

Lecture Notes in Mechanical Engineering

R. K. Tyagi  
Pallav Gupta  
Prosenjit Das  
Rajiv Prakash *Editors*

# Advances in Engineering Materials

Select Proceedings of FLAME 2022

 Springer

# Lecture Notes in Mechanical Engineering

## Series Editors


Fakher Chaari, National School of Engineers, University of Sfax, Sfax, Tunisia

Francesco Gherardini , Dipartimento di Ingegneria “Enzo Ferrari”, Università di Modena e Reggio Emilia, Modena, Italy

Vitalii Ivanov, Department of Manufacturing Engineering, Machines and Tools, Sumy State University, Sumy, Ukraine

Mohamed Haddar, National School of Engineers of Sfax (ENIS), Sfax, Tunisia

## Editorial Board

Francisco Cavas-Martínez , Departamento de Estructuras, Construcción y Expresión Gráfica Universidad Politécnica de Cartagena, Cartagena, Murcia, Spain

Francesca di Mare, Institute of Energy Technology, Ruhr-Universität Bochum, Bochum, Nordrhein-Westfalen, Germany

Young W. Kwon, Department of Manufacturing Engineering and Aerospace Engineering, Graduate School of Engineering and Applied Science, Monterey, CA, USA

Justyna Trojanowska, Poznan University of Technology, Poznan, Poland

Jinyang Xu, School of Mechanical Engineering, Shanghai Jiao Tong University, Shanghai, China

**Lecture Notes in Mechanical Engineering (LNME)** publishes the latest developments in Mechanical Engineering—quickly, informally and with high quality. Original research reported in proceedings and post-proceedings represents the core of LNME. Volumes published in LNME embrace all aspects, subfields and new challenges of mechanical engineering.

To submit a proposal or request further information, please contact the Springer Editor of your location:

**Europe, USA, Africa:** Leontina Di Cecco at [Leontina.dicecco@springer.com](mailto:Leontina.dicecco@springer.com)

**China:** Ella Zhang at [ella.zhang@springer.com](mailto:ella.zhang@springer.com)

**India:** Priya Vyas at [priya.vyas@springer.com](mailto:priya.vyas@springer.com)

**Rest of Asia, Australia, New Zealand:** Swati Meherishi at [swati.meherishi@springer.com](mailto:swati.meherishi@springer.com)

Topics in the series include:

- Engineering Design
- Machinery and Machine Elements
- Mechanical Structures and Stress Analysis
- Automotive Engineering
- Engine Technology
- Aerospace Technology and Astronautics
- Nanotechnology and Microengineering
- Control, Robotics, Mechatronics
- MEMS
- Theoretical and Applied Mechanics
- Dynamical Systems, Control
- Fluid Mechanics
- Engineering Thermodynamics, Heat and Mass Transfer
- Manufacturing
- Precision Engineering, Instrumentation, Measurement
- Materials Engineering
- Tribology and Surface Technology

**Indexed by SCOPUS, EI Compendex, and INSPEC.**

All books published in the series are evaluated by Web of Science for the Conference Proceedings Citation Index (CPCI).

To submit a proposal for a monograph, please check our Springer Tracts in Mechanical Engineering at <https://link.springer.com/bookseries/11693>.

R. K. Tyagi · Pallav Gupta · Prosenjit Das ·  
Rajiv Prakash  
Editors

# Advances in Engineering Materials

Select Proceedings of FLAME 2022

 Springer



*Editors*

R. K. Tyagi  
Department of Mechanical Engineering  
Amity School of Engineering  
and Technology  
Amity University  
Noida, Uttar Pradesh, India

Pallav Gupta  
Department of Mechanical Engineering  
Amity School of Engineering  
and Technology  
Amity University  
Noida, Uttar Pradesh, India

Prosenjit Das  
Department of Materials Engineering  
Indian Institute of Science Bangalore  
Bengaluru, Karnataka, India

Rajiv Prakash  
School of Materials Science  
and Technology  
Indian Institute of Technology BHU  
Varanasi, India

ISSN 2195-4356

ISSN 2195-4364 (electronic)

Lecture Notes in Mechanical Engineering

ISBN 978-981-99-4757-7

ISBN 978-981-99-4758-4 (eBook)

<https://doi.org/10.1007/978-981-99-4758-4>

© The Editor(s) (if applicable) and The Author(s), under exclusive license to Springer Nature Singapore Pte Ltd. 2024

This work is subject to copyright. All rights are solely and exclusively licensed by the Publisher, whether the whole or part of the material is concerned, specifically the rights of translation, reprinting, reuse of illustrations, recitation, broadcasting, reproduction on microfilms or in any other physical way, and transmission or information storage and retrieval, electronic adaptation, computer software, or by similar or dissimilar methodology now known or hereafter developed.

The use of general descriptive names, registered names, trademarks, service marks, etc. in this publication does not imply, even in the absence of a specific statement, that such names are exempt from the relevant protective laws and regulations and therefore free for general use.

The publisher, the authors, and the editors are safe to assume that the advice and information in this book are believed to be true and accurate at the date of publication. Neither the publisher nor the authors or the editors give a warranty, expressed or implied, with respect to the material contained herein or for any errors or omissions that may have been made. The publisher remains neutral with regard to jurisdictional claims in published maps and institutional affiliations.

This Springer imprint is published by the registered company Springer Nature Singapore Pte Ltd.

The registered company address is: 152 Beach Road, #21-01/04 Gateway East, Singapore 189721, Singapore

Paper in this product is recyclable.

# Preface

This book is a collection of articles from the third biennial international conference on Future Learning Aspects for Mechanical Engineering (FLAME-2022), which was held at Amity University Uttar Pradesh, Noida, India, from August 3 to 5, 2022. The articles cover a wide range of perspectives on mechanical engineering.

FLAME-2022's major aim was to create a forum for academicians, scientists, and researchers around the world to communicate their scientific ideas and vision in the advancement of material, thermal, design, industrial, production, and multidisciplinary fields of mechanical engineering. FLAME-2022 was critical in bridging the gap between academics and industry.

Around 600 people attended the conference to discuss scientific ideas. During the three-day event, researchers from academia and industry shared their latest cutting-edge findings, had scientific brainstorming sessions, and discussed perspectives on current socioeconomic challenges. This meeting also gave us an opportunity to develop a network for academic and industrial engagement. The major focus of the plenary and keynote presentations was on new advances and innovations in various sectors of mechanical engineering. It was backed by the University of Leicester, the UK, and the Budapest University of Technology and Economics, Hungary.

This book focuses on the latest advances in the field of engineering materials. This book includes many sections related to the advances in material such as design, development, manufacturing, and applications. The content of book will be fruitful for scholars, industry persons, and research organization. The present piece of work can be considered as reference book.

The editors would like to thank all of the participants, management of Amity University Noida, Science and Engineering Research Board (SERB), the Department of Science and Technology (DST), the Council of Science and Technology Uttar Pradesh, the Council of Scientific and Industrial Research, E-Spin Nanotech, Begell House, etc. who contributed to this book directly/indirectly.

The editors are also grateful to all plenary, keynote speakers, industry partners, faculty members, staff members, students, etc. The success of FLAME-2022 was impossible without their co-operation and support.

The editors would like to express their gratitude to Springer Nature for publishing the selected proceedings of FLAME-2022 in the LNME series. Finally, the editors would like to express their gratitude to the respected Dr. Ashok K. Chauhan, Founder President of Amity University, for his unwavering support and blessings.

In spite of sincere care, there might be typos, and there is always possibility of perfection. The editors would appreciate any suggestions from the reader's side.

Noida, India  
Noida, India  
Bengaluru, India  
Varanasi, India  
November 2022

Dr. R. K. Tyagi  
Dr. Pallav Gupta  
Dr. Prosenjit Das  
Dr. Rajiv Prakash

# About This Book

This volume is a compilation of papers presented at FLAME-2022, the third biennial international conference on Future Learning Aspects of Mechanical Engineering, held at Amity University Uttar Pradesh, Noida, India, from August 3 to 5, 2022, and fifty-one chapters cover a wide range of topics related to engineering materials.

In the modern era, the advancement of technology is directly associated with the development of new smart materials with modified properties in different sectors such as automobile, electronics, construction, aerospace, medical, and thermal.

The Advances in Engineering Materials continues to be the premier proceedings for all the latest research in materials. The goal of this proceeding is to provide recent development and innovation in the field of materials. It is expected that proceeding on topic “Advances in Engineering Materials” would stimulate further interest in the advancement of modern materials.

Potential topics of interest in proceeding “Advances in Engineering Materials” include but are not limited to the following areas:

- Surface science and coating technology
- Non-destructive testing of materials
- Bio-medical materials
- Intermetallic
- Phase change materials
- Modern manufacturing techniques of materials
- Ceramics
- Numerical simulation techniques for material behavior
- Micro-/Nanomanufacturing
- Properties optimization.
- Composite materials

# Contents

<b>Improvement in Flow Distribution for Effective Thermal Management in Thermoelectric Generator for Waste Heat Recovery</b> .....	1
Chander Veer, Shobhana Singh, and Jasa Ram	
<b>Microstructure Characterisation and Analysis of AA2024/SiC/Carbonised Eggshell-Reinforced Hybrid Green Aluminium Matrix Composite</b> .....	13
Yatan Nagpal, Rohit Sharma, Neeraj Sharma, and R. K. Tyagi	
<b>Passive Thermal Management of a PV Module Using Fins of Various Geometries: A Numerical Study</b> .....	23
Vipul Kumar, Vibhor Kumar Gupta, Shwetanshu Goel, and Akhilesh Arora	
<b>Experimental Investigation for Mechanical Performance of Plant Fiber-Based Polymer Composites</b> .....	35
Apurv Upadhyay, Swabhi Dinesh Bajpai, Vijay Chaudhary, Sumit Gupta, and Pallav Gupta	
<b>Al 6063 Hybrid Metal Matrix Reinforced Composites with TiC Nanoparticles and NEEM Leaf Ash Using Stir Casting Method for Bicycle Frame</b> .....	51
Umesh Kumar Vates, Nirav Khattar, Rohit Kumar, Ansh Bhardwaj, Bhupendra Prakash Sharma, Nand Jee Kanu, Eva Gupta, Gyanendra Kumar Singh, and Sivaraos Subramanian	
<b>Microwave Sintering of Aluminum Composite</b> .....	67
Vishal Naranje, Sachin Salunkhe, Vinod Kumar Shukla, and Purushottam Sharmad	

<b>Analysis of Energy-Efficient Copper Mining Processes Using Solar Energy: A Review</b> .....	75
Prem Nath Suman, Ravindra Kannojiya, Manish Kumar Ojha, and Anoop Kumar Shukla	
<b>Effect of Notch on Strength and Ductility of a Martensitic Stainless Steel in Tensile Test</b> .....	85
Jai Singh and S. K. Nath	
<b>Effect of Substitution of Fly Ash on the Strength of Geopolymer Concrete</b> .....	95
Arun Kumar Parashar, Prashant Sharma, and Neha Sharma	
<b>Effect on Vibration Characteristics of Fiber Metal Laminates Reinforced with Jute/glass Fibers</b> .....	105
Abhijeet Pidge, Aniket Salve, Ashok Mache, Aparna Kulkarni, and Yashwant Munde	
<b>Human–Computer Interaction: Comparison of Different Contributions Based on Opinion and Survey</b> .....	117
Krishnakant Dixit and Kanchan Yadav	
<b>Framework and Challenges for Mobile Satellite System</b> .....	127
Reeya Agrawal and Aditi Saxena	
<b>A Short Review on the Development of Rare Earths Containing Magnesium Alloys for Biomedical Applications</b> .....	137
Voleti Sri Sai Harsha Vardhan, Ambuj Sharma, Ravikumar Dumpala, and Ratna Sunil Buradagunta	
<b>Design and Simulation for Brake Pedal of Aluminium Alloy</b> .....	147
Charan Singh, Utkarsh Jain, Rishabh Singh, and Brahma Nand Agrawal	
<b>Recent Advancements and Challenges of Abrasive Jet Machining: A Review</b> .....	157
Bhaskar Chandra Kandpal, S. P. Singh, Nitin Johri, Khalid Nafees, Ajay Singh Raghav, Arshad, and Amit Gupta	
<b>Optical, Thermal, and Mechanical Properties of Scheelite Molybdate and Tungstate Materials Using Atomistic Simulations</b> .....	169
Yamini Sudha Sistla, Ramesh Gupta Burela, Ankit Gupta, and Nabila Tabassum	
<b>A Comprehensive Review on Aluminium MMC Fabricated by Liquid-Phase Fabrication Methodologies</b> .....	185
Dinesh Chawla, Manoj Nayak, and Pallav Gupta	

**Prediction of Effective Elastic Properties of PEEK-CF Composites Subjected to Thermomechanical Loading** ..... 203  
 Brahma Nand Agrawal, Pawan Kumar Singh Nain, Saksham Bisht, and Aniket Srivastava

**Mori–Tanaka Modeling of Polymer Nanocomposites: Interface Effect on the Moduli** ..... 211  
 Brahma Nand Agrawal, Pawan Kumar Singh Nain, Abhishek Patwal, and Akash Abrol

**Static Engine Test on CTN Model Rocket Engine with 1/2 A6-2 Propellant** ..... 219  
 Sarath Raj, Nour Alaa Elsonbaty, and Sathiyagayathiri Ramamoorthy

**Mordernistic Aspects of MXenes and Its Applications** ..... 231  
 Swarnima Sharma and Surbhi Sharma

**Synthesis of Five-Membered Heterocyclic Compounds and Their Anticorrosive, Thermal, Electron Transfer, and Biological Properties** ..... 247  
 Archana Thakur and Anam Ansari

**Optimization of Drilling Operation Using Work Material Al 7075 Alloy Reinforced with Boron Carbide** ..... 263  
 Sohail Akhtar and Imtiaz Ali Khan

**Critical Analysis of Manufacturing of Manganese Steel Liners Used in Crushing and Mining Sector for Improved Performance** ..... 275  
 Rahul Nagar, Anant Prakash Agrawal, Ajay Kumar, and Shyam Lal

**Productivity Improvement Using Systematic Layout Planning: A Cement Refractory Case Study** ..... 295  
 Ramkrishna Bharsakade, Atharwa Kharkar, Himanshu Kurzekar, Arnav Hardas, Ameya Panshikar, and Nilay Diwan

**Study on the Flexural Strength of Glass Fiber-Reinforced M20 Grade Self-Healing Concrete Using a Novel Technique Microbial-Induced Calcite Precipitation** ..... 307  
 S. Hemanth and B. Ramesh

**Spectroscopic Study of Eco-Friendly Slow Release Micronutrient Delivery System** ..... 321  
 Manpreet Kaur Takkar and Khushbu Gumber

**Mechanical Behavior of Friction Stir Welded Al-Alloy AA6063 + 5% SiC<sub>p</sub>** ..... 327  
 Pardeep Gahlot, Narinder Kaushik, Naveen Hooda, Rajkumar Duhan, and Rakesh Kumar Phanden

**3D Printing of Phase Change Materials: Issues and Challenges** ..... 337  
Deepak Kumar Yadav, Basant Singh Sikarwar, Arvind Kumar Gupta,  
and Rajeev Kumar Singh

**Challenges and Possibilities in the Welding of Advanced  
High-Strength Steels** ..... 351  
Marcell Gáspár and Raghawendra P. S. Sisodia

**CNT-Reinforced Metal Matrix Composites: A Review** ..... 357  
Garvit Kumar, Anirudh Sharma, Bhavish Sharma, and Prateek Mittal

**Nonlinear Static and Dynamic Analysis of Composite Riser** ..... 369  
Manander Singh, Rajeev Kumar Singh, Sanatan Ratna,  
Shubham Sharma, and Priyank Srivastava



# About the Editors



**Dr. R. K. Tyagi** is Professor at Department of Mechanical Engineering, Amity University, Noida, India. He did his Master's and Ph.D. in the area of Design Engineering. His research interest includes spray technology, agricultural equipment's, automobile engineering, pollution. He has published numerous research articles and many patents are also granted on his name.



**Dr. Pallav Gupta** completed his B.Tech. from Department of Mechanical Engineering, Integral University, Lucknow, INDIA in the year 2009, Qualified GATE in 2009 and then completed his M.Tech. from I.I.T. (B.H.U.), INDIA in the year 2011 followed by Ph.D. in the year 2015 from I.I.T.(B.H.U.), INDIA. Dr. Gupta is presently working as an Assistant Professor (Grade-III) in Department of Mechanical Engineering, Amity School of Engineering and Technology, Amity University Uttar Pradesh, Noida. His area of research includes Material Processing; Composite Materials; Metal Matrix Nanocomposites; Coatings/Nanocoatings; Wear; Mechanical Behavior. Dr. Gupta has over 08 years of teaching and research experience. In this period of time he has published 50 research papers in peer reviewed international journals having good impact factor and 52 research papers in reputed international and national conferences in India as well as in abroad.

Apart from this he has also published 13 chapters in books published by Springer, Taylor & Francis and Elsevier. Authored 02 books and Edited 06 books of reputed International Publisher like Springer, Taylor and Francis and IGI Global.



**Dr. Prosenjit Das** is currently working as an Assistant Professor in Department of Materials Engineering, Indian Institute of Science-Bangalore. Academy of Scientific and Innovative Research (AcSIR), CMERI campus. Dr. Das joined CSIR-CMERI as a Scientist, after completion of his masters from Department of Metallurgical and Materials Engineering, Indian Institute of Technology (IIT) Roorkee. He completed his B.Tech. in Mechanical Engineering in 2008 from Kalyani Government Engineering College, and completed his Ph.D. from Indian Institute of Science (IISc) Bangalore. Dr. Das has worked in the field of casting and solidification, bio-inspired manufacturing, metallurgical/manufacturing process modelling, fracture mechanics, etc. He has gained expertise over the years in light alloy/composite development and processing front, adopting melting/casting and semi solid processing route as well as processing of metal/ceramic powders towards product development, adopting macro and micro injection molding techniques. His research findings till date have yielded approx. 35 SCI journal publications. He is guiding 5 Ph.D. students at present.



**Prof. Rajiv Prakash** received his M.Tech. degree in Materials Technology from the Institute of Technology Banaras Hindu University (IIT BHU) and completed his Ph.D. work from Tata Institute of Fundamental Research (TIFR), India in 1999. He is Professor at School of Materials Science and Technology, I.I.T.(B.H.U.). Currently he is on deputation from I.I.T.(B.H.U.) and is the Director of I.I.T.-Bhilai. His areas of research include polymers and nanocomposites, organic electronics and sensor devices and energy storage devices. He has over 225 publications in international journals of repute and 22 patents in his credit. He has been the recipient of Young Scientist Award (Council of Science and Technology), Young Engineer (INAE) Awards of India and Materials Research Society (MRSI) Medal Award of

India. He is on the Editorial Board of several National and International Journals. He is a member of various national committees including DST-TIFAC for India Vision 2035 and MHRD “IMPRINT” the program, Member of the Accelerator Users Committee of Inter-University Accelerator Centre, New Delhi, Member Defense Corridor Project of Government of India and Member Program Advisory Committee for Technology development program (TDP) of DST, New Delhi, India.

# Improvement in Flow Distribution for Effective Thermal Management in Thermoelectric Generator for Waste Heat Recovery



Chander Veer , Shobhana Singh , and Jasa Ram

**Abstract** In an automobile, only one-third of the total fuel energy is used for propulsion, and the remaining two-third is lost to engine coolant and the exhaust as waste. Thermoelectric generators (TEG) demonstrate huge potential in automotive applications by recovering the exhaust waste heat and converting it into direct electric power. TEG helps escalate the engine's fuel efficiency. However, extracting waste heat from automobile exhaust using TEG manifests practical difficulties attributed to thermoelectric materials, design, and operating conditions. Ineffective configurations and heat exchanger designs lead to non-uniform flow and temperature distribution on the hot and cold sides of TEG, causing undesirable power output, which lowers the entire system's efficiency. In this study, the flow distribution of exhaust gas through the automotive TEG with pin fin heat exchanger is simulated using Computational Fluid Dynamics (CFD). Improvement in the flow pattern using passive flow distributors such as guide vanes at different angles is analyzed to attain the temperature uniformity through the hot heat exchanger surface. A detailed analysis of flow distribution and its influence on the local and average temperature distribution is presented. Results provide critical design recommendations to improve the flow distribution in an automotive TEG for exhaust waste energy recovery.

**Keywords** Thermoelectric generator · Heat exchanger · Flow distribution · Temperature uniformity · Computational fluid dynamics

## *Nomenclature*

$h$  Specific enthalpy (J/kg K)  
 $k$  Thermal conductivity (W/m K)

---

C. Veer · S. Singh (✉)  
Indian Institute of Technology Jodhpur, Jodhpur, Rajasthan 342037, India  
e-mail: [shobhana@iitj.ac.in](mailto:shobhana@iitj.ac.in)

J. Ram  
Defense Laboratory Jodhpur, Jodhpur, Rajasthan 342011, India

$k'$	Turbulent kinetic energy (J/kg)
$p$	Pressure (Pa)
$u, v, w$	Velocities (m/s) in $x, y,$ and $z$ directions respectively
$V$	Velocity vector (m/s)

### ***Greek Symbols***

$\rho$	Density (kg/m <sup>3</sup> )
$\theta$	Temperature (K)
$\omega'$	Specific rate of dissipation of turbulent kinetic energy (1/s)
$\mu$	Dynamic viscosity (Pa s)

### ***Subscripts***

$x, y, z$  Directions corresponding to Cartesian coordinates

## **1 Introduction**

The transportation sector alone accounts for 55% of the total fossil fuel usage, and this consumption is increasing at an annual rate of 1.4% [1]. Increasing fossil fuel consumption and demand has raised significant concerns regarding the sustainability of natural resources and petroleum products. Many avenues can be explored to reduce energy consumption, and improving the fuel efficiency of automobiles is one of them. For a typical automobile engine, 40% of the fuel energy is wasted in the form of exhaust [2]. Recovering this waste heat can significantly improve fuel efficiency and reduce harmful emissions. Thermoelectric generators have proven to be a promising device in waste heat recovery from automobile exhaust, which can directly convert the exhaust waste heat into useful electrical energy using the Seebeck effect. In order to achieve a high power output from the Automotive Exhaust Thermoelectric Generator (AETEG), a high temperature on the hot side of the Thermoelectric (TE) is needed. This necessitates the design of an efficient heat exchanger, which can extract the maximum heat from the exhaust air and maintain a uniform temperature over the heat exchanger surface. For AETEG, the most decisive factors that affect its performance are the temperature and flow distribution.

To achieve a uniform and high temperature on the surface of the heat exchanger, several heat exchanger designs have been studied. Kumar et al. [3] tested three heat exchanger configurations, namely triangular, rectangular, and hexagonal. The

author concluded that a rectangular heat exchanger exhibits a more balanced performance among the three. In addition to the hot heat exchanger’s shape, the hot heat exchanger’s internal geometry is an essential criterion in AETEG application. A flat-shaped heat exchanger with three different internal configurations, i.e., accordion, fishbone, and scattered was investigated by Su et al. [4]. The author concluded that an accordion-shaped heat exchanger is best suited for the application in AETEG.

Improving airflow distribution can significantly improve the temperature distribution over the heat exchanger surface. Nagesh et al. [5] conducted an experimental study to evaluate the thermal performance of AETEG using the flow straighteners with varying porosity at different locations. It is inferred from their study that by placing the flow straightener having a porosity of 0.4–0.5 in the middle of the exhaust channel, the power output is maximized. There is a scarcity of literature that address the problem of flow maldistribution. The focus of the present study is to improve the flow distribution inside a pin fin heat exchanger using guide vanes. Guide vanes at three different angles are placed at the inlet diffuser section, and their effect on the thermal–hydraulic performance of the heat exchanger and temperature uniformity over the heat exchanger surface is studied.

## 2 Physical Model

Figure 1a depicts the physical model of AETEG. The heat exchanger has a cross section area of 200 mm × 100 mm and a length of 250 mm. Circular pin fins of diameter 10 mm and length of 100 mm are used inside the heat exchanger, keeping the volume of pin fins 1/10th to that of the heat exchanger volume. Air with temperature-dependent properties is used as the working fluid (see Table 1). The inlet and outlet diffuser, hot heat exchanger, and heat sink material are taken as aluminum. Bismuth telluride is taken as the thermoelectric material, and for insulation, asbestos is selected. All material properties are listed in Table 2.

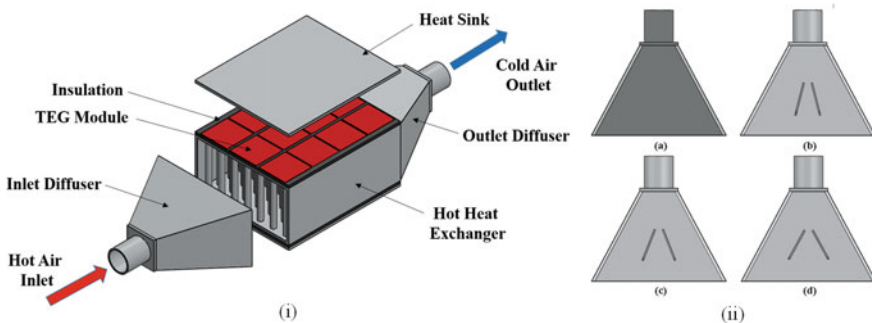


**Fig. 1** Physical model of AETEG (i) Components of AETEG (ii) inlet diffuser **a** without guide vanes and guide vanes at different angles **b** 30° **c** 45° **d** 60°

**Table 1** Thermophysical properties of air

Property	Expression
Density (kg/m <sup>3</sup> )	$3.7771 - 1.5884 \times 10^{-2} \theta + 3.3564 \times 10^{-5} \theta^2 - 3.7685 \times 10^{-8} \theta^3 + 2.1407 \times 10^{-11} \theta^4 - 4.8308 \times 10^{-15} \theta^5$
Specific heat capacity (J/kg K)	$1013.1890 + 0.2336 \theta - 2.3511 \times 10^{-3} \theta^2 + 7.3109 \times 10^{-6} \theta^3 - 9.2297 \times 10^{-9} \theta^4 + 5.3424 \times 10^{-12} \theta^5 - 1.1797 \times 10^{-15} \theta^6$
Thermal conductivity (W/m K)	$1.0132 \times 10^{-3} + 9.0445 \times 10^{-5} \theta - 2.9040 \times 10^{-8} \theta^2 + 4.6490 \times 10^{-12} \theta^3$
Dynamic viscosity (Pa s)	$2.7545 \times 10^{-6} + 6.1156 \times 10^{-8} \theta - 3.0361 \times 10^{-11} \theta^2 + 8 \times 10^{-15} \theta^3$

**Table 2** Thermophysical properties of aluminum, asbestos, and bismuth telluride

Material	Density (kg/m <sup>3</sup> )	Specific heat capacity (J/kg K)	Thermal conductivity (W/m K)
Aluminum	2719	871	202
Asbestos	2400	566	0.15
Bismuth telluride	7500	544	1.5

TE module has a cross section of 60 mm × 60 mm and a height of 5 mm. A diffuser section is provided before the hot heat exchanger to distribute the flow before reaching the inlet heat exchanger. The diffuser has a length of 140 mm, and the cross section expands from 50 mm × 50 mm to 200 mm × 100 mm.

For this study, guide vanes at three different angles (30°, 45°, and 60°) are placed in the inlet diffuser section, as shown in Fig. 1b. The performance of the heat exchanger has been evaluated based on different thermal–hydraulic parameters such as flow streamlines, temperature uniformity index, and power output from the thermoelectric modules.

### 3 Numerical Model

A three-dimensional CFD model is studied to analyze the effect of guide vanes at different angles on flow and heat transfer behavior. Only half of the geometry is simulated to simplify the model and solution process, and symmetry boundary condition is imposed on the symmetric plane.

The following assumptions have been taken into account while solving the numerical model,

1. The airflow is steady, incompressible, and turbulent.
2. Radiation heat transfer is neglected.
3. Perfect thermal contact between contact surfaces such that the contact resistance is neglected.

Using the above assumptions, the governing equations are reduced to the form, Continuity equation,

$$\nabla \cdot (\rho \mathbf{V}) = 0 \quad (1)$$

Momentum equation,

$$\nabla(\rho u \mathbf{V}) = -\nabla p_x + \mu \nabla^2 u \quad (2)$$

$$\nabla(\rho v \mathbf{V}) = -\nabla p_y + \mu \nabla^2 v \quad (3)$$

$$\nabla(\rho w \mathbf{V}) = -\nabla p_z + \mu \nabla^2 w \quad (4)$$

Energy equation,

$$\nabla \cdot (k \nabla \theta) = \nabla \cdot (\rho h \mathbf{V}) \quad (5)$$

SST  $k$ - $\omega$  model,

$$\nabla \cdot (\rho \mathbf{V} k') = \nabla \cdot [\rho \nabla k' (\mu + \sigma_{k'} \mu_t)] + \rho (P_k - \epsilon) \quad (6)$$

$$\begin{aligned} \nabla \cdot (\rho \mathbf{V} \omega') &= \rho \omega' \left( \frac{\gamma P_k}{k'} - \beta \omega \right) + 2(1 - F_1) \left( \frac{\rho \sigma_{\omega'} \omega'}{\omega'} \right) \nabla k' \nabla \omega' \\ &+ \nabla \cdot [\rho \nabla \omega' (\mu + \sigma_{\omega'} \mu_t)] \end{aligned} \quad (7)$$

where  $\sigma_{k'} = 0.5$ ,  $\sigma_{k_2} = 0.5$ ,  $\sigma_{\omega'} = 0.5$ ,  $\sigma_{\omega_2} = 0.856$ ,  $\beta_1 = 0.075$ ,  $\beta_2 = 0.0828$  [6].

Following are the boundary conditions that are imposed on the CFD model: Inlet velocity of exhaust air is set to 6.5 m/s and inlet temperature as 473 K. The Reynolds number at the inlet is 23,965 and flow is in a turbulent region. At the outlet, pressure outlet condition is used with a gauge pressure value set to 0 Pa. To have a perfect thermal contact at every interface, the coupled wall boundary condition is used. A constant wall temperature condition with a temperature of 298 K is employed on the heat sink. All surfaces exposed to ambient have an insulated boundary condition with the heat flux value set to 0 W/m<sup>2</sup>.

The numerical model of AETEG is solved using ANSYS Fluent 2020R2. SST  $k$ - $\omega$  model is employed to simulate the turbulent flow of exhaust air. To achieve the pressure-velocity coupling, the COUPLED scheme is used. The gradients are calculated using the Least Square Cell-Based method, and pressure is discretized using the PRESTO scheme. To conserve the energy, turbulent kinetic energy, specific dissipation rate, and momentum equation, the second-order upwind scheme is used. The convergence criteria are set to  $10^{-3}$  for continuity and  $10^{-6}$  for  $k'$ ,  $\omega'$ , momentum equation, and energy equation.



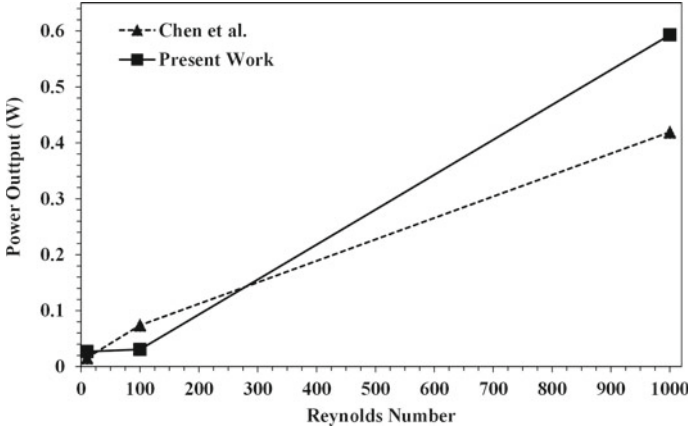


**Fig. 2** Numerical validation between the present work and the work reported by Chen et al.

For the model's accuracy, a mesh independence study is performed with number of elements from 43,909 to 24,61,819. The air outlet temperature and pressure drop converged as the mesh size increased. To balance accuracy and computational time, a grid size of 2.5 mm is selected with the number of elements 12,75,373.

The numerical model discussed in the present research is validated by a study reported by Chen et al. [7]. The average surface temperature on the cold side and hot side of TE modules is compared. It is observed that the variation between the present numerical model and the previously reported study is less than 2%.

The numerical validation is also performed with respect to the power output from the TEG. The performance parameter comparison between the present study and the analysis conducted by Chen et al. [7] is shown in Fig. 2.

## 4 Results and Discussion

Using the solution methodology described above, the model is numerically investigated to study the effect of guide vanes placed at three different angles on the thermal-hydraulic performance of the hot heat exchanger. Keeping in mind the goal of temperature uniformity over the heat exchanger surface, the performance of the hot heat exchanger is analyzed with the temperature uniformity index ( $\gamma$ ) [8], which can be defined as,

$$\gamma = 1 - \frac{1}{n} \sum_{j=1}^n \frac{\theta_j - \theta_{\text{avg}}}{\theta_{\text{avg}}} \quad (8)$$

Here,  $n$  is the total number of modules,  $\theta_j$  is the average temperature of the  $j$ th module (K), and  $\theta_{\text{avg}}$  is the average temperature of the heat exchanger surface (K).

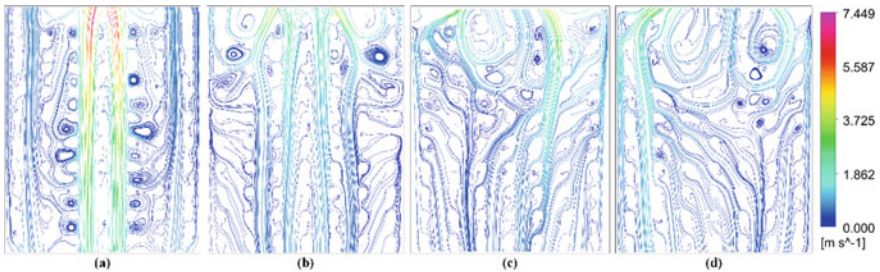
One important parameter to judge the performance of AETEG is the power output from the modules. For simplicity, the electrical simulations have not been included in the present study, and theoretical power output has been calculated based on the following equation,

$$\text{Power Output} = n \frac{\alpha^2 \Delta\theta^2}{4R} \quad (9)$$

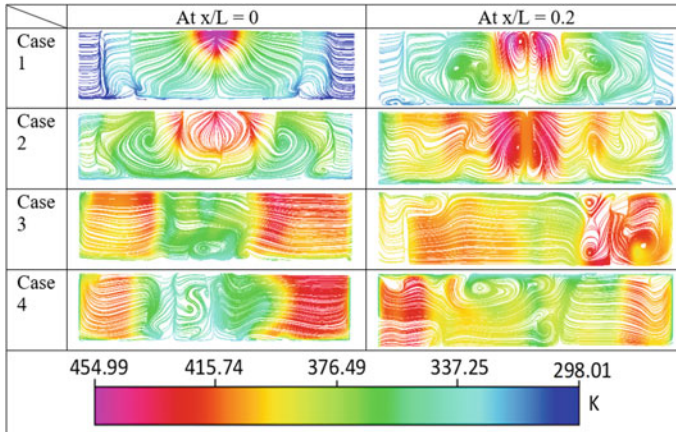
Here,  $n$  is the number of modules,  $\alpha$  is the Seebeck coefficient (V/K),  $\Delta\theta$  is the temperature difference across a single module (K), and  $R$  is the electrical resistance of the module (ohm). For simplicity, the results are represented as Case 1—Without any guide vanes, Case 2—Guide Vanes at  $30^\circ$ , Case 3—Guide Vanes at  $45^\circ$ , and Case 4—Guide Vanes at  $60^\circ$ .

#### 4.1 Flow Analysis

The velocity streamlines on the symmetric plane of the hot heat exchanger are shown in Fig. 3. From the streamlines flow on the symmetry plane, it can be concluded that if no guide vanes are present, the flow is going straight from inlet to outlet, and no airflow is occurring near sidewalls. The vortices forming due to flow separation by fins are also limited to the middle portion of the hot heat exchanger. However, as soon as the guide vanes are inserted in the inlet diffuser, a change in the flow pattern of exhaust air is observed. As we start to increase the angle of guide vanes, more and more air is deflected toward the sidewalls of the hot heat exchanger. With the use of guide vanes, an increase in vortices can also be observed. Also, these vortices are not limited to the middle portion. Instead, they are distributed in the whole hot heat exchanger.



**Fig. 3** Flow streamlines on the symmetric plane of hot heat exchanger **a** case 1 **b** case 2 **c** case 3 **d** case 4



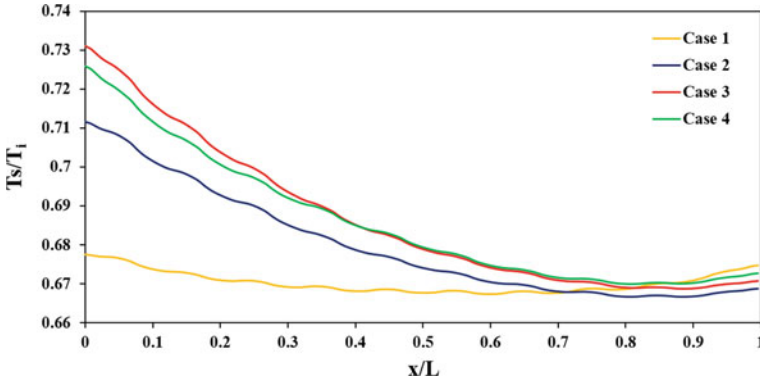
**Fig. 4** Flow streamlines on transverse planes of hot heat exchanger drawn at two different locations

Figure 4 represents the streamlines on two transverse planes, one at the hot heat exchanger inlet and the second after two rows of pin fins. In the table,  $x$  represents the distance from the heat exchanger inlet, and  $L$  represents the total heat exchanger length. The color code represents the temperature of exhaust air. It is inferred that, for the case 1, most part of the hot air is going straight from inlet to the outlet diffuser and that too through the middle part of heat exchanger. There is no direct contact between the hot air and the heat exchanger surface. So most of the heat transfer to the heat exchanger surface is by conduction through pin fins.

However, when guide vanes are present, hot air is also deflected toward the bottom surface of the heat exchanger. Now the heat is transferred to the surface by conduction through fins as well as the direct contact of air, resulting in a high heat transfer rate and higher surface temperature. At an angle of  $30^\circ$  (case 2), most of the hot air flow is still through the middle portion of the heat exchanger. However, if the angle is increased to  $60^\circ$  (case 4), the flow is more directed toward the sidewalls of the hot heat exchanger. Guide vanes kept at an angle of  $45^\circ$  (case 3), present a more balanced flow than the other two resulting in a more uniform distribution of hot air throughout the hot heat exchanger.

## 4.2 Thermal Analysis

The variation in average surface temperature of hot heat exchangers along the length is shown in Fig. 5. The abscissa represents the normalized heat exchanger length and the ordinate represents the normalized surface temperature of hot heat exchanger with respect to the air inlet temperature. In comparison with the base case, i.e., no guide vanes, there is an increase of about 5–7% in the average surface temperature



**Fig. 5** Variation of surface temperature along the length of the hot heat exchanger

at the heat exchanger inlet. This increase in surface temperature is highest for case 3 and lowest for case 2.

These results are also in-line with the flow distribution of exhaust gas, in which it is observed that flow was more uniform in case 3 as compared to case 2 and case 4. This increase in surface temperature is attributed to the fact that with the use of guide vanes, the flow gets deflected toward a larger area of hot heat exchanger, and more and more hot air gets in contact with the hot heat exchanger, resulting in a higher heat transfer rate. Moving along the length of heat exchanger, a temperature gradient is observed on the heat exchanger surface. This temperature gradient is steeper for cases 2, 3, and 4, because the air is more distributed at the inlet of the hot heat exchanger. Further, the air temperature reduces along the length due to the continuous exchange of heat thereby reducing the exergy of air. This results in a low heat transfer rate near the hot heat exchanger outlet and consequently a low temperature on the surface.

### 4.3 Temperature Uniformity Index and Power Output

One of the goals in designing a heat exchanger for AETEG is to obtain a uniform temperature distribution over the surface. To have an idea of temperature uniformity in all cases, the temperature uniformity index is calculated and the results are given in Table 3. The results suggest that using guide vanes reduces the temperature uniformity over the surface. This is observed because the air is deflected toward a larger area at the heat exchanger inlet, resulting in increased heat transfer and a high surface temperature at the heat exchanger inlet.

Table 3 represents the maximum rated power output that is obtained from the AETEG. It can be seen that there is an increase of 58%, 113%, and 101% in power output from AETEG for cases 2, 3, and 4, respectively. This is due to the fact that the modules that are present near the inlet position of the hot heat exchanger are subjected to a much higher temperature difference than the case with no guide vanes.

**Table 3** Performance parameters of heat exchanger for AETEG

Case	Case 1 (without guide vanes)	Case 2 (guide vanes at 30°)	Case 3 (guide vanes at 45°)	Case 4 (guide vanes at 60°)
Temperature uniformity index	0.991	0.976	0.967	0.971
Power output (W)	5.714	9.068	12.171	11.535

Also, the temperature near the outlet of the hot heat exchanger for cases 2, 3, and 4 is comparable to case 1, hence the modules which are present at the rear end of the hot heat exchanger generated power equivalent to case 1. The overall outcome is that the design with the guide vanes performs better in terms of power output than the design without guide vanes.

## 5 Conclusion

In this study, the effect of guide vanes placed inside the inlet diffuser at three different angles (30°, 45°, and 60°) on the flow and heat transfer behavior of exhaust gas is analyzed. The power output and temperature uniformity index are calculated for all four cases. It is concluded that there is a significant change in the performance of AETEG when the guide vanes are used. Following are the concluding remarks based on the present study:

1. The guide vanes significantly improve the flow distribution of hot air and the surface temperature of the hot heat exchanger.
2. The theoretical power output of AETEG is increased by 113%, with the guide vanes at an angle of 45°.
3. The design with no guide vanes present a higher value of temperature uniformity index, but when it comes to the overall performance, guide vanes perform better in terms of surface temperature and power output.

**Acknowledgements** Present work is carried out in collaboration with Defense Research Laboratory, Jodhpur under the research project (Project Number-S/DRDO/SHS/20210056).

## References

1. González-Montaña JR, Alonso Diez AJ, Alonso de la Varga ME, Avila Téllez S (2016) “Por Determinar,” *Internacional de Ovinocultura. Asociación mexicana de especialistas en ovinocultura (AMTEO)* 2016:127–137
2. Khan MQ, Malarmannan S, Manikandaraja G (2018) Power generation from waste heat of vehicle exhaust using thermoelectric generator: a review. *IOP Conf Ser Mater Sci Eng* 402(1). <https://doi.org/10.1088/1757-899X/402/1/012174>

3. Kumar CR, Sonthalia A, Goel R (2011) Experimental study on waste heat recovery from an internal combustion engine using thermoelectric technology. *Therm Sci* 15(4):1011–1022. <https://doi.org/10.2298/TSCI100518053K>
4. Su CQ, Wang WS, Liu X, Deng YD (2014) Simulation and experimental study on thermal optimization of the heat exchanger for automotive exhaust-based thermoelectric generators. *Case Stud Therm Eng* 4:85–91. <https://doi.org/10.1016/j.csite.2014.06.002>
5. Negash AA, Choi Y, Kim TY (2021) Experimental investigation of optimal location of flow straightener from the aspects of power output and pressure drop characteristics of a thermoelectric generator. *Energy* 219:119565. <https://doi.org/10.1016/j.energy.2020.119565>
6. Menter FR (1994) Two-equation eddy-viscosity turbulence models for engineering applications. *AIAA J* 32(8):1598–1605. <https://doi.org/10.2514/3.12149>
7. Chen WH, Lin YX, Bin Chiou Y, Lin YL, Wang XD (2020) A computational fluid dynamics (CFD) approach of thermoelectric generator (TEG) for power generation. *Appl Therm Eng* 173:115203. <https://doi.org/10.1016/j.applthermaleng.2020.115203>
8. Su CQ, Huang C, Deng YD, Wang YP, Chu PQ, Zheng SJ (2016) Simulation and optimization of the heat exchanger for automotive exhaust-based thermoelectric generators. *J Electron Mater* 45(3):1464–1472. <https://doi.org/10.1007/s11664-015-4077-x>

# Microstructure Characterisation and Analysis of AA2024/SiC/Carbonised Eggshell-Reinforced Hybrid Green Aluminium Matrix Composite



Yatan Nagpal, Rohit Sharma, Neeraj Sharma, and R. K. Tyagi

**Abstract** The driving force behind this work is to investigate the microstructure of hybrid green aluminium matrix composite (AMMCs) made of AA2024/SiC/carbonised eggshell by using the stir casting method. The stir casting procedure is utilised in this study to allow (SiC and carbonised ES) hybrid reinforcement particles to mix equally in AA2024 matrix. The composition of reinforcements in this study varies from 3 to 12 wt% of SiC and ES particles together in a step of 3, i.e. (3, 6, 9, 12) as per earlier researchers. The microstructure characterisation of AA2024/carbonised eggshell/SiC composite was carried by SEM and XRD technique. The results revealed the strong bonding and uniform distribution between particles and matrix at 3% and 6%, respectively, and agglomeration and clustering of particles is being observed with increase in wt% of reinforcement beyond 6%. The term “Green” is being added to signify waste reduction from the environment by using ES as a waste reinforcement and to make our environment sustainable and eco-friendly.

**Keywords** Waste eggshells · AMCs · Hybrid composite · Green composite · AMMCs · Stir casting · SEM · XRD · Silicon carbide · Eggshell

## 1 Introduction

Metal matrix composites (MMCs) have witnessed considerable progress in recent years. MMCs which are made by combining two or more components are regarded as sophisticated materials whose customised properties are being researched. The main goal of producing MMCs was to concatenate the desirable properties ceramic and

---

Y. Nagpal (✉)

Amity University Uttar Pradesh, Noida, India

e-mail: [yatannagpal@gmail.com](mailto:yatannagpal@gmail.com)

R. Sharma · R. K. Tyagi

Mechanical Engineering Department, Amity University Uttar Pradesh, Noida, India

N. Sharma

Mechanical Engineering Department, Maharishi Markandeshwar University, Ambala, India

high strength metals such as high elasticity modulus and ductility to create a newer material that possesses intermediate mechanical properties in between ceramic reinforcement and matrix alloy, where the continuous phase was referred to as matrix and the discontinuous phase or component as reinforcement [1, 2]. Aluminium-based MMCs as an engineering material have the advantages of high strength, toughness and wear resistance and have gained increasing attention in the recent decades [3]. Al reinforced with SiC, Al<sub>2</sub>O<sub>3</sub> or B<sub>4</sub>C is often used MMCs with improved qualities and cheaper manufacturing costs which has inspired many researchers to employ AMMCs for various applications such as drive shafts, pistons, brake rotors and cylinder liners [4]. In the recent years, Al–Si alloy has grown in popularity due to its widespread use in aviation and ship radar equipment due to improved mechanical properties, lower density, good heat dissipation properties and so on as compared to pure Al [5]. Due to its yield strength and higher tensile with reduced elongation, Al–Cu–Mg alloy is also one of the most often used aluminium-copper alloys in forging and also as rivets for truck wheels, aircraft industries, aircraft frames, hardware and so on [6]. A great deal of environmental damage caused by industrial waste inspired our societies/researchers to use these waste items in research domains. Recently, recycling or waste materials such as melon shell ash, fly-ash, rice husk ash, red mud, bagasse ash and eggshell waste particles have been used. The environmental impact of chicken eggshell (ES), an aviculture by-product, is one of the worst, especially in nations where the egg product sector is well established. According to a recent survey, the USA alone has disposed of around 150,000 tonnes of this material as waste [7–10]. The use of chicken ES as a reinforcement material has many benefits, including the ability to be used as a biofiller to improve the mechanical and thermal properties of a composite, its lighter weight, availability in large quantities, affordability and environmental friendliness which make it suitable to use as one of the green reinforcements in composite fabrication [11–14]. The evaluation and characterisation of mechanical and physical properties of AMMCs reinforced with eggshell particles is a vast field of study. Due to their ease of availability and low cost, these composites are mostly created using various casting procedures such as electromagnetic and mechanical stir casting [15, 16]. Several researchers have tried to develop various Al-reinforced composites as below.

Hassan and Aigbodion [16] developed Al–Cu–Mg/ES-reinforced AMCs by the technique of stir casting. The microstructure and mechanical properties were inspected and assessed. As carbonised ES particles were included as reinforcement in the composite, the physical and mechanical properties improved when compared with the uncarbonised ES particles. It has also been demonstrated experimentally that the inclusion of ES particles can improve mechanical results by up to 12 wt%.

Salleh et al. [17] produced the eggshell by mixing and sieving it into particles smaller than 160  $\mu\text{m}$  using a ball milling process. The results showed that ES filler improved creep strain at 34 and 80 °C operating temperatures.

Toro et al. [7] produced and used chicken ES in various amounts of different particle sizes as a biofiller in a polypropylene composite. The outcomes showed that increasing the ES content as reinforcement improved the Young's Modulus ( $E$ ).



Lunge et al. [18] researched and synthesised a novel alumina-supported carbon composite material termed “eggshells composite” (EC) from ES waste as a calcium source for selective fluoride adsorption from water. The results demonstrated that EC is a viable, indigenous and cost-effective adsorbent for fluoride removal.

Depending on the literature survey, it was found that most researchers employed eggshell as a biofiller material and only a significant researchers used chicken ES as a reinforcement material to produce aluminium base green MMC by stir casting. From literature, it was also observed that very little or negligible work is being carried out using ES waste as one of the primary reinforcement material and SiC as secondary reinforcement material [19–33] in development of low cost and less dense Al–Cu–Mg (AA2024) hybrid green metal matrix composite. Also, very few researchers have worked on mechanical characterisation of hybrid green AMCs using AA2024 as matrix.

Hence, in view of above facts, the contemporary work deals with the microstructure analysis of AA2024/SiC/eggshell-reinforced hybrid green MMC with the help of stir casting technique by SEM and XRD. In the present work, SiC is termed as secondary reinforcement as from literature, because of low cost of SiC and good wettability property.

## 2 Materials and Methods

The AA2024 aluminium alloy (Al–Cu–Mg) was chosen as the matrix material in this study, and its chemical composition is reported in Table 1. Because of its inexpensive cost, light weight, high strength-to-weight ratio and good fatigue strength, the AA2024 matrix material was chosen. Furthermore, because of fatigue resistance and high strength, it is widely utilised in aircrafts, particularly in fuselage and wing components, hence AA2024 material has been chosen for future applications in the aeronautical industry.

Table 2 gives the chemical composition of carbonised eggshell powder, which was chosen as a primary reinforcement material. An eggshell is the hard-shelled egg’s exterior covering. Recently, researchers used chicken ES as a biofiller material in conjunction with a conductive polymer to improve characteristics. According to comprehensive literature data, chicken eggshell waste contains 94–95% calcium carbonate ( $\text{CaCO}_3$ ) and has the ability to be used as a raw material and reinforcement in composites. The eggshell covering layer was removed from the chicken ES by cleaning it and drying it in the sun [34]. The powdered eggshell was created by ball milling the dry eggshell. The carbonaceous material, such as the membrane of an

**Table 1** AA2024 elemental composition used as matrix material (wt%)

Element	Si	Fe	Cu	Mn	Mg	Cr	Zn	Ti	Al
%	0.6	0.4	4.1	0.5	1.6	0.2	0.26	0.16	Bal.

**Table 2** Eggshell chemical composition (wt%)

Elements	Weight percentage (%)
Calcium carbonate ( $\text{CaCO}_3$ )	94.5
Magnesium carbonate ( $\text{MgCO}_3$ )	1.5
Calcium phosphate ( $\text{Ca}_3(\text{PO}_4)_2$ )	1.5
Organic matter	2.5

eggshell, was then removed by carbonization at 500 °C for three hours [16]. Due to low cost and low density and presence of calcium carbonate for enhancing hardness of a composite, chicken eggshell in carbonised powder form is selected as primary reinforcement in this study.

SiC was selected as the secondary reinforcing material due to its high strength, low density, wear resistance, high temperature strength and good wettability property. Several researchers have discovered that using SiC as reinforcement improves the mechanical properties of a composite such as high tensile strength and hardness [35]. SiC is used in several applications such as semiconductors processing equipments, fixed and moving turbine components, ball valve parts, heat exchangers, bearings, and pump vanes.

The reinforcing compositions (SiC and carbonised eggshell) were chosen based on the previous study results [36, 37]. In AA2024 matrix material, the total percentage of both reinforcements ranges from 3 to 12 wt% in three-step increments, i.e. (3, 6, 9, 12) in AA2024. A composite's mechanical and physical properties cannot be further improved or altered if the reinforcing content exceeds 12 wt% [16].

The stir casting method was to produce AA2024/SiC/carbonised ES hybrid green MMC utilised in this investigation as the process of using stirrer with graphite crucible was found to be much more economical with less cost and easy availability. The parameters of this process were 11A (current), 170 s (time) and 650 °C (temperature of pouring of molten matrix) extruded on UTM machine at 65 MPa in order to remove porosity [34]. The matrix material was heated in a muffle furnace while maintaining a high liquid temperature in order to obtain it in molten form. ES was sun dried and carbonised and was about to be preheated at 500 °C to reduce the wettability issues. The molten AA2024 alloy at 700 °C was poured in graphite crucible. The preheated SiC and carbonised powdered ES particles were added in graphite crucible containing liquid AA2024. The mixture was stirred and mixed thoroughly using stir casting. The argon gas was added in a mixture to ensure uniform distribution and to remove porosity. To reduce porosity, the melt was placed into a cast iron chamber and pressure was exerted by the UTM machine. The mixture was consolidated, and the samples were removed from the crucible using the machining process.

### 3 Results and Discussion

#### 3.1 Microstructure Characterisation

##### 3.1.1 SEM Analysis

In the microstructure, pictures of these composites were obtained using a scanning electron microscope (SEM) at (3, 6, 9, 12%), respectively. The SEM analysis is been carried out at Inter-University Accelerator Centre (IUAC), New Delhi. The result of the microstructural analysis of MMCs has been demonstrated in Figs. 1 and 2 at 400X and 1000X magnification, respectively. The black patches represent agglomeration, whereas the white spots represent the existence of eggshell powder.

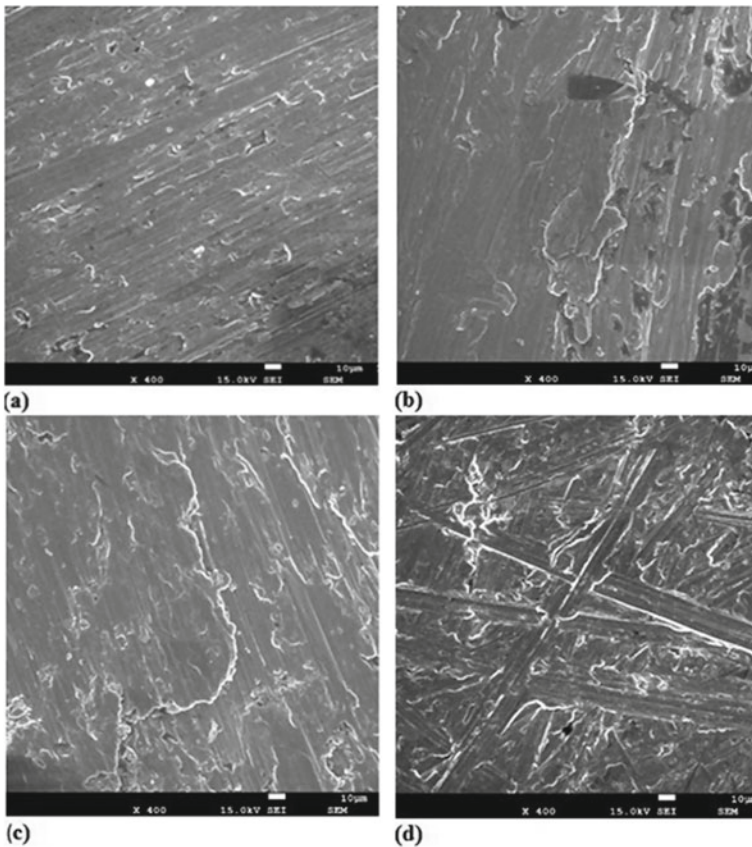


**Fig. 1** SEM micrograph of developed composite at 400X: **a** SEM micrograph for 3% reinforcement; **b** SEM micrograph for 6% reinforcement; **c** SEM micrograph for 9% reinforcement; **d** SEM micrograph for 12% reinforcement

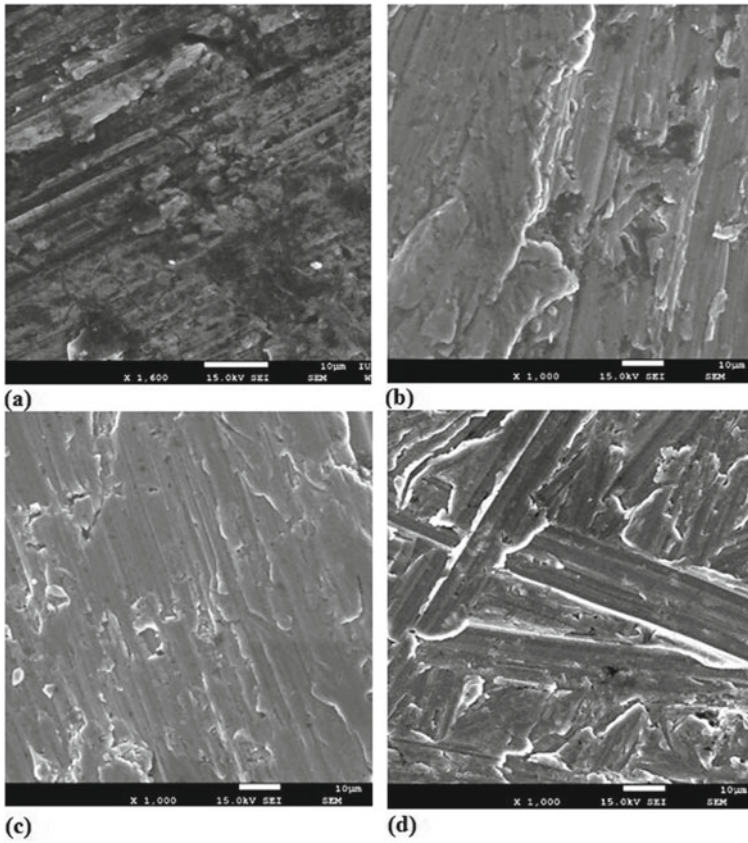


**Fig. 2** SEM micrograph of developed composite at 1000X: **a** SEM micrograph for 3% reinforcement; **b** SEM micrograph for 6% reinforcement; **c** SEM micrograph for 9% reinforcement; **d** SEM micrograph for 12% reinforcement

The findings demonstrate that eggshell and silicon carbide reinforcements are distributed uniformly and equally in the AA2024 aluminium metal matrix at percentages of 3 and 6, respectively. Additionally, there was no egg particle aggregation, which supports the wettability of eggshell as reinforcement with aluminium metal matrix.

The strong interfacial bonding is also being observed at lower percentages of reinforcement. But on increasing the wt% of reinforcement particles beyond 6%, clustering and agglomeration of ES particulates are being observed along with pores and cracks.

### 3.1.2 X-ray Diffraction Analysis

The XRD analysis is also been carried out at Inter-University Accelerator Centre (IUAC), New Delhi to get the graph pattern at (3, 6, 9, 12%), respectively. The graph depicts the composition of ES powder, AA2024 and SiC. The greatest peaks in Fig. 3 represent the AA2024 proportion, which is highest, whereas the small peaks indicate the presence of ES powder and other elements. Figure 3 depicts the peak details for all samples. Small peaks represent the elements in the composition in lower percentages. The existence of little peaks in all of the diagrams below demonstrates the decent wettability of ES powder with aluminium AA2024 base metal, while many little peaks certify the non-appearance of agglomeration of ES powder in matrix.

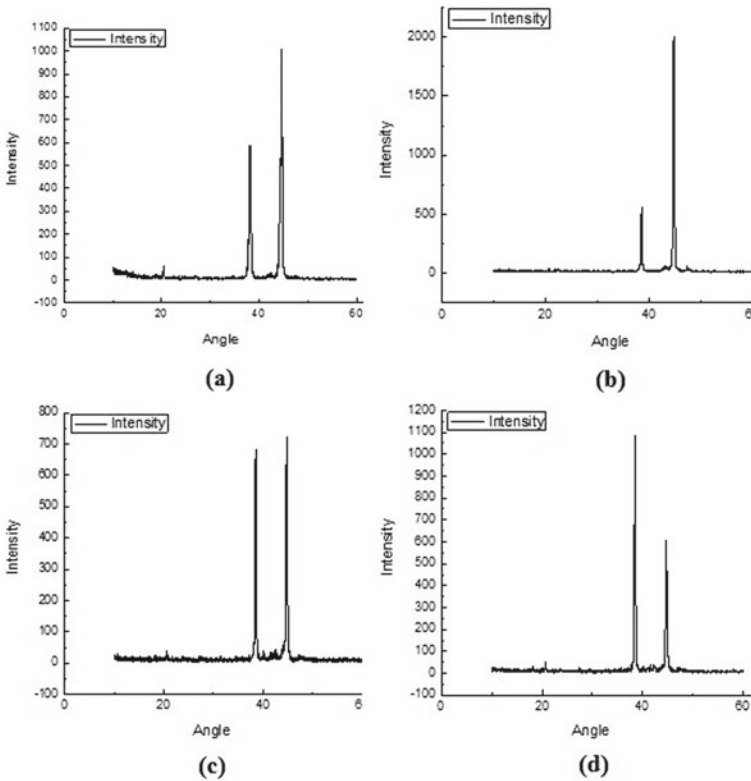


**Fig. 3** XRD of developed composite: **a** XRD for 3% reinforcement; **b** XRD for 6% reinforcement; **c** XRD for 9% reinforcement; **d** XRD for 12% reinforcement

## 4 Conclusion

From this study, the microstructure characterisation is successfully been analysed for AA2024 hybrid green MMCs using carbonised ES and SiC as reinforcements fabricated by the technique of stir casting by SEM and XRD. The results revealed that—

1. The ES and SiC reinforcements were uniformly distributed in AA2024 matrix.
2. Strong bonding and uniform distribution in reinforcement particles have been observed more at 3 and 6%, respectively, that indicated good wettability of eggshell as reinforcement.
3. The clustering and agglomeration of ES particulate along with pores and cracks were being observed on increasing the wt% of reinforcement particles beyond 6%, respectively.
4. The X-ray and SEM diffraction images demonstrate the white spots of eggshell (ES) powder, indicating that as porosity increases as the vol.% of ES powder increases in the composite.

**Acknowledgements** “Authors are thankful to IUAC for extending FE-SEM facility funded by Ministry of Earth Sciences (MoES) under Geochronology project [MoES/P.O.(Seismic)8(09)-Geochron/2012]”.

**Funding** “This research received no external funding”.

## References

1. Hashim J, Looney L, Hashmi MSJ (1999) Metal matrix composites: production by the stir casting method. *J Mater Process Technol* 92:1–7. [https://doi.org/10.1016/S0924-0136\(99\)00118-1](https://doi.org/10.1016/S0924-0136(99)00118-1)
2. Kala H, Mer KKS, Kumar S (2014) A review on mechanical and tribological behaviors of stir cast aluminum matrix composites. *Procedia Mater Sci* 6:1951–1960. <https://doi.org/10.1016/j.mspro.2014.07.229>
3. Anilkumar HC, Hebbar HS, Ravishankar KS (2011) Mechanical properties of fly ash reinforced aluminium alloy (Al6061) composites. *Int J Mech Mater Eng* 6:41–45
4. Ramanathan A, Krishnan PK, Muraliraja R (2019) A review on the production of metal matrix composites through stir casting—furnace design, properties, challenges, and research opportunities. *J Manuf Processes* 42:213–245. <https://doi.org/10.1016/j.jmapro.2019.04.017>
5. Bandil K, Vashisth H, Kumar S, Verma L, Jamwal A, Kumar D, Singh N, Sadasivuni KK, Gupta P (2019) Microstructural, mechanical and corrosion behaviour of Al–Si alloy reinforced with SiC metal matrix composite. *J Compos Mater* 53:4215–4223. <https://doi.org/10.1177/0021998319856679>
6. Rao JB, Rao DV, Murthy IN, Bhargava NR (2012) Mechanical properties and corrosion behaviour of fly ash particles reinforced AA 2024 composites. *J Compos Mater* 46:1393–404. <https://doi.org/10.1177/0021998311419876>
7. Toro P, Quijada R, Yazdani-Pedram M, Arias JL (2007) Eggshell, a new bio-filler for polypropylene composites. *Mater Lett* 61:4347–50. <https://doi.org/10.1016/j.matlet.2007.01.102>



8. Rath MK, Choi BH, Ji MJ, Lee KT (2014) Eggshell-membrane-templated synthesis of hierarchically-ordered NiO–Ce0.8Gd0.2O1.9 composite powders and their electrochemical performances as SOFC anodes. *Ceram Int* 40:3295–304. <https://doi.org/10.1016/j.ceramint.2013.09.105>
9. Bootklad M, Kaewtatip K (2013) Biodegradation of thermoplastic starch/eggshell powder composites. *Carbohydr Polym* 97:315–320. <https://doi.org/10.1016/j.carbpol.2013.05.030>
10. Severa L, Němeček J, Nedomová Š, Buchar J (2010) Determination of micromechanical properties of a hen's eggshell by means of nano indentation. *J Food Eng* 101:14651. <https://doi.org/10.1016/j.jfoodeng.2010.06.013>
11. Hassan TA, Rangari VK, Rana RK, Jeelani S (2013) Sonochemical effect on size reduction of CaCO<sub>3</sub> nanoparticles derived from waste eggshells. *Ultrason Sonochem* 20:1308–1315. <https://doi.org/10.1016/j.ultsonch.2013.01.016>
12. Chaithanyasai A, Vakchore PR, Umasankar V (2014) The micro structural and mechanical property study of effects of EGGSHELL particles on the Aluminum 6061. *Procedia Eng* 97:961–967. <https://doi.org/10.1016/j.proeng.2014.12.372>
13. Mosaddegh E, Hassankhani A, Pourahmadi S, Ghazanfari D (2013) Ball mill–assisted preparation of nano-CaCO<sub>3</sub> as a novel and green catalyst-based eggshell waste: a green approach in the synthesis of pyrano [4, 3-B] pyrans. *Int J Green Nanotechnol* 1:1943089213507160. <https://doi.org/10.1177/1943089213507160>
14. Ghabeer T, Dweiri R, Al Khateeb S (2013) Thermal and mechanical characterization of polypropylene/eggshell biocomposites. *J Reinf Plast Compos* 32:402–409. <https://doi.org/10.1177/731684412470015>
15. Yew MC, Sulong NR, Yew MK, Amalina MA, Johan MR (2013) The formulation and study of the thermal stability and mechanical properties of an acrylic coating using chicken eggshell as a novel bio-filler. *Prog Org Coat* 76:1549–1555. <https://doi.org/10.1016/j.porgcoat.2013.06.011>
16. Hassan SB, Aigbodion VS (2015) Effects of eggshell on the microstructures and properties of Al–Cu–Mg/eggshell particulate composites. *J KingSaudUniv Eng Sci* 27:49–56. <https://doi.org/10.1016/j.jksues.2013.03.001>
17. Salleh MR, Kamely A, Tajul A (2011) Characterizing chicken eggshell reinforced polypropylene (PP). *Adv Mater Res* 264:871–879 (TransTechPublicationsLtd.) <https://doi.org/10.4028/www.scientific.net/AMR.264-265.871>
18. Lunge S, Thakre D, Kamble S, Labhsetwar N, Rayalu S (2012) Alumina supported carbon composite material with exceptionally high defluoridation property from eggshell waste. *J Hazard Mater* 237:161–169. <https://doi.org/10.1016/j.jhazmat.2012.08.023>
19. Chandel R, Sharma N, Bansal SA (2021) A review on recent developments of aluminum-based hybrid composites for automotive applications. *Emergent Mater* 4(5):1243–1257
20. Singh G, Chan SLI, Sharma N (2018) Parametric study on the dry sliding wear behaviour of AA6082–T6/TiB<sub>2</sub> in situ composites using response surface methodology. *J Braz Soc Mech Sci Eng* 40(6):1–12
21. Sharma N, Khanna R, Singh G, Kumar V (2017) Fabrication of 6061 aluminum alloy reinforced with Si<sub>3</sub>N<sub>4</sub>/n-Gr and its wear performance optimization using integrated RSM-GA. *Part Sci Technol* 35(6):731–741
22. Singh G, Goyal S, Miranda G, Sharma N (2018) Parametric study of the dry sliding wear behaviour of AA6082–T6/SiC and AA6082–T6/B<sub>4</sub>C composites using RSM. *J Mech Sci Technol* 32(2):579–592
23. Sharma P, Paliwal K, Dabra V, Sharma S, Sharma N, Singh G (2018) Influence of Silicon Carbide/Graphite addition on properties of AA6082 reinforced composites. *Aust J Mech Eng*
24. Singh G, Sharma N, Goyal S, Sharma RC (2021) Comparative measurements of physical and mechanical properties of AA6082 based composites reinforced with B<sub>4</sub>C and SiC particulates produced via stir casting. *Met Mater Int* 27(11):4333–4345
25. Sharma P, Dabra V, Sharma S, Khanduja D, Sharma N, Sharma R, Saini K (2019) Microstructure and properties of AA6082/(SiC+ graphite) hybrid composites. *Refract Ind Ceram* 59(5):471–477

26. Singh G, Sharma N (2021) Study on the influence of T4 and T6 heat treatment on the wear behavior of coarse and fine WC particulate reinforced LM28 Aluminium cast composites. *Compos Part C Open Access* 4:100106
27. Sharma P, Sharma N, Singh G, Dabra V (2020) Abrasive wear study of AA7075/ZrB<sub>2</sub> reinforced composites. *Refract Ind Ceram* 60(5):506–509
28. Dwivedi SP, Maurya M, Saxena A, Sharma S (2022) Synthesis and characterization of spent alumina catalyst and grinding sludge reinforced aluminium-based composite material. *Proc Inst Mech Eng C J Mech Eng Sci* 236(10):5523–5534
29. Chintada S, Dora SP, Kare D (2022) Mechanical behavior and metallographic characterization of microwave sintered Al/SiC composite materials—an experimental approach. *Silicon* 14(12):7341–7352
30. Brodova IG, Petrova AN, Shirinkina IG, Rasposienko DY, Yolshina LA, Muradymov RV, Shorokhov EV et al (2021) Mechanical properties of submicrocrystalline aluminium matrix composites reinforced by “in situ” graphene through severe plastic deformation processes. *J Alloy Compd* 859:158387
31. Bhuvaneswari V, Rajeshkumar L, Ross KNS (2021) Influence of bioceramic reinforcement on tribological behaviour of aluminium alloy metal matrix composites: experimental study and analysis. *J Mater Res Technol* 15:2802–2819
32. Khanna V, Kumar V, Bansal SA (2021) Mechanical properties of aluminium-graphene/carbon nanotubes (CNTs) metal matrix composites: advancement, opportunities and perspective. *Mater Res Bull* 138:111224
33. Ao M, Liu H, Dong C, Feng S, Liu J (2021) Degradation mechanism of 6063 aluminium matrix composite reinforced with TiC and Al<sub>2</sub>O<sub>3</sub> particles. *J Alloy Compd* 859:157838
34. Dwivedi SP, Sharma S, Mishra RK (2016) Synthesis and mechanical behaviour of green metal matrix composites using waste eggshells as reinforcement material. *Green Process Synth* 5:275–282. <https://doi.org/10.1515/gps-2016-0006>
35. Tham LM, Gupta M, Cheng L (2001) Effect of limited matrix–reinforcement interfacial reaction on enhancing the mechanical properties of aluminium–silicon carbide composites. *Acta Mater* 49:3243–3253. [https://doi.org/10.1016/S1359-6454\(01\)00221-X](https://doi.org/10.1016/S1359-6454(01)00221-X)
36. Dwivedi SP, Sharma S, Mishra RK (2016) Characterization of waste eggshells and CaCO<sub>3</sub> reinforced AA2014 greenmetal matrix composites: a green approach in the synthesis of composites. *Int J Precis Eng Manuf* 17:1383–1393. <https://doi.org/10.1007/s12541-016-0164-z>
37. Dwivedi SP, Sharma S, Mishra RK (2017) A comparative study of waste eggshells, CaCO<sub>3</sub>, and SiC-reinforced AA2014 green metal matrix composites. *J Compos Mater* 51:2407–2421. <https://doi.org/10.1177/0021998316672295>



# Passive Thermal Management of a PV Module Using Fins of Various Geometries: A Numerical Study



Vipul Kumar, Vibhor Kumar Gupta, Shwetanshu Goel, and Akhilesh Arora

**Abstract** The working temperature of a photovoltaic (PV) module is an essential attribute that influences both its power output and lifespan. Some of the working challenges encountered after the installation of solar PV modules in regions with high solar irradiance include the reduction in electrical output efficiency due to the rise in the surface temperature. Adding fins to the rear side of a PV module is one of the passive cooling solutions for lowering operating temperatures. In this paper, the working temperature of a monocrystalline silicon PV module with an air-cooled heat sink was studied numerically. The heat sink, in the form of pin fins, rectangular fins, and rectangular fins with single step change (RFSSC), was made of copper, because of its high thermal conductivity and attached to the bottom face of the PV module. The conversion efficiency and cell temperature have been investigated for these three configurations of fin geometry for varying flux conditions. The cooling effectiveness was established by comparing numerically computed 3D models of the module to investigate the influence of operating temperatures over the module's performance. It was observed that adding RFSSC to the PV module resulted in maximum improvement in the power output to the tune of 20.85% owing to the reduction in average operating temperature by 28 °C.

**Keywords** Thermal management · Photovoltaic module · Operating temperature · Passive cooling · Heat transfer · Heat sink · Numerical study · Fins

---

V. Kumar (✉) · V. K. Gupta (✉) · S. Goel · A. Arora  
Delhi Technological University, Shahbad Daultapur, Delhi 110042, India  
e-mail: [kvipulk02@gmail.com](mailto:kvipulk02@gmail.com)

V. K. Gupta  
e-mail: [vibhorkumar8755@gmail.com](mailto:vibhorkumar8755@gmail.com)

## 1 Introduction

A photovoltaic (PV) solar cell is a technology that directly creates electricity from solar energy with unlimited potential, quiet operation, and very little upkeep. PV cells are a type of photo-electric cell whose electrical characteristics such as resistance, voltage, or current vary when the cell is introduced to light. PV cells may be grouped as modules to form solar panels. PV systems have applications ranging from small rooftops mounted systems of tens of kilowatts to large-scale power plants [1].

The conversion efficiency of the PV module is 6–20%, depending on the PV cell type, ambient temperature, wind speed, solar radiation, and installation orientation [1, 2], with the remaining incident solar radiation being converted to heat and raising the PV module's temperature. The relation of operating temperature of PV cells with power output has been a domain of much interest. Various studies have demonstrated that efficiency decreases when operating temperature rises [1–3], with an inverse linear relationship between the two [4]. This happens as a considerable drop in  $V_{oc}$  (open-circuit voltage) overcomes a slight increase in  $I_{sc}$  (short-circuit current) [5]. This results in a decreased conversion efficiency in the range of 0.4–0.5%/°C [6, 7]. Without any cooling, the PV temperatures can even elevate to 80 °C [8] and the resulting thermal stress causes irreversible damages such as micro-cracks, delamination, and deformation to the PV cells [9]. Studies have been conducted keeping these constraints in mind to study the performance of PV systems with various proposed solutions for better heat dissipation.

Numerous PV cooling solutions systems have been proposed in the past. Some of the most commonly used active and passive solutions include phase change materials (PCM), natural, and forced convection using heat sinks, photovoltaic/thermal system (PV/T), floating cooling system (FCC), thermoelectric system, hydraulic techniques involving immersion, spraying, forced flow over surfaces, and photonic crystal cooling and heat pipes among others [10–13]. However, the quantitative work for the thermal performance improvement using these solutions has been scarce.

An active cooling system requires water to run continually and thus more pumping energy is necessary. Liquid immersion cooling, spraying, and forced water circulation are some examples of an active cooling system [14]. Using the immersion cooling technology, photovoltaic modules can be installed underwater. Water absorbs heat from PV panels, resulting in high-efficiency improvements. According to Mehrotra et al. [15] this type of cooling method is not ideal for solar systems of floating type despite its low impact on the environment and significant potential to reduce temperature. Krauter [16] circulated water in holes drilled into PV's surface with the help of a pump. The PV cell's surface was cooled and overcame the effects of drift and dust on the cell's efficiency and eventually improved the cell's electrical efficiency by 9%. However, the resulting increased maintenance and cost and the low value of the net-power gain, considering the power losses of a circulation pump and the PV power gain, remains a nagging issue.

A passive cooling method for PV modules and balancing systems involves utilizing air instead of mechanical procedures. The most used cooling method is

arguably natural convection because of its simplicity, requirement of no additional working parts, and cost effectiveness. Convection transports heat away from PV panels [14]. In an experimental study by Elbreki et al. [17] fins were used for cooling PV panels. The highest performance was observed with passive cooling employing lapping fins, with an average temperature of 24.6 °C lower than the reference PV module. Another research by Popovici proposed a computational method for lowering the temperature of solar panels utilizing air-cooled heat sinks. Simulations showed that the temperature is reduced by at least 10 °C compared to the baseline situation [18]. Setyohandoko investigated the performance of PV panels with aluminum fins under various heat fluxes using a computer model. As a result, an average temperature drops of 13.1 °C was obtained, as well as an increase in PV module efficiency of 0.8% [19]. Pin fins were employed to increase the performance of PV panels in theoretical research conducted by Sedaghat et al. [20]. Based on an analytical model, concluding this passive cooling method as effective, with the panel’s yearly mean temperature of surface dropping by 2.3–7.8 °C.

## 2 Methodology

The PV module consisted of four layers for the simulations, i.e., glass, EVA, PVC, and PVF. The physical properties and dimensions of each of these layers can be seen in Table 1. The heat sink made of copper is considered to be a thin plate with the copper fins implanted on it, and further, this plate is fixed at the bottom face of the PV module to assist in heat dissipation and improve the module’s performance (Fig. 1).

**Table 1** Layer properties of photovoltaic (PV) panel

Layer	Thickness (mm)	Thermal conductivity (W/m K)	Density (kg/m <sup>3</sup> )	Specific heat capacity (J/kg K)
Glass	32	0.7	2450	790
EVA	5	0.311	960	2090
PV cell	2	130	2330	677
PVF	3	0.15	1200	1250

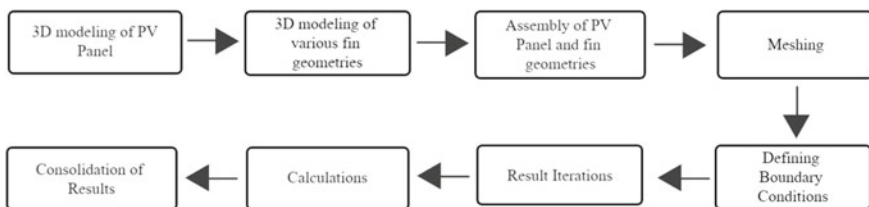
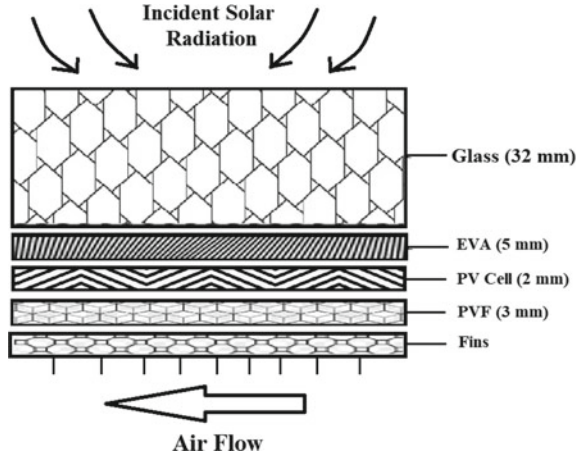


**Fig. 1** Methodology flowchart

**Fig. 2** PV panel layers



For the numerical experimentation, three types of heat sink geometries were considered to study the effect of various geometry of fins over the operating temperatures of the photovoltaic module. The geometries considered were as follows (Fig. 2):

- Rectangular fins
- Rectangular fins with single step change (RFSSC)
- Pin fins

The heat sink in the form of fin geometries and the PV module was modeled using the design modeler and then was imported in the fluent flow module. The dimensions of the fins can be seen in Table 2. After modeling the heat sink and the PV module, a fluid domain of a width of 100 mm was formed around the fins' surface.

Meshing was done with varying refinement for the heat sink, the photovoltaic module, and the fluid domain. For the module and the heat sink, the mesh cell size considered was of size 5 mm and that for the fluid domain was taken to be 10 mm.

The module's thermal and fluid flow analysis was performed by considering a steady-state condition for the control volume. The solar irradiation on the photovoltaic module was applied in heat flux inputs in the range of 800–1000 W/m<sup>2</sup>.

**Table 2** Dimensions of fins

Specifications	Size (mm)
Fin height	10
Fin length	500
Fin thickness	2
Heat sink base length	500
Heat sink base width	500
Heat sink base thickness	1

These heat fluxes were applied generally on the upper face of the glass layer of the module. For the ambient conditions, the temperature was taken as 35 °C. The inlet velocity through the fluid domain was considered to be 5.4 km/h, and the related Reynolds number was found to be 13,100 [21], which was acquired from the equation given below,

$$Re = \rho V L \mu$$

A turbulent flow regime was considered for the above Reynolds number. For the airflow inside the fluid domain, a re-normalization  $k-\varepsilon$  turbulence model was applied [2] and the turbulence intensity considered was 4.8% which was found using the equation

$$I = 0.16 \cdot Re^{-18}$$

### 3 Results

The results of the simulations are depicted as temperature distribution contours for various fin geometries and different heat fluxes.

- Figure 3 represents the temp. distribution for the PV panel without the use of fins. The average temperatures in this case reached 83 °C, 77 °C, and 72 °C for heat fluxes of 1000 W/m<sup>2</sup>, 900 W/m<sup>2</sup>, and 800 W/m<sup>2</sup>, respectively.
- Figure 4 represents the temperature distribution for the PV panel when rectangular fins are used as heat sinks. In this case, the average temperatures were reduced to 64 °C, 61 °C, and 57 °C for heat fluxes of 1000 W/m<sup>2</sup>, 900 W/m<sup>2</sup>, and 800 W/m<sup>2</sup>, respectively.
- Figure 5 represents the temperature distribution for the PV panel when double layered rectangular fins are used as heat sinks. In this case, the average temperatures were reduced to 55 °C, 53 °C, and 49 °C for heat fluxes of 1000 W/m<sup>2</sup>, 900 W/m<sup>2</sup>, and 800 W/m<sup>2</sup>, respectively.
- Figure 6 represents the temp. distribution for the PV panel when pin fins are used as heat sinks. In this case, the average temperatures were 79 °C, 73 °C, and 69 °C for heat fluxes of 1000 W/m<sup>2</sup>, 900 W/m<sup>2</sup>, and 800 W/m<sup>2</sup>, respectively.

The values of average temperatures when fins are used as heat sinks show an improvement in the thermal performance in contrast to that of the PV panel without any fins (Figs. 7 and 8 and Table 3).

The maximum decrease in temperature was 28 °C between that of module without fins and when RFSSC fins were used (Fig. 9).

The efficiency of a photovoltaic module, as given by Dubey et al. [2], in the form of a linear expression for the photovoltaic electrical efficiency is given as below:

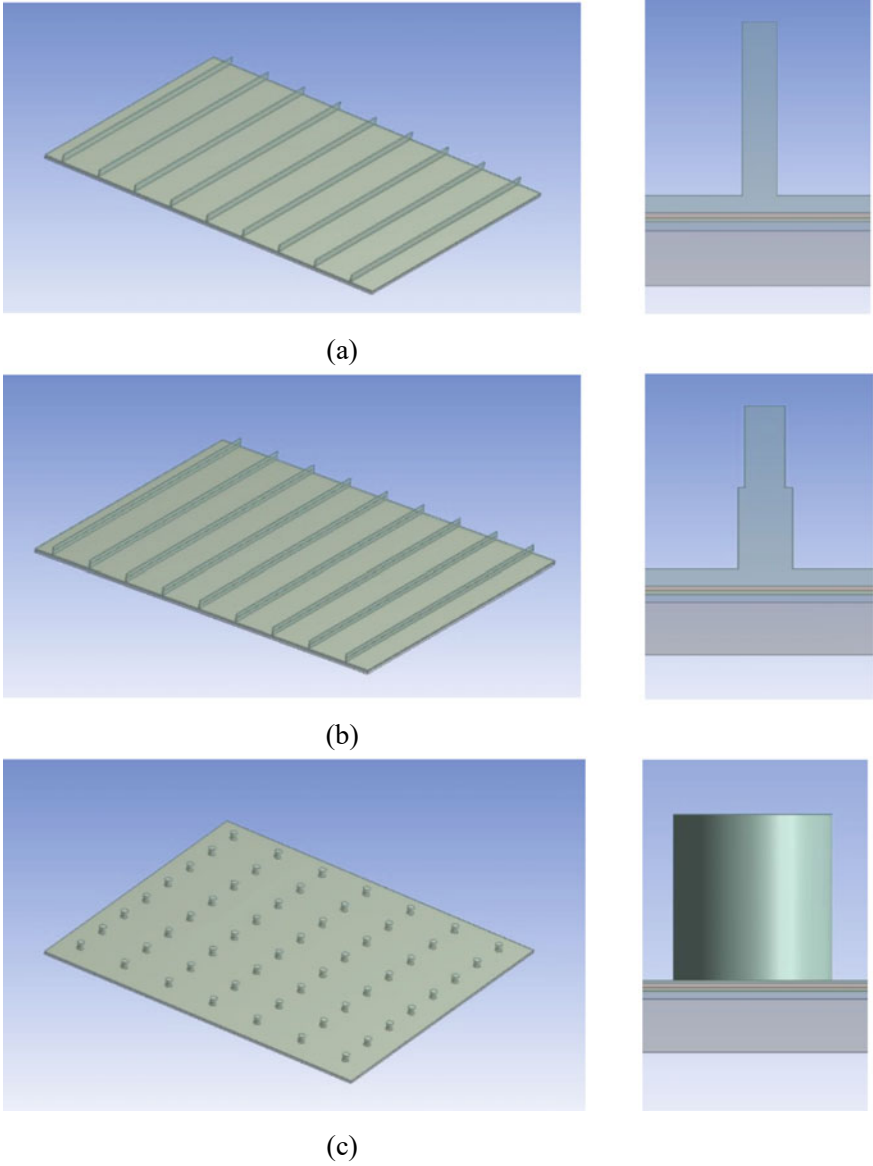


**Fig. 3** Fin geometries **a** rectangular fins **b** rectangular fins with single step change **c** pin fins

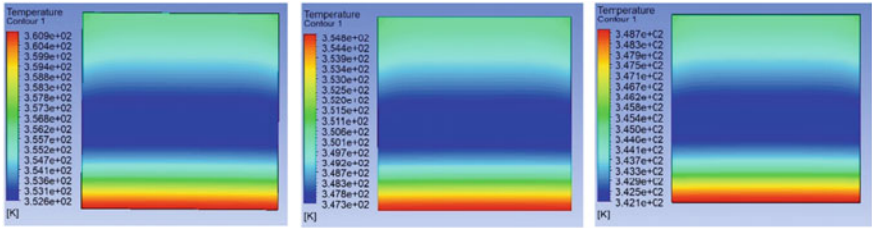


Fig. 4 Temp. contours for a PV panel without fins for a heat flux of 1000, 900, and 800 W/m<sup>2</sup>

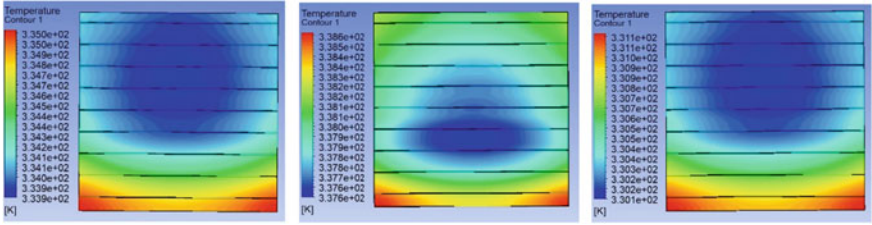


Fig. 5 Temp. contours for a PV panel with rectangular fins for a heat flux of 1000, 900, and 800 W/m<sup>2</sup>

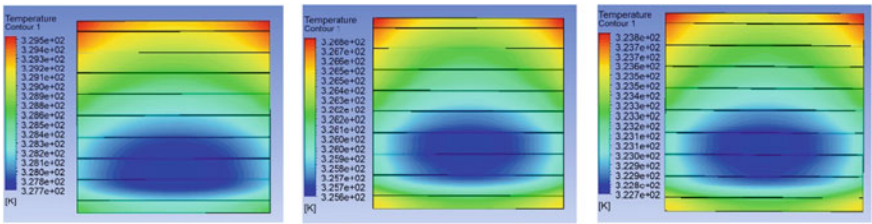


Fig. 6 Temp. contours for a PV panel with RFSSC for a heat flux of 1000, 900, and 800 W/m<sup>2</sup>

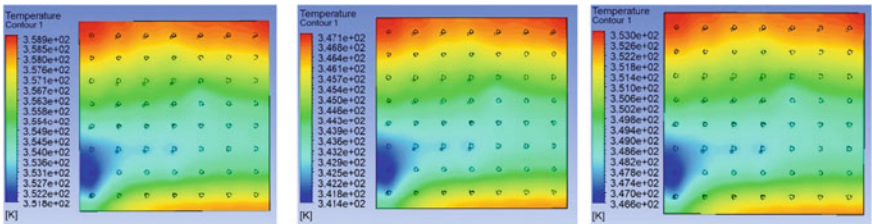
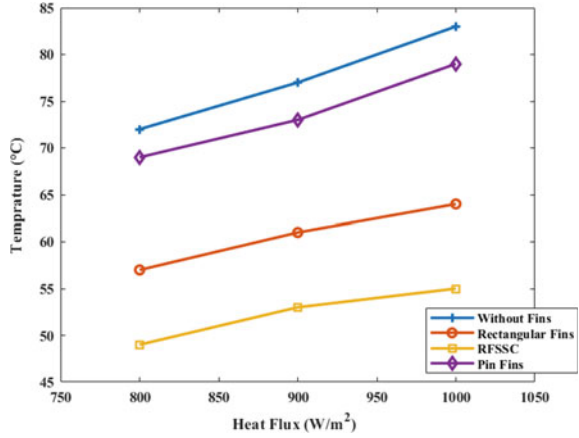


Fig. 7 Temp. contours for a PV panel with pin fins for a heat flux of 1000, 900, and 800 W/m<sup>2</sup>

**Fig. 8** Average module temperature under variable heat flux



**Table 3** Influence of fin geometry on PV module

Geometry	Heat flux (W/m <sup>2</sup> )	$T_{avg}$ (°C)	$\eta$	$P_{el}$ (W)
Without fins	1000	83	0.114	42.358
	900	77	0.118	39.825
	800	72	0.121	36.662
Pin fins	1000	79	0.117	43.619
	900	73	0.120	40.961
	800	69	0.123	37.419
Rectangular fins	1000	64	0.126	48.350
	900	61	0.128	44.367
	800	57	0.130	40.446
(RFSSC)	1000	55	0.132	51.189
	900	53	0.133	46.637
	800	49	0.135	42.465

$$\eta_c = \eta T_{ref} [1 - \beta_{ref}(T_C - T_{ref})]$$

As evident in the graph of heat flux vs efficiency, the rise of efficiency produced at 1000 W/m<sup>2</sup> flux of RFSSC fins was 15.78% more than that of PV module without fins (Figs. 10 and 11).

For a photovoltaic module, the max. power produced at a given heat flux, as given by Marion [22] in the PVFORM model, is given below:

$$P_{mp} = (S/S_{ref}) P_{mp,ref} [1 + \gamma(T - T_{ref})]$$

The power output with RFSSC was 20.85% more than that of without when the heat flux is taken to be 1000 W/m<sup>2</sup>. The results and observations of the numerical



**Fig. 9** Efficiency under variable heat flux

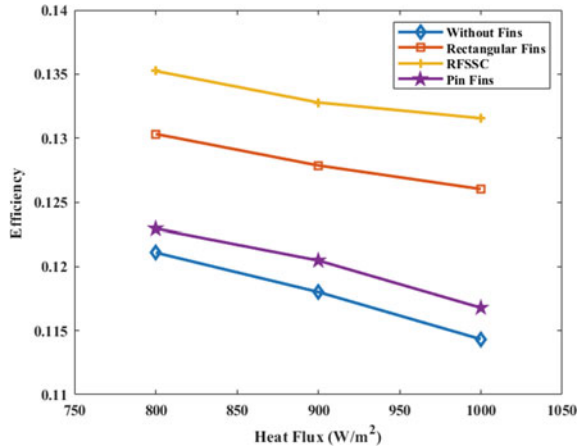
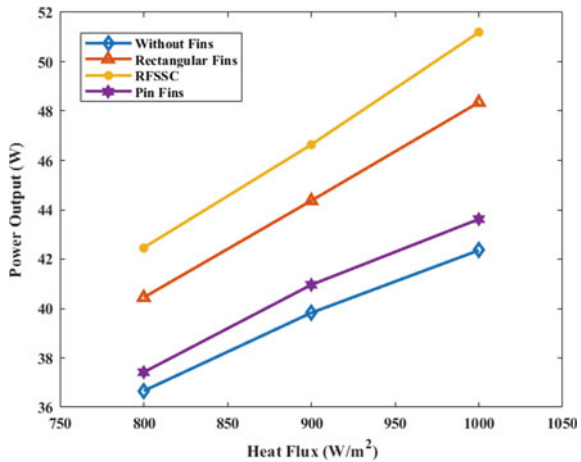


**Fig. 10** Power under variable heat flux

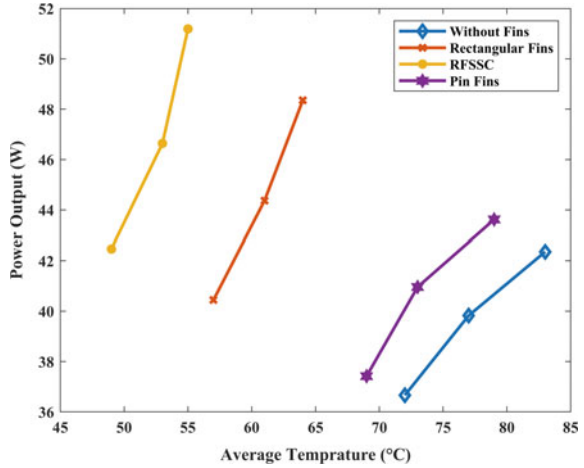


experimentation align with the results of various studies conducted by researchers in an effort to improve the thermal performance of PV modules. The temperature results of our PV module without heat sink and that with rectangular fins are similar to the studies performed by Ahmed [23] and Egab et al. [24]. Other geometries considered by us in the numerical experimentation improve upon these results to indicate an increase in the thermal performance of the PV module. The use of fins resulted in an increase of area for convection. Referring to the formula,

$$Q = hA\Delta T$$

heat transfer rate for convection is directly proportional to the exposed surface area. Consequently, the heat transfer from the bottom layer of the solar panel was enhanced

**Fig. 11** Power versus average temperature



as compared to the solar panel without any fins. This enabled the heat accumulated due to the solar heat flux to escape to the atmosphere at a higher rate. As is evident from the graphs, the highest decrease in temperature was found in rectangular fins with single step change, lesser in rectangular fins, and the least in pin fins due to their decreasing exposed surface area.

### 4 Future Scope

A logical continuation of this project would be the optimization of the size and design of the fins to maximize the heat dissipation by taking a genetic algorithm approach and then modifying this numerical study to the resultant fin dimensions. Fabrication of a commercial-level prototype will enable the team to verify the numerical results and make suitable adjustments, if required and also helping in studying the cost effectiveness and structural stability of the modification made to the PV module and convert it to a fully functional PV panel. An even further progression of this work can be incorporation of phase change materials (PCM) inside hollow fins or the use of other passive cooling systems such as heat pipes.

### 5 Conclusion

The operating temperatures of the photovoltaic module play a pivotal role in influencing the conversion efficiency. This is evident from the results as the conversion efficiency for various fin geometries increases with a decrease in the average operating temperatures of the module. Considering the results, it can be concluded that

among the three fin geometries used in our study, the PV module that uses RFSSC fins as heat sinks has the best performance. Pin fins were the worst performing geometry due to the lesser exposed surface area for heat dissipation compared to rectangular and RFSSC fins. This method could be an economical solution to reduce operating temperatures for existing PV modules.

## References

1. Krishan O, Suhag S (2019) Techno-economic analysis of a hybrid renewable energy system for an energy poor rural community. *J Energy Storage* 23:305–319
2. Dubey S, Sarvaiya JN, Seshadri B (2013) Temperature dependent photovoltaic (PV) efficiency and its effect on PV production in the world—a review. *Energy Procedia* 33:311–321
3. Griffith JS, Rathod MS, Paslaski J (1981) Some tests of flat plate photovoltaic module cell temperatures in simulated field conditions. In: 15th photovoltaic specialists conference, pp 822–830
4. Hussein KH et al (1995) Maximum photovoltaic power tracking: an algorithm for rapidly changing atmospheric conditions. *IEE Proc Gener Transm Distrib* 142(1):59–64
5. Radziemska E (2003) The effect of temperature on the power drop in crystalline silicon solar cells. *Renew Energy* 28(1):1–12
6. Lorenzo E (1994) *Solar electricity: engineering of photovoltaic systems*. Earthscan/James & James
7. Wu S, Xiong C (2014) Passive cooling technology for photovoltaic panels for domestic houses. *Int J Low-Carbon Technol* 9(2):118–126
8. Skoplaki E, Palyvos JA (2009) On the temperature dependence of photovoltaic module electrical performance: a review of efficiency/power correlations. *Sol Energy* 83(5):614–624
9. Reddy SR, Ebadian MA, Lin C-X (2015) A review of PV–T systems: thermal management and efficiency with single phase cooling. *Int J Heat Mass Transf* 91:861–871
10. Dong J et al (2018) Numerical analysis of a multi-channel active cooling system for densely packed concentrating photovoltaic cells. *Energy Convers Manage* 161:172–181
11. Hasanuzzaman M et al (2016) Global advancement of cooling technologies for PV systems: a review. *Sol Energy* 137:25–45
12. Du D, Darkwa J, Kokogiannakis G (2013) Thermal management systems for photovoltaics (PV) installations: a critical review. *Sol Energy* 97:238–254
13. Siecker J, Kusakana K, Numbi BP (2017) A review of solar photovoltaic systems cooling technologies. *Renew Sustain Energy Rev* 79:192–203
14. Dwivedi P, Sudhakar K, Soni A, Solomin E, Kirpichnikova I (2020) Advanced cooling techniques of P.V. modules: a state of art. *Case Stud Therm Eng* 21
15. Mehrotra S, Rawat P, Debbarma M, Sudhakar K (2014) Performance of a solar panel with water immersion cooling technique. *Int J Sci Environ Technol* 3:1161–1172
16. Krauter S (2004) Increased electrical yield via water flow over the front of photovoltaic panels. *Sol Energy Mater Sol Cells* 82:131–137
17. Elbreki M, Muftah AF, Sopian K, Jarimi H, Fazlizan A, Ibrahim A (2021) Experimental and economic analysis of passive cooling PV module using fins and planar reflector. *Case Stud Therm Eng* 23
18. Popovici CG, Hudişteanu SV, Mateescu TD, Cherecheş NC (2016) Efficiency improvement of photovoltaic panels by using air cooled heat sinks. *Energy Procedia* 85
19. Setyohandoko G, Sutanto B, Rachmanto RA, Prija Tjahjana DDD, Arifin Z (2021) A numerical approach to study the performance of photovoltaic panels by using Aluminium heat sink. *J Adv Res Fluid Mech Therm Sci* 70(2):97–105

20. Sedaghat A, Karami MR, Eslami M (2020) Improving performance of a photovoltaic panel by pin fins: a theoretical analysis. *Iran J Sci Technol Trans Mech Eng* 44:997–1004
21. Fox RW, McDonald AT, Pritchard PJ, Leylegian JC (2011) *Fluid mechanics*, 8th edn
22. Marion B (2008) Comparison of predictive models for photovoltaic module performance
23. Ahmed I (2018) Enhancement the performance of PV panel by using fins as heat sink. *Eng Technol J* 36:798–805
24. Egab K, Okab A, Dywan HS, Oudah SK (2020) Enhancing a solar panel cooling system using an air heat sink with different fin configurations. *IOP Conf Ser Mater Sci Eng*

# Experimental Investigation for Mechanical Performance of Plant Fiber-Based Polymer Composites



Apurv Upadhyay, Swabhi Dinesh Bajpai, Vijay Chaudhary, Sumit Gupta,  
and Pallav Gupta

**Abstract** The demand of biocomposites has been increased in the past few years due to their improved mechanical properties such as light weight, high strength and thermal stability. Most of composites are not biodegradable or even recyclable damaging the flora and fauna. Several research and modification has been done to make biocomposites capable to stand against the conventional or synthetic composites and to increase spectrum of usability as biocomposites are non-toxic, ecofriendly and can be recycled or decomposed under controlled environment. The present work reports the fabrication of biocomposites from hem and hemp-linen in the form of mat from. All the samples were prepared using hand layup technique. Fabricated specimens will be subjected to various mechanical characterizations. It is expected that the present class of fabricated biocomposites will be used for wide engineering applications.

## 1 Introduction

The demand of biocomposites has been increased rapidly in last few years. Due to rise in global warming and plastic waste, private and government bodies are putting effort in development of materials that are better alternative, have all the characteristics of conventional polymers and biodegradable too. Although, the modern synthetic polymers such as carbon fiber, PLA and fiber glass are made from petrochemicals and other substances can be recycled using various techniques. In past few years, it become possible to manufacture composites with natural derivatives (natural fiber coir, hemp, linen etc.; bio matrix soy-based resin, cellulose, etc.). They are not only biodegradable but also possess mechanical characteristics identical to

---

A. Upadhyay · S. D. Bajpai · V. Chaudhary (✉) · S. Gupta · P. Gupta (✉)  
Department of Mechanical Engineering, Amity School of Engineering and Technology, Amity  
University Uttar Pradesh, Sector125, Noida 201313, India  
e-mail: [vchaudhary2@amity.edu](mailto:vchaudhary2@amity.edu)

P. Gupta  
e-mail: [pgupta7@amity.edu](mailto:pgupta7@amity.edu)

conventional polymers [1]. Natural fibers exhibit natural acoustic and thermal insulation due to specific built-in properties such as low density, typical cellular structure and resistance against water absorption. These days, bioplastics are being used to do the production of structural and non-structural components in construction industry, automobile industry, etc. While the manufacturing of biocomposites, the natural reinforced fibers in the form of matt or in random order are soaked with bioresin uniformly layer by layer, and this process is repeated until desired dimension is achieved. The nature of polymer matrix can be thermoplastic (e.g., lignin, teflon) or thermosetting (epoxy, silicones), and for fiber reinforcement, there are variety of material available such as, hemp, coir, linen and bamboo. Natural fibers not only have significant loading bearing capacity but also can be processed at quite low cost as compare to synthetic fibers [1, 2]. The cultivation of some of the natural fibers such as hemp contributes in lowering down the emission of greenhouse gases as specifically hemp is a wild plant which can grow in climate and helps in maintaining the natural elements of soil irrespective of how many times the crop is grown on same land. Natural fibers are reinforced with polymer matrix to develop the polymeric composite materials. Developed composite showed the better properties as compared to single polymer and fiber [3].

This study is conducted to examine the characteristics of natural fiber-reinforced composites prepared from hemp-linen and hemp in the form of matt in bi-directional structure infused with epoxy resin. No such hybrid structure (hemp-linen) as per author's knowledge and literature has been tested/reviewed. The aim is to study the upshot of hybrid structure of reinforced biocomposites on its mechanical characteristics like tensile, flexural and impact strength and fractured regions are examined through scanning electron microscopy (SEM) [1].

## 2 Literature Review

Vijay Chaudhary et al. [1] had put forward the technique to infuse the natural fibers with thermoset polymer resin to develop natural fiber-reinforced composite having characterization potential based on tensile strength, flexural strength, etc. The motive of this research was to do study on mechanical and morphological characterization of prepared natural fiber (jute/hemp/flex)-reinforced composite. According to study, the percentage change in density was minimum in hemp/epoxy-reinforced composite that was around 6.112% and was maximum in flex/epoxy-reinforced composite about 8.089%. This variation in change in density is due to presence of interfacial voids, where air got trap while the fusion of reinforced fiber with resin. The quality of fabrication due to inconsistency in the fabrication process also signifies the reason of change in density.

Prepared flax/hemp/recycled paper-reinforced biocomposites infused with modified soybean oil in the form of acrylated epoxidized soybean oil (acrylated epoxidized soybean oil) using VARTM method (vacuum-assisted resin transfer method). Both mechanical and dynamic mechanical were done for the characterization of

constituents of reinforced composites (resin and fibers) [4]. The research was done to develop a reinforced biocomposites for high volume applications. Studied shown that the recycled paper-reinforced biocomposites shown high storage modulus around 5242 MPa with lowest of flax reinforced biocomposites with 2176 MPa. Due to less viscosity of resin, there were less voids making composite ideal for high volume construction such as automotive and housing [5].

Devireddy et al. [6] manufactured samples of banana-jute fiber infused with epoxy resin. The fibers were chopped with an average length of 15 mm kept in three ratios of 1:1, 1:3 and 3:1 for banana-jute fiber-reinforced composite. The motive of the study was to review the thermos-physical properties of hybrid composites. According to study, the composite with ratio of 3:1 showed significant percentage of voids due to low adhesion between resin and banana fiber, while other two sample performed well due to good interface bonding between jute fiber and matrix (resin). Based on water absorption test, the banana-fiber sample having excess fibers showed high water absorption due to presence of significant polar hydroxide group and voids. As the percentage of jute fiber increased in composite, water absorption decreased as jute is bast fiber and have more percentage of lignin which is more than cellulosic compound. The thermal conductivity of three samples is measured by guarded heat flow meter between 30 and 120 °C. Due to the evaporation of moisture content in fibers, the thermal conductivity found to increase. The is a significant effect on thermal conductivity of fiber loading in the composite sample.

with high content of jute fiber showed less thermal conductivity due to very less water absorption tendency, whereas composite with high banana-fiber percentage showed high thermal conductivity due to water absorption tendency, i.e., the thermal conductivity of composite with high jute fiber content showed the decrease in thermal conductivity by 34.16% and composite with high banana-fiber content showed the decrease in thermal conductivity by 31.13%.

According to study, as per study, the composite material with banana-jute fiber ratio of 1:3 exhibits appreciable thermal insulation properties which makes it suitable for building construction and automobile components reducing the dependency on conventional material for insulation and other applications [6].

### 3 Materials and Fabrication Process

#### 3.1 Fibers and Resin (Matrix)

Natural fibers like hemp and hemp-linen hybrid of 150–170/cm<sup>2</sup> of thread count in the form of mat bi-directionally woven as shown in Fig. 1 used to manufacture biocomposites and were supplied by Compact Buying Services, Faridabad, Haryana, India. Epoxy resin is used as a matrix for fabrication which was sourced by Alcos India Pvt. Ltd., Meerut, Uttar Pradesh.

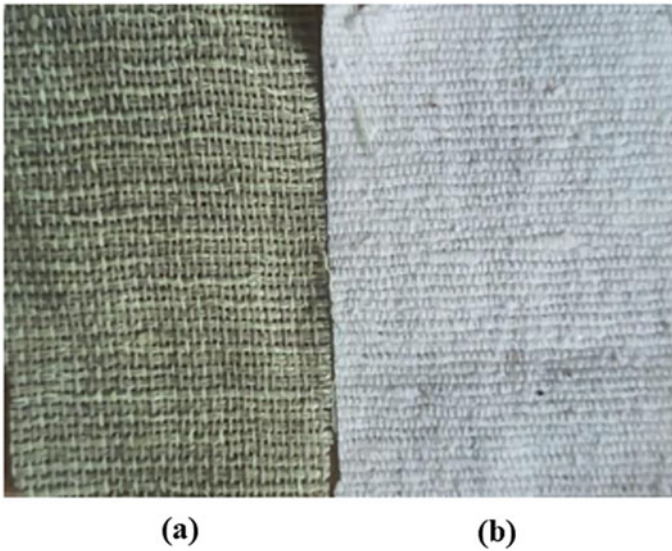


**Fig. 1** a Hemp-linen mat; b hemp mat

### **3.2 Manufacturing Technique**

For the manufacturing of reinforced biocomposites, hand layup process was used as shown in Fig. 2. The fiber content by weight used in fabrication was around 23–26%. In case of hybrid fiber mat, the ratio of constituents was 3:2, i.e., hemp and linen. To create a laminated sheet of composite, two iron plates were used. Firstly, the surface preparation before initiating the fabrication process and for that a coat of silica gel/wax was applied on the face of mold. It acts like a releasing agent or to prevent the sticking of the surface of the mold with resin coat. After applying the coat of a releasing agent, a coat of resin was applied which is a mixture of resin and hardener in ratio of 2:1. The next step was to carefully place the fiber mat/chopped fiber/long fibers according to desired properties on the coat of the resin by a roller, the fiber sheet was covered by resin by pushing the fiber sheet into resin coat. After making the first fiber sheet completely we, another coat of resin was applied and another layer of fiber sheet was placed over it [7]. Until the desired thickness achieved the process was repeated. After this, the second plate of iron coated with silica gel is placed over the fresh site of composite, and some weight around 10–15 kg was placed uniformly on the iron plate to make the interface bonding between fiber and resin uniformly and to remove air bubbles got trapped while fabrication process. Another reason of putting some amount of weight is to fill the voids that is between the fibers and made due to incomplete bonding between fiber and resin due to viscosity of resin which was impossible without exerting pressure. If voids were not taken into consideration, it may lead to the failure of composite material due to break down from the section where voids are present. After placing the second iron plate, the wet composites



sheets were left over for 48 h to get freeze/settle according to the curing duration of epoxy resin. To prepare the biocomposites, four sheet of hemp-linen mat and hemp mat of 210 \* 297 mm dimension were used. The quantity of resin consumed in the fabrication of hemp-linen composite was 465 ml and for hemp composite was 620 ml. According to curing duration of resin, it took 48 h to get the composites prepared. The upper plate was carefully removed as shown in Figs. 3 and 4 and the composites were taken out. The irregular edges were trimmed out by a cutter and excess silica gel was cleared off by tissue paper. After preparing the reinforced composite sheet, they got cut into pieces according to ASTM dimension standards, i.e., ASTM D3039 for tensile testing and ASTM D 790 for flexural testing shown in Figs. 5, 6 and 7. The total number of fiber mat were four used in the preparation each hemp-linen and hemp-reinforced biocomposite to achieve thickness of 4 mm as per ASTM standard.

**Fig. 2** Schematic diagram of hand layup technique

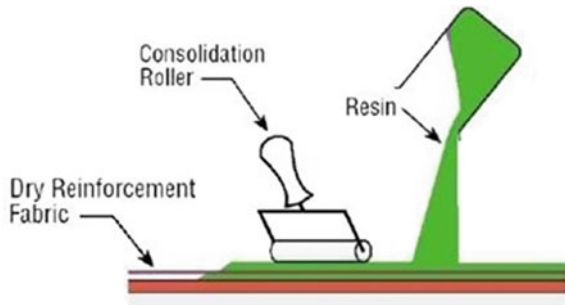


**Fig. 3** Hemp-epoxy-reinforced biocomposites





**Fig. 4** Hemp-linen hybrid and epoxy-reinforced biocomposites

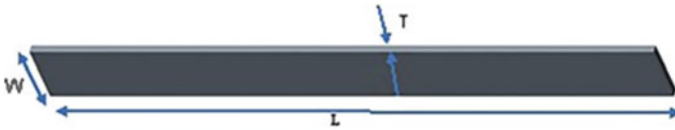


**Fig. 5**  $L = 250$  mm;  $W = 25$  mm;  $T = 4$  mm (specimen dimensions according to ASTM D3039) (for tensile testing)

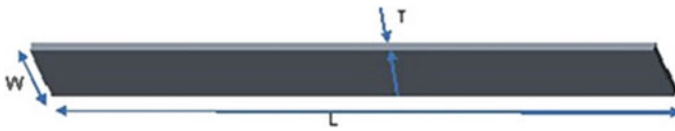


**Fig. 6**  $L = 127$  mm;  $W = 13$  mm;  $T = 4$  mm (specimen dimensions according to ASTM D790) (for flexural testing)

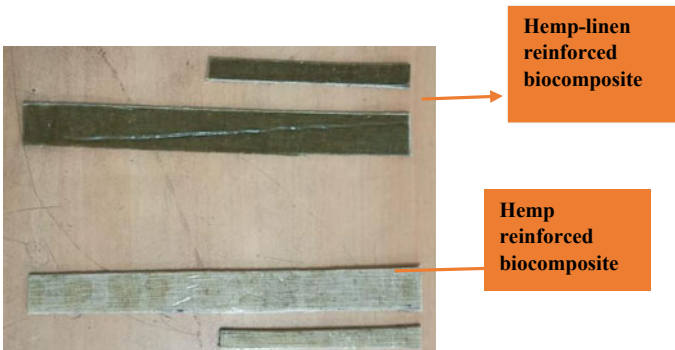


**Fig. 7** Hemp-linen and hemp-reinforced biocomposites according to ASTM dimension standards

## 4 Mechanical Characterization

### 4.1 Tensile Testing

The samples of biocomposites were prepared according to ASTM 3039 (ASTM standard D3039 2008) [8] which is for to measure the force required to break polymer-based composites. To conduct the tensile test, Banbros WDW-5 was taken in use having speed of 5 mm/min at ITS Engineering College, Greater Noida, Uttar Pradesh as shown in Fig. 8. While conducting test, a stress-strain curve was obtained for hemp-linen composite and hemp composite as depicted in Fig. 9.

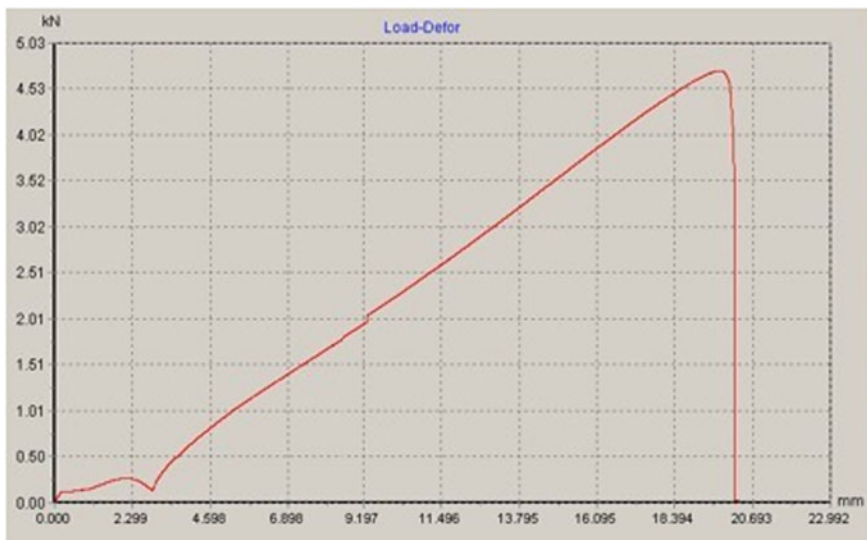
In Fig. 9, the result of experiment done on hemp-linen and hemp-reinforced biocomposites by Universal Testing Machine for tensile modulus elongation before break is depicted in detail. Fusion of various reinforced fiber mat such as hybrid of hemp- linen hemp fiber mat in with matrix (resin) increased the tensile strength to various extant depending on interfacial bonding between fiber and resin, strength of fiber and percentage of voids left in composite after curing.

According to experiment result, the hemp-linen-reinforced biocomposite performed well with 53.6 kN of tensile strength while hemp-reinforced biocomposites exhibited 48.00 kN of tensile strength while testing as depicted in Fig. 10. The developed composites performed well as compared to neat epoxy biocomposites that have tensile strength between 35 and 50 kN depending upon the polymer structure and other parameters like thermal stability, curing time, etc. There are a variety of reasons for the influence of the properties of composites such as good interfacial adhesion between fiber reinforcement and polymer matrix, selection of manufacturing process,

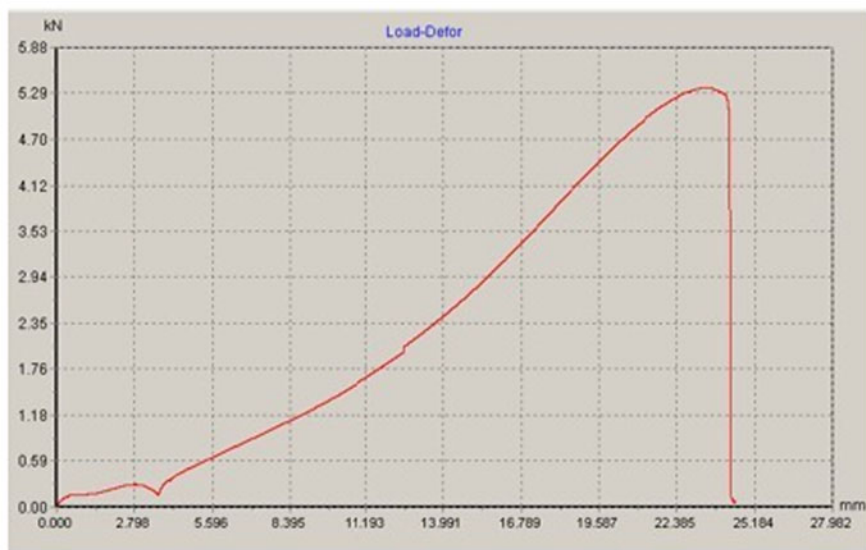


(a) Hemp-linen/epoxy reinforced biocomposites under tensile strength testing      (b) Hemp-epoxy biocomposites under tensile strength testing

**Fig. 8** Tensile strength test of **a** hemp-linen/epoxy composite **b** hemp-epoxy biocomposites



(a)



(b)

**Fig. 9** Stress versus strain curve diagram obtained during tensile test **a** hemp-linen **b** hemp-reinforced composites

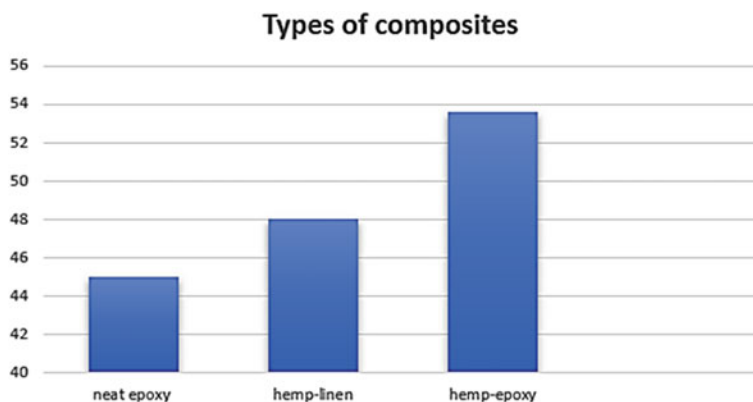


**Fig. 10** Tensile strength of composites (neat epoxy, hemp-linen, hemp-epoxy)

percentage of reinforcement and matrix etc. Tensile test helps to determine the various properties such as ductility and brittleness while elongation before getting break. The hemp-linen-reinforced biocomposites showed the maximum percentage elongation of 41.5% while hemp-resin infused biocomposites exhibited 34.6% of elongation at max load which depicts the ductility and brittleness of materials.

Tensile strength in case of hybrid composite (hemp-linen) is affected by several factors such as different surface properties of fibers present in the reinforced woven mat, i.e., interaction of fiber surface with matrix and due to direction or orientation of the applied resin while preparation of composites, the nature of composite to respond according to the load varies at different point in composites due to the direction of lamination in while fabrication. In case of single fiber composite, the tensile strength depends on various factors such as, woven pattern, fiber diameter, interfacial interaction between fiber and matrix and percentage of voids cured/left while fabrication process.

## 5 Flexural Test

The three-point bending test was performed on Instron Universal Testing Machine to calculate the various flexural properties of different biocomposites as depicted in Figs. 11 and 12. Flexural strength of the developed biocomposites showed a good enhancement because of expected interfacial adhesion between fiber and resin in hemp-linen and hemp-epoxy biocomposites as depicted in Fig. 13. Hybrid reinforced biocomposite of hemp-linen withstand the maximum load of 169.1 kN which was more then expected while on the other hand composite of hemp fiber reinforced in resin withstand the maximum load of 34.8 kN which is also more then expectation as hemp fiber exhibits less tensile strength compared to linen fiber [9].

There are certain parameters which directly influence the properties of composites such as different reinforced woven fiber mats (unidirectional, bidirectional, chopped), surface properties of fiber reinforcement etc. Which also affects the interfacial adhesion between fiber and matrix.

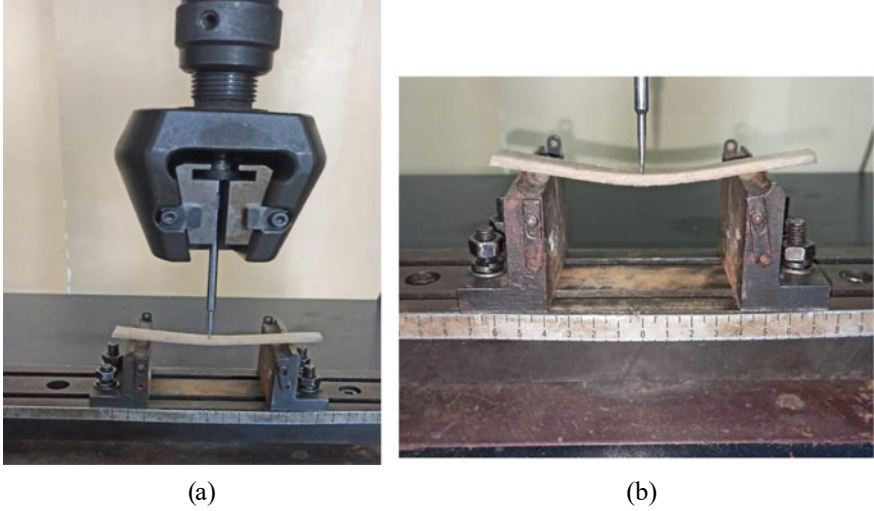


**Fig. 11** Three-point bending test of **a** hemp-linen/epoxy-reinforced composite and **b** hemp/epoxy-reinforced biocomposites

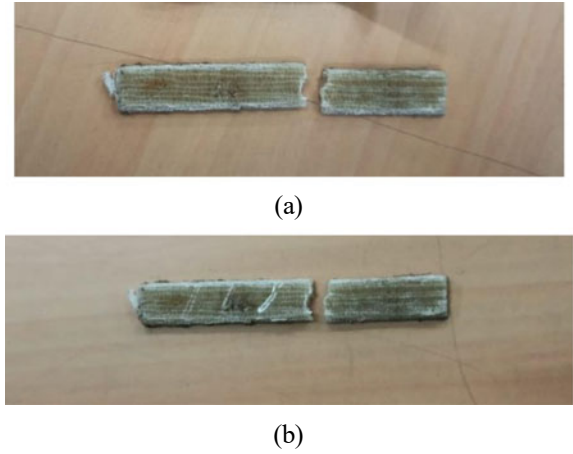
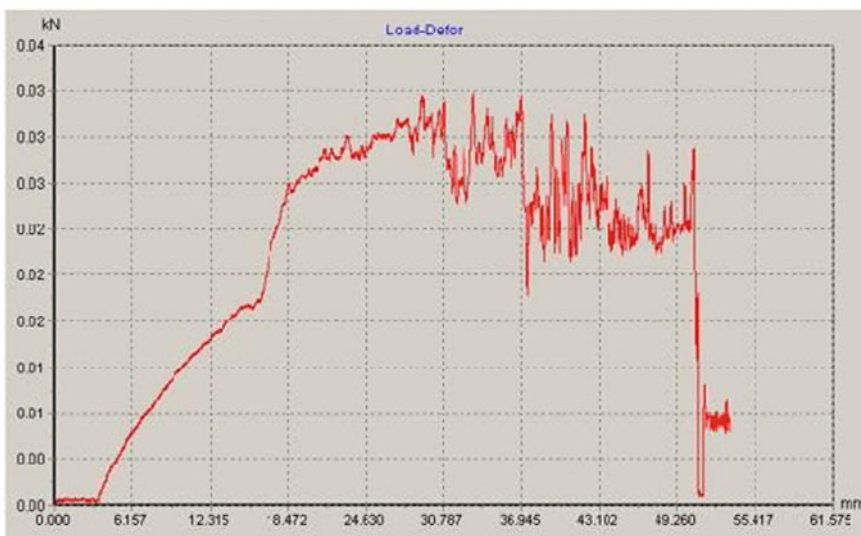


**Fig. 12** Effect of bending force in **a** hemp-resin reinforced biocomposite **b** hemp/line-resin reinforced biocomposite



(a)



(b)

**Fig. 13** Load versus extension curve while flexural test: **a** hemp-linen/epoxy **b** hemp/epoxy

## 6 Interface Observation

To study the interface behavior against fracture happened while performing tensile test and flexural test, scanning electron microscopy was used as shown in Figs. 14 and 15. Firstly, the samples went through gold plating with the help of vacuum gold plating apparatus to create a conductive surface for electrons in SEM. As the gold plating was done, multiple photographs were taken of both hemp-linen hybrid biocomposite and hemp biocomposites to study the influence of tensile test and flexural test which led to various categories of failure as a result causing fiber rupture, bond breakage between fiber matrix due to pulling effect and bending. SEM also helps to pin out the basic reasons responsible for the failure of a biocomposites such as uniformity of matrix throughout the composite, percentage of voids and distortion in fiber orientation while fabrication process. These factors act as keywords to study the structure of biocomposites after going through certain type of testing at microscale level. The quality of bonding between fiber and matrix (resin) primarily depends on the texture of fiber doesn't matter whether it is natural fiber or synthetic [1] (Fig. 16).

The diameter of threads in fiber mat affects the surface property in good or bad way. If the diameter of thread is less then the degree of adhesion/bonding between fiber and matrix will be good as the percentage of voids will be less. if the diameter of thread in a fiber mat is more then there will be significant number of voids which will lead to improper bonding between fiber and matrix ending with underperformance of composite. The uniformity of bonding between fiber and matrix also usually gets hampered by the properties of matrix (resin) such as viscosity and stability used while preparation. If the viscosity of resin is high, then the chances of generation of voids are higher as due to high surface tension and phenomenon of capillary repulsion which results in formation of voids or vacuum space between the crosslinks of thread in mat weakening the inconsistent adhesion between matrix and fiber. There is another reason which if it is ignored can affect the performance of composite and might

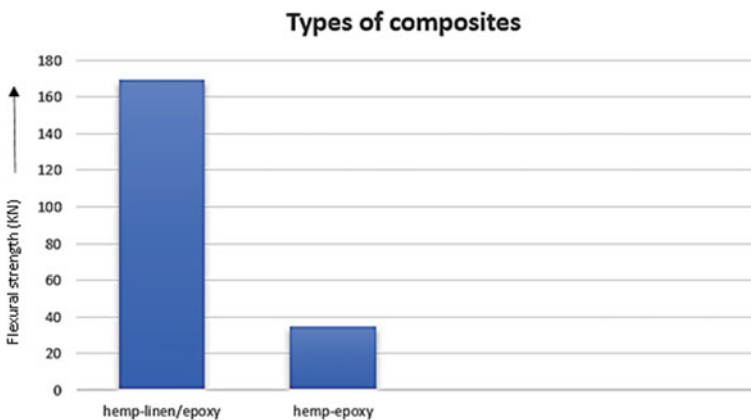


**Fig. 14** Flexural strength of hemp-linen/epoxy biocomposite and hemp-epoxy biocomposite



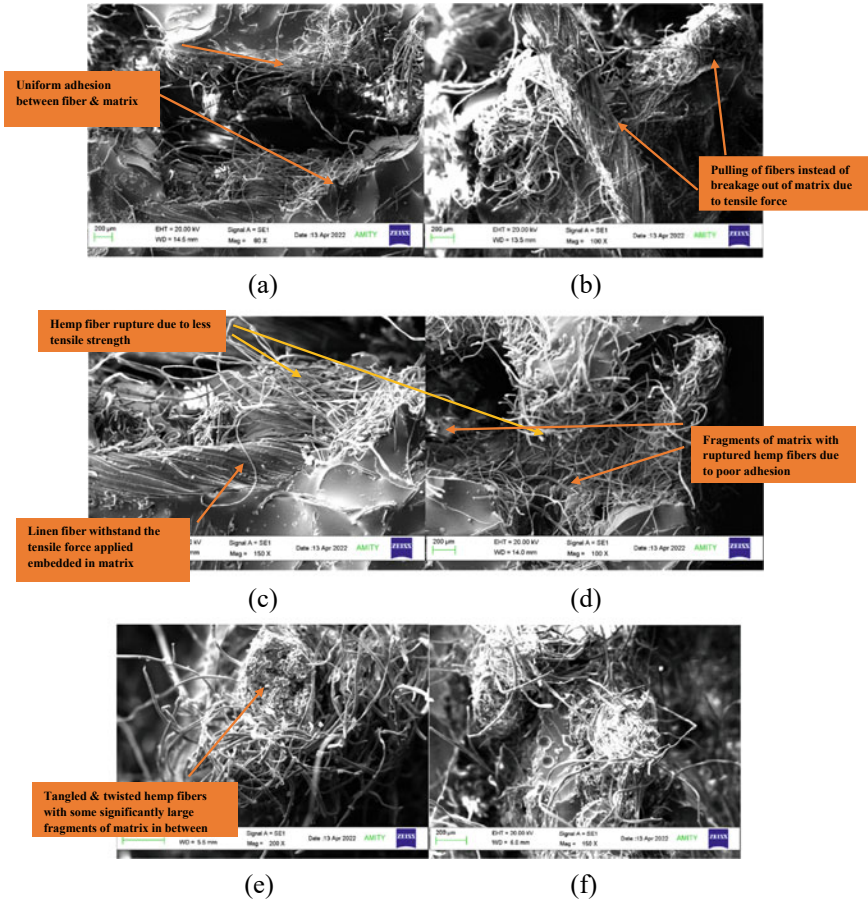


**Fig. 15** Ruptured surface of hemp/linin/epoxy (a–c) and hemp/epoxy composites after going through tensile testing (d–f)

not be able to withstand the expected load that is impurity. If certain amount of oil, gel or wax is present on the fiber, it can influence the adhesion between the matrix (resin) and natural fiber mat. This generally happens while fabrication doing surface preparation which is very first step before putting a layer of resin and fiber in mat or any other form. When natural fiber or resin solution encounters with hands or tools contaminated with oil or wax, the chances of inconsistent bonding between fiber and resin become prominent [1, 7].

To calculate the maximum flex limit of biocomposites, flexural test was performed using three-point bending test under gradual loading with speed of 5 mm/min and as similar to tensile strength testing, there are certain factors here too such as surface and mechanical characteristics, woven orientation, presence of any sort of contamination, etc., can influenced the performance of biocomposites sample while going

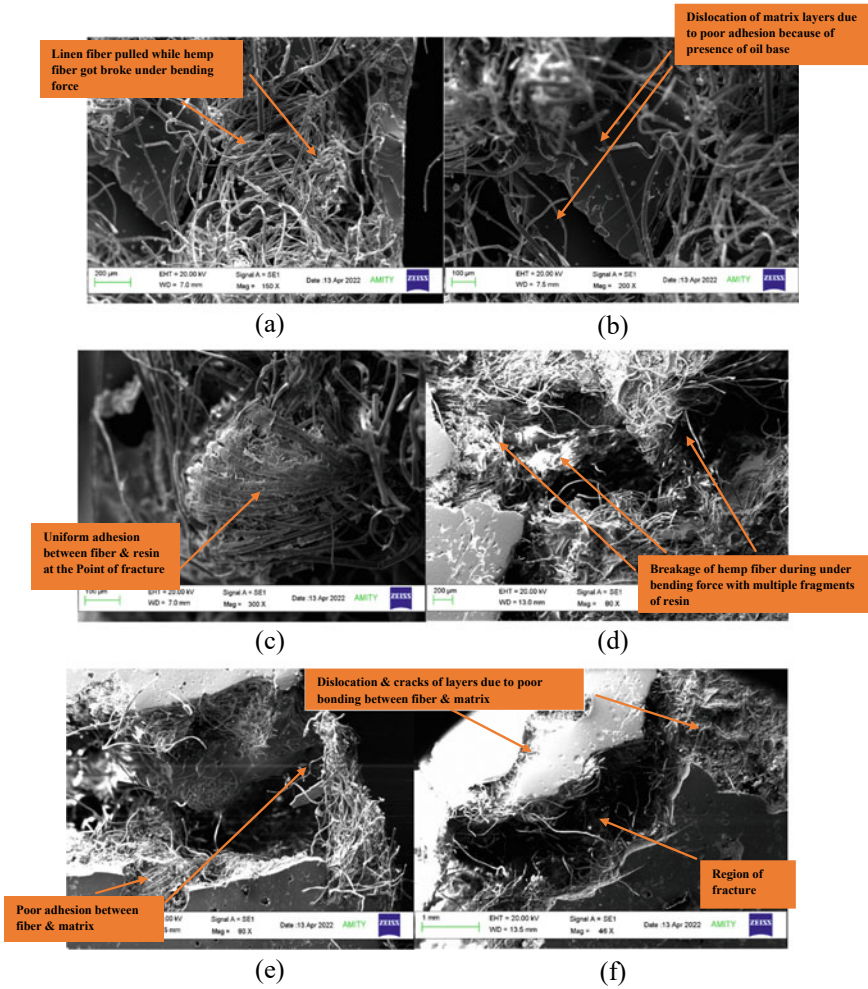


**Fig. 16** Ruptured surface of hemp/linen/epoxy and hemp/epoxy after going through flexural test

through testing leading to distortion in matrix and fiber interface, fiber breaking, breakdown of composite into its constituent layers and breaking of matrix into small fragments or edgy chips. According to test result and photographs recovered from SEM, it was noticed that hemp/linen/epoxy-reinforced biocomposites performed while withstanding against max load of 169.1 kN with minimum layer breakdown and fiber breakage. hemp/epoxy-reinforced biocomposite was able to cope 34.8 kN of load before showing significant fiber breakage and layer breakdown. Through result it was clear that the surface properties play an important role to judge the strength of a composite. Natural composites with high thread diameter tends to fail early while testing as the percentage of voids hampers the adhesion between fiber and matrix.

Increasing the thread count and decreasing the diameter of thread, adhesion between fiber and matrix can be increased significantly.

## 7 Conclusion

To conduct this study, sample of hemp/epoxy biocomposite and hybrid biocomposite of hemp/linen/epoxy was prepared using hand layup technique to conduct the testing of various mechanical properties and to study the impact of certain types of tests on microstructure of biocomposite using SEM.

The points which can be concluded in this study are:

1. According to experimental results, it is clear that the strength of biocomposites can be enhanced by using hybrid structure of reinforced fibers, i.e., by doing doping of fibers of different characteristics. Hybrid structure of hemp/linen was used to enhance both strength and flexibility. As a result, hemp/linen/epoxy biocomposites was able to take ultimate tensile load of 53.6 kN and flexural load of 169.1 kN.
2. Hemp/epoxy biocomposites didn't performed well, with 34.8 kN flexural load and 48 kN of tensile load. There are multiple reasons behind the poor performance such as insufficient adhesion between matrix and fiber due to vacuum space/voids present in interface between matrix and fibers.
3. By increasing the thread count and decreasing the thread diameter, both flexural and tensile strength can be enhanced.
4. Through SEM, the impact of tensile and flexural loading on microstructure of biocomposites is depicted clearly.

## References

1. Chaudhary V, Bajpai PK, Maheshwari S (2018) Studies on mechanical and morphological characterization of developed jute/hemp/flax reinforced hybrid composites for structural applications. *J Nat Fibers* 15(1):80–97
2. Das PP, Chaudhary V (2010) Tribological and dynamic mechanical analysis of bio-composites: a review. In: *Materials today: proceedings*
3. Du Y, Wu T, Yan N, Kortschot MT, Farnood R (2013) Pulp fiber-reinforced thermoset polymer composites: effects of the pulp fibers and polymer 48:10–17
4. Adekunle K, Cho SW, Patzelt C, Blomfeldt T, Skrifvars M (2011) Impact and flexural properties of flax fabrics and Lyocell fiber-reinforced bio-based thermoset. *J Reinf Plast Compos* 30(8):685–697
5. Zhang MH, Chen JK, Zhao F, Bai SL (2016) A new model of interfacial adhesive strength of fiber-reinforced polymeric composites upon consideration of cohesive force. *Int J Mech Sci* 106:50–61
6. Devireddy SBR, Biswas S (2016) Thermo-physical properties of short banana-jute fiber-reinforced epoxy-based hybrid composites. *Proc Instit Mech Eng (Part L J Mater Des Appl)*

7. Chaudhary V, Bajpai PK, Maheshwari S (2018) Effect of moisture absorption on the mechanical performance of natural fiber reinforced woven hybrid bio-composites. *J Nat Fibers* 1–1 (2018). <https://doi.org/10.1080/15440478.2018.1469451>
8. Standard DA (2008) Tensile properties of polymer matrix composite materials. ASTM International, West Conshohocken. [www.astm.org](http://www.astm.org)
9. Standard DA (2010) Standard test methods for flexural properties of unreinforced and reinforced plastics and electrical insulating materials. ASTM International, West Conshohocken (2010). <http://www.astm.org>

# Al 6063 Hybrid Metal Matrix Reinforced Composites with TiC Nanoparticles and NEEM Leaf Ash Using Stir Casting Method for Bicycle Frame



Umesh Kumar Vates, Nirav Khattar, Rohit Kumar, Ansh Bhardwaj, Bhupendra Prakash Sharma, Nand Jee Kanu, Eva Gupta, Gyanendra Kumar Singh, and Sivaraos Subramanian

**Abstract** Aluminium metal matrix composites (AMMCs) are the trustful materials for marine, aerospace, defence, advanced structural, aviation applications and also in automobile vehicles due to its favourable properties. The hybrid metal matrix composites are manufactured using stir casting process, which is the simplest and most convenient form of manufacturing a material. In this present research work, aluminium alloy 6063 has been bolstered with TiC and neem leaf ash. Seven samples have been fabricated sample 1 (Al 6063 hundred%), sample 2 (Al 6063 ninety-five% + TiC 4% + neem ash 1%), sample 3 (Al 6063 ninety-six and half % + TiC 2% + neem leaf ash 1.5%), sample 4 (Al 6063 ninety-three and half % + TiC 6% + neem leaf ash half%), sample 5 (Al 6063 ninety-seven and half % + TiC 2% + neem leaf ash half %), sample 6 (Al 6063 ninety-five and half % + TiC 4% + neem leaf ash half %) and sample 7 (Al 6063 ninety-three% + TiC 6% + neem leaf ash 1%). After manufacturing these samples, the hardness test, strength and fatigue test have been

---

U. K. Vates (✉) · N. Khattar · R. Kumar · A. Bhardwaj · B. P. Sharma  
Mechanical Engineering Department, ASET, Amity University Uttar Pradesh, Noida, India  
e-mail: [u.k.vates@gmail.com](mailto:u.k.vates@gmail.com)

N. J. Kanu (✉)  
Mechanical Engineering Department, S. V. National Institute of Technology, Surat, India  
e-mail: [nandssm@gmail.com](mailto:nandssm@gmail.com)

Mechanical Engineering Department, JSPM Narhe Technical Campus, Pune, India

E. Gupta  
Electrical Engineering Department, ASET, Amity University Uttar Pradesh, Noida, India

Electrical Engineering Department, TSSM's Bhivrabai Sawant College of Engineering and Research, Pune, India

G. K. Singh  
Mechanical Engineering Department, School of Mechanical, Chemical and Materials Engineering, Adama Science and Technology University, Adama, Ethiopia

S. Subramanian  
Manufacturing Engineering Department, Universiti Teknikal Malaysia Melaka, Melaka, Malaysia

conducted. Optimal combination of TiC and neem leaf ash particles in the Al matrix is improving mechanical properties as per the desire for bicycle frame.

**Keywords** Aluminium 6063 grade · TiC nanoparticles · Neem leaf ash · Stir casting process · Aluminium metal matrix composite · Wear properties

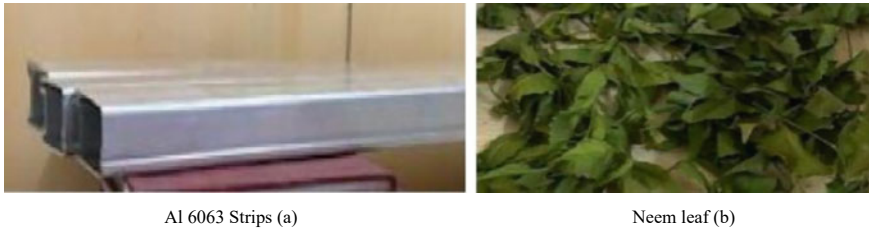
## 1 Introduction

Aluminium metal matrix composites are the most widely used in automotive components to increase their strength. MMCs are the toughened material also which do not lose their parent properties at various environmental condition. Process methods to make aluminium composites are the critical factors to change the mechanical, physical and metallurgical properties of MMCs [1–3]. It possesses high strength to weight ratio for wider applications even in bicycle frame application. MMCs are being reinforced with various nanofillers to further improve the specific properties. Properties of composites are mainly concern on the properties of their constituent materials, their distribution in the matrix and the interaction among them. Metal matrix composites (MMCs) generally offer higher specific strength, higher stiffness and better wear resistance resulting in increasing use in the aerospace, automotive and biomedical industries [4–6]. Popular reinforcement materials for these composites are silicon carbide, silicon nitride, boron carbide, alumina particles, with aluminium, titanium and magnesium being the most common matrix materials [7–10]. The aluminium-based composite materials having ceramic reinforcements are found to reveal improved quality, specific strength, higher temperature properties, higher wear resistance and lower thermal expansion coefficient with better corrosion resistance in comparison with their base alloy matrixes [11–13]. At present, more research consideration is being directed towards identifying hybrid composites having more than one reinforcing component.

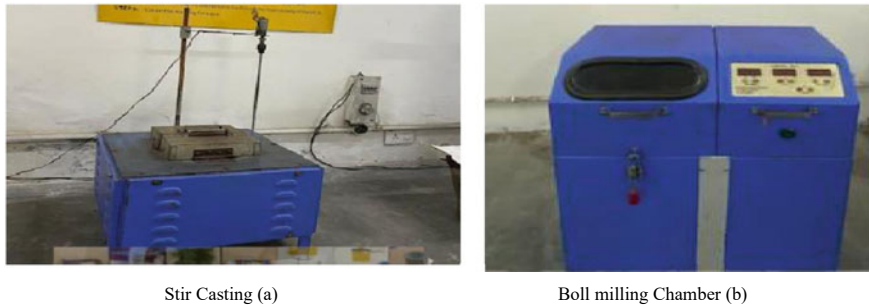
## 2 Experimentations

In present work, hybrid reinforcements like TiC and neem leaf ash have been explored to improve the aluminium metal matrix composite. Figure 1 represents that Al6063 aluminium alloys strips for matrix were arranged for the experimental purpose and neem leaf were burned and ash prepared. Neem ash was also ground for the hybrid reinforcement.

In this study, aluminium have been taken as a matrix, and TiC is primary reinforcement particle. TiC is one of the best reinforcements in making composite with aluminium which has already been proved by many researchers. Neem leaf is being used as hybrid reinforcements [14–16].



**Fig. 1** Al 6063 matrix and neem leaf



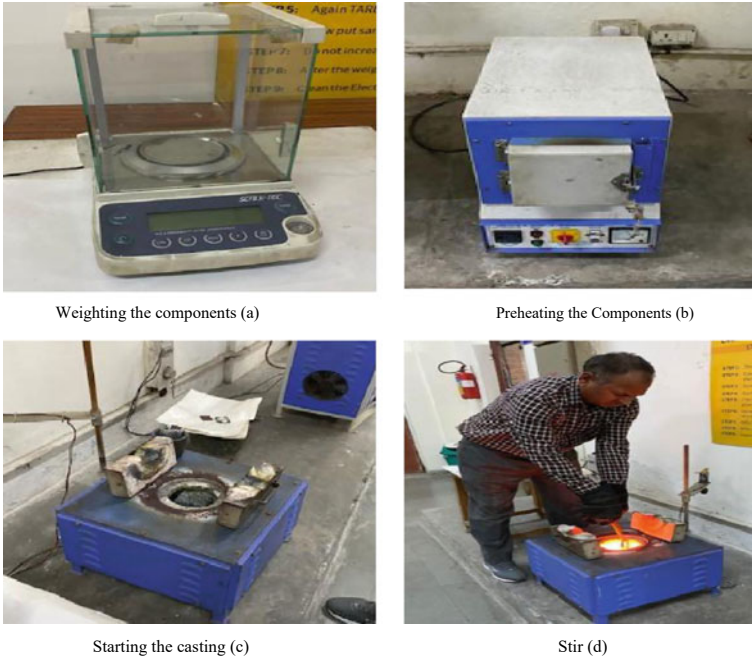
**Fig. 2** Stir casting setup

Figure 2a is the stir casting setup to perform the stir casting process to make the metal matrix composite at various conditions as the design of experiments. Figure 2b is the ball milling setup it being used to mixing of the reinforcements like TiC and neem ash at different ratios. Both the reinforcements were taken at various weight ratio and mixed at various speed and total span of time as per the design of experiments [17–20].

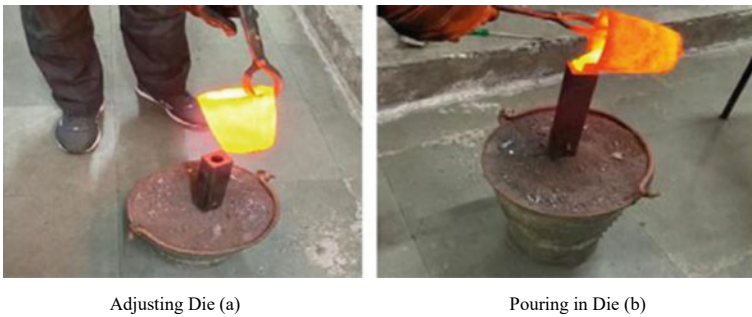
It is evident that the reinforcement quantities of TiC and neem leaf were calculated in weight ratio in milligram and performed the weighting process as Fig. 3a. Figure 3b is the preheating chamber to remove the moisture contents in the reinforcements. Preheat processes were generally performed for 30 min and at 250 °C, and it was constant for every samples. Moisture contents and foreign particles were generally removed from the mixed reinforced particles [21–23]. Figure 3c is the stir casting setup which are having the provision of for pencil heater having capacity 1 KW each. Figure 3d is concern to live stir casting process at 1150 °C.

Figure 4a is the live demonstration of molten material in crucible and it is pouring in designed die to make the desire shaped specimen as shown in Fig. 4b. Generally, it is heated as per the designed temperature limit and after successfully pouring it may be allowed sufficient time for proper solidifications with constant cooling rate [24–26].





**Fig. 3** Weighing and stir casting



**Fig. 4** Pouring of molten materials in die

### 3 Result and Discussion

Experiments were conducted using specific components for each sample and passed through stir casting process.

Stir casting process parameters were also selected critically depending on the literature. Conducted process with their responses were given in Table 1.



**Table 1** Stir casting experiments using critical parameters and their responses

Sl. No	Stir casting temperature in °C	Stirring time (m)	Percentage of Al6063 matrix	Percentage of TiC nanoparticles (W <sub>1</sub> )	Percentage of Neem leaf ash (W <sub>2</sub> )	Hardness (BHN)	Compressive strength (KN)	Fatigue test (RPM)
1	955	0	100	0	0	53.33	53	1256
2	1055	2	95	4	1	226.15	57	2086
3	1155	4	96.5	2	1.5	155.9	55	1977
4	955	6	93.5	6	0.5	309.6	59	2563
5	1055	2	97.5	2	0.5	155.8	55	1833
6	1155	4	95.5	4	0.5	246.2	56	1982
7	955	6	93	6	1	312.1	60	2688

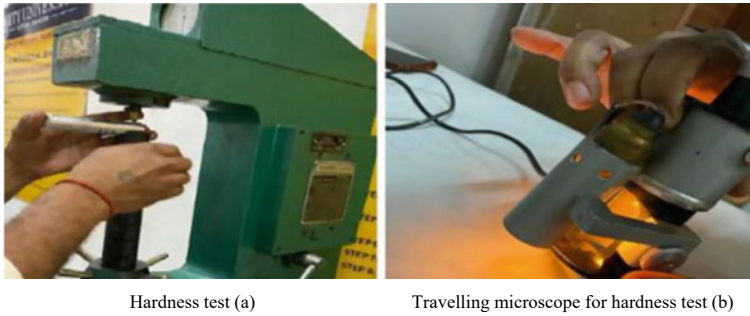


**Fig. 5** Conducting hardness test

Figure 5a indicates about hardness test of produced samples. It has provision to apply pressure and produced indentation on the test sample under the given conditions [27–30]. Depending on the available hardness of sample, indentation diameters generally appear on the surface [31–37]. This indentation diameters are being measured with help of travelling microscope as shown in Fig. 5b.

The universal testing machine where tensile and compressive strength test is being conducted for all the specimen is shown in Fig. 6.

Figure 7 is the live demonstration of fatigue test which have been conducted for all the samples. Round per minutes were recorded for each sample where it was got failure. Test was conducted on the available setup where provision available to hold the sample at one end of motor and supporting end. RPM was recorded at the failure points.

Figures 8, 9 and 10 are the scanning electron microscopy test results for the optimal sample at various magnification stages. It is directly indicating the homogeneous distribution of the reinforcement and its hybrid reinforcements in the composite. Sometimes the white spots are the carbide formed due to rapid cooling rate which are the very hard structures. Gold sputtering was made on the optimal sample as shown in Fig. 13. It helps to fill the peak and bellies appeared on the test sample surface. Gold sputtering is also done because there are some non-conducting reinforcements added in it. Figure 11 indicates the percentage distribution of the elements inside the test sample. Figure 12 and Table 2 are concern to the macrograph of test sample and its percentage distributions with atomic weight.

Figures 14, 15 and 16 have been plotted between critical stir casting process parameters, material properties and responses like harness, compressive strength and fatigue strength. It is evident from Fig. 14 that hardness is increasing with low value of stir temperature, high stir time, low Al percentage, high percentage of TiC combination and moderate value of neem ash to revile the high hardness. Similarly, in Fig. 15, it is indicated that compressive strength may be increased with low value of stir temperature, high stir time, low Al percentage, high percentage of TiC combination and moderate value of neem ash. Also in Fig. 16, fatigue strength are increasing with low value of stir temperature, high stir time, low Al percentage,



**Fig. 6** Conducting tensile strength test on UTM



Fatigue test setup (a)



Sample for fatigue test (b)

**Fig. 7** Conducting tensile strength test

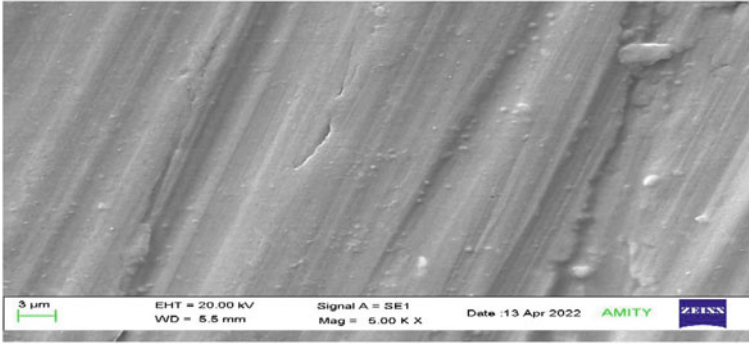


Fig. 8 Scanning electron microscopy 1

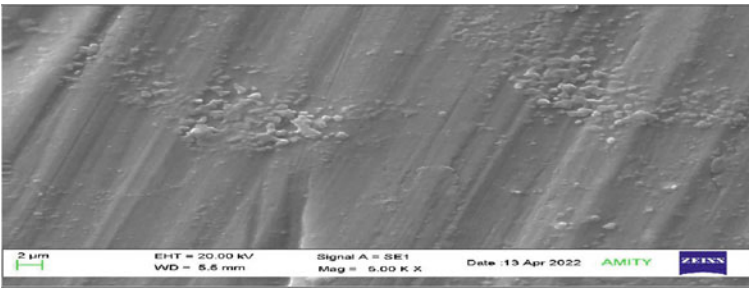


Fig. 9 Scanning electron microscopy 2

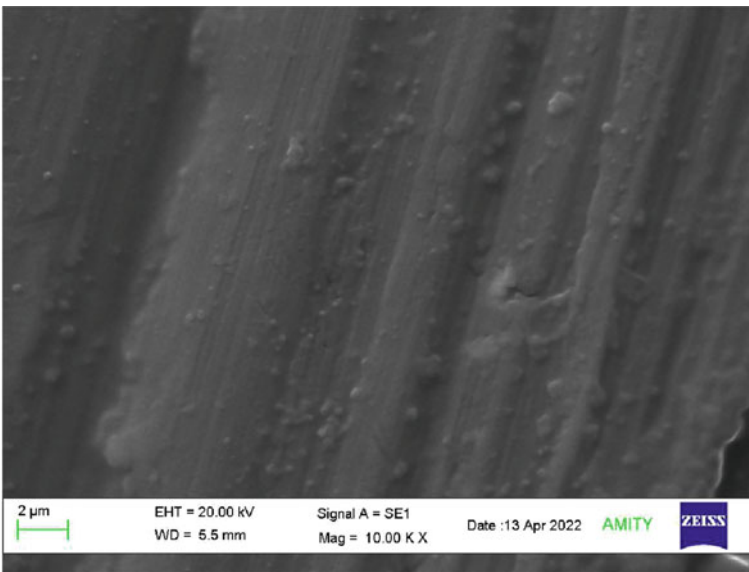


Fig. 10 Scanning electron microscopy 3

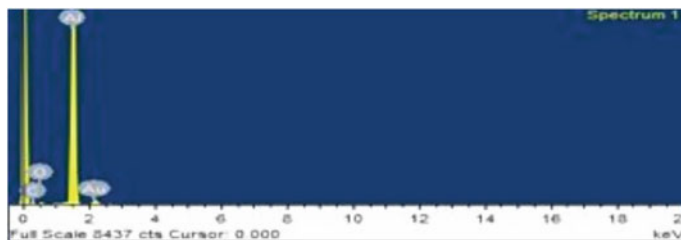


Fig. 11 EDX micrograph for the sample for optimal result

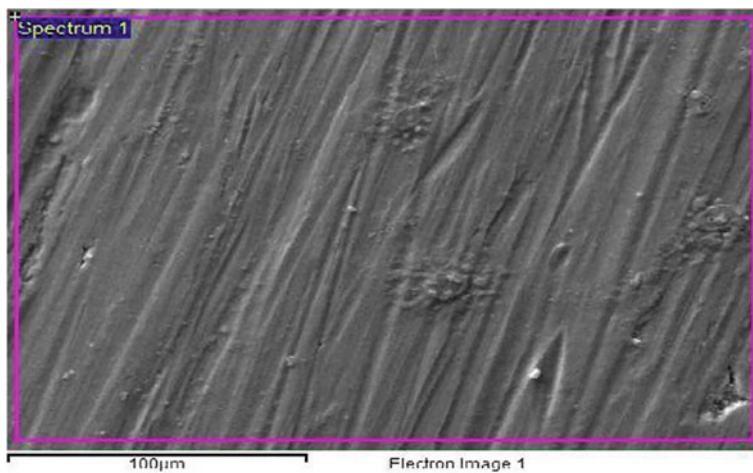


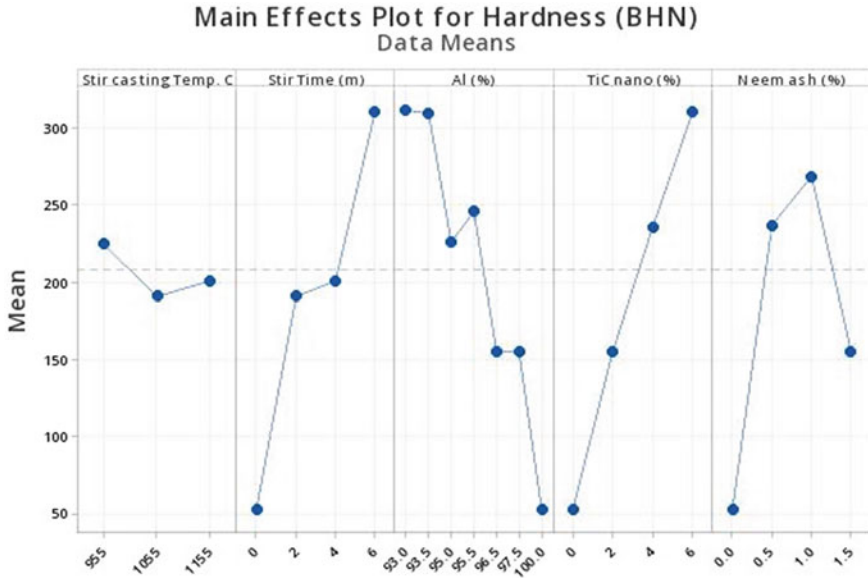
Fig. 12 SEM image for the sample giving optimal result



Fig. 13 Gold sputtering on optimal composite sample

**Table 2** Composition in the test sample

Element	Weight%	Atomic%
C K	23.55	42.16
O K	6.55	8.80
Al K	60.21	47.98
Ti K	0.03	0.01
Au M	9.67	1.06
Totals	100.00	



**Fig. 14** Main effect plots on stir casting parameters versus hardness (BHN)

high percentage of TiC combination and moderate value of neem ash. In Fig. 17, all the above relations are also represented in terms of surface plot.

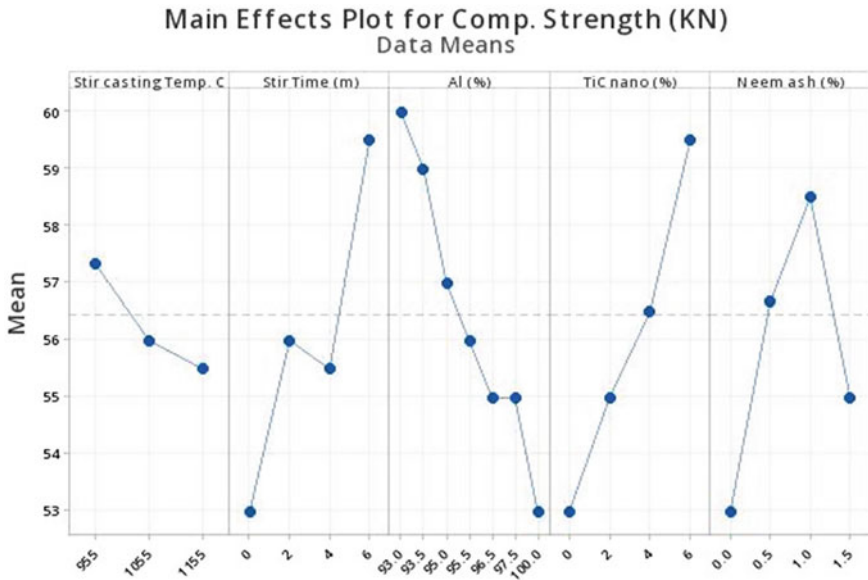


Fig. 15 Main effect plots on stir casting parameters versus comp. strength (KN)

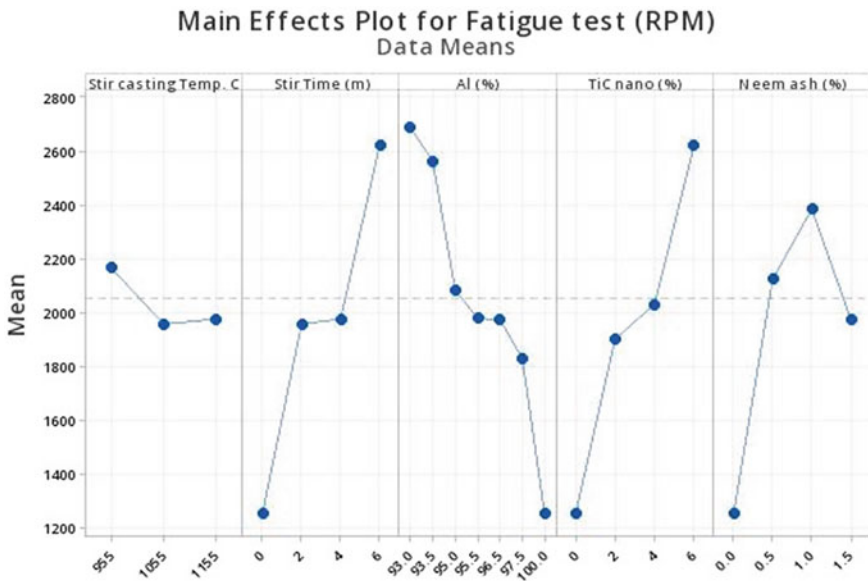
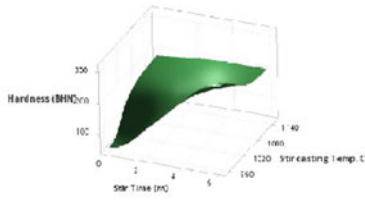


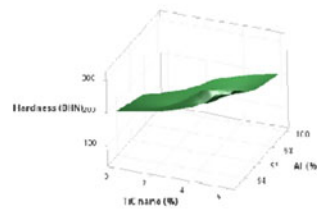
Fig. 16 Main effect plots on stir casting parameters versus fatigue (RPM)

Surface Plot of Hardness (BHN) vs Stir casting Temp. C, Stir Time (m)



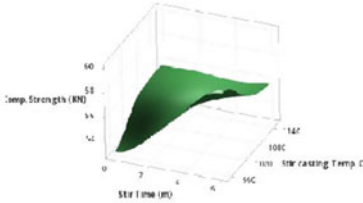
(a) Stir Casting Parameters Vs. BHN

Surface Plot of Hardness (BHN) vs Al(%) ,TiC nano (%)



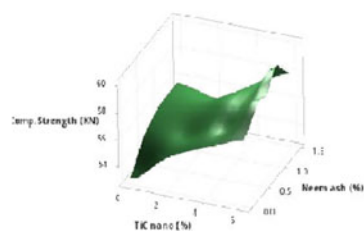
(b) Stir Casting Parameters Vs. BHN

Surface Plot of Comp. Strength ( vs Stir casting Tem, Stir Time (m)



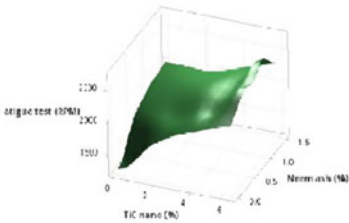
(c) Stir Casting Parameters Vs. M

Surface Plot of Comp. Strength (KN) vs Neem ash (%), TiC nano (%)



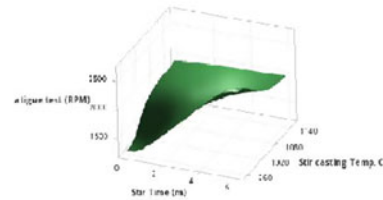
(d) Stir Casting Parameters Vs. M

Surface Plot of Fatigue test (RPM) vs Neem ash (%), TiC nano (%)



(e) Stir Casting Parameters Vs. RPM

Surface Plot of Fatigue test (RP vs Stir casting Tem, Stir Time (m)



(f) Stir Casting Parameters Vs. RPM

Fig. 17 Surface plots on stir casting parameters versus selected responses

### 4 Conclusion

It has been observed that bicycle frame generally get failure due to fatigue loading condition and road jerks. In this work, it was depicted that higher the TiC amount reinforcement makes sample higher compressive strength, high hardness and lower chances to fatigue failure. Similarly higher the neem ash amount plays an important role in increasing the mechanical properties as required for bicycle frame. It is suggested that high amount of TiC nanocomposite with neem leaf ash will be more suitable composite materials for bicycle frame applications.



## References


1. Kanu NJ, Gupta E, Vates UK, Singh GK (2019) An insight into biomimetic 4D printing. *RSC Adv* 9:38209–38226. <https://doi.org/10.1039/C9RA07342F>
2. Kanu NJ, Gupta E, Vates UK, Singh GK (2019) Self-healing composites: a state-of-the-art review. *Compos A Appl Sci Manuf* 121:474–486. <https://doi.org/10.1016/j.compositesa.2019.04.012>
3. Kanu NJ, Vates UK, Singh GK, Chavan S (2019) Fracture problems, vibration, buckling, and bending analyses of functionally graded materials: a state-of-the-art review including smart FGMS. *Part Sci Technol* 37:583–608. <https://doi.org/10.1080/02726351.2017.1410265>
4. Vates UK, Sharma BP, Kanu NJ, Daniel NA, Subramanian S, Sharma P (2020) Optimization of process parameters of galvanizing steel in resistance seam welding using RSM. In: *Proceedings of International Conference in Mechanical and Energy Technology*, Springer, Singapore, pp 695–706. [https://doi.org/10.1007/978-981-15-2647-3\\_65](https://doi.org/10.1007/978-981-15-2647-3_65)
5. Gupta E, Kanu NJ (2020) An insight into the simplified RP transmission network, concise baseline and SIR models for simulating the transmissibility of the novel coronavirus disease 2019 (COVID-19) outbreak. *Am J Infect Dis* 16:89–108. <https://doi.org/10.3844/ajidsp.2020.89.108>
6. Kanu NJ, Patwardhan D, Gupta E, Vates UK, Singh GK (2020) Numerical investigations of stress-deformation responses in fractured paediatric bones with prosthetic bone plates. *IOP Conf Ser Mater Sci Eng* 814:012038. <https://doi.org/10.1088/1757-899X/814/1/012038>
7. Lal A, Kanu NJ (2020) The nonlinear deflection response of CNT/nanoclay reinforced polymer hybrid composite plate under different loading conditions. *IOP Conf Ser Mater Sci Eng* 814:012033. <https://doi.org/10.1088/1757-899X/814/1/012033>
8. Kanu NJ, Gupta E, Vates UK, Singh GK (2020) Electrospinning process parameters optimization for biofunctional curcumin/gelatin nanofibers. *Mater Res Express* 7:035022. <https://doi.org/10.1088/2053-1591/ab7f60>
9. Gupta E, Kanu NJ, Munot A, Sutar V, Vates UK, Singh GK (2020) Stochastic and deterministic mathematical modeling and simulation to evaluate the novel COVID-19 pandemic control measures. *Am J Infect Dis* 16:135–170. <https://doi.org/10.3844/ajidsp.2020.135.170>
10. Kanu NJ, Gupta E, Vates UK, Singh GK (2021) An insight into smart self-lubricating composites. *Smart Polym Nanocomposites Biomed Environ Appl* 85–101. <https://doi.org/10.1016/B978-0-12-819961-9.00012-8>
11. Kanu NJ, Patwardhan D, Gupta E, Vates UK, Singh GK (2021) Finite element analysis of mechanical response of fracture fixation functionally graded bone plate at paediatric femur bone fracture site under compressive and torsional loadings. *Mater Today Proc* 38:2817–2823. <https://doi.org/10.1016/j.matpr.2020.08.740>
12. Pandey V, Kanu NJ, Singh GK, Gadissa B (2021) AZ31-alloy, H13-die combination heat transfer characteristics by using inverse heat conduction algorithm. *Mater Today Proc* 44:4762–4766. <https://doi.org/10.1016/j.matpr.2020.11.258>
13. Chauhan A, Vates UK, Kanu NJ, Gupta E, Singh GK, Sharma BP, Gorrepati SR (2021) Fabrication and characterization of novel nitinol particulate reinforced aluminium alloy metal matrix composites (NiTip/AA6061 MMCs). *Mater Today Proc* 38:3027–3034. <https://doi.org/10.1016/j.matpr.2020.09.326>
14. Daniel NA, Vates UK, Sharma BP, Kanu NJ, Subramonian S (2021) Optimization of inconel die-in EDD steel deep drawing with influence of punch coating using RSM. In: *Advances in industrial and production engineering: select proceedings of FLAME 2020. Lecture notes in mechanical engineering*. Springer, Singapore, pp 721–738. [https://doi.org/10.1007/978-981-33-4320-7\\_64](https://doi.org/10.1007/978-981-33-4320-7_64)
15. Jain N, Kanu NJ (2021) The potential application of carbon nanotubes in water treatment: a state-of-the-art-review. *Mater Today Proc* 43. <https://doi.org/10.1016/j.matpr.2021.01.331>
16. Kanu NJ, Gupta E, Sutar V, Singh GK, Vates UK (2021) An insight into biofunctional curcumin/gelatin nanofibers. In: *Nanofibers. Nanofibers—synthesis, properties and applications*, Brajesh Kumar. IntechOpen. <https://doi.org/10.5772/intechopen.97113>

17. Kanu NJ, Patil SA, Sutar V, Gupta E, Singh GK, Vates UK, Chavan S (2021) Design and CFD analyses of aluminium alloy-based vortex tubes with multiple inlet nozzles for their optimum performances in sustainable applications. *Mater Today Proc* 47:2808–2813. <https://doi.org/10.1016/j.matpr.2021.03.482>
18. Kadam S, Chavan S, Kanu NJ (2021) An insight into advance self-healing composites. *Mater Res Express* 8:052001. <https://doi.org/10.1088/2053-1591/abfba5>
19. Gupta E, Kanu NJ, Agrawal MS, Kamble AA, Shaikh AN, Vates UK, Singh GK, Chavan SS (2021) An insight into numerical investigation of bioreactor for possible oxygen emission on Mars. *Mater Today Proc* 47:4149–4154. <https://doi.org/10.1016/j.matpr.2021.04.059>
20. Halwe AD, Deshmukh SJ, Kanu NJ, Gupta E, Tale RB (2021) Optimization of the novel hydrodynamic cavitation based waste cooking oil biodiesel production process parameters using integrated L9 Taguchi and RSM approach. *Mater Today Proc* 47:5934–5941. <https://doi.org/10.1016/j.matpr.2021.04.484>
21. Kumbhalkar MA, Rambhad KS, Kanu NJ (2021) An insight into biomechanical study for replacement of knee joint. *Mater Today Proc* 47:2957–2965. <https://doi.org/10.1016/j.matpr.2021.05.202>
22. Kanu NJ, Mangalam A, Gupta E, Vates UK, Singh GK, Sinha DK (2021) Investigation on secondary deformation of ultrafine SiC particles reinforced LM25 metal matrix composites. *Mater Today Proc* 47:3054–3058. <https://doi.org/10.1016/j.matpr.2021.05.640>
23. Pandey V, Bekele A, Ahmed GMS, Kanu NJ, Singh GK (2021) An application of conjugate gradient technique for determination of thermal conductivity as an inverse engineering problem. *Mater Today Proc* 47:3082–3087. <https://doi.org/10.1016/j.matpr.2021.06.073>
24. Kanu NJ, Guluwadi S, Pandey V, Suyambazhahan S (2021) Experimental investigation of emission characteristics on can-combustor using Jatropha based bio-derived synthetic paraffinic kerosene. *Smart Sci.* <https://doi.org/10.1080/23080477.2021.1938503>
25. Jain N, Gupta E, Kanu NJ (2021) Plethora of carbon nanotubes applications in various fields—a state-of-the-art-review. *Smart Sci.* <https://doi.org/10.1080/23080477.2021.1940752>
26. Kale SM, Kirange PM, Kale TV, Kanu NJ, Gupta E, Chavan SS, Vates UK, Singh GK (2021) Synthesis of ultrathin ZnO, nylon-6, 6 and carbon nanofibers using electrospinning method for novel applications. *Mater Today Proc* 47:3186–3189. <https://doi.org/10.1016/j.matpr.2021.06.289>
27. Vates UK, Kanu NJ, Gupta E, Singh GK, Sharma BP, Pandey V (2021) Optimization of electro discharge critical process parameters in tungsten carbide drilling using L9 Taguchi approach. *Mater Today Proc* 47:3227–3234. <https://doi.org/10.1016/j.matpr.2021.06.438>
28. Ayushi, Vates UK, Mishra S, Kanu NJ (2021) Biomimetic 4D printed materials: a state-of-the-art review on concepts, opportunities, and challenges. *Mater Today Proc* 47:3313–3319. <https://doi.org/10.1016/j.matpr.2021.07.148>
29. Kanu NJ (2021) Modeling of stress wave propagation in matrix cracked laminates. *AIP Adv* 11:085217. <https://doi.org/10.1063/5.0057749>
30. Kanu NJ, Bapat S, Deodhar H, Gupta E, Singh GK, Vates UK, Verma GC, Pandey V (2021) An insight into processing and properties of smart carbon nanotubes reinforced nanocomposites. *Smart Sci.* <https://doi.org/10.1080/23080477.2021.1972913>
31. Asre CM, Kurkute VK, Kanu NJ (2021) Power generation with the application of vortex wind turbine. *Mater Today Proc.* <https://doi.org/10.1016/j.matpr.2021.08.228>
32. Vates UK, Kanu NJ, Gupta E, Singh GK, Daniel NA, Sharma BP (2021) Optimization of FDM 3D printing process parameters on ABS based bone hammer using RSM technique. *IOP Conf Ser Mater Sci Eng* 1206:012001. <https://doi.org/10.1088/1757-899X/1206/1/012001>
33. Sakhare SA, Pendkar SM, Kanu NJ, Gupta E, Vates UK, Singh GK, Verma GC (2022) Design suggestions on modified self-sustainable space toilet. *SN Appl Sci* 4:13. <https://doi.org/10.1007/s42452-021-04878-w>
34. Vates UK, Sharma BP, Kanu NJ, Gupta E, Singh GK (2021) Modeling and optimization of IOT factors to enhance agile manufacturing strategy-based production system using SCM and RSM. *Smart Sci.* <https://doi.org/10.1080/23080477.2021.2017543>

35. Kanu NJ, Lal A (2022) Nonlinear static and dynamic performance of CNT reinforced and nanoclay modified laminated nanocomposite plate. *AIP Adv* 12:025102. <https://doi.org/10.1063/5.0074987>
36. Kanu NJ, Lal A (2022) Nonlinear static analysis of CNT/nanoclay particles reinforced polymer matrix composite plate using secant function based shear deformation theory. *Smart Sci*. <https://doi.org/10.1080/23080477.2022.2066052>
37. Gonfa BK, Sinha D, Vates UK, Badruddin IA, Hussien M, Kamangar S, Singh GK, Ahmed GMS, Kanu NJ, Hossain N (2022) Investigation of mechanical and tribological behaviors of aluminum based hybrid metal matrix composite and multi-objective optimization. *Materials* 15(16):5607. <https://doi.org/10.3390/ma15165607>

# Microwave Sintering of Aluminum Composite



Vishal Naranje , Sachin Salunkhe, Vinod Kumar Shukla,  
and Purushottam Sharmad

**Abstract** Microwave heating has a long history in the industry, most notably in the food processing industry. Furthermore, it is used in the processing of organic and inorganic materials. This technology is increasingly being used in the manufacture of sintered composite materials. In this paper, the properties of aluminum alloy powders—microwave sintering at a temperature of 5500 C (Al–SiC–B<sub>4</sub>C)—are investigated. The influence of various Al, SiC, and B<sub>4</sub>C compositions' mechanical and physical properties are also investigated. It is observed that as apparent density increases, the tendency to shrink during sintering appears to decrease. Boron carbide has a greater tap density (93%) than silicon carbide (90%), which is greater than the tap density of aluminum. The microhardness of the metal matrix composite increased linearly with increasing boron carbide content.

**Keywords** Microwave sintering · Al composite · Tap density · Microhardness first section

## 1 Introduction

Due to the high microwave susceptibility of water molecules in food, microwave heating is the most common method of heating food. A growing number of materials—including plastics, ceramics, metals, minerals, and various chemicals—are being heated using microwaves. Other potential uses for microwave heating include remediating contaminated soil and repurposing various waste materials. The growing

---

V. Naranje (✉) · V. K. Shukla  
Amity University Dubai, Dubai 345019, UAE  
e-mail: [vnaranje@amityuniversity.ae](mailto:vnaranje@amityuniversity.ae)

S. Salunkhe  
Department of Mechanical Engineering, Vel Tech Rangarajan Dr. Sagunthala R&D Institute of Science and Technology, Chennai, India

P. Sharmad  
Amity University Uttar Pradesh, Noida, India

body of literature on the microwave processing of various materials, on the other hand, shows that microwave processing has recently gained increasing attention. The process is sped up by volumetric and rapid processing. Unlike other methods, this can process a wide range of materials, including novel materials that cannot be processed conventionally. As an added benefit, microwave heating can improve the properties of materials that have already been processed. Reinforcement materials such as SiC and B<sub>4</sub>C are the most commonly used in Al alloys. Due to its high metallurgical and hardness properties, it is also becoming more popular for reinforcing purposes. Aluminum composites have been the subject of several studies in recent years. Physical and mechanical properties of Al/B<sub>4</sub>C composites with a reinforcement content of 5 and 10% were studied by Yusof et al. [1]. Aluminum alloys and silicon carbide particles reinforced with solid lubricants were studied by Asif et al. [2] for their tribological properties. The mechanical properties of three distinct Al composites (Al 6061, Al 6063, and Al 7072) reinforced with silicon carbide particulates were examined by Reddy and Zitoun [3]. B<sub>4</sub>Cp/2024Al composite morphology and microstructure were studied by Nie et al. [4]. The mechanical properties of an aluminum composite reinforced with silicon carbide and boron carbide particles were studied by Bodukuri et al. [5]. Aluminum alloy composites reinforced with B<sub>4</sub>Cp and SiCp particles were studied by Ceren [6] to determine the effect of Zr on the microstructure as well as the wear properties. Carbon-containing Al–SiC(n) hybrid composites were studied by Hekner et al. [7] for their tribological properties. Several researchers in aluminum matrix composites have studied copper additives. The most common sintering methods in powder metallurgy are microwave sintering and spark plasma sintering (SPS) (Hu et al. [8] and Manohar et al. [9]). To avoid the formation of intermetallic compounds, quick and low-temperature sintering times and processing conditions are used in these mechanisms (Viala et al. [10] and Azarniya et al. [11]). High-temperature plasma regions are formed in the SPS process by spark discharges between adjacent particles. Boron carbide (B<sub>4</sub>C) and silicon carbide (SiC) particles, the most commonly used reinforcement materials in aluminum matrix composites (AMCs), have been discovered by numerous researchers to reinforce the matrix structure and provide high resistance, good wear resistance, and high thermal stability. An Al composite's microstructure and mechanical properties will be studied using microwave sintering parameters and varying SiC and B<sub>4</sub>C content. SiC and B<sub>4</sub>C, two commonly used reinforcing materials, have unique properties. In the author's information, no research has been done on the mechanical properties of microwave sintered SiC, B<sub>4</sub>C composite. Al–SiC–B<sub>4</sub>C composite sintering mechanisms were studied in this study. Additional work was done to determine the microstructural analysis of various Al–SiC–B<sub>4</sub>C percentages.

## 2 Experimental Procedures

Figure 1 presents the procedure for experimental design with the help of flowchart.

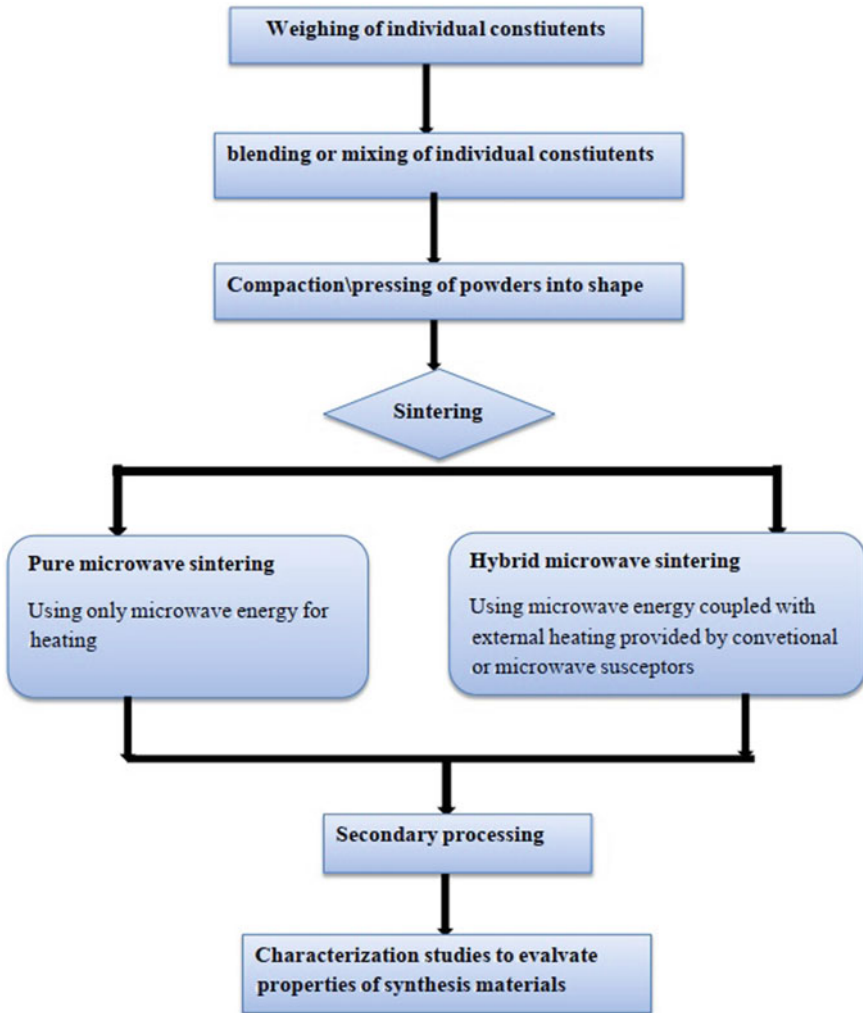


Fig. 1 Flow chart for experimental design

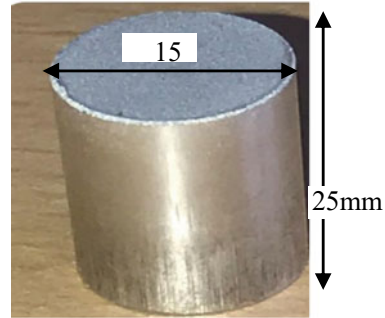
Al powder was combined with various weight fractions of SiC and B<sub>4</sub>C to make Al composites, with the resulting chemical compositions shown in Table 1.

Using BSS pans numbered 144, 100, 120, 200, and a lid, the particle size of aluminum powder was determined. Simultaneously, the same-sized pans were used to characterize silicon carbide powders. A variety of BSS pans were used to examine the properties of boron carbide powders. All of the combined powders were milled for 2 h at a speed of 200 rpm in a planetary ball mill to achieve a homogeneous particle distribution. This stage was completed without the use of balls. Cold compacting of the blended powders into cylindrical pellets with a uniaxial pressure of 150 MPa

**Table 1** Weight fractions of SiC and B<sub>4</sub>C with the chemical compositions

Batch	Al (wt%)	SiC (wt%)	B <sub>4</sub> C (wt%)
A	95	5	0
B	93	5	2
C	91	5	4
D	89	5	6
E	87	5	8

**Fig. 2** Sample of produced Al composite



into billets was used. For homogeneous mixtures, a BCR of 5:1 is maintained. The compacted cylindrical billets were sintering at 550 °C for 30 min. Similarly, the other metal matrix composites were prepared in the same manner. This procedure is repeated for every three compositions, and the powders' apparent and tap densities are determined once more.

The samples were sintered in a graphite bed without soaking time using a single-mode microwave furnace. Figure 2 illustrates a sintered sample. Following sintering, these rods were used for characterization experiments.

### 3 Result and Discussion

#### 3.1 Microstructural Analysis

SEM was used to analyze the morphology and microstructure of advanced composites containing a variety of reinforcements. SEM micrographs of A, B, and C composites are shown in Fig. 3. Figure 3a–d shows typically, homogeneous distribution of B<sub>4</sub>C reinforcements in the Al matrix; however, A composite, compared to B composite, exhibits some porosity around the B<sub>4</sub>C reinforcement particles as shown in Fig. 4. It appears as though the addition of Co improves the adhesion of the Al matrix to B<sub>4</sub>C particles. SEM of an Al—20% B<sub>4</sub>C—2% Co sintered composite at 850 °C.

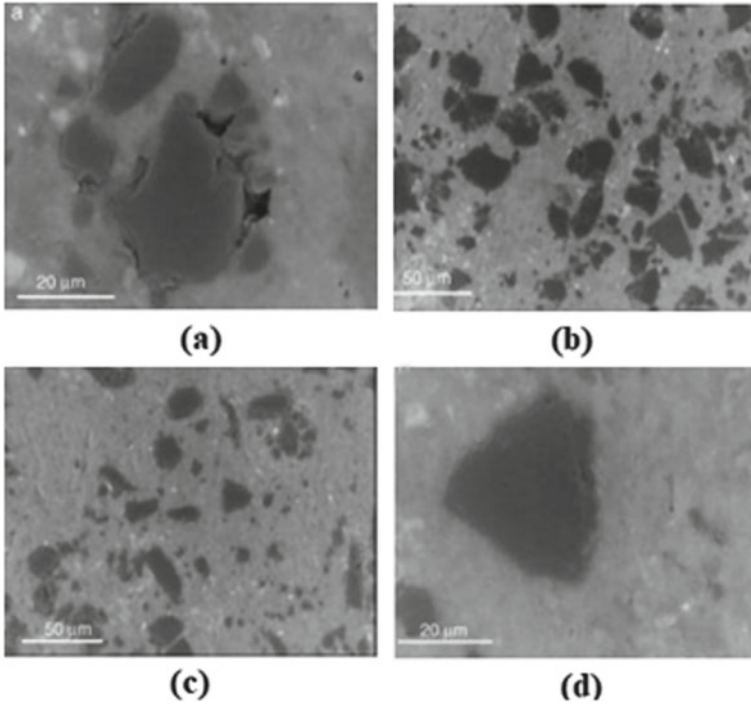


Fig. 3 SEM micrographs of Al composite

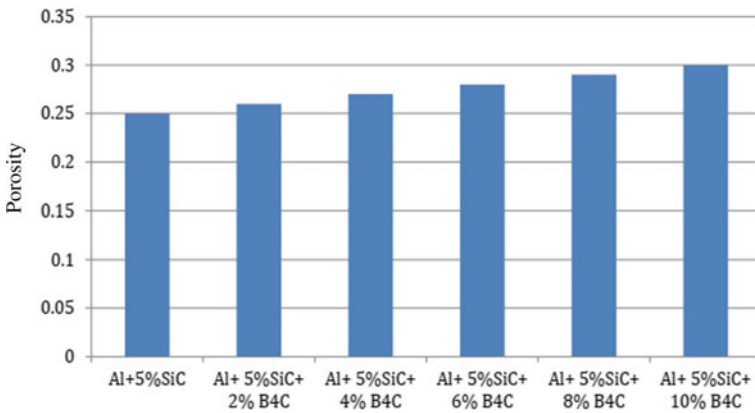


Fig. 4 Porosity of Al composite



### 3.2 Densification

The tendency to shrink during sintering seems to decrease with the increase in apparent density. The greatest increase in tap density occurs during the initial tapping period and eventually, the tap density becomes constant as shown in Fig. 5. The tap density of boron carbide is more than silicon carbide which is more when compared to that of aluminum as shown in Table 2. Tap density of 90% Al 5% SiC 4% B<sub>4</sub>C is greater than tap density of 90% Al 5% SiC 6% B<sub>4</sub>C which is greater than that of 90% Al 5% SiC 2% B<sub>4</sub>C. Green density of 90% Al 5% SiC 2% B<sub>4</sub>C is greater than green density of 90% Al 5% SiC 4% B<sub>4</sub>C, which is greater than that of 90% Al 5% SiC 6% B<sub>4</sub>C. Sintered density of 90% Al 5% SiC 6% B<sub>4</sub>C is greater than that of 90% Al 5% SiC 2% B<sub>4</sub>C, is greater than that of 90% Al 5% SiC 4% B<sub>4</sub>C.

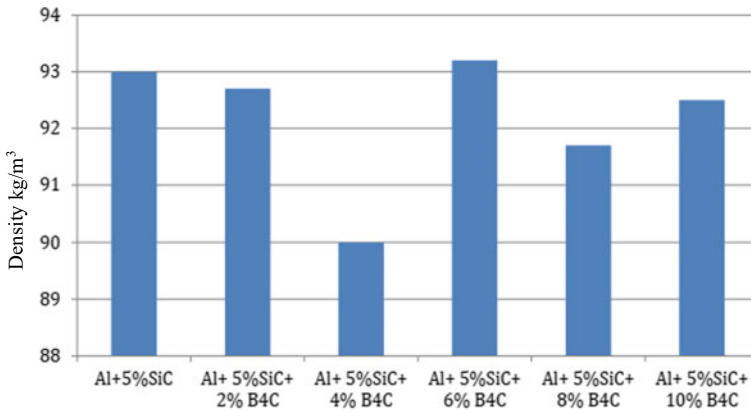
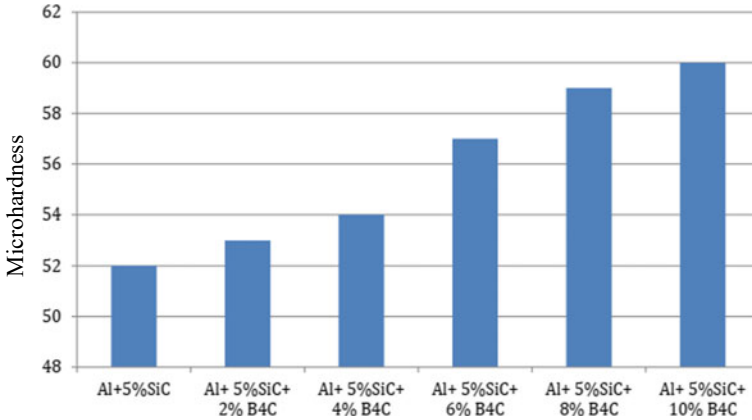


Fig. 5 Density of Al composite

Table 2 Density (green and sintered) of Al composition

S.No.	Microwave sample	Green density	Sintered density
1	Al + 5%SiC	4.75	7.75
2	Al + 5%SiC + 2%B <sub>4</sub> C	4.76	7.76
3	Al + 5%SiC + 4%B <sub>4</sub> C	4.76	7.77
4	Al + 5%SiC + 6%B <sub>4</sub> C	4.77	7.78
5	Al + 5%SiC + 8%B <sub>4</sub> C	4.78	7.79
6	Al + 5%SiC + 10%B <sub>4</sub> C	4.78	8



**Fig. 6** Microhardness of Al composite

### 3.3 Hardness

Hardness measurements are used to determine the mechanical properties of sintered samples. Microhardness or Vickers hardness tests are used in this study. An applied load of 250 gf and dwell of 15 s is used to measure the hardness. The recorded data points are separated by 0.3 mm on the two orthogonal axes (*X* and *Y* axes) with a point of intersection at (0, 0) at the center of the disk. Ninety percentage hardness Al5 percentage SiC6 percentage B<sub>4</sub>C has a higher melting point than 90% SiC6 percentage B<sub>4</sub>C. Al 5 percentage SiC 54 percentage B<sub>4</sub>C has a higher melting point than 90% Al5 percentage SiC 2 percentage B<sub>4</sub>C. The hardness value decreases as the percentage of boron carbide increases (Fig. 6).

## 4 Conclusion

The investigation was carried out using microwave sintering on Al–SiC–B<sub>4</sub>C composites in this study. As a result, shrinkage during sintering has been found to decrease as apparent density increases. The sintered density of 90% Al 5% SiC 6% B<sub>4</sub>C is higher than that of 90% Al 5% SiC 2% B<sub>4</sub>C. The addition of B<sub>4</sub>C reinforcement increases the composite’s microhardness. As the percentage of B<sub>4</sub>C in the metal matrix composite increases, the microhardness of the composite increases significantly. Due to their high stiffness values due to SiC content, these composite materials can be used in the industrial, defense, and aviation sectors because graphite acts as a lubricating medium.

## References

1. Yusof A, Yusof MR, Muhammad A, Kamarudin N, Sylvester PW, Zali NM (2012) Al/B4C composites with 5 and 10 wt% reinforcement content prepared by powder metallurgy. *J Nucl Relat Technol* 2012(1):42–47
2. Asif M, Chandra K, Misra PS (2011) Development of aluminium based hybrid metal matrix composites for heavy duty applications. *J Miner Mater Charact Eng* 10(14):1337–1344
3. Reddy AC, Zitoun E (2010) Matrix Al-alloys for silicon carbide particle reinforced metal matrix composites. *Indian J Sci Technol* 3:1184–1187
4. Nie C-Z, Gu J, Liu J-L, Zhang D (2007) Production of boron carbide reinforced 2024 aluminum matrix composites by mechanical alloying. *Mater Trans* 48(5):990–995
5. Bodukuri AK, Eswaraiah K, Rajendar K, Sampath V (2016) Fabrication of Al–SiC–B4C metal matrix composite by powder metallurgy technique and evaluating mechanical properties. *Perspect Sci* 8:428–431.
6. Ceren G (2013) Mechanical properties of hot pressed SiCp and B4Cp/Alumix 123 composites alloyed with minor Zr. *Compos B Eng* 54:34–40
7. Hekner B, Myalski J, Valle N, Botor-Probierz A, Sopicka-Lizer M, Wieczorek J (2017) Friction and wear behavior of Al–SiC(n) hybrid composites with carbon addition. *Compos B Eng* 108:291–300
8. Hu ZY, Zhang ZH, Cheng XW, Wang FC, Zhang YF, Li SL (2020) A review of multi-physical fields induced phenomena and effects in spark plasma sintering: fundamentals and applications *mater. Des* 191:108662. <https://doi.org/10.1016/j.matdes.2020.108662>
9. Manohar G, Pandey KM, Maity SR (2021) Effect of sintering mechanisms on mechanical properties of AA7075/B4C composite fabricated by powder metallurgy techniques. *Ceram Int* 47:15147–15154. <https://doi.org/10.1016/j.ceramint.2021.02.073>
10. Viala JC, Bouix J, Gonzalez G, Esnouf C (1997) Chemical reactivity of aluminium with boron carbide. *J Mater Sci* 32:4559–4573. <https://doi.org/10.1023/A:1018625402103>
11. Azarniya A, Azarniya A, Abdollah-zadeh A, Madaah Hosseini HR, Ramakrishna S (2019) In situ hybrid aluminum matrix composites: a review of phase transformations and mechanical aspects. *Adv Eng Mater* 21:1801269. <https://doi.org/10.1002/adem.201801269>. LNCS Homepage, <http://www.springer.com/lncs>. Last accessed 2016/11/21

# Analysis of Energy-Efficient Copper Mining Processes Using Solar Energy: A Review



Prem Nath Suman, Ravindra Kannojiya, Manish Kumar Ojha, and Anoop Kumar Shukla

**Abstract** The copper mineral processing sector faces challenging circumstances due to rising demand, volatile cost of energy, declining grade ore that lead to higher resources usage, and greater public awareness of the GHG emission. In this paper, state of solar technology now is describe. It explains how solar thermal and solar photovoltaic technology are used in copper mining processes to provide electricity and heat. While solar thermal technologies can be used to provide electricity, heat, in copper extraction PV technologies can be used to generate energy for crushing and grinding machines and electrolysis. The research also takes a more comprehensive look at the usable applications of these techs in the management and development of novel sun energy in copper extraction. The researchers came to the conclusion that integrating sun energy into copper extraction processes can be done in a number of practical ways. The major objective of the article is to advance knowledge of sun energy technology and its use in copper mining sector so that people can deal with energy and environmental problems more pro-actively and strategically. In this study, current advances in solar energy for the mining sector are discussed.

**Keywords** Energy efficiency · Solar technology · GHG emission · Energy costing · Mining

## 1 Introduction

Copper mining processes rely heavily on renewable energy sources to extract copper from its ore. Copper is used extensively in automobiles, computers, household appliances, and consumables. High grade and low grade energy is needed in the copper mining to extract and produce copper from its ore [1]. Energy costs are currently high due to their widespread use in various industries. Various clients have noticed a significant increase in CO<sub>2</sub> emissions during copper mining procedures, which is not good for the environment, and scientists have warned that it could lead to massive

---

P. N. Suman · R. Kannojiya (✉) · M. K. Ojha · A. K. Shukla  
Amity University, Noida, Uttar Pradesh 201301, India  
e-mail: [ravindra.k36@gmail.com](mailto:ravindra.k36@gmail.com)

© The Author(s), under exclusive license to Springer Nature Singapore Pte Ltd. 2024  
R. K. Tyagi et al. (eds.), *Advances in Engineering Materials*, Lecture Notes in Mechanical Engineering, [https://doi.org/10.1007/978-981-99-4758-4\\_8](https://doi.org/10.1007/978-981-99-4758-4_8)

greenhouse emissions [2]. Since a few years ago, copper production has been rising, but the demand for energy and power has increased six times more quickly than copper production as a result of a continuously dropping ore grade that necessitates more energy [3]. Sun energy can be input to power extraction processes activities in order to determine variation in energy usage caused by ore properties [4].

There are two ways to get copper out of the ground: underground mining or open pit mining. When copper ore is not discovered near the earth's surface, underground mining is employed to obtain it. Copper ore is extracted through open pit mining close to the earth's surface [5]. However, the majority of copper is currently mined using open pit methods. These both techniques for copper mining processes use fossil fuels to operate. As of now most of world primary source of energy production is fossil fuels, but our target is to replace it from solar, or we can say that copper mining methods should incorporate solar energy [6]. As fossil fuels largely contribute in greenhouse gas emissions, it pollutes the environment; so clean energy like solar energy should be used to tackle the reduction of greenhouse gas emissions [7].

The two main methods for harvesting solar energy are solar thermal, which typically take the form of CSP and PV cells, which convert sun radiation directly into electricity to produce heat [2, 5]. Most of mining areas are located in remote areas which are far away from grid which makes mining industry to mostly rely on fossil fuels for electricity to operate the mining [8]. As copper mining industry is located in remote areas, we can use sunlight radiation to generate electricity, and to produce heat in the form of solar energy, this way we can replace fossil fuels with solar energy. We find that the usage of concentrated solar power (CSP) and solar photovoltaic (PV) significantly reduces greenhouse gas emissions [9].

Renewable energy sources have recently been thought of as a fossil fuel alternative because of the sharp rise in energy usage. Due to its clean energy, safety, and sustainability, solar energy has been examined more recently as a potential alternative for fossil fuels [10].

Many nations have been working on creating their own solar power generating in recent years. Each nation has a national policy that outlines how much solar energy will cost, how much will be demanded, how it will be integrated into the economy, and other factors [11]. To this end, governments are taking steps to cut their greenhouse gas emissions [12].

This paper tries to incorporate energy from sun into the copper mining sector. The current work in this paper consists of the following:

- A review of solar technology or, more precisely, a study of solar technology integration in copper mining processes.
- Examine the solar technology and resources that can be incorporated into different copper mineral processing methods.
- Provides some insight into potential problems and studies into the usage of sun energy in mining operations.

The summary of the processing of copper ore is given in Sect. 3 after that. The technologies used for solar energy now are described in Sect. 4. The state of solar resources and technologies that can be used in various copper mineral processing

is given in Sect. 5. Section 6 discusses upcoming difficulties and research toward incorporating solar power in the mining industry. The paper is concluded in Sect. 7.

## 2 Recent Trends and Method Adopted

Figure 1 shows the current trends, the approach to be taken, and the work that needs to be done to include solar energy in copper mining. The literature review was conducted based on the copper mining business by in-depth investigation and thorough searching in ScienceDirect, which contains a wide variety of journals and proceedings, as well as through the Google search engine. This essay seeks to give the readers essential knowledge in easy-to-follow instructions. After highlighting the issues facing the copper mining sector, particularly those pertaining to energy, we included the major trends and difficulties affecting the mining sector and stoking interest in the use of solar energy in mining operations.

Understanding sun energy and how it can asset in the mining sector requires understanding of both copper extraction and sun energy technology [13]. The study and challenges of incorporating sun energy into the mining business were also explored.

This paper highlights how sun radiation can be applied to the mining sector using solar energy.

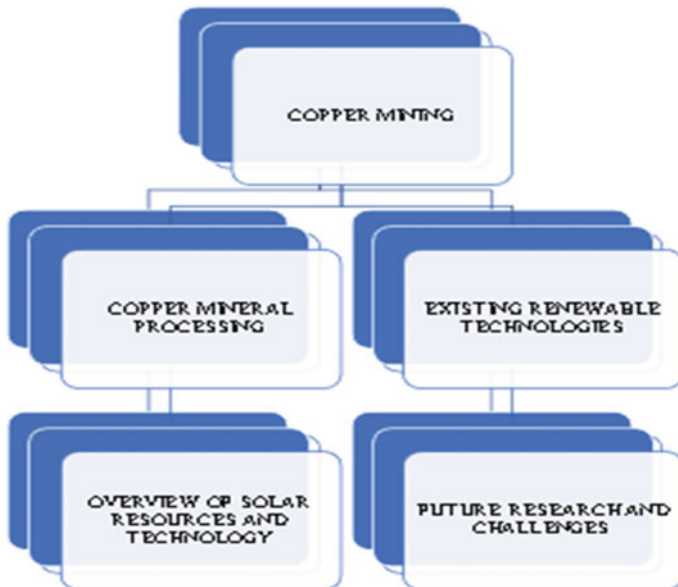


Fig. 1 Recent trends and method to be adopted in copper mining industry

### 3 Copper Mineral Processing

Because copper ores are complicated, several mining and extraction techniques are needed to produce pure copper, which is measured at 99.99% [14]. Electricity, explosives, heat, hydrocarbon fuels including diesel, natural gas, coal, and fuel oil, as well as the energy equivalent of materials consumed, are all needed for the manufacture of copper [15]. There are two main processes used to treat copper ores: hydrometallurgy and pyrometallurgy [16]. In hydrometallurgy oxides ore are generally processed to obtain Cu-minerals. It is a less expensive process. Hydrometallurgy uses aqueous solution in simple we can say electrolysis for extraction of copper from its oxides ores, to obtain 99.99% pure copper [17]. In pyrometallurgy sulfide ores are generally processed to obtain Cu minerals. It is just a pricey process. High temperatures are necessary in pyrometallurgy to extract and purify copper from copper sulfide ores, and this process typically entails the following steps: froth flotation, smelting, converting, anode and refining and casting (electrolysis), and electro-refining. High temperatures and extensive electricity use are needed in these processes to produce pure copper [18].

### 4 Existing Renewable Technologies

In this section, information of current renewable technology can be used to produce heat and energy.

#### 4.1 Photovoltaic Solar

Sun cell or a photovoltaic cell is an energy harvesting technology that converts sunlight directly into electricity with no moving parts and is operated quietly with no emission [19]. It required little maintenance. PV modules which are commercially available convert sunlight into energy with approximately 5–15% efficiency [20]. Majority of photovoltaic solar cells are made of silicon, which is used in materials ranging from amorphous to poly crystalline silicon forms with increasing efficiency and decreasing cost shown in Table 1. Unlike electric generators, solar cells use sun energy to generate electricity without the need for fuel [21]. The PV plant that is highlighted is the most widely used in Chile [3]. Solar photovoltaic cells may be deployed on small, big, or both scales. Because of the size of its installations, the copper mining sector requires large-scale applications. First-generation polycrystalline silicon solar cells The copper mining sector now uses solar PV technologies [5]. Solar photovoltaic cells may be deployed on small, big, or both scales. Because of the size of its installations, the copper mining sector requires large-scale applications. Off-the-shelf PV technology is affordable and provides a clear solution

**Table 1** Percentage efficiency of solar PV cell [5]

Different solar PV cell	Percentage (%)
Polycrystalline cell	15–18
Monocrystalline cell	16.5–19
Polycrystalline PERC cell	17–19.5
Monocrystalline PERC cell	17.5–20
Monocrystalline N-type cell	19–20.5
Monocrystalline N-type cell	19–21.7
Monocrystalline N-type IBC cell	20–22.8

for mining and mineral processing. The manufacturing of copper uses high-energy electrolysis techniques based on PV electro-refining and electrowinning, where the currents generated are supported by massive transformers and powerful rectifiers.

## 4.2 Solar Thermal

Various solar thermal collector types, including concentrating and non-concentrating collectors [22]. A method called solar thermal power collects and concentrates sunlight to create the intense heat (thermal) required to produce electricity [23]. Utilizing solar energy for thermal energy is involved (heat). Solar thermal methods typically use parabolic or flat collectors that focus sunlight onto a receiver, mostly employing mirrors to gather and focus sunlight [24].

Flat plate collectors are the most widely utilized solar thermal technique in Europe. The most often used solar thermal technology worldwide is evacuated tube collectors. In general, evacuated tubes will be more expensive than flat plate collectors [25].

## 4.3 Solar-Hybrid Photovoltaic Thermal

To promote the advantages of solar radiation and PV efficiency, a PV thermal hybrid solar collector was proposed [26]. When used independently, PV thermal is more efficient than both PV and thermal collector systems. PVT is appropriate for areas with restricted surface area [6]. Uncoupled and coupled PV-T systems are the two different configurations for PVT systems. A PV thermal hybrid solar collector was suggested to promote the benefits of solar radiation and PV efficiency [27]. PV thermal is more effective than both PV and thermal collector systems when used alone. PVT is suitable for spaces with less surface area [28]. The two different PV-T system configurations are linked and uncoupled PV-T systems [13].



## 5 Overview of Solar Resources and Technology that Can Be Integrated in Various Copper Mineral Processing

Mineral extraction and processing account for 20% of the energy used in copper mining activities, while the global energy consumption is just 10% [14]. In the mineral sector, solar energy is frequently used since it is economically viable, lowers our reliance on fossil fuels, and has been shown to cut greenhouse gas emissions [29]. Integration of solar technology depends on the solar resources that are accessible at every given place [30]. On specific location, the amount of sunlight can be measured.

In Fig. 2, there are numerous methods for capturing solar energy. Each solar energy collecting technique's technical and operational viability at every location so it is reliable on the available sun energy resource [31].

Electrolysis involves electro-refining and electrowinning is a high energy consuming stage in copper extraction [32]. As a result, it contributes significantly to the copper mining industry's high GHG emissions [2]. The use of sun energy in electrowinning and electrorefining has a lot of potential [14]. When a system has two loops, the indirect heat idea is used. After going through many case study, full utilization of solar energy is yet to be done in copper mining industry; few of them have integrated solar energy but not at its full potential like Chile has implemented solar technologies in copper ore process like in electrowinning [33].

COPPER MINERAL PROCESSING	SOLAR TECHNOLOGY
CRUSHING & GRINDING	SOLAR PV
FROTH FLOTATION	SOLAR PV
ROASTING	SOLAR THERMAL
SMELTING	SOLAR THERMAL
ELECTROLYTIC REFINING	SOLAR PV

Fig. 2 Technology that can be integrated in copper mineral processing

## 6 Future Challenges and Research in Integrating Solar Energy in Mining Industry

Governments, customers, and other important stakeholders are increasingly requesting that the mining industry operates in a sustainable manner [1]. Energy security concerns and resource efficiency are driving changes in the sector's energy mix [17]. The rising cost of conventional energy sources and the availability of alternative energy sources will undoubtedly speed up the transition [20]. Moreover, taking into account the extensive timeframe for While “bridging” fuels like shale gas and nuclear power are desirable in the short run, it is not obvious if these technologies can appeal in long duration [34]. For mining companies operating in distant areas with limited energy resources, solar energy holds out a lot of promise. The possibility for utilities to become more financially viable, for mining businesses to dramatically reduce their energy costs, and for the general public to gain from a speedier grid development are what the future holds [35]. The primary issue for future research will be to create environmentally conscious, safe, and effective solar systems. Electrolysis produces high purity copper for commercial use. 20% of the annual production of copper uses electrowinning [36]. Existing copper mining techniques can be greatly improved and modified to make better use of solar energy. Minor modifications were made to the hybrid PV-T system to enable it to power processes like electrowinning and electro-refining [37]. The requirement for current copper mining techniques could be satisfied by a few cutting-edge solar energy technologies [38]. PV that isn't little—Self-contained hybrid renewable energy plants that integrate biomass, wind, and solar power could also be a viable option, particularly in dry mines [39].

## 7 Conclusion

The copper mining processing sector has the potential to employ solar energy to address current energy problems, especially green house gas emissions. An intriguing approach for extensive sun energy integration might help to optimize alterations to current procedures to take into account the availability of solar resources. Solar technology can assist mining companies in making financial savings since power is one of the most expensive components. More installations will be driven in large part by the expansion of the solar sector as well as the declining cost of solar technologies. In order to spread cutting-edge technologies from the energy sector, transfer of technology should also be supported. Technology development and research into the behavior and transformation of solar energy will be crucial in upcoming year.

This paper aims at integrating sun energy in the copper mining industry, gives information about technologies which can be integrated furthermore in mining industry, and makes it possible to full work solar energy, thus also reducing the GHG emission and lowering the consumption of fossil fuels. Technology can always be upgraded.

At different location, copper mining industry is situated, and there are different ways to integrate solar technologies at different location on the basis of its energy requirement for copper mining industry to extract copper.

After going through various case studies, sun energy used in copper mining is not fully utilized, there is lot of scope of improvement, and very few copper mining industry have used solar energy.

## References

1. Fernandez V (2021) Copper mining in Chile and its regional employment linkages. *Resour Policy* 70:1–17. <https://doi.org/10.1016/j.resourpol.2018.03.017>
2. Norgate T, Haque N (2010) Energy and greenhouse gas impacts of mining and mineral processing operations. *J Clean Prod* 18:266–274. <https://doi.org/10.1016/j.jclepro.2009.09.020>
3. Moreno-Leiva S, Díaz-Ferrán G, Haas J, Telsnig T, Díaz-Alvarado FA, Palma- Behnke R, Kracht W, Román R, Chudinzow D, Eltrop L (2017) Towards solar power supply for copper production in Chile: assessment of global warming potential using a life-cycle approach. *J Clean Prod* 164:242–249. <https://doi.org/10.1016/j.jclepro.2017.06.038>
4. Singh B, Sharma U, Kumar S (2018) Standalone photovoltaic water pumping system using induction motor drive with reduced sensors. *IEEE Trans Ind Appl* 54:3645–3655. <https://doi.org/10.1109/TIA.2018.2825285>
5. Behar O, Peña R, Kouro S, Kracht W, Fuentealba E, Moran L, Sbarbaro D (2021) The use of solar energy in the copper mining processes: a comprehensive review. *Clean Eng Technol* 4:100259. <https://doi.org/10.1016/J.CLET.2021.100259>
6. Pai S, Zerriffi H, Jewell J, Pathak J (2020) Solar has greater techno-economic resource suitability than wind for replacing coal mining jobs. *Environ Res Lett* 15:034065. <https://doi.org/10.1088/1748-9326/AB6C6D>
7. The Warren Centre (2019) Zero emission copper mine of the future. *Oper Idris*, pp 242–243
8. Haas J, Moreno-Leiva S, Junne T, Chen PJ, Pamparana G, Nowak W, Kracht W, Ortiz JM (2020) Copper mining: 100% solar electricity by 2030? *Appl Energy* 262:114506. <https://doi.org/10.1016/J.APENERGY.2020.114506>
9. Chandia E, Zaversky F, Sallaberry F, Sánchez M (2016) International journal of sustainable engineering analysis of the energy demand of the Chilean mining industry and its coverage with solar thermal technologies analysis of the energy demand of the Chilean mining industry and its coverage with solar thermal technologies. *Int J Sustain Eng* 9:240–250. <https://doi.org/10.1080/19397038.2016.1148797>
10. Nwokolo SC, Amadi SO, Obiwulu AU, Ogbulezie JC, Eyibio EE (2022) Prediction of global solar radiation potential for sustainable and cleaner energy generation using improved Angstrom-PreScott and Gumbel probabilistic models. *Clean Eng Technol* 6. <https://doi.org/10.1016/j.clet.2022.100416>
11. Huang YF, Chang SH (2017) Mining optimum models of generating solar power based on big data analysis. *Sol Energy* 155:224–232. <https://doi.org/10.1016/J.SOLENER.2017.06.035>
12. Lakshmanan PK, Singh S, Asta Lakshmi S (2017) The Paris agreement on climate change and India. *J Clim Change* 3:1–10. <https://doi.org/10.3233/JCC-170001>
13. Pamparana G, Kracht W, Haas J, Ortiz JM, Nowak W, Palma-Behnke R (2019) Studying the integration of solar energy into the operation of a semi-autogenous grinding mill. Part I: framework, model development and effect of solar irradiance forecasting. *Miner Eng* 137:68–77. <https://doi.org/10.1016/j.mineng.2019.03.017>
14. Schipper BW, Lin HC, Meloni MA, Wansleebe K, Heijungs R, van der Voet E (2018) Estimating global copper demand until 2100 with regression and stock dynamics. *Resour Conserv Recycl* 132:28–36. <https://doi.org/10.1016/j.resconrec.2018.01.004>

15. Bardi U (2014) Corrigendum: the mineral question: how energy and technology will determine the future of mining [Front. Energy Res., 1, 9, (2013)]. <https://doi.org/10.3389/fenrg.2013.00009>. Front Energy Res 2. <https://doi.org/10.3389/FENRG.2014.00015>
16. Pietrzyk S, Tora B (2018) Trends in global copper mining—a review. IOP Conf Ser Mater Sci Eng 427. <https://doi.org/10.1088/1757-899X/427/1/012002>
17. Jose-Luis P, Abadias A, Valero A, Valero A, Reuter M (2019) The energy needed to concentrate minerals from common rocks: the case of copper ore. Energy 181:494–503. <https://doi.org/10.1016/j.energy.2019.05.145>
18. Curry JA, Ismay MJL, Jameson GJ (2014) Mine operating costs and the potential impacts of energy and grinding. Miner Eng 56:70–80. <https://doi.org/10.1016/j.mineng.2013.10.020>
19. Lai CS, Jia Y, Lai LL, Xu Z, McCulloch MD, Wong KP (2017) A comprehensive review on large-scale photovoltaic system with applications of electrical energy storage. Renew Sustain Energy Rev 78:439–451. <https://doi.org/10.1016/j.rser.2017.04.078>
20. Behar O, Sbarbaro D, Morán L (2020) A practical methodology for the design and cost estimation of solar tower power plants. Sustainability 12:1–16. <https://doi.org/10.3390/SU12208708>
21. Nasirov S, Agostini CA (2018) Mining experts' perspectives on the determinants of solar technologies adoption in the Chilean mining industry. Renew Sustain Energy Rev 95:194–202. <https://doi.org/10.1016/J.RSER.2018.07.038>
22. Quiñones G, Felbol C, Valenzuela C, Cardemil JM, Escobar RA (2020) Analyzing the potential for solar thermal energy utilization in the Chilean copper mining industry. Sol Energy 197:292–310. <https://doi.org/10.1016/j.solener.2020.01.009>
23. Murray C, Platzer W, Petersen J (2017) Potential for solar thermal energy in the heap bioleaching of chalcopyrite in Chilean copper mining. Miner Eng 100:75–82. <https://doi.org/10.1016/j.mineng.2016.09.022>
24. Herez A, El Hage H, Lemenand T, Ramadan M, Khaled M (2020) Review on photovoltaic/thermal hybrid solar collectors: classifications, applications and new systems. Sol Energy 207:1321–1347. <https://doi.org/10.1016/J.SOLENER.2020.07.062>
25. Ju X, Xu C, Han X, Du X, Wei G, Yang Y (2017) A review of the concentrated photovoltaic/thermal (CPVT) hybrid solar systems based on the spectral beam splitting technology. Appl Energy 187:534–563. <https://doi.org/10.1016/j.apenergy.2016.11.087>
26. Dambhare MV, Butey B, Moharil SV (2021) Solar photovoltaic technology: a review of different types of solar cells and its future trends. J Phys Conf Ser 1913:012053. <https://doi.org/10.1088/1742-6596/1913/1/012053>
27. Baig MH, Surovtseva D, Halawa E (2015) The potential of concentrated solar power for remote mine sites in the northern territory, Australia. J Sol Energy 2015:1–10. <https://doi.org/10.1155/2015/617356>
28. Paredes Sánchez JP (2018) Solar energy applications in mining: a case study. Green Energy Technol 273–285. [https://doi.org/10.1007/978-3-319-54199-0\\_15](https://doi.org/10.1007/978-3-319-54199-0_15)
29. Bamisile OO, Dagbasi M, Abbasoglu S (2019) Energy and exergy analyses of a novel solar PTC assisted multi-generation system. Int J Exergy 28:158–182. <https://doi.org/10.1504/IJEX.2019.097978>
30. Pamparana G, Kracht W, Haas J, Ortiz JM, Nowak W, Palma-Behnke R (2019) Studying the integration of solar energy into the operation of a semi-autogenous grinding mill. Part II: effect of ore hardness variability, geometallurgical modeling and demand side management. Miner Eng 137:53–67. <https://doi.org/10.1016/j.mineng.2019.03.016>
31. Zurita A, Castillejo-Cuberos A, García M, Mata-Torres C, Simsek Y, García R, Antonanzas-Torres F, Escobar RA (2018) State of the art and future prospects for solar PV development in Chile. Renew Sustain Energy Rev 92:701–727. <https://doi.org/10.1016/j.rser.2018.04.096>
32. Cuevas F, Murray C, Platzer W, Heimsath A (2015) Large scale solar plants integration in electro-winning copper recuperation process. Energy Procedia 70:605–614. <https://doi.org/10.1016/J.EGYPRO.2015.02.167>
33. Chandia E, Zaversky F, Sallaberry F, Sánchez M (2016) Analysis of the energy demand of the Chilean mining industry and its coverage with solar thermal technologies. Int J Sustain Eng 9:240–250. <https://doi.org/10.1080/19397038.2016.1148797>

34. Awuah-Offei K (2018a) Energy efficiency in the minerals industry: best practices and research directions, p 329
35. Awuah-Offei K (ed) (2018b) Energy efficiency in the minerals industry. <https://doi.org/10.1007/978-3-319-54199-0>
36. Sohn HY, Malfliet A, Scheunis L, Jones PT, Blanpain B (2014) Copper production
37. Ushak S, Grágeda M, Pulido D, Of E, Cabeza LF (2014) Application of solar heating on the electrolyte conditioning for electrowinning process: thermosolar plant performance. *Energy Procedia* 57:2930–2936. <https://doi.org/10.1016/j.egypro.2014.10.328>
38. Sturla-Zerene G, Figueroa BE, Sturla M (2020) Reducing GHG global emissions from copper refining and sea shipping of Chile's mining exports: a world win-win policy. *Resour Policy* 65:101565. <https://doi.org/10.1016/j.resourpol.2019.101565>
39. Kaur H, Gupta S, Dhingra A (2021) Analysis of hybrid solar biomass power plant for generation of electric power. *Mater Today Proc* 48:1134–1140. <https://doi.org/10.1016/j.matpr.2021.08.080>

# Effect of Notch on Strength and Ductility of a Martensitic Stainless Steel in Tensile Test



Jai Singh  and S. K. Nath

**Abstract** Tensile properties characterize the quality of the product and forecast the performance for design purpose. There is no clear evidence that the tensile results obtained from a different type of specimen are comparable or interchangeable. This study investigates the effect of notch on the tensile properties of stainless steel by conducting uniaxial tensile tests on notched and round specimens at room temperature. A flat specimen was also tested to compare the tensile properties of notched and round specimens. The ultimate tensile strength (UTS), while being higher for notched specimen, was found to be consistent with the type of specimens. The tri-axial stress at the notch root was responsible to the increased UTS of the notched specimen. The higher strain hardening in flat specimen attributed to the reduced ductility. The tensile results of flat stainless steel specimen were found to be more consistent with the standard (round smooth) specimen. The formation of dimples on the fractured surfaces identified a ductile type of fracture for all three types of tensile specimens. Local strain hardening and cracking in notched specimen might have resulted in facets on the fractographs.

**Keywords** Tensile test · Tensile specimens · Notched tensile specimen · Flat tensile specimen · Ultimate tensile strength · Ductility

## 1 Introduction

Tensile test characterizes the mechanical properties of the materials which include yield strength, yield point phenomenon, ultimate tensile strength, young's modulus, and ductility (% elongation). These properties define the quality of the material and

---

J. Singh (✉)

Department of Mechanical Engineering, Gandhi Institute of Technology and Management (GITAM) Deemed to be University, Bengaluru 561203, India  
e-mail: [jsingh@nt.iitr.ac.in](mailto:jsingh@nt.iitr.ac.in); [jsingh@gitam.edu](mailto:jsingh@gitam.edu)

S. K. Nath

Department of Metallurgical and Materials Engineering, IIT Roorkee, Roorkee 247667, India  
e-mail: [indiafmt@iitr.ac.in](mailto:indiafmt@iitr.ac.in)

forecast its performance, e.g., wear performance [1]. Further, these can be utilized for design, analysis, simulation, and opportunity for property improvement. The shape, size, and type of the tensile specimens are prescribed by some standards/documents [2, 3]. These documents specify the shape and the relationships between different dimensions of the specimens; for example, a round smooth specimen should have a gauge length to diameter ratio as 5 [2]. Generally, round and flat (rectangular) specimens are used in practice. Sometimes, it is not possible to adhere to the prescribed standard size due to scarcity of material. Miniaturization of specimens is also being approached rapidly. Modern engineering is very much starving for weight reduction of the components. In this scenario, maintaining an appropriate strength is the key. Also, strength (tensile) tested with the help of specimens having conventional standard sizes may not represent the actual strength required used in thin applications. In such circumstances, the question of inter-comparison of results obtained from a different type of tensile specimens remains unclear.

Many studies addressed the effect of sizes on tensile properties for a particular type of tensile specimens. The effect of thickness on tensile properties of a rectangular specimen was investigated for structural steels (X80, and FH550) [4], ultra-fine grained copper [5]. Strnadel and Brumek [6] investigated the effect of thickness for rectangular and effect of diameter for round specimens. Different sizes of rectangular tensile specimens for titanium alloy were studied by Masete et al. [7]. All these studies identified the independence of YS and UTS on the size of the specimens. In other studies, the effect of specimen diameter on round tensile specimens was investigated [8, 9]. Yang et al. [10] compared a miniature and standard specimen of 1.25Cr–0.5Mo steel and found the influence of geometric size of the specimen in the post-necking region. Small punch test and micro-tensile test specimens were compared for mild steel [11]. The research on the size effects of tensile specimens is well established.

Literature has addressed the effect of sizes for a particular type of specimen, while the studies on a different type of specimen are scarce. This study investigated three types of tensile specimens including round, flat, and notched. The round (smooth) specimen was prepared as per the ASTM standard. Flat stainless steel (ss-3)-type tensile specimen [12–15] is also gaining importance in many circumstances of limited material or thickness. Notched tensile specimens are being widely used for testing the weldments [16–19]. CA6NM steel (turbine steel, 13-4 MSS) is taken as research material in this study. This steel is an important material for hydro turbine underwater parts including buckets, guide vanes due to its high wear, and corrosion resistance [20]. As enough research is being carried out on 13-4 MSS [21, 22], it is worth to study the interchangeability of tensile results for various kinds of tensile specimen. The obtained tensile results of round smooth (standard) specimen were compared with the results of the other two. The investigations on the influence of notch on UTS and ductility are emphasized. Furthermore, the interchangeability of tensile test results for different types of specimens is elucidated.



## 2 Materials and Experiments

CA6NM steel (turbine steel, 13-4 MSS) is tested in this study. Spark emission spectroscopy (Thermo Jarrell Ash) was used to determine the chemical composition of 13-4 MSS. It consists of 0.07% C, 13.51% Cr, 3.35% Ni, 0.06% Cu, 0.32% Mo, 0.62% Mn, 0.64% Si, 0.01% P, and rest Fe. The optical micrograph of 13-4 MSS having a typical lath morphology is shown in Fig. 1.

The three different types and different size tensile specimens were cut to exact dimensions using CNC wire cut electric discharge machine (EDM). The schematic geometries of all the three tensile specimens are shown in Figs. 2, 3 and 4. Figure 2 shows the schematic geometry of round smooth specimen which is round in shape. The smooth specimen is having a 20 mm gauge length and 40 mm total length. Tensile tests for smooth specimen were conducted on Tinius Olsen H25KS machine with a cross-head speed of 0.01 mm/s. Load versus elongation data were converted to engineering stress and strain. The smooth tensile specimen is designated as ‘Smooth’ in this article. Three samples were tested, and the mean values along with standard deviation are reported.

Figure 3 shows the schematic geometry of notched tensile specimen. This is designated as ‘Notched’ in the article. This is a round specimen (70 mm length and 10 mm diameter). It consists of a round notch of a 3 mm radius in the middle of the length. The minimum radius inside the notch was 6 mm. The tests for the notched specimen were conducted on Tinius Olsen H75KS machine with a cross-head speed of 0.01 mm/s. Three samples were tested, and the mean values along with standard

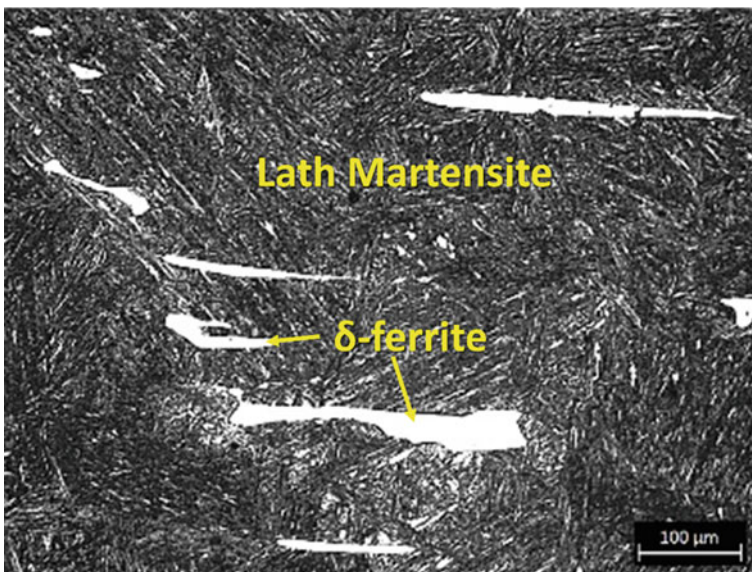


**Fig. 1** Optical microstructure of 13-4 MSS having a typical lath morphology



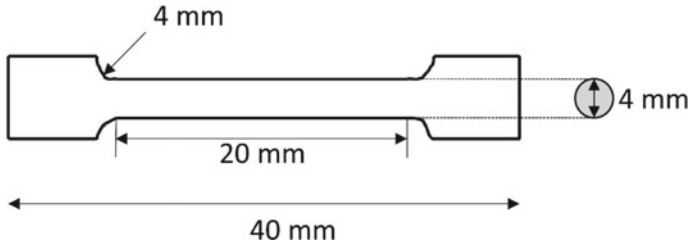


Fig. 2 Schematic geometry of round smooth tensile specimen having 20 mm gauge length

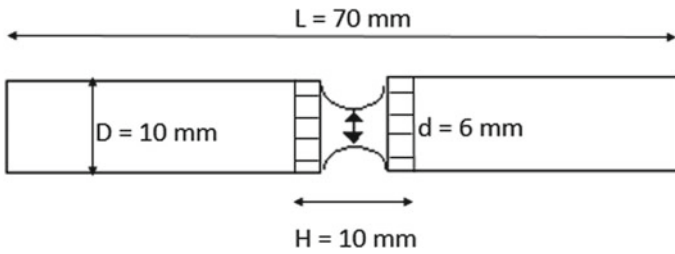


Fig. 3 Schematic geometry of notched tensile specimen having 6 mm diameter in the notch

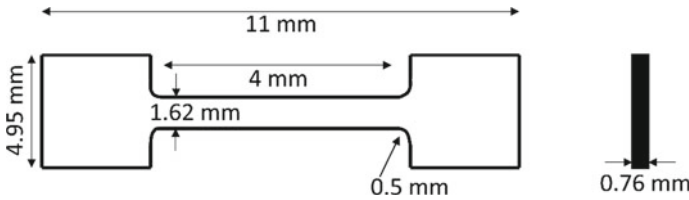


Fig. 4 Geometry of flat specimen (ss-3 type) having 4 mm gauge length

deviation are reported. Notched tensile data were recorded while performing the test. This data, along with the shape factor, was further utilized to get engineering tensile data. All the tests for all types of specimens were conducted at room temperature.

The geometry of flat specimen (ss-3 type) [23, 24] is shown in Fig. 4. This specimen is designated as ‘Flat’ in this article. The flat specimen is having a 4 mm gauge length and 11 mm total length. The thickness of the specimen was 0.76 mm, and the width was 1.62 mm. Tinius Olsen H25KS tensile testing machine was utilized to test the flat samples, and the cross-head speed was kept 0.01 mm/s. Load and extension data were recorded during the test. Engineering stress and strain data were obtained from the load versus extension data. In the case of flat specimen, the length (total) was so small that a specimen may not represent the actual behavior in such a small length. So, for better accuracy, five samples were tested, and the mean values along with standard deviation are reported.

To visualize the difference in the fractographs and identify the fracture mechanism of different tensile specimens tested, fractography was performed by using FEI QUANTA 200FESEM. The hardness at various locations was measured by UHL VMHT microhardness tester. A load of 50 g was applied for a 15 s dwell time.

### 3 Results and Discussion

The results of ultimate tensile strength (UTS) and yield strength (YS) are shown in Fig. 5a. Load versus elongation data were converted to engineering stress and engineering strain for smooth and flat specimens. The notched tensile data were converted to engineering tensile data with the help of shape correction factor (G) as in [25]. The calculation of UTS and ductility was performed for notched specimen, and yield strength was not performed in this study.

The UTS is somewhat consistent for smooth and flat specimens while there is a significant difference in the yield strength (YS) for the concerned specimens. The UTS for notched specimen is quite on higher side. Though the UTS results for notched specimen is comparable with the UTS of flat, it is not consistent with the UTS of smooth specimen. This is owing to the existence of tri-axial state of stress due to the presence of notch [26]. Therefore, larger force is required to cause the deformation.

The percentage elongation term is defined as ductility for smooth and flat specimens. The strain percentage (i.e., ductility) for the notched specimen was calculated as in [25] which is found to be  $27 \pm 1$ . The ductility for smooth specimen was found to be  $23.4 \pm 0.3$  while for flat specimen  $21.0 \pm 0.5$ . It can be perceived that the ductility for flat specimen is somewhat consistent with the ductility of the standard specimen (smooth). But, as the ductility of the notched specimen was calculated by

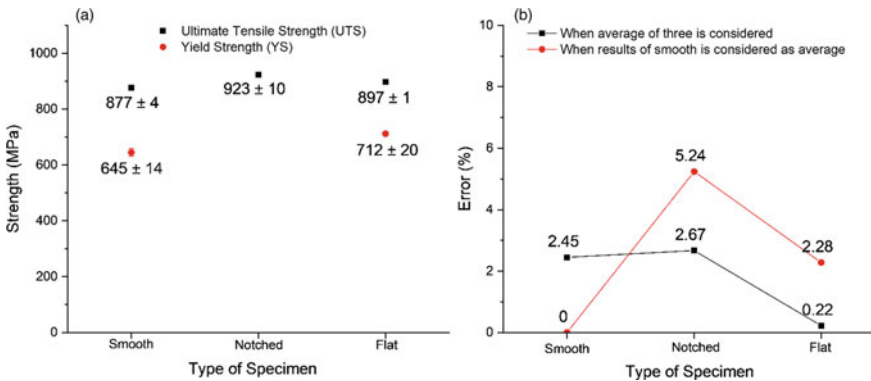


**Fig. 5** a Results of ultimate tensile strength (UTS) and yield strength (YS), and b deviation (%) of UTS from the mean value for various specimens

utilizing the initial diameter and the diameter after fracture, it cannot be directly compared with the ductility results of the other specimens tested in this study.

To compare the results of UTS for various specimens, the error % was calculated using the average value. The average value was calculated by using the results of all three specimens, and deviations from the average (mean) value were computed as per Eq. (1).

$$\text{error \%} = \left( \frac{|\text{Average value} - \text{Obtained value}|}{\text{Average value}} \right) \times 100 \quad (1)$$

The error % for UTS of the three specimens are illustrated in Fig. 5b. Initially, the average value was computed by taking the results of all three specimens and the calculated error %. Finally, the results of the standard specimen (smooth) were considered as average value, and the error % was computed likewise. The UTS for all three specimens falls in the  $\pm 2.67\%$  range when the average was computed by taking all the three values. From that, it can be concluded that the UTS obtained is within a permissible range. The error % results of the flat specimen are much closer to the average value.

As the results of smooth specimen are considered the average value (in the second case), the error % for smooth specimen is zero. The UTS for notched specimen has quite deviated (5.24%) but still looks considerable while little deviation (2.28%) can be observed for flat specimen. Overall, the UTS results fall within  $\pm 5\%$  error and can be considered consistent.

To better understand the tensile behavior of all the specimens, the deformed specimens were investigated for microhardness at various locations and fractographic analysis. The microhardness was measured at four different locations (base metal (0), start of the gauge length (1), onset of necking (2), and close to fracture point (3)) of each specimen and the results for which are presented in Fig. 6. It can be observed that the notched specimen has undergone quite lesser strain hardening particularly in post-necking region. This may be due to the presence of tri-axial state of stress present at the root of the notch and local strain hardening [26]. While the flat specimen undergone higher strain hardening at all locations which might have limited the plastic deformation. Therefore, the flat specimen possessed lesser ductility as compared to the round specimen. It can also be noted that the difference in ductility was mainly caused by the post-necking deformation owing to strain hardening capability of the specimens.

The fracture morphologies of the tensile tested specimens for all the specimens are shown in Fig. 7. The formation of different size dimples can easily be identified on the fractographs of all the specimens. The fractograph of notched specimen, along with the dimples, consists of facets over a small region which adds little brittleness. This owing to the high local strain hardening and cracking due to the presence of notch which may restrict the deformation and lead to somewhat brittle fracture. Therefore, the actual ductility of the notched specimen should be lesser irrespective of the larger dimple size. The dimple sizes were computed using quantitative metallurgy that are shown in Table 1. As the dimple size is generally considered as a measure of the

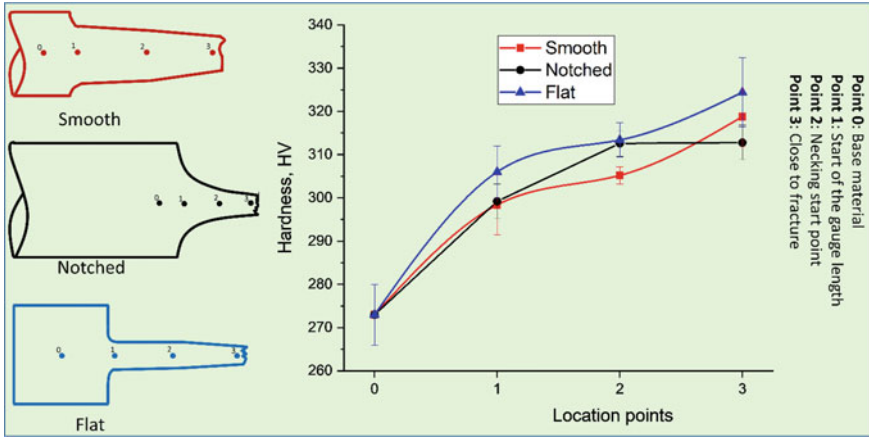


**Fig. 6** Microhardness variation at different location of deformed tensile specimens

ductility of a specimen [27]. The larger the size of the dimples the more the ductility is. The dimple sizes from Table 1 clearly support the ductility results of various specimens.

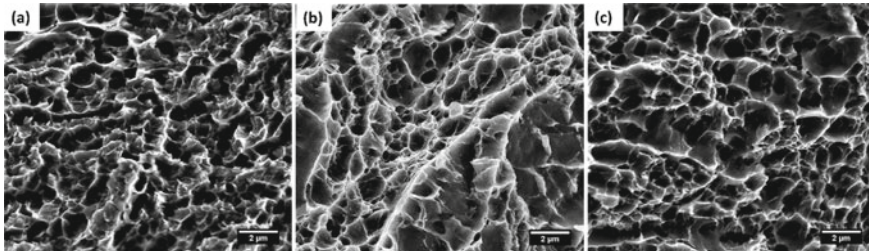


**Fig. 7** Comparison of fractographs of different specimens: **a** smooth specimen, **b** notched tensile specimen, and **c** flat ss-3 type specimen

**Table 1** Average dimple size calculated from the fractographs of various specimens

Specimen type	Smooth	Notched	Flat
Dimple size, mean ± s.d. (μm)	0.68 ± 0.08	0.87 ± 0.17	0.72 ± 0.1

## 4 Conclusions

Three different types and sizes of tensile specimens were investigated for the interchangeability or comparability of tensile results. The results were compared with each specimen, and the following conclusions can be made:

- The notched specimen has higher UTS than the counterparts of flat and smooth specimens. This is due to the tri-axial state of stress at the notch root. Still, the UTS results for flat and notched tensile specimens fall within a considerable limit (5%) when compared to the standard (smooth) specimen. The yield strength (YS) results were not conclusive.
- The ductility for flat specimen is less consistent with the ductility of the round (standard) specimen, while the ductility of the notched specimen cannot be directly compared. The higher strain hardening in flat specimen reduced its ductility.
- The fractured surfaces were found to have dimples on the major area and ductile fracture mode for all the specimens. The fractograph for notched specimen consisted facets along with the dimples which can increase the tendency of somewhat brittle fracture.
- It is concluded that these specimen types tested in this study may be interchangeably used according to the application and the available resources within specified limits.

## References

1. Singh J, Nath SK (2020) Improved slurry erosion resistance of martensitic 13wt%Cr–4wt%Ni steel subjected to cyclic heat treatment. *Wear* 460–461:203476. <https://doi.org/10.1016/j.wear.2020.203476>
2. ASTM E8/E8M standard test methods for tension testing of metallic materials 1, pp 1–27 (2010). <https://doi.org/10.1520/E0008>
3. ISO Standard 6892-1:2016. Metallic materials—tensile testing—part 1: method of test at room temperature
4. Yuan WJ, Zhang ZL, Su YJ, Qiao LJ, Chu WY (2012) Influence of specimen thickness with rectangular cross-section on the tensile properties of structural steels. *Mater Sci Eng A* 532:601–605. <https://doi.org/10.1016/j.msea.2011.11.021>
5. An J, Wang YF, Wang QY, Cao WQ, Huang CX (2016) The effects of reducing specimen thickness on mechanical behavior of cryo-rolled ultrafine-grained copper. *Mater Sci Eng A* 651:1–7. <https://doi.org/10.1016/j.msea.2015.10.091>
6. Strnadel B, Brumek J (2013) Effect of tensile test specimen size on ductility of R7T steel. In: *Met. 2013—22nd international conference on metallurgy and materials proceedings*, pp 560–565
7. Masete MS, Muchavi NS, Chikosha S (2018) The effect of specimen geometry on tensile properties of titanium alloy metal sheet. *IOP Conf Ser Mater Sci Eng* 430. <https://doi.org/10.1088/1757-899X/430/1/012015>
8. Hwang JK (2019) Effects of diameter and preparation of round shaped tensile specimen on mechanical properties. *Mater Sci Eng A* 763:138119. <https://doi.org/10.1016/j.msea.2019.138119>

9. Yuan WJ, Zhou F, Zhang ZL, Su YJ, Qiao LJ, Chu WY (2013) An analysis on necking effect and stress distribution in round cross-section specimens of pure copper with different diameters. *Mater Sci Eng A* 561:183–190. <https://doi.org/10.1016/j.msea.2012.10.077>
10. Yang B, Sun WQ, Jiang WC, Wang ML, Li MC, Chen JK (2019) Comparative study of the tensile properties of a 1.25Cr–0.5Mo steel characterized by the miniature specimen and the standard specimen. *Int J Press Vessel Pip* 177:103990. <https://doi.org/10.1016/j.ijvp.2019.103990>
11. Konopik P, Farahnak P, Rund M, Prochazka R, Dzuga J (2018) Application of micro-tensile test for material characterization of mild steel DC01. *Ubiquity Proc* 1:33. <https://doi.org/10.5334/uproc.33>
12. Kishor B, Chaudhari GP, Nath SK (2016) Slurry erosion of thermo-mechanically processed 13Cr4Ni stainless steel. *Tribol Int* 93:50–57. <https://doi.org/10.1016/j.triboint.2015.08.048>
13. Kishor B, Chaudhari GP, Nath SK (2018) Slurry erosion behaviour of thermomechanically treated 16Cr5Ni stainless steel. *Tribol Int* 119:411–418. <https://doi.org/10.1016/j.triboint.2017.11.025>
14. Farrell K, Byun TS (2003) Tensile properties of ferritic/martensitic steels irradiated in HFIR, and comparison with spallation irradiation data. *J Nucl Mater* 318:274–282. [https://doi.org/10.1016/S0022-3115\(03\)00102-8](https://doi.org/10.1016/S0022-3115(03)00102-8)
15. Hyde TH, Sun W, Williams JA (2007) Requirements for and use of miniature test specimens to provide mechanical and creep properties of materials: a review. *Int Mater Rev* 52:213–255. <https://doi.org/10.1179/174328007X160317>
16. Tu Z, Ren S, Nyhus X, Akselsen B, He OM, Zhang J (2018) A special notched tensile specimen to determine the flow stress-strain curve of hardening materials without applying the Bridgman correction. *Eng Fract Mech* 179:225–239. <https://doi.org/10.1016/j.engfractmech.2017.04.039>
17. Kumar S, Chaudhari GP, Nath SK, Basu B (2012) Effect of preheat temperature on weldability of martensitic stainless steel. *Mater Manuf Process* 27:1382–1386. <https://doi.org/10.1080/10426914.2012.700150>
18. Zhang ZL, Hauge M, Thaulow C, Ødegård J (2002) A notched cross weld tensile testing method for determining true stress-strain curves for weldments. *Eng Fract Mech* 69:353–366. [https://doi.org/10.1016/S0013-7944\(01\)00075-3](https://doi.org/10.1016/S0013-7944(01)00075-3)
19. Olden ZL, Zhang V (2002) Material characterisation for ductile fracture by testing of notched tensile specimens. In: ECF14, Cracow, 2002. <https://www.gruppofrattura.it/ocs/index.php/esis/ECF14/schedConf/presentations>
20. Mann BS, Arya V (2001) Abrasive and erosive wear characteristics of plasma nitriding and HVOF coatings: their application in hydro turbines. *Wear* 249:354–360
21. Singh J, Nath SK (2021) Dissolution of delta ferrite through cyclic treatment and its influence on the hydro abrasive erosion and mechanisms. *Tribol Int* 161:107056. <https://doi.org/10.1016/j.triboint.2021.107056>
22. Singh J, Nath SK (2021) Thermal cycling effects on microstructural evolution and hardness of martensite 13wt%Cr–4wt%Ni steel. In: *Lecture Notes in Mechanical Engineering*. Springer Singapore, Singapore, pp 239–246. [https://doi.org/10.1007/978-981-33-6029-7\\_23](https://doi.org/10.1007/978-981-33-6029-7_23)
23. Singh J, Nath SK (2022) Microstructural characterization and investigation of slurry erosion performance of cyclically heat treated martensite steel. *Eng Fail Anal* 131:105833. <https://doi.org/10.1016/j.engfailanal.2021.105833>
24. Singh J, Nath SK (2020) Improvement in mechanical properties and wear resistance of 13Cr–4Ni martensitic steel by cyclic heat treatment. *Trans Indian Inst Met* 73:2519–2528. <https://doi.org/10.1007/s12666-020-02043-2>
25. Singh J, Nath SK (2020) Effects of cyclic heat treatment on microstructure and mechanical properties of 13%Cr–4%Ni martensitic stainless steel. *J Mater Eng Perform* 29:2478–2490. <https://doi.org/10.1007/s11665-020-04787-w>
26. Dieter SL, Kuhn GE, Semiati HA (2003) *Handbook of workability and process design*. ASM international
27. Möser M (n.d.) Chapter 15 fractography with the SEM (failure analysis)

# Effect of Substitution of Fly Ash on the Strength of Geopolymer Concrete



Arun Kumar Parashar, Prashant Sharma, and Neha Sharma

**Abstract** Concrete is most often used construction material for infrastructure, which includes structures such as buildings, bridges, roads, dams, and a variety of other structures. To fulfill the increased demand for constructing infrastructure, worldwide output of ordinary Portland cement (OPC) is increasing. This suggests that concrete will continue to be the most widely used construction material for a long time. Cement production consumes a lot of energy and emits a lot of CO<sub>2</sub> into the atmosphere. Another ecologically friendly concrete option is to utilize geopolymer, which is an inorganic alumina silicate polymer created from natural or waste resources such as fly ash, which is high in silicon and aluminum. Geopolymer is an inorganic alumina silicate polymer that may be manufactured from natural resources or waste products such as fly ash. This research looked at how various elements impact the mechanical characteristics of concrete and how the concrete mix behaves. To do this, concrete mixtures were created. There are many factors to consider when designing a geopolymer manufactured from fly ash, including how much cement it contains, how much cement it replaces, and how much activator solution it contains. The testing revealed that utilizing a fly ash-based geopolymer instead of fly ash improved the durability of concrete. Concrete with a 50% replacement ratio is more durable than other forms of concrete. It outperforms other kinds of concrete in terms of splitting tensile strength, compressive strength, and flexural strength.

**Keywords** Fly ash · Compressive strength · Cement · Flexural strength

## 1 Introduction

The major building materials utilized in reinforced concrete constructions are ordinary Portland cement and steel. Manufacturing of Portland cement and concrete, on other hand, are both energy demanding and produce significant CO<sub>2</sub> emissions [1–4]. Cement manufacturing alone is estimated to be responsible for 4–8% of all CO<sub>2</sub>

---

A. K. Parashar (✉) · P. Sharma · N. Sharma  
Department of Civil Engineering, GLA University, Mathura 281406, India  
e-mail: [arun.parashar@gla.ac.in](mailto:arun.parashar@gla.ac.in)

© The Author(s), under exclusive license to Springer Nature Singapore Pte Ltd. 2024  
R. K. Tyagi et al. (eds.), *Advances in Engineering Materials*, Lecture Notes in Mechanical Engineering, [https://doi.org/10.1007/978-981-99-4758-4\\_10](https://doi.org/10.1007/978-981-99-4758-4_10)

emissions globally, with 1 tonne of cement creating 1 tonne of CO<sub>2</sub>. Because Portland cement is made in large amounts across the globe, even a slight decrease in output might result in huge CO<sub>2</sub> emission reductions. However, since Portland cement is currently the most often used cementitious binder in concrete building, research into ecologically acceptable alternatives is becoming more important [5–8]. Inorganic waste materials from various industrial sectors have long been utilized as partial substitute for Portland cement. A substantial amount of research on these materials combined with Portland cement in binary and ternary combinations has recently been published, highlighting the increased mechanical and durability qualities above plain Portland cement. The goal of modern cement and concrete material development is to achieve great strength and durability while retaining a reasonable energy cost of manufacturing. There is a lot of possibility for the development of cement-free binders since Portland cement has a high embodied energy and contributes considerably to global CO<sub>2</sub> emissions. This is an area where the drive for more ecologically friendly construction materials and practices might have a substantial influence [9–11]. This project aims on employing chemical pre-treatment of fly ash to make a 19 geopolymer that will set and harden and might be utilized as a viable alternative to Portland cement. It is well-known that adding alkali to fly ash or slag can induce these materials to set and harden on their own, resulting in alkali-activated systems. It differs greatly from other alkali-activated materials in that it produces a polymer rather than a C-S-H gel (such as activated slag). The development of geopolymeric binders and their characteristics has received a lot of attention in recent years [12–14]. The geopolymer produced, on the other hand, come in a variety of mix patterns and activators. The focus of previous study has been on the qualities of these materials, with notable differences in performance. There has been limited research into how the fly ash and activators interact and how their relative amounts affect the performance and quality of the geopolymer concrete formed, as well as the underlying chemistry that causes these changes. As was indicated before, one possibility is to use binders that are activated by alkali and are manufactured from industrial byproducts that include silicate minerals [3]. Fly ash is a typical example of an industrial byproduct that is put to use in order to improve the cements and concretes' ability to improve their physical, chemical, and mechanical qualities. In the European Union (EU), a cement alternative called fly ash is employed, and it makes up roughly 30% of the overall output. Calcium silicate hydrate, also known as C-S-H, is produced when the Ca(OH)<sub>2</sub> produced during the hydration of Portland cement reacts with fly ash [15, 16]. Therefore, the reaction between Portland cement and fly ash will not start until the Portland cement first starts to hydrate. Because of this lag, the strength of mixed Portland cements develops at an earlier age and at a slower rate than that of Portland cement by itself. As a result, an upper limit of 40% fly ash substitution for Portland cement may be employed while preserving adequate strength and durability [17].



## 2 Materials

The study used BIS 8112: 2013 [18] standard grade 43 ordinary Portland cement. Care has been taken to ensure that the same cement company and quality are used throughout the research. Local river sand, devoid of organic pollutants and compliant with IS: 383–1970 [19], was used for the purpose of the fine aggregate. All three of the aforementioned properties of the fine aggregate—its bulk density, specific gravity, and fineness modulus—were determined in accordance with IS: 2386–1963 [20]. The coarse aggregate that was used in geopolymer and OPC concrete was typically spherical in shape, was well graded, and had a maximum size that was smaller than the coarse aggregate that was utilized in standard 64 concrete. The coarse aggregate utilized ranged in size from 10 to 20 mm. Graded aggregate is especially crucial for casting concrete in severely crowded reinforcement or small-diameter formwork. In this study, crushed granite metal with diameters ranging from 20 to 10 mm was procured from locally accessible quarries. In the building industry, fly ash is one of the most often utilized additional cementitious materials. It is an inorganic, noncombustible, finely split residue that forms from any industrial furnace's exhaust gases. Solids, cenospheres, and plerospheres are among the particles found in fly ash. Typical size of fly ash particles is less than 20 m, although they can be as small as 1 m or as large as 100 m. Its surface area varies between 300 and 500 m<sup>2</sup>/kg. Silica, alumina, iron, and calcium are the main components of silicate glass, which constitutes most fly ash. Fly ash has a grey hue and a specific gravity of between 1.9 and 2.8. Commercially accessible sodium silicate solutions come in a number of grades, while powdered water glass performs less effectively than liquid water glass. A silicate solution with a SiO<sub>2</sub> to Na<sub>2</sub>O ratio (by mass) of 2.0, along with an 8–16 M activator, should be mixed 24 h before usage for optimal effects. In the manufacturing of geopolymers, NaOH is often utilized as an alkaline activator. The properties of the paste are determined by the concentration and molarity of this activating solution (Fig. 1).

## 3 Methodology

The process of developing concrete mixes is a laborious one that is frequently determined by the required level of performance. In the process of designing a mix, the performance factors that are selected include the workability of new concrete and the compressive strength of concrete after it has had time to set. In the course of this investigation, 12 M sodium hydroxide was utilized. The compressive strength of geopolymer concrete was influenced, both directly and indirectly, by the quantities and qualities of the component elements that make up the geopolymer paste. The geopolymer paste is produced as a result of the reaction between the alkaline liquid and the silicon and aluminum oxides that are present in the low-calcium fly ash. The loose coarse and fine aggregates, as well as any extra components that have not yet



**Fig. 1** a Fly ash b NaOH flakes

reacted to generate the geopolymer concrete, are subsequently bound by this paste after it has been applied. In the same way as they do in OPC concrete, coarse and fine aggregates make up around 75–80% of the mass in GPC concrete. This is likewise the case with polymer-modified concrete (PC concrete). The flakes of sodium hydroxide were first dissolved in distilled water at least one day before their application in order to facilitate the production of a solution with a concentration of 12 M. Fly ash and aggregates were mixed together in a pan mixer with a capacity of 80 L, and the mixture was churned for close to three minutes. After thoroughly combining the 12 M sodium hydroxide with the extra water, it was added to the dry components, where it was stirred for about four minutes. The mold was filled with new concrete. The specimens were crushed using a rod to place three layers and press them down. This was followed by a 10-s vibration on a vibrating table, after which the molds were held at room temperature for ambient curing. In this study, fly ash was used to substitute cement to the tune of 0 to 100%. Table 1 shows the fly replacement level with cement.

**Table 1** Sample ID of concrete mix

Sample ID	Cement (%)	Fly ash (%)
C100F0	100	0
C80F20	80	20
C50F50	50	50
C20F80	20	80
C0F100	0	100

## 4 Testing

The amount of uniaxial compressive stress that a material is subjected to before it completely gives way is referred to as its compressive strength. In this investigation, cube specimens with dimensions of 150 mm on each side and 150 mm on top were analyzed in accordance with the international standard IS: 516–1969 [21]. The compression testing was carried out with equipment that had a capacity of 200 tonnes when it was being compressed. The split tensile strength test is one example of a technique used in indirect tension testing. During the compression test, a cylindrical specimen was put horizontally between the loading faces of a compression testing machine, and a load was applied until the cylinder failed along the vertical diameter. This continued until the force was released. When the cylinder did not work properly, the test was considered successful. A concrete cylinder with a diameter of 150 mm and a height of 300 mm was subjected to a compressive force that was delivered to two sides that were opposite to one another. The 87 cylinder was compressed at the loaded section, and uniform tensile stress was applied across the length of the cylinder. For all of the grades, 100 × 100 × 500 mm beams were produced. The flexural strength test is performed using a 100 kN capacity flexure testing equipment under two point stresses.

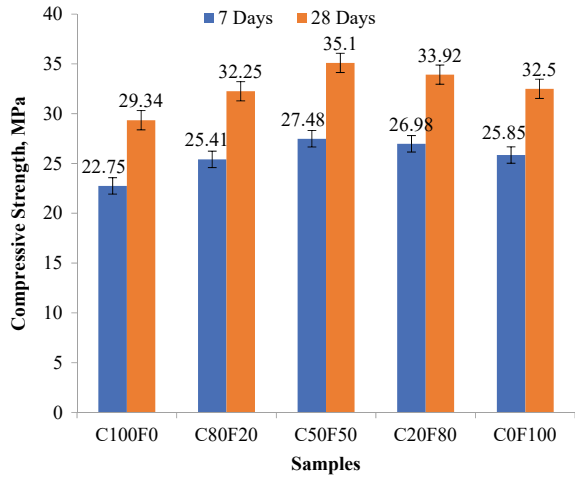
## 5 Result and Discussion

### 5.1 Compressive Strength

The compression strength of all kinds of samples was evaluated using compression testing equipment in accordance with IS: 516–1959. Figure 2 depicts the results of testing for ordinary concrete, partial cement replacement concrete, and complete cement replacement concrete.

Compressive strength, which is a component of mechanical strength, was measured after 7 and 28 days of curing in ambient air, respectively. The results of the compression strength test are displayed in Fig. 1. After 7 days of testing, C100F0 samples had compressive strengths of 22.75 MPa, whereas after 28 days of testing, those same samples had compressive strengths of 29.34 MPa. The compressive strength of C80F20 samples was 25.41 MPa after 7 days and 32.25 MPa after 28 days, respectively. Compressive strengths of samples made from C50F50 range from 27.48 MPa to 35.1 MPa, respectively. At 7 days and 28 days, the compressive strengths of C20F80 and C0F100 samples were 26.98 MPa and 25.85 MPa, respectively. C20F100 samples exhibited a compressive strength of 32.5 MPa. According to the findings, compressive strength improved up to the point where 50% of the cement was substituted with fly ash; however, when the amount of fly ash was increased, compressive strength began to decrease.

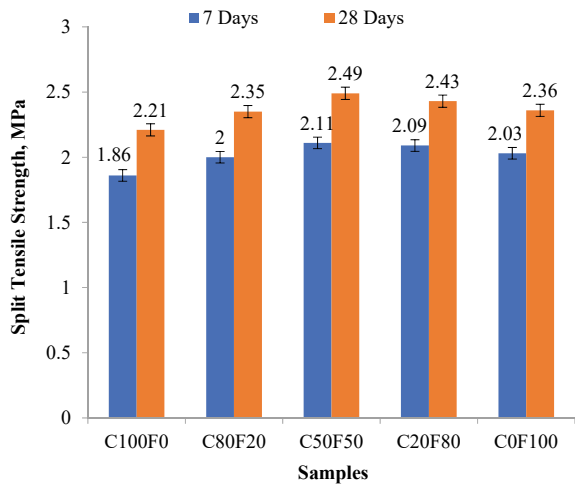
**Fig. 2** Compressive strength of standard and fly ash concrete



### 5.2 Split Tensile Strength

The splitting test or the indirect tensile test was used to measure the tensile strength of the geopolymer concrete that was based on fly ash. We used different amounts of cement to make thirty cylindrical specimens with diameters of one hundred millimeters and heights of two hundred millimeters. Each specimen had a height of two hundred millimeters. The results of the tests are shown in Fig. 3, which compares conventional concrete to concrete with partial cement replacement, complete cement replacement, and no cement replacement at all.

**Fig. 3** Split tensile strength of standard and fly ash concrete



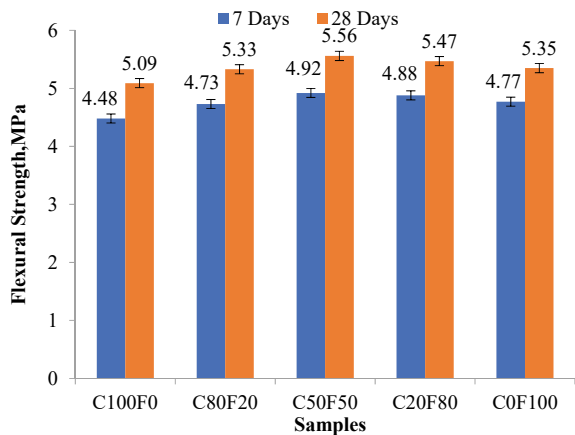
Split tensile strength, which is a component of mechanical strength, was tested before, after seven days of curing in ambient air and then again after twenty-eight days of curing. C100F0 samples were found to have a strength of 1.86 MPa after 7 days of testing, and after 28 days of testing, they were found to have a strength of 2.21 MPa. After seven days, the split tensile strength of C80F20 samples is determined to be 2 MPa, whereas after 28 days, it is determined to be 2.35 MPa. Both the split and tensile strengths of the C50F50 samples came in at 2.11 MPa, with the latter sample coming in at 2.49 MPa. After 7 days and 28 days, the split tensile strength of C20F80 and C0F100 samples was 2.09 MPa and 2.03 MPa, respectively, while at 14 days and 28 days, it was 2.43 MPa and 2.36 MPa, respectively. According to the findings, the strength rose all the way up to a cement replacement rate of fifty percent when using fly ash; however, after increasing the amount of fly ash, split tensile strength started to drop.

### 5.3 Flexural Strength

The outcomes of flexural testing for a range of cement replacement percentages are illustrated in Fig. 4. In geopolymer concrete, the optimal tensile strength of the material is determined by using the flexural strength of the first crack in the material. The influence that the replacement ratio has on flexure strength is illustrated in Fig. 3. When the replacement ratio is increased up to fifty percent, it has been demonstrated that flexural strength rises; however, after this point, there is no substantial difference evident.

The flexural strength of the material was evaluated after 7 and 28 days of curing in ambient air. This evaluation was included in the analysis of the material’s overall mechanical strength. After 7 days of testing, C100F0 samples showed flexural strengths of 4.48 MPa, and after 28 days of testing, those strengths increased to

**Fig. 4** Flexural strength of standard and fly ash concrete



5.09 MPa. The flexural strength of C80F20 samples was 4.73 MPa after 7 days and 5.33 MPa after 28 days, respectively. Flexural strengths of samples made from C50F50 range from 4.92 MPa to 5.56 MPa, respectively. The flexural strength of C20F80 and C0F100 samples was measured to be 4.88 MPa, 4.77 MPa, and 5.47 MPa, 5.35 MPa, respectively, after 7 and 28 days of curing. According to the data, flexural strength increased up to a replacement of 50% of the cement with fly ash; however, as the quantity of fly ash grew, flexural strength began to decrease.

## 6 Conclusion

1. The impact of varied levels of fly ash on geopolymer concrete was investigated in this research. When the percentage of fly ash substituted with cement was increased to 50%, the strength of the geopolymer mix increased. The following are some of the conclusions that may be derived from the study.
2. The compressive strength, splitting tensile strength, and flexural strength of mixes prepared with 0–100% cement replacement ratios were found to be the highest at 50% cement substitution ratio 2.
3. The compressive strengths of C100F0 and C80F20 samples were 29.34 MPa and 32.25 MPa, respectively. At 28 days of testing, the compressive strength of C50F50 samples was 35.1 MPa. At 28 days, the compressive strengths of C20F80 and C0F100 samples were 25.85 MPa and 32.5 MPa, respectively. When 50% of the cement was replaced with fly ash, the compressive strength increased to 19.63.
4. The strength of the C100F0 and C80F20 samples was 2.21 MPa and 2.35 MPa, respectively. At 28 days, the strength of C50F50 samples was 2.49 MPa. At 28 days, the strength of C20F80 and C0F100 samples was 2.03 MPa and 2.36 MPa, respectively.

## References

1. Gupta N, Gupta A, Saxena KK, Shukla A, Goyal SK (2021) Mechanical and durability properties of geopolymer concrete composite at varying superplasticizer dosage. *Mater Today Proc* 44:12–16
2. Sharma P, Sharma N, Singh P, Verma M, Parihar HS (2020) Examine the effect of setting time and compressive strength of cement mortar paste using iminodiacetic acid. *Mater Today Proc* 32:878–881
3. Kishore K, Gupta N (2021) Mechanical characterization and assessment of composite geopolymer concrete. *Mater Today Proc* 44:58–62
4. Parashar AK, Gupta A (2021) Experimental study of the effect of bacillus megaterium bacteria on cement concrete. In: IOP conference series: materials science and engineering, vol 1116, no 1. IOP Publishing, p 012168

5. Gupta A, Parashar AK (2022) Development of sustainable concrete using slag and calcined clay. In: Proceedings of international conference on innovative technologies for clean and sustainable development (ICITCSD–2021). Springer, Cham, pp 369–377
6. Sharma N, Sharma P, kr Verma S (2021) Influence of Diatomite on the properties of mortar and concrete: a review. In: IOP conference series: materials science and engineering, vol 1116, no 1. IOP Publishing, p 012174
7. Parashar AK, Gupta A (2022) Assessment of the impact of *Bacillus Cereus* Bacteria on strength and water absorption capacity of sustainable concrete. In: Proceedings of international conference on innovative technologies for clean and sustainable development (ICITCSD–2021). Springer, Cham, pp 379–388
8. Kadapure SA, Kulkarni GS, Prakash KB (2017) A laboratory investigation on the production of sustainable bacteria-blended fly ash concrete. *Arab J Sci Eng* 42(3):1039–1048
9. Nagar PA, Gupta N, Kishore K, Parashar AK (2021) Coupled effect of *B. Sphaericus* bacteria and calcined clay mineral on OPC concrete. *Mater Today Proc* 44:113–117
10. Gupta A, Gupta N, Saxena KK, Goyal SK (2021) Investigation of the mechanical strength of stone dust and ceramic waste based composite. *Mater Today Proc* 44:29–33
11. Kumar Tiwari P, Sharma P, Sharma N, Verma M (2020) An experimental investigation on metakaoline GGBS based concrete with recycled coarse aggregate. *Mater Today Proc* 40
12. Gupta N, Kumar P, Mishra A, Srivastava RP (2015) Characterization and application of rice husk ash as pozzolanic material in concrete. *IOSR J Mech Civil Eng* 12(3):28–32
13. Praveenkumar S, Sankarasubramanian G (2019) Behavior of high performance fibre reinforced concrete composite beams in flexure. *Rev Rom Mater* 49(2):259–266
14. Rajasekar A, Arunachalam K, Kottaisamy M, Saraswathy V (2018) Durability characteristics of ultra high strength concrete with treated sugarcane bagasse ash. *Constr Build Mater* 171:350–356
15. Achal V, Pan X (2011) Characterization of urease and carbonic anhydrase producing bacteria and their role in calcite precipitation. *Curr Microbiol* 62(3):894–902
16. Kadapure SA, Kulkarni GS, Prakash KB (2019) Study on properties of bacteria-embedded fly ash concrete. *Asian J Civil Eng* 20(5):627–636
17. Mounanga P, Khokhar MIA, El Hachem R, Loukili A (2011) Improvement of the early-age reactivity of fly ash and blast furnace slag cementitious systems using limestone filler. *Mater Struct* 44(2):437–453
18. BIS 8112 (2013) BIS 8112: 2013 ordinary portland cement, 43 grade specification. *Bur Indian Stand*
19. B. of I. S. (BIS) (1970) IS 383: 1970 specification for coarse and fine aggregates from natural sources for concrete. *Indian Stand*
20. Bureau of Indian Standards (BIS) (1963) IS: 2386 (Part II)—1963: methods of test for aggregates for concrete. *Indian Stand*
21. IS:516–1959 (2004) BJR£AU Indian stand Manak Shavan 9 Bahadtjr Shah Zafar Marg New Delhi 110002. Published online 2004

# Effect on Vibration Characteristics of Fiber Metal Laminates Reinforced with Jute/glass Fibers



Abhijeet Pidge, Aniket Salve, Ashok Mache, Aparna Kulkarni, and Yashwant Munde

**Abstract** Fiber metal laminate has outperformed aluminum alloys and fiber-reinforced polymer composites due to its superior mechanical characteristics and reduced density. They are commonly employed in aerospace applications. This paper investigates the damping capacities of fiber metal laminates, including stainless steel, glass fiber, and jute ply, as well as their virgin counterparts. The hand layup method is used to create laminates with eleven plies, which are subsequently compression molded. The plies are held together by epoxy adhesive. Tensile strength, modulus, and damping properties of composite laminates are all tested. The damping ratio and modal frequencies are also determined using experimental modal analysis. The influence of hybridization is investigated for modal and damping parameters obtained from damping experiments under fixed-free boundary conditions. The results of the experiments show that as the free length increases, the modal frequency decreases. The bigger the number of jute pies at the extreme ends, the better the damping properties. These compositions have a greater damping ratio as compared to other configurations.

**Keywords** Jute · Fiber metal laminate · Hybrid composite · Damping

---

A. Pidge · A. Salve · A. Mache (✉) · A. Kulkarni  
Vishwakarma Institute of Information Technology, Pune, India  
e-mail: [ashok.mache@viit.ac.in](mailto:ashok.mache@viit.ac.in)

A. Salve  
e-mail: [aniket.salve@viit.ac.in](mailto:aniket.salve@viit.ac.in)

A. Kulkarni  
e-mail: [aparna.kulkarni@viit.ac.in](mailto:aparna.kulkarni@viit.ac.in)

Y. Munde  
Cummins College of Engineering for Women, Pune, India



## 1 Introduction

Fiber metal laminates (FML's) are hybrid materials made up of thin metal sheets laminated together with layers of composite materials. Fibers integrated into adhesive system make up the composite layers. The FML takes the advantage of metal and results in enhanced properties like low density, metal fatigue, corrosion resistance, impact resistance, etc. The FML's advantages include its lightweight and strong strength-to-weight ratio [1–3]. Conventional metals such as aluminum and iron are replaced by the fiber metal laminates for manufacturing [1, 4, 5]. The combination of low density fiber and high density stainless steel sheet results in the requisite thickness and improved characteristics. The comparatively high density of stainless steel renders it unsuitable for aeroplane applications. Despite the fact that stainless steel has a specific stiffness comparable to aluminum alloys, its uses result in a thin sheet thickness and a high sensitivity to compression molding. Fiber metal laminates are high-performance and adaptable materials used in the aerospace sector. In technological applications, components are frequently subjected to a wide spectrum of vibrations. As a result, materials with good damping properties are preferred. Vibrations are designed into stiff and lightweight constructions. Because of their improved fatigue performance, fiber metal laminates are used for lightweight applications.

The most challenging aspect of any fiber metal laminate is to create an adhesive bond between the metal and the fiber. To solve this problem, numerous researchers used a combination of chemical and mechanical treatments [6, 7]. The metal surface can be mechanically treated using sand paper to increase its adhesion. As a result, the roughness of the metal surface provides peaks and valleys that promote adhesion [7]. The removal of metal oxide from the metal surface is essential during mechanical treatment for better adhesion. Acetone is used to remove dirt and greasy contaminants from metal surfaces. Various types of surface treatments are used, among which the sandblasting stainless steel surface shows better adhesion [8, 9]. The mechanical treatment is followed by the chemical treatment. The most common treatment is based on nitric-hydrofluoric acid etch. Stainless steel sheets are immersed in a nitric acid and hydrofluoric acid solution at 18 °C in this procedure for 12 min [10]. Delamination is the first failure which results in a decrease in overall strength and stiffness. Studies are reported, where FML is prepared using SS304 and glass fiber, and the results are studied under tensile load. It concludes that the surface treatment of metals shows a remarkable effect on fracture toughness [11]. Another researcher investigated stainless steel-based FML with glass fiber and concluded that it had improved corrosion resistance and peel strength. This study focuses on the use of stainless steel grade 304, as well as glass fiber and jute ply. Stainless steel shows good tensile strength. The use of stainless steel as the outer layer protects the fabrics inside the composite. This gives overall increase in the resistance to foreign object's impact and environmental effect on the fabrics. Fiber metal laminates are also used, considering the vibration characteristics. The fibers have increased viscoelasticity due to enhanced fiber matrix interaction at the microstructure level. As a result, composites' damping capacity increases. The modal frequency and damping characteristics are

influenced by the different parameters such as the stacking sequence and fiber orientation. The study uses a fiber metal laminate with eight fiber plies and three stainless steel sheets. An increase in jute fiber content leads to an increase in natural frequency of vibration. Pre-treatment of the fiber with acetic acid, silane, or sodium hydroxide results in an improvement of mechanical properties [12]. The natural frequency, and damping capacity can be affected with improvement in the mechanical properties [13]. The study by Daoud et al. [14] explores the vibration and damping characteristics of flax fiber reinforced composites with a natural viscoelastic layer through experiments and finite element modeling, yielding close alignment with experimental results and insightful parametric insights.

The purpose of this research is to develop a fiber metal laminate with SS304, glass, and jute fiber as reinforcement and to investigate its damping properties. The jute fiber based composite have been studied earlier for their performance under static and impact loading conditions [15–18] and found to be effective. In this study, eight plies of glass fiber and jute with different stacking sequences and three sheets of SS304 of 0.3 mm thickness are used to prepare the laminates. The hand layup method is used for the process, followed by compression molding. Tensile tests were carried out for mechanical properties. The modal frequency and the damping ratio are evaluated from the vibration tests. The vibration tests are carried out on different lengths to find out the effect of free length on the damping factor and frequencies.

In the current work, fiber metal laminate with SS304 and woven jute fiber as reinforcement with epoxy (Bond Tite) as an adhesive is prepared and studied for its mechanical and vibration properties. To the best of author's knowledge, this study is been reported first time. The outcome of this research work will provide valuable information to research community for developing low cost FML's for low and medium end structural applications.

## 2 Materials and Manufacturing Methods

### 2.1 Composite Constituents

Jute and glass fiber were procured locally in Pune, India, and were used to reinforce plain weave in the FML. Glass fibers weighing 360 GSM (grams per square meter) were employed in the method. The epoxy adhesive (Bond Tite, fast, and clear) and SS304 were acquired locally. Sand paper is utilized to prepare the stainless steel sheets of 0.3 mm thickness employed in this investigation for adhesive bonding. The fiber metal laminates were prepared by hand layup followed by compression molding and curing for about an hour at room temperature. The laminates developed demonstrate good adhesive bonding between metal and fibers without any chemical treatment. Equation (1) is used to calculate the volume fraction for each laminate. Variations in the volume fractions of the fibers and matrix are caused by resin impregnation provided by fibers, as well as their architecture and manufacturing flaws. Laminate

**Table 1** Volume fraction of FML and its virgin composites

Laminate configuration	Thickness (mm)	Density (Kg/mm <sup>3</sup> )	Volume fraction			
			Stainless steel 304	Glass	Jute	Matrix
SS-GGGG-SS-GGGG-SS	4.3	2453	0.131	0.351	–	0.516
SS-JJJJ-SS-JJJJ-SS	9.8	1186	0.162	–	0.296	0.541
SS-JGGG-SS-GGGJ-SS	4.9	2318	0.187	0.374	0.086	0.353
SS-JJGG-SS-GGJJ-SS	6.5	1916	0.175	0.234	0.160	0.429
SS-JJJG-SS-GJJJ-SS	7.9	1732	0.156	0.104	0.215	0.523
JJJJJJJ	5.6	1234	–	–	0.376	0.629
GGGGGGGG	2.0	1805	–	0.389	–	0.607

configurations and corresponding volume fractions are shown in Table 1.

$$VF_f = \frac{m_f / \rho_f}{m_f / \rho_f + m_m / \rho_m + m_s / \rho_s} \quad (1)$$

where  $VF_f$  = Volume fraction of fiber,  $m_f$  = mass of fiber,  $m_m$  = mass of matrix,  $m_s$  = mass of steel,  $\rho_f$  = density of fiber,  $\rho_m$  = density of matrix, and  $\rho_s$  = density of steel.

## 2.2 Mechanical Characterization

Tensile tests were conducted using Universal Testing Machine with a 100 kN capacity, as shown in Fig. 1, to obtain tensile strength and modulus of FML. Tensile tests were performed on specimens measuring  $250 \times 25 \times t$  mm. ASTM D3039 was used to determine tensile strength and modulus. The mechanical properties of hybridization and stacking sequence were examined.

## 2.3 Vibration Characteristics

Vibration test specimens with dimensions of  $340 \times 50 \times t$  mm were cut from the laminates and analyzed under fixed-free boundary conditions with a free length of 300 mm and a clamping length of 40 mm. The modal frequencies are obtained using the fast Fourier transform (FFT) analyzer to obtain and understand the damping behavior of the prepared composite specimens. The diagram of the experimental setup and the cantilever beam test specimen for modal analysis is shown in Fig. 2. The signal for acceleration versus frequency and acceleration versus time is captured with the help of Brüel & Kjær accelerometer mounted on the cantilever composite

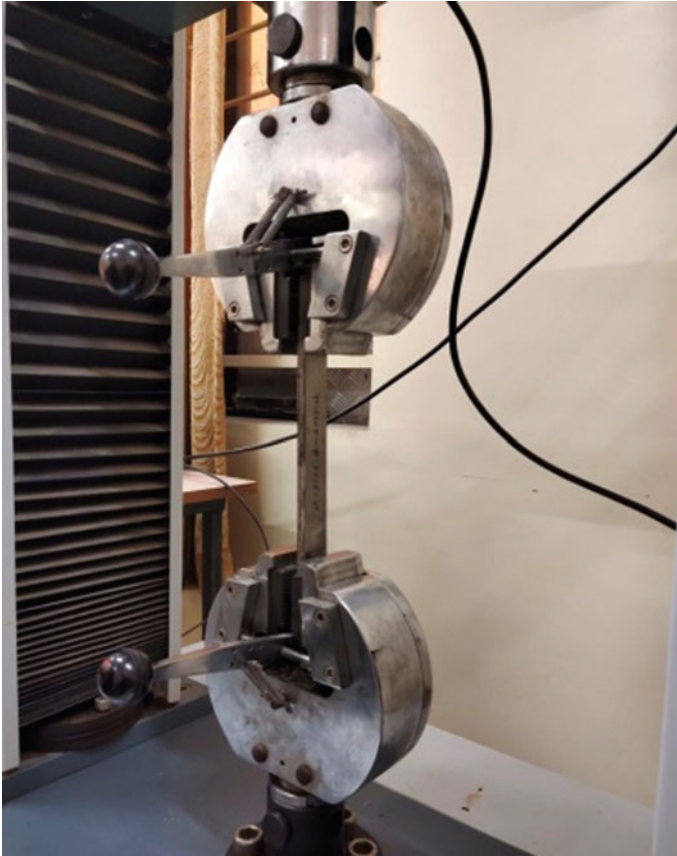


**Fig. 1** FML under tensile test

specimen under test. The inherent mass of the accelerometer has minimum effect on the vibration specimens. Only one channel of the accelerometer is connected to the fast Fourier transform (FFT) to obtain a frequency domain signal from the time domain acceleration signal. The modal frequencies are represented by the peaks in the acceleration versus frequency graph. To convert the time domain signal to the frequency domain signal, the Brüel & Kjaer data gathering system is utilized in conjunction with the RT Pro Photon software.



**Fig. 2** **a** Test setup for modal analysis of cantilever beam using FFT analyzer, **b** Cantilever beam test specimen used for modal analysis

The damping ratio is evaluated using logarithmic decrement method and half power bandwidth method.

(i) Logarithmic Decrement:

$$\delta = \frac{1}{n} \ln \frac{x_i}{x_{n+i}} \quad (2)$$

and

$$\zeta = \frac{1}{\sqrt{1 + \left(\frac{\delta}{2\pi}\right)^2}} \quad (3)$$

where  $\delta$  = Logarithmic decrement,  $x_i$  =  $i$ th acceleration amplitude,  $x_{n+i}$  =  $(n + i)$ th acceleration amplitude, and  $\zeta$  = damping ratio.

(ii) Half power bandwidth method:

$$\zeta = \frac{\omega_2 - \omega_1}{2\omega_n} \quad (4)$$

## 3 Results and Discussion

### 3.1 Experimental Test Results

#### Tensile Properties

Tensile test specimens are shown in Fig. 3a and Fig. 3b depicts the specimens that failed in tensile test. During the tensile test of FML, the specimen breaks due to delamination at the weakly bonded surface of metal and fiber. The stress–strain

curves for fiber metal laminates and their virgin equivalents loaded at a rate of 2 mm/min are shown in Fig. 4. The modulus and tensile strength changes are shown in Table 2. Glass/epoxy composites have the maximum tensile strength of 373 MPa among virgin composites, whereas jute/epoxy has the lowest strength of around 46 MPa. The fiber metal laminate with the stacking sequence (SS-GGGG-SS-GGGG-SS) observed a tensile strength of 277 MPa. This configuration’s lower strength as compared to pure glass/epoxy composite is due to inadequate bonding between glass fiber and SS304. The FML with jute ply and stainless steel has a low tensile strength. The composite structure with glass fiber as the inner layer has a higher tensile strength.

The FML with the stacking sequence: SS-GGGG-SS-GGGG-SS has a tensile strength of 277 MPa, which is greater than the jute fiber reinforcement, which has a 40% loss in strength by adding jute ply at the extreme end following stainless steel. This study shows that the external layers play an important role in damping. The modulus of the FML is increased by 26% when jute plies are added at the extreme ends following stainless steel.

**Table 2** Tensile properties of fiber metal laminates and its virgin composite

Laminate configuration	Tensile strength (MPa)	Young’s modulus (GPa)	Breaking strain %
SS-GGGG-SS-GGGG-SS	277	2.97	10.37
SS-JJJJ-SS-JJJJ-SS	90	0.98	9.01
SS-JGGG-SS-GGGJ-SS	167	1.90	9.23
SS-JJGG-SS-GGJJ-SS	91	1.23	7.99
SS-JJJG-SS-GJJJ-SS	160	2.24	7.86
JJJJJJJ	46	1.15	4.35
GGGGGGGG	373	4.31	9.35



**Fig. 3** a Tensile test specimens, b FML specimen failure after tensile test

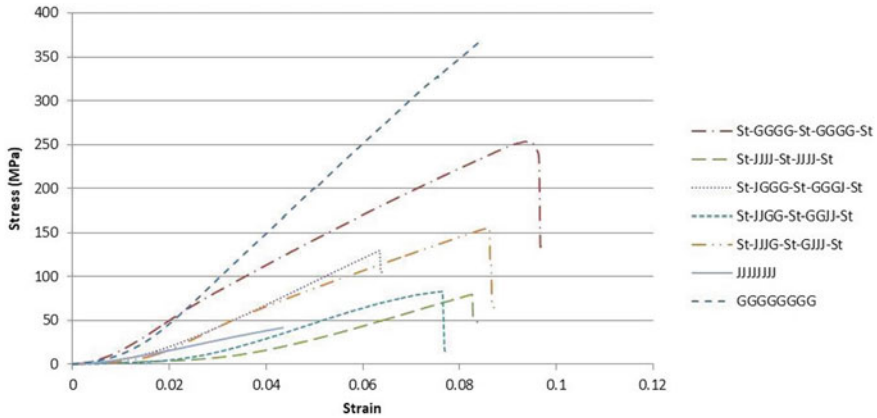


**Fig. 4** Stress–strain curve for fiber metal laminate and its virgin composites

**Natural frequency and damping ratio**

The damping ratio and first modal frequency of the FML for various free lengths are shown in Tables 3 and 4, respectively. It indicates that as the free length increases, the modal frequencies decrease. In terms of free length, all of the pieces have the same relative performance. The frequencies and damping behavior of FML depend on volume fraction of the matrix, fiber, and SS304. Additionally, it can also depend upon the surface treatment of the metal surface. The composition: SS-JJJJ-SS-JJJJ-SS, SS-JJGG-SS-GGJJ-SS, and SS-JJGG-SS-GJJJ-SS shows an increase in damping factor due to the presence of high viscoelastic natural fiber at the extreme end after stainless steel that dissipate more vibration energy. The composition: SS-JGGG-SS-GGGJ-SS, SS-GGGG-SS-GGGG-SS shows lower damping capacity due to increase in stiffness. The effect of free length of the cantilever beam over the frequency is shown in Fig. 5.

The damping capacity and stiffness act inversely in FML, which means that increasing the stiffness reduces the damping capacity of the FML.

**Table 3** Damping factor of composite specimen for different free length

Free length (mm)	100	150	200	250	300
Sequence	Damping ratio				
SS-GGGG-SS-GGGG-SS	0.0554	0.0290	0.0340	0.0355	0.0330
SS-JJJJ-SS-JJJJ-SS	0.0715	0.0590	0.0670	0.0514	0.0538
SS-JGGG-SS-GGGJ-SS	0.0234	0.0239	0.0332	0.0214	0.0230
SS-JJGG-SS-GGJJ-SS	0.0860	0.0464	0.0478	0.0273	0.0344
SS-JJGG-SS-GJJJ-SS	0.0771	0.0753	0.0512	0.0548	0.0469
JJJJJJJ	0.0645	0.0202	0.0197	0.0245	0.022
GGGGGGGG	0.0411	0.0465	0.038	0.0234	0.0293

**Table 4** First modal frequency of composite specimens for different free length

Free length (mm)	100	150	200	250	300
Sequence	First modal frequency				
SS-GGGG-SS-GGGG-SS	226	110	68	46	32
SS-JJJJ-SS-JJJJ-SS	262	155	91	68	52
SS-JGGG-SS-GGGJ-SS	256	140	82	57	39
SS-JJGG-SS-GGJJ-SS	218	140	83	55	37
SS-JJJG-SS-GJJJ-SS	193	99	65	47	32
JJJJJJJ	98	49	30	21	15
GGGGGGGG	55	27	16	11	9

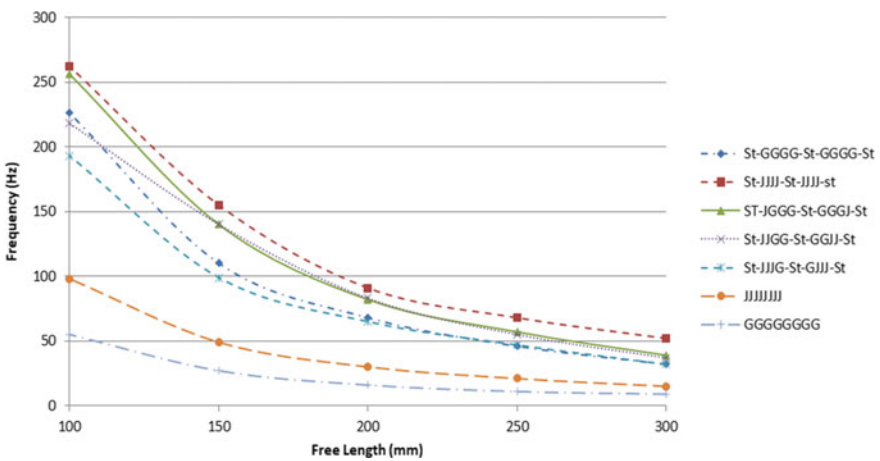


**Fig. 5** Frequency versus free length for different fiber metal laminates compositions

### 3.2 Numerical Results

To study the vibration characteristics of the fiber metal laminate, the finite element method is used. The parameters such as metal thickness, number of layers, fiber thickness, and their effect on damping is studied. The natural frequencies of the FML specimens were obtained numerically using ANSYS. The obtained frequencies and analyzed results are represented in Table 5 and Fig. 6, respectively. The theoretically calculated frequencies using the Euler Bernoulli equation are compared to the numerical data. The theoretically calculated frequencies are closer to the numerically evaluated frequencies.

The experimentally obtained frequencies are verified through analytical approach using Euler Bernoulli beam theory as shown in Eq. (5).



**Table 5** Theoretical and numerical obtained frequency

Stacking sequence	Theoretical frequency (Hz)			Numerical frequency (Hz)		
	Mode1	Mode 2	Mode 3	Mode 1	Mode 2	Mode 3
SS-GGGG-SS-GGGG-SS	1.80	11.30	31.64	1.55	9.70	27.14
SS-JJJJ-SS-JJJJ-SS	2.40	15.31	42.86	2.45	9.79	42.45
SS-JGGG-SS-GGGJ-SS	0.87	5.45	15.27	0.93	5.85	16.38
SS-JJGG-SS-GGJJ-SS	1.82	11.45	32.06	1.84	11.51	32.16
SS-JJGG-SS-GJJJ-SS	2.95	18.54	51.91	2.99	16.02	52.12
JJJJJJJ	1.92	12.05	33.75	1.95	12.20	34.17
GGGGGGG	0.87	5.49	15.37	0.87	5.50	20.55

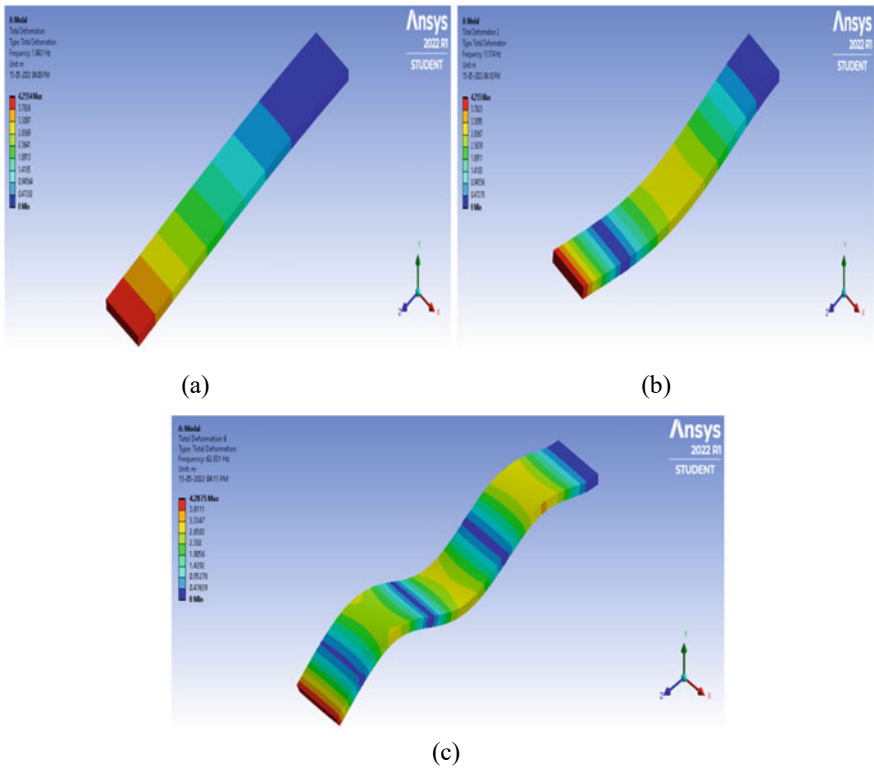


**Fig. 6** Numerically obtained modal analysis results

$$\omega = \frac{\beta^2}{2\pi} \left( \sqrt{\frac{EI}{\rho AL^4}} \right) \tag{5}$$

**Table 6** Natural frequency obtained experimentally

Stacking sequence	Experimental frequency (Hz)		
	Mode 1	Mode 2	Mode 3
SS-GGGG-SS-GGGG-SS	1	17	24
SS-JJJJ-SS-JJJJ-SS	1	14	46
SS-JGGG-SS-GGGJ-SS	1	6	23
SS-JJGG-SS-GGJJ-SS	1	22	28
SS-JJG-SS-GJJJ-SS	1	6	40
JJJJJJJ	1	7	23
GGGGGGGG	1	3	15

where  $\omega$  = natural frequency,  $A$  = area of cross-section,  $L$  = free length,  $\rho$  = density of specimen,  $E$  = Young’s modulus,  $I$  = moment of inertia,  $\beta = 1.875, 4.694$  and  $7.854$  for the first, second, and third mode, respectively. The experimentally determined frequencies fall within the range of theoretical and numerical frequencies, as indicated in Table 6.

## 4 Conclusion

The vibration characteristics, such as modal frequency and damping factor, of FML made of SS304, glass, and jute fiber, were examined in this work. The tensile strength of FML with greater number of glass plies and stainless steel in the core having a configuration of SS-JGGG-SS-GGGJ-SS is greater than that of other stacks. The greater the number of jute plies at the extreme end (SS-JJG-SS-GJJJ-SS), the better the damping. Furthermore, when free length decreases, the modal frequency and damping ratio rise in FMLs with different stacking. The FML adhesive bonding demonstrates that no chemical treatment is required. Mechanical treatment of stainless steel using sand paper can improve adherence. Using ANSYS, modal analysis simulation on fiber metal laminates yields satisfactory modal frequency results. Higher frequencies were seen in the FML, with more glass fibers in the middle and less at the extremes. Among the virgin composites, the jute/epoxy composite shows a higher frequency. When jute plies are added at the extreme ends of the FML, the modulus increases by 26%.

## References

1. Mouritz AP, Gellert E, Burchill P, Challis K (2001) Review of advanced composite structures for naval ships and submarines, vol 53

2. Khalid MY, Arif ZU, Al Rashid A, Shahid MI, Ahmed W, Tariq AF, Abbas Z (2021) Inter-laminar shear strength (ILSS) characterization of fibre metal laminates (FML's) manufactured through VARTM process. *Forces Mech* 4
3. Aniket S, Ratnakar K, Ashok M (2016) A review: fibre metal laminates (FML's) manufacturing, test methods and numerical modelling. *Int J Eng Technol Sci* 3(2)
4. Kavitha K, Vijayan R, Sathishkumar T (2019) Materials today: proceedings fibre metal laminates: a review of reinforcement and formability characteristics. *Mater Today Proc*
5. Khalid MY, Rashid AA, Sheikh MF (2021) Effect of anodizing process on inter laminar shear strength of GLARE composite through T-Peel test: experimental and numerical approach. *Exp Tech*
6. Sinmazcelik T, Avcu E, Bora MO (2011) A review: fibre metal laminates, background, bonding types and applied test methods. *Mater Des* 32(7):3671–3685
7. Thirukumaran M, Winowlin Jappes JT, Siva I, Ramanathan R, Brintha NC, On the interfacial adhesion of fibre metal laminates using surface modified aluminium 7475 alloy for aviation industries—a study. *J Adhes Sci Technol*
8. Sarlin E, Heinonen E, Vuorinen J, Vippola M, Lepistö T (2014) Adhesion properties of novel corrosion resistant hybrid structures. *Int J Adhes* 49:51–57
9. Singh S, Angra S (2018) Experimental evaluation of hygrothermal degradation of stainless steel fibre metal laminate. *Eng Sci Technol Int J* 21(1):170–179
10. ASTM, Standard guide for preparation of metal surfaces for adhesive bonding
11. Kanerva M, Sarlin E, Saarela O (2013) Variation in mode II dominated interface fracture of stainless steel-epoxy bonds. Part I: mechanical testing. *Eng Fract Mech* 99:147–158
12. Li X, Tabil LG, Panigrahi S (2007) Chemical treatments of natural fiber for use in natural fiber-reinforced composites: a review. *J Polym Environ* 15(1):25–33
13. Harshad P, Ashok M, Yashwant M, Siva I, Synergy of inter-laminar glass fibre hybridization on mechanical and dynamic characteristics of jute and flax fabric reinforced epoxy composites. *J Nat Fibres*
14. Daoud H, El Mahi A, Rebière JL, Taktak M, Haddar M (2017) Characterization of the vibrational behaviour of flax fibre reinforced composites with an interleaved natural viscoelastic layer. *Appl Acoust* 128:23–31
15. Mache A, Deb A (2013) A comparative study on the axial impact performance of jute and glass fibre-based composite tubes. *SAE Technical Paper*, 01-1178
16. Ashok M, Anindya D, Narinder G (2020) An Experimental Study on performance of Jute-Polyester composite tubes under axial and transverse impact loading. *Polym Compos* 41(5):1796–1812
17. Aninsya D, Sumitesh D, Ashok M, Rokesh L (2017) A study on mechanical behaviour of jute-polyester composites. *Procedia Eng* 173:631–638
18. Harshad P, Ashok M, Yashwant M, Siva I (2021) A comprehensive review on drop weight impact characteristics of bast natural fiber reinforced composites. *Mater Today Proc* 44(5):3872–3880

# Human–Computer Interaction: Comparison of Different Contributions Based on Opinion and Survey



Krishnakant Dixit and Kanchan Yadav

**Abstract** Human–computer interaction (HCI) has a long and contentious history of “technology.” The academic and consistent status of HCI is regularly called into question, resulting in hollow rhetoric. In the 1970s, it grew quickly from research laboratories, coinciding with the term of the Decennial conferences. Since its inception, there have been concerns regarding his standing as a normal academic object, on which many of them have concentrated their attention. In this paper, a comparative study was conducted between the main parameters of human–computer interaction, which are analytical and theoretical contribution. Three types of discoveries are described here: the first is conceptual, the second is operational, and the third is analytical. HCI is widely recognised as an interdisciplinary study topic. It takes years and years for new types of knowledge and information to arise, integrate, and stabilise in HCI. Several sorts of study findings have evolved over time, and the gaps in this research were identified using opinion datasets and survey contributions. This makes it easy to comprehend how much human–computer interaction is feasible in real time.

**Keywords** Multi-disciplinary · Human computer interaction cognitive study · Technology · Conceptual · Operational · Analytical

## 1 Introduction

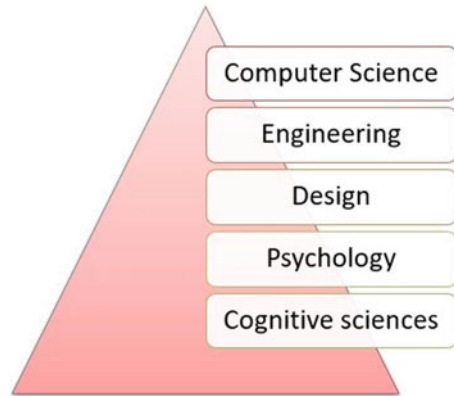
The study and creation of interactive technologies is referred to as HCI stands for human–computer interaction, and it has a strong and diverse scientific community [1–5]. Discussions on different roles of technology in HCI may be outlined the talks between Campbell, Card, Newell, and Carroll in beginning of the 1980s on the

---

K. Dixit (✉) · K. Yadav  
GLA University, Mathura, India  
e-mail: [krishnakant.dixit@gla.ac.in](mailto:krishnakant.dixit@gla.ac.in)

K. Yadav  
e-mail: [kanchan.yadav@gla.ac.in](mailto:kanchan.yadav@gla.ac.in)

**Fig. 1** HCI-related research fields



application of cognitive psychology in the design and development of the science of the interaction between human and computer [6–10]. Subsequently there have been intermittent assertions of a wish to create some kind of technical disciplinary for HCI. This may be seen in recent years at ACM CHI conference, which has featured workshop and lectures on themes like scientific imitation and collaborative science when compared to other true examples, HCI is a bad scientific field. HCI is discovered to be lacking of central motor themes, which are believed to be hallmark of through scientific fields, implying that the HCI program has failed. More work is needed to make HCI “more scientific, as Greenberg and Thimble noted in 1992.” This study covers a number of cognate themes in HCI, including science, disciplinary, and design, in addressing these complicated disputes and point out in this work that the concern of HCI as an academic’s goal is a consequence of the first stages of research. This way, cognitivist perspective was used to scientific reasoning with the design notion of Simon in order to generate a particular research idea known as the space of science design. This informs both our understanding of and our exploration of human–computer interactions. Figure 1 shows HCI-related research fields.

In this paper, a comparison is made between the current contributions to the field of human–computer interaction, namely analytical research, artifact contribution, and theoretical contribution, and then, the conclusions are validated using various datasets and expert opinions.

### ***1.1 Analytical Study***

The foundation of science is analytical studies. The survey and collection of data adds to new knowledge. Data might be qualitative or quantitative, objective or non-population-based in laboratories or in the field. Experiments, test users, surveys, surveys, target groups, journals, ethnography, field observations, and surveys all contribute to the analytical contributions from HCI (Fig. 2).

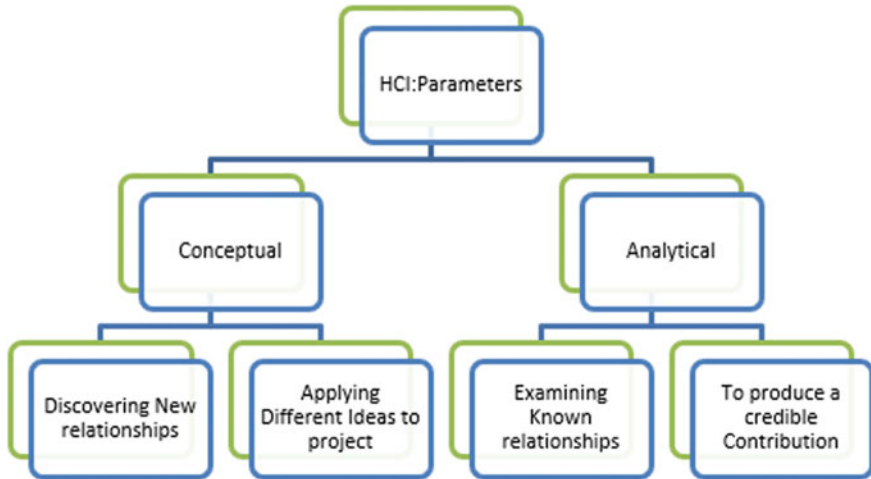


Fig. 2 Flow chart indicating comparative parameters of conceptual and analytical contributions

Table 1 Analytical data distribution

Percentage distribution	Analytical study of system use	Analytical study of people
Percentage of submission	44	29
Percentage of program	45	32
Acceptance rate	24	26

Analytical research is mostly used to assess the significance of their findings and the soundness of their methodologies [11, 12]. Table 1 shows analytical data distribution, and Fig. 3 shows analytical data distribution graph.

## 2 Artifact Contributions

The conception and deployment of interactive artifacts is driven by HCI [13–15]. Artifacts are created through generative design activities, whereas analytical contributions are obtained from descriptive discovery (science) activities (invention). New systems, archaeologies, tools, toolkits, technologies, skits, mock-ups, and settings, often prototypes, open up new opportunities, facilitate new explorations, and drive us to contemplate future potential. The objects and materials that come with them become part of and manifest new knowledge. The value of artifact research contributions is determined on the type of item. They often go with analysis, but not always. They are often combined with analytical investigations. The evaluation of novel systems, architectures, techniques, and techniques in reference to what has been done and what has not been done. On the other hand, new input and interaction

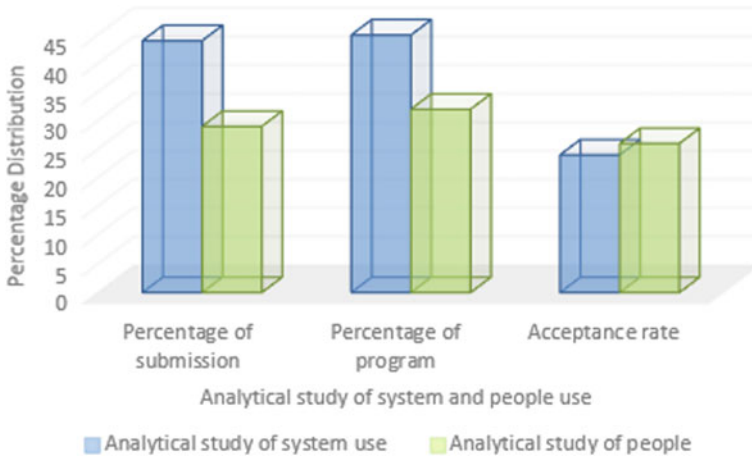


**Fig. 3** Analytical data distribution graph

**Table 2** Artifact’s data distribution

Percentage distribution	Artifacts
Percentage of submission	23
Percentage of program	24
Acceptance rate	21

strategies are thoroughly and scientifically examined in order to extract their human advantages. Images of fresh design expressions that are intelligent, compelling, and innovative are examined, including drawings, mock-ups, and visions. How you negotiate trade treaties and balance opposing agendas is crucial to consider. Table 2 shows artifact’s data distribution, and Fig. 4 shows artifact’s data distribution graph.

### 3 Methodological and Theoretical Contribution

#### 3.1 Methodological

The contribution of methodological research produces fresh knowledge that guides how our work is carried out [16]. This has the potential to improve research or practice. You have the ability to influence our approach to science and design. You can improve the way things are detected, measured, analysed, created, or built. For methodological research contributions, the usefulness, reproductivity, dependability, and legitimacy of an original process or process improvement are evaluated. Approaches for reproducing and providing reliable and valid results are rated

positively. To understand a method’s properties, it must be validated repeatedly. Table 3 shows methodological data distribution, and Fig. 5 shows methodological data distribution graph.

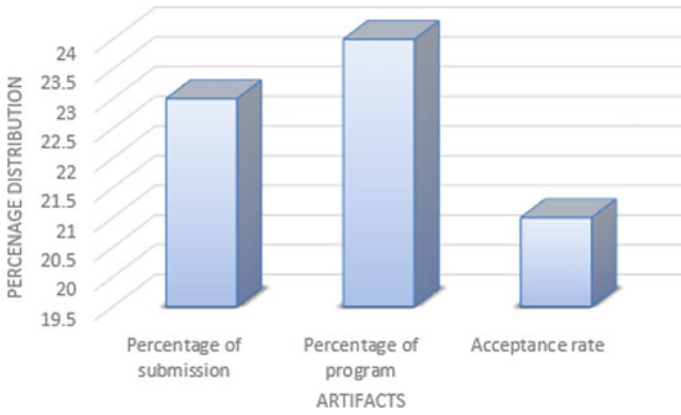


**Fig. 4** Artifacts data distribution graph

**Table 3** Methodological data distribution

Percentage distribution	Methods
Percentage of submission	19
Percentage of program	14
Acceptance rate	17

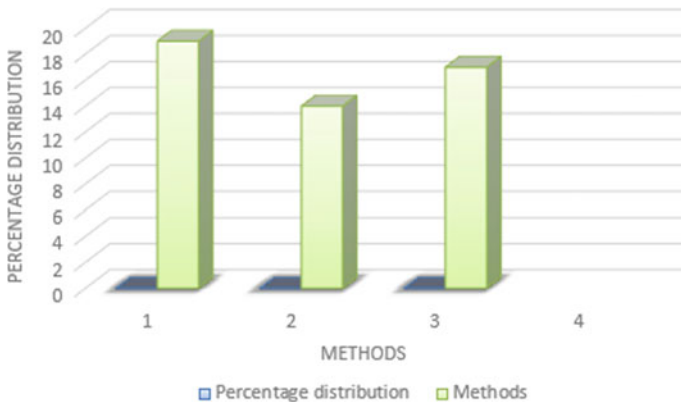


**Fig. 5** Methodological data distribution graph



### 3.2 Conceptual Contribution

Conceptual research contributions include new or better concepts, definitions, models, principles, or frameworks. They are thought-generating vehicles. While methodological contributions have an impact what is done, what we do, why we do so, and what we desire influences conceptual contributions. Qualitative or quantitative theories can be employed. It can be both descriptive and predictive; it can also show how this phenomenon works by the distillation of the key features of a phenomenon. Fully developed theories not only examine it, but also explain why accounts of explanation. Theories must be testable and forgery-proof; otherwise, they should not be considered. Table 4 describes conceptual data distribution, and Fig. 6 shows conceptual data distribution graph.

**Table 4** Conceptual data distribution

Percentage distribution	Conceptual
Percentage of submission	6
Percentage of program	4
Acceptance rate	18

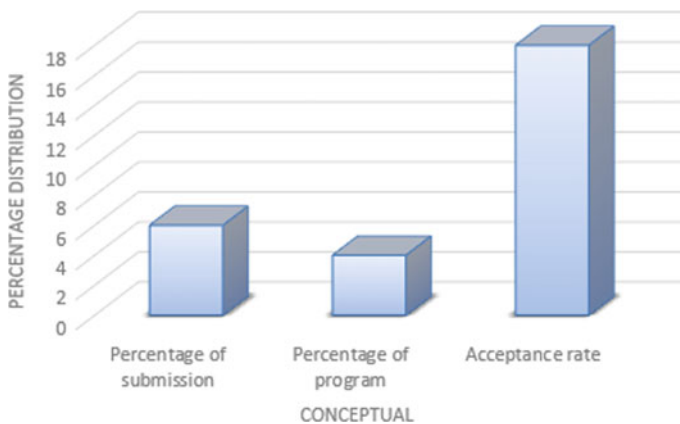


**Fig. 6** Conceptual data distribution graph

**Table 5** Dataset distribution

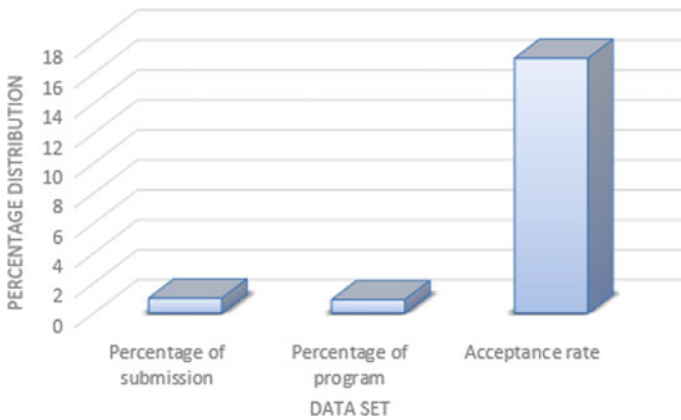
Percentage distribution	Dataset
Percentage of submission	1
Percentage of program	0.9
Acceptance rate	17

## 4 Results and Discussion Based on Different Parameters

### 4.1 Opinion Dataset and Survey Contribution Results

#### 4.1.1 Dataset

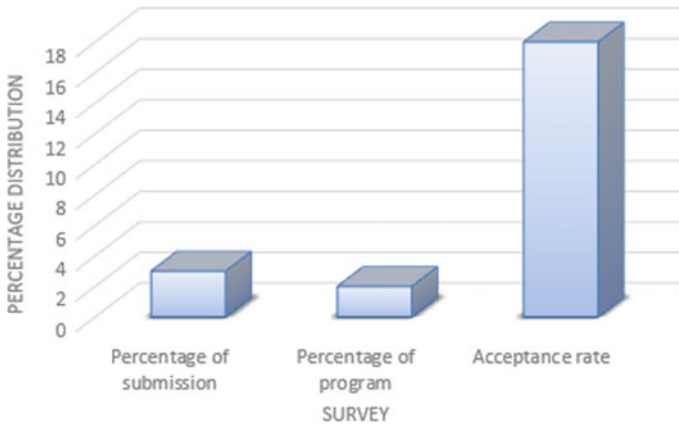
A dataset contribution gives the research community a fresh and relevant collection of data, and it is often accompanied by a description of its features. Datasets may be accompanied by the standardisation of comparison benchmark tests. These datasets enable the evaluation of new algorithms, systems, or methods for shared repositories. The value of datasets in research is proportional to extent which the research community can test and measure a useful and representative. To allow scientists to work with new corpus, datasets are frequently published using new tools. Contributions to datasets are frequently accompanied by methods for executing the dataset in which a new method is intended. Table 5 shows dataset distribution, and Fig. 7 shows dataset distribution graph.



**Fig. 7** Dataset distribution graph

**Table 6** Survey data distribution

Percentage distribution	Survey
Percentage of submission	3
Percentage of program	2
Acceptance rate	18

**Fig. 8** Survey distribution graph

## 4.2 Study Contributions

In order to discover patterns and gaps, survey studies and other meta-analysis assess and create literature on certain issue. After a certain level of maturity has been reached, survey contributions are appropriate. Hundreds of references are not unusual in surveys. The periodical ACM Computing Surveys mostly publish survey investigations. Regularly in the journal Foundations and Trends in HCI. In basic terms, survey contributes and meta-analyses are assessed in order to organise and identify novel research paths, which is previously known about a subject. Table 6 shows survey data distribution, and Fig. 8 shows survey data distribution graph.

## 4.3 Opinion Contribution

Contributions to opinion research, also known as essays or arguments, attempt to persuade people to change their minds. Despite the fact that the word “opinion” may refer to a less scientific endeavour, it is founded on all of the aforementioned contributions. Opinion is considered a separate category of research contribution, whether or not it lacks a research foundation, but because its aim is to convince instead of merely educating.

## 5 Conclusion

The current contributions to the field of human–computer interaction, including analytical research, artifact contribution, and theoretical contribution, are compared in this study, and the conclusions are validated using diverse data sets and expert opinions.

As the HCI area evolves, the information it generates and the forms it takes should be acknowledged. Reflection can be tough in a wide variety of subjects, and while we should avoid limiting our creativity, it can be challenging. The purpose of opinion and argument submissions is to stimulate thought, dialogue, and discussion. Opinion analysis submissions are rated according to their assertion. Strong claims rely on objective evidence to present opposing opinions. They address matters of widespread interest and should be readily accessible. This handy map can help newbies navigate the HCI sector as they take their first steps. Certainly, these newcomers will expand our horizons and enrich our experience. All of these studies and opinions aid us in analysing the real-time feasibility of human–computer connection and the public's acceptance of it.

## References

1. Sun Y, Wen Z, Zhang S (2021) Experience in teaching design of human-computer interaction through evaluation and research. In: International conference on applied human factors and ergonomics. Springer, Cham
2. Kumar A, Sharma K, Dixit AR (2020) Role of graphene in biosensor and protective textile against viruses. *Med Hypotheses* 144:110253
3. Xu W et al (2021) From human-computer interaction to human-AI interaction: new challenges and opportunities for enabling human-centered AI. arXiv preprint [arXiv:2105.05424](https://arxiv.org/abs/2105.05424)
4. Saxena A, Kumar J, Deolia VK, Roy D (2022) Assessment of traditional and hybrid controller for controlling robotic manipulator system. In: Recent advances in industrial production. Springer, Singapore, pp 509–515
5. Bouzekri E et al (2021) Should I add recommendations to my warning system? The RCRAFT framework can answer this and other questions about supporting the assessment of automation designs. In: IFIP conference on human-computer interaction. Springer, Cham
6. Shukla MK, Sharma K (2019) Effect of functionalized graphene/CNT ratio on the synergetic enhancement of mechanical and thermal properties of epoxy hybrid composite. *Mater Res Express* 6(8):085318
7. Schmid D (2021) Single pilot operations along the human-centered design lifecycle: reviewing the dedicated support concept. In: Congress of the international ergonomics association. Springer, Cham
8. Benne D, Schöbel S, Janson A (2021) Persuasive design for smart personal assistants—a theory-motivated state-of-the-art analysis
9. Jarosz M et al (2021) Multi-platform intelligent system for multimodal human-computer interaction. *Comput Inf* 40(1):83–103
10. Bressa N et al (2021) What's the situation with situated visualization? A survey and perspectives on situatedness. In: IEEE transactions on visualization and computer graphics
11. Ramírez AJ, Reijers HA, Enríquez JG (2021) 9 Human–computer interaction analysis for RPA support. In: Robotic Process Automation. De Gruyter Oldenbourg, 2021, pp 169–186

12. Roodbandi J, Sadat A et al (2021) Research outputs in ergonomics and human factors engineering: a bibliometric and co-word analysis of content and contributions. *Int J Occup Safety Ergon* just-accepted:1–42
13. Saxena A, Kumar J, Sharma K, Roy D (2022) Designing and analysis of dynamic model for robotic manipulator. In: *Advances in energy technology*. Springer, Singapore, pp 683–691
14. Mao C-C, Chen C-H (2021) Augmented reality of 3D content application in common operational picture training system for army. *Int J Hum Comput Interact* 1–17
15. Ahmed S et al (2021) Hand gestures recognition using radar sensors for human-computer-interaction: a review. *Remote Sens* 13(3):527
16. Schmidt A, Alt F, Mäkelä V (2021) Evaluation in human-computer interaction—beyond lab studies. In: *Extended abstracts of the 2021 CHI conference on human factors in computing systems*

# Framework and Challenges for Mobile Satellite System



Reeya Agrawal and Aditi Saxena

**Abstract** In satellite communications, as in other businesses, the demand for broadband has increased. Satellites carry global client information, including satellite TV, radio, and the Internet, via spacecraft. Satellite communication also provides global speech delivery. They are also vital for the recovery of natural disasters and other emergencies, as communications following natural disasters are crucial. While some spacecrafts are used primarily for data delivery, all spacecraft require communications systems. For example, remote satellites may collect environmental data, but both the data gathered and the satellites' locations are unknown. The limited storage capacity on board necessitates a high-speed data connection in order to prevent data loss when collecting massive amounts of information. The use of satellites to communicate with others, such as (interplanetary) space, necessitates the creation of new algorithms and protocols for each network tier; satellite communication is constrained by the relatively narrow bandwidth and high transmission power required for satellite transmission. The rising demand for high-speed data impacts the whole telecoms and satellite communications industry. Continuing demand growth and dynamically shifting markets are the key drivers of satellite communication trends.

**Keywords** Broadband · Satellite communication · Remote sensing · Links · Data distribution

## 1 Introduction

For many decades, satellites have been used for communication. Satellite networks have frequently been added to terrestrial infrastructure-based fixed, wireless, or mobile communications systems. For example, early satellite communications

---

R. Agrawal (✉) · A. Saxena  
GLA University, Mathura, India  
e-mail: [reeya.agrawal@gla.ac.in](mailto:reeya.agrawal@gla.ac.in)

A. Saxena  
e-mail: [aditi.saxena@gla.ac.in](mailto:aditi.saxena@gla.ac.in)

networks were technically and geographically unavailable to the maritime industry on any ground-based network. As the need for all-encompassing personal communications increases rapidly, satellites are filling the void in rural areas not served by either fixed-line or mobile networks. Moreover, when all other lines of communication fail during natural disasters, satellite communication has become indispensable. Satellite communication networks must surmount a number of obstacles in order to achieve widespread consumer adoption. From a network perspective, satellite communication is plagued by challenges relating to both the height of the network and physical layers. Long-term delays, packet losses, and intermittent connection and connection disruptions are examples of high-level difficulties for which well-known network protocol stacks such as TCP/IP are inadequate solutions. New network architectures, such as the delay and interrupt network tolerance (DTN) architecture, may present an alternative solution [1, 2]. Physical layer constraints include the requirement for satellite line-of-view (LOS), which limits user access to the satellite network, particularly in congested urban regions where LOS requirements are not met. Furthermore, Table 1 displays customer data for three major satellite telephone companies (as of the end of the third quarter of 2010) [3]. The figures show how satellite services compete with cellular networks.

Within the next five years, mobile data demand will climb by 25–50 times current levels, and while technology will continue to advance, the spectral performance

**Table 1** Important satellites comparative information

Cost	Operational	Services	Life- time	Satellites	Orbit	Name
N/A	1995	GPS	N/A	21	MEO	Glonass
Receiver: \$600–40,000	1995	GPS	18 years	33	MEO	GPS
Terminal: \$2000	1998		5 years	36	LEO	Orb-comm
Terminal: \$800 Air-time: \$40–50/min	2000	Broadband	N/A	80	Broadband LEO	Sky Bridge
N/A	Est. 2008	Broadband	11 years	288	Broadband LEO	Tele desic
Hand-set: \$800 Air-time: \$0.70–4/min	2000	V, D, F, P	13 years	10	MEO	ICO
Air-time: \$2–1.50/min	1999	V, D, F, P, GPS	11 years	48	B- LEO	Global Star
Hand-set: \$4000 Air-time: \$2–2.50/min	Nov, 1998	V, D, F, P	6 years	66	B- LEO	Iridium

of existing 4G orthogonal frequency-division (OFDM)-based solutions approaches maximum predicted bounds. The Federal Communications Commission (FCC) predicts that mobile broadband will be technologically and economically viable [4]. Although satellites are only a small portion of the telecommunications industry, they are a significant financial sector. The satellite industry, worth more than US\$190 billion, accounts for almost 60% of the total in both the telecommunications and space industries. In terms of the responsibilities of those in orbit today, around 38% are commercial communications satellites, 20% are for civilian or military communications, and satellites play the most prominent role. As previously indicated, communications technology should be employed by people whose primary responsibility is not communications [5].

## 2 Architecture of Communication Satellite

This consists of two halves, space and ground, also known as uplink and downlink. Space segment: the space segment is comprised of three major systems: (a) the fuel system, (b) the satellite control and communications system, and (c) the transponders. Utilizing the fuel device, the satellite is operational for years. It is equipped with solar panels that provide the energy required to power the satellite. The telecontrol system and satellite are used to transmit satellite commands and information about on-board systems to ground stations. The transponder is a communication device that functions as an interplanetary transmitter. The transponder collects, amplifies, and transmits ground station signals [6, 7]. There are a number of terrestrial stations in the ground sector. In a network with a star structure, there will be a central station called the center and a number of distant stations. At each remote station, a very small aperture terminal (VSAT) antenna measuring between 1 and 2.5 meters will be accessible. In addition to the antenna, an external device (ODU) containing radio equipment will be utilized to transport and improve the signal. The radio signal is transmitted to an IDU, which modulates and performs the required baseband processing. The IDU is the radio transmission. IDUs are linked to a PC, LAN, or PBX-like apparatus. At the central station, a huge antenna (ranging from 5.5 to 12 meters) and the corresponding equipment are located. In addition, there will be a network control center (NCC) that executes all management tasks, such as remote station configuration, remote station database maintenance, remote station healthcare management, and traffic analysis. According to the needs, the NCC's primary task is to transfer the appropriate channels to various remote systems. The path between a ground station and a satellite is known as the uplink. The connection between a satellite and a ground station is known as the contact connection. Utilize distinct frequencies for uploading and downloading (Fig. 1) [8, 9].



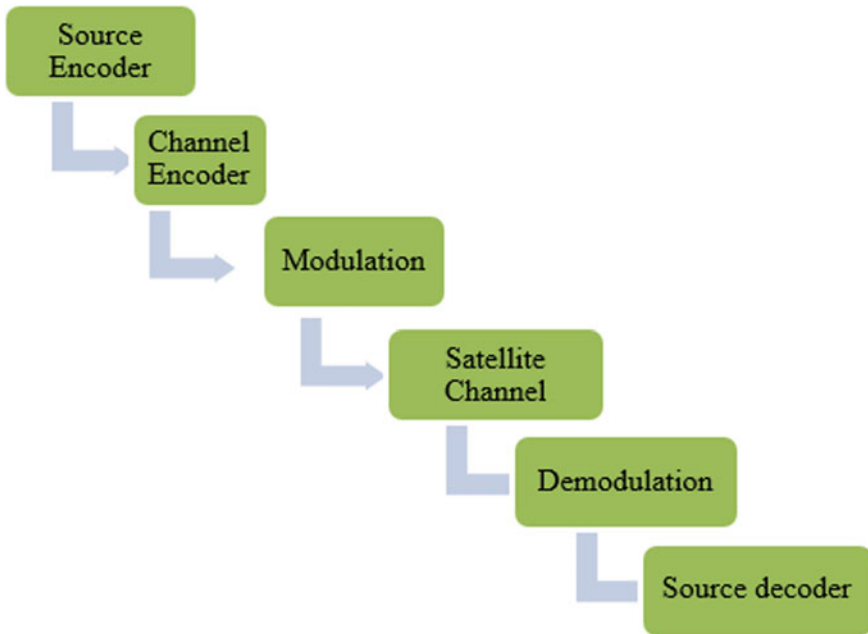


Fig. 1 Satellite communication block diagram

### 2.1 Operational Frequencies

C band, Ku band, and Ka band are the three frequency bands most widely used in satellite communication systems. As frequency increases, antenna size decreases. However, at higher frequencies, the effect of rain is greater. For broadcast purposes, the Ka band is utilized with an uplink frequency strip of (27.7–30.8) GHz and a downlink frequency strip of (17.9–21.1) GHz. Direct satellites provide video programming to the home directly (rather than via cable TV networks). Due to the higher service frequency of the Ku band, the antenna size would be significantly smaller than that of the C band. Rain has a greater impact on the Ku band as opposed to the C band. For some years, satellite communication has been limited to the C band. As a result of advancements in radio components such as amplifiers, filters, and modulators, rain impacts on the Ku band can be mitigated with the necessary amplification. Currently, the Ku band is widely used for communication (Table 2) [10, 11].

Table 2 Various bands of operation

Downlink frequency	Uplink frequency	Bands
(11.9–12.1 GHz)	(14.1–14.4 GHz)	Ku Bands
(3.9–4.1 GHz)	(6.025–6.325 GHz)	C Bands
(17.9–21.1 GHz)	(27.7–30.8 GHz)	Ka Bands

### 3 Mobile Satellite System

Fixed satellite services (FSS) and mobile satellite services (MSS) are the two types of satellite communication services (MSS). MSS will examine the future of global satellite communications in this article. Since the late 1970s, mobile satellite telephone services have been available. In terms of penetration, however, the competitiveness of mobile technology, a safer and less expensive alternative that approaches global coverage, makes a significant difference in comparison with satellite-based telephone. In addition, satellite networks require LOS, which is difficult to accomplish indoors in urban settings and very impossible to secure. In the early twenty-first century, satellite network operators were able to persuade telecom regulators in several parts of the world, including North America, the European Union, and Japan, to grant their authorization to integrate ground elements into a number of previously discussed issues, thereby making satellite communication more appealing to the mass market. On the inclusion of the soil section, more information is offered. The use of keywords close to mobile networks may constitute a satellite spot beam. The user’s travel through cellular cells necessitates a handoff from one base station to the next. In the case of non-geostationary satellites, however, cells are not geographically stable because they move to a specific spot-on Earth. As a result, stationary users must also transfer from one satellite to another [12]. In modern MSSs, the satellite uses relatively small antennas with modestly low power transmission, whereas the client uses a high-power device with a comparatively large antenna. Future MSS satellites will contain enormous antennas so that user terminals can transmit with a high level of power (Table 3).

Traditional satellites, specifically GEOS, function like curved pipes. This means that they are essentially a buffer between two geographical locations. In contrast, some satellites facilitate OBP’s use of channels and increase bandwidth. OBP

**Table 3** Various parameters of satellite communication

Life time	Mass	Frequ ency band	Attitude	Inclination	Orbit range	Number of orbital planes	Num ber of satellites	Mobile satellite system
4–10	45–172	L	670–825	45	LEO	8	59	Orbcomm
15	700	C, L, S	1400	52	LEO	8	24	Global star
15	6910	L	35,200	4	GEO	2	2	Terre Star
15	5390	L	35,777	0, 2	GEO	2	2	Light squared
15	3200	L	35,800	0	GEO	1	2	Thuraya
10	6100	L, S	35,786	0	GEO	1	12	Inmarsat
10	4500	C	35,900	0	GEO	1	1	Aces
15	860	L, K	781	86.4	LEO	6	66	Iridium Next
8	690	L, K	781	86.4	LEO	6	66	Iridium

also enables direct connection between satellites within the same constellation, enabling the provision of Intersatellite Links (ISL) directly via ISL for faster calling. This reduces the typical latency in the field of satellite voice transmission-based space diversity. Multiple satellites (usually two) communicate with user devices to improve satellite visibility. In order to provide a range of connections, OBP must integrate signals from both satellites. The spatial diversity of forward linkages is another alternative. However, the fundamental satellite diversity can suffice in this circumstance.

## 4 Challenges and Issues of Satellite Communication

Satellite communication has surely altered the manner in which people throughout the world connect with one another. It has contributed in the eradication of physical barriers and the creation of a massive global information society by giving people from all over the world a strong voice and access to communication. However, there are still places in the world, particularly in rural areas, where phone and Internet connections are not available. According to one estimate, only 40% of the world's population has access to the Internet. Satellite communication has the potential to alleviate the accessibility problem if the following obstacles to its development and acceptance are appropriately addressed (Table 4).

**Table 4** Issues with satellite communication

Satellite	Aerial platform	Terrestrial	Issue
Complex	Substantial	Substantial	Indoor
MEO/LEO: in stages GEO: 1 Stand—alone	Minimum of one platform/ground station	In stages	Deployment timing
Upto 15 years	Upto 5 years	Long term	Lifetime
50–500 km	0.5–10 km	100 m–2 km	Cell diameter
GEO/MEO: high	Very Low	Varies	Propagation delay
GEO: large regions MEO/LEO: Global > 500 km	Upto 400 km per Platform	Few Km per BS	Geographical coverage
Land and sea	Land and Sea	Land and coastline	Coverage
1, 2, 4, 6, 12–18, 27–40 GHz	1, 2, 4, 6, 12–18, 27–40 GHz	Few GHz	Frequency band
750–36,000 km	0.1–20 km	Upto 250 m	Altitude above ground
Solar panels	Fuel, propellers, and solar panels	Electricity	Power supply
Low	Low	High	Power consumption

### ***4.1 High Expenses***

From developing equipment to establishing a link, satellite communication is a pricey affair. In addition, the price of satellite communication services is projected to increase as satellite technology becomes more complex. Thus, it is impossible for underdeveloped nations to afford such an expensive communication medium.

### ***4.2 Delay in Spreading***

Delay in propagation is the time required for a satellite to link with the Earth. This delay may vary greatly depending on the satellite's distance from the location. Furthermore, this delay can echo telephone connections.

### ***4.3 Slow Speed***

Current web experiences are mainly focused on faster uploads and downloads, making satellite communication on the front somewhat deceiving. The current average satellite speed is approximately 1Mbps, frequently impeded by interference and noise.

### ***4.4 Facilitating Right Solutions of the International Sky Group***

International Sky Group (ISG) is a one-of-a-kind initiative aiming to address the aforementioned satellite communication challenges, hence granting users more seamless and cost-effective access to phone and Internet services. The network has built an efficient 'Satellite Communication System' that is compatible with both the existing telecommunications network and can function independently. The system is also based on a constellation of low-orbit satellite communications that enables the global dissemination of high-speed information to consumers.

## **5 Conclusion**

Increasing useable bandwidth, adapting to rising consumer demands, and improving satellite fleets to efficiently transfer data over worldwide coverage areas are the primary trends.

Combined with the increased longevity of satellites, this need for adaptability drives the desire for technology that enables satellite operators to transfer satellite capabilities between coverage areas.

As the industry strives for additional bandwidth, it extends beyond the Ka band and into higher frequency bands, which offer larger capacity. Work is undertaken to gain a deeper understanding of the channel's characteristics and the mature techniques that permit the usage of specific frequency bands. These include GaN, which has the potential to produce extremely reliable solid-state power outputs, but experiments are currently being conducted in practice.

New channelers, phased display antennas, reflector antennas, and reflect arrays are a few of the technologies that allow improved adaptation and diversity in the distribution of broadband data throughout coverage zones. Clearly, satellite communication offers numerous opportunities to improve communication. The aforementioned difficulties are crucial to their development and acceptance by the general populace. However, the International Sky Group provides a forum for effectively addressing the challenges and providing solutions for enhancing the effectiveness, reliability, and security of satellite communications.

## References

1. Holmes M (2013) Technology preview: Satellite 2013. *Satellite Today* [Online]. <http://www.satellitetoday.com/publications/2013/02/01/technology-preview-satellite-2013/>
2. Boeing company Web site [Online]. [http://www.boeing.com/boeing/defense-space/space/bss/factsheets/702/wgs/wgs\\_factsheet.page](http://www.boeing.com/boeing/defense-space/space/bss/factsheets/702/wgs/wgs_factsheet.page)
3. Runton D, Aichele D, LeFevre M, Burns C (2010) Defining application spaces for high power GaN. In: Proceedings of IEEE MTT-S international microwave symposium workshop, GaN for high power, high bandwidth applications: finally fulfilling the promise, pp 1–27
4. Ishida T (2011) GaN HEMT technologies for space and radio applications. *Microw J* 54(8):56
5. Nicol FE, Mangus BJ, Grebliunas JR (2013) TWTA versus SSPA: a comparison update of the Boeing satellite fleet on-orbit reliability. In: Proceedings of IEEE 14th international vacuum electronics conference, pp 169–170
6. Cheron J, Campovecchio M, Qu  r   R, Schwantuschke D, Quay R, Ambacher O (2013) High-efficiency power amplifier MMICs in 100 nm GaN technology at Ka-band frequencies. In: Proceedings of 8th European microwave integrated circuits conference European microwave week, Nurnmberg, Germany, pp 492–495
7. Saxena A, Kumar J, Sharma K, Roy D (2022) Controlling of manipulator for performing advance metal welding. In: Recent innovations in mechanical engineering. Springer, Singapore, pp 41–48
8. Campell C (2012) A K-band 5 W Doherty amplifier MMIC utilizing 0.15 $\mu$ m GaN on SiC HEMT technology. In: Proceedings of compound semiconductor integrated circuit Symposium, La Jolla, CA, pp 1–4
9. Sharma K, Shukla M (2014) Three-phase carbon fiber amine functionalized carbon nanotubes epoxy composite: processing, characterisation, and multiscale modeling. *J Nanomater*
10. Quay R, Walterit P, K  hn J, Brueckner P, van Heijningen M, Jukkala P, Hirche K, Ambacher O (2013) Submicron-AlGaIn/GaN MMICs for space applications. In: Proceedings of International Microwave Symposium, Piscataway, NJ

11. Singh PK, Sharma K (2018) Mechanical and viscoelastic properties of in-situ amine functionalized multiple layer graphene/epoxy nanocomposites. *Curr Nanosci* 14(3):252–262
12. Kumar A, Sharma K, Dixit AR (2020) A review on the mechanical and thermal properties of graphene and graphene-based polymer nanocomposites: understanding of modelling and MD simulation. *Mol Simul* 46(2):136–154

# A Short Review on the Development of Rare Earths Containing Magnesium Alloys for Biomedical Applications



Voleti Sri Sai Harsha Vardhan , Ambuj Sharma ,  
Ravikumar Dumpala , and Ratna Sunil Buradagunta 

**Abstract** Development of Mg-based degradable implants for several medical applications is an active research field in biomedical engineering. Owing to its biocompatibility, degradability, and non-toxic nature, Mg has gained tremendous attention among material engineers across the globe to use as a potential candidate for manufacturing medical implants. In spite of its promising properties, degradation control is an important area of research to tailor Mg as promising implant material. Alloying of any metal significantly alters its bulk properties and performance during the application. Several Mg alloys were developed for biomedical applications. Among them, rare earths (RE) containing Mg alloys occupy a prominent place. Different RE elements have been used to improve several properties of Mg. The objective of the current review is to present a brief summary of the developments in Mg–RE alloys targeted for biodegradable medical applications. The role of these alloying elements in enhancing the essential bulk properties required for medical applications is presented. The promising future perspectives and challenges involved in developing Mg-RE alloys for medical applications are also briefly discussed.

**Keywords** Mg alloys · Rare earths · Biodegradable · Implants · Orthopedics · Corrosion

---

V. S. S. H. Vardhan · A. Sharma (✉)  
School of Mechanical Engineering, VIT-AP University, Amaravati, Andhra Pradesh 522237, India  
e-mail: [ambujsharma08@gmail.com](mailto:ambujsharma08@gmail.com)

R. Dumpala  
Department of Mechanical Engineering, Visvesvaraya National Institute of Technology,  
Nagpur 440010, India

R. S. Buradagunta (✉)  
Department of Mechanical Engineering, Bapatla Engineering College, Bapatla 522101, India  
e-mail: [bratnasunil@gmail.com](mailto:bratnasunil@gmail.com)

## 1 Introduction

The growing demand for novel materials and processes to counter the present problems and to improve the performance of the existing biomedical implants led the material scientist to develop novel engineered materials in the biomedical field. Research on developing Mg-based implants is one such potential area that has gained tremendous attention in the past two decades [1]. Being a metal, Mg can be a better choice for manufacturing bio-implants due to its biocompatibility and safe degradability [2]. The potential applications of Mg implants include screws, nails, bone fixing plates, and scaffolds for short-duration orthopedic implants. However, its rapid degradation is a limitation that leads to a mismatch in the new bone formation rate and the implant degradation rate and eventually results in a gap at the implant–tissue interface and affects the mechanical integrity, as schematically shown in Fig. 1. Alloying of metals helps to enhance several properties, including mechanical performance, electrical properties, corrosion resistance, tribological behavior, creep, and fatigue properties. Alloying of Mg also has been proven as a potential strategy to improve the aforementioned material properties [3]. Particularly, alloying with suitable elements is a promising strategy to enhance the performance of Mg, as reported in the literature [4].

Initially, commercial-based alloys, including AZ series alloys, were widely investigated. Later on, several other alloy systems were developed with specially designed chemical compositions. Based on the alloying elements, the properties of Mg alloys are significantly altered. Depending on the microstructural factors, Mg alloys can be classified as Zr-free alloys and Zr-containing alloys. The addition of Zr influences the microstructure, and hence, the classification from the microstructure perspective can be done considering Zr presence [5]. On the other hand, by considering the toxicity

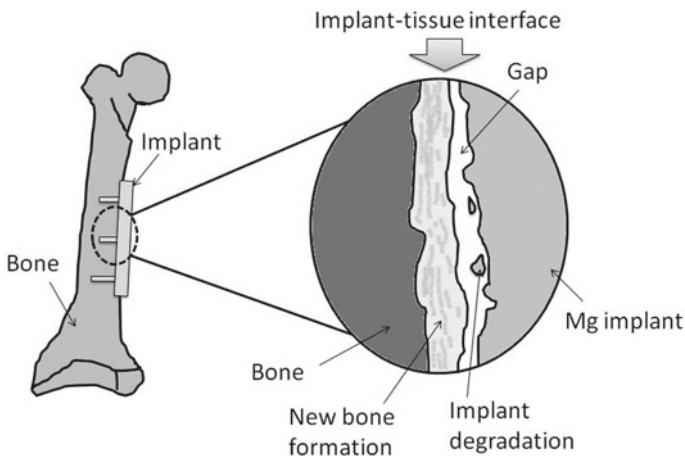


**Fig. 1** Schematic representation of new bone formation and Mg degradation at the implant-tissue interface



effect associated with Al, Mg alloys are also classified considering the Al presence [4]. Besides, rare earths (RE) containing Mg alloys were also studied for biomedical applications, as seen from the recent works [6, 7]. The present paper summarizes the developments in biodegradable RE containing Mg alloys with a discussion on the advantages and challenges. Rare earth (RE) elements include lanthanides on the periodic table plus Sc and Y. RE elements such as Ce, La, Pr, Nd, Ga, Eu, and Dy are widely used in several industries, including cosmetics, high-performing alloys, electronics, medical, and aerospace applications [8]. Using RE elements in appropriate amounts in Mg enhances the mechanical performance and electrochemical properties. However, a few elements, such as La, Pr, and Ce, induce toxicity effects at higher concentrations which must be considered while designing the composition of the Mg alloy for biomedical applications [9].

## 2 Mg–RE Alloys as Biomaterials

Binary and ternary Mg alloys with RE elements that were investigated for biomedical applications can be widely seen in the literature. In binary alloys, Mg with any one of the RE elements is added to produce the Mg alloy. Ce, La, Gd, Nd, and Gy are examples of such binary Mg-RE systems. Willbold et al. [10] studied Mg binary alloys with Ce, Nd, and La as the alloying elements as implant materials by conducting in-vivo experiments using rabbit as the animal model for four weeks. From the results, the evolution of gas was not detected, and the healing was found to be excellent. Gd and Dy, known as heavy RE elements, were also alloyed with Mg to produce binary alloys for medical applications [9]. From the literature, it is understood that the stress shielding effect can be minimized by using Mg–Gd and Mg–Dy alloys which possess mechanical properties close to the bone compared with the other alloys [11]. Yang et al. [12, 13] studied Mg–Dy alloy, and excellent corrosion was observed after solutionizing heat treatment followed by aging against cell culture medium. Y is another promising alloying element to develop Mg alloy, which promotes corrosion resistance in the aggressive physiological environment [14, 15]. Peng et al. [16] also produced Mg–8Y binary alloy, and better corrosion resistance was observed.

Ternary alloys and multi-element alloys with Zn, Ca, Al, and Li as the main constituting alloying elements are the other Mg alloy systems widely investigated in the literature. Mg–Zn system with additional RE elements in different fractions was prepared as potential implant material and investigated. The presence of Zn as an alloying element in Mg promotes better mechanical properties. It is a common observation that the Zn is added to several commercial Mg alloys. The presence of Zn in Mg alloy does not cause abnormal issues as the human body needs Zn on a regular basis for metabolic activities [17]. Additionally, RE elements are used to produce ternary alloys with Mg–Zn base system. It can be learned that the presence of Gd in Mg–Zn–Gd alloy [18] and Y in Mg–Zn–Y alloy [19] has a profound effect on improving the mechanical performance of Mg–Zn system. From the works of Bian

et al. [20], the corrosion resistance of Mg–Zn–Gd alloy was observed as higher in the in-vitro studies. Furthermore, better cell activities were also reported against VSMC, MG63, and L929 cell lines. From the in-vivo experiment, the alloy was observed with excellent structural integrity with the host tissue. In other words, adding Gd to the Mg–Zn system has shown better degradation resistance against Hank's solution and improved mechanical performance [21]. The presence of Y and Zr was also found to be beneficial in enhancing the mechanical performance and controlling the corrosion rate of Mg alloys [22–25]. Adding Nd to the Mg–Zn system in smaller amounts in view of its toxicity associated with higher fractions was also reported in the recent literature [26]. Niu et al. [27] developed Nd containing Mg–Zn alloy, and safe degradation was noticed from the in-vivo studies carried out for 18 months.

Mg–Ca alloys with additional RE elements are the other alloys investigated for biomedical applications. Basically, Ca promotes grain refinement in Mg and also contributes to increasing the corrosion resistance when used in smaller quantities. Li et al. [28] produced Mg–Ca–Y alloy, and better mechanical properties and increased corrosion resistance were observed. You et al. [29] also studied the role of Y while developing Mg alloy on the mechanical performance, and from the results, higher UTS and % elongation were observed. From the studies of Tong et al. [30] and Zhang et al. [31], adding La and Ca to Mg–Zn–Ca alloy has shown a significant role in enhancing mechanical performance. With the increased fraction of La and Ce from 0.5% to 1%, the degradation rate of the alloys was noticed to be significantly decreased. Mg–Al system is another type of Mg alloy that can be used to produce wrought products if the Al content is limited to less than 3%. Studies on RE containing the Mg–Al system for possible implant applications can be seen in the earlier reports. Yokobayashi et al. [32] developed a ternary alloy of Mg–Al–Gd, and precipitation of Mg<sub>5</sub>Gd intermetallic was observed after heat treatment. From the works of Lu et al. [33], Mg–Al–Gd alloy has shown better corrosion properties after the heat treatment due to the Mg<sub>5</sub>Gd precipitates. Toxic issues are the important limitation with the combination of Al and Gd in Mg alloy. The presence of Al in higher concentrations leads to neurological health issues. On the other hand, the presence of Gd also must be in the lower amounts in view of the toxicity in the presence of the biological system [34, 35].

Mg–Li alloys are the other group of RE containing Mg alloys studied for medical applications. Among these alloys, LAE442 with the chemical composition of Li (4 wt.%), Al (4 wt.%), Ce (1.3 wt.%), Nd (0.37 wt.%), La (0.5 wt.%), and remaining Mg has been widely studied in the scientific literature. Witte et al. [35] carried out degradation studies of LAE442 alloy and AZ91D alloy by in-vitro and in-vivo routes. From the in-vitro studies, corrosion resistance of AZ91D has been observed as better compared with LAE442 alloy. On the contrary, from the in-vivo studies, the LAE442 alloy exhibited higher corrosion resistance compared with the AZ91D alloy. In another study, Witte et al. [36] produced MgF<sub>2</sub> coatings on LAE442, and a further decreased corrosion rate was observed from the in-vivo studies. Krause et al. [37] also used LAE442 alloy as an implant material and compared the performance of WE42 (Mg–Y–RE) alloy by carrying out in-vivo experiments for 6 months. Zhou et al. [38] also investigated the mechanical behavior, corrosion properties, and bioproperties

of Mg–Al–Li and Mg–Al–Li–RE alloys. Interestingly, the presence of RE elements significantly enhanced the strength of the alloy, and the intermetallics deteriorated the corrosion performance. Several other Mg–RE alloys with other alloying elements were also investigated to develop biomedical implants. Among them, the Mg–Y–RE alloy system occupies prominent space. WE43 is the best example for such alloy which has a great potential to manufacture degradable implants. Yttrium enhances the mechanical strength and improves the corrosion performance in Mg alloys [39]. Several reports demonstrated increased corrosion resistance due to the yttrium oxide ( $Y_2O_3$ ) produced on the heat-treated WE43 Mg alloy when exposed to a corroding environment [40–42]. ZE41 and ZK60 are the other RE containing Mg alloys investigated to understand the degradation behavior, which exhibited better mechanical performance and lower corrosion rates [43, 44].

### 3 Properties Influenced by RE Elements in Mg Alloys

The majority of the properties which are significantly affected by alloying Mg with RE elements can be grouped into three categories which include mechanical properties, corrosion properties, and bioproperties. Table 1 presents the effect of individual RE elements on different material properties. Mechanical properties are the first group of bulk properties significantly altered due to alloying Mg with RE elements.

**Table 1** Effect of RE elements on material properties of Mg alloys

S. No	Element	Influence on material properties	Reference
1	Ce	<ul style="list-style-type: none"> <li>• Induces grain refinement</li> <li>• Higher amount of Ce decreases the corrosion resistance and increases the toxicity</li> </ul>	[9, 45]
2	Gd	<ul style="list-style-type: none"> <li>• More soluble in Mg compared with the remaining RE elements</li> <li>• Improves mechanical properties</li> </ul>	[9, 46]
3	Dy	<ul style="list-style-type: none"> <li>• More soluble in Mg similar to Gd</li> <li>• Improves ultimate tensile strength and yield strength</li> <li>• Enhances corrosion resistance</li> </ul>	[9, 12, 13]
4	Sc	<ul style="list-style-type: none"> <li>• Acts as the best grain refiner compared with other RE elements</li> <li>• Improves corrosion resistance</li> </ul>	[47, 48]
5	Y	<ul style="list-style-type: none"> <li>• Improves corrosion resistance</li> <li>• Improves new bone formation rate</li> </ul>	[14, 16, 37]
6	La	<ul style="list-style-type: none"> <li>• Improves corrosion resistance</li> <li>• Higher amounts induce toxicity</li> </ul>	[9, 35]
7	Nd	<ul style="list-style-type: none"> <li>• Enhances mechanical properties and corrosion resistance</li> <li>• Improves stress corrosion cracking resistance</li> <li>• Higher amounts of Nd induce toxicity</li> </ul>	[26, 27, 49]

It has been observed from the reported literature that the range of tensile strength varies from 70 to 350 MPa, yield strength varies from 45 to 300 MPa, and the % elongation is varied from 1% to more than 50% with different alloying elements. Mg-RE binary alloys exhibit improved mechanical properties. However, the ductility is significantly decreased, as reflected in the lower % of elongation. Among all the RE containing alloys, WE43 with aging conditions exhibits higher ductility (60% elongation). Next comes the most promising ZW21 and ZEK100 Mg alloys with higher ductility (round 35% elongation) [6]. Furthermore, the alloys subjected to mechanical processing followed by heat treatment have shown improved mechanical properties [50]. Corrosion properties are also significantly affected due to the added RE elements in Mg alloys. For degradable implant applications, the material is intended to function well with good mechanical integrity with the host tissue for at least 4–6 months until the new bone formation is completed. In this context, RE containing alloys exhibit relatively longer life span in the biological environment. Among all the alloys, WE43 and LAE442 alloys exhibited lower corrosion rates, as observed from the reported works [37]. Usually, the mechanical properties deteriorate when the material is subjected to corrosion. Corrosion-initiated pits and cracks accelerate the mechanical failure of Mg alloys when used as bio-implants. Since the targeted application is orthopedic implants where the implant material is subjected to mechanical loads, understanding the role of degradation on the mechanical failure of the Mg alloys is important. WE43 Mg alloy has shown better mechanical performance after 3 months of exposure to a corroding environment in bending tests [51]. However, a few studies also suggested producing surface coatings to minimize the degradation process of Mg alloys during the initial days [52, 53]. The toxicity of RE containing Mg alloys has been investigated against different cell lines, including L929, MC3T3, VSMC, and ECV304 [10, 20]. From the detailed preliminary studies, RE containing Mg alloys exhibited non-toxic nature, as reported by several authors [54, 55]. The cell culture studies clearly established the non-toxic nature of body tolerance of RE containing Mg alloys. However, detailed studies on the level of allowable concentration of these elements in Mg alloys in the context of localized toxicity and the effect on the functioning of other organs are essentially required.

## 4 Future Scope and Challenges

Compared with pure Mg, the toxicity of RE containing Mg is lower. The evolution of hydrogen gas as a byproduct during the corrosion of Mg-RE alloys is lower compared with the degradation of pure Mg, which is the prime reason behind the higher cell availability with the Mg-RE alloys. Therefore, the increased cell viability as observed in the Mg-RE alloys is claimed to be the localized favorable conditions from the absence of hydrogen gas perspective rather than the effect of the alloying element. A few RE elements, for example, Nd, Gd, and Dy, are allowed in smaller fractions in view of their toxicity with higher concentrations. Hence, detailed studies on the toxicity of different RE elements are required to fully get benefited from RE

elements in developing Mg-based implants. Some of the alloys exhibited more than 100% cell viability. This can be possible with the cell growth during the incubation period, as also reported by the other authors with the other Mg alloys, where the presence of Mg ions helps toward cell growth and proliferation [45, 46]. From the economic perspective, the cost of RE elements is relatively higher compared with the other alloying elements, and therefore, the overall cost of the Mg alloy is increased when multiple RE elements are used to develop these alloys. In addition to alloy development, adopting subsequent thermo-mechanical treatments to refine the microstructure can be adopted to improve the performance of the Mg alloys [56–58]. Furthermore, heat treatment processes, particularly for the alloys, which can be hardened by aging treatment, improve the mechanical and corrosion properties by precipitating fine intermetallic phases. Using Mg–RE alloys as matrix materials, highly bioactive phases such as Ca/P phases can be dispersed to develop metal matrix composites to achieve hybrid properties coupled with a higher level of bioactivity, which increases the healing rate and controls the degradation rate. Additionally, by providing surface coatings from an external source or by developing surface oxide layers from the substrate itself, the degradation can be controlled, and special properties such as antibacterial and antimicrobial properties can be imparted to the Mg–RE implants.

## 5 Conclusions

Mg–RE alloys occupy a special place in developing Mg-based degradable implants due to their excellent mechanical performance and lower degradation compared with other Mg alloys. Among them, WE43 alloy and LAE442 alloy were observed with better corrosion resistance compared with all other Mg–RE alloys. Every RE element has its advantages and limitations with respect to enhancing mechanical and corrosion properties but induces toxicity if they present in higher concentrations. Elements such as Y, Gd, and Sc result in higher grain refinement compared with other elements. On the other hand, La and Ce are relatively toxic compared with the other elements. WE43 Mg alloy exhibited higher % of elongation (60%) compared with the other alloys. Even though the in-vitro studies establish the potential of these alloys, additional studies to assess the consequences of leaching of these REs on individual organs and the effect of these ions on the other health conditions are required. Furthermore, studies on the effect of RE elements in the physiological environment for longer periods are also required to be carried out. The status of the research in developing Mg–RE alloys for biodegradable implants is promising, and further research efforts will certainly bring development to witness the commercial implants in the medical industry in the near future.

## References

1. Witte F, Hort N, Vogt C et al (2008) Degradable biomaterials based on magnesium corrosion. *Curr Opin Solid St Mater Sci* 12:63–72
2. Zeng R, Dietzel W, Witte F et al (2008) Progress and challenge for magnesium alloys as biomaterials. *Adv Eng Mater* 10(8):B3–B14
3. Avedesian M, Baker MH (1999) ASM specialty handbook, Magnesium and magnesium alloys, ASM International, USA
4. Kirkland NT, Birbilis N (2014) Magnesium biomaterials design, testing, and best practice. Springer Science and Business Media; New York, USA, pp 1–131
5. Fridrich HE, Mordike BL (2006) Magnesium technology. Springer, Germany
6. Liua D, Yang D, Li X, Hu S (2019) Mechanical properties, corrosion resistance and biocompatibilities of degradable Mg–RE alloys: a review. *J Mater Res Technol* 8(1):1538–1549
7. Jamel MM, Jamel MM, Lopez HF (2022) Designing advanced biomedical biodegradable Mg alloys: a review. *Metals* 12:85
8. Voncken JHL (2015) The rare earth elements: an introduction. Springer
9. Feyerabend F, Fischer J, Holtz J, Witte F, Willumeit R, Drücker H et al (2010) Evaluation of short-term effects of rare earth and other elements used in magnesium alloys on primary cells and cell lines. *Acta Biomater* 6(5):1834–1842
10. Willbold E, Gu X, Albert D, Kalla K, Bobe K, Brauneis M et al (2015) Effect of the addition of low rare earth elements (lanthanum, neodymium, cerium) on the biodegradation and biocompatibility of magnesium. *Acta Biomater* 11:554
11. Chino Y, Kado M, Mabuchi M (2008) Enhancement of tensile ductility and stretch formability of magnesium by addition of 0.2 wt%(0.035 at%)Ce. *Mater Sci Eng A* 494(1–2):343–349
12. Yang L, Ma L, Huang Y, Feyerabend F, Blawert C, Höche D et al (2017) Influence of Dy in solid solution on the degradation behavior of binary Mg–Dy alloys in cell culture medium. *Mater Sci Eng C* 75:1351–1358
13. Yang L, Hort N, Laipple D, Höche D, Huang Y, Kainer KU et al (2013) Element distribution in the corrosion layer and cytotoxicity of alloy Mg–10Dy during in vitro biodegradation. *Acta Biomater* 9(10):8475–8487
14. Wang XM, Zeng XQ, Wu GS, Yao SS (2006) Yttrium ionimplantation on the surface properties of magnesium. *Appl Surf Sci* 253(5):2437–2442
15. Liu M, Schmutz P, Uggowitzer PJ, Song G, Atrens A (2010) The influence of yttrium (Y) on the corrosion of Mg–Y binary alloys. *Corros Sci* 52(11):3687–3701
16. Peng Q, Huang Y, Zhou L, Hort N, Kainer KU (2010) Preparation and properties of high purity Mg–Y biomaterials. *Biomaterials* 31(3):398–403
17. MacDonald RS (2000) The role of zinc in growth and cell proliferation. *J Nutr* 130:1500S–S1508
18. Yuan G, Liu Y, Ding W, Lu C (2007) Effects of extrusion on the microstructure and mechanical properties of Mg–Zn–Gd alloy reinforced with quasi crystalline particles. *Mater Sci Eng A* 474(1):348–354
19. Yamasaki M, Hashimoto K, Hagihara K, Kawamura Y (2011) Effect of multimodal microstructure evolution on mechanical properties of Mg–Zn–Y extruded alloy. *Acta Mater* 59(9):3646–3658
20. Bian D, Deng J, Li N, Chu X, Liu Y, Li W et al (2018) In vitro and in vivo studies on biomedical magnesium low-alloying with elements gadolinium and zinc for orthopaedic implant applications. *ACS Appl Mater Inter* 10(5):4394–4408
21. Miao H, Huang H, Shi Y, Zhang H, Pei J, Yuan G (2017) Effects of solution treatment before extrusion on the microstructure, mechanical properties and corrosion of Mg–Zn–Gd alloy in vitro. *Corros Sci* 122(01):90–99
22. Zhao X, Shi LL, Xu J (2013) Mg–Zn–Y alloys with long-period stacking ordered structure: in vitro assessments of biodegradation behavior. *Mater Sci Eng C* 33(7):3627–3637

23. Kraus T, Fischerauer SF, Hänzi AC, Uggowitzer PJ, Löffler JF, Weinberg AM (2012) Magnesium alloys for temporary implants in osteosynthesis: in vivo studies of their degradation and interaction with bone. *Acta Biomater* 8(3):1230–1238
24. Hänzi AC, Gerber I, Schinhammer M, Löffler JF, Uggowitzer PJ (2010) On the in vitro and in vivo degradation performance and biological response of new biodegradable Mg-Y-Zn alloys. *Acta Biomater* 6(5):1824–1833
25. Waizy H, Weizbauer A, Modrejewski C, Witte F, Windhagen H, Lucas A et al (2012) In vitro corrosion of ZEK100 plates in Hank's balanced salt solution. *Biomed Eng Online* 11(1):1–14
26. Zhang X, Yuan G, Niu J, Fu P, Ding W (2012) Microstructure, mechanical properties, biocorrosion behavior, and cytotoxicity of as-extruded Mg-Nd-Zn-Zr alloy with different extrusion ratios. *J Mech Behav Biomed* 9(3):153–162
27. Niu J, Xiong M, Guan X, Zhang J, Huang H, Pei J et al (2016) The in vivo degradation and bone-implant interface of Mg-Nd-Zn-Zr alloy screws: 18 months post-operation results. *Corros Sci* 113:183–187
28. Li Y, Hodgson PD, Wen C (2011) The effects of calcium and yttrium additions on the microstructure, mechanical properties and biocompatibility of biodegradable magnesium alloys. *J Mater Sci* 46(2):365–371
29. You S, Huang Y, Kainer KU, Hort N (2018) Influences of yttrium content on microstructure and mechanical properties of as-cast Mg-Ca-Y-Zr alloys. In: TMS meeting exhibition. Springer, Cham, pp 91–97
30. Tong LB, Zhang QX, Jiang ZH, Zhang JB, Meng J, Cheng LR et al (2016) Microstructures, mechanical properties and corrosion resistances of extruded Mg-Zn-Ca-xCe/La alloys. *J Mech Behav Biomed* 62:57–70
31. Zhang Q, Tong L, Cheng L, Jiang Z, Meng J, Zhang H (2015) Effect of Ce/La micro alloying on microstructural evolution of Mg-Zn-Ca alloy during solution treatment. *J Rare Earth* 33(1):70–76
32. Yokobayashi H, Kishida K, Inui H, Yamasaki M, Kawamura Y (2011) Enrichment of Gd and Al atoms in the quadruple close packed planes and their in-plane long-range ordering in the long period stacking-ordered phase in the Mg-Al-Gd system. *Acta Mater* 59(19):7287–7299
33. Lu F, Ma A, Jiang J, Guo Y, Yang D, Song D et al (2015) Significantly improved corrosion resistance of heat-treated Mg-Al-Gd alloy containing profuse needle-like precipitates within grains. *Corros Sci* 94:171–178
34. El-Rahman SSA (2003) Neuropathology of aluminum toxicity in rats (glutamate and GABA impairment). *Pharmacol Res* 47:189–194
35. Witte F, Fischer J, Nellesen J, Crostack H-A, Kaese V, Pisch A et al (2006) In vitro and in vivo corrosion measurements of magnesium alloys. *Biomaterials* 27:1013–1018
36. Witte F, Kaese V, Haferkamp H, Switzer E, Meyer-Lindenberg A, Wirth CJ et al (2005) In vivo corrosion of four magnesium alloys and the associated bone response. *Biomaterials* 26:3557–3563
37. Krause A, Höh N, Bormann D, Krause C, Bach FW, Windhagen H et al (2009) Degradation behaviour and mechanical properties of magnesium implants in rabbit tibiae. *J Mater Sci* 45:624–632
38. Zhou WR, Zheng YF, Leeftang MA, Zhou J (2013) Mechanical property, biocorrosion and in vitro biocompatibility evaluations of Mg-Li-(Al)-(RE) alloys for future cardiovascular stent application. *Acta Biomater* 9(10):8488
39. Soćjusz-Podosek M, Lityńska L (2003) Effect of yttrium on structure and mechanical properties of Mg alloys. *Mater Chem Phys* 80:472–475
40. Hänzi AC, Gunde P, Schinhammer M, Uggowitzer PJ (2009) On the biodegradation performance of an Mg-Y-RE alloy with various surface conditions in simulated body fluid. *Acta Biomater* 5(1):162–171
41. Liu D, Ding Y, Guo T, Qin X, Guo C, Yu S et al (2014) Influence of fine-grain and solid-solution strengthening on mechanical properties and in vitro degradation of WE43 alloy. *Biomed Mater* 9(1):015014

42. Chu PW, Marquis EA (2015) Linking the microstructure of a heat-treated WE43 Mg alloy with its corrosion behavior. *Corros Sci* 101:94–104
43. Jamesh MI, Wu G, Zhao Y, Mckenzie DR, Bilek MMM, Chu PK (2015) Electrochemical corrosion behavior of biodegradable Mg-Y-RE and Mg-Zn-Zr alloys in Ringer's solution and simulated body fluid. *Corros Sci* 91:160–184
44. Praveen Kumar N, Naveen C, Sujatha D, Anandarao D, Naga Sireesha J, Anand Kumar S, Siva I, Venkateswarlu B, Jagannatham M, Ratna Sunil B (2018) Developing composites of ZE41 Mg alloy—naturally derived hydroxyapatite by friction stir processing: investigating in vitro degradation behavior. *Mater Technol* 33(9):603–611
45. Zhang F, Aibin MA, Song D, Jiang J, Lu F, Zhang L, Yang D, Chen J (2015) Improving in-vitro biocorrosion resistance of Mg-Zn-Mn-Ca alloy in Hank's solution through addition of cerium. *J Rare Earths* 33:93–101
46. Hort N, Huang Y, Fechner D, Störmer M, Blawert C, Witte F et al (2010) Magnesium alloys as implant materials—principles of property design for Mg-RE alloys. *Acta Biomater* 6(5):1714–1725
47. Lee Y, Dahle A, St JD (2000) The role of solute in grain refinement of magnesium. *Metall Mater Trans A* 31:2895–2906
48. Brar HS, Berglund IS, Allen JB, Manuel MV (2014) The role of surface oxidation on the degradation behavior of biodegradable Mg-RE (Gd, Y, Sc) alloys for resorbable implants. *Mater Sci Eng C* 40:407–417
49. Hakimi O, Aghion E, Goldman J (2015) Improved stress corrosion cracking resistance of a novel biodegradable EW62magnesium alloy by rapid solidification, in simulated electrolytes. *Mater Sci Eng C* 51:226–232
50. Alizadeh R, Mahmudi R, Langdon TG (2014) Superplasticity of a fine-grained Mg–9Gd–4Y–0.4Zr alloy evaluated using shear punch testing. *J Mater Res Technol* 3(3):228–232
51. Li N, Zheng YF (2013) Novel magnesium alloys developed for biomedical application: a review. *J Mater Sci Technol* 29(6):489–502
52. He MF, Hu WB, Zhao S, Liu L, Wu YT (2012) Novel multilayer Mg–Al intermetallic coating for corrosion protection of magnesium alloy by molten salts treatment. *Trans Nonferrous Met Soc China* 22:s74–s78
53. Chu CL, Han X, Bai J, Xue F, Chu PK (2014) Surface modification of biomedical magnesium alloy wires by micro-arc oxidation. *Trans Nonferrous Met Soc China* 24:1058–1064
54. Du ZQ, Yang P (2011) Comparative study on apoptosis and membrane potassium current of dorsal root neurons induced by rare earth ions of lanthanum, lanthanum and strontium. *J Chin Soc Rare Earth* 29(4):496–503
55. Zhang Y, Xu J, Ruan YC, Yu MK, O'Laughlin M, Wise H et al (2016) Implant-derived magnesium induces local neuronal production of CGRP to improve bone-fracture healing in rats. *Nat Med* 22(10):1160
56. Ratna Sunil B, Sampath Kumar TS, Chakkingal U, Nandakumar V, Mukesh Doble NV (2014) Friction stir processing of magnesium—nanohydroxyapatite composites with controlled in vitro degradation behaviour. *Mater Sci Eng C* 39:315–324
57. Ratna Sunil B, Sampath Kumar TS, Chakkingal U, Mukesh Doble NV (2014) Nano-hydroxyapatite reinforced AZ31 magnesium alloy by friction stir processing: a solid state processing for biodegradable metal matrix composites. *J Mater Sci Mater Med* 25:975–988
58. Kundurti SC, Sharma A, Tambe P, Kumar A (2022) Fabrication of surface metal matrix composites for structural applications using friction stir processing – a review. *Mater Today Proc* 561468–561477. <https://doi.org/10.1016/j.matpr.2021.12.337>



# Design and Simulation for Brake Pedal of Aluminium Alloy



Charan Singh , Utkarsh Jain , Rishabh Singh ,  
and Brahma Nand Agrawal 

**Abstract** A brake pedal is a significant pedal after the acceleration pedal as it is used in controlling the vehicle's speed. An optimized brake pedal is designed to improve the design and other parameters. FEA analysis shows that several test cycles are performed very well. In this paper, an analysis of the design of the brake pedal of a vehicle and testing the strength of the brake pedal are performed and tested according to the criterion. Brake pedal models are designed and constructed using SolidWorks 2018 software. Aluminum alloy is selected as the material for analysis. It is concluded that aluminum is good for the vehicle brake pedal at the beginning of the test. The test is performed on the pedal physical as well as internal buildup characteristics in the material as well as in the design. This study reveals more strength and durability in design with material placed at the required location.

**Keywords** FEA analysis · Brake pedal · Aluminum alloy(6065) · Software analysis · SolidWorks

---

C. Singh · U. Jain · R. Singh · B. N. Agrawal (✉)  
Department of Mechanical Engineering, Galgotias University, Greater Noida, Uttar Pradesh, India  
e-mail: [brahma.agrawal@galgotiasuniversity.edu.in](mailto:brahma.agrawal@galgotiasuniversity.edu.in)

© The Author(s), under exclusive license to Springer Nature Singapore Pte Ltd. 2024  
R. K. Tyagi et al. (eds.), *Advances in Engineering Materials*, Lecture Notes in  
Mechanical Engineering, [https://doi.org/10.1007/978-981-99-4758-4\\_15](https://doi.org/10.1007/978-981-99-4758-4_15)

147

## 1 Introduction

A significance of a braking system is to enhance thermal efficiency and driving stability with security. An optimized design geometry of the brake pedal is designed to improve energy economy and with other parameters [1]. A vehicle must acquire appropriate braking techniques for actual control of the brake pedal under certain operational conditions. The comparative study was taken out to identify the pedal material and design of the pedal under the different operating conditions concerning the environmental condition [2]. The application of pedal while accidental braking was predicted during the sudden application of the brakes by the person. The study was conducted when various simulation strategies with the accidental behavior of the person were predicted [3]. The acceptance of the tolerance of force applied on the brake pedal concerning a person's behavior and material strength. The identification of rapid force exerted on the pedal design concerning the safety measures was created [4]. Demonstrating the utilization of a one-pedal drive system for managing both braking and acceleration, alongside the incorporation of regenerative algorithms employed in braking, is pivotal in heavy-duty and electric vehicles. This application holds relevance in modern vehicular systems [5].

Employing varying brake pedal ratios is a common practice, both during normal driving conditions and in panic situations, as controlled by the driver. Enhancing its efficiency while considerably reducing the cost of the pedal can be achieved through the implementation of optimization techniques during the manufacturing process [6]. The software test of the pedal was conducted which was manufactured using a new effective as well as the more efficient process of design in the additive manufacturing field which is available. The designed pedal was tested in more practical condition imitation that can be possible with software [7]. An average comparative analysis/study was performed on drivers and brake operation on the mountain slope and the connection of their heart-beating time-concerning sudden brake application. Force comparison of the acceleration pedal and the brake pedal was conducted physically by monitoring the behavior of body and wheel dynamics [8]. The making of a more reliable and viable brake pedal used for FSAE championship and other motorsport is taken into consideration within maximizing the strength of the pedal while significantly reducing the cost with effective manufacturing tech [9]. To render the braking pedal more suitable for patients experiencing knee issues or who have undergone an operation, specific modifications are required. Different force output is recorded with the time [10].

By employing simulations of the brake pedal encompassing various processes inherent to a single-pedal operating system in a vehicle, improvements can be achieved. To enhance the overall braking efficiency in electric vehicles is the intended outcome [11]. Utilizing advanced computing to analyze instances of inadvertent brake pressing during panic conditions by the driver, along with the control offered by the car's computer, is the approach taken [12]. Incorporating the additive manufacturing process to develop a more complex and lightweight brake pedal design/

geometry. This process to optimize the structure by design, strength, and performance characteristics in this study [13].

The study of this paper is conducted on stress, strain, and other physical analyses on the brake pedal designed in a virtual analysis and design software to find the impact on the specified material (Aluminum alloy) by providing the actual condition for the test by specifying it in the software boundary conditions and as well as physical condition and analysis results were added in the study.

## **2 Brake Pedal**

A brake pedal is used in vehicles to control the speed of the vehicle, and when it is fully pressed, it stops the vehicle completely. It is located at the left foot of the driver. Pressing the brake pedal by the driver automatically applies the optimum pressure to stop or slow the vehicle down.

### ***2.1 Methodology***

- Designing and modeling on the software (SolidWorks 2018).
- Specifying material and setting parameters.
- Conducting the analysis of the model as required.
- Generating Results and noting them down.

### ***2.2 CAD Model***

A model brake pedal is designed and then drawn in SolidWorks. The made brake pedal has a pedal ratio of 6:1, a total length of 6 inches, and a thickness of 1 inch. The CAD model of the brake pedal can be seen in (the isometric view) in Fig. 1. Also, the properties are specified in the software as required to be.

### ***2.3 Material Selection***

In most, modern-day vehicles material used to construct the brake pedal is some iron alloy with nylon to cover it with short fiber but due to material availability and cost factor. Aluminum 6065 is used for the brake pedal. Properties of aluminum 6065 are defined in Table 1.

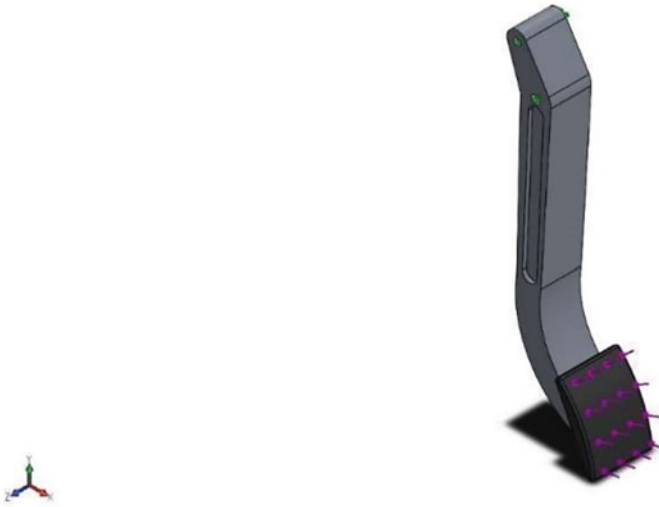


**Fig. 1** Brake pedal

**Table 1** Material properties of aluminum 6065 [14]

Failure analysis on:	Max von Stress
Max. tensile strength:	1.240841 e + 008 N/m <sup>2</sup>
Max. yield strength:	5.514851 e + 007 N/m <sup>2</sup>
Material Poisson's ratio:	0.331
Modulus of elastic:	6.91 e + 010 N/m <sup>2</sup>
Material shear modulus:	2.6 e + 010 N/m <sup>2</sup>
Material mass density:	2700 kg/m <sup>3</sup>
Coefficient of thermal expansion:	2.4e-005 /Kelvin


Volumetric properties aluminum 6065:

- Mass of material: 0.254468 kg
- Volume occupied: 9.424731 e-005 m<sup>3</sup>
- The density of material: 2700 kg/m<sup>3</sup>
- Weigh of material: 2.493781 N

## 2.4 Meshing

Solid Mesh is provided to the brake pedal, with reference to Table 1 and volumetric properties as mentioned in material selection. Shown mesh details after meshing was noted in Fig. 2.

Element Size	Tolerance	Total Nodes	Total Elements
0.152338 in	0.00761691 in	22193	13823



**Fig. 2** Mesh brake pedal

### 3 Result and Discussion

#### 3.1 Static Analysis

For this analysis, considered that the pedal experiences the force of 200 N on its surface. The force is provided as it is provided during the operation of a vehicle by the person who is driving it. For this given force, various parameters are taken as an essential criterion for the preferred analysis which the study shows. The following as

- Stress,
- Displacement,
- Strain,
- Factor of safety.

These factors are calculated in the simulation software known as SolidWorks which has helped in analyzing it up close with a great deal of actual operation-like environment.

#### 3.2 Simulations

The simulations are conducted in the order as mentioned in Fig. 3 the shown below shows the test for “stress” which the pedal has experienced during the test run. The color blue shows the least stress in the point areas, and the color green shows the

stress value in the areas which is higher than the blue area that experiences it with the maximum limit at the red area on the scale.

The same is performed in Fig. 4 for the displacement, and the colors show the displacement change of the material on the points of the color change in the simulation for the pedal.

The strain analysis for the maximum is also performed in the same manner in Fig. 5 for the pedal with strain development shown/depicted with change in the colored area according to the effect on the pedal during the test run.

In Fig. 6, a measure of the safety factor is analyzed for the pedal and the depiction for the test outcomes remains as the change in color within the required parameters for the pedal to be safe when constructed by the specified material within the limits described for the pedal.

A compilation of the results is presented below that can be gathered from the above simulation:

Name of factor	Min.	Max.
Stress	1.401e + 003 N/m <sup>2</sup>	3.295e + 007 N/m <sup>2</sup>
Displacement	000e + 000 mm	5.667e-001 mm
Strain	1.011e-007	3.677e-004
Factor of safety	1.674e + 000	3.937e + 004

- The stress developed is  $3.295 \times 10^7$  which is less than tensile and yields stress on the material.
- Displacement and strain are also within the permissible limit.
- The factor of safety is between 3 and 5.

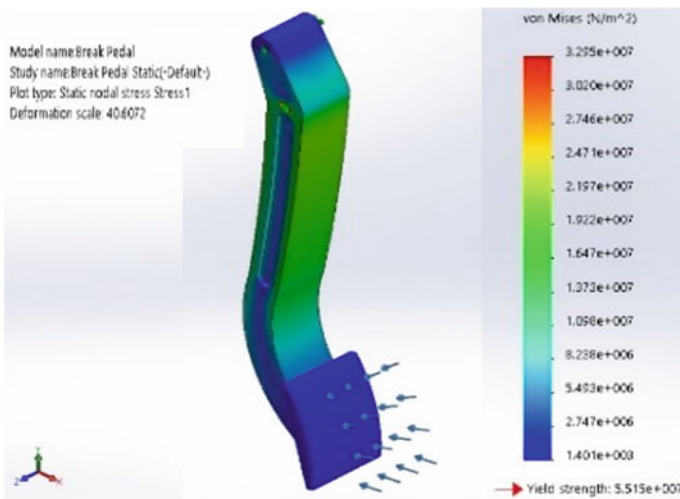


Fig. 3 Equivalent stress

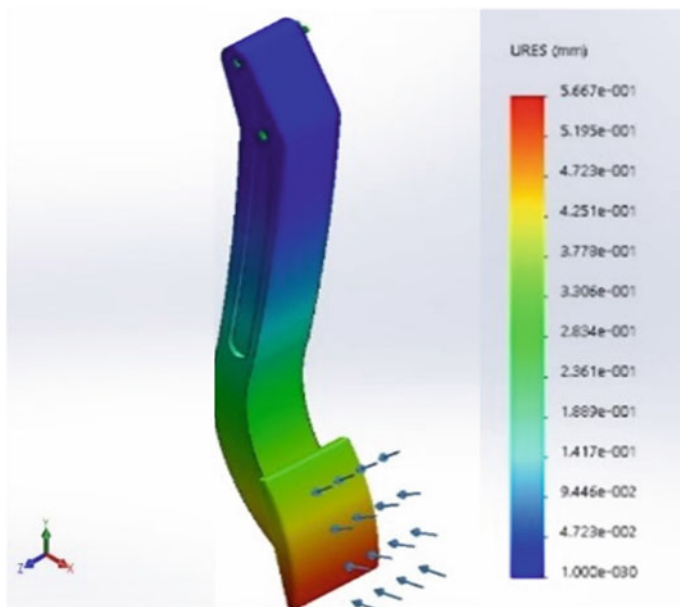


Fig. 4 Brake pedal displacement

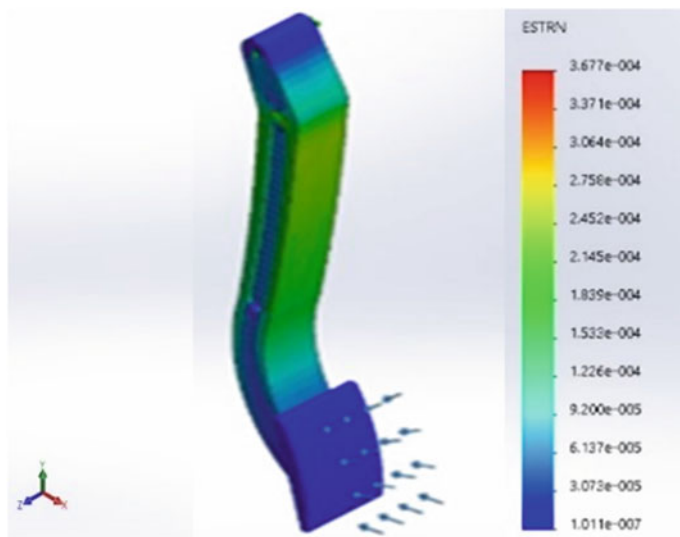
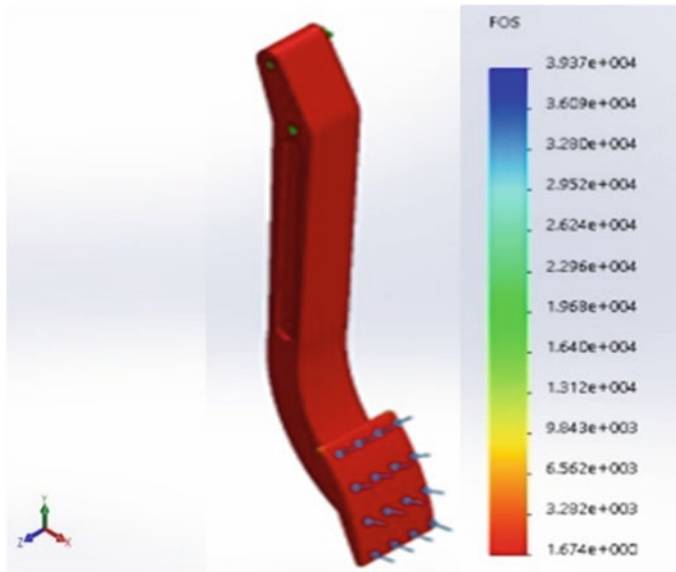


Fig. 5 Equivalent strain



**Fig. 6** Factor of safety

## 4 Conclusion

In this test simulation for the pedal, some interesting factors were revealed, which can help in defining a better brake pedal design. This included design based on different thicknesses in the pedal design according to the force buildup at a different location during application. It is more practical and efficient to use a pedal constructed out of aluminum alloy. The pedal analysis also tests the limits which are offered by the material with the design and the working analysis for the pedal.

The results concluded that the pedal has effectiveness according to the design of the pedal with a maximum tensile stress yield of  $3.295 \times 10^7$  which is offered by the material. The pedal design has a lower yield of tensile stress in the design. But the displacement and strain are within the permissible limit with a factor of safety between 3 and 5 points on a 5-point scale.

## References

1. He H, Wang C, Jia H, Cui X (2020) An intelligent braking system composed single-pedal and multi-objective optimization neural network braking control strategies for an electric vehicle. *Appl Energy* 259. <https://doi.org/10.1016/j.apenergy.2019.114172>
2. Shi J et al (2020) Prediction of brake pedal aperture for automatic wheel loader based on deep learning. *Autom Constr* 119. <https://doi.org/10.1016/j.autcon.2020.103313>.



3. Wu Y, Boyle LN, McGehee DV (2018) Evaluating variability in foot to pedal movements using functional principal components analysis. *Accid Anal Prev* 118:146–153. <https://doi.org/10.1016/j.aap.2018.02.011>
4. Wiggermann N, Zhou J (2018) Relationships among static strength, dynamic strength, and psychophysically determined levels of acceptable force for a pushing task and foot pedal actuation task. *Int J Ind Ergon* 65:68–73. <https://doi.org/10.1016/j.ergon.2018.01.010>
5. Cuma MU, Ünal ÇD, Savrun MM (2021) Design and implementation of algorithms for one-pedal driving in electric buses. *Eng Sci Technol Int J* 24(1):138–144. <https://doi.org/10.1016/j.jestch.2020.12.014>
6. Singh YD, Varma SVM, Khakhar P (2018) Analysis on multi linkage brake system with variable pedal ratio [Online]. [www.sciencedirect.com/www.materialstoday.com/proceedings](http://www.sciencedirect.com/www.materialstoday.com/proceedings)
7. Sargini MIM, Masood SH, Palanisamy S, Jayamani E, Kapoor A (2021) Additive manufacturing of an automotive brake pedal by metal fused deposition modeling. *Mater Today Proc* 45:4601–4605. <https://doi.org/10.1016/j.matpr.2021.01.010>
8. Deng TM, hou Fu J, Shao YM, shuan Peng J, Xu J (2019) Pedal operation characteristics and driving workload on slopes of mountainous road based on naturalistic driving tests. *Safety Sci* 119:40–49. <https://doi.org/10.1016/j.ssci.2018.10.011>
9. Romero J, Queipo NV (2018) An ANOVA approach for accounting for life-cycle uncertainty reduction measures in RBDO: the FSAE brake pedal case study. *Struct Multi Optim* 57(6):2109–2125. <https://doi.org/10.1007/s00158-018-1983-6>
10. Kirschbaum S et al (2021) Reaction time and brake pedal force after total knee replacement: timeframe for return to car driving. *Knee Surg Sports Traumatol Arthrosc* 29(10):3213–3220. <https://doi.org/10.1007/s00167-020-06105-2>
11. Liu W, Qi H, Liu X, Wang Y (2020) Evaluation of regenerative braking based on single-pedal control for electric vehicles. *Front Mech Eng* 15(1):166–179. <https://doi.org/10.1007/s11465-019-0546-x>
12. Yusuf R, Tanev I, Shimohara K (2019) Affective computing to help recognize mistaken pedal-pressing during accidental braking. *Artif Life Robot* 24(2):212–218. <https://doi.org/10.1007/s10015-018-0515-1>
13. Kulangara AJ, Rao CSP, Cherian J (2021) Topology optimization of lattice structure on a brake pedal. *Mater Today Proc* 47:5334–5337. <https://doi.org/10.1016/j.matpr.2021.06.059>
14. Mohanta M, Kar S, Mohanta D, Mohanty AM (2018) Experimental analysis and parametric optimization of 6065-aluminium alloy in rotary friction welding, vol 8, no 1, pp 111–118

# Recent Advancements and Challenges of Abrasive Jet Machining: A Review



Bhaskar Chandra Kandpal, S. P. Singh, Nitin Johri, Khalid Nafees, Ajay Singh Raghav, Arshad, and Amit Gupta

**Abstract** Advanced processing methods such as abrasive jet machining can perform various processing such as deburring, polishing, and cutting, and can process even minute dimensions effectively and efficiently. This research paper provides a comprehensive overview of the work done in this area and highlights the complex analysis that has been done to date. This paper provides an overview of the latest technology used in this machining and also discusses the issues related to machining. The review also highlights different materials and methods used under different conditions. Various optimization techniques to improve material removal rate (MRR) and improve kerf width and surface finish are also discussed. This review paper may represent current research challenges and also foresee the development of scopes in this area of advance machining.

**Keywords** AJM · AWJM · Sandblasting · Mechanism of material removal · Nozzle wear

## 1 Introduction

The industrial revolution from Industry 1.0 to Industry 4.0 has dramatically changed human life. Industrialization with high productivity, zero defect quality, increased efficiency, significant time savings, and much better connectivity are some of the main advantages, but at the expense of environmental damage. To overcome the challenges, sustainable manufacturing processes are of great importance worldwide. The term sustainability is the ability of a process, system, product, or service to function efficiently without impacting the environment. Sustainability measures are taken from the processing of raw materials to the delivery of the final product.

---

B. C. Kandpal (✉) · S. P. Singh · K. Nafees · A. S. Raghav · Arshad · A. Gupta  
Department of Mechanical Engineering, Inderprastha Engineering College, Ghaziabad, India  
e-mail: [kandpalbhaskar2000@gmail.com](mailto:kandpalbhaskar2000@gmail.com)

N. Johri  
Department of Mechanical Engineering, Graphic Era (Deemed to be) University, Dehradun,  
Uttarakhand, India

© The Author(s), under exclusive license to Springer Nature Singapore Pte Ltd. 2024  
R. K. Tyagi et al. (eds.), *Advances in Engineering Materials*, Lecture Notes in  
Mechanical Engineering, [https://doi.org/10.1007/978-981-99-4758-4\\_16](https://doi.org/10.1007/978-981-99-4758-4_16)

157

Sustainability interventions include a range of strategies and techniques to conserve natural resources and protect the environment. Machining is an important segment in manufacturing for producing technical parts and components of capital and consumer goods using typical processes. These processes ultimately lead to a high ecological footprint. It required the development of green machining techniques such as hybrid machining such as abrasive jet machining, green lubrication methods, dry cutting, and energy efficient auxiliary machining methods. Environmentally friendly processing technology is expected to contribute to the success of the industrial revolution.

In abrasive jet machining, jet of inert gas and fine abrasive particles strike the workpiece at a very high speed (300–500 m/s). The material is removed by the erosive action of abrasive particles. The kinetic energy of an abrasive particle converts into force and erodes the material. AJM process is commonly used for cutting, deburring, etc. This process is effective on hard/brittle materials. It can produce fine and complicated details.

### **Principle of AJM**

In the AJM process, fine particles are accelerated in a gas stream. The particles are directed toward the focus of machining (less than 1 mm from the tip). As the particles impact the surface, it causes a small fracture, and the gas stream carries both the abrasive particles and the fractured particles (wear) away.

### **Mechanism of AJM**

In the AJM process, cavity dimension changes with the change of NTD. The abrasive particles repeatedly hit on the workpiece. A brittle fracture separates tiny particles to produce a cavity. In the AJM process, the cavity width will be greater than or equal to the nozzle inner diameter (depending on NTD). During the brittle erosion process, particle impact produces different types of cracks and chips, with negligible plastic deformation. In the case of ductile materials, the material is removed by plastic deformation and cutting wear, or plastic strain and deformation wear. Different types of abrasives are used in the AJM process for different applications, such as  $\text{Al}_2\text{O}_3$ , SiC, and glass beads. Abrasive jet machining (AJM) is an efficient method of machining employed for brittle and hard materials employing fine abrasive particles focused stream with striking of the workpiece by highly pressurized air. This results in the removal of material from the surface on account of mechanical erosion. Abrasive particles get high kinetic energy from high-pressure air leaving the nozzle thereby impacting the workpiece and resulting in material removal from small fractures on impact. Fractured material and abrasive particles are carried away by the air stream. Wide application of AJM both on the macro-scale as well as microscale like micro-machining generating microholes, microchannels, and microdevice manufacturing is seen. Process parameters of the AJM process need to be optimized for enhanced material removal rate (MRR) with good surface quality.

## 2 Parameters of AJM

The impacts of feed rate, nozzle angle, pressure, grit size of abrasive grain particles, SOD, and MRR were studied. Glass specimens were machined using aluminum and carbide powder. AJM readily machined these specimens, but only compressive layers of toughened glass could be machined; no holes could be drilled. The exit nozzle was severely worn; although the mixing chamber and entry nozzle were a little worn [1]. A study on the shape of the surface [2] generated by AJM was done using an analytical approach as given in Table 1 to generate a semi-empirical equation to obtain the shape of the surface generated by AJM. They investigated the effects of grain size SOD, center line, and peripheral velocities of the jet on produced shape.

It examined [3] the influence of pressure and viscosity on MRR and surface polish in abrasive flow machining in their research work. The material of the workpiece also plays a role in the AJM process. Surface quality increased considerably over the first few cycles, according to scanning microscopy. The near-surface profile derived by wavelength decomposition improved surface formation mechanics. They studied [4] the susceptibility of alumina particles' impact on AJM. The application of abrasive grits has a considerable influence on the material responsiveness to impact. Experiments found that aluminum oxide abrasives roughened surfaces, whereas carbide abrasives smoothed them. Synthetic diamond abrasive produced more roughness on impact. This study examines the processes that impact surface roughness. To determine the influence of operating parameters on hole creation on GFRP ceramic material, the research was conducted [5]. The study used a statistical method called DOE. Abrasive flow and jet pressure were employed together with nominal hole diameter and SOD. The appropriate cutting feed, abrasive MRR, jet pressure, and SOD are all crucial for high-quality cuts, dimensional tolerances, and profitability, according to an assessment of the parameters. Abrasive water jet cut aluminum plates were investigated for surface [6] roughness by utilizing cutting abrasive of the appropriate mesh size. The surface roughness changed as the abrasive flow mass rate changed, affecting the bottom cut transverse speed and other abrasive water jet cutting parameters. Materials cut with an abrasive water jet have two surface textures, according to scientists. The first texture had a smooth start and a rough finish. They studied [7]

**Table 1** Results at different parameter levels [1]

Effect of input parameters	Results	Reasons
Increasing particle size	Increase MRR and penetration rate	The increased kinetic energy of the particles
Increasing standoff distance	Increased entry side diameter	Increased equivalent jet radius
Increased peripheral velocity	Increased MRR and edge radius	The increased kinetic energy of the particles
Increasing jet centerline velocity	Increased penetration depth and MRR	Erosion is proportional to $V^2$

machining of aluminum oxide ( $\text{Al}_2\text{O}_3$ ) due to its ductile and high tensile properties given in Table 2.

Different abrasive water jet machining (AWJM) processes are reviewed [8], on basis of parameters like work materials, factor influences, and modeling process. Parameters influencing AWJM process were categorized as hydraulic, abrasive, mixing, and cutting parameters. Modeling process for AWJM like neural network, statistical, numerical, dimensional, analytical, and differential equation model were investigated. Comparative analysis among different research works on basis of their experiment and subsequent performance was done. Challenges like low penetration depth and low rate of material removal along with their future scope were addressed. Pressure applied, NTS, MRR, offset distance, nozzle angle, and additional processing constraints were employed in this investigation. This study's major objective was to assess the design's productivity and machining accuracy. It was found that [9] aluminum oxide as corundum as an abrasive powder to drill a glass workpiece. To test MRR and overcut, SOD and pressure were used as OC. The impact of MRR and OC was studied using the Taguchi design. The findings show that SOD and applied pressure are critical for material removal percentage, whereas only applied pressure is significant for OC. Individual parameter modifications reduce OC and increase MRR. They employed an experimental method to study the impacts of rate offered, nozzle angle, applied pressure, abrasive mesh size, SOD, and MRR. Corundum and carbide powder was used to machine glass specimens. AJM readily machined these specimens, but only compressive layers of toughened glass could be machined; therefore, drilling was not possible. The exit nozzle was severely worn, whereas the mixing chamber and entry nozzle were a little worn. It was observed [10] the influence of material thickness on drilling time using abrasive jet machining on fragile glass, ceramic, and fiber sheets in their research work. Various-sized holes were drilled into each material. They observed that drilling time is not directly linked to material thickness, and that material machinability has a significant influence on drilling time. It was discovered that when SOD diminishes, the cut breadth decreases, and so drilling time increases as kerf grows. The machining parameters were discussed in Tables 3 and 4.

It explored [11] process parameters such as the space between the nozzle face and the work surface. The diameter of the hole rises with the space between the nozzle face and the work surface. Because a longer nozzle tip distance permits the jet to expand before impingement, it is more susceptible to external drag. Shorter nozzle

**Table 2** Limitation values of the control factors [6]

Control factor	Label	Low	High	Unit
Pressure	A	1300	1800	Bar
Nozzle transverse speed	B	2	3	Min/sec
Abrasive flow rate	C	6.38	13.62	g/min
Offset diameter	D	0.15	0.20	Mm
Impact angle	E	0	15	degree

**Table 3** Parameters used in AJM [10]

Medium of fabric	Air, nitrogen, and oxides of carbon
Type of abrasive	SiC, Al <sub>2</sub> O <sub>3</sub> , and glass beads
Abrasive flow	3–20 g/min
Flow velocity	150–300 m/min
Pressure	2–8 kg/cm <sup>2</sup>
Nozzle specification	0.05–0.40 mm
Material used (Nozzle)	Sapphire and tungsten carbide
Lifespan (Nozzle)	Max. 300 h
SOD	Maintain between 0.25 and 15 mm (The most appropriate distance is 8 mm)
Workpiece material	Glass, granite, ceramics, alloys of silicon, germanium, etc
Application	Cutting, cleaning, drilling, and deburring

**Table 4** Limitation values of the control factors [9]

Control factor	Label	Low	High	Unit
Pressure	A	1300	1800	Bar
Nozzle transverse speed	B	2	3	Min/sec
Abrasive flow rate	C	6.38	13.62	g/min
Offset diameter	D	0.15	0.20	Mm
Impact angle	E	0	15	degree

tip distances result in a smoother surface owing to enhanced K.E. The connection is between nozzle tip distance and hole bottom surface diameter at 5.5 kg/cm<sup>2</sup>. In this case, the NTD is 0.79 mm. The hole diameter is 1.50 mm for NTD 10.01 mm. They investigated [12] CFD, the flow field resolution, and the physical interactions between carrying and abrasive media. The anticipated particle velocity improved as the abrasive medium sharpness was adjusted from 1 to 0.6. The sphericity of the particles did not influence the air jet flow field. They used [13] the novel shadow mask technology to control particle size and SOD. Experiments employing shadow mask and clamped mask technologies were used to analyze the X-sectional shapes of channels for numerous jet passages. Mask depth and SOD were studied to produce an adequate mask for cutting a form. It investigated [14] the demand for energy in AJM. They studied the influence of input process variables on machining energy. An experimental approach combining MARS and GP was used for computer simulation. Choosing the optimal machining time and abrasive type is crucial to enhancing environmental performance.

### 3 Optimization of AJM Process

One of the versatile processing techniques for materials “Abrasive jet bombarding” finds application in abrasive jet machining, fast cleaning, deburring, polishing, surface preparation erosion testing, and shot-peening [15]. Current issues in R&D are identified as specific operation types like microchannel polishing and micro-machining. Critical issues involving material processing using an abrasive jet are subsequently reviewed and presented here. Optimal process constraints like SR and MRR are found for the water AJM process using the Taguchi method and ANOVA [16], for the prediction of optimal parameters like abrasive flow rate, applied pressure, NTS, and SOD as well as effective machining. Experiments carried out with L9 orthogonal array combination show surface roughness being majorly affected by abrasive flow rate, whereas MRR is affected by SOD, respectively. Carrier media is seen to play an important role in material removal using abrasive jet machining [17]. Hot air is attempted to be used as this carrier media, and robust design analysis using a modified Taguchi approach is attempted for optimal process parameters combination. The roughness of the machined surface and material removal rate is seen to be significantly affected by air temperature along with good agreement among experimental and predicted optimization values. Higher plastic deformation supplemented by brittle fracture failure at high temperatures is seen as evidence resulting in minimal and enhanced MRR. MCDM techniques involving product assessment and weighted aggregated sum are discussed in [18]. Responses of carbide coated nozzle in improved air-based AJM for nickel-233 alloy are considered against abrasive mesh size 400  $\mu\text{m}$ , injecting pressures 0.686 MPa and SOD 9 mm, as process variables for MRR maximization and SR minimization along with minimization of taper angle. Brittle material glass is machined by abrasive jet machining with high-speed abrasive particle stream application carried through a gas medium via nozzle [19]. Gas pressure impact using abrasive jet machining on the material removal rate is also emphasized. AJM as an untraditional industrial process for increased productivity is shown as a means for enhancing the manufacturer’s capability and efficiency. Micromachining process, abrasive machining which involves processes like lapping polishing, grinding, honing, super finishing, etc., is analyzed for improved material removal rate and flow rate using computational fluid dynamics [20] for modified elliptical nozzle shape instead of regular circular and rectangular nozzle shape. Analysis has shown elliptical design nozzle resulting in improved material removal rate and flow rate, respectively, thereby enhancing design. Optimization of parametric constraints of AJM like abrasive flow rate, applied pressure, nozzle diameter, and SOD is attempted using the Taguchi technique and ANOVA [21], for assessment of process parameters influence on fiberglass kerf and material removal rate, respectively. Pressure is seen to have a significant effect on material removal rate along with a major effect on kerf by a stand of distance. L16 orthogonal array for varying process parameters was utilized with the conduct of four experiments for the analysis. They [22] made use of abrasive water jet (AWJ) machining to machine difficult-to-cut

materials because of the fascinating feature of minimal tool wear and material independence. When cutting through a material, however, AWJ machining has limitations in terms of the geometries that may be produced. This constraint was overcome by using AWJ milling procedures, which were time consuming. To address this problem, the authors presented and investigated an improved AWJ milling operation intending to increase the number of geometries that can be produced. It [23] evaluated the cutting performance of the hot abrasive jet machining (HAJM) method, as well as the machinability of hardstone quartz in terms of three parameters, viz. taper angle, surface roughness, and material removal rate based on some control parameters. The author(s) analyzed experimental results using analysis of variance (ANOVA) and employed the genetic algorithm technique to carry out multi-objective optimization. Based on all analyses and experiments, the authors have concluded that hot abrasive jet machining has enhanced cutting performance and high material removal rate. They [24] investigated machinability on various compositions of aluminum hybrid composites using an abrasive water jet machining process. In this study, the effect of variation in factors such as transverse rate, water jet pressure, abrasive flow rate, and abrasive mesh size was observed on other parameters like surface roughness, material removal rate, and depth of cut. All experimentation concluded that the abrasive mesh size results in reducing surface roughness with a higher depth of cut and material removal rate. It [25] established the role of adding SiC super hard ceramic to garnet and determined the best input variable that influences material removal rate and surface finish during the process as. According to the findings, particle size was the most important factor in achieving high MRR and low surface roughness. They [26] made an effort to machine channels on silicon wafers. The effect of process parameters, e.g., feed rate, air pressure, and standoff distance was studied on other parameters, e.g., width and depth of the channel, material removal rate, and surface roughness. Experiments showed that the machined channels have adequate depth and a satisfactory surface polish with no heat-impacted zones and resolidification. It was [27] investigated the effect of slicing parameters on single crystal silicon by abrasive water jet machining (AWJM). The authors combined the gray relational analysis with fuzzy logic to optimize the response characteristics of the sliced surface and determine the highly preferable responses.

To identify and correlate the surface properties of the sliced silicon samples, these were examined by a 3D optical profilometer, scanning electron microscope (SEM), and atomic force microscope (AFM). The effect of surface irregularity on the optical properties of sliced samples for various sizes of abrasive particles was investigated. Variation of abrasive temperature and its effect on machining of features like target surface reliability; stress-free defects, surface roughness, and erosion rate were analyzed. Surface contours of the generated workpiece with the rate of erosion are shown to be a function of constraints of machining not influence characteristics of the flow of air-abrasive. Process parameters influence dimensional accuracy obtained in glass drilling by abrasive jet machining which is analyzed [28]. The effects of nozzle diameter, standoff distance, applied pressure, and grain size of particles was analyzed on kerf taper while drilling holes from glass sheets. A precise model based on the artificial neural network technique was established as a



process parameter's function. Optimization of the model using a genetic algorithm for kerf taper minimization was done. Standoff distance effect on kerf taper is seen to be major from results along with substantial reduction seen in the same on the application of axial feed toward nozzle resulting in constant standoff distance while performing machining. An experiment-based study of varying process parameters on abrasive jet machining is done [29]. The use of sand as an abrasive powder is made in drilling test series on glass workpieces. Process parameters like standoff distance, particle grain size, applied air pressure, impact angle, and nozzle diameter on machining performance were evaluated in terms of resulting material removal rate (MRR). MRR is seen to be majorly based on abrasive particles' kinetic energy and dominant parameter as applied pressure. Optimization of the model using a genetic algorithm with MRR maximization conditions identification was also done. Good agreement between obtained experimental results and genetic algorithm and artificial neural network-based predictions is seen. Process parameters' influence on dimensional accuracy obtained in glass drilling by abrasive jet machining is analyzed [28]. The effects of nozzle diameter, standoff distance, applied pressure, and grain size of particle were analyzed on kerf taper while drilling holes from glass sheets. A precise model based on artificial neural network technique was established as a process parameter's function. Optimization of the model using genetic algorithm for kerf taper minimization was done. Standoff distance effect on kerf taper is seen to be major from results along with substantial reduction seen in the same on application of axial feed toward nozzle resulting in constant standoff distance while performing machining. An experimental based study of varying process parameters on abrasive jet machining is done [29]. Use of sand as an abrasive powder is made in drilling test series on glass workpieces. Process parameters like standoff distance, particle grain size, applied air pressure, impact angle, and nozzle diameter on machining performance were evaluated in terms of resulting material removal rate (MRR). MRR is seen to be majorly based on abrasive particles kinetic energy and dominant parameter as applied pressure. Optimization of model using genetic algorithm with MRR maximization conditions identification was also done. Good agreement between obtained experimental results and genetic algorithm and artificial neural network-based predictions is seen. Analysis of effect of electrode wear ratio, rate of material removal, and surface finish of workpiece on process parameters of electrical discharge machining during SKD61 manufacture was made [30]. Optimal settings for the process parameters were proposed by a hybrid method comprising of genetic algorithm (GA), back propagation neural network (BPNN), and response surface methodology (RSM). Based on Taguchi table of orthogonal array, various specimens were made under varying processing conditions of EDM and prediction of ratio of relative electrode wear, rate of material removal, and roughness average were done on basis of results of experimental runs. Analysis of variance (ANOVA) implementation for significant factor identification in EDM process parameters was also done. Comparison of results from integrated BPNN and GA against RSM approach were made with the results showing superior prediction and confirmation by GA approach as compared to RSM. Surface roughness optimization for die sinking based on input parameters effect using electric discharge machining was aimed [31]. Surface roughness

values based at peak voltage and current were measured. Neuro solutions package based model of multiperceptron neural network were developed. Weighing factors of network were optimized using genetic algorithm. Effects of factors having relative influence on performance measure were analyzed based on sensitivity analysis. Material type is seen to have an effective influence over performance measures.

### **Challenges in AJM Process**

Process parameters of AJM process need to be optimized for enhanced material removal rate (MRR) with good surface quality. Hot abrasive jet machining process (HAJM) is a non-traditional machining process which utilizes stream of hot abrasive and relative high-speed air for generating tapered holes and microchannels with high accuracy. HAJM is seen as a technique with competence over other manufacturing techniques on account of defect free surfaces with better surface reliability. An approach toward computational fluid dynamics technique and experimental study in hot abrasive jet machining is discussed [32], with an aim toward predicting extent of erosive footprint and its constraint on target rate of surface erosion and surface roughness of intricately generated tapered shape holes. Abrasive particles of hot silicon carbide selection for achieving suitable holes of intricate shapes on zirconia ceramic were done. Variation of abrasive temperature and its effect on machining of features like target surface reliability; stress-free defects, surface roughness, and erosion rate were analyzed. Surface contours of generated work piece with rate of erosion are shown to be function of constraints of machining having no influence on characteristics of flow of air–abrasive.

## **4 Conclusion**

Throughout this discussion, a comprehensive description of AJM research and development will be offered. Because there is so much room for experimentation, there is a lot of room to see ideal values of critical regulating factors, such as SOD, applied pressure, and material feed rate, for a variety of materials. Nozzle designs were often modified to boost production speed. A wide range of experimental investigations may be carried out to better understand the relationship between various process factors.

**Acknowledgements** This research was supported by inderprastha Engineering College, Ghaziabad. We thank our colleagues from Inderprastha Engineering College Ghaziabad who provided insight and expertise that greatly assisted the research, although they may not agree with all of the conclusions of this paper.

## References

1. Balasubramaniam R, Krishnan J, Ramakrishnan N (2002) A study on the shape of the surface generated by abrasive jet machining. *J Mater Process Technol* 121:102–106
2. Williams RE, Rajurkar KP (1989) Metal removal and surface finish characteristics in abrasive flow machining. In: *Mechanics of deburring and surface finishing processes*. Presented at the winter annual meeting of the American society mechanical. American Society of Mechanical Engineers, New York, USA
3. Wakuda M, Yamauchi Y, Kanzaki S (2003) Material response to particle impact during abrasive jet machining of alumina ceramics. *J Mater Process Technol* 132(1–3):177–183
4. Ibraheem HMA, Iqbal A, Hashemipour M (2015) Numerical optimization of hole making in GFRP composite using abrasive water jet machining process. *J Chin Inst Eng Trans Chin Inst Eng* A38:66–76
5. Begic-Hajdarevic D, Cekic A, Mehmedovic M, Djelmic A (2015) Experimental study on surface roughness in abrasive water jet cutting. *Procedia Eng* 100:394–399
6. Dittrich M, Dix M, Kuhl M, Palumbo B, Tagliaferri F (2014) Process analysis of water abrasive fine jet structuring of ceramic surfaces via the design of experiment. *Procedia CIRP* 14:442–447
7. Padhy JP, Nayak KC (2014) Optimization and effect of controlling parameters on AJM using Taguchi technique. *J Eng Res Appl* 4:598–604
8. Anu Kuttan A, Rajesh R, Dev Anand M (2021) Abrasive water jet machining techniques and parameters: a state of the art, open issue challenges and research directions. *J Brazilian Soc Mech Sci Eng* 43
9. Rao PSVR, Naidu AL, Kona S (2018) Design and fabrication of abrasive jet machine (AJM). *Mech Mech Eng* 22:1471–1482
10. Reddy CAK, Danushyam B, Anil P (2018) Fabrication of abrasive jet machine with parameters investigation. *Int J Inn Sc Eng Tech* 5:15–18
11. Kulkarni PP, Suryawanshi D, Patil P (2019) Study of abrasive jet machine. *Int Res J Eng Technol* 06:264–268
12. Li H, Lee A, Fan J, Yeoh GH, Wang J (2014) On DEM-CFD study of the dynamic characteristics of high-speed micro-abrasive air jet. *Powder Technol* 267:161–179
13. Nouri A, Sookhak Lari MR, Spelt JK, Papini M (2015) Implementation of a shadow mask for direct writing in abrasive jet micro-machining. *J Mater Process Technol* 223:232–239
14. Vijayaraghavan R, Garg A, Vijayaraghavan V, Gao L (2015) Development of energy consumption model of the abrasive machining process by a combined evolutionary computing approach. *Meas. J Int Meas Confed* 75:171–179
15. Haldar B, Adak DK, Ghosh D, Karmakar A, Habtamu E, Ahmed M, Das S (2018) Present status and some critical issues of abrasive jet materials processing: a review. *Procedia Manuf* 20:523–529
16. Nagdeve L, Chaturvedi V, Vimal J (2012) Implementation of Taguchi approach for optimization of abrasive water jet machining process parameters. *Int J Instrum Control Autom* 224–228
17. Jagannatha N, Hiremath SS, Sadashivappa K (2012) Analysis and parametric optimization of abrasive hot air jet machining for glass using Taguchi method and utility concept. *Int J Mech Mater Eng* 7:9–15
18. Prasad SR, Ravindranath K, Devakumar MLS (2019) Experimental study and optimization in modified air abrasive jet machining on nickel-233 alloy using MCDM techniques. *Manuf Technol* 19:1010–1019
19. Rout IS (2014) Effect of pressure on material removal rate on glass using abrasive jet machining. *Int J Eng Res Technol* 3:483–487
20. Baranitharan P, Zeelan BN (2015) Design and analysis of elliptical nozzle in AJM process using computational fluid dynamics. *Sci Technol Arts Res J* 7522:171–179
21. Srikanth DV, Rao MS (2014) Application of optimization methods on abrasive jet machining of ceramics. *Int J Ind Eng Technol* 4:23–32
22. Uhlmann E, Mannel C, Braun T (2020) Efficient abrasive water jet milling for near-net-shape fabrication of difficult-to-cut materials. *Int J Adv Manuf Technol* 111:685–693

23. Pradhan S, Das SR, Drupal D (2021) Performance evaluation of recently developed new process HAJM during machining hardstone quartz using hot silicon carbide abrasives: an experimental investigation and sustainability assessment. *SILICON* 13:2895–2919
24. Thamizhvalavan P, Yuvaraj N, Arivazhagan S (2022) Abrasive water jet machining of Al6063/B4C/ZrSiO4Hybrid composites: a study of machinability and surface characterization analysis. *SILICON* 14:1093–1121
25. Saravanan K, Francis JX, Sudeshkumar MP, Maridurai T, Suyamburajan V, Jayaseelan V (2022) Optimization of SiC abrasive parameters on machining of Ti-6Al-4V alloy in AJM using taguchi-grey relational method. *Silicon* 14:997–1004. <https://doi.org/10.1007/s12633-020-00918-z>
26. Tomy A, Hiremath SS (2022) Machining, characterization, and optimization: a novel approach for machining channels on silicon wafer using tailor-made micro abrasive jet machining. *SILICON* 14:2317–2328
27. Sundararaj ONR, Sethuramalingam P (2022) Experimental investigation of AWJ slicing of single crystal silicon using fuzzy grey relational analysis (FGRA). *Silicon*
28. Nassef A, Elkaseer A, Abdelnasser ES, Negm M, Qudeiri JA (2018) Abrasive jet drilling of glass sheets: effect and optimization of process parameters on kerf taper. *Adv Mech Eng* 10
29. Abdelnasser ES, Elkaseer A, Nassef A (2016) Abrasive jet machining of glass: experimental investigation with artificial neural network modeling and genetic algorithm optimization. *Cogent Eng* 3
30. Krishna Mohana Rao G, Rangajanardhaa G, Hanumantha Rao D, Sreenivasa Rao M (2009) Development of hybrid model and optimization of surface roughness in electric discharge machining using artificial neural networks and genetic algorithm. *J Mater Process Technol* 209:1512–1520
31. Kuriakose S, Shunmugam MS (2005) Multi-objective optimization of wire-electro discharge machining process by Non-Dominated Sorting Genetic Algorithm. *J Mater Process Technol* 170:133–141
32. Pradhan S, Das SR, Jena PC, Dhupal D (2022) Machining performance evaluation under recently developed sustainable HAJM process of zirconia ceramic using hot SiC abrasives: An experimental and simulation approach. *Proc Inst Mech Eng Part C J Mech Eng Sci* 236:1009–1035

# Optical, Thermal, and Mechanical Properties of Scheelite Molybdate and Tungstate Materials Using Atomistic Simulations



Yamini Sudha Sistla, Ramesh Gupta Burela, Ankit Gupta,  
and Nabila Tabassum

**Abstract** Solid-state Raman-active materials are instrumental in the development of advanced eye-safe lasers, laser guide stars, remote sensing, and medical diagnosis and treatment. Present work focuses on studying the properties of Scheelite crystal structures of  $\text{BaWO}_4$ ,  $\text{CaWO}_4$ ,  $\text{BaMoO}_4$ , and  $\text{CaMoO}_4$  using atomistic simulations, to evaluate their suitability as Raman-active materials. Properties at zero external hydrostatic pressure such as band gap, dielectric function, refractive index, and thermal conductivity were studied using plane-wave density functional theory. Mechanical properties such as elastic constants, bulk modulus, shear modulus, young's modulus, Debye temperature, average sound velocity, and anisotropy index were also calculated. The calculated properties were in close correspondence with the available experimental and theoretical literature values. A good Raman-active material should possess high thermal conductivity, good absorption in visible and near-infrared region, and low micro-hardness. Among the four crystals studied,  $\text{CaWO}_4$  showed higher thermal conductivity and lowest hardness (more flexible and therefore easy to process) and highest fracture toughness. Further,  $\text{CaMoO}_4$  showed highest refractive index indicating its suitability for optoelectronic applications to develop transparent/anti-reflective materials. Analysis of elastic constants and various mechanical properties infer that the barium based materials and specifically tungstate material is more ductile. Barium-based crystals showed superior anisotropy compared to calcium based crystals. Young's modulus values infer that  $\text{BaMoO}_4$  is more ductile than  $\text{BaWO}_4$ ,  $\text{CaMoO}_4$ , and  $\text{CaWO}_4$ . Among the four crystals studied,  $\text{CaWO}_4$  showed highest thermal conductivity followed by  $\text{CaMoO}_4$ . Overall comparison indicates the suitability of calcium-based molybdate and tungstate as Raman-active materials which offer more ease of processing.

**Keywords** Raman-active materials · Scheelite materials · Density functional theory · Mechanical properties · Thermal conductivity · Dielectric function

---

Y. S. Sistla (✉) · N. Tabassum

Department of Chemical Engineering, Shiv Nadar University, Greater Noida, India  
e-mail: [yamini.sistla@snu.edu.in](mailto:yamini.sistla@snu.edu.in)

R. G. Burela · A. Gupta

Department of Mechanical Engineering, Shiv Nadar University, Greater Noida, India

© The Author(s), under exclusive license to Springer Nature Singapore Pte Ltd. 2024  
R. K. Tyagi et al. (eds.), *Advances in Engineering Materials*, Lecture Notes in  
Mechanical Engineering, [https://doi.org/10.1007/978-981-99-4758-4\\_17](https://doi.org/10.1007/978-981-99-4758-4_17)

169

## 1 Introduction

Ceramic materials have undergone a huge spike in popularity over the last two decades, resulting in considerable advancements in their development and application [1, 2]. Recently scheelite-type crystalline ceramics were reported to be promising materials for application in optoelectronic applications such as solid-state lasers and optical fibers due to their Raman-active nature [3, 4]. The Raman-active materials are widely used in optical remote sensing, laser guiding star, medical diagnosis, and treatment and coastal bathymetry to name a few. Some of the reported Raman-active materials include  $\text{CaWO}_4$ ,  $\text{SrWO}_4$ ,  $\text{BaWO}_4$ , and  $\text{YVO}_4$ . The metal tungstates ( $\text{WO}_4$ ) and molybdates ( $\text{MoO}_4$ ) have a general formula as  $\text{ABO}_4$  comprising of  $\text{A}^{+2}$  ( $\text{A} = \text{Ca}$ ,  $\text{Sr}$ ,  $\text{Ba}$ ,  $\text{Ni}$ ,  $\text{Mg}$ , and  $\text{Co}$ ) cations and  $\text{BO}_4^{-2}$  ( $\text{B} = \text{Mo}$ , and  $\text{W}$ ). The metal tungstates ( $\text{WO}_4^{-2}$ ) and molybdates ( $\text{MoO}_4^{-2}$ ) exist in various forms such as wolframite and scheelite structures [4–8]. These materials are known as self-Raman crystals which show laser and Raman properties. When the transition metal ‘W’ or ‘Mo’ show tetrahedral coordination, it is known as scheelite structure while a sixfold coordination would give them wolframite structure. The coordination depends on the ionic radius of the metal cation  $\text{A}^{+2}$ . When the ionic radius of bivalent cation is greater than 0.99 Å, scheelite structure will form, and when the ionic radius is less than 0.77 Å, wolframite structure will form [9]. The ionic radius of  $\text{Ba}^{+2}$  is 1.35 Å, and the ionic radius of  $\text{Ca}^{+2}$  is 1.00 Å. Therefore, both  $\text{Ba}^{+2}$  and  $\text{Ca}^{+2}$  form scheelite structures of tungstate and molybdate. The luminescent properties of scheelite materials have been studied by various researchers. Among the metal molybdates,  $\text{BaMoO}_4$  has a scheelite structure and produce green luminescence and therefore is reportedly suitable for producing optical fibers [10]. Luo et al. [4] have produced  $\text{BaMoO}_4$  nest-like nanostructures assembled with single-crystal nanosheets which exhibited green luminescence. Pontes et al. [5] have developed thin films out of  $\text{BaWO}_4$  and  $\text{PbWO}_4$  having a tetragonal scheelite structure. Marques et al. [6] have developed amorphous and crystalline thin films of  $\text{BaMoO}_4$  and studied their photoluminescence properties. They reported that the amorphous  $\text{BaMoO}_4$  thin film can be a great candidate for photo-luminescent applications [6]. The tungstate-based material  $\text{BaWO}_4$  (barium tungstate) is reportedly well suited for applications such as laser host material and scintillator in high-energy physics detectors. Ge et al. [7] have used iridium crucible to develop a single large crystal of  $\text{BaWO}_4$  using Czochralski method. They studied the molar enthalpy of fusion, molar entropy of fusion, thermal expansion coefficients, thermal conductivity, and micro-hardness of the  $\text{BaWO}_4$  single crystal [7]. Among the thermal properties, thermal conductivity of the material is very important in designing Raman lasers. The availability of thermal conductivity of single crystals of the barium- and calcium-based molybdate and tungstate materials is very limited in the literature. The Raman-active materials should possess good thermal properties such as high thermal conductivity and low thermal expansion. Similarly, mechanical stability of the material is also critical in developing robust Raman lasers with low processing cost. Especially, the elastic constants of single crystals is difficult to measure experimentally.

Atomistic simulations provide fundamental macroscopic perspective of materials which is critical for rational development of new and advanced materials with improved properties for a particular application. Further, atomistic simulations can also predict such properties which are difficult to determine experimentally especially single-crystal thermal conductivity, elastic constants, and dielectric functions to name a few [10, 11]. Therefore, the objective of the present work is to study and compare the optoelectronic, thermal, and mechanical properties of scheelite crystal materials  $\text{BaWO}_4$ ,  $\text{CaWO}_4$ ,  $\text{BaMoO}_4$ , and  $\text{CaMoO}_4$  using first principles based atomistic simulations. Such fundamental studies are very limited in the open literature. A validation of theoretical methods with experiments would be a stepping stone for developing new materials with improved properties.

## 2 Computational Methods

Initially, the stable energy configurations of bimetallic oxide ceramics ( $\text{BaWO}_4$ ,  $\text{CaWO}_4$ ,  $\text{BaMoO}_4$ , and  $\text{CaMoO}_4$ ) were obtained by studying the phase diagram and various conformational structures [12]. All the density functional theory and atomistic simulation calculations were performed using Biovia Material Studio 2022 software [13]. The geometry optimization of the crystal structures were done using plane-wave pseudopotential method as implemented in CASTEP (Cambridge Serial Total Energy Package). The exchange correlation function was calculated by using generalized gradient approximation (GGA) with the functional Perdew–Burke–Ernzerhof (PBE). On-the-fly generation (OTFG) ultrasoft pseudopotential were implemented with Koelling–Harmon scalar relativistic treatment. The integration over Brillouin zone was done over Monkhorst–pack grid scheme by setting  $k$ -points grid sampling at  $6 \times 6 \times 4$  in order to improve accuracy of results. The plane-wave cutoff energy was set at 700 eV. For the geometry optimization, Broyden–Fletcher–Goldfarb–Shanno (BFGS) minimization algorithm was used. The convergence tolerance criteria was set as: energy— $1.0 \times 10^{-5}$  eV/atom; maximum force—0.3 eV/atom; maximum stress—0.05 GPA; maximum displacement—0.001 Å. After the geometry optimization via energy minimization, the total density of states, band structure, thermodynamic properties, and magnetic moments were studied. The geometry optimization was performed at zero external hydrostatic pressure. After the geometry optimization, the elastic properties were studied by analyzing stress–strain curves for a maximum strain amplitude of 0.003. The properties such as bulk modulus ( $B$ ), shear modulus ( $G$ ), Young’s modulus ( $E$ ), and Poisson’s ratio ( $\sigma$ ) were computed from elastic constants ( $C_{ij}$ ). The optical properties such as refractive index were calculated from dielectric function in the electromagnetic photon incident frequency range of 0–80 eV (corresponding to the region of infrared to ultraviolet). Molecular dynamic simulations were used to compute the thermal conductivity of the crystalline materials using a supercell of the structure having lattice parameters of  $45.46 \text{ \AA} \times 22.73 \text{ \AA} \times 136.40 \text{ \AA}$ . The thermal conductivity was calculated by fixed

energy exchange method between atoms of different layers of the simulation cell. Simulations were run in a canonical ensemble (NVT) at a temperature of 500 K.

### 3 Results and Discussion

#### 3.1 Electronic Properties

The metal–oxygen bond length, lattice dimensions, cell volume, density, and band gap of the optimized structures of the crystals at zero external hydrostatic pressure are presented in Table 1. The lattice parameters and the crystal density values computed in the present work are very close to the reported experimental values as mentioned in brackets of Table 1 [7, 14, 15]. In general, a band gap greater than 3 eV usually considered as insulator property. Based on the band gap values, among the four crystals studied, it is clear that BaWO<sub>4</sub> is a good insulator and CaMoO<sub>4</sub> is a weak insulator and could show semiconductor properties.

The energy bands of the crystals were analyzed with the help of partial density of states of individual atoms each crystal made up of. Figure 1 shows the total density of states (DOS) and partial density of states (PDOS) of the four crystals studied. The conduction band of BaWO<sub>4</sub> is around 15 eV wide, whereas the valance band is 4.70 eV wide consisting of 2 sub bands. The conduction band is majorly created by 5d and 6p of barium (Ba) followed by 2p of oxygen (O) and 5d of tungsten (W). The first part of valance band (−1.98 to 0.3 eV) formed purely from 2p states of oxygen.

**Table 1** Lattice dimensions ( $a$ ,  $c$ ) unit cell volume  $V$  and density of the crystals obtained using density functional method

Crystal	Bond length (Å)	Lattice dimension ( $a$ , $c$ ) (Å)	Volume (Å <sup>3</sup> )	Density (g/cm <sup>3</sup> )	Band gap (eV)
BaWO <sub>4</sub>	Ba–O: 2.77 (2.75) [7] W–O: 1.81 (1.78) [7]	$a = 5.74$ (5.63) $c = 12.89$ (12.79) [7]	424.73	6.136 (6.35) [7]	5.159
CaWO <sub>4</sub>	Ca–O: 2.47 W–O: 1.80	$a = 5.33$ (5.24) $c = 11.50$ (11.37) [15]	327.50	5.896 (6.12) [15]	4.577
BaMoO <sub>4</sub>	Ba–O: 2.79 (2.73) [14] Mo–O: 1.78 (1.78) [14]	$a = 5.70$ $c = 13.07$	425.51	4.645 (4.94) [14]	4.509
CaMoO <sub>4</sub>	Ca–O: 2.48 Mo–O: 1.78	$a = 5.31$ $c = 11.59$	327.07	4.116 (4.40) [3]	3.862

<sup>a</sup>The numbers in the bracket are the reference values



The second sub band ( $-3.96$  to  $-1.98$  eV) is also created by 2p states of oxygen while a minor contribution from 5d of tungsten. The conduction band of  $\text{CaWO}_4$  is around 18 eV wide while the valance band is 5.00 eV wide consisting of 2 sub bands. The conduction band majorly created by 3d and 4p of calcium (Ca) followed by 2p of oxygen (O) and a minor contribution from 5d of tungsten (W). The first part of valance band ( $-2.25$  to  $0.34$  eV) formed purely from 2p states of oxygen. The second sub band ( $-4.82$  to  $-2.25$  eV) is also created by 2p states of oxygen while a minor contribution from 4d of tungsten. The conduction band of  $\text{BaMoO}_4$  is around 16.5 eV wide while the valance band is 4.40 eV wide consisting of 2 sub bands. The conduction band majorly created by 5d and 6p of barium (Ba) followed by 2p of oxygen (O) and a minor contribution from 4d of molybdenum (Mo). The first part of valance band ( $-2.31$  to  $0.30$  eV) formed purely from 2p states of oxygen. The second sub band ( $-4.10$  to  $-2.31$  eV) is also created by 2p states of oxygen while a minor contribution from 4d of molybdenum. The conduction band of  $\text{CaMoO}_4$  is around 19 eV wide while the valance band is 5.02 eV wide consisting of 2 sub bands. The conduction band majorly created by 3d and 4p of calcium (Ca) followed by 2p of oxygen (O) and a minor contribution from 4d of molybdenum (Mo). The first part of valance band ( $-2.70$  to  $0.28$  eV) formed purely from 2p states of oxygen. The second sub band ( $-4.98$  to  $-2.70$  eV) is also created by 2p states of oxygen while a minor contribution from 4d of molybdenum. Therefore, Fig. 1 concludes that both the conduction band and valance band of barium-based tungstate and molybdate crystals are comparatively narrower than their calcium-based counterparts. In all the four crystals, the conduction band is made up of bivalent metal ion ( $\text{Ba}^{+2}$  and  $\text{Ca}^{+2}$ ) and the valance band is majorly made up of oxygen atoms. The tetravalent transition metal ions do not seem to be part of conduction band or valance band to any significant level.

### 3.2 Optical Properties

For solids, the dielectric constant represents optical conductivity. The optical conductivity is the electrical conductivity of the material in the alternating electric field. The optical properties in a way represent the electronic band structure of the solid material. The complex refractive index  $N$  is directly related to the complex dielectric function ( $\varepsilon_1$  and  $\varepsilon_2$ ) derived from Maxwell relations. The mathematical relationships between complex dielectric constant ( $\varepsilon(\omega)$ ), complex refractive index ( $N(\omega)$ ), and optical conductivity ( $\sigma(\omega)$ ) are as shown below [16].

$$N(\omega) = \sqrt{\varepsilon(\omega)} = n(\omega) + ik(\omega) \quad (1)$$

$$\varepsilon(\omega) = \varepsilon_1(\omega) + i\varepsilon_2(\omega) \quad (2)$$

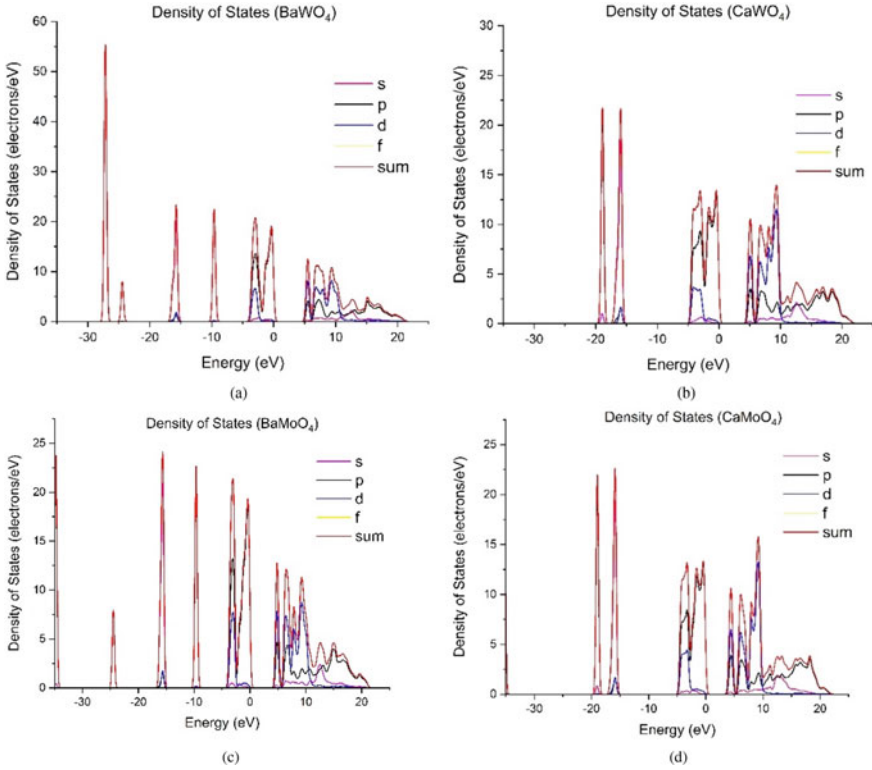


**Fig. 1** Density of states of crystals at zero external pressure **a** BaWO<sub>4</sub> **b** CaWO<sub>4</sub> **c** BaMoO<sub>4</sub> **d** CaMoO<sub>4</sub>

$$\varepsilon_1(\omega) = n_{(\omega)}^2 - k_{(\omega)}^2; \quad \varepsilon_2(\omega) = 2n_{(\omega)}k_{(\omega)} \quad (3)$$

$$\sigma(\omega) = -i \frac{\omega}{4\pi} (\varepsilon(\omega) - 1) \quad (4)$$

where ‘ $n$ ’ is the usual refractive index and ‘ $k$ ’ is the extinction coefficient, ‘ $\omega$ ’ is the angular frequency of incident electromagnetic photon wave, and ‘ $\varepsilon(\omega)$ ’ is the complex dielectric constant. Further, ‘ $\varepsilon_1(\omega)$ ’ is the real part of ‘ $\varepsilon(\omega)$ ’ and ‘ $\varepsilon_2(\omega)$ ’ is the complex part of ‘ $\varepsilon(\omega)$ ’. The dielectric constant typically describes a causal response. The imaginary part ( $\varepsilon_2(\omega)$ ) describes the real transitions between occupied and unoccupied electronic states. The absorption and emission of photons is caused due to transition between both filled and unfilled states. Therefore, imaginary part ( $\varepsilon_2(\omega)$ ) is obtained from the momentum matrix between the occupied and the unoccupied electronic states as represented by the equation shown below [16].

$$\varepsilon_2(q \rightarrow O_{\hat{u}}, \hbar\omega) = \frac{2e^2\pi}{\Omega\varepsilon_0} \sum_{k,v,c} |\langle \Psi_k^c | u \cdot r | \Psi_k^v \rangle|^2 \delta(E_k^c - E_k^v - \hbar\omega) \quad (5)$$

where ‘ $\omega$ ’ represents the angular frequency of electromagnetic photon, ‘ $u$ ’ represents the vector indicating the polarization of the incident electric field, and ‘ $e$ ’ represents the electronic charge. Further,  $\Psi_k^v$  and  $\Psi_k^c$  represent the wave functions of valance band and conduction band at ‘ $k$ ’. The real ( $\varepsilon_1$ ) and imaginary parts ( $\varepsilon_2$ ) are linked through Kramers–Kronig transform [17]. The complex refractive index ‘ $N$ ’ indicates the difference in the propagation of an electromagnetic wave through vacuum and the material being studied. The complex refractive index ( $N$ ) in vacuum is real ( $n$ ) and is equal to unity. Further,  $N$  is merely real ( $n$ ) for transparent materials. The imaginary part ( $k$ ) is related to the absorption coefficient ( $\eta$ ) as per the formula  $\eta = 2k\omega/c$  [16]. The absorption coefficient ( $\eta$ ) designates the fraction of energy lost by the wave when the wave passes through the material. More details of the theory and calculations can be found in CASTEP theory of Biovia Material Studio user guide [13].

The dielectric function ( $\text{Re}(\varepsilon)$  and  $\text{Im}(\varepsilon)$ ) against frequency (eV) for the four crystals is presented in Fig. 2. The optical properties of material in general depends on wavelength/frequency of incident light. The real and imaginary parts of ‘ $\varepsilon$ ’ are calculated using Kramers–Kronig relation [17]. The frequency of infrared, near-infrared, visible, and ultraviolet (UV) incident beam are 0.0414–0.41 eV, 0.49–1.65 eV, 1.65–3.10 eV, and 4.15–413 eV, respectively. The refractive index of a material changes with frequency of incident light. This is because the absorption coefficient ( $\eta$ ) and the extinction coefficient ( $k$ ) are functions of frequency of incident light [16]. In “normal dispersion phase/region, the refractive index of material increases with increase in frequency while in anomalous dispersion”, the refractive index decreases with frequency [17–19]. The calculated average refractive index of the crystals  $\text{BaWO}_4$ ,  $\text{CaWO}_4$ ,  $\text{BaMoO}_4$ , and  $\text{CaMoO}_4$  in the absorption region of infrared to visible range is 1.88, 1.84, 1.81, and 1.78, respectively. The refractive index versus frequency (eV) for all the four crystals is presented in Fig. 3a, b. The optical conductivity ( $\sigma(\omega)$ ) of the four crystals is presented in Fig. 4a, b. The computed refractive index values in the range of infrared–visible region match well with the experimental values reported by various researchers. Voronina et al. [20] have developed  $\text{BaWO}_4$  crystals using Czochralski method. They reported that the refractive index of  $\text{BaWO}_4$  as 1.87 at in a frequency range of 2–4 eV measured using goniometer. This is in close correspondence with the values computed in the present study. Wang et al. [18] have developed  $\text{CaWO}_4$  single crystals using Bridgman method from  $\text{CaWO}_4$  bulk crystals. They reported the refractive index of the single  $\text{CaWO}_4$  crystal in the range of 2.0–1.80 in the frequency range of 1.86–3.26 eV. This observation is in close correspondence with the values computed using DFT method in the present study. Among the four crystals studied, in the frequency range of 0–5 eV,  $\text{CaMoO}_4$  has the highest refractive index and optical conductivity, whereas  $\text{BaWO}_4$  has lowest values of refractive index and optical conductivity. Lower refractive index indicates higher speed of light in the material, and high refractive index indicates slow travel of light through the medium. High refractive index materials have significant applications in optoelectronic and

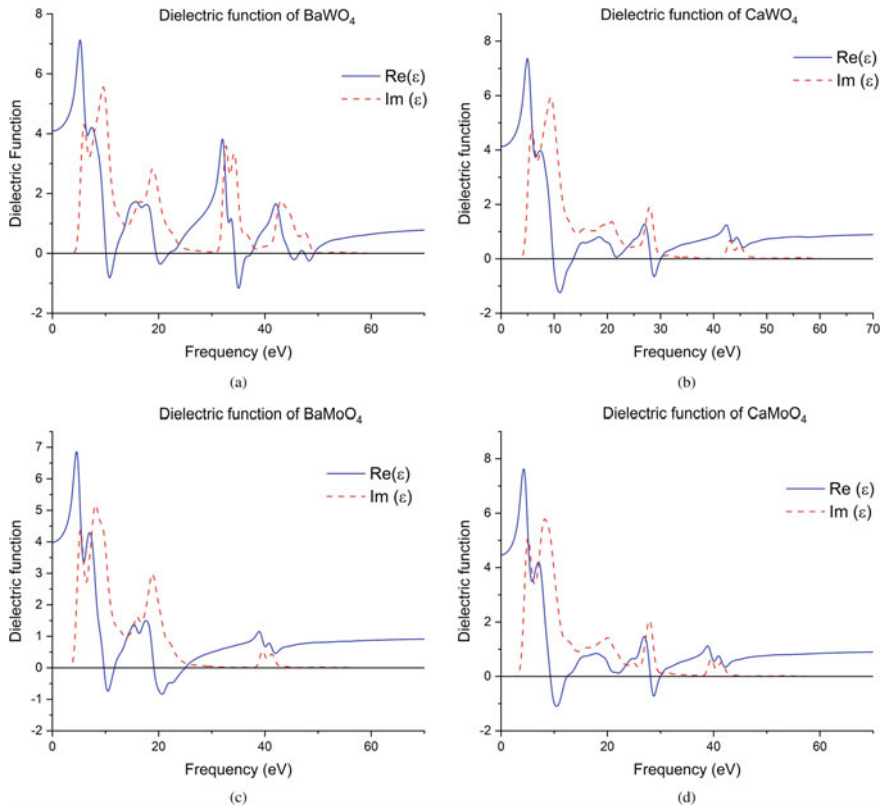


**Fig. 2** Dielectric function of the crystals at zero pressure

are suitable in applications of developing transparent materials. Another application of high refractive index materials is in developing anti-reflective materials. To this end, among the four crystals studied,  $\text{CaMoO}_4$  followed by  $\text{CaWO}_4$  could make a better choice in terms of application is transparent/anti-reflective materials.

### 3.3 Mechanical Properties

The elastic properties are typically described by the elastic moduli  $C_{ij}$ . A tetragonal crystal will show seven symmetry elements such as  $C_{11}$ ,  $C_{33}$ ,  $C_{44}$ ,  $C_{66}$ ,  $C_{12}$ ,  $C_{13}$ , and  $C_{16}$ . The elastic moduli of the four crystals studies at zero external pressure are presented in Table 2. The elastic constant  $C_{11}$  represents the resistance to linear compression in the  $(a, b)$  direction while  $C_{33}$  represents the resistance to linear compression in ' $c$ ' direction. The elastic constant  $C_{44}$  represents the shear elastic modulus along (010) direction on the (001) plane. The constant  $C_{66}$  represents the

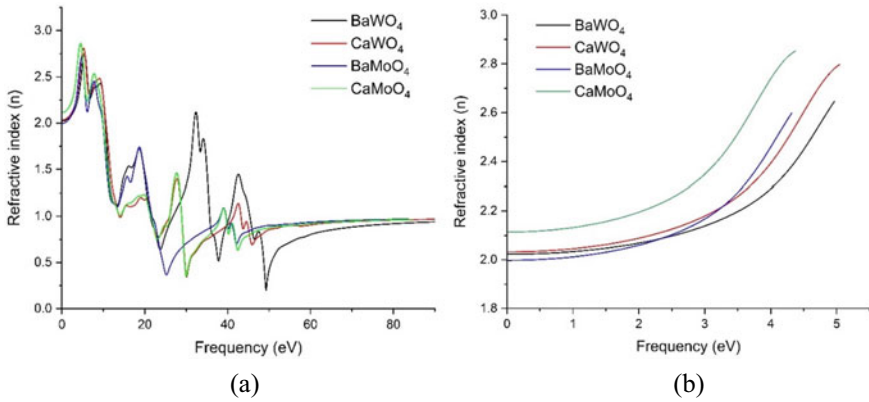


**Fig. 3** Refractive index of the crystals BaWO<sub>4</sub>, CaWO<sub>4</sub>, BaMoO<sub>4</sub>, and CaMoO<sub>4</sub>

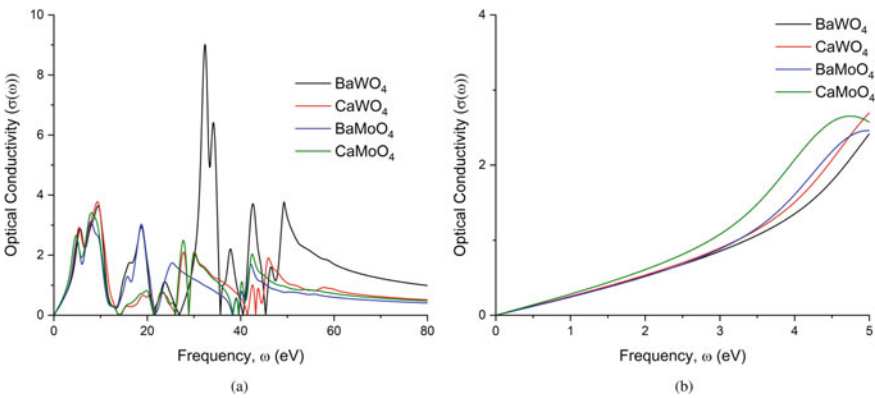


**Fig. 4** Optical conductivity of the crystals BaWO<sub>4</sub>, CaWO<sub>4</sub>, BaMoO<sub>4</sub>, and CaMoO<sub>4</sub>

shear elastic modulus along the (100) direction on the (010) plane. A crystal is considered to show elastic stability when the following conditions of elastic constants are met [10]:  $C_{11} > 0$ ;  $C_{33} > 0$ ;  $C_{44} > 0$ ;  $C_{66} > 0$ ;  $C_{11} - C_{12} > 0$ ;  $C_{11} + C_{33} - 2C_{13} > 0$ ;  $2(C_{11} + C_{12}) + C_{33} + 4C_{13} > 0$ .

All the four crystals studied meet the elastic stability conditions indicating that the structures are mechanically stable at zero external pressure. For all the four crystals studied,  $C_{33}$  is less than  $C_{11}$ . This represents that the crystal is more compressible in ‘c’-axis than the ‘a’ and ‘b’ axis. The lowest  $C_{33}$  and  $C_{11}$  values of BaMoO<sub>4</sub> indicates that, among the studied four crystals, BaMoO<sub>4</sub> is more compressible. The values if  $C_{44}$  and  $C_{66}$  being very less in comparison with  $C_{11}$  and  $C_{33}$  indicate that the structures have low resistance to the monoclinic shear distortion. Further,  $C_{44} < C_{66}$  indicates that [100](001) shear is more easier than [100](010) shear. It is quite clear from Table 2 that all the elastic constants of the barium (Ba)-based crystals (BaWO<sub>4</sub> and

**Table 2** Calculated elastic constants  $C_{ij}$  (GPa) of the tetragonal crystals at zero pressure

	$C_{11}$	$C_{33}$	$C_{44}$	$C_{66}$	$C_{12}$	$C_{13}$	$C_{16}$
BaWO <sub>4</sub>	90.28 (89.66) [22]	81.16 (91) [22]	24.65 (22) [22]	30.93 (32.86) [22]	48.34 (46.4) [22]	41.2 (39.45) [22]	10.23 (9.96) [22]
CaWO <sub>4</sub>	139.07 (143.87) [23]	115.99 (121.84) [23]	32.2 (33.5) [23]	38.94 (38.7) [23]	55.91 (60.90) [23]	46.09 (40.28) [23]	11.12 (11.91) [23]
BaMoO <sub>4</sub>	86.76	72.35	25.99	29.64	47.13	38.32	-10.59
CaMoO <sub>4</sub>	128.58 (144.7) [24, 25]	109.49 (126.5) [24, 25]	30.1 (36.9) [24, 25]	37.81 (37.4) [24, 25]	50.47 (66.4) [24, 25]	45.69 (46.6) [24, 25]	-8.33

<sup>a</sup>References are the experimental values

BaMoO<sub>4</sub>) are significantly less than those of calcium (Ca)-based crystals (CaWO<sub>4</sub> and CaMoO<sub>4</sub>), this indicates that the same external pressure should produce more deformations to the barium-based crystals than their calcium-based counterparts.

Table 3 presents the mechanical properties such as bulk modulus ( $B$ ), shear modulus ( $G$ ), Young's modulus, Poisson's ratio, and ductility index. The bulk and shear modulus are calculated via Voigt–Reus–Hill approach. The properties are compared (mentioned in brackets in Tables 2 and 3) with some of the available literature values are observed to be in close correspondence. As per the Pugh's approach, the ductility of a material can be measured by the ratio of bulk modulus to the shear modulus,  $B/G$ . In general, a material is brittle when  $B/G$  is less than 1.75 and is ductile when  $B/G$  is greater than 1.75. The data in Table 3 shows that all the crystals are ductile and the increase in ductility follows the order BaWO<sub>4</sub> > BaMoO<sub>4</sub> > CaMoO<sub>4</sub> > CaWO<sub>4</sub>. The Cauchy pressure ( $C_{12}$ – $C_{44}$ ) indicates the toughness of the material. If the Cauchy pressure is positive, then the material is known to be ductile whereas the crystal is usually brittle when the Cauchy pressure is negative [21]. All the three Cauchy pressures  $C_{12}$ – $C_{66}$ ,  $C_{13}$ – $C_{44}$ ,  $C_{12}$ – $C_{44}$  for the four crystals is positive indicating the ductile nature of the crystals. Furthermore, higher the Cauchy pressure, higher will be the toughness of the material.

Table 2 suggests that the order of materials studied in terms of toughness (Cauchy pressure) is CaWO<sub>4</sub> > BaWO<sub>4</sub> > BaMoO<sub>4</sub> > CaMoO<sub>4</sub>. The  $C_{ij}$  values computed using DFT method are compared with the available experimental values and mentioned in superscripted brackets in Table 2 at respective positions. Young's modulus (stress/strain) indicates the stiffness of the material and how easy it is to bend or stretch the material. The crystal BaMoO<sub>4</sub> is the most easily stretchable material among the four crystals studied followed by BaWO<sub>4</sub>, CaMoO<sub>4</sub>, and CaWO<sub>4</sub>. This indicates that among the bivalent metals, Ba<sup>+2</sup> gives flexibility and among the tetravalent materials and the molybdate-based compounds are more stretchable. The velocity of sound is highest in CaMoO<sub>4</sub> followed by CaWO<sub>4</sub>, BaMoO<sub>4</sub>, and BaWO<sub>4</sub> indicating the order of the crystals as CaMoO<sub>4</sub> > CaWO<sub>4</sub> > BaMoO<sub>4</sub> > BaWO<sub>4</sub> based on elasticity. The

**Table 3** Computed mechanical properties of the tetragonal crystals at zero pressure

	Elastic properties	BaWO <sub>4</sub>	CaWO <sub>4</sub>	BaMoO <sub>4</sub>	CaMoO <sub>4</sub>
Bulk modulus (B)	Bulk modulus (Voigt) (GPa)	58.13 (56.54) [25]	76.7	54.82	72.26
	Bulk modulus (Reus) (GPa)	57.70 (56.03) [25]	75.71	53.87	71.67
	Bulk modulus (Hill) (GPa)	57.92	76.2	54.34	71.97
	Bulk modulus (GPa)	57.71 (56.28) [25]	75.71 (78.5) [25]	53.87	71.67
Shear modulus (G)	Shear modulus (Voigt) (GPa)	24.78 (26.18)	37.07	24.46	34.59
	Shear modulus (Reus) (GPa)	22.63 (24.03)	35.45	21.76	33.52
	Shear modulus (Hill) (GPa)	23.71 (25.11) [25]	36.26	23.11	34.05
	Shear modulus (GPa)	23.7	36.26 (39.8) [25]	23.11	34.05
	Young's modulus (GPa)	65.08 (65.68) [25]	95.78	63.89	89.49
	Poisson's ratio	0.31 (0.3) [25]	0.29	0.3	0.29
	Ductility index (B/G)	2.43 (2.24) [25]	2.08	2.33	2.1
	Fracture toughness (Mpa m <sup>0.5</sup> )	0.61	0.82	0.58	0.77
	Universal anisotropy index	0.48	0.24	0.64	0.17
	Elastic Debye temperature (K)	251.49	344.51 (356) [15]	282.07	400.67 (438) [26]
	Velocity of sound (m/s)	2190.13	2758.57	2452.57	3203.07

elastic anisotropy indicates the tendency of the crystals toward developing micro-cracks [27]. The universal anisotropy index quantifies the anisotropy of the material. For an isotropic crystal, the universal anisotropy index will be zero. The anisotropy of studied crystals are in the order of  $\text{BaMoO}_4 > \text{BaWO}_4 > \text{CaWO}_4 > \text{CaMoO}_4$ . The Debye temperature calculated from elastic constants is reported in Table 3. The elastic Debye temperature of calcium-based tungstate and molybdate is higher than the barium-based counterparts. The elastic Debye temperature of the calcium-based crystals are in close corresponding with the theoretical values reported in literature as mentioned in superscripted brackets of Table 3.

### 3.4 Thermal Properties

Thermal conductivities of the four crystals at a temperature of 500 K were computed using molecular simulations. After geometry optimization of single unit cell of the crystal structure, Mulliken partial charges were applied to each atom. The super-cell of the crystal having dimensions of  $45 \text{ \AA} \times 22 \text{ \AA} \times 136 \text{ \AA}$  was generated and used for further simulations. The simulation cell was initially geometry optimized. The resulting cell was divided into 50 layers in the Z-direction. All the simulations were conducted in canonical ensemble (NVT, constant volume, and temperature for a fixed number of molecules). The thermal conductivity was calculated by using fixed energy exchange method between the atoms in different layers of the simulation cell. The energy exchange was fixed at a value of 1.0 kcal/mol [28]. Thermal conductivity of all the materials was studied at a temperature of 500 K. Temperature was controlled by Berendsen thermostat with a decay constant of 0.1. Universal force field was applied for the system. Atom-based summation method was used for the long range van der Waals interactions. During equilibration, 1000 exchange steps were run and 2500 energy exchange steps were run during production with 100 time steps between the two exchanges. A time step of 1 fs (femto sec) was used. The initial velocities were assigned to the atoms by running NVT simulation for 100 steps. The velocity of the molecules depends on the temperature. During the transfer of heat energy, the velocity of the fastest atom in one region will be replaced by the velocity of the slowest atom in a different region. As a result, the first region becomes colder and the other region becomes hotter due to exchange in velocities. In this manner, the atoms in the system will interact by virtue of flowing energy from hot to colder region until a steady state is achieved. The thermal conductivity is computed as the ratio of energy flux and temperature gradient. The thermal conductivity of the four crystal materials are presented in Table 4. The values from molecular simulations are compared with some of the experimental values available in the literature. It is clear from Table 4 that the molecular simulations were able to predict the thermal conductivity of materials. Figure 5 shows the temperature fields along the supercell of the crystal at steady state of the simulation at temperature of 500 K. The results from Table 4 infer that the thermal conductivity of the four crystals is in the order of  $\text{CaWO}_4 > \text{CaMoO}_4 >$



**Table 4** Thermal conductivity of the crystals at 500 K

Crystal	Thermal conductivity (this work) W/m K	Thermal conductivity (literature value) W/m K
BaWO <sub>4</sub>	1.945	2.35 [29]
CaWO <sub>4</sub>	3.953	3.5 [15]
BaMoO <sub>4</sub>	1.999	2.8 [30]
CaMoO <sub>4</sub>	2.79	

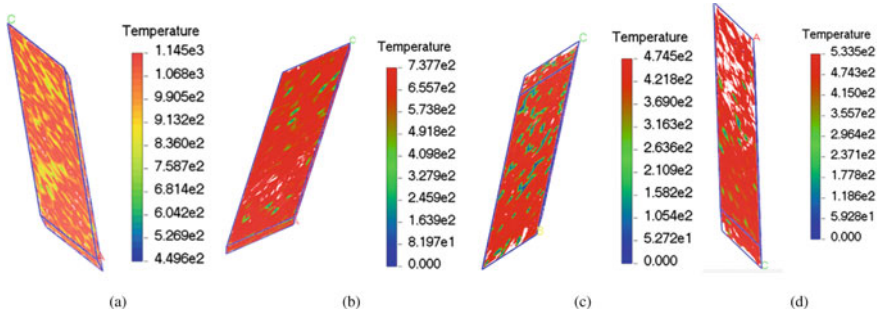


**Fig. 5** Temperature fields of the crystals **a** BaWO<sub>4</sub> **b** BaMoO<sub>4</sub> **c** CaWO<sub>4</sub> **d** CaMoO<sub>4</sub>

BaMoO<sub>4</sub> > BaWO<sub>4</sub>. This trend indicates that the calcium-based materials are more conducting than barium-based ones.

## 4 Conclusions

The optoelectronic, mechanical, and thermal properties of the scheelite crystal materials BaWO<sub>4</sub>, CaWO<sub>4</sub>, BaMoO<sub>4</sub>, and CaMoO<sub>4</sub> were studied using density functional theory and molecular simulations. All the properties of crystal structures were studied at zero external hydrostatic pressure. Electronic and optical properties such as lattice constants, density, band gap, dielectric function, and refractive index were studied using plane-wave density functional theory. The mechanical properties such as elastic constants, bulk modulus, shear modulus, young’s modulus, Debye temperature, average sound velocity, anisotropy index, and ductility index were also calculated. Thermal conductivity was computed using molecular simulations. The calculated properties were compared with the available experimental and theoretical literature values and are observed to be in close correspondence. The band gap of the four studied materials suggests that BaWO<sub>4</sub> is a good insulator and CaMoO<sub>4</sub> is a weak insulator and could show semiconductor properties. The conduction band of the studied crystal materials is majorly made up of bivalent metal ion (Ba<sup>+2</sup> and Ca<sup>+2</sup>),

and the valance band is majorly made up of oxygen atoms. However, the contribution of tetravalent transition metal ions to the conduction band or valance band is not significant. Further, both the conduction band and valence band of barium-based tungstate and molybdate crystals are comparatively narrower than their calcium-based counterparts. The crystal  $\text{CaMoO}_4$  has shown the highest refractive index whereas  $\text{BaWO}_4$  has lowest refractive index. This indicates that  $\text{CaMoO}_4$  is most suitable for optoelectronic applications while developing transparent/anti-reflective materials. The analysis of elastic constants and various mechanical properties infer that the barium-based materials and specifically tungstate material is more ductile. The materials can be arranged in decreasing order of ductility as follows:  $\text{BaWO}_4 > \text{BaMoO}_4 > \text{CaMoO}_4 \geq \text{CaWO}_4$ . Based on elasticity, the studied materials are in the order of  $\text{CaMoO}_4 > \text{CaWO}_4 > \text{BaMoO}_4 > \text{BaWO}_4$ . The anisotropy of studied crystals are in the order of  $\text{BaMoO}_4 > \text{BaWO}_4 > \text{CaWO}_4 > \text{CaMoO}_4$ . Young's modulus values infer that the crystal  $\text{BaMoO}_4$  is the most easily stretchable material among the four crystals studied followed by  $\text{BaWO}_4$ ,  $\text{CaMoO}_4$ , and  $\text{CaWO}_4$ . Among the four crystals studied,  $\text{CaWO}_4$  has the highest thermal conductivity followed by  $\text{CaMoO}_4$ . Overall comparison of the properties indicates the suitability of the  $\text{Ca}^{+2}$  based tungstate and molybdate materials as Raman-active materials.

**Acknowledgements** The authors would like to acknowledge the SNU-Dassault Centre of Excellence (SDC) for providing the computational resources.

## References

1. Orera VM, Merino RI (2015) Ceramics with photonic and optical applications. *BOL SOC ESP CERÁM VIDR* 54(1):1–10
2. Xiaoa Z, Yub S, Lia Y, Ruanc S, Kongc LB, Huangd Q, Huangd Z, Zhoue K, Suf H, Yaog Z, Queh W, Liui Y, Zhangj T, Wangj J, Liuji P, Shenj D, Allixk M, Zhang Z, Tang D (2019) Materials development and potential applications of transparent ceramics: a review. *Mater Sci Eng R Rep Elsevier* 139:100518. <https://doi.org/10.1016/j.mser.2019.100518ff.hal-02391441>
3. Oliveira FKF, Oliveira MC, Gracia L, Tranquilin RL, Paskocimas CA, Motta FV, Longo E, Andres J, Bomio MRD (2018) Experimental and theoretical study to explain the morphology of  $\text{CaMoO}_4$  crystals. *J Phys Chem Solids* 114:141–152
4. Luo Z, Li H, Shu H, Wang K, Xia J, Yan Y (2008) Synthesis of  $\text{BaMoO}_4$  nestlike nanostructures under a new growth mechanism. *Cryst Growth Des* 8(7):2275–2281
5. Pontes FM, Maurera MAMA, Souza AG, Longo E, Leite ER, Magnani R, Machado MAC, Pizani PS, Varel JA (2003) Preparation, structural and optical characterization of  $\text{BaWO}_4$  and  $\text{PbWO}_4$  thin films prepared by a chemical route. *J Eur Ceram Soc* 23:3001–3007
6. Marques APA, de Melo DMA, Longo E, Paskocimas CA, Pizani PS, Leite ER (2005) Photoluminescence properties of  $\text{BaMoO}_4$  amorphous thin films. *J Solid State Chem* 178:2346–2353
7. Ge WW, Zhang HJ, Wang JY, Liu JH, Xu XG, Hu XB, Jiang MH, Ran DG, Sun SQ, Xia HR, Boughton RI (2005) Thermal and mechanical properties of  $\text{BaWO}_4$  crystal. *J Appl Phys* 98:013542
8. Tuersley IP, Jawaid A, Pashby IR (1994) Review: various methods of machining advanced ceramic materials. *J Mater Process Technol* 42:377–390
9. Wang X, Fan Z, Yu H, Zhang H, Wang J (2017) Characterization of  $\text{ZnWO}_4$  Raman crystal. *Optical Mater Express* 7(6):1732–1744

10. Benmakhlof A, Bentabet A (2015) First principles study of structural and elastic properties of BaWO<sub>4</sub> Scheelite phase structure under pressure. *Int J Phys Math Sci* 9(6):329–333
11. Wu D-H, Wang H-C, Wei L-T, Pan R-K, Tang B-Y (2014) First-principles study of structural stability and elastic properties of MgPd<sub>3</sub> and its hydride. *J Mag Alloys* 2:165–174
12. Jain A, Ong SP, Hautier G, Chen W, Richards WD, Dacek S, Cholia S, Gunter D, Skinner D, Ceder G, Persson KA (2013) The materials project: a materials genome approach to accelerating materials innovation. *APL Mater* 1(1):011002
13. Biovia (2022) Dassault systèmes, material studio version 22. Dassault Systèmes, San Diego
14. Xiao E-C, Li J, Wang J, Xing C, Guo M, Qiao H, Wang Q, Qi Z-M, Dou Z, Shi F (2018) Phonon characteristics and dielectric properties of BaMoO<sub>4</sub> ceramic. *J Materiomics* 4:383–389
15. Senyshyn A, Kraus H, Mikhailik VB, Yakovyna V (2004) Lattice dynamics and thermal properties of CaWO<sub>4</sub>. *Phys Rev B* 70:214306
16. Palik ED (1985) Handbook of optical constants of solids. Academic Press, Orlando
17. Kozak MI, Zhikharev VN, Puga PP, Loya VY (2017) The Kramers-Kronig relations: validation via Calculation Technique. *Int J Innov Sci Eng Technol* 4(12):152–159
18. Wang Z, Jiang L, Chen Y, Chen P, Chen H, Mao R (2017) Bridgman growth and scintillation properties of calcium tungstate single crystal. *J Cryst Growth* 480:96–101
19. Mytsyk BG, Kost YP, Demyanyshyn NM, Andrushchak AS, Solskii IM (2015) PiezoOptic coefficients of CaWO<sub>4</sub> crystals. *Crystallogr Rep* 60(1):130–137
20. Voronina IS, Ivleva LI, Basiev TT, Zverev PG, Polozkov NM (2003) Active Raman media: SrWO<sub>4</sub>:Nd<sup>3+</sup>, BaWO<sub>4</sub>:Nd<sup>3+</sup>. Growth and characterization. *J Optoelectron Adv Mater* 5(4):887–892
21. Eberhart ME, Jones TE (2012) Cauchy pressure and the generalized bonding model for nonmagnetic bcc transition metals. *Phys Rev B* 86:134106
22. Kavitha C, Narayana C, Ramachandran BE, Gargn N, Sharma SM (2015) Acoustic phonon behavior of PbWO<sub>4</sub> and BaWO<sub>4</sub> probed by low temperature Brillouin spectroscopy. *Solid State Commun* 202:78–84
23. Farley JM, Saunders GA (1971) The elastic constants of CaWO<sub>4</sub>. *Solid State Commun* 9(13), 965–969
24. Alton WJ, Barlow AJ (1967) Acoustic-wave propagation in tetragonal crystals and measurements of the elastic constants of calcium molybdate. *J Appl Phys* 38(10)
25. Najafvanzadeh N, López-Moreno S, Errandonea D, Pavone P, Drax C (2020) First-principles study of elastic and thermal properties of scheelite-type molybdates and tungstates. *Mat Today Commun* 24:101089
26. Senyshyn A, Kraus H, Mikhailik VB, Vasylechko L, Knapp M (2006) Thermal properties of CaMoO<sub>4</sub>: lattice dynamics and synchrotron powder diffraction studies. *Phys Rev B* 73:014104
27. Kube CM (2016) Elastic anisotropy of crystals. *AIP Adv* 6:095209
28. Mueller-Plathe F (1997) A simple nonequilibrium molecular dynamics method for calculating the thermal conductivity. *J Chem Phys* 106:6082
29. Liu Y, Jia D, Zhou Y, Zhou Y, Zhao J, Li Q, Liu B (2020) Discovery of ABO<sub>4</sub> scheelites with the extra low thermal conductivity through high-throughput calculations. *J Materiomics* 6:702–711
30. Bsaibess E, Delorme F, Monot-Laffez I, Giovannelli F (2021) Ultra-low thermal conductivity in scheelite and A-deficient scheelite ceramics. *Scripta Mater* 201:113950

# A Comprehensive Review on Aluminium MMC Fabricated by Liquid-Phase Fabrication Methodologies



Dinesh Chawla, Manoj Nayak, and Pallav Gupta

**Abstract** The need for advanced materials has always been desirable in all kinds of industries such as mechanical, aeronautical, civil and automobile. Almost all industries are looking for low-cost materials with better properties. These are the main components that attract every engineer or industrialist to produce an advanced and new material. This requirement may be attained in the form of composite materials. The better mechanical properties and light weight of composite mainly depend upon fabrication method and reinforcement used in the composite. This paper attempts to review the single and hybrid reinforcement used to prepare aluminium MMCs and liquid-phase fabrication method. Various liquid-phase fabrication methods were discussed which is used for the production of Al MMCs but especially put effort on stir casting technique.

**Keywords** Aluminium · Metal matrix composite (MMC) · Hybrid · Reinforcement · Liquid-phase processing methods

## 1 Introduction

MMC was developed in the year 1970, and the main support was from aerospace industries, but currently eighty percent of MMC is used in transportation industry, and hence, the support for further development is from transportation industries. Due to increase in demand in terms of both safety and fuel efficiency, industries like automotive, aerospace and marine is expected to fuel advanced materials [1]. States laying down stringent norms to cut down vehicular weight, which affect less

---

D. Chawla (✉) · M. Nayak

Department of Mechanical Engineering, Manav Rachna International Institute of Research and Studies, Faridabad 121003, India  
e-mail: [dineshchawla.fet@mriu.edu.in](mailto:dineshchawla.fet@mriu.edu.in)

P. Gupta

Department of Mechanical Engineering, A.S.E.T., Amity University Uttar Pradesh, Noida 201313, India  
e-mail: [pgupta7@amity.edu](mailto:pgupta7@amity.edu)

fuel consumption and further reduces the emissions of gases. This is compelling to indulge in research and development to meet the anticipated demand of metal matrix composite. Adding on to the existing demand is the rising disposable income of individuals along with the increasing trade practices which is the need of passenger car and commercial vehicle. Efficient performance requirements of aircraft ask for light weight material in aerospace industry which may likely fuel the market growth and anticipated demand. Therefore, high manufacturing cost and low productivity may act as a barrier for aforesaid market expansion. Hence, major industries are investing huge money in their research and development to produce metal matrix composites with lightness, enhanced durability, and high strength-to-weight ratio.

Metal matrix composites are materials with a metal matrix of aluminium, magnesium, titanium, iron, nickel, cobalt, and silver with ceramic reinforcement of silicon carbides, aluminium oxides, boron carbides, titanium carbides, titanium borides, and graphite. Morphology of reinforcement material plays a significant role to determine the property/cost combination. The various morphology are whisker fibre, particulate fibre along with continuous fibre. There is another category of hybrid composites primarily consisting one matrix and more than two reinforcement material of varying properties with the existing matrix phase, thereby reducing the weight of up to 50% in comparison with pure alloys [2]. But the aluminium matrix composites find wide applications in use or making prototyping of space shuttle, commercial aircrafts, automobiles, electronics substrate, which in fact requires the matrix properties of super alloys, titanium, magnesium, and copper. Aluminium metal matrix family covers wide range of varying composition of aluminium matrix with varying properties of stiffness, density, strength, weight, thermal and electrical properties which can be obtained by varying the reinforcement material, the orientation and location of reinforcement, the matrix alloy, the shape and volume of the reinforcement, heat treatment and the production methods tailored to achieve desired properties [3].

## 2 Reinforcement

The use of reinforcement type plays an important part in enhancing mechanical properties of composite, and its main use is to carry load [4]. Reinforcement type is divided into three categories: continuous reinforcement, whiskers and particulates. The most researched continuous reinforcement includes fibres made up of silicon carbide (SiC),  $\text{Al}_2\text{O}_3$ , carbon and monofilament wires. The continuous reinforcement showed better result in terms of strength and specific stiffness in comparison with discontinuous reinforcement. Carbon fibres are the lightest because of low density, so it offers greater saving in weight. The main disadvantage of the continuous reinforcement is its high cost along with higher cost of composite production [5]. The material used for making whisker includes metal, halides, carbides, oxides and organic compounds. The main class used for preparing whiskers mainly includes SiC,  $\text{Al}_2\text{O}_3$  and  $\text{Si}_3\text{N}_4$ . The whiskers reinforcement composites are more costly as compared to particles based composite, but it offer potential for enhanced properties. In general,

Particle and whiskers reinforcement are less expensive than continuous fibres [6]. Discontinuous reinforcement includes particles (WC, B<sub>4</sub>C, SiC, Al<sub>2</sub>O<sub>3</sub>, TiC) and whiskers are used [7]. Particulates reinforcement is cost effective as compared to whiskers and continuous reinforcement. The material used as reinforcement alloying are boron carbide, silicon carbide, graphite and Al<sub>2</sub>O<sub>3</sub> which are less costly industry-based particulates that showed excellent enhancement in mechanical behaviour and wear properties. The high melting temperature reinforcement like titanium carbide (TiC), WC, and magnesium oxide (MgO), produce advantageous properties like better strength and hot hardness of MMCs [8].

## 2.1 Single Reinforced Composites

Single reinforced composites are those materials that are produced by reinforcing single reinforcement materials within a matrix. The use of single reinforcement within a matrix is given in Table 1.

**Table 1** Literature review on use of single reinforcement in matrix

S. no	Matrix	Reinforcement	Literature review
1	LM13	SiC	Khan and Dixit [9] reported a work on LM13/SiC reinforced (0, 10, 15 wt%) particulates that were synthesized by liquid metallurgy method
2	AA6061	Al <sub>2</sub> O <sub>3</sub>	Singh et al. [10] worked on AA6061/Al <sub>2</sub> O <sub>3</sub> (aluminium oxide) by 1–3 wt% based material which was synthesized and processed via ultrasonic stir casting process followed by ultrasonic-assisted squeeze casting process
3	AA6082	Red mud	Samal et al. [11] carried out his experimental work on the fabrication of AA6082 composite reinforced with red mud particles by varying 2–6 wt%. Micro-hardness, yield strength and ultimate tensile strength increased on the addition of particulates; moreover, there was reduction in impact strength for both cast sample as well as sample treated by heat treatment
4	AA6082	Al <sub>2</sub> O <sub>3</sub>	Lukose et al. [12] performed an experimental study on the fabrication of AA6082 based composite reinforced with Al <sub>2</sub> O <sub>3</sub> by varying 1–3 wt%

## 2.2 Hybrid Reinforced Composite

Hybrid reinforced composites are materials that are produced by reinforcing two or more reinforcement materials within a single matrix. The use of hybrid reinforcement within a matrix is given in Table 2.

## 3 AMC Liquid-Phase Fabrication Methodologies

In past few years, the metal matrix composite has gained so much attention over alloy in the industries due to improved mechanical properties which make the composite material more suitable for special application such as aircraft industry and automotive industry. The processing cost of composite is high, still composite has gain attraction towards industry. The properties of the MMC are greatly influenced by

**Table 2** Literature review on use of hybrid reinforcement in matrix

S. no	Matrix	Reinforcement	Literature review
1	AA6061 T6	SiC/TiB2	James et al. [13] performed an experimental study on AA 6061 T6/SiC/TiB2 by 1–10 wt% based material which was fabricated by gravity die casting method. The addition of hybrid reinforcement (up to 10 wt%) enhanced the hardness, but reduction in strength was observed on the addition of TiB2 only
2	ADC 12	Groundnut shell ash/B4C	Venkatesh et al. [14] carried out experimental work on ADC 12/groundnut shell ash/B4C aluminium alloy-based hybrid composites was fabricated by squeeze casting method. The reinforcement contents were varied from 2.5 to 7.5 wt% and enhancement in hardness of 17% and ultimate tensile strength increased by 18.3%
3	AA 6063	SiC/PBA (pride of Barbados seed ash)	Oladayo et al. [15] reported a work on AA 6063/SiC/PBA (pride of Barbados seed ash) based hybrid MMC which was processed using stir casting technique with reinforcement variation of 10 weight percent in ratio of 0:10, 2.5:7.5, 5:5, 7.5:2.5, and 10:0
4	Al 6061	Al <sub>2</sub> O <sub>3</sub> /Bagasse ash	Chandla et al. [16] worked on hybrid reinforced composites Al 6061/5 wt% Al <sub>2</sub> O <sub>3</sub> /4, 6, 8 wt% bagasse ash were processed by using stir casting technique assisted with vacuum mechanism. The result showed max increment of 16.5% in Vickers hardness and strength reached a value of 151.1 MPa for 5 wt%Al <sub>2</sub> O <sub>3</sub> -6 wt% bagasse ash sample

fabrication technique. The selection of fabrication technique depends upon types of reinforcement and matrix, melting temperature of matrix and amount of composite to be produced. There are several fabrication techniques used in the industry to fabricate metal matrix composite. There is no unique technique available which is suitable for all type of composite. The fabrication method is majorly divided into two categories:

- Solid-phase fabrication method
- Liquid-phase fabrication method

Present study will discuss the liquid-phase fabrication methods, which involves the incorporation of reinforcement into the molten material. The mixing of matrix and reinforcement is performed with the help of some stirring mechanism and followed by solidification process. Generally, liquid-phase fabrication apparatus are easy to operate and cost effective in comparison with solid-phase fabrication method because of longer processing time. Any composite fabrication technique generally depends upon the application, type of reinforcement, distribution of reinforcement, melting temperature of matrix and amount of composite to be produced. Number of liquid-phase methods for the fabrication of high performance composite have been developed and reported by various researchers. Liquid-phase fabrication method mainly includes casting technique and infiltration technique. Various researchers have reported a study on the fabrication of composite using liquid-phase fabrication methods have been explained below.

### ***3.1 Stir Casting Processing***

Stir casting is a liquid-phase technique, in which discontinuous type of reinforcement is mixed with a molten matrix material by using mechanical stirring, followed by solidification process. It is an economical procedure for the production of low melting point matrix. Various researchers proposed an experimental work on stir casting method as discussed below.

Samal et al. [11] reported a work on fabrication AA6082 based MMC reinforced with red mud particles varying from 0 to 6 wt% with a step 2 wt%. The calculated amount of matrix melted at 800 °C in electric furnace and preheated reinforcement wrapped with aluminium foil were added into molten metal. The stirring process was performed by three axial mechanical stirrers at 500 rpm followed by formation of vortex field for the uniform dispersion of particles. The molten slurry was poured into die for solidification of the composite [11].

Dolata et al. [17] fabricated AlSi<sub>12</sub>/SiCp based MMC by using centrifugal casting technique. Initially, the alloy was melted performed under argon atmosphere in the PTA200/PrG station with the addition of Mg and Sr in desired wt% to improve wettability condition. The mixture was mixed under reduced pressure condition followed by addition of preheated reinforcement SiC (10 wt%) onto vortex of molten alloy. Then, degassing of the composite suspension was performed for 2 h and composite suspension was cast. Afterwards, the composite ingot was again melted in furnace



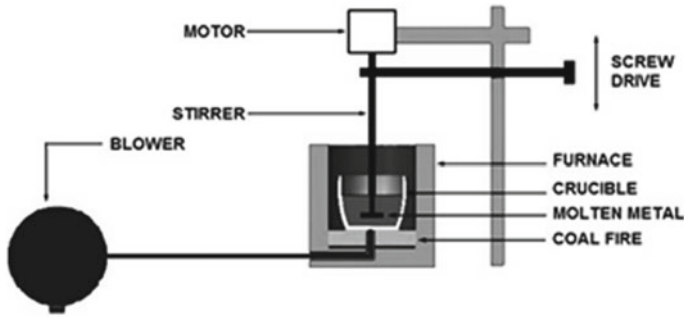


**Fig. 1** Stir casting set up [20]

and the tapping of suspension was directly made into centrifugal mould rotating in vertical axis [17].

Reddy et al. [18] worked on stir casting process to produce AA6063/TiC based composite varying from 5 to 15 wt% reinforcement content. In this technique, the reinforcement agent was incorporated into molten matrix followed by stirring the mixture with the help of rotating impeller and allowed the mixture to solidify.

Dwivedi et al. [19] presented a work on stir casting technique to develop AA6061/ $\text{Al}_2\text{O}_3$ /fly ash based hybrid composite with reinforcement variation of 0–15 wt%. This method involves the mixing of preheated ceramic particles and then reinforced into molten material at 700 °C. The stirring was performed by mechanical stirrer for proper mixing of reinforcement particles into molten metal and was poured into metallic mould for solidification of composite [19]. The layout diagram of stir casting set up is shown in Fig. 1 [20].

Singh et al. [21] fabricated AA6063/SiC composite by using advanced vacuum mould stir casting set up. This method involved the preheating of alloy matrix in the inbuilt crucible set up at 700 °C for 1 h and subsequently reinforcement was preheated at 500 °C. After preheating, complete melting of matrix was done at 800 °C and then temperature lowered to 575 °C to maintain slurry in semi-solid state. The mixing of reinforcement into slurry was performed by mechanical stirrer rotating at 350–500 rpm, and inert argon gas was injected into molten metal. The degassing process was performed at 800 °C to remove impurities followed by pouring of slurry into mould for solidification of composite [21].

Khan and Dixit [9] prepared LM13 alloy based composite reinforced with SiC (0, 10, 15 wt%) by using liquid metallurgy method. This method involves the incorporation of preheated reinforcement on the vortex of the molten alloy. The reinforcement particles was preheated at 200 °C and dispersed on the vortex of molten alloy at the temperature of 800 °C. The vortex formation was performed by mechanical stirrer rotating at 600 rpm, and after dispersion of particles, molten alloy was poured into mould to get solidified casting [9].

Senemar et al. [22] presented an experimental work on Al AMC/HTV silicone-based composite prepared by stir casting technique assisted with pyrolysis of HTV.

This method involves the addition of vulcanization silicone was gradually added into molten metal at 750 °C followed by stirring process with impeller at 600 rpm. The radiation and gas was released from the melt on each addition of reinforcement which indicates its reaction duration. Then, the slurry was poured into die and allowed to solidify [22].

Vinod et al. [23] presented a work on double stir casting method to fabricate hybrid composite A356/RHA/fly ash with different weight fraction from 0 to 12.5%. In this experimental study, initially the matrix was heated above liquidus temperature (>650 °C) in a furnace with preheating of reinforcement particles to 250 °C in a separate crucible to improve wettability. The inert argon gas was charged into furnace and cooling of molten metal was allowed to semi-solid state at 600 °C. This was followed by mixing of reinforcement particles into semi-solid state alloy, and stirring process was performed on the slurry for 10 min manually. After this, it was followed by second process mechanical stirring at 400 rpm for 15 min with superheating of mixture to 750 °C for the uniform distribution of reinforcement particles [23].

Singh et al. [10] performed an experimental work on AA6061/Al<sub>2</sub>O<sub>3</sub> based MMC fabricated by combination process of ultrasonic stir casting process and ultrasonic-assisted squeeze casting process. In ultrasonic squeeze casting process, the molten metal was mixed with preheated reinforcement and then poured into preheated die which was placed on the platform of the press. Afterwards the desired pressure was applied on the molten metal by using punch until complete solidification. The ultrasonic stir casting process involved the mixing of preheated reinforcement into the vortex of molten metal at 800 °C. The mechanical stirring was performed at 200 rpm by using stirrer for proper mixing of reinforcement particles. After stirring, the stirrer was replaced by ultrasonic probe for the uniform dispersion of particles in the matrix [10].

James et al. [13] presented a work on fabrication of AA 6061 T6/SiC/TiB<sub>2</sub> based hybrid MMC by using gravity die casting process. This method started with preheating of reinforcements and then added into the molten metal at 750 °C followed by stirring process at 350 rpm. Afterwards, molten metal was poured into mould by gravity casting and then solidified [13]. The results obtained of the various composite material fabricated by stir casting technique are presented in Table 3.

### ***3.2 Squeeze Casting Processing***

Squeeze casting is a hybrid technique that combines a process of casting and forging. This method involves the pouring of molten material in specific amount into a preheated bottom half die which is closed at ends, and subsequently pressure is applied by upper-half die to the solidified metal to get the final shape. Some researchers proposed an experimental work on squeeze casting method as discussed below.

**Table 3** Matrix, reinforcement and metallurgical properties of AMCs fabricated by stir casting technique

Sr. no	Matrix/reinforcement	Fabrication technique	Properties/result
1	Aluminium (99.6% purity)/waste colliery shale material	Stir casting process	Wear resistance and abrasion are higher for composite, yield strength, toughness and tensile strength improved [24]
2	A356/ZrO <sub>2</sub>	Stir casting process	Hardness, UTS and dislocation density improved with reinforcement content [25]
3	AA 6061 T6/ SiC and TiB <sub>2</sub>	Gravity die casting	Tensile strength decreased, wear resistance improved; SiC addition improved the tensile strength [13]
4	AA6082/graphite	Stir casting process	Hardness reduced with Gr addition to Al6082, addition of Gr is advantageous for wear properties. Non-uniform distribution of Gr [26]
5	AA6063/ Al <sub>2</sub> O <sub>3</sub> , rice husk ash, Gr	Two step stir casting process	Hardness decreased with addition of RHA and Gr, tensile strength and toughness higher at 0.5 wt% Gr, wear resistance decreased with Gr content [27]
6	AA7075/graphite and bagasse ash	Stir casting process	UTS and YS increased with increasing reinforcement, ductility decreased and hardness increase with reinforcement addition [28]
7	AA6061/ Al <sub>2</sub> O <sub>3</sub> and red mud	Vortex method (liquid metallurgy technique)	Hardness and tensile strength improved, uniform distribution of particles with small cluster at some places and porosity [29]
8	LM24/B4C	Stir casting process	Impact strength, UTS and hardness improved with increasing wt% of reinforcement [30]
9	AA8011/fly ash	Stir casting technique	Vickers hardness and wear resistance increased with fly ash reinforcement % [31]
10	Nickel plated A356.2/RHA	Stir casting technique	Achieved better adhesion between nickel and Al substrate, corrosion resistance increased [32]
11	A356/RHA, fly ash	Double stir casting method	Micro-hardness and density increased, porosity decreased [23]
12	AA8011/TiC, graphite	Stir casting method	Tensile strength, micro-hardness, impact strength and corrosion resistance increased with addition of TiC, corrosion rate increase with addition of Gr [33]
13	AA6061/ Al <sub>2</sub> O <sub>3</sub> /fly ash	Stir casting method	Tensile strength and hardness improved, toughness and ductility reduced [19]
14	AA6061/SiC, Gr	Liquid metallurgy route	Hardness decreased in case of Gr content, hardness increase in case of SiC content, hardness improved due to aging, wear resistance increased in case of SiC reinforced composite, but decreased in case of hybrid composite [34]

(continued)

**Table 3** (continued)

Sr. no	Matrix/reinforcement	Fabrication technique	Properties/result
15	AA6063/TiC	Stir casting method	Tensile strength, micro-hardness improved and % elongation decreased, wear coefficient increase with reinforcement wt % [18]
16	AlSi12/SiCp	Centrifugal casting process	Coefficient friction and friction force increased, abrasion resistance increased [17]
17	AA6082/red mud particles	Stir casting method	Micro-hardness, yield strength and UTS improved and impact strength reduced, wear resistance increased with red mud reinforcement wt% [11]

Soundararajan et al. [35] worked on squeeze casting process to fabricate A413 based composite reinforced with B<sub>4</sub>C. The fabrication started with the melting of matrix in the furnace with mechanical stirring at 6000 rpm. The preheating reinforcement was gradually added in to the molten matrix and followed by pouring process in to die cavity. The pouring molten metal was then subjected to squeeze pressure by using hydraulically operated power press for the solidification of molten metal [35]. The pictorial view of the squeeze casting experimental setup is shown in Fig. 2 [36].

Baghi et al. [37] used combination of vortex and squeeze casting method to prepare A413 based composite reinforced with short carbon fibres. The electric furnace was used for melting of matrix at 680 °C, and then coated short carbon fibres were gradually added into molten alloy with continuous stirring process by using mechanical three blade stirrer. After mixing, the slurry was poured into squeeze casting die and then immediately placed on bed of press. Afterwards, it undergone squeeze pressure of 80 MPa for 30 s followed by solidification of composite, and after solidification, the composite was extracted [37].

The results obtained of the various composite material fabricated by squeeze casting technique are presented in Table 4.

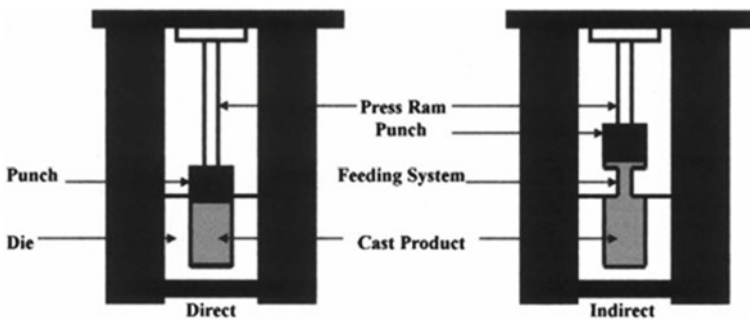


**Fig. 2** Squeeze casting experimental set up [36]

**Table 4** Matrix, reinforcement and metallurgical properties of AMCs fabricated by squeeze casting technique

Sr. no	Matrix/reinforcement	Method	Properties/result
1	AA 6061/Al <sub>2</sub> O <sub>3</sub>	Ultrasonic-assisted squeeze casting process	Tensile strength, compressive strength and hardness of ultrasonic-assisted squeeze casting processed composite are higher than ultrasonic-assisted stir casting [10]
2	AA 6061/CuO coated aluminium borate whiskers (ABO w)	Squeeze casting process	CuO coated composites having better mechanical properties as compared to without coating [38]
3	AA7075/SiC and nano-alumina	Squeeze casting process	Tensile strength and hardness improved, uniform distribution of particles, agglomeration was observed above 2 wt% nanoparticles [39]
4	A413/coated CSF	Squeeze casting process	Density decreased and porosity increased with addition of CSF, UTS and hardness increased up to 2 vol.% with uncoated CSF, UTS and hardness increased up to 3 vol.% with coated CSF [37]
5	A413/B4C	Squeeze casting process	Microporosity and defects eliminated at optimum process parameter, hardness, YS and UTS increased with B4C wt% [35]
6	Wrought aluminium alloy 2024	Ultrasonic-assisted squeeze casting process	UTS, YTS and percentage elongation improved, microstructure refined with increase in ultrasonic power [40]

### 3.3 Infiltration Processing

Infiltration is a technique used for producing various metal matrix composite-based components. This technique involves the flow of the molten metal into a preform made up of reinforcing material. Some of the researchers proposed an experimental work on infiltration technique as discussed below.

Zhang et al. [41] reported a study on the fabrication of Al<sub>2</sub>O<sub>3</sub> p/Al composite by mechanical pressure infiltration method. In this research work, ball milling process was initially used to prepare Al<sub>2</sub>O<sub>3</sub> scaffold, obtained by mixing Al<sub>2</sub>O<sub>3</sub> powder (1.2 wt%) and glycerol (10 wt%). The resulting sample produced after unidirectional solidification was undergone freeze drying process at -40 °C temp to remove the content of solvent. Afterwards, the frozen samples were subjected to sintered process at 1500 °C followed by cooling and Al<sub>2</sub>O<sub>3</sub> scaffold was prepared. Then, composite Al<sub>2</sub>O<sub>3</sub> p/Al was prepared by using mechanical pressure infiltration method that involves preheating of Al<sub>2</sub>O<sub>3</sub> p/Al in a mould at 500 °C along with melting of aluminium alloy at 900 °C. The resulting mixture was subjected to mechanical pressure of 5 MPa for 10 min and then allowed to cool [41].

Kim et al. [42] worked on fabrication of A356/CNT/Al<sub>2</sub>O<sub>3</sub> aluminium metal matrix hybrid composite by using infiltration technique followed by hot extrusion method. Initially, CNT and Al<sub>2</sub>O<sub>3</sub> fibres were mixed with required amount of binder and water to improve the viscosity of the slurry. This was followed by mechanical agitation in a controlled condition with mixing of cationic starch for flocking effect. The other additive added with starch was subsequently subjected to ultrasonic vibration for the uniform dispersion of additives. Water content present in the slurry was removed through vacuum pump, and the slurry was poured into mould for solidification [42].

Che et al. [43] prepared Al metal matrix composite reinforced with Ti coated diamond particles by using gas pressure infiltration method. In this method, the chamber containing reinforcement with aluminium matrix on the top were placed in a furnace and evacuated at a very low pressure of 0.1 Pa. Afterwards, the furnace was heated to 800 °C at a rate of 50 °C/min followed by applying pressurized gas on the molten metal until a pressure of 1 MPa pressure. This pressurized gas forced the matrix to infiltrate into reinforcement and then allowed to cool [43].

The results obtained of the various composite material fabricated by infiltration technique are presented in Table 5.

**Table 5** Matrix, reinforcement and metallurgical properties of AMCs fabricated by pressure infiltration technique

Sr. no	Matrix/reinforcement	Method	Properties/result
1	A356/CNTs and Al <sub>2</sub> O <sub>3</sub>	Ultrasonic infiltration method	Homogenous distribution of CNT, deformation resistance higher in case of hybrid composite compared to base alloy, increase in hardness were observed in core area [42]
2	Aluminium (99.99% purity)/Ti and diamond particle	Gas pressure infiltration method	Tensile, compressive and bending strength increased monotonically [44]
3	Commercial Al (purity 99.97%)/Ti-coated diamond particle	Gas pressure infiltration	Optimized thermal conductivity was attained as decreasing the thickness of TiC coating due to less thermal resistance at interface [43]
4	Al–Mg–Si alloy/Al <sub>2</sub> O <sub>3</sub> scaffold	Mechanical pressure infiltration method	Hardness behaviour is isotropic, compressive strength higher in transverse direction (anisotropic), strength improved in transverse direction [41]

## 4 Finding and Discussion

In liquid-phase methodologies, stir casting process is quite successful method for the uniform dispersion of particulates in base material [45]. An experimental study was attempted to fabricate AA7075 based composite reinforced with SiC and TiC composite by using stir casting technique, and it was observed that uniform dispersion of reinforcement particles was achieved [46]. The study revealed homogeneous distribution of reinforcement particles in hybrid composite AA7075/SiC/Al<sub>2</sub>O<sub>3</sub> fabricated by stir casting technique [47]. Stir casting process is an economical method to fabricate particulate reinforced composite as compared to other method. The processing parameter such as stirring time and stirring temperature greatly affects the mechanical behaviour of the composite. Minimum stirring time is required to form a bond between reinforcement and matrix, and higher stirring temperature would lead to improved distribution [48]. Stir casting technique assisted with extrusion process showed significant result in reduction of porosity, grain refinement, and matrix grain size [49].

The particles agglomeration problem in case of light reinforcement was overcome by using advanced shear technology and significantly improved ductility as well as strength of the fabricated sample [50]. Homogeneous dispersion of CNT and Al<sub>2</sub>O<sub>3</sub> was achieved in matrix A356 fabricated by using infiltration method and hot extrusion process [42]. Uniform distribution of particles was achieved in HPDC composite due to fluid shear generated, and significant improvement was observed in HPDC composite as compared to GDC composite [51]. It has been observed that induction melting have great potential to overcome the problem of dispersion of CNT in Al molten metal [52]. An attempt was carried out to predict the performance of A356.2 based composite reinforced with RHA and SiC. It was found that composite with up to 8% SiC and RHA reinforcement particles can be fabricated easily by stir casting technique and uniform dispersion of particles was achieved [53].

Aluminium silicon carbide based material was found to have excellent properties for power transmission elements like transmission gear under steady loadings [54]. A356/20%SiC/10%Al<sub>2</sub>O<sub>3</sub> based composite is found to be suitable material for the application of heavy vehicle such as clutch pressure and face plate [55]. Aluminium/silicon carbide based composite material is found as one of the option for power transmission component like spur gear [54].

The study revealed decrement in mechanical properties of AA-4032/SiC composite with increasing reinforcement content beyond 6% [56]. It was found that mechanical properties of the AA6061 based composite enhanced with increasing alumina particles reinforcement weight fraction but reduction in mechanical properties was observed with increase of reinforcement wt. fraction of MoS<sub>2</sub> [57]. A study was performed to fabricate Al-Si alloy based composite reinforced with 0D ball reinforcement. 1D rod reinforcement and 2D sheet reinforcement individually by using microcasting techniques [58].

## 5 Conclusion

Composites materials attained extensive demand in the manufacturing industries as well as in research due to their advantageous properties that is difficult to obtain by any of the constituent materials in the form of reinforcement acting alone. The literature reveals that the extensive effort put by researcher towards various problems that may be reduced to make composite strengthen. The mechanical and morphological properties of the matrix and type of reinforcement material used such as graphite,  $Al_2O_3$ , silicon carbide, titanium carbide, boron carbide, TiB<sub>2</sub> and graphene greatly affect the mechanical behaviour of composite. Several type of reinforcement particulates were used to fabricate the composite, but hybrid reinforced composite found to have better mechanical properties as compared to single reinforced composite. The addition of reinforcement like agro waste and industry waste in the Al matrix produce composites with enhanced properties.

Various processing methods were used by several researchers to make composite with better properties. The liquid-phase processing methods have been found to have remarkable attribute for volume production of composite due to their reduced composite production cost. The literature reveals that various researcher reported an experimental work on stir casting process to fabricate composites due to its less operating cost. The stir casting technique was found to have magnificent performance for producing composite because of better control on processing parameter, availability of the apparatus, viability and easy to use. The stir casting is found suitable for matrix having low melting temperature such as aluminium, copper and magnesium.

## 6 Future Scope

Despite of major research efforts made in the field of composite manufacturing, there is enormous scope to develop advanced material. Further work is possible on industrial and agriculture materials such as reinforcement towards the volume production of qualitative and low cost Al MMCs. Consequently, 3D printing technologies form of additive manufacturing has been found to have excellent potential, and more research work is needed for producing new part.

## References

1. Dhingra AK (1986) Metals replacement by composites. JOM 38(3):17–17. <https://doi.org/10.1007/bf03257887>
2. Clyne T (2000) An introductory overview of MMC systems, types, and developments. *Compreh Com Mater* 1–26. <https://doi.org/10.1016/b0-08-042993-9/00001-2>
3. Bunsell A (1980) Foreword. *Adv Comp Mater* 1-2. <https://doi.org/10.1016/b978-1-4832-8370-8.50004-8>



4. Diler EA, Ipek R (2013) Main and interaction effects of matrix particle size, reinforcement particle size and volume fraction on wear characteristics of Al–sicp composites using central composite design. *Compos B Eng* 50:371–380. <https://doi.org/10.1016/j.compositesb.2013.02.001>
5. Natrayan L, Senthil Kumar M (2018) Study on squeeze casting of aluminum matrix composites—a review. *Adv Manuf Mater Sci* 75–83. [https://doi.org/10.1007/978-3-319-76276-0\\_8](https://doi.org/10.1007/978-3-319-76276-0_8)
6. Rajesh AM, Kaleemulla M (2016) Experimental investigations on mechanical behavior of aluminium metal matrix composites. *IOP Conf Ser Mater Sci Eng* 149:012121. <https://doi.org/10.1088/1757-899x/149/1/012121>
7. Daniel Silas Kumar M, Jagadamba P, Srikiran S, Pujari S (2019) Mechanical behavioural aspects of Al-356 under the influence of boron carbide and magnesium. *Lecture notes on multi-disciplinary industrial engineering*, pp 437–447. [https://doi.org/10.1007/978-981-13-7643-6\\_35](https://doi.org/10.1007/978-981-13-7643-6_35)
8. Chen F, Gupta N, Behera RK, Rohatgi PK (2018) Graphene-reinforced aluminum matrix composites: a review of synthesis methods and properties. *JOM* 70(6):837–845. <https://doi.org/10.1007/s11837-018-2810-7>
9. Khan MM, Dixit G (2019) Evaluation of microstructure, mechanical, thermal and erosive wear behavior of aluminum-based composites. *Silicon* 12(1):59–70. <https://doi.org/10.1007/s12633-019-00099-4>
10. Singh M, Rana R, Purohit R, Sahu K (2015) Development and analysis of Al-matrix Nano composites fabricated by ultrasonic assisted squeeze casting process. *Mater Today Proc* 2(4–5):3697–3703. <https://doi.org/10.1016/j.matpr.2015.07.146>
11. Samal P, Mandava RK, Vundavilli PR (2020) Dry sliding wear behavior of al 6082 metal matrix composites reinforced with red mud particles. *SN Appl Sci* 2(2). <https://doi.org/10.1007/s42452-020-2136-2>
12. Lukose L, Babu K, Srinivasan S (2020) Development of aluminium 6082 alloy reinforced with Al<sub>2</sub>O<sub>3</sub> by die casting and investigation of microstructural and mechanical properties. *Mater Today Proc* 27:2520–2525. <https://doi.org/10.1016/j.matpr.2019.09.229>
13. James SJ, Venkatesan K, Kuppan P, Ramanujam R (2014) Hybrid aluminium metal matrix composite reinforced with sic and TiB<sub>2</sub>. *Procedia Eng* 97:1018–1026. <https://doi.org/10.1016/j.proeng.2014.12.379>
14. Venkatesh L, Arjunan TV, Ravikumar K (2019) Microstructural characteristics and mechanical behaviour of aluminium hybrid composites reinforced with groundnut shell ash and B4C. *J Braz Soc Mech Sci Eng* 41(7). <https://doi.org/10.1007/s40430-019-1800-1>
15. Oladayo O, Sikirat AK (2019) Mechanical and electrochemical behaviour of aluminum-based hybrid composites reinforced with silicon carbide and pride of barbardos seed ash produced by stir casting. *Mater Sci Eng Int J* 3(5). <https://doi.org/10.15406/mseij.2019.03.00110>
16. Chandla NK, Yashpal Kant S, Goud M, Jawalkar C (2020) Experimental analysis and mechanical characterization of al 6061/alumina/bagasse ash hybrid reinforced metal matrix composite using vacuum-assisted stir casting method. *J Com Mater* 54(27):4283–4297. <https://doi.org/10.1177/0021998320929417>
17. Dolata AJ, Mróz M, Dyzia M, Jacek-Burek M (2020) Scratch testing of AlSi12/SiCp composite layer with high share of reinforcing phase formed in the centrifugal casting process. *Materials* 13(7):1685. <https://doi.org/10.3390/ma13071685>
18. Reddy PV, Prasad PR, Krishnuudu DM, Goud EV (2019) An investigation on mechanical and wear characteristics of al 6063/TiC metal matrix composites using RSM. *J Bio Tribo Corros* 5(4). <https://doi.org/10.1007/s40735-019-0282-0>
19. Dwivedi S, Srivastava A, Maurya N, Maurya M (2019) Microstructure and mechanical properties of al 6061/Al<sub>2</sub>O<sub>3</sub>/fly-ash composite fabricated through stir casting. *Annales de Chimie - Science des Matériaux* 43(5), 341–346. <https://doi.org/10.18280/acsm.430510>
20. Kumar UKAV (2017) Method of stir casting of aluminum metal matrix composites: a review. *Mater Today Proc* 4(2):1140–1146

21. Singh J, Jawalkar CS, Belokar RM (2019) Analysis of mechanical properties of AMC fabricated by vacuum stir casting process. *Silicon* 12(10):2433–2443. <https://doi.org/10.1007/s12633-019-00338-8>
22. Senemar M, Niroumand B, Maleki A, Rohatgi PK (2017) Synthesis of the in situ aluminum matrix composite through pyrolysis of high temperature vulcanization silicone. *J Compos Mater* 52(1):123–134. <https://doi.org/10.1177/0021998317702955>
23. Vinod B, Ramanathan S, Ananthi V, Selvakumar N (2018) Fabrication and characterization of organic and in-organic reinforced A356 aluminium matrix hybrid composite by improved double-stir casting. *Silicon* 11(2):817–829. <https://doi.org/10.1007/s12633-018-9881-5>
24. Venkata Siva SB, Sahoo KL, Ganguly RI, Dash RR, Singh SK, Satpathy BK, Srinivasarao G (2013) Preparation of aluminum metal matrix composite with novel in situ ceramic composite particulates, developed from waste colliery shale material. *Metall and Mater Trans B* 44(4):800–808. <https://doi.org/10.1007/s11663-013-9832-x>
25. Abdizadeh H, Baghchesara MA (2013) Investigation on mechanical properties and fracture behavior of A356 aluminum alloy based ZrO<sub>2</sub> particle reinforced metal-matrix composites. *Ceram Int* 39(2):2045–2050. <https://doi.org/10.1016/j.ceramint.2012.08.057>
26. Sharma P, Sharma S, Khanduja D (2015) A study on microstructure of aluminium matrix composites. *J Asian Ceram Soc* 3(3):240–244. <https://doi.org/10.1016/j.jascer.2015.04.001>
27. Alaneme KK, Sanusi KO (2015) Microstructural characteristics, mechanical and wear behaviour of aluminium matrix hybrid composites reinforced with alumina, rice husk ash and graphite. *Eng Sci Technol Int J* 18(3):416–422. <https://doi.org/10.1016/j.jestech.2015.02.003>
28. Imran M, Khan AA, Megeri S, Sadik S (2016) Study of hardness and tensile strength of aluminium-7075 percentage varying reinforced with graphite and bagasse-ash composites. *Resour Efficient Technol* 2(2):81–88. <https://doi.org/10.1016/j.refffit.2016.06.007>
29. Quader SM, Murthy BS, Ravinder Reddy P (2016) Processing and mechanical properties of Al<sub>2</sub>O<sub>3</sub> and red mud particle reinforced AA6061 hybrid composites. *J Miner Mater Charact Eng* 04(02):135–142. <https://doi.org/10.4236/jmmce.2016.42013>
30. Singh K, Rana R, Pandey A (2017) Fabrication and mechanical properties characterization of aluminium alloy LM24/B 4 C composites. *Mater Today Proc* 4(2):701–708. <https://doi.org/10.1016/j.matpr.2017.01.075>
31. Magibalan S, Senthilkumar P, Palanivelu R, Senthilkumar C, Shivasankaran N, Prabu M (2018) Dry sliding behavior of aluminum alloy 8011 with 12% fly ash composites. *Mater Res Express* 5(5):056505. <https://doi.org/10.1088/2053-1591/aabf46>
32. Prasad DS, Ebenezer NS, Shoba C, Raju P, Rao PS (2018) The effect of T6 heat treatment on corrosion behavior of nickel electroplated metal matrix composites. *Silicon* 11(4):2025–2032. <https://doi.org/10.1007/s12633-018-0023-x>
33. Karthikeyan A, Jinu GR (2019) Investigation on mechanical and corrosion behaviour of AA8011 reinforced with tic and graphite hybrid composites. *Mater Res Express*. <https://doi.org/10.1088/2053-1591/ab3e87>
34. Karuppusamy T, Velmurugan C, Thirumalaimuthukumaran M (2019) Experimental study on the mechanical properties of heat treated aluminium composites. *Mater Res Express* 6(9):096552. <https://doi.org/10.1088/2053-1591/ab2ebb>
35. Soundararajan R, Ramesh A, Sivasankaran S, Vignesh M (2017) Modeling and analysis of mechanical properties of aluminium alloy (A413) reinforced with boron carbide (B 4 C) processed through squeeze casting process using artificial neural network model and statistical technique. *Mater Today Proc* 4(2):2008–2030. <https://doi.org/10.1016/j.matpr.2017.02.047>
36. Ghomashchi MR, Vikhrov A (2000) Squeeze casting: an overview. *J Mater Process Technol* 101(1–3):1–9
37. Baghi M, Niroumand B, Emadi R (2017) Fabrication and characterization of squeeze cast A413-CSF composites. *J Alloy Compd* 710:29–36. <https://doi.org/10.1016/j.jallcom.2017.03.136>
38. Yue H, Wang B, Gao X, Zhang S, Lin X, Yao L, Guo E (2017) Effect of interfacial modifying on the microstructures, mechanical properties and abrasive wear properties of aluminum borate whiskers reinforced 6061Al composite. *J Alloy Compd* 692:395–402. <https://doi.org/10.1016/j.jallcom.2016.09.082>

39. Kannan C, Ramanujam R (2017) Comparative study on the mechanical and microstructural characterisation of AA 7075 nano and hybrid nanocomposites produced by stir and squeeze casting. *J Adv Res* 8(4):309–319. <https://doi.org/10.1016/j.jare.2017.02.005>
40. Chen G, Yang M, Jin Y, Zhang H, Han F, Chen Q, Zhao Z (2019) Ultrasonic assisted squeeze casting of a wrought aluminum alloy. *J Mater Process Technol* 266:19–25. <https://doi.org/10.1016/j.jmatprotec.2018.10.032>
41. Zhang Q, Dong S, Ma S, Hou X, Yang W, Zhang Y, Wu G (2020) Microstructure and compressive behavior of lamellar Al<sub>2</sub>O<sub>3</sub>p/Al composite prepared by freeze-drying and mechanical-pressure infiltration method. *Sci Eng Compos Mater* 27(1):1–9. <https://doi.org/10.1515/secm-2020-0001>
42. Kim HH, Babu JS, Kang CG (2014) Hot extrusion of A356 aluminum metal matrix composite with carbon nanotube/Al<sub>2</sub>O<sub>3</sub> hybrid reinforcement. *Metall and Mater Trans A* 45(5):2636–2645. <https://doi.org/10.1007/s11661-014-2185-5>
43. Che Z, Wang Q, Wang L, Li J, Zhang H, Zhang Y, Wang X, Wang J, Kim MJ (2017) Interfacial structure evolution of ti-coated diamond particle reinforced al matrix composite produced by gas pressure infiltration. *Compos B Eng* 113:285–290. <https://doi.org/10.1016/j.compositesb.2017.01.047>
44. Zhang H, Wu J, Zhang Y, Li J, Wang X (2015) Effect of metal matrix alloying on mechanical strength of diamond particle-reinforced aluminum composites. *J Mater Eng Perform* 24(6):2556–2562. <https://doi.org/10.1007/s11665-015-1527-9>
45. Inegbenebor AO, Bolu CA, Babalola PO, Inegbenebor AI, Fayomi OS (2016) Aluminum silicon carbide particulate metal matrix composite development via stir casting processing. *Silicon* 10(2):343–347. <https://doi.org/10.1007/s12633-016-9451-7>
46. Sambath kumar M, Navaneethakrishnan P, Ponappa K, Sasikumar K (2017) Mechanical and corrosion behavior of Al7075 (Hybrid) metal matrix composites by two step stir casting process. *Latin Am J Solids Struct* 14(2):243–255. <https://doi.org/10.1590/1679-78253132>
47. Am R, Kaleemulla M, Doddamani S, Kn B (2019) Material characterization of sic and Al<sub>2</sub>O<sub>3</sub>–reinforced hybrid aluminum metal matrix composites on wear behavior. *Adv Comp Lett* 28:096369351985635. <https://doi.org/10.1177/0963693519856356>
48. Soltani S, Azari Khosroshahi R, Taherzadeh Mousavian R, Jiang Z, Fadavi Boostani A, Brabazon D (2015) Stir casting process for manufacture of al–sic composites. *Rare Met* 36(7):581–590. <https://doi.org/10.1007/s12598-015-0565-7>
49. Mohana kumara, K., Rajashekar, H., Ghanaraja, S., & Ajitprasad, S. (2014) Development and mechanical properties of sic reinforced cast and extruded al based metal matrix composite. *Procedia Mater Sci* 5:934–943. <https://doi.org/10.1016/j.mspro.2014.07.381>
50. Barekar N, Tzamtzis S, Dhindaw BK, Patel J, Hari Babu N, Fan Z (2009) Processing of aluminum-graphite particulate metal matrix composites by advanced shear technology. *J Mater Eng Perform* 18(9):1230–1240. <https://doi.org/10.1007/s11665-009-9362-5>
51. Hu Q, Zhao H, Li F (2017) Microstructures and properties of sic particles reinforced aluminum-matrix composites fabricated by vacuum-assisted high pressure die casting. *Mater Sci Eng A* 680:270–277. <https://doi.org/10.1016/j.msea.2016.10.090>
52. Mansoor M, Shahid M (2016) Carbon nanotube-reinforced aluminum composite produced by induction melting. *J Appl Res Technol* 14(4):215–224. <https://doi.org/10.1016/j.jart.2016.05.002>
53. Prasad DS, Shoba C, Ramanaiah N (2014) Investigations on mechanical properties of aluminum hybrid composites. *J Market Res* 3(1):79–85. <https://doi.org/10.1016/j.jmrt.2013.11.002>
54. Pawar P, Utpat AA (2014) Development of aluminium based silicon carbide particulate metal matrix composite for spur gear. *Procedia Mater Sci* 6:1150–1156. <https://doi.org/10.1016/j.mspro.2014.07.187>
55. Dhanasekaran S, Sunilraj S, Ramya G, Ravishankar S (2015) SiC and Al<sub>2</sub>O<sub>3</sub> reinforced aluminum metal matrix composites for heavy vehicle clutch applications. *Trans Indian Inst Met* 69(3):699–703. <https://doi.org/10.1007/s12666-015-0542-8>
56. Kumar D, Singh PK (2019) Microstructural and mechanical characterization of al-4032 based metal matrix composites. *Mater Today Proc* 18:2563–2572. <https://doi.org/10.1016/j.matpr.2019.07.114>

57. Pitchayyapillai G, Seenikannan P, Raja K, Chandrasekaran K (2016) Al6061 hybrid metal matrix composite reinforced with alumina and molybdenum disulphide. *Adv Mater Sci Eng* 2016:1–9. <https://doi.org/10.1155/2016/6127624>
58. Shao C, Zhao S, Wang X, Zhu Y, Zhang Z, Ritchie RO (2019) Architecture of high-strength aluminum–matrix composites processed by a novel micro casting technique. *NPG Asia Mater* 11(1). <https://doi.org/10.1038/s41427-019-0174-2>

# Prediction of Effective Elastic Properties of PEEK-CF Composites Subjected to Thermomechanical Loading



Brahma Nand Agrawal, Pawan Kumar Singh Nain, Saksham Bisht, and Aniket Srivastava

**Abstract** The micromechanics approach to studying the effect of filler's mass fraction on the effective elastic properties of the composites is investigated. Poly(ether ether ketone) (PEEK) as matrix and carbon fiber as fillers are used due to excellent nucleation density compared to pure PEEK. The scheme used depends on the single inclusion problem which effectively predicted the mechanical properties considering the orientation, aspect ratio, and mass fraction of the fillers. The main outcome of the study is the moduli variation for 10, 20, and 30% mass fraction reinforced PEEK composites subjected to mechanical and thermal loading simultaneously. It has been observed that above 63 °C, the composite's elastic properties decrease by 30% mass fraction of CF in PEEK. The maximum failure strength of the composite is 105.32 MPa obtained for a 30% mass fraction of CF in PEEK. In general, the moduli and strength of the composites decrease with the increase in temperature due to the structural change in the polymer.

**Keywords** PEEK · Carbon fiber · Thermomechanical · Elastic · Mass fraction

## 1 Introduction

The quantitative determination of elastic properties of composites using micromechanical approaches has become necessary due to the heterogeneous nature of the composites. PEEK reinforced with CF has been gaining popularity due to the excellent time-dependent creep properties of the composites [1]. These constituents have shown good bonding when fused with any manufacturing processes. Also, the mechanical properties obtained experimentally are remarkable. But, studying these composites for the effective determination of the elastic properties when subjected to coupled loading conditions is an ongoing topic.

Mori–Tanaka was applied by various researchers to study the mechanical properties of the composites [2–17]. The scheme was successfully applied to unidirectional

---

B. N. Agrawal (✉) · P. K. S. Nain · S. Bisht · A. Srivastava  
Department of Mechanical Engineering, Galgotias University, Greater Noida, India  
e-mail: [brahma.agrawal@galgotiasuniversity.edu.in](mailto:brahma.agrawal@galgotiasuniversity.edu.in)

© The Author(s), under exclusive license to Springer Nature Singapore Pte Ltd. 2024  
R. K. Tyagi et al. (eds.), *Advances in Engineering Materials*, Lecture Notes in  
Mechanical Engineering, [https://doi.org/10.1007/978-981-99-4758-4\\_19](https://doi.org/10.1007/978-981-99-4758-4_19)

203

**Table 1** Properties of CF [1]

Properties	Values
Young's modulus (axial) (GPa)	23.4
Young's modulus (inplane) (GPa)	15
Poisson's ratio (inplane)	0.2
Poisson's ratio (transverse)	0.49
Shear modulus (transverse) (GPa)	7
Thermal expansion coefficient (axial)	$-3.8 \times 10^{-7}$
Thermal expansion coefficient (inplane)	$1.2 \times 10^{-6}$

composites, but it has been observed that it also shows reliable results for randomly distributed composites. The coupled loading conditions were also studied by many researchers for high aspect ratio composites [18–20]. The scheme has gained popularity as amendments can be made easily as per the loading conditions. The scheme has been applied successfully to thermoplastic and thermosetting polymers with different fillers.

PEEK-CF composites were studied to estimate the elastic properties using Mori-Tanaka [10]. PEEK has been used with mainly two fillers, i.e., carbon-nanotubes (CNTs) and carbon fibers (short or spherical). A vast literature on the PEEK-CNTs is available, but limited study on the thermomechanical loading condition of PEEK-CF is available [1, 10, 21, 22]. Therefore, the present study is focused on the application of the scheme to PEEK-CF composites to study the effective elastic properties subjected to coupled loading conditions. The loading condition used in the present study is mechanical loading in a thermal environment. The conditions used in this article can easily be created in an experimental setup for determining the moduli.

## 2 Materials

The materials used for evaluating the mechanical properties are carbon fiber (CF) as fillers and poly(ether ether ketone) (PEEK) as matrix have been used. The fillers CF have transversely isotropic elasticity and thermoelastic constitutive law as represented in Table 1. CFs have aspect ratio as 1. The matrix, i.e., PEEK, has been used as thermoelastic with J2 plasticity and isotropic hardening law as represented in Table 2.

## 3 Mori–Tanaka Scheme

For a heterogeneous and anisotropic material, the generalized Hooke's law is defined as:

**Table 2** Properties of PEEK [1]

Properties	Values
Young's modulus (GPa)	3.4
Poisson's ratio	0.37
Thermal expansion coefficient	$4.7 \times 10^{-5}$
Yield stress (MPa)	40
Hardening modulus (MPa)	50
Hardening exponent	240
Linear hardening modulus (MPa)	20

$$\sigma_{ij} = C_{ijkl}\varepsilon_{ij} \tag{1}$$

The effective properties after applying the boundary conditions can be obtained from Eqs. (2) and (3) as follows [12]:

$$C_{abcd}^{\text{eff}} = \frac{1}{V} \int_V c_{abij}(r) A_{ijcd}(r) dV \tag{2}$$

$$C^{\text{eff}} = c^0 + \sum_{X=1}^N V_X (c^X - c^0) : \mathbf{A}^X \tag{3}$$

Here, 0 and X are used for matrix and filler, C is the stiffness matrix, the strain concentration tensor (A) and the volume (V) subjected to far-field stress or strain.

The average strain field is approximated by calculating the strain in the matrix. Thus, following this assumption, the stiffness matrix evaluated by Mori–Tanaka is given as [12]:

$$C^{\text{Mori-Tanaka}} = \sum_{X=0}^N V_X C^X \mathbf{A}^X = \left( V_0 c^0 + \sum_{X=1}^N V_X C^X \mathbf{a}^X \right) : \mathbf{A}^0 \tag{4}$$

where the global strain tensor  $A^0$ .

It is represented as follows [12]:

$$\mathbf{A}^0 = \mathbf{a}^0 : \langle \mathbf{a}^X \rangle^{-1} = \left( V_0 X + \sum_{X=1}^N V_X \mathbf{a}^X \right)^{-1} \tag{5}$$

## 4 Results and Discussion

The composites are evaluated to conclude the effective or overall elastic properties using a homogenization scheme, i.e., Mori–Tanaka. In this scheme, the properties used for the constituents are already mentioned in Tables 1 and 2. The homogenized properties for 10%, 20%, and 30% CF reinforced PEEK composites at different temperatures are presented in Tables 3, 4, and 5, respectively.

**Table 3** Elastic properties of 10% CF reinforced polymer composites at different temperatures

Temperature (°C)	Young's modulus (axial) (GPa)	Young's modulus (inplane) (GPa)	Poisson's ratio (inplane)	Poisson's ratio (transverse)	Shear modulus (inplane) (GPa)	Shear modulus (transverse) (GPa)
23	3.95	3.76	0.3657	0.3675	1.37	1.39
43	3.26	3.13	0.3654	0.3668	1.14	1.15
63	2.57	2.48	0.3649	0.3661	0.91	0.914
83	1.92	1.87	0.3645	0.3654	0.68	0.69
103	1.59	1.55	0.3643	0.365	0.57	0.57

**Table 4** Elastic properties of 20% CF reinforced polymer composites at different temperatures

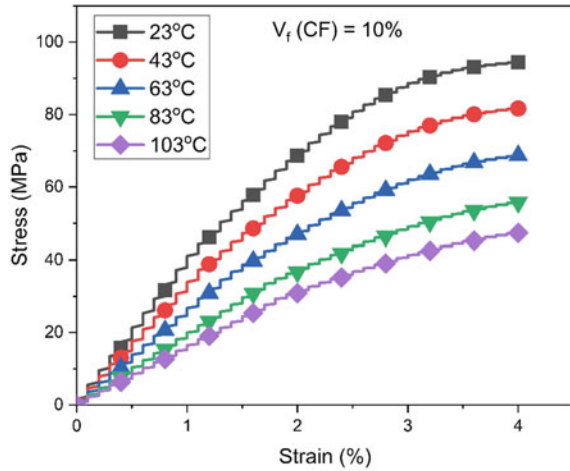
Temperature (°C)	Young's modulus (axial) (GPa)	Young's modulus (inplane) (GPa)	Poisson's ratio (inplane)	Poisson's ratio (transverse)	Shear modulus (inplane) (GPa)	Shear modulus (transverse) (GPa)
23	4.64	4.19	0.36	0.3649	1.54	1.56
43	3.84	3.51	0.3595	0.3636	1.29	1.31
63	3.03	2.82	0.3588	0.3622	1.03	1.04
83	2.27	2.14	0.3582	0.3608	0.789	0.794
103	1.87	1.78	0.3579	0.36	0.657	0.66

**Table 5** Elastic properties of 30% CF reinforced polymer composites at different temperatures

Temperature (°C)	Young's modulus (axial) (GPa)	Young's modulus (inplane) (GPa)	Poisson's ratio (inplane)	Poisson's ratio (transverse)	Shear modulus (inplane) (GPa)	Shear modulus (transverse) (GPa)
23	5.52	4.69	0.3527	0.3625	1.73	1.76
43	4.57	3.97	0.3521	0.3605	1.47	1.49
63	3.61	3.22	0.3516	0.3583	1.19	1.2
83	2.7	2.47	0.351	0.3563	0.91	0.92
103	2.23	2.07	0.3507	0.3551	0.77	0.77



**Fig. 1** Stress–strain curve of 10% CF reinforced polymer composites at different temperatures



It is evident from Table 1 that the elastic properties are decreasing with the increase in temperature of the simulation. The composites have shown maximum axial and in-plane Young’s modulus at 23 °C; thereafter, it is below the modulus of the polymer as presented in Table 3. This indicates that the polymer starts degrading after that. Although the mass percentage reinforcement of CF is also 10% in this case which may be the reason for low moduli after 23 °C. From Fig. 1, it is indicated that the ultimate stress and yield stress are also decreasing with a temperature rise. The nonlinear nature can be observed from the curves shown in Fig. 1.

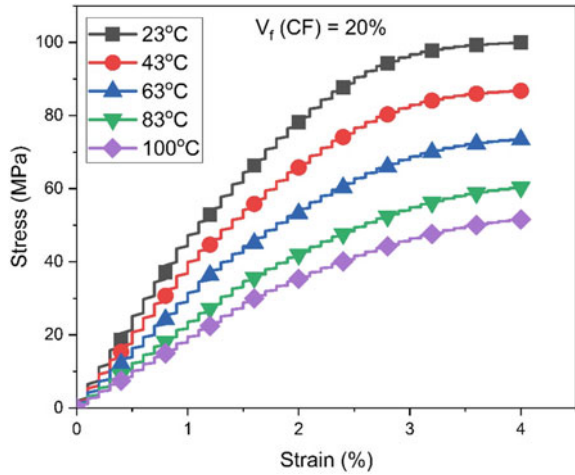
Table 4 represents the effective elastic properties of PEEK-CF composites with 20% CF reinforcement. The composites have shown good moduli up to 43 °C, and thereafter, the degradation in the structure of the polymer could be the probable reason for low elastic properties. The stress–strain curves as shown in Fig. 2 also represent the nonlinear nature of the composites. The curve starts decreasing the plasticity as the temperature is increasing which shows the debonding or low load transfer of CF to PEEK.

Table 5 represents the elastic properties of 30% CF reinforced PEEK composites. These composites have shown effective elastic properties up to 63 °C, and degradation in the elastic properties has been observed after that. Also, the nonlinear nature of the curves can be seen in Fig. 3. These composites have shown maximum stress at all temperatures compared to 10% and 20% CF reinforced composites.

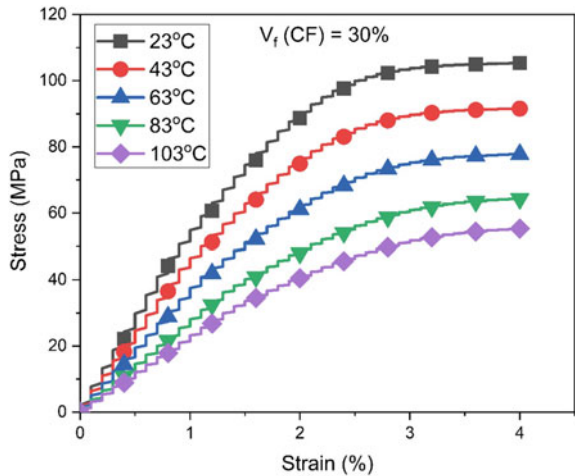
## 5 Conclusions

1. Mori–Tanaka has been successfully applied to determine the overall or effective properties of PEEK-CF composites.
2. The scheme predicted the maximum results for a 30% mass fraction of CF.

**Fig. 2** Stress–strain curve of 20% CF reinforced polymer composites at different temperatures



**Fig. 3** Stress–strain curve of 30% CF reinforced polymer composites at different temperatures



3. The temperature dependence of elastic and other mechanical properties has been observed.
4. Young's modulus for 10%, 20%, and 30% decreases significantly, whereas other elastic properties have not shown much variation.
5. The composites lose strength due to a decrease in strength of the polymer at elevated temperatures and debonding of CF.

## References

1. Chen CH, Chang yi H, Cheng ho C (2016) Micromechanics and creep behavior of fiber-reinforced polyether-ether-ketone composites, vol 29, pp 359–371. <https://doi.org/10.1177/002199839502900304>
2. Lielens G, Pirotte P, Coumiot A, Dupret F, Keunings R (1998) Prediction of thermo-mechanical properties for compression moulded composites. *Compos Part A Appl Sci Manuf* 29:63–70
3. Noor AK, Shah RS (1993) Effective thermoelastic and thermal properties of unidirectional fiber-reinforced composites and their sensitivity coefficients. *Compos Struct* 26:7–23
4. Kammoun S, Doghri I, Brassart L, Delannay L (2015) Micromechanical modeling of the progressive failure in short glass-fiber reinforced thermoplastics—first pseudo-grain damage model. *Compos Part A Appl Sci Manuf* 73:166–175
5. Kundalwal SI (2017) Review on modeling of mechanical and thermal properties of nano- and micro-composites
6. Doghri I, Brassart L, Adam L, Gérard JS (2011) A second-moment incremental formulation for the mean-field homogenization of elasto-plastic composites. *Int J Plast* 27:352–371
7. Dong C (2014) Mechanical and thermo-mechanical properties of carbon nanotube reinforced composites. *Int J Smart Nano Mater* 5:44–58
8. Padmanabhan S, Gupta A, Arora G, Pathak H, Burela RG, Bhatnagar AS (2020) Meso–macro-scale computational analysis of boron nitride nanotube-reinforced aluminium and epoxy nanocomposites: a case study on crack propagation. *Proc Inst Mech Eng Part L J Mater Des Appl* 1–16
9. Bhatnagar AS, Gupta A, Arora G, Padmanabhan S, Burela RG (2021) Mean-field homogenization coupled low-velocity impact analysis of nano fibre reinforced composites. *Mater Today Commun* 102089
10. Katouzian M, Vlase S (2020) Mori–Tanaka formalism-based method used to estimate the viscoelastic parameters of laminated composites. *Polym* 12:2481
11. Weng GJ (1990) The theoretical connection between Mori-Tanaka’s theory and the Hashin-Shtrikman-Walpole bounds. *Int J Eng Sci* 28:1111–1120
12. Mori T, Tanaka K (1973) Average stress in matrix and average elastic energy of materials with misfitting inclusions. *Acta Metall* 21:571–574
13. Benveniste Y (1987) A new approach to the application of Mori-Tanaka’s theory in composite materials. *Mech Mater* 6:147–157
14. Peng RD, Zhou HW, Wang HW, Mishnaevsky L (2012) Modeling of nano-reinforced polymer composites: microstructure effect on Young’s modulus. *Comput Mater Sci* 60:19–31
15. Hua Y, Gu L (2013) Prediction of the thermomechanical behavior of particle-reinforced metal matrix composites. *Compos Part B Eng* 45:1464–1470
16. Arora G, Pathak H (2019) Modeling of transversely isotropic properties of CNT-polymer composites using meso-scale FEM approach. *Compos Part B Eng* 166:588–597
17. Arora G, Pathak H (2019) Numerical study on the thermal behavior of polymer nano-composites. *J Phys Conf Ser* 1240
18. Mura T (1991) *Metal matrix composites: thermomechanical behavior*
19. Zhai J, Cheng S, Zeng T, Wang Z, Jiang L (2017) Thermo-mechanical behavior analysis of 3D braided composites by multiscale finite element method. *Compos Struct* 176:664–672
20. Ansari R, Hassanzadeh Aghdam MK (2016) Micromechanics-based viscoelastic analysis of carbon nanotube-reinforced composites subjected to uniaxial and biaxial loading. *Compos Part B Eng* 90:512–522
21. Katouzian M, Vlase S (2021) Creep response of carbon-fiber-reinforced composite using homogenization method. *Polym* 13:867
22. Maniak I, Melnikov B, Semenov AS, Saikin S (2015) Experimental investigation and finite element simulation of fracture process of polymer composite material with short carbon fibers. *Appl Mech Mater* 725–726:943–948

# Mori–Tanaka Modeling of Polymer Nanocomposites: Interface Effect on the Moduli



Brahma Nand Agrawal, Pawan Kumar Singh Nain, Abhishek Patwal, and Akash Abrol

**Abstract** Polymer nanocomposites have gained popularity due to ease in manufacturing and enhanced elastic properties and strength compared to polymers. The main focus of the study is on the determination of elastic properties of polymer nanocomposites reinforced with 1, 2, 5, and 10% volume fractions of nanoparticles. The scheme used for the study is Mori–Tanaka. It is established on Eshelby’s sole filler problem and effectively determines the elastic properties of the nanocomposites. The cases studied in this paper are no, soft, medium-stiff, and stiff interface of 0.6 nm thickness for the determination of Young’s modulus, Poisson’s ratio, and Shear modulus of the nanocomposites. It has been observed that a 27% increment in the moduli with a stiff interface has been achieved compared to no interface case. The medium-stiff interface has a positive effect on the elastic properties. A 10% and 3% increase in E and G, respectively, have been observed compared to no interface case. A remarkable increment of 27% for both E and G has been observed for the stiff interface case compared to the no interface case.

**Keywords** Mori–Tanaka · Polymer · Nanocomposites · Young’s modulus · Eshelby

## 1 Introduction

Polymer nanocomposites have been studied extensively to mend their mechanical properties [8, 11, 12, 14, 18, 20, 22, 27, 28]. Researchers are not only interested in manufacturing these nanocomposites but have shown interest in studying the effect of volume fraction ( $V_f$ ), shape, size, orientation, and curviness (having high aspect ratio fillers) on the mechanical, thermal, and electrical properties [9, 13, 15, 21, 29, 30]. The bonding between the constituents also shows an essential part in improving the nanocomposite’s overall properties. Therefore, researchers have applied analytical, numerical, or computational techniques to determine the nature of the composites

---

B. N. Agrawal (✉) · P. K. S. Nain · A. Patwal · A. Abrol  
Department of Mechanical Engineering, Galgotias University, Greater Noida, India  
e-mail: [brahma.agrawal@galgotiasuniversity.edu.in](mailto:brahma.agrawal@galgotiasuniversity.edu.in)

© The Author(s), under exclusive license to Springer Nature Singapore Pte Ltd. 2024  
R. K. Tyagi et al. (eds.), *Advances in Engineering Materials*, Lecture Notes in  
Mechanical Engineering, [https://doi.org/10.1007/978-981-99-4758-4\\_20](https://doi.org/10.1007/978-981-99-4758-4_20)

211

at different scales. As nanocomposites consist of nanoscale filler and macroscale matrix, therefore analyzing the nanocomposites at a small scale has become the primary objective of the researchers.

The literature on studying these composites at a small scale consists of many techniques like Mori–Tanaka, finite element method, molecular dynamics, etc. [7, 10, 17, 19, 23, 24, 26]. Each has its advantages and disadvantages. Mori–Tanaka is constructed on the mean-field homogenization principle. It provides the effective material properties for a nanocomposite by applying Eshelby’s single inclusion solution. Thus, it converges quickly compared to other techniques. But, the disadvantage of the scheme is that it only provides reliable results up to 25%  $V_f$  for short aspect ratio fillers whereas it can be used for higher  $V_f$  for higher aspect ratio fillers.

The micromechanical techniques are also useful in determining the effective properties of the nanocomposites [1–7, 24]. But, some techniques do not take into account the effect of reinforcing effects of the nano-fillers. However, numerical techniques like the finite element method are quite effective in considering the bonding effect, clustering, and coating influence on the nanocomposite’s overall mechanical properties. The finite element method has been used by many researchers to study the waviness of high aspect ratio fillers, stiffness of clay flakes, interface effect, aspect ratio effect, distribution, and orientation effect of the nano-fillers on the mechanical properties.

In the most available literature, it has been observed that the interface effect is the critical one to accomplish the desired mechanical properties. Therefore, in this article, the effectiveness of Mori–Tanaka for different interface conditions has been studied. The method, i.e., Mori–Tanaka, is effective at up to 25%  $V_f$  for short aspect ratio fillers, therefore in this study, the maximum  $V_f$  of the nanoparticles is 10%. Also, the absolute thickness of the interface is 0.6 nm (constant) for each interface condition. The matrix used for the study is having Young’s modulus of 4.2 GPa and Poisson’s ratio of 0.4 [25]. The nanoparticles have Young’s modulus of 88.7 GPa and Poisson’s ratio of 0.3 [25]. The perfect bonding between the constituents has been assumed.

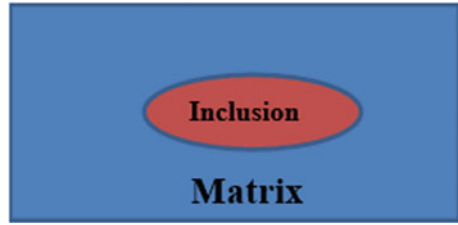
## 2 Mori–Tanaka Modeling

Mori–Tanaka modeling works on the principle of a problem solved by Eshelby. He has considered an ellipsoidal volume subjected to uniform strain and then calculated uniform stresses, further to determine the elastic properties.

Eshelby considered an infinite body shown in Fig. 1. The infinite body is the matrix in this case with a uniform stiffness  $S_m$ . An ellipsoidal volume in the model is the filler/inclusion which is subjected to Eigen strain  $\varepsilon_e$ . Therefore, Eshelby isolates the inclusion and applies the Eigen strain and then plugin back at the same location in the matrix and determines the strain in the inclusion as follows [16]:

$$\varepsilon(x) = \zeta(O_r, S_m) : \varepsilon_e, \quad \forall x \in (O_r),$$

**Fig. 1** Eshelby’s model to study two-phase composites



where  $\zeta(O_r, S_m)$  is Eshelby's tensor. (1)

Mori–Tanaka 1973 applied the solution mentioned in Eq. (1) to two-phase composites. Mori and Tanaka initiate that the strain concentration tensor can be determined by taking the volumetric average of strain considering all fillers in the matrix to the average strain in the matrix only. It is represented as follows [16]:

$$B^\varepsilon = H^\varepsilon(O_r, S_m, S_i) \quad (2)$$

where  $B^\varepsilon$  is the strain concentration tensor linking the strains in the matrix and inclusion, and  $H^\varepsilon$  is the strain concentration tensor for a single inclusion case (Fig. 2).

### 3 Results and Discussion

Four cases have been discussed to obtain the properties (elastic) of polymer nanocomposites.

#### 3.1 No Interface is Present Between the Constituents

The elastic properties of the nanocomposites were determined for no interface case as shown in Table 1. The elastic properties like Young's modulus ( $E$ ), Poisson's ratio ( $\nu$ ), and shear modulus ( $G$ ) were evaluated for diverse volume fractions ( $V_f$ ) of nanoparticles present in the polymeric matrix. It is evident from the values that  $E$  and  $G$  increase with an increase in  $V_f$  and thus showing strong dependence of nanoparticles on the elastic properties. However, the decrease in Poisson's ratio reflects the small change in strain.  $E$  and  $G$  have increased to 19% and 20%, respectively, with 10%  $V_f$  of the nanocomposites. An insignificant change has been observed in Poisson's ratio, i.e., 0.5%.

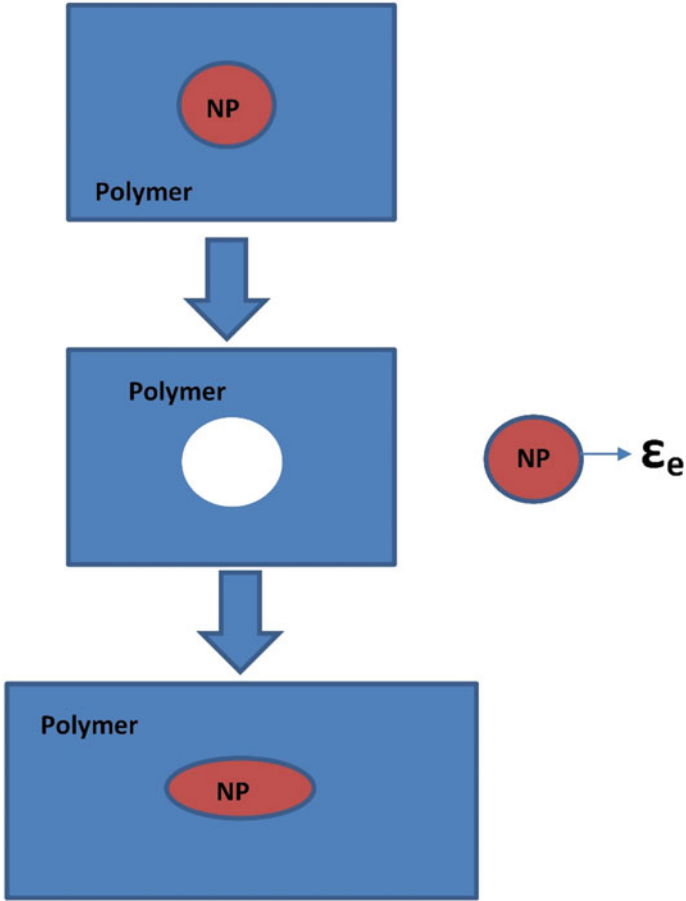


**Fig. 2** Application of Mori–Tanaka to two-phase composite (NP is nanoparticle)

**Table 1** Moduli of polymer nanocomposites (aspect ratio = 1, radius = 1 nm) with no interface

$V_f$ of nanoparticles (%)	$E$ (GPa)	$\nu$	$G$ (GPa)
1	4.28	0.4000	1.53
2	4.37	0.3996	1.56
5	4.64	0.3987	1.66
10	5.11	0.3979	1.84

### 3.2 A Soft Interface is Present Between the Constituents

The effect of a 0.6 nm thick soft interface having 3.5 GPa modulus and 0.4 Poisson’s ratio on the properties (elastic) of nanocomposites is evaluated. The evaluated elastic

**Table 2** Moduli of polymer nanocomposites (aspect ratio = 1, radius = 1 nm) with a soft interface (0.6 nm absolute thickness)

$V_f$ of nanoparticles (%)	$E$ (GPa)	$\nu$	$G$ (GPa)
1	4.25	0.3992	1.52
2	4.31	0.3984	1.54
5	4.47	0.3959	1.60
10	4.76	0.3918	1.71

**Table 3** Moduli of polymer nanocomposites (aspect ratio = 1, size = 1 nm) with medium interface (0.6 nm absolute thickness)

$V_f$ of nanoparticles (%)	$E$ (GPa)	$\nu$	$a$ (GPa)
1	4.30	0.3991	1.56
2	4.40	0.3983	1.60
5	4.73	0.3956	1.71
10	5.58	0.3914	1.92

properties are represented in Table 2. A 12% increase in the elastic properties, i.e.,  $E$  and  $G$  at 10%  $V_f$  of the nanoparticles is observed. However, a remarkable change in the Poisson's ratio, i.e., 1.85% has been observed for 10%  $V_f$  of the nanoparticles.

### 3.3 A Medium Interface is Present Between the Constituents

In this case, a medium-stiff interface of 4.2 GPa modulus, 0.4 Poisson's ratio, and 0.6 nm thickness is present between the constituents to find out the nanocomposite's elastic properties. The evaluated  $E$  and  $G$  have shown 29% and 23% increments at 10%  $V_f$  of the nanoparticles. This means that the effectiveness of the medium-stiff interface on the properties is high. On the other hand, the Poisson's ratio has decreased to 1.9% for 10%  $V_f$  of the nanoparticles, thus highlighting the effect of strain on the nanocomposites (Table 3).

### 3.4 A Stiff Interface is Present Between the Constituents

The stiff interface of 8.4 GPa modulus, 0.4 Poisson's ratio, and 0.6 nm thickness effect on the nanocomposite's elastic properties is given in Table 4. The elastic and shear modulus of the nanocomposites has increased to 47%, and the Poisson's ratio has decreased to nearly 2.8%. These results show the nanocomposite's enhanced elastic properties.



**Table 4** Moduli of polymer nanocomposites (aspect ratio = 1, radius = 1 nm) with stiff interface (0.6 nm absolute thickness)

$V_f$ of nanoparticles (%)	$E$ (GPa)	$\nu$	$G$ (GPa)
1	4.39	0.3985	1.59
2	4.58	0.3971	1.64
5	5.22	0.3930	1.87
10	6.49	0.3872	2.34

## 4 Conclusions

- The conclusion from the study is that for a two-phase nanocomposite, the Mori–Tanaka scheme can be applied successfully for determining the elastic properties of up to 10% volume fraction of the nanoparticles.
- The study also concludes the effect of no, the soft, medium-stiff, and stiff interface on the elastic properties.
- The soft interface has a negative effect on the elastic properties compared to the no interface case. A decrement of 10% has been observed in the moduli for soft interface compared to no interface.
- The medium-stiff interface has a positive effect on the elastic properties. A 10% and 3% increase in  $E$  and  $G$ , respectively, have been observed compared to no interface case.
- A remarkable increment of 27% for both  $E$  and  $G$  has been observed for the stiff interface case compared to the no interface case.
- All cases were studied for the same interface thickness of 0.6 nm. The study can be extended for different interface thicknesses and orientations of the nanoparticles.

## References

1. Arora G, Pathak H (2019) Multi-scale fracture analysis of fibre-reinforced composites. *Mater Today Proc* 18:687–695. <https://doi.org/10.1016/j.matpr.2019.06.469>
2. Arora G, Pathak H (2019b) Numerical study on the thermal behavior of polymer nanocomposites. *J Phys Conf Series* 1240(1). <https://doi.org/10.1088/1742-6596/1240/1/012050>
3. Arora G, Pathak H (2019) Modeling of transversely isotropic properties of CNT-polymer composites using meso-scale FEM approach. *Compos B Eng* 166:588–597. <https://doi.org/10.1016/J.COMPOSITESB.2019.02.061>
4. Arora G, Pathak H (2020) Experimental and numerical approach to study mechanical and fracture properties of high-density polyethylene carbon nanotubes composite. *Mater Today Commun* 22:100829. <https://doi.org/10.1016/j.mtcomm.2019.100829>
5. Arora G, Pathak H (2021) Nanoindentation characterization of polymer nanocomposites for elastic and viscoelastic properties: experimental and mathematical approach. *Compos Part C Open Access* 4:100103. <https://doi.org/10.1016/j.jcomc.2020.100103>

6. Arora G, Pathak H, Zafar S (2019) Fabrication and characterization of microwave cured high-density polyethylene/carbon nanotube and polypropylene/carbon nanotube composites. *J Compos Mater* 53(15):2091–2104. <https://doi.org/10.1177/0021998318822705>
7. Bhatnagar AS, Gupta A, Arora G, Padmanabhan S, Burela RG (2021) Mean-field homogenization coupled low-velocity impact analysis of nano fibre reinforced composites. *Mater Today Commun* 102089. <https://doi.org/10.1016/j.mtcomm.2021.102089>
8. Cao HL, Wang P, Li Y (2010) Preparation of poly(lactic acid)/na-montmorillonite nanocomposite by microwave-assisted in-situ melt polycondensation. *Macromol Res* 18(11):1129–1132. <https://doi.org/10.1007/s13233-010-1113-9>
9. Chen J, Han J, Xu D (2019) Thermal expansion properties of the polycaprolactam nanocomposites reinforced with single-walled carbon nanotubes. *Results Phys* 12:1645–1652. <https://doi.org/10.1016/j.rinp.2019.01.067>
10. Doghri I, Brassart L, Adam L, Gérard JS (2011) A second-moment incremental formulation for the mean-field homogenization of elasto-plastic composites. *Int J Plast* 27(3):352–371. <https://doi.org/10.1016/j.ijplas.2010.06.004>
11. Fischer H (2003) Polymer nanocomposites: from fundamental research to specific applications. *Mater Sci Eng. C* 23(6–8):763–772. <https://doi.org/10.1016/j.msec.2003.09.148>
12. Gogna E, Kumar R, Anurag, Sahoo AK, Panda A (2019) A comprehensive review on jute fiber reinforced composites. Lecture notes in mechanical engineering, pp 459–467. [https://doi.org/10.1007/978-981-13-6412-9\\_45/COVER/](https://doi.org/10.1007/978-981-13-6412-9_45/COVER/)
13. Gupta AK, Harsha SP (2016) Analysis of mechanical properties of carbon nanotube reinforced polymer composites using multi-scale finite element modeling approach. *Compos B Eng* 95:172–178. <https://doi.org/10.1016/J.COMPOSITESB.2016.04.005>
14. Hu K, Kulkarni DD, Choi I, Tsukruk VV (2014) Graphene-polymer nanocomposites for structural and functional applications. *Prog Polym Sci* 39(11):1934–1972. <https://doi.org/10.1016/j.progpolymsci.2014.03.001>
15. Huang C, Qian X, Yang R (2018) Thermal conductivity of polymers and polymer nanocomposites. In arXiv
16. Kammoun S, Doghri I, Brassart L, Delannay L (2015) Micromechanical modeling of the progressive failure in short glass-fiber reinforced thermoplastics—first pseudo-grain damage model. *Compos A Appl Sci Manuf* 73:166–175. <https://doi.org/10.1016/j.compositesa.2015.02.017>
17. Kanouté P, Boso DP, Chaboche JL, Schrefler BA (2009) Multiscale methods for composites: a review. *Arch Comput Methods Eng* 16(1):31–75. <https://doi.org/10.1007/s11831-008-9028-8>
18. Khandai S, Nayak RK, Kumar A, Das D, Kumar R (2019) Assessment of mechanical and tribological properties of flax/Kenaf/glass/carbon fiber reinforced polymer composites. *Mater Today Proc* 18:3835–3841. <https://doi.org/10.1016/J.MATPR.2019.07.322>
19. Kurska M, Kowalczyk-Gajewska K, Lewandowski MJ, Petryk H (2018) Elastic-plastic properties of metal matrix composites: validation of mean-field approaches. *Eur J Mech A/Solids* 68:53–66. <https://doi.org/10.1016/j.euromechsol.2017.11.001>
20. Lau K, Gu C (2006) A critical review on nanotube and nanotube/nanoclay related polymer composite materials. *Compos B Eng* 37(6):425–436. <https://doi.org/10.1016/J.COMPOSITESB.2006.02.020>
21. Luo JJ, Daniel IM (2003) Characterization and modeling of mechanical behavior of polymer/clay nanocomposites. *Compos Sci Technol* 63(11):1607–1616. [https://doi.org/10.1016/S0266-3538\(03\)00060-5](https://doi.org/10.1016/S0266-3538(03)00060-5)
22. Mishra RR, Panda A, Sahoo AK, Kumar R (2022) Research progress on nano-metal matrix composite (NMMC) fabrication method: a comprehensive review. *Mater Today Proc* 56:2104–2109. <https://doi.org/10.1016/J.MATPR.2021.11.437>
23. Mozafari H, Dong P, Ren K, Han X, Gu L (2019) Micromechanical analysis of bioresorbable PLLA/Mg composites coated with MgO: effects of particle weight fraction, particle/matrix interface bonding strength and interphase. *Compos Part B Eng* 162(October 2018):129–133. <https://doi.org/10.1016/j.compositesb.2018.10.106>

24. Padmanabhan S, Gupta A, Arora G, Pathak H, Burela RG, Bhatnagar AS (2020) Meso-macro-scale computational analysis of boron nitride nanotube-reinforced aluminium and epoxy nanocomposites: a case study on crack propagation. *Proc Inst Mech Eng Part L J Mater Design Appl* 0(0):1–16. <https://doi.org/10.1177/1464420720961426>
25. Peng RD, Zhou HW, Wang HW, Mishnaevsky L (2012) Modeling of nano-reinforced polymer composites: microstructure effect on Young's modulus. *Comput Mater Sci* 60:19–31. <https://doi.org/10.1016/j.commatsci.2012.03.010>
26. Shajari AR, Ghajar R, Shokrieh MM (2018) Multiscale modeling of the viscoelastic properties of CNT/polymer nanocomposites, using complex and time-dependent homogenizations. *Comput Mater Sci* 142:395–409. <https://doi.org/10.1016/J.COMMATSCI.2017.10.006>
27. Shi X, Sitharaman B, Pham QP, Liang F, Wu K, Edward Billups W, Wilson LJ, Mikos AG (2007) Fabrication of porous ultra-short single-walled carbon nanotube nanocomposite scaffolds for bone tissue engineering. *Biomaterials* 28(28):4078–4090. <https://doi.org/10.1016/j.biomaterials.2007.05.033>
28. Singh K, Das D, Nayak RK, Khandai S, Kumar R, Routara BC (2020) Effect of silanization on mechanical and tribological properties of kenaf-carbon and kenaf-glass hybrid polymer composites. *Mater Today Proc* 26:2094–2098. <https://doi.org/10.1016/J.MATPR.2020.02.452>
29. Zhang X, Tan W, Smail F, De Volder M, Fleck N, Boies A (2018) High-fidelity characterization on anisotropic thermal conductivity of carbon nanotube sheets and on their effects of thermal enhancement of nanocomposites. *Nanotechnology* 29(36). <https://doi.org/10.1088/1361-6528/aacd7b>
30. Zhu J, Zare Y, Rhee KY (2017) Analysis of the roles of interphase, waviness and agglomeration of CNT in the electrical conductivity and tensile modulus of polymer/CNT nanocomposites by theoretical approaches. *Colloids Surf, A*. <https://doi.org/10.1016/j.colsurfa.2017.12.001>

# Static Engine Test on CTN Model Rocket Engine with 1/2 A6-2 Propellant



Sarath Raj, Nour Alaa Elsonbaty, and Sathiyagayathiri Ramamoorthy

**Abstract** Solid propellant rocket engines are characterized as the basic model for rocket propellants. They are highly utilized in the industry due to their simplicity and high combustible range. Even though solid rocket engines are widely used, the concept still appears to be lacking for some engineers, hence developing a working prototype of a unique design is proposed. This will help study the advantages and prove the concept of solid rocket engines through visual tests. This paper focuses on the construction of a mini-solid fuel rocket engine, stand test, and the conduction of static test to evaluate the prototype performance and thrust production.

**Keywords** Rocket engine · Static test · Solid propellant · ANSYS · Rocket propulsion · Engine design

## 1 Introduction

The solid propellant rocket engine is an engine that uses solid fuel as its propellant. They contain both the fluid and oxidizer together in the chemical itself. The solid propellant rocket technology got a boost in the mid-twentieth century when the government initiatives were developing military missiles [1]. The basic design of the engine consists of the fuel grain or the solid fuel, motor casing, and the nozzle. The fuel grain is placed inside the motor casing where the combustion process takes place. The combustion process of the solid fuel engine contains multiple phases of which when the propellant changes from solid to liquid to gas state [2]. They are mainly used in various applications because of their easy storage, it is easily handled compared to other types of propellants, and due to their high-density property, and it has a compact size [3].

Solid rocket motors are utilized on aerial and air-to-ground rockets, on model rockets, and as sponsors for satellite launchers. In this type of rocket, the fuel and oxidizer are combined as one into a strong charge which is stuffed into a strong

---

S. Raj (✉) · N. A. Elsonbaty · S. Ramamoorthy  
Amity University, Dubai, UAE  
e-mail: [sraj@amityuniversity.ae](mailto:sraj@amityuniversity.ae)

© The Author(s), under exclusive license to Springer Nature Singapore Pte Ltd. 2024  
R. K. Tyagi et al. (eds.), *Advances in Engineering Materials*, Lecture Notes in  
Mechanical Engineering, [https://doi.org/10.1007/978-981-99-4758-4\\_21](https://doi.org/10.1007/978-981-99-4758-4_21)

219

chamber [4]. An opening through the chamber fills in as an ignition chamber. At the point when the blend is touched off, burning happens outside of the charge [5]. Solid rocket engines are consistent with four main parts, initially is the motor casing which acts as the engine's protective shell. The second part is the combustion chamber designed to withstand the combustion process load. The third component is the fuel grain (solid propellant) and lastly is the nozzle used to increase, expand, and accelerate the combusted gas to produce the desired thrust [6].

Solid fuel rocket engines are also used in experimental rockets used in the aviation industry to prove the concept of rocket engines and estimate the developments required in the design and performance [7]. It is beneficial for research and aerospace students to conduct various tests and help visualize the concept of any rocket engine. Solid fuels are mainly used as experimental rockets due to their simple design and favorable results [8]. It is also the safest among other experimental rockets because it can be made or bought based on the quantity needed however precaution is always needed with any experimental rocket engines, and they also are powered by a solid oxidizer-fuel mixture which makes its ignition easier, prevent leakage issues, and help decrease the delay time [9].

## 2 Objective

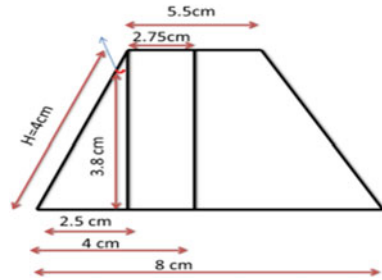
The paper focuses on the procedures initiated to design and construct the engine prototype along the stand test evaluating its performance, efficiency, and durability. Over the above, static tests shall be performed to test the engine design and prove its working principle, where the estimation of the burn time and combustibility rate will be calculated. Furthermore, durability tests will be conducted to determine and measure the strength of the test stand.

## 3 Design and Construction

### 3.1 Engine Design

The design adopted is the casing-throttle-nozzle (CTN) design, which is developed by maintaining all three components in one motor piece. This design has been selected due to its simplicity and clear visualization of the combustion process. Furthermore, it improves the engine performance by reducing gas leakage and size accommodation [10]. The engine is constructed of a motor casing which is a cylindrical tube of 2 cm outer diameter, a 1.8 cm inner diameter, and a length of 10 cm, designed to hold a small amount of solid propellant due to its high combustible rate and to withstand a high amount of internal loads. The material used for it is copper since it is durable, has high tensile strength, and is non-corrosive [11].

**Fig. 1** Nozzle frustum diagram



The nozzle is fabricated of a steel sheet due to its high durability and the amount of thermal load it can withstand. It is 7.4 cm long and has a diameter of 2.2 cm. The nozzle is fabricated using the frustum calculations, then based on them were drawn and the nozzle was shaped like a cone and sealed using the soldering iron inside out to ensure it is secured [12]. Then a durability test has been conducted on the nozzle after the fabrication, and as it passed, it was added to a room temperature room until use (Fig. 1).

$$h = \sqrt{a^2 + b^2} = 4 \text{ cm} \tag{1}$$

$$\cos \theta = \frac{3.8}{4} \text{ \& } \theta = 18.2^\circ \tag{2}$$

1/2 A6-2 Estes rocket motor was used as the solid propellant which is consisted of a mixture of potassium nitrate, sulfur, and the choral to form the fuel grain [13]. In addition, the fuel grain is wrapped in a paper casing to act as the insulator [14]. The engine also contains a delay charge to allow the rocket to reach maximum altitudes safely and provide a clear visual of the flight path [15]. Furthermore, ignition wires and safety plugs are installed to secure and initiate the ignition process [16].

Finally, the ignition system Estes Launch controller is used as the main power supply. It consists of the main electrical system of which is the main power supply, the connecting wires which helps connect the ignition wires/igniters to the electrical system, and the safety key used to prevent any insecure ignition and alerts in case of any system is not working or in case the connecting wires are not connected properly [17] (Fig. 2).

### 3.2 Stand Test Design

The stand test design is based on a three-legged stand design, where it is designed to help measure the thrust using the thrust meter. The stand test is designed in a way to handle the engine and the load acted by the engine. The stand test design consists of one aluminum metal plate of a length 50 cm, a width of 10 cm and a thickness of

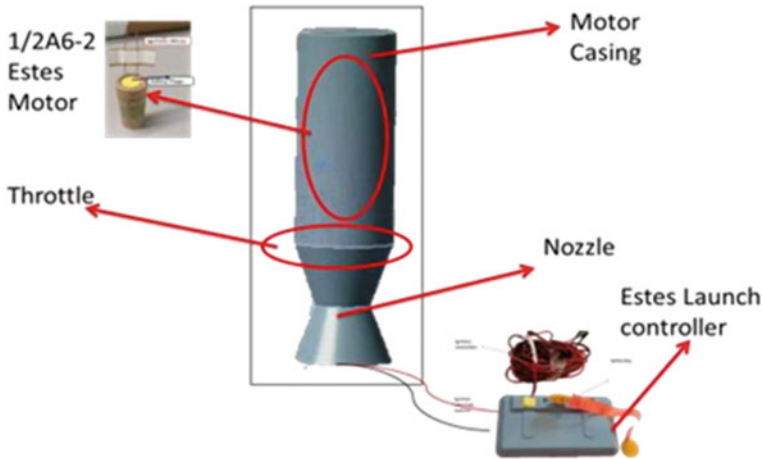


**Fig. 2** Engine design

0.15 cm, three aluminum angle legs of a length of 50 cm and a width of 10 cm to support the plate, and angle brackets that are  $5 \times 5$  cm [17].

To start first, the angle legs were taken and assembled into the angle brackets at an angle of  $45^\circ$ . Both the angle brackets and the legs were then drilled into 6 mm in size using the drilling machine. They were then attached by the bolt and secured using the bolt nut. The same procedure was followed for all three legs. After assembling the legs, the plate was taken and placed on its rougher surface. Then the metal glue adhesive metal glue was prepared by mixing hardener and resin. A generous amount of glue was then added to the angle brackets that are attached to the legs and were attached to the plate. After placing the legs, several heavy loads were added to it to help secure it in place. The stand was left then for 5 h to harden. After finishing the primary assembly, a stability test was performed to check the durability of the test by adding loads on the top part of the stand test [18]. The first test failed due to the lack of the proper amount of glue on it and the stand test assembly failed after holding the weights for 2 min. After several inspections and detecting the problem, the stand test got cleaned and the legs were glued again with an excessive amount of glue from the bottom and secured on the sides and were left overnight to dry. The next day, the durability test was performed once more and was found to be a success as that the legs handled the loads acting on it for 10 min without moving and without getting deforming and so it was ready for the second assembly phase.

After that the sliding drawer is attached using two angle brackets, one of them is placed at the beginning of the plate and the second is placed at the middle-end of the plate. The angle brackets are then drilled into the same size as the drilled hole in the sliding drawer of 4 mm. The angle brackets are then glued to the plate with the adhesive hardener-rinse glue mix and are left for 5 h to dry. After that, the sliding drawer is attached to the drilled angle brackets with the bolt and is secured with the bolt nut. The materials used for the stand test plate, legs, and angle brackets



Fig. 3 Stand test design

aluminum have been used because it is durable, lightweight, non-corrosive, and it has high tensile strength. And for the sliding drawer, galvanized steel has been used because it is corrosion resistant and has a high tensile and yield strength, as well as it is very protective and safe [19] (Fig. 3).

## 4 Structural Analysis

The assessment of the effects of loads on physical structures and their components is known as structural analysis. All structures that must sustain loads are susceptible to this sort of study. ANSYS software and Solidworks were used to determine the structural effects on the body.

### 4.1 Thermal Analysis

The effects of heat and thermal energy were tested on the structure of the engine. A strain temperature of 298 k was added to the engine as the analysis thermal load. The minimum heat flux of the engine is  $5.4801 \times 1010 \text{ W/m}^2$  and the maximum is  $2.4387 \times 1017 \text{ W/m}^2$ . With the material used and the built design, the average heat flux the engine reached is  $2.4387 \times 108 \text{ W/m}^2$ .



### 4.2 Pressure Analysis

In order to identify the amount of load, the engine can withstand and the deformation of the engine.

$$\text{The weight total surface acting area on the of engine the engine} = AF \quad (3)$$

where

$$F = 8 \text{ N and Total surface area } A = 1064.527 \text{ cm}^2$$

Substituting the above values in the given equation, we obtain that approximately the pressure magnitude acting on the engine is  $1.79 \times 10^2$  Pa and the results obtained were only the tips of the nozzle reached the max distortion value because of the exhaust velocity. The engine was in the safe zone throughout the analysis.

### 4.3 Combined Load Analysis

Combined load analysis was performed on both Solidworks and ANSYS which had a combination of the thermal load of a 3000 C and pressure load of  $1.79 \times 10^2$  Pa. Based on this analysis, it was visualized that the nozzle is the area which reached the highest deformation value of  $1.066 \times 10^{-8}$  Pa because the nozzle is the area with the highest point of thermal load due to the exhaust velocity.

It was also visualized that the engine did not reach the maximum distortion value and reach the average critical value because of the design implementation and the material used, and so there was no structural defects or damages in the engine structure (Fig. 4).

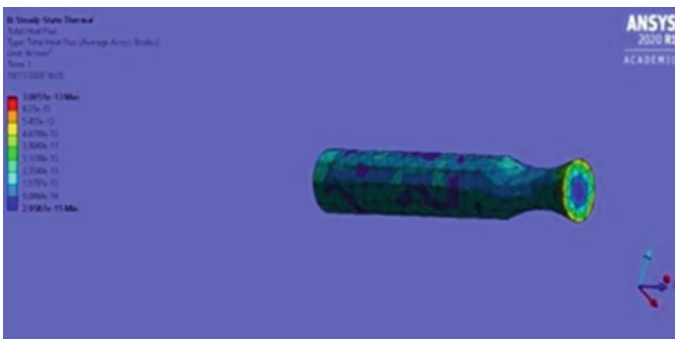


Fig. 4 Engine analysis

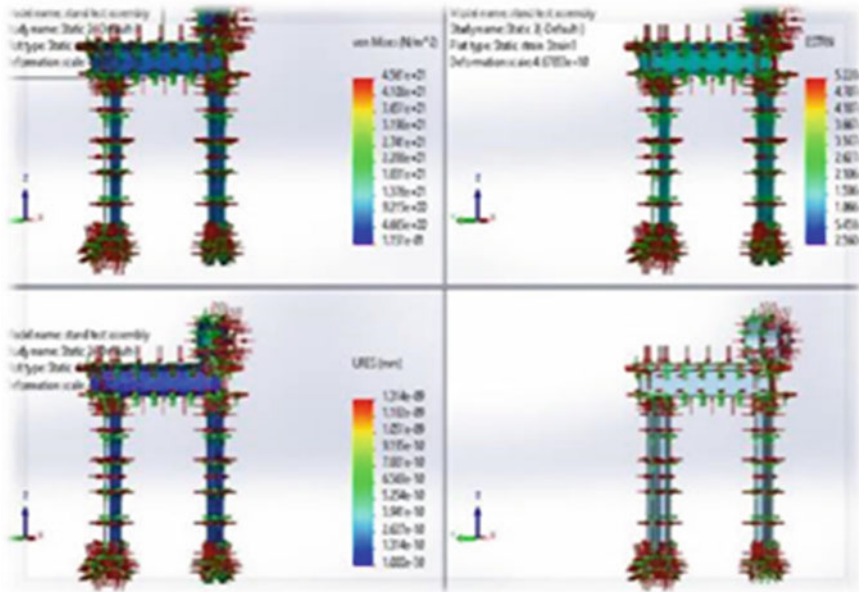


Fig. 5 Stand test analysis

### 5 Stand Test Analysis

Solidwoks analysis was conducted to evaluate the durability, strength, and safety of the stand test model, with a mesh size of 15 mm and mesh type of solid mesh of a thermal load of and a pressure load of 0.00010 mpa. Through the analysis, it was visualized that the stand test reached a distortion value of  $1.376 \times 10 \text{ N/m}^2$  which is way below the maximum distortion value of  $4.561 \times 10 \text{ N/m}^2$  of the material. These result concluded that the stand test did not reach the maximum distortion value, and hence it is safe to start its actual building and is safe to conduct various tests on it (Fig. 5).

### 6 Fluid Flow Analysis

The fluid flow analysis was conducted on ANSYS Fluent, in which boundary conditions of outer temperature = 22 °C and inner temperature = 300 °C. At the end of the analysis, it could be concluded that the engine was able to withstand the high temperature implemented by the propellant. The flow through the engine was described to be turbulent, which is not preferred as it may cause an uneven ignition process and cause an internal damage in the engine. Extra precautionary methods were taken to

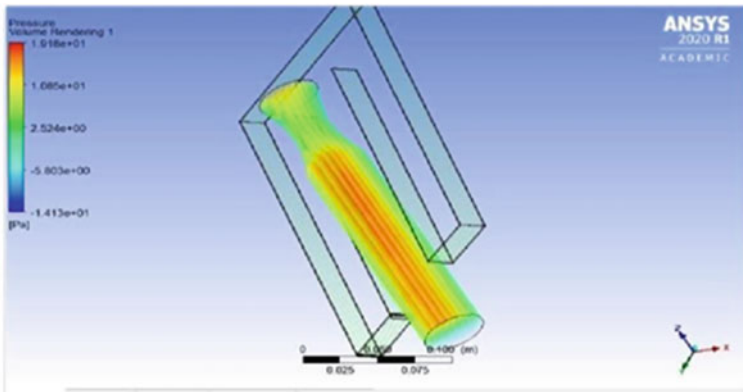


**Fig. 6** CFD analysis

ensure that the ignition process is smooth and that the flow is laminar and construct further enhancements in the engine design (Fig. 6).

## 7 Tests and Results

### 7.1 Tests

Before testing, the stand test was placed in the testing area and several inspections were made and restricted the movement of people to ensure safety, as well as, assembled the safety equipment concerning the area. The fire extinguisher was to be placed near the test section in case of any accident; the ignition system was placed at a 1-m gap, to ensure the safety of the students conducting the test. The engine parts are assembled and the hose clamps are attached to the static test stand in order to hold the engine in place. There were two tests conducted, the solid propellant static test which is done to test the combustibility of the propellant and the force it will implement, and the second is engine static test where it helps to test the performance of the CTN design.

To check the combustibility of the propellant, it must be attached to the static test stand arrangement and the ignition wires are connected to the propellant. Once the system is connected, the safety key is added to the main electrical power supply and the red light turns on, it means that the system is prepared for the ignition, hold on the red and yellow buttons to start the ignition process. When the power reaches the ignition wires, it will create a spark inside the propellant throat which will start the ignition processes of the propellant.

After the combustibility of the propellant is tested, the propellant is inserted into the CTN engine. The connecting wires are then added and the ignition process starts.

**Fig. 7** Engine static test arrangements

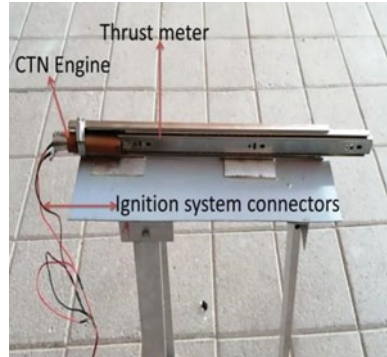


**Fig. 8** CTN static test

During the CTN tests, the ignition processes failed twice. And several inspections were made during the testing processes. After inspection, it can be concluded that the ignition wires were not secured properly because the safety plug was not tidily compressed inside of the propellant throat and so the spark did not reach the propellant. The wire connectors were loose and so the power supplied by the electrical system did not reach the ignition wires and so prevented the occurrence of the ignition spark. The hose clamps were loose and the engine was not tightly secured.

After detecting the mistakes, the wires were reconnected and before starting the ignition process. The engine was secured properly and the ignition process was a success (Figs. 7 and 8).

## 7.2 Results

The solid propellant force from the live demonstration:

Initial distance = 56.4 cm Final distance = 58 cm

Total time ( $\Delta t$ ) = 5 s

$\Delta V = 0.32$

$\Delta x = 1.6$  cm;  $a = 0.064$  cm

$\Delta m = 125$ ;  $F = 8$  N.

CTN design:

Initial distance = 49 cm Final distance = 50 cm

Total time ( $\Delta t$ ) = 5 s

$\Delta V = 0.2$

$\Delta x = 1$  cm;  $a = 0.04$  cm

$\Delta m = 200$ ;  $F = 8$  N

Rocket Ignition: Force = 8 N

Total Area = Area of cylinder (motor casing) + Area of circle (nozzle) (4)

$$\text{Total Area} = 2\pi(9)(70) + 2\pi(9)2$$

$$\text{Total Area} = 4407.3447 \text{ mm}^2 \text{ or } 44.67 \text{ cm}^2$$

$$\text{Pressure} = \text{Force/Area} \quad (5)$$

$$\text{Pressure} = 8/44.67 = 1.79 \times 10^{-3} \text{ pa}$$

$$\text{Mass Flow Rate; } \dot{m} = A^* \left( \frac{P_t}{\gamma_t} \right) \sqrt{\frac{\gamma}{R} \left( \frac{\gamma + 1}{2} \right)^{\frac{-\gamma+1}{2(\gamma+1)}}} \quad (6)$$

$$\dot{m} = 5.263 \times 10^{-5} \text{ g}$$

$$A_e = A = \pi r^2 = 50.24 \text{ mm}^2 \quad (7)$$

$$V_e = M_e \sqrt{\gamma R T_c} = 59.09 \quad (8)$$

$$P_0 = 101.1 \times 10^2$$

$$\text{Thrust; } F = \dot{m} V_e + (P_e - P_0) A_e = 50.69 \text{ N} \quad (9)$$

## 8 Conclusion

At the end of the experiment, the concept of solid rocket propulsion was understood, and by performing the static test, the maximum thrust and the force produced were calculated. The materials that have been used for the engine proved that they are durable, reliant, and is highly tensile at the end of the static test. The design of the static test stand is a little complicated and requires proper material and testing before it can be used for the static test. It has proved that the static test stand model is also perfectly designed and the component selection was perfect. A durability test was done on the static test stand model and it was able to withstand it. Various tests were done on the engine and the static test stand model on software such as ANSYS and

Solidworks. These tests proved that the design of the engine and static test stand was perfect. Despite having disadvantages, the performance of this type of engine is highly efficient and widely used in the industry.

## References

1. Nazri M, Jaafar m (2014) Development of solid rocket propulsion system at UTM
2. Kuo KK (ed) (1984) Fundamentals of solid-propellant combustion. American Institute of Aeronautics and Astronautics
3. Williams FA, Barrère M, Huang NC (1969) Fundamental aspects of solid propellant rockets. Advisory group for aerospace research and development Neuilly-Sur-Seine (France)
4. Schüttauf K et al (2016) Operation of solid rockets in comparison with hybrid rockets during the STERN project. SpaceOps 2016 conference, 13 May 2016. <https://doi.org/10.2514/6.2016-2613>
5. Beckstead MW, Derr RL, Price CF (1970) A model of composite solid-propellant combustion based on multiple flames. *AiAA J S*(12):2200–2207
6. Davenas A (ed) (2012) Solid rocket propulsion technology. Newnes
7. Kirtas M, Disseau M, Scarborough D, Jagoda J, Menon S (2002) Combustion dynamics in a high aspect ratio engine. *Proc Combust Inst* 29(1):917923
8. Zohari N, Keshavarz MH, Seyedsadjadi SA (2013) The advantages and shortcomings of using nano-sized energetic materials. *Central Eur J Energ Mater*
9. Niemi Jr EE (2002) Using model rocketry to introduce students to aerospace engineering. *Age* 7:1
10. George K, Panda BP, Mohanty S, Nayak SK (2018) Recent developments in elastomeric heat shielding materials for solid rocket motor casing application for future perspective. *Polym Adv Technol* 29(1):8–21
11. Manesh HD, Taheri AK (2003) The effect of annealing treatment on mechanical properties of aluminum clad steel sheet. *Mater Des* 24(8):617–622
12. Stephenson J, Undergraduate J Math
13. Mathematical Modeling: One + Two Modeling: One + Two Design of Nozzle for High-Powered
14. Solid Rocket Propellant Design of Nozzle for High-Powered Solid Rocket Propellant. *J Math Model One + Two* 9(1). <https://doi.org/10.5038/2326-3652.9.1.4895>
15. Chen SL, Chang HJ, Lee JN, Chen ST (2013) Cone frustum part simulation performance of turn-mill five-axis machine tool. In: *Applied mechanics and materials* (vol 284). Trans Tech Publications Ltd., pp 638–644
16. Davis JR (ed) (2001) Copper and copper alloys. ASM International
17. Fedel M, Olivier M, Poelman M, Deflorian F, Rossi S, Druart ME (2009) Corrosion protection properties of silane pre-treated powder coated galvanized steel. *Prog Org Coat* 66(2):118–128
18. Klyatis L (2012) Accelerated reliability and durability testing technology, 2nd edn. Wiley, USA
19. MY (2021) Corrosion and electrochemical properties of bulk metallic glasses and nano-crystalline materials, 2nd edn. The Electrochemical Society, Japan

# Mordernistic Aspects of MXenes and Its Applications



Swarnima Sharma and Surbhi Sharma

**Abstract** Since last decades identification of  $Ti_3C_2$ , the collection of 2D transition metal carbides, carbonitrides, and nitrides has become fastly grown topic. MXenes are two-dimensional (2D) materials that are synthesized from MAX different stages. The numerous implications of 2D MXenes in nanomedicine, spintronics, microwave absorption, and energy storage devices have been promoted by their exfoliation. Scientists at Drexel University were the first to characterize a monolayer from a M phase of  $Ti_3C_2$ . Distinctive features of MXenes include strong rigidity and high electrical conductivity. In terms of crystallographic and structural complexity, the MAX phase family, and its descendant, the use of MXenes and related nanostructured materials in (photo) electrocatalysis and traditional chemical processing is highlighted in recent conceptual advancements. MXenes are expanding rapidly. Day-by-day rising interest and advancement of MXene-based research and technology in the area of MXenes applications like catalysts, ion batteries, gas storage medium, and sensors are continuously attracting the researchers to have a assembled review studies for its structure activity prospects. This review paper will definitely serve the path for the development of a new generation of MXene-based a compound with exciting potential. In this paper, we have discussed the synthesis, composition, and characteristics of MXenes, and their different applications with highlighting the challenges to look forward for research.

**Keywords** MXenes · Metal carbides · Max phase · 2D materials · Energy storage

## 1 Introduction

Due to their particular electric platforms, MXenes are certainly large, and two-dimensional (2D) compound tends to be encouraging candidates for several electric and power applications. MXenes have very unique properties, and every property has defined application, nowadays, it is often seen when we start using substance for

---

S. Sharma · S. Sharma (✉)

Department of Chemistry, Chandigarh University, Garuah Mohali, Gharuan, Punjab 140301, India  
e-mail: [surbhi.e9299@cumail.in](mailto:surbhi.e9299@cumail.in)

separating layers, we use methods like sonication and exfoliation [1], it is specially for modifying formation and size of 2D materials from 3-dimensional that are multi-layered substances which are held by binding substances. Gogotsi et al. presented 2D matter that is novel transition diamniotic form of carbons (carbides), N-3, and carbon nitrides ( $C_3N_{4+x}H_y$ ) (MXenes) to the people in the groups and get trigger another trend of passion for study of these advanced ideas [2]. Chemical formula for MXenes is  $M_{n+1}X_nT_x$ . MXenes may be categorized as arranged mono-M means single, bought solid-solution and double-M M compounds metal metal compounds predicated on the bases of its particular atom lattices and structure. MXenes are made through selective etching of acid, and their origin can be MAX and non-MAX. These are the places that signify group elements A from decades different type of max diamniotic form of carbons and N-3(nitrides) variants were being identified devoting great to the MXene family because of this many types of MXenes produced [3]. Researchers facing some problems like due to MXenes great price and scarcity, the use of noble metals like platinum and Ru as electrocatalysts is severely constrained for large-scale applications; because of the challenging synthesis of monolayer  $Ti_3C_2T_x$  MXene, low structural stability caused quick reaction with  $H_2O$  and extremely delicate management of single-layer or few-layer structures, the realistic use of monolayer  $Ti_3C_2T_x$  MXene as a photocatalyst is constrained, top most obstacle is the low yield and high expense of MXenes, but MXenes are presently mostly made in laboratories with low yields. The development of a method for the huge manufacture of MXenes that is economical, productive, and environmentally sustainable will help to progress studies in this area and will offer up new opportunities for MXenes' potential commercial uses but because of 2D material MXene is in demand showing their unique properties.

## 1.1 Electronic Properties

Commonly, MXenes tend to be metallic matter having a thickness in Fermis because of the level of group B elements which are metal. The density of MXenes is nearby the Fermis which is intimidated through group B metal elements and electrons of  $D$  orbits, whereas the electrons from  $p$  orbits associated with number of atoms can call it  $x$ , and this signifies that outer layers of MXenes tend to be relax and play an even more important part within their electric properties compared to the internal group b element metals. Because hydroxy and fluorine groups can get just 1 e, they have identical impact on MXenes electric platforms, and oxygen can take 2 e and therefore produce a unique impact, and [4] the moiety groups also affect the electronic transference and this is always find in F-termi MXenes. Wherever F-termi MXenes show the greatest electric transference and monetization by O atoms, this will show contribution to a large reduced amount of the transference. The major number of MXenes fit in with the group of trivial-metals, semi-metals, or semiconductors. The metallic behavior of MXenes or behavior that is semiconducting nature shown by MXenes is mostly dependent on their monolayers of MXenes [5]. The terminations can cause electron to be almost free near the Fermi degree in some MXenes, like,



e.g.,  $\text{Ti}_2\text{C}(\text{aOH})_2$ ,  $\text{Zr}_2\text{C}_2$ ,  $\text{Zr}_2\text{N}(\text{OH})_2$ ,  $\text{Hf}_2\text{C}(\text{OH})_2$ ,  $\text{Hf}_2\text{N}(\text{OH})_2$ ,  $\text{Nb}_2\text{C}(\text{OH})_2$ , and  $\text{Ta}_2\text{C}(\text{OH})_2$ , and MXenes can provide networks which can help in break-free electron moment [6]. MXenes with 100% in valley-spintronics and ferromagnetic applications and polarization rotational property are shown at the Fermi level that play a very important part in products; thus, they get awareness that is exceptional [7].

## 2 Optical Properties/Photonic Properties

The optical properties in case of linear example are consumption, but in linear form, photo-luminescence and optical characteristics being nonlinear [8]. Example saturated absorption and the dispersion of linear and nonlinear dielectric function of MXenes are extremely influenced by energy structures, but there are the weakness that is various other low-dimensional matter show [9]. MXenes show sizable excitonic impact which is revolutionary in the world of 2D materials. For evaluating 2D materials that will require e-hole fundamental connections to be calculated under consideration so that researchers can quantitatively find and show absorption profiles. In X-ray, ultraviolet, infrared, and microwave spectra for the  $\text{Mo}_2\text{CO}_2/\text{W}_2\text{CO}_2$  heterostructure signify Type II band arrangement followed [10]. Different optical characteristics of compound such as the transmittance, usage, reflectivity, refractive index, and power waste [11] are predicted according to theory via research associated with genuine and fictional aspects of the complex dielectric constant [12]. Optical properties of pristine  $\text{Ti}_2\text{C}$ ,  $\text{Ti}_2\text{N}$ ,  $\text{Ti}_3\text{C}_2$ , and  $\text{Ti}_3\text{N}_2$  were examined utilizing the random stage approximation method. Because these have metallic form of conductivity and have no optical gap they show functions that is shown by dielectric materials. The reliance of optical characteristics and true amount of MXene layers calculated and been known.

### 2.1 Magnetic Properties

2-dimensional layer of the MXene materials provides range that is rich in magnetic characteristics. The magnetic moments of the group b elements and the magnetized MXenes mainly observed from the loss of electrons that is nominal for the b group elements like carbon-, nitrogen-, fluorine-, OH-, and oxygen-, as well as by finding the coord no the group b elements it is notice that additional functions are performed by MXenes [13] This is because of *d* electrons in MXenes. In case of bonding, one of the MXenes is formed nearby the Fermi surface located between the bonding and anti-bonding region. It is presented that fluorine, oxygen, hydrogen, and hydroxy group are functional and that show specific features of MXenes [14]. MXenes are magnetic; however, some of them show ferro-magnetic to anti-ferro-magnetic transitions. The properties of MXenes characterizations are obtained from the orbital of *d* shell of chromium atoms [6]. Given that the energy difference in the

ferro and anti-ferro-magnetic configuration of chromium-based MXenes is incredibly big, and this type of programs sticks to their characteristics at temperature of room [15].

## 2.2 Surface Properties

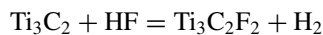
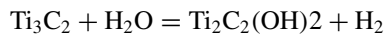
The work function describes as the essential change in the Fermi level while the vacuum potential shows the usefulness of materials which can be additionally utilized for the formation of one type of applications [16]. The work functions of compound having pyraclostrobin and boscalid are calculated based on MXenes, and MXenes derived with fluorine, hydroxy group, and oxygen are calculated and should be in the variation of 3.3–4.8, 3.1–5.8, 1.6–2.8, and 3.3–6.7 eV, correspondingly [17]. The variations affect the work purpose of MXenes after functionalization when treated with pristine MXenes which are described due to its magnetic dipole moments and because of its specifications [18]. MXenes can be used to create links which can be schottkya- barrier-free and between other 2D semiconductors too, by all hydroxyl-terminated (some oxygen-terminated) MXenes can produce e-(vacuum) fillers.

## 3 Synthesis and Processing of MXenes

### 3.1 Etching

To obtain 2D materials, we need to isolate one or some atomic layers from wadded compounds, wherein the layers-to-layers bonding which is much fragile compared to the bonds in the layers (Fig. 1). As an example, in  $\text{Mo}_2\text{Ga}_2\text{C}$ , 2 Ga layers are etched. In  $\text{Zr}_3\text{Al}_3\text{C}_5$  and  $\text{Hf}_3(\text{Al}, \text{Si})_4\text{C}_6$ ,  $\text{Al}_3\text{C}_3$  and  $(\text{Al}, \text{Si})_4\text{C}_4$  are etched to produce  $\text{Zr}_3\text{C}_2\text{Tz}$  that is 2D correspondingly. This etching is supportive in aqueous mode only [11]. MXenes mostly form high area terminations, with help of some chemicals such as  $-\text{F}$ ,  $-\text{OH}$ , and  $-\text{O}$  at high temperature, but MXenes are obtained in max phases and having hexagonal structure are only show these types of terminations (Fig. 2).

During synthesis, some reactions are processed



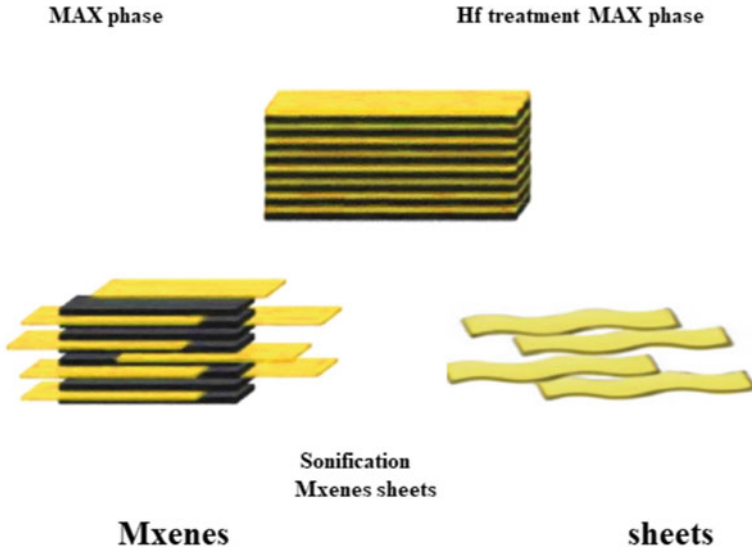


Fig. 1 General synthesis steps and shape of MXenes

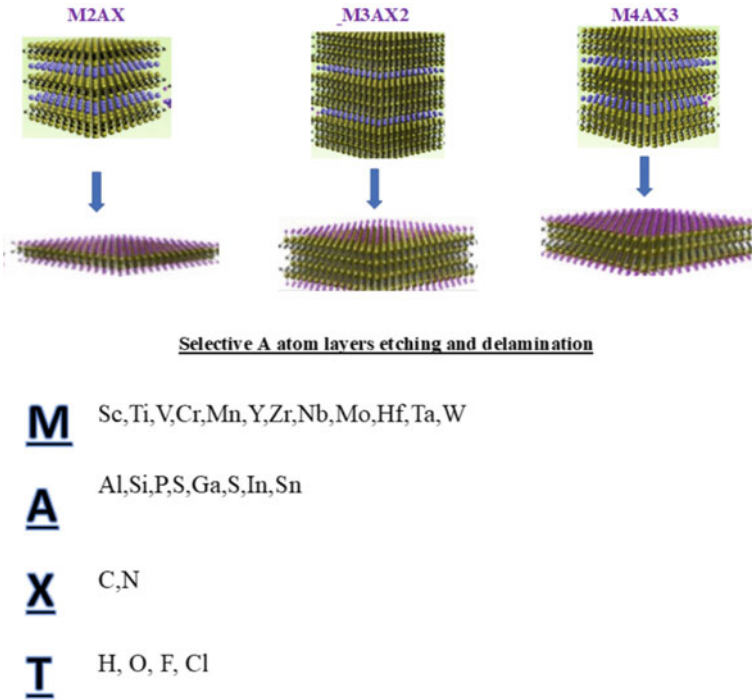


Fig. 2 Different types of mono-M max phases

## 4 Exfoliation

After etching, the uniquely mixed atomic layers are changed by different terminations plus the material that is result of  $M_{n+1}X_nTz$  multilayers (MLs) kept collectively by hydrogen and or van der Waals bonds [19]. In the MAX duration, MXenes substance shows some great benefits which are (i) less intense reactants when compared with HF; (ii) paid down sonicating times (put another way., at the very least four times), (iii) high yield, with around 70% about the fragment with 1 or 2 levels, (iv) under quantity of vacant spaces, and (v) highly very adjustable shapeable and versatile clay-like MXenes. HF acid is one of the main components for MXene production. Mxenes are amazing crystal structures associated with MAX stage, and MXenes had been characterized by a PANalytical. Some artificial methods like freeze-drying have been trusted to fabricate porous 2D, spray. Drying out is definitely a method that can be an alternative to fabricate porous 2D materials, and some of the methods are capillary pressed crumpling and self-construction, but in case of this, the formation rate is low [20]. V2C MXene is tough to synthesize. The electric conductivity depends on the three solid-solution for MXene, and it is calculated on the bases vacuum-filtered by using a examine technique that is four-point. MXenes offer some properties like surface interlayer groups that are tunable, and these functional teams are basically associated with the work function, which is vital for electronic devices applications and structure-dependent properties. Suspended MXene membranes have twisted elastically which is really a topic of concerns because of this sure technical failure occurs. MXenes are metallic structures having electrons that is nearby the Fermi measure. Density concept of MXenes is functional, and sometime, molecular characteristics were used to recreate the technical properties of MXenes. The change among the practical and theoretical mechanical characteristics of MXene is principally described during the time of traits of nanosheets, because of these characteristics, they truly utilized in many applications [21]. Table 1 is summarizing the novelty and applications of recently reported MXenes.

## 5 Applications of MXenes

### 5.1 Energy Storage

MXenes have larger capability to create ideal chemicals and have features which are structural other than 2D materials. Therefore, they're extremely guaranteeing as materials for anodes in additional batteries. As the applicability of  $Nb_2C$  MXene in Li-ion batteries. And MXenes like as  $Zr_2C$ ,  $Zr_3C_2$ ,  $Zr_2CO_2$ ,  $Zr_3C_2O_2$ ,  $Ti_3C_2$  MXene/CNT compounds were all found to be ideal for Na ion batteries Because  $Nb_2C$  can be performed with the help of HF and  $H_2O$  because of the availability of O, F, and OH groups [22]. Monolayers are the layers having greater desirable than other 2D materials in opto-electronics, spintronics,  $Ti_3C_2$  that is photocatalysis and

**Table 1** Summary of different MXenes and their uses via highlighting the novelty of each

Application	Research group	MXenes used	Advancement or novelty
Energy storage	Professor Zhi Chunyi and Assistant Professor Dr. Fan Jun	Zr <sub>2</sub> C, Zr <sub>3</sub> C <sub>2</sub> , Zr <sub>2</sub> CO <sub>2</sub> , Zr <sub>3</sub> C <sub>2</sub> O <sub>2</sub> , Ti <sub>3</sub> C <sub>2</sub> MXene	Sensors, strain sensors, electrochemical biosensors, gas sensors, thermal heaters
Photoavoltaic devices	Edmond Becquerel	Ti <sub>3</sub> C <sub>2</sub> T <sub>x</sub> MXene	Mass silicon, Si thin films, C nanostructures, photo-sensitized pigments, functional group conjugated polymers, and dipole fusion organic–inorganic materials
Thermoelectric power generation	Jean Charles Athanase Peltier	Sc <sub>2</sub> CT <sub>x</sub> , Zr <sub>2</sub> CT <sub>x</sub> , Ti <sub>2</sub> CT <sub>x</sub> , and Hf <sub>2</sub> CT <sub>x</sub>	Bioimaging and heavy metal ion and dye adsorption for environmental water treatment
Solar steam production photothermal	Auguste Mouchout	Cr <sub>2</sub> M''C <sub>2</sub> T <sub>2</sub> (M'' = titanium, T = Fluorine, hydroxy, and Oxygen)	Magnetic change dichalcogenides
Surface plasmonics	Rufus Ritchie	Titanium (IV) carbide MXene	Bio, chemical, and optical detectors, as well as surface-enhanced Raman spectroscopy (SERS)
MRI	Paul C. Lauterbur	Manganese oxide and titanium carbide	Weight-bearing MRI exams
Ferroelectricity	Joseph Valasek	Sc <sub>2</sub> CO <sub>2</sub>	Dielectric constant capacitors, pyroelectric devices, transducers for medical diagnostic

were utilized as co-catalysts to improve the photoactivity for C<sub>3</sub>N<sub>4</sub> and H<sub>2</sub> during the time of fabrication. MXenes have actually superb conductivity because of its metallic character it is about 5000 to over 15,000 S cm<sup>-1</sup>, and now, we discovered applications where superior electrical conductivity is recognized as pivotal, and it is needed in many applications like sensors, strain sensors, electrochemical biosensors, gas sensors, and thermal heaters [23]. All-MXene hydrogels are the connections among MXene nanosheets and binded by covalent bond.

Researchers outline the intercalation of several cations, namely lithium+, sodium+, and potassium+, within Mo1.33C nanostructure in order to provide a

preliminary assessment of the promise of *i*-MXenes for metal-ion capacitors and secondary-ion batteries. The  $(\text{Mo}_{2/3}\text{Sc}_{1/3})_2\text{AlC}$  phase was used to produce the d-Mo1.33C “tissue” electrode, Mo1.33C electrode displayed rectangular CV curves in 3 electrolytes, demonstrating surface-controlled capacitance charge storage behavior, with the exception of a small variance in working voltage range. The electrochemical properties of conventional MXenes, namely  $\text{Ti}_3\text{C}_2$  and  $\text{Ti}_2\text{C}$ , in superior catalytic applications have been improved using a variety of methods. For instance, MXene layers can be treated to increase the ionically surface by creating a 3D system which is considered, or they can be adorned with electrochemically active substances like  $\text{RuO}_2$  and  $\text{MnO}_2$  [24]. We provide multiple methods for enhancing the charge storage capacity of a d-Mo1.33C “paper” electrode: the creation of a gel made of MXene and the post-etch annealed of the *i*-MXene electrodes. The most potential MXenes are those with minimal chemical weights, including  $\text{Ti}_2\text{C}$ ,  $\text{Nb}_2\text{C}$ ,  $\text{V}_2\text{C}$ , and  $\text{Sc}_2\text{C}$ . Thus,  $\text{M}_2\text{X}$  electrodes should have greater gravimetric capabilities than their  $\text{M}_3\text{X}_2$  and  $\text{M}_4\text{X}_3$  counterparts. It is plausible to believe that ions only enter between the MXene sheet so the bonds with M and X are too powerful to be quickly disrupted. The most researched MXene for electrolytic devices is  $\text{Ti}_3\text{C}_2\text{T}_x$ . It has been shown that frameless  $\text{Ti}_3\text{C}_2\text{T}_x$  paper electrodes have volumetric capacitances of 300–400  $\text{F cm}^3$  in neutral and basic electrolytes; these exceptional values surpass the best all-carbon electrical double-layer capacitors. Additionally,  $\text{Ti}_3\text{C}_2\text{T}_x$  exhibits excellent capacitive performance even at relatively large charge and discharge rates. This contrasts with the gradual ion intercalation often seen in other multilayer materials utilized in battery applications, like graphite [21].

## 5.2 Photovoltaic Devices

A photovoltaic device is made up of a semiconductor structure where with change of position composition will also change, and it is made up of 2 materials that establishes a connection for the photoinduced electron–hole pair splitting and the consequent charge movement to electrodes for the creation of photocurrent [25]. Semiconducting *p*–*n*, *p*–*i*, and metal/semiconductor are part of Schottky junctions and find useful during heterostructures studies. Mass silicon, Si thin films, C nanostructures, photo-sensitized pigments, functional group conjugated polymers, and dipole fusion organic–inorganic materials are the energy accepting materials used in solar cells. Once the photocurrent output is low because of very thin, mainly atom-thin, 2D materials, then we use photovoltaic devices in solar cells for solar energy conversion [23]. MXenes offer unique features that make them ideal for photoelectronic energy transfer, including changeable electronic properties for metallic or semiconducting conductivity, customizable work functions, and excellent optical transmittance. MXenes’ work functions are strongly affected by their surface functional groups; for example, hydroxy groups reduce work functions while oxygen groups raise them [26].

### 5.3 Thermoelectric Power Generation

$\text{Sc}_2\text{CT}_x$ ,  $\text{Zr}_2\text{CT}_x$ ,  $\text{Ti}_2\text{CT}_x$ , and  $\text{Hf}_2\text{CT}_x$  are among the MXenes expected to be semi-conducting with non-zero band gaps. These MXenes have strong Seebeck, with 1140 mV/K for  $\text{Ti}_2\text{CO}_2$  and 2200 mV/K for  $\text{Sc}_2\text{C}(\text{OH})_2$  at 100 K, according to calculations.  $\text{MoCF}_2$  also has a higher thermoelectric power factor. These characteristic has led to many other useful applications, like hydrogen storage media, semiconductive films, field-effect, detectors, photoactive classifying agents for bioimaging, and heavy metal ion and dye adsorption for environmental water treatment, in addition to energy applications [27]. MXenes also provide enriching substrates for novel processes, such as Ohmic contact with other semiconductive two-dimensional materials to generate field-effect transistor, topological insulator in o2 MXenes, and selectable two-dimensional photogenerated electron-hole gas for spin orbitronics, useful in the area of physics.

### 5.4 Solar Steam Production Photothermal

MXenes, at light absorption which is visible, exhibit extra-ordinary efficiencies that is almost used in solar-thermal industries. For instance, a  $\text{Ti}_3\text{C}_2$  membrane layer attained 100% light-to-heat transformation efficiency as calculated in a droplet beam heating process [28]. Under sun exposure, a high solar steam generation efficiency of 84% shows the exceptional energy conversion efficiency. This show efficiency of MXenes as photothermal materials. Numerous various MXenes of  $\text{Cr}_2\text{M}''\text{C}_2\text{T}_2$  ( $\text{M}'' = \text{titanium}$ ,  $\text{T} = \text{fluorine}$ ,  $\text{hydroxy}$ , and  $\text{oxygen}$ ) have been investigated with regards to their magnetic features. Like magnetic change dichalcogenides, MXenes adjust its magnetism by structural reformation and improving magnetic moments of MXenes and its transitions [29]. Two-dimensional levels, such as n3 and carbide, can be made up of just one layer, which is so thin in the shape of an atom that it has a lot of changeability in its properties. In particular, the existence of a low-dimensional group b metal n3 with a peculiar spin-character exhibiting a quality that is most of its polarization and also a 12 metallic sort of conductivity has caused a shift. The  $\text{Fe}_2\text{C}$  MXene is expected to be metal that possess intrinsic ferro-magnetic properties which is 2D and show a total magnetic spin of 3.95  $\mu\text{B}$  for every cell, but when the material is forming [30], it may considerably affect the electromagnetic characteristics of MXenes, because of the existence of un-paired electrons within the orbitals of d shell which can be spin-split. Some MXenes like  $\text{cr}_2\text{c}$ ,  $\text{cr}_2\text{n}$ ,  $\text{cr}_2\text{n}$ ,  $\text{ta}_3\text{c}_2$ ,  $\text{cr}_3\text{c}_2$  expected to become ferromagnets that can be separated from their surfaces and 2D titanium carbide and titanium(II) Nitride are anti-ferro-magnets.

## **5.5 Surface Plasmonics**

Two-dimensional layer of MXenes' showing metallic characteristics provides an ideal substrate for photoelectron interaction at their surface. Surface plasmonic emission applications offered in a large range of fields, including bio, chemical, and optical detectors, as well as surface-enhanced Raman spectroscopy (SERS) [31]. Mauchamp et al. showed that the surface plasmonic frequency of Titanium (IV) carbide MXene layers may be controlled in the IR region by changing layers functions and thickness using high-resolution transmission e-energy-loss spectroscopy (EELS). Just like a large number of other 2D matters, example graphite, boron nitride, and molybdenum (IV) sulfide, have almost free e-(NFE) states and have spatial area throughout the surfaces toward the free space. MXenes could be useful for specific gas detectors and heavy-element filtration applications [32].

## **5.6 Photon-Phonon Conversion**

The photothermal effect causes how MXenes convert photons to phonons based on the input light characteristics. In comparison with non-MXenes, MXenes may have a greater photothermal energy and photo-luminescent property. MXene quantum dots may have a poor nonradiative photothermal efficiency, but photothermal effects based on MXene have lately been used in biological diagnostics and therapies, which will be explored in some other area [33].

## **5.7 Biomedical Application**

Bio-compatible MXenes can be a good photothermal conversion agent, beneficial for local tumor ablations, and this is all because of their metallic or narrow bandgap features and nonradiative nature. 36.4 and 45.65% of photothermal transformation efficiencies are shown by niobium carbide, and MXene has a wavelength of 808 nm and a wavelength of 1064 nm, and because all of its, these properties as well as high specific area nanosheets of MXenes make them perfect for drug loading and transport [34].

## **5.8 Biosensing**

In compare to conventional nanoparticle-based biosensing, 2D nanomaterials have two distinct advantages in biosensing. For label-free dopamine detection and monitoring spiking activity in primary hippocampal neurons, an extremely sensitive



device based on MXene-FET-based biosensor with high sensitivity was developed. MXenes are promising for biosensing alternatives because of their great sensitivity to signal disruption of electrochemistry. MXenes are interesting options for biosensing replacements due to their great sensitivity feature to signal disruption of electrochemistry [35].

### ***5.9 Magnetic Resonance Imaging (MRI)***

Combination of functional components with extra thin two-dimensional nanosheets opens up new possibilities for the use of two-dimensional nanomaterials, in the area of diagnostic and imaging applications. For example, the combination of manganese oxide and titanium carbide improves manganese-based MRI, which was examined for detecting tumor MR imaging is one of the most often utilized imaging techniques in clinics due to its enhanced spatial resolution and favorable tissue contrast [36].

### ***5.10 Electrocatalysts***

MXenes having greater surface area, increased surface water solubility, and high surface activity observed as catalysts or catalyst support. MXenes always examined to perform applications work on bases of H<sub>2</sub>O electrolysis in which hydrogen and oxygen are generated by a hydrogen evolution reaction (HER) at the cathode and an oxygen evolution reaction (OER) occur at anode end and are the most well-studied concept. Platinum is the best beneficial water splitting catalysts, but it has limitations like expensive price and limited availability [37].

### ***5.11 Capacitors***

MXenes are useful in this field of capacitors because of their 2-dimensional lamellar structure and unique properties specifically in field of mechanics, as well as their rapid ion intercalation behavior, as a product we get a large electrochemically accessible reactive surface and pseudocapacitive mechanism always react in acid and having aqueous and non-aqueous electrolytes [38].

### ***5.12 MXenes in Membrane Separation of Pollutants***

2D nanomaterials from carbon family, such as graphene and (GO), show promising features as molecular and ionic sieving materials. Ren et al. were the first to report on

the MXene-based water purification membrane [39]. The membrane was created by assembling two-dimensional MXene nanostructures into a freestanding membrane using a VAF. The layer was created by assembling 2D  $\text{Ti}_3\text{C}_2\text{T}_x$  MXene nanostructures into a sheet that can be freestanding using a vacuum-assisted filtering process. The MXene membrane, which was based on an anodic aluminum oxide substrate, had a water permeability of more than  $1000 \text{ L m}^2 \text{ h}^{-1} \text{ bar}^{-1}$  and a cancellation rate of more than 90% for molecules bigger than 2.5 nm. Other substrates with a comparable rejection rate performed worse than the MXene-based membrane [40].

### 5.13 *Electrocatalytic Sensors*

These electrocatalytical sensors are produced for removing pollutants from the environment as MXenes play a very vital part in this sensors, it provide a wide surface area to sensors to absorb pollution and detect it from environment. Multiferroelectricity may also be created in organized transition metal MXenes, such as  $\text{Hf}_2\text{V}$  and  $\text{C}_2\text{F}_2$ , where the helical spin states cause an electrical polarization on the surface, according to current theoretical work [41].

### 5.14 *Ferroelectricity*

The binding energy required as barrier for changing from ferromagnetic material to antiferromagnetic phase is 0.53 eV per formula unit, which is high enough to operate at room temperature [42]. Because of their dipole structures, noncentrosymmetric 2D semiconductors can show ferroelectric or piezoelectric properties. A ferroelectric substance is a polar system that can have its polarity reversed with the application of an electric field.  $\text{Sc}_2\text{CO}_2$  is the only MXene family member with in-plane and out-of-plane polarizations [43].

### 5.15 *Piezoelectricity*

Piezoelectrics are a class of conductive matter having in-plane noncentrosymmetry that may create an electrical field due to movements in the centers of positive (+) and negative (−) charges when mechanical strain is applied [44]. This increase the possibility of some conducting MXenes being used as piezoelectrics. Many piezoelectric two-dimensional metals, such as boron nitride, gallium arsenide, calcium sulfate, and aluminum antimonide in the range of  $0.5\text{--}3.0 \text{ pmV}^{-1}$ , as well as mass materials, such as quartz, wurtzite GaN, and wurtzite AlN, respectively, are often utilized in factories [45].

## 5.16 Thermoelectricity

Despite the fact that metallic MXenes have excellent electrical conductivities, their Seebeck coefficients are extremely low, resulting in a low-power factor ( $S^2$ ). Highly conductive MXenes, on the other hand, have high Seebeck values and strong electrical conductivity, resulting in a high-power factor. Further studies [46] show that MXenes have thermal conductivities in the range of  $10\text{--}60 \text{ Wm}^{-1}\text{K}^{-1}$ , which is similar to that of transition metal dichalcogenides [47].

In this article, we have lightened the applications of MXenes correspond to its properties which are base for many applications like magnetic properties of MXenes play vital role in strain modulation spin filter, magnetic tunnel junctions, magnetic random access memory, and electronic properties used in energy storage, electronics, gas separations, batteries, and supercapacitors. Optical properties are shown by sensors, biomedicine, optical devices, and transparent conductive thin film. Where surface property used in heavy-element filtration, specific gas sensors and also concerns about challenges faced by researchers while handling MXenes as two-dimensional material and try to elaborate their solutions.

## 5.17 Conclusion

Over 50 different varieties of MXenes have previously been generated by specific etching, transformations, and bottom-up constructions, with many more potentially possible. MXenes provide a supporting environment for basic and trans-disciplinary study due to their complex physics and chemistry concepts.  $\text{Ti}_3\text{C}_2\text{T}_x$  was created by Liu and colleagues as a reagent for the hydroxylation of ethylbenzene, and the enzyme was additionally durable for 40 h while being tested, obtaining a max styrene selectivity of 97.5% at a conversions of about 21%. Pure MXenes have been utilized for prototype presentations of semiconductive electrodes, effective EMI shielding, and in absorption due to their low optical dispersion and strong electrical conductivity. A variety of obstacles must be solved in order to improve this area of research and that are (1) due to MXenes great price and scarcity, the use of noble metals like platinum and Ru as electrocatalysts is severely constrained for large-scale applications. But MXenes could serve as an example of a flexible, open-ended research field in materials research for the conversion of energy via photocatalysis by helping in this concern  $\text{Ti}_3\text{C}_2$  is attracting a lot of attention in the fabrication of MXene-depend photocatalysts as a competitor to increase the transistor photocatalyst productivity. (2) Because of the challenging synthesis of monolayer  $\text{Ti}_3\text{C}_2\text{T}_x$  MXene, low structural stability caused quick reaction with  $\text{H}_2\text{O}$ , and extremely delicate management of single-layer or few-layer structures, the realistic use of monolayer  $\text{Ti}_3\text{C}_2\text{T}_x$  MXene as a photocatalyst is constrained. (3) Introducing  $\text{Ti}_3\text{C}_2\text{T}_x$  MXene is quite well for further photocatalysis investigation despite these important problems that need to be solved. On a wide variety of substrates,  $\text{Ti}_3\text{C}_2$

MXene inks have been created and successfully used for direct writing of conductivity features for electronic systems and energy storage devices. (4) Because of increased resistance of the electrocatalysts, paper-based supercapacitors not be used which are not able to produce non-rectangular CV graphs without the need for additional post-processing or current collectors, MXenes exhibit strong electrochemical performance with improved capacity and help in identifying cv graphs. (5) Top most obstacle is the low yield and high expense of Mxenes, but MXenes are presently mostly made in laboratories with low yields. The development of a method for the huge manufacture of MXenes that is economical, productive, and environmentally sustainable will help to progress studies in this area and will offer up new opportunities for MXenes' potential commercial uses. For mass manufacturing, it is anticipated that the expense will be quite low.

It is necessary to investigate the potential of MXenes as an adsorbent in ongoing operation systems. An environmentally sustainable method for the production of MXene can be guaranteed by replacing HF with renewable compounds. (6) Additional challenge for researchers is the requirement for sub-0 temperatures for MXene storage. The creation of an effective technique is essential for long-term, oxidation-free storage of MXene solution but had to be searched. Synthesis process for MXenes, such as 3D printing, has yet to be confirmed. Despite quick advancement and successful achievements in the discovery of unique, MXene synthesis procedures and different opto-electro-magnetic characteristics, there is still a significant difference between theoretical and experimental confirmations. But there will be advancement in MXenes in future and going to vast its field of applications.

**Acknowledgements** Authors are grateful to the Chandigarh University—Chemistry Department, Mohali, Punjab.

## References

1. Verger L, Natu V, Carey M, Barsoum MW (2019) MXenes: an introduction of their synthesis, select properties, and applications. *Trends Chem* 1(7):656–669. <https://doi.org/10.1016/j.trechm.2019.04.006>
2. Liu G, Jin W, Xu N (2016) Two-dimensional-material membranes: a new family of high-performance separation membranes. *Angew Chemie Int Ed* 55(43):13384–13397. <https://doi.org/10.1002/anie.201600438>
3. Xu M, Liang T, Shi M, Chen H (2013) Graphene-like two-dimensional materials. *Chem Rev* 113(5):3766–3798. <https://doi.org/10.1021/cr300263a>
4. Gogotsi Y, Anasori B (2019) The rise of MXenes. *ACS Nano* 13(8):8491–8494. <https://doi.org/10.1021/acsnano.9b06394>
5. Nemani SK et al (2021) High-entropy 2D carbide MXenes: TiVNbMoC<sub>3</sub> and TiVCrMoC<sub>3</sub>. *ACS Nano* 15(8):12815–12825. <https://doi.org/10.1021/acsnano.1c02775>
6. Han M et al (2020) Tailoring electronic and optical properties of MXenes through forming solid solutions. *J Am Chem Soc* 142(45):19110–19118. <https://doi.org/10.1021/jacs.0c07395>
7. Naguib M, Barsoum MW, Gogotsi Y (2021) Ten years of progress in the synthesis and development of MXenes. *Adv Mater* 33(39):1–10. <https://doi.org/10.1002/adma.202103393>

8. Gogotsi Y, Huang Q (2021) MXenes: two-dimensional building blocks for future materials and devices. *ACS Nano* 15(4):5775–5780. <https://doi.org/10.1021/acsnano.1c03161>
9. Wei Y, Zhang P, Soomro RA, Zhu Q, Xu B (2021) Advances in the synthesis of 2D MXenes. *Adv Mater* 33(39):1–30. <https://doi.org/10.1002/adma.202103148>
10. Ronchi RM, Arantes JT, Santos SF (2019) Synthesis, structure, properties and applications of MXenes: current status and perspectives. *Ceram Int* 45(15):18167–18188. <https://doi.org/10.1016/j.ceramint.2019.06.114>
11. Tang H, Wang R, Shi L, Sheremet E, Rodriguez RD, Sun J (2021) Post-processing strategies for improving the electrical and mechanical properties of MXenes. *Chem Eng J* 425(August):131472. <https://doi.org/10.1016/j.cej.2021.131472>
12. Shuck CE, Ventura-Martinez K, Goad A, Uzun S, Shekhirev M, Gogotsi Y (2021) Safe synthesis of MAX and MXene: guidelines to reduce risk during synthesis. *ACS Chem Heal Saf* 28(5):326–338. <https://doi.org/10.1021/acs.chas.1c00051>
13. Yazdanparast S, Soltanmohammad S, Fash-White A, Tucker GJ, Brennecke GL (2020) Synthesis and surface chemistry of 2D TiVC solid-solution MXenes. *ACS Appl Mater Interfaces* 12(17):20129–20137. <https://doi.org/10.1021/acscami.0c03181>
14. Bu F, Zagho MM, Ibrahim Y, Ma B, Elzatahry A, Zhao D (2020) Porous MXenes: synthesis, structures, and applications. *Nano Today* 30(xxxx):100803. <https://doi.org/10.1016/j.nantod.2019.100803>
15. Kim H, Wang Z, Alshareef HN (2019) MXetronics: electronic and photonic applications of MXenes. *Nano Energy* 60:179–197. <https://doi.org/10.1016/j.nanoen.2019.03.020>
16. Ibragimova R, Erhart P, Rinke P, Komsa HP (2021) Surface functionalization of 2D MXenes: trends in distribution, composition, and electronic properties. *J Phys Chem Lett* 12(9):2377–2384. <https://doi.org/10.1021/acs.jpcclett.0c03710>
17. Lipatov A et al (2018) Elastic properties of 2D  $Ti_3C_2T_x$  MXene monolayers and bilayers. *Sci Adv* 4(6):1–8. <https://doi.org/10.1126/sciadv.aat0491>
18. Gao L et al (2020) MXene/polymer membranes: synthesis, properties, and emerging applications. *Chem Mater* 32(5):1703–1747. <https://doi.org/10.1021/acs.chemmater.9b04408>
19. Zhu J, Chronos A, Schwingenschlöggl U (2015) Nb-based MXenes for Li-ion battery applications. *Phys Status Solidi Rapid Res Lett* 9(12):726–729. <https://doi.org/10.1002/pssr.201510358>
20. Alrebdi TA, Amin B (2020) Optoelectronic and photocatalytic applications of hBP-XYM ( $M = Mo, W; (X \neq Y) = S, Se, Te$ ) van der Waals heterostructures. *Phys Chem Chem Phys* 22(40):23028–23037. <https://doi.org/10.1039/d0cp03926h>
21. Liu Y, Bhattarai P, Dai Z, Chen X (2019) Photothermal therapy and photoacoustic imaging: via nanotheranostics in fighting cancer. *Chem Soc Rev* 48(7):2053–2108. <https://doi.org/10.1039/c8cs00618k>
22. Shahzad F, Iqbal A, Kim H, Koo CM (2020) 2D transition metal carbides (MXenes): applications as an electrically conducting material. *Adv Mater* 32(51):1–23. <https://doi.org/10.1002/adma.202002159>
23. Gao L, Bao W, Kuklin AV, Mei S, Zhang H, Ågren H (2021) Hetero-MXenes: theory, synthesis, and emerging applications. *Adv Mater* 33(10):1–43. <https://doi.org/10.1002/adma.202004129>
24. Pang J et al (2019) Applications of 2D MXenes in energy conversion and storage systems. *Chem Soc Rev* 48(1):72–133. <https://doi.org/10.1039/c8cs00324f>
25. Jiang X et al (2020) Two-dimensional MXenes: from morphological to optical, electric, and magnetic properties and applications. *Phys Rep* 848:1–58. <https://doi.org/10.1016/j.physrep.2019.12.006>
26. Zhu Q, Li J, Simon P, Xu B (2021) Two-dimensional MXenes for electrochemical capacitor applications: progress, challenges and perspectives. *Energy Storage Mater* 35:630–660. <https://doi.org/10.1016/j.ensm.2020.11.035>
27. Sun Y et al (2019) 2D MXenes as co-catalysts in photocatalysis: synthetic methods. *Nano-Micro Lett* 11(1). <https://doi.org/10.1007/s40820-019-0309-6>
28. Prasad C et al (2020) Recent advances in MXenes supported semiconductors based photocatalysts: Properties, synthesis and photocatalytic applications. *J Ind Eng Chem* 85:1–33. <https://doi.org/10.1016/j.jiec.2019.12.003>

29. Wu Y, Sun Y, Zheng J, Rong J, Li H, Niu L (2021) MXenes: advanced materials in potassium ion batteries. *Chem Eng J* 404:126565. <https://doi.org/10.1016/j.cej.2020.126565>
30. Lin H, Chen Y, Shi J (2018) Insights into 2D MXenes for versatile biomedical applications: current advances and challenges ahead. *Adv Sci* 5(10). <https://doi.org/10.1002/adv.201800518>
31. Zhang T, Wang H, Zhao J (2019) Heterostructures of doped graphene and MoX<sub>2</sub> (X = S and Se) as promising anchoring materials for lithium-sulfur batteries: a first-principles study. *New J Chem* 43(24):9396–9402. <https://doi.org/10.1039/c9nj02065a>
32. Zhang H, Yang G, Zuo X, Tang H, Yang Q, Li G (2016) Computational studies on the structural, electronic and optical properties of graphene-like MXenes (M<sub>2</sub>CT<sub>2</sub>, M = Ti, Zr, Hf; T = O, F, OH) and their potential applications as visible-light driven photocatalysts. *J Mater Chem A* 4(33):12913–12920. <https://doi.org/10.1039/c6ta04628b>
33. Khazaei M, Mishra A, Venkataramanan NS, Singh AK, Yunoki S (2019) Recent advances in MXenes: from fundamentals to applications. *Curr Opin Solid State Mater Sci* 23(3):164–178. <https://doi.org/10.1016/j.cossms.2019.01.002>
34. Abergel DSL, Apalkov V, Berashevich J, Ziegler K, Chakraborty T (2010) Properties of graphene: a theoretical perspective. *Adv Phys* 59(4):261–482. <https://doi.org/10.1080/00018732.2010.487978>
35. Xin M, Li J, Ma Z, Pan L, Shi Y (2020) MXenes and Their applications in wearable sensors. *Front Chem* 8(April):1–14. <https://doi.org/10.3389/fchem.2020.00297>
36. Zhang K et al (2021) Insights into different dimensional MXenes for photocatalysis. *Chem Eng J* 424(April):130340. <https://doi.org/10.1016/j.cej.2021.130340>
37. Mallakpour S, Behranvand V, Hussain CM (2021) MXenes-based materials: structure, synthesis, and various applications. *Ceram Int* 47(19):26585–26597. <https://doi.org/10.1016/j.ceramint.2021.06.107>
38. Yin L et al (2021) MXenes for solar cells. *Nano-Micro Lett* 13(1):1–17. <https://doi.org/10.1007/s40820-021-00604-8>
39. Chirica IM, Mirea AG, Neațu Ș, Florea M, Barsoum MW, Neațu F (2021) Applications of MAX phases and MXenes as catalysts. *J Mater Chem A* 9(35):19589–19612. <https://doi.org/10.1039/d1ta04097a>
40. Hemanth NR, Kim T, Kim B, Jadhav AH, Lee K, Chaudhari NK (2021) Transition metal dichalcogenide-decorated MXenes: promising hybrid electrodes for energy storage and conversion applications. *Mater Chem Front* 5(8):3298–3321. <https://doi.org/10.1039/d1qm00035g>
41. Pu JH et al (2019) Multilayer structured AgNW/WPU-MXene fiber strain sensors with ultrahigh sensitivity and a wide operating range for wearable monitoring and healthcare. *J Mater Chem A* 7(26):15913–15923. <https://doi.org/10.1039/c9ta04352g>
42. Huang K et al (2020) Photocatalytic applications of two-dimensional Ti<sub>3</sub>C<sub>2</sub>MXenes: a review. *ACS Appl Nano Mater* 3(10):9581–9603. <https://doi.org/10.1021/acsnm.0c02481>
43. Zhang YZ et al (2020) MXene hydrogels: fundamentals and applications. *Chem Soc Rev* 49(20):7229–7251. <https://doi.org/10.1039/d0cs00022a>
44. Khan R, Andreescu S (2020) Mxenes-based bioanalytical sensors: design, characterization, and applications. *Sensors (Switzerland)* 20(18):1–19. <https://doi.org/10.3390/s20185434>
45. Chaudhari NK, Jin H, Kim B, San Baek D, Joo SH, Lee K (2017) MXene: an emerging two-dimensional material for future energy conversion and storage applications. *J Mater Chem A* 5(47):24564–24579. <https://doi.org/10.1039/c7ta09094c>
46. Tunesi MM, Soomro RA, Han X, Zhu Q, Wei Y, Xu B (2021) Application of MXenes in environmental remediation technologies. *Nano Converg* 8(1). <https://doi.org/10.1186/s40580-021-00255-w>
47. Khazaei M, Mishra A, Venkataramanan NS, Singh AK, Yunoki S (2019) Recent advances in MXenes: from fundamentals to applications. *Curr Opinion Solid State Mater Sci*

# Synthesis of Five-Membered Heterocyclic Compounds and Their Anticorrosive, Thermal, Electron Transfer, and Biological Properties



Archana Thakur and Anam Ansari

**Abstract** In organic science, heterocyclic compounds are considered the biggest family of organic chemicals. The role of heterocyclic compounds in our daily lives is critical. In medicinal chemistry and agrochemicals, it has a wide range of uses. Developers, corrosion inhibitors, sanitizers, copolymers, antioxidants, and dyestuff all use it. The importance of an efficient process for synthesizing novel heterocycle moiety cannot be overstated. According to a literature review, more than 85–95% of novel medications contain heterocycles, providing valuable scientific insight into the biological system. I concentrated on five-membered heterocyclic compounds in my review. The current article review discusses the extremely active heterocyclic compounds which demonstrate antifungal, anti-inflammatory, antibacterial, antidepressant, antiulcer, anthelmintic, anticorrosive, thermal, and electron-transfer properties.

**Keywords** Heterocycles · Anticorrosive · Imidazole · Furans · Electron-transfer

## 1 Introduction

Medicinal chemistry is considered a chemical subfield particularly related to determining the effects of chemical structure on biological activity. It arose from an empirical strategy that involves the chemical-free synthesis of new compounds mainly based on structural modification, followed by testing of biological activity. The Medicinal Chemistry branch refers to the finding, expansion, interpretation, and recognition of physiologically active chemical mechanisms of action at the molecular level. The study of heterocyclic molecules is crucial to medical chemistry. Heterocyclic chemistry is the most challenging branch of chemistry. Its industrial and

---

A. Thakur · A. Ansari (✉)

Department of Chemistry, University Institute of Sciences, Chandigarh University, Gharuan, Punjab, India

e-mail: [anam.e11775@cumail.in](mailto:anam.e11775@cumail.in)

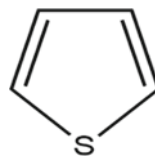
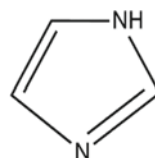
medical consequences, as well as the variety of its synthetic technique and theoretical implications, are all intriguing. Synthetic heterocyclic chemistry has a significant impact on every aspect of human life, with applications in agriculture, health, polymers, and a variety of industries. Anticonvulsants, hypnotics, anti-neoplastic, antiseptics, antihistaminic, antiviral, anti-tumor, and other synthetic heterocyclic compounds are utilized as drugs. Every year, pharmacopeia introduces a considerable number of heterocyclic medications. The physicochemical features of the mother scaffold were greatly influenced by the length and types of ring structures, as well as the required alternate groups. Heterocyclic compounds play an important function in medicine as antiviral, antibacterial, anti-inflammatory, antifungal, and anti-tumor medications, among other things. The broad uses of heterocycles are as numerous as they are diverse, and they are far from the range of this review. Alkaloids are determined as a form of natural-appearing heterocyclic chemicals that have several ranges of biological actions. The majority of alkaloids have basic nitrogen atoms. Organic synthetic techniques based on heterocyclic chemistry have lately evolved as successful approaches for chemists to make a useful large number of molecules and chemicals. Economic reasons are affecting their strategy, as seen by higher reaction yield and sterility, but also here, the environmental factors are becoming more relevant.

Heterocyclic compounds are a large family of chemicals that make up more than fifty percent of all called organic compounds. A carbocyclic substance is an organic cyclic compound in which the carbon atoms are completely arranged in rings. On the other hand, in heterocyclic compounds, other than the carbon at least one element is present in the ring configuration. The constant heteroatoms are oxygen, sulfur, and nitrogen, apart from this, the heterocyclic rings which have extra heteroatoms are also popular [1].

There are mainly two types of heterocyclic compounds, the first is called aliphatic heterocyclic compounds, and the other is known as aromatic heterocyclic compounds. The cyclic analogs of ethers, thioethers, amides, amines, and other aliphatic heterocycles are known as aliphatic heterocycles. The qualities have mainly impacted the result of the ring's tension. Such compounds frequently contain both small (3 and 4-membered) and common (5 to 7-membered) ring structures. On the other hand, in aromatic heterocyclic compounds, the heteroatom is present in the ring, and in many ways, the characteristics of the complaint can be compared to benzene. DNA and RNA, chlorophyll, hemoglobin, vitamins, and a variety of other biological substances contain them. Heterocyclic compounds, which have one to three heteroatoms in their nucleus, are essential for all live cells' metabolism [2].

Thiophene is considered one of the most important five-membered heterocyclic compounds (Scheme 1). Thiophene is a heterocyclic molecule with the formula  $C_4H_4S$ , which has a five-membered ring with one sulfur as a heteroatom. Petroleum and coal both contain thiophene and its compounds. Thiophene is derived from the Greek words *theion*, which means sulfur, and *phaino*, which means shining. Thiophene's structure can be found in various natural compounds, as well as in a variety of pharmacologically active substances. Thiophene derivatives are well-known in medicinal chemistry for their therapeutic uses. Simple thiophenes are stable liquids



**Scheme 1** Thiophene**Scheme 2** Imidazole

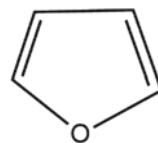
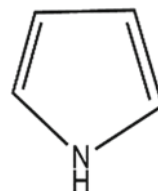
that, in terms of boiling point and even smell, are quite similar to their benzene counterparts. They are in distillates of coal tar. One of the most well-known instances in organic chemistry involved the discovery of thiophene in coal tar benzene. Thiophene was detected in benzene as a contaminant. When isatin (1H-indole-2, 3-Dione) is combined with sulfuric acid and crude benzene, it produces a blue dye. Victor Meyer was successful in isolating the chemical that caused this reaction. Thiophene was discovered to be a heterocyclic chemical.

Another important five-membered heterocyclic compound is imidazole. Imidazoles are essential heterocyclic compounds that have important properties in a variety of medicines (Scheme 2). Imidazole is a planar ring molecule with five members that dissolves in both polar solvents and water. Due to the fact that any one of the two nitrogen atoms can accept a hydrogen atom, hence it usually appears in mainly 2 standard tautomeric forms. A computed dipole moment of 3.61D indicates that it is a polar molecule. An imidazole molecule is classified as aromatic if it has a sextet of electrons, each of which is built of electron pairs on the nitrogen atom. Because imidazole is amphoteric, it has the ability to act both as an acid and a base.

Anticancer, antifungal, antimalarial, anti-inflammatory, and antibacterial capabilities are among the properties of imidazoles. In order to boost their activity, researchers are still working on improving imidazole moiety synthesis and functionalization at various locations. Harsh conditions, numerous name reactions, multicomponent reactions, and the usage of base and acid of Lewis, free from metal conditions, expensive transition metal catalysts, or insolvent environments are all examples of these procedures.

Furan is another five-membered heterocyclic compound (Scheme 3). Furan is a monocyclic heteroarene with the formula  $C_4H_4O$  with a five-membered ring having four carbons and one oxygen. It is a volatile, toxic, liquid that is colorless and has a boiling point below  $31\text{ }^\circ\text{C}$ . It functions as a carcinogen, a hepatotoxic agent, and a result of the Maillard reaction. It is a monocyclic heteroarene with a mancude organic heteromonocyclic parent. It belongs to the furan family.

Pyrrole is a heterocyclic chemical molecule that is made of mainly 4 carbon atoms as well as 1 nitrogen atom and forms a ring structure (Scheme 4). In the

**Scheme 3** Furan**Scheme 4** Pyrrole

pyrrole family, the pyrrole is considered a basic part with  $C_4H_5N$  as its chemical formula. In amino acids proline and the hydroxyproline, the pyrrole ring system is mainly found, also it can be found in some colored natural products like chlorophyll and heme (a component of hemoglobin). The pyrrole molecules are also present in alkaloids, which is a huge group of alkaline organic nitrogen compounds mainly made by trees.

## 1.1 History

Along with the growth of organic chemistry, in the 1800s, heterocyclic chemistry originated. The following are a few important developments:

- In 1818, alloxan is isolated from uric acid by Brugnatelli.
- In 1832, Dobereiner combines starch with sulfuric acid to produce furfural (a furan).
- In 1834, Runge produces pyrrole through bone dry distillation (“fiery oil”).
- Friedlander invented indigo dye in 1906, which gave permission to synthetic chemistry to move ahead of many agricultural companies.
- In 1936, Treibs discovers the biological origins of petroleum by synthesizing chlorophyll derivatives from crude oil.
- In the genetic code, Chargaff’s 1951 guidelines are applied to explain the importance of heterocyclic compounds (pyrimidines and purine bases).

## 2 Anticorrosive Activity

Prevention of corrosion is a very significant issue for the industry as well as society at large. Many compounds have been investigated for their anticorrosive properties. No wonder organic compounds are also emerging in this as an important anticorrosive agent. They can donate electrons to unoccupied orbitals of a metal surface or to adsorption sites in the surface of an oxide/passive film to form coordinate covalent bonds or may also accept free electrons from the metal surface by using their antibonding orbitals are generally good corrosion inhibitors. Recently, many researchers have studied several five-membered heterocycles including imidazole, an imidazole derivative, and thiophene as inhibitors of metal corrosion and shown good inhibition efficiency.

Al-Najjar and Al-Baitai synthesized a novel Schiff-based imidazole derivative which acts as a corrosion inhibitor for carbon steel in an acidic medium. As carbon steel is one of the most important industrial materials having several applications, and its protection is of high significance. The authors describe that the synthesized compound was tested as an inhibitor in controlling the corrosion of carbon steel in 0.1 M hydrochloric acid solution by using open circuit potential. The results from both experimental and theoretical analysis showed that the synthesized compound can be considered as an effective inhibitor of carbon steel. The inhibition efficiency (IE%) was increased with increasing the concentrations, but it decreased with rising the solution temperature and the maximum [3]. Guo et al. reported a computational study of thiophene derivatives as anticorrosive agents against iron [4].

## 3 Thermal and Electron-Transfer Properties

The knowledge of the thermodynamic properties of heterocyclic compounds enables a better understanding of their chemical behavior and, consequently, leads to an important background for the future development of their practical applications. Freitas et al. used a number of experimental methods, namely calorimetric and effusion techniques, namely static and rotating bomb combustion calorimetry, vacuum sublimation/vaporization drop micro calorimetry, and Knudsen effusion methods, to derive reliable thermodynamic values for the several five-membered heterocyclic compounds [5]. This study allowed the characterization of the structural and energetic properties of a set of heterocyclic compounds. Villar et al. reported ab initio SCF molecular calculations for five-membered heterocycles, such as pyrrole, furan, and thiophene and analyzed their electronic structure. The bandgap is found to follow a direct relationship with the ionization potential of the heteroatom which indeed plays a primary role in the position of the LUMO [6]. Hildebrandt and Lang reported electron-transfer studies of five-membered heterocyclic compounds conjugated with ferrocenyl units. By comparing, for example, ferrocenyl thiophenes featuring all possible substitution patterns, it could be shown that ferrocenyl groups in positions

2 and 5 of the heterocyclic core interact more strongly with each other than with ferrocenyls in positions 3 and 4. Furthermore, it could be shown electron-rich heterocycles tend to show enhanced electron transfer, in comparison with electron-poor connecting units [7].

## 4 Biological Activity

The majority of natural ingredients, vitamins, and biologically active substances contain heterocycles, as do anticancer, anti-HIV, antibiotic, antidepressant, insecticidal agents, antimalarial, antibacterial, antifungal, antiviral, antidiabetic, herbicidal, and antidepressant. In medical chemistry and agriculture, they are found as a common structural unit.

### 4.1 Antifungal Activity

Microorganisms called fungi are heterotrophic that do not have the capacity to photosynthesize. Posaconazole is an antifungal medication that belongs to the triazole family. It is effective against candida, aspergillus, and zygomycetes germs. Fluconazole, isavuconazole, hexaconazole, epoxiconazole, difenoconazole, tebuconazole, and other indole derivatives and triazole compounds are employed as fungicides [8].

### 4.2 Anti-inflammatory Activity

The capacity of a drug to reduce inflammation is referred to as anti-inflammatory. Anti-inflammatory medications account for nearly half of all analgesics, and they relieve pain by lowering inflammation while having little effect on the central nervous system. Anti-inflammatory properties have been discovered in pyrido [2, 3,—d] pyrimidinone derivatives. Triazine derivatives have anti-inflammatory properties as well [9].

### 4.3 Antiulcer Activity

Antiulcer drugs work by reducing the excess acidity in the stomach, which causes ulcers to develop. Omeprazole and other substituted benzimidazole compounds have antisecretory and hence antiulcerative properties in the stomach. Several omeprazole equivalents, such as lansoprazole and pantoprazole, have been launched recently [10].

#### ***4.4 Antibacterial Activity***

Bacteria are the simplest and tiniest unicellular creatures that can be found in groups or singly. The medicinal chemist aiming to synthesize novel antibacterial medicines has stiff competition from a huge number of worthy, and generally, non-toxic medications are found for the cure of bacterial infections. Antibacterial activity has been discovered in several triazine derivatives [11].

#### ***4.5 Antimalarial Activity***

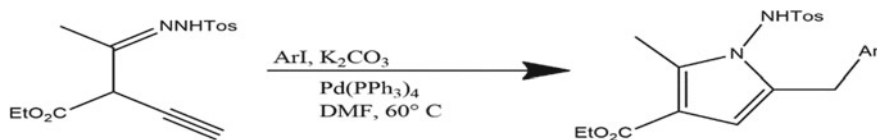
Malaria affects a substantial portion of the world's population. Quinine, chloroquine, and primaquine are recognized for their increased antimalarial activity and lesser toxicity [12].

#### ***4.6 Antidepressants***

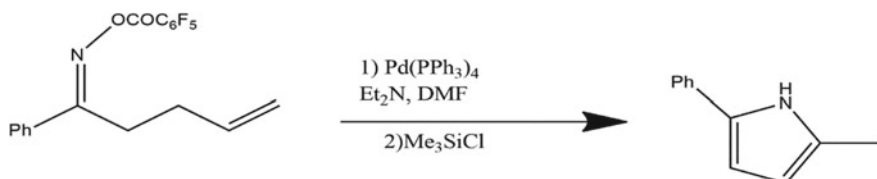
Antidepressants are psychiatric medications that help people with mood disorders such as serious depression. Paroxetine and reboxetine are antidepressants with a heterocyclic moiety. Antidepressant effects can be seen in some piperidine and pyrimidine compounds. Antidepressant action has been demonstrated in a range of small molecule nano-peptide heterocyclic [13].

#### ***4.7 Anticancer Activity***

The anticancer word describes a set of illnesses caused by many factors such as chemical compounds and radiant light. Cancer is defined as the unregulated and abnormal division of cells that results in tumors and invasion of normal tissue in varying degrees of malignancy. These medicines are used to treat cancer by either killing or modifying the development of cancer cells. Anticancer medications have long been interested in compounds that alkylated DNA. Quinazolines and pyrimidine derivatives of various kinds have anticancer properties [14].



**Scheme 5** Synthesis of pyrrole



**Scheme 6** Synthesis of pyrrole derivatives

## 5 Synthesis

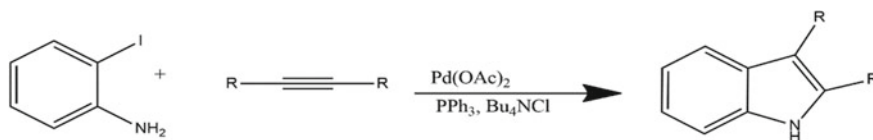
### 5.1 Preparation of Pyrroles

Sonogashira coupling of an alkyne chain containing a tosyl hydrazone with aryl iodides led to 2-benzyl substituted pyrroles in 40–70% of the cases; not in the presence of aryl iodide, 2-methyl substituted pyrroles were generated (Scheme 5) [15].

$\text{Pd}(\text{PPh}_3)_4$  catalyzed olefinic moiety of Heck-type animation to produce substituted pyrroles from, unsaturated ketone O-pentafluorobenzoyloximes (Scheme 6) [16].

### 5.2 Synthesis of Indoles and Other Nitrogen-Containing Heterocycles

The utility of the nucleus in numerous physiologically active chemicals has made the synthesis of indole the most frequently investigated topic in this series. Different cyclization strategies can be used to make palladium-catalyzed indole synthesis. Some will make indoles right away from the accurate initial material, while the rest will need to make the requisite initial ingredients first. A first coupling reaction is typically used for this. First, the single-step approach to the indole nucleus will be described. Ortho-halo-anilines or their analogs, such as triflates, were used to begin the synthesis. Amides might be used to preserve the amines, or an alkyl group could be replaced. Larock et al. disclosed an effective process for preparing indoles in 1991, which used palladium-catalyzed oxidation. Larock et al., in 1991 introduced a Palladium-catalyzed heteroannulation of internal alkynes with o-iodoanilines method



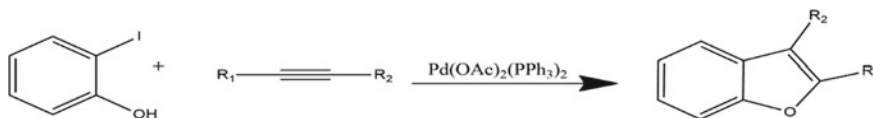
**Scheme 7** Synthesis of pyrrole derivatives from alkynes

for making indoles (Scheme 7). With the presence of unsymmetrical alkynes, the cyclization was regioselective [17].

### 5.3 Synthesis of Compounds Containing Benso[b] Furans and Oxygen

The o-indophenol is used to make benzofurans in a single-step procedure which is opposite to o-iodoanilines. Arcadi et al. [18] employed Pd (OAc)<sub>2</sub>(PPh<sub>3</sub>)<sub>2</sub> and CuI to create a 25–88% yield from 2-iodophenols variably substituted benzofurans and acetylenic derivatives (R<sub>2</sub> = H) [18]. The method was extended to the compound of furo[3, 2-b] pyridines. Kundu et al. switched palladium dichloride, CuI, and Et<sub>3</sub>N into a base and were able to make benzofuran derivatives [19]. A thorough analysis of this heteroannulation was published afterward [20]. For the synthesis of 2-substituted benzofurans solid phase, by using an ester function on the 5-carboxylic acid, the iodophenol was attached to a resin (Scheme 8) [21]. Internal alkynes were used for the condensation of benzofurans, which proved to be more challenging than the indole synthesis. Higher temperatures were required, regioselectivity was diminished, and it was restricted to alkynes with inhibited carboxy, silyl, and aryl groups [22].

One-pot coupling strategy of a multicomponent was used to make 2,3-disubstituted benzofurans, which included first deprotonating a combination of both a terminal alkyne and o-iodophenol alkyne and, then coupling with palladium, and at last, it reacts with the alkenyl triflates or aryl iodide [23]. In the same article, an example of indole derivative synthesis was presented. At the time when the reaction takes place in the existence of carbon monoxide in the final step, the 3-acyl derivative was produced. O-indophenol and terminal alkynes underwent the same research as indole synthesis using microwave activation and KF/Al<sub>2</sub>O<sub>3</sub> [24]. The yields, in this case, varied from fair to outstanding.

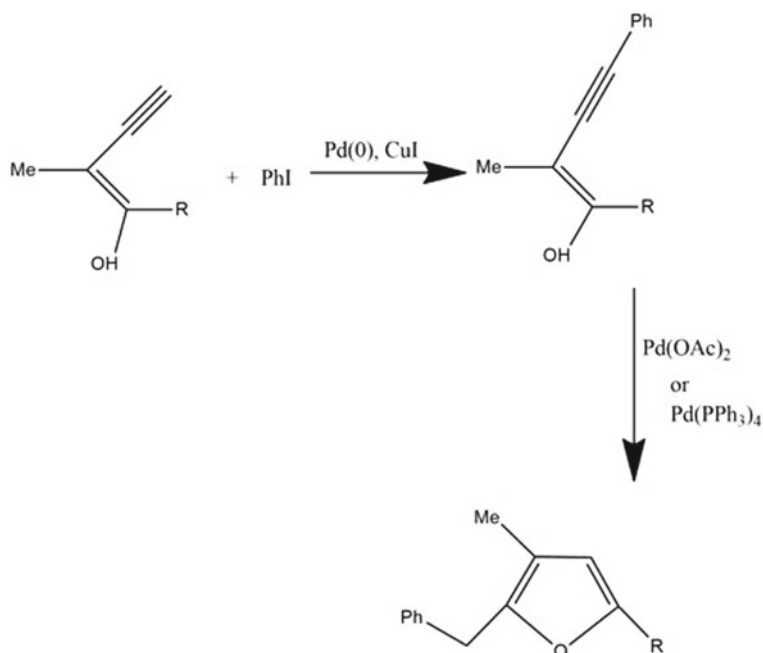


**Scheme 8** Synthesis of indole derivatives

## 5.4 Synthesis of Furans

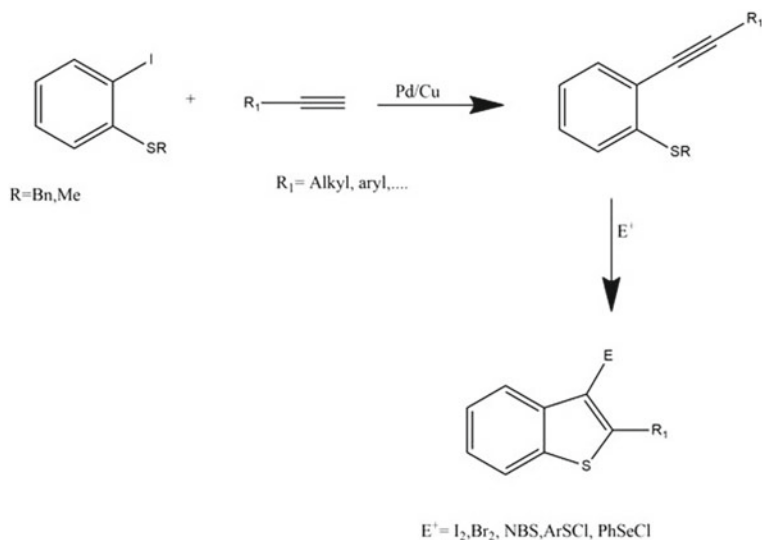
In the class of starting material, the Alkynyl substituted allylic alcohols are important for the furans synthesis. The alcohols were made by combining both Iodoalkenes or terminal alkynes with copper iodide and Pd (0) and the suitable aryl iodide, or terminal alkynes. The produced allylic alcohols were cyclized using a variety of palladium catalysts (Scheme 9) [25–27].

Balme and colleagues proposed a two-step synthesis pathway to furans. On the basis of 3 component reaction where intermediate tetrahydrofuran derivative is raised with an additional conjugate, as well as palladium coupling, which was also decarboxylated to make trisubstituted furan [27]. Apart from this, the reaction can also be conducted in a two-step one-pot method, with the interposed being cyclized immediately to produce the actual products, yielding similar results to the previous example (40–60% compared to 45–65%).



**Scheme 9** Synthesis of furan





**Scheme 10** Synthesis of thiophene derivatives

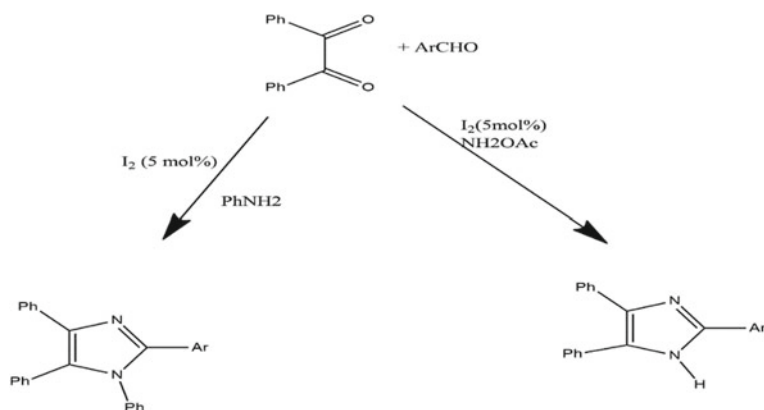
### 5.5 Synthesis of Benzo[b]Thiophenes

For the benzo[b]thiophenes synthesis, the Palladium-catalyzed techniques have received little attention, owing to palladium's incompatibility with sulfur-containing compounds. In the indicated synthesis, electrophilic substitution on o-alkynylthiophenoethers was performed via Sonogashira coupling of o-iodothiophenoethers with terminal alkynes.

Flynn et al. [28] used a palladium-catalyzed for the o-iodobromobenzene coupling with benzyl thiol to make the benzyl thioether. The iodo-compound was formed by cyclizing with iodine, and it was employed in the following coupling procedure to insert aryl substituents (Scheme 10). The cyclization conditions were expanded by LaRock and Yue to other electrophiles, allowing for alternative replacements in the three locations [29]. It should be noted that when bromine was used to cyclize a trimethylsilyl derivative ( $R_1 = \text{SiMe}_3$ ), the result was 2,3-dibromobenzo[b]thiophene.

### 5.6 Synthesis of Imidazole

M. Kidwai and colleagues in 1991 created a one-pot multicomponent tri- and tetra-substituted imidazole with the help of using a catalyst molecular iodine substituted nitrogen sources (a diketo system, ammonium acetate, and substituted aldehyde) as well as a substituted amine as a nitrogen source. They proposed a procedure in

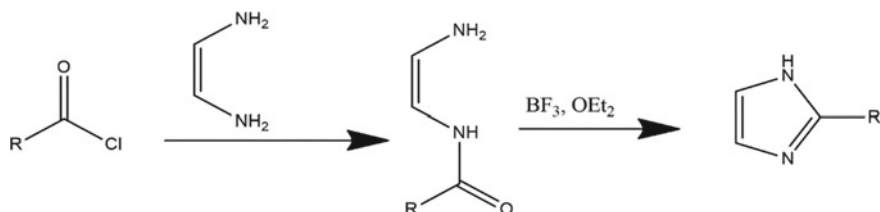


**Scheme 11** Synthesis of imidazole derivatives

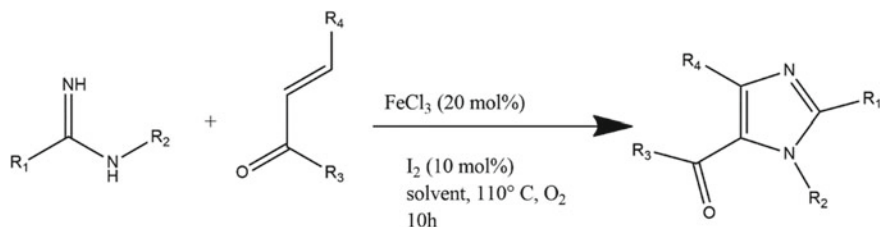
which to activate the parent diketone carbonyl system the iodine serves as a gentle Lewis acid, apart from this, iodine also initiates the making of a diamine intermediate, which leads to the production of iso-imidazole, then dehydration, and at last the sigma topic rearrangement, which leads to the production of imidazole (Scheme 11) [30].

S. Sharma and colleagues synthesized *N*-acyl-1,2-ethylenediamine derivatives in 2008 by substituting imidazole for ethylenediamine as well as acid chloride for ethylenediamine at 0 °C in a non-polar solvent, dry dioxane, and stirring at room temperature, followed by the insertion of effective Lewis acid trifluoroboronetherate (Scheme 12). This study, the acid chloride-containing long-chain alkyl group, is not commercially present. This was achieved by fabricating hydroxyl olefinic and olefinic long acids chains in situ [31].

In 2015, Jianli Li and colleagues used a  $\text{FeCl}_3/\text{I}_2$ -catalyzed aerobic oxidative coupling procedure to make an easy and useful method for producing tetra-substituted imidazoles with amidines and chalcones (Scheme 13). With a higher tolerance for functional groups and moderate reaction conditions, this reaction is highly regioselective [32].



**Scheme 12** Synthesis of imidazole from acid chloride



**Scheme 13** Synthesis of imidazole derivatives unsaturated ketone

## 6 Conclusions

Heterocyclic compounds are a type of organic compounds that can be seen in many natural products as well as medications. The heterocyclic nucleus is a major structural component in anti-microbial, antiviral, anti-cancerous, antihypertensive, anti-malarial, antidepressant, anthelmintic, anti-inflammatory, and other drugs categories. The five-membered heterocyclic compounds have also found there used as anticorrosive and electron-transfer agents. Thermal properties and band gap properties help in the evaluation of further application of these compounds.

Heterocycles are ubiquitous in biological and pharmacological substances, and research shows that heterocyclic synthesis is becoming more popular. The majority of the reactions mentioned here have paved the way for the low-cost production of several synthetically valuable chemicals, such as active biomolecules. The advantages of the reactions of multicomponent, like the capacity to integrate numerous reaction steps into a one-operation and the insertion of many reactive functionalities into molecules in lesser stages, involve simplified and accelerated complex heterocycles synthesis. With the combination of both reactive and worthy functional groups, these methods permit better transformation. The majority of the approaches presented here have substantial advantages, such as moderate reaction conditions, a good economy of the atom, and more tolerance of the functional group. Apart from the synthesis, their biological, anticorrosive, and thermal and electron-transfer properties are mentioned with the intention that the application of these five-membered compounds would shed a light on to why the synthesis is important. We hope that the present review will encourage and help the research community to further enhance the synthetic methodology of these compounds with a wide range of applications based upon our little contribution to the whole ocean of knowledge about the heterocyclic compounds.

**Acknowledgements** I am thankful to Dr. Atul Pratap Singh for providing me with the opportunity to write this paper and to support me in all aspects to complete my goal. Major support from Chandigarh University and faculty to help me.

## References

1. Katritzky A (1985) *R. Handbook of heterocyclic chemistry*. Pergamon Press, New York
2. Mauras N, Bishop K, Merinbaum D, Emeribe U, Agbo F, Lowe E (2009) *J Clin Endocrinol Metab* 94(8):2975–2978
3. Al-Najjar S, Al-Baitai A (2022) Synthesized of novel imidazole-derived Schiff Base as a corrosion inhibitor of carbon steel in acidic medium supported by electrochemical and DFT studies. *Phys Chem Res* 10(2):179–194
4. Guo L, Safi ZS, Kaya S, Shi W, Tüzün B, Altunay N, Kaya C (2018) Anticorrosive effects of some thiophene derivatives against the corrosion of iron: a computational study. *Front Chem* 6:155
5. Freitas VLS, Ribeiro da Silva MDMC (2015) Oxygen and sulfur heterocyclic compounds. *J Therm Anal Calorim* 121:1059–1071
6. Spassova M, Enchev V (2004) Ab initio investigation of the structure and nonlinear optical properties of five-membered heterocycles containing sulfur. *Chem Phys* 11:1–4
7. Hildebrandt A, Lang H (2013) (Multi) Ferrocenyl five-membered heterocycles: excellent connecting units for electron transfer studies. *Organometallic* 32(20):5640–5653
8. Chen Q, Zhu X-L, Jiang L-L, Liu Z-M, Yang G-F (2008) Synthesis, antifungal activity and CoMFA analysis of novel 1,2,4-triazolo[1,5-a] pyrimidine derivatives. *Eur J Med Chem* 43(3):595–603
9. Erhan P, Şahin G, Pelin K (2001) Synthesis and anti-inflammatory activity of 1-acylthiosemicarbazides, 1,3,4-oxadiazoles, 1,3,4-thiadiazoles and 1,2,4-triazole-3-thiones. *II Farmaco* 57(2):101–107
10. Zhao WG, Chen HS, Li ZM, Han YF, Yan H, Lai JY, Wang SH (2001) Synthesis of pyrazolyl-heterocycles and their activities. *Chin J Chem* 22:939–942
11. Srinivas K, Srinivas U, Bhanuprakash K, Harakishore K (2006) Synthesis and antibacterial activity of various substituted s-triazines. *Eur J Med Chem* 41:1240–1246
12. Chen HS, Li ZM, Li JF (2000) Synthesis of 2-pyrazoyl-5-substituted-1,3,4-oxadiazoles and their biological activities. *Chem J Chin Univ* 21:1520–1523
13. Chin YW, Balunas MJ, Chai HB, Kinghorn AD (2006) Drug discovery from natural sources. *AAPS J* 8(2):239–253
14. Ahmed AS, Hamdy RM, Nadia MM (2006) Novel 5-(2 hydroxyphenyl)-3- substituted-2,3-dihydro-1,3,4-oxadiazole-2-thione derivatives: promising anticancer agents. *Bioorg Med Chem* 14:1236–1246
15. Arcadi A, Anarcordio R, D'Anniballe G, Gentile M (1997) Synthesis of 1,2,3,5-substituted pyrroles through palladium-catalyzed reaction of ethyl 2-acetyl-4-pentynoate tosylhydrazone with aryl iodides. *Synlett* 11:1315–1317
16. Tsutsui H, Narasaka K (1999) Synthesis of pyrrole derivatives by the heck-type cyclization of  $\gamma,\delta$ -unsaturated ketone-pentafluorobenzoyloximes. *Chem Lett* 28(1):45–46
17. Larock RC, Yum EK (1991) Synthesis of indoles via palladium-catalyzed heteroannulation of internal alkynes. *J Am Chem Soc* 113(17):6689–6690
18. Arcadi A, Marinelli F, Cacchi S (1986) Palladium-catalyzed reaction of 2-hydroxyaryl and hydroxyheteroaryl halides with 1-alkynes: an improved route to the benzo[b]furan ring system. *Synthesis* 9:749–751
19. Kundu NG, Pal M, Mahanty JS, Dasgupta SK (1992) Palladium-catalysed heteroannulation of acetylenic compounds: a facile method for the synthesis of benzofurans. *J Chem Soc Chem Comm* 1:41–42
20. Kundu NG, Pal M, Mahanty JS, De M (1997) Palladium-catalysed heteroannulation with acetylenic compounds: synthesis of benzofurans. *J Chem Soc Perkin Trans* 1, 19, 2815–2820
21. Fancelli D, Fagnola MC, Severino D, Bedeschi A (1997) Solid phase synthesis of 2-substituted benzofurans via the palladium-catalysed heteroannulation of acetylenes. *Tetrahedron Lett* 38:2311–2314
22. Larock CR, Yum EK, Doty MJ, Sham KKC (1995) *J Org Chem* 60:3270

23. Chaplin JH, Flynn BL (2000) Palladium-catalysed C-X bond formations. *J Chem Soc Chem Comm* 17:1594
24. Kabalka GW, Lei W, Pagni RM (2001) Sonogashira coupling and cyclization reactions on alumina: a route to aryl alkynes, 2-substituted-benzo[b]furans and 2-substituted-indoles. *Tetrahedron* 57:8017
25. Sellier B, Bruneau C, Dixneuf P (1995) Synthesis of furans by cyclization of 2-En-4-yn-1-ols in the presence of ruthenium and palladium catalysts. *Tetrahedron* 51:13089
26. Qing F-L, Gao W-Z, Ying J (2000) Synthesis of 3-trifluoroethylfurans by palladium-catalyzed cyclization—isomerization of (Z)-2-alkynyl-3-trifluoromethyl allylic alcohols. *J Org Chem* 65:2003–2006
27. Garçon S, Vassiliou S, Cavicchioli M, Hartmann B, Monteiro N, Balme G (2001) An effective one-pot synthesis of 3-benzylfurans and their potential utility as versatile precursors of 3,4-dibenzyltetrahydrofuran Lignans. Formal synthesis of (±)-Burseran. *J Org Chem* 66:4069–4073
28. Flynn BL, Verdier-Pinard P, Hamel E (2001) A novel palladium-mediated coupling approach to 2,3-disubstituted benzo[b]thiophenes and its application to the synthesis of tubulin binding agents. *Org Lett* 3:651–654
29. Larock RC, Yue D (2001) Synthesis of benzo[b]thiophenes by electrophilic cyclization. *Tetrahedron Lett* 42(35):6011–6013
30. Kidwai M, Mothsra P, Bansal V, Somvanshi RK, Ethayathulla AS, Dey S, Singh TP (2007) One-pot synthesis of highly substituted imidazoles using molecular iodine: a versatile catalyst. *J Mol Catal A* 265:177–182
31. Sharma S, Gangal S, Rauf A (2009) Convenient one-pot synthesis of novel 2-substituted benzimidazoles, tetrahydrobenzimidazoles and imidazoles and evaluation of their in vitro antibacterial and antifungal activities. *Eur J Med Chem* 44:1751–1757
32. Zhu Y, Li C, Zhang J, She M, Sun W, Wan K, Wang Y, Yin B, Liu P, Li JA (2015) Facile FeCl<sub>3</sub>/I<sub>2</sub>-catalyzed aerobic oxidative coupling reaction: synthesis of tetrasubstituted imidazoles from amidines and chalcones. *Org Lett* 17(15):3872–3875

# Optimization of Drilling Operation Using Work Material Al 7075 Alloy Reinforced with Boron Carbide



Sohail Akhtar and Imtiaz Ali Khan

**Abstract** In the present study, a metal matrix composite containing Al 7075 alloy and boron carbide (6% wt) was fabricated with the help of stir casting method. After the fabrication of the composite, the drilling operation was done on the conventional radial drilling machine, manufactured by Atlas Engineering Co. London. The dimensions of the work piece samples were 75 mm × 75 mm × 25 mm. The drill sizes were 5, 6.5, and 8.5 mm in diameter. The drills bits used were of HSS manufactured by Miranda Gold (India). Feed rate, speed, and drill bit diameter were chosen as process parameters. For the design of experiment, Taguchi's L9 orthogonal array was used with three level of factor. For finding out the optimum level of process parameters for multi-performance characteristics that is MRR and surface roughness, grey relational analysis was used. After optimization, it was found that the largest values of grey relational grade for feed rate, spindle speed, and drill diameter are at the level 740 rpm, 0.015 in/rev, and 5 mm, respectively. Hence, these are the recommended levels of process parameter when better MRR and optimum surface roughness have to be obtained simultaneously.

**Keywords** Metal matrix composite · Stir casting · Taguchi · MRR · Surface roughness · Grey relational analysis

## 1 Introduction

A composite material is made up of two or more than material but there these components are in different phases. Means if a composite is made up of two components  $X$  and  $Y$ , and we take a cross section of the composite, we can still distinguish between the material  $X$  and  $Y$ . But this is not in the case of alloys. The constituent

---

S. Akhtar (✉) · I. A. Khan

Department of Mechanical-Engineering, Zakir-Husain College of Engineering and Technology, Aligarh-Muslim University, Aligarh, India  
e-mail: [sohail3422@gmail.com](mailto:sohail3422@gmail.com)

I. A. Khan

e-mail: [iakhan.me@amu.ac.in](mailto:iakhan.me@amu.ac.in)

elements save their own characters implies they don't union or break up totally into each other in spite of the fact that they demonstration in show. Regularly, the constituents show an interface between each other and can be physically recognized. These days, composites are widely used in many fields and hence the ease of machining and good characteristic performance. To know the machining characteristic of a composite, one can perform a study taking a very common machining process (such as drilling) using composite. With the quickly developing advancements, quality and profitability are the significant concern. Profitability is worried about the material removal rate (MRR) during machining activity and quality alludes to the item attributes. So the quality and profitability can be improved through parameters optimization. There are number of examination works identified with different drilling parameters optimization for accomplishing the required value of performance characteristics. Among them, surface roughness and material removal rate (MRR) are the significant performance characteristics.

## 2 Literature Review

Rana and Lata [1], study was carried out in which basically drilling parameters were optimized for multi-performance characteristics of aluminium-based composite Al-MgO. Stir casting process was used to fabricate metal matrix composite. The composite base alloy was Al 5052 and reinforcement used was MgO. The parameters selected were feed, spindle speed, and drill diameter. These parameters were optimized by using genetic algorithm-based multi-performance characteristics which were temperature and burr height [2] played out the optimization of drilling procedure which was done on carbon fibre strengthened polymer (CFRP) utilizing different boring apparatus of width 0.70 mm, 0.80 mm, and 0.90 mm by Taguchi GRA. Feed rate, spindle speed, and drill diameter were taken as process parameters for micro-drilling process. The experimental design was decided by using Taguchi L27 orthogonal array. The performance parameters chosen were MRR and delamination factor [3]. Performed a study in which investigation of effect of different machining parameters such as feed, speed, and depth of cut on different performance parameters such as MRR, surface roughness, and thrust force was done for dry turning operation on AISI 304 austenitic stainless steel. Tool used was the ISO P30 grade uncoated cemented carbide inserts. Machining parameters chosen were  $V = 45, 35, 25$  m/min,  $f = 0.2, 0.15, 0.1$  mm/rev, and  $t = 1.00, 1.125, 1.50$  mm, and the design of the experiment adopted was L27 orthogonal array. Optimization of the parameters was performed using GRA approach [4]. In other study, the effects on tribological behaviour of Al 7075 composite of  $B_4C$  were identified. Al 7075- $B_4C$  composites were fabricated by casting process and various mechanical properties were tested, such as tensile strength, hardness flexural, and compression strength. The observations were made that by mechanical properties enhanced to some extent by the addition of reinforcement [5]. Presented a study in which optimization of nature of surface in drilling process was performed by using response surface method. In

**Table 1** Components of Al 7075 alloy

Elements	(Zn)	(Mg)	(Cu)	(Mn)	(Fe)	(Si)	(Cr)	(Ti)	(Al)
Weight-(%)	5.40	2.41	1.41	0.14	0.43	0.42	0.22	0.02	89.57

this study, by using the parameters such as spindle speed, feed, and drill diameters, the effects on surface roughness and nature of surface of drilled holes were found out. After the optimization, it was established that for the speed of 2000 rpm, feed of 78 mm/min, and drill diameter of 2.5 mm, the minimum surface roughness was found out to be 1.06 mm. It was also observed that surface roughness decreases by increasing feed rate, speed, and diameter. Hence feed rate, spindle speed, and depth of cut have collective effects on surface roughness [6–8].

### 3 Experimentation

#### 3.1 Raw Materials

Al alloy (Al 7075) was purchased online from a firm called Plus Metals, Mumbai, B<sub>4</sub>C makes CDH 150 mesh powder which was purchased from Gulmarg Materials, Aligarh.

##### Al Alloy

Base material in studies is Al 7075 because it has great strength and very important light weight properties. It has very prominent use in the aircraft and automobile industries [9]. The components present and the percentage is given in Table 1.

##### B<sub>4</sub>C Powder

B<sub>4</sub>C is a well-known material for its hardness, thermal properties, and strength. It has a density of about 2.52 g/cm<sup>3</sup> and hardness of HV = 78. It is becoming very popular as reinforcement for aluminium alloys. It provides various excellent properties to alloy that are impossible to get in a plain alloy.

#### 3.2 Work Piece Fabrication

##### Stir Casting Method

The reinforcing material used is boron carbide. Since the stir casting method ensures the uniform distribution of alloy and reinforcement, this method was used to fabricate composites with B<sub>4</sub>C (6% wt) and Al 7075 alloy. The aluminium alloy rod was cut into small pieces and melted in crucible on furnace. And the mechanical stirrer was provided to give required 400 rpm. The reinforcement was preheated in a muffle





**Fig. 1** Radial drilling machine and machined work piece

furnace to about 460 °C. The stirrer was allowed to stir the melts for about 10 min and then the work piece was casted.

### **Drilling Operation**

Drilling operation was done on the conventional radial drilling machine, manufactured by Atlas Engineering Co. London shown in Fig. 1. The dimensions of the work piece samples used for conducting the experiments were 75 mm × 75 mm × 25 mm. The drill sizes were 5, 6.5, and 8.5 mm in diameter and its helix angle was 30°, the point angle used was 118°. The drills used were HSS manufactured by Miranda Gold (India).

## **3.3 Performance Parameters**

### **MRR Measurement**

MRR means the volume of the machined material removed per minute. If we increase the feed rate, value of MRR will increase.

$$\text{MRR} = (\pi \times D^2 \times F/4) \text{ mm}^3/\text{min}$$

Here,

$D$  Depth of cut, mm

$F$  Feed rate, mm.

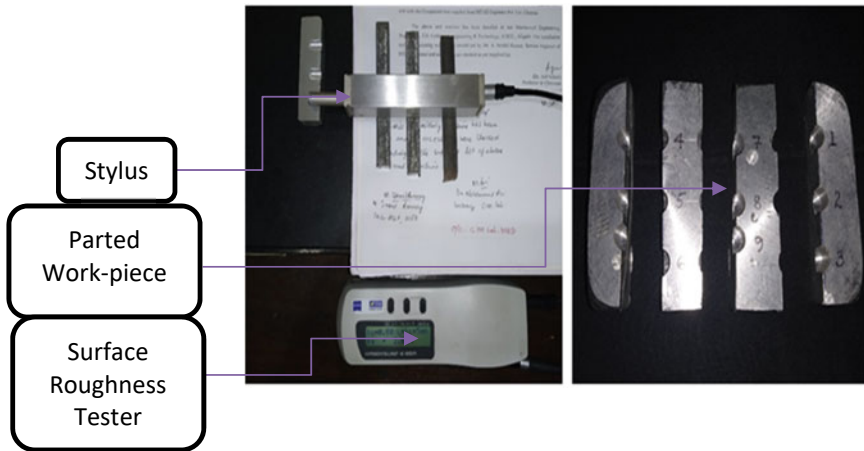


Fig. 2 Photograph of surface roughness tester and parted work piece

**Surface Roughness Measurement**

After drilling, the work piece sample was parted to measure the roughness of the surface using the tester make-Zeiss. The surface roughness values were taken at three different positions or each case, and then, mean was calculated for each experiment (Fig. 2).

**3.4 Design of Experiment**

**Taguchi’s-Orthogonal Array (OA)**

For the design of experiment as discussed earlier,  $L_9$  ( $3^3$ ) orthogonal array with three levels of process parameters was used. Different levels of parameters given in Table 2. The corresponding design of experiment is given in Table 3.

Table 2 Machining parameters and level

Control parameters	Symbols	Level		
		1	2	3
Speed (RPM)	A	555	740	1030
Feed (in/rev)	B	0.005	0.010	0.015
Drill diameter (mm)	C	5	6.5	8.5

### 3.5 Grey Relational Analysis

In this study, 9 experiments were performed on drilling operations according to the design of experiments suggested by Taguchi L9 array. Then, the assessment was done by using the GRA. The aim of this study maximizes the MRR and minimizes the surface roughness. And for this, the optimum combination of process parameters occurred when GRG value is highest. The basic steps during the GRA were as follows, (i) determine the S/N values of the performance characteristics; (ii) then S/N ratios should be normalized; (iii) after that GR coefficients were calculated; (iv) then by averaging the values in step three, we get GRG values; (v) the GRG values were then statically analysed; (vi) optimal levels of parameters were selected; (vii) verification through confirmation test [10].

When data of the experiment has the smaller-the-better nature, then it can be normalized by using the following equation

$$X_i(k) = \frac{\max x_i(k) - x_i(k)}{\max x_i(k) - \min x_i(k)} \quad (1)$$

where the normalized value is denoted by  $X_i(k)$ , the output value of experiment is represented by  $x_i(k)$ , maximum value for the  $k$ th response of the experiment is symbolized by  $\max x_i(k)$ , and the minimum value by  $\min x_i(k)$ .

When data of the experiment has the larger-the-better nature, then it can be normalized by using the following equation

$$X_i(k) = \frac{y_i(k) - \min .y_i(k)}{\max y_i - \min .y_i(k)} \quad (2)$$

where the normalized value is denoted by  $X_i(k)$ , the output value of experiment is denoted by  $y_i(k)$ , maximum value for the  $k$ th response of the experiment is represented by  $\max y_i(k)$ , and the minimum value by  $\min y_i(k)$ .

Then, the grey relational coefficient can be calculated as follows.

$$\xi_i(k) = \frac{\Delta \min + \psi \Delta \max .}{\Delta 0_i(k) + \psi \Delta \max .} \quad (3)$$

where

$\xi_i(k)$  is the GR coefficient,

$\Delta 0_i(k) = \|X_0(k) - X_i(k)\|$

$\Delta 0_i(k) = \|X_0(k) - X_i(k)\|$  is the difference of  $X_0(k)$  and  $X_i(k)$ ,

$\Psi$  is the distinguishing coefficient.  $0 \leq \Psi \leq 1$ , mostly taken as 0.5,

The smallest value of  $\Delta 0_i$  is represented by  $\Delta \min$  and largest value of  $\Delta 0$  is represented by  $\Delta \max_i$ .

Now, the GRG values can be calculated as follows,

$$\gamma_i = \frac{1}{n} \sum \xi_i.(k) \tag{4}$$

where  $\gamma_i$  represents the GRG and the number of response is represented by  $n$  [11].

## 4 Results-And-Discussion

### 4.1 Grey Relational Analysis

Table 3 gives the observations of the experiment, which was conducted according to the Taguchi design. Then, the analysis was carried out by the procedure we have discussed earlier. S/N ratios for each row were found out by using Eqs. (1) and (2). After that deviation sequence  $\Delta 0_i(k)$  was calculated (Tables 4 and 5).

Then, the grey relational coefficients were calculated by using the Eq. (3), and taking  $\psi$  equal to 0.5. After finding grey relational coefficient, grey relational grade is calculated using Eq. (4). Closeness of the results to the normalized values can be predicted by the GRG values. High GRG values indicate that results are more close to normalized values. Experiment 6 has the highest GRG value, it means that this experiment run corresponds to best output results.

The value of overall GRG value is also calculated as given in Table 6. The greater the GRG value better will be the multiple performance characteristic is. The various levels of mean GRG value have been shown in the graph. The graph indicates that the optimum parametric setting is  $A_2B_3C_1$ , i.e. spindle speed at the level 2 (740 RPM), feed at the level 3 (0.015 in/rev), and drill bit diameter at the level 3 (5 mm). After

**Table 3** Experimental results for Al 7075 and B<sub>4</sub>C composite using L<sub>9</sub> orthogonal array

S. No.	A	B	C	Ra (μm)	MRR (mm <sup>3</sup> /min)	S/N Ra	S/N MRR
1	555	0.005	5	1.06	1383.96	- 0.50612	62.8225
2	555	0.010	6.5	1.76	4677.82	- 4.91025	73.4009
3	555	0.015	8.5	2.30	11,999.02	- 7.23456	81.5829
4	740	0.005	6.5	0.87	3118.54	1.20961	69.8790
5	740	0.010	8.5	0.90	10,665.80	0.91515	80.5599
6	740	0.015	5	0.53	5535.88	5.51448	74.8637
7	1030	0.005	8.5	1.40	7422.81	- 2.92256	77.4114
8	1030	0.010	5	2.00	5136.89	- 6.02060	74.2140
9	1030	0.015	6.5	1.46	13,022.03	- 3.28706	82.2936

**Table 4** Deviation sequence

Deviation sequence = $\Delta O_i(k) = \ X_0(k) - X_i(k)\ $		
No. of experiments	Surface roughness	MRR
1	0.4722	1.0000
2	0.8177	0.4567
3	1.0000	0.0365
4	0.3377	0.6376
5	0.3608	0.0890
6	0.0000	0.3816
7	0.6618	0.2507
8	0.9048	0.4150
9	0.6904	0.0000

**Table 5** Grey relational coefficients and GRG values

S. No.	A	B	C	Grey relational coefficient		Grey relational grade	Rank
				Ra	MRR		
1	555	0.005	5	0.5143	0.3333	0.4238	9
2	555	0.010	6.5	0.3795	0.5226	0.4510	8
3	555	0.015	8.5	0.3333	0.9320	0.6326	4
4	740	0.005	6.5	0.5969	0.4395	0.5182	6
5	740	0.010	8.5	0.5809	0.8488	0.7149	2
6	740	0.015	5	1.0000	0.5672	0.7836	1
7	1030	0.005	8.5	0.4304	0.6660	0.5482	5
8	1030	0.010	5	0.3559	0.5465	0.4512	7
9	1030	0.015	6.5	0.4200	1.0000	0.7100	3

this, ANOVA is applied on grey relational grade to find out the contribution of each process parameter on performance characteristics in the next section (Fig. 3).

**Table 6** Overall GRG value

Symbol	Machining parameter	Grey relational grade			Main effect (max–min)	Rank
		Level 1	Level 2	Level 3		
A	Speed	0.5025	0.6722 <sup>a</sup>	0.5698	0.1697	2
B	Feed	0.4967	0.5390	0.7087 <sup>a</sup>	0.2120	1
C	Drill diameter	0.6319 <sup>a</sup>	0.5579	0.5529	0.0790	3

Total mean value of grey relational grade  $\xi_m = 0.5815$

<sup>a</sup>Levels of optimum GRG

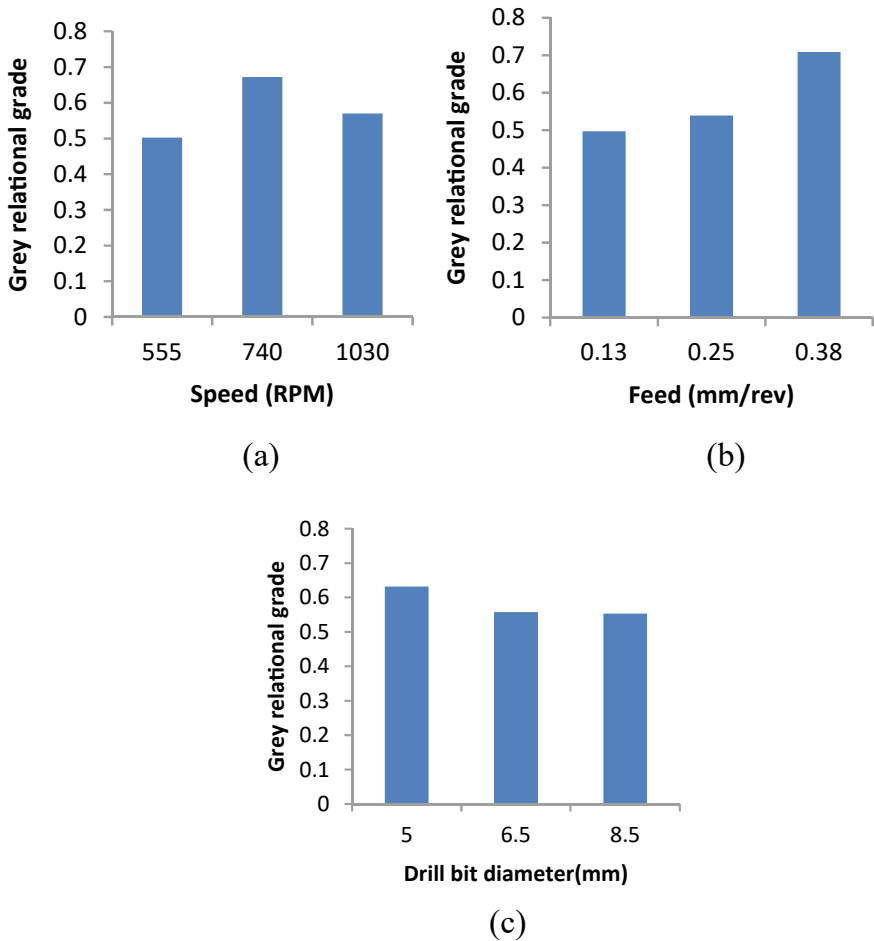


Fig. 3 Response graphs of the a speed, b feed, and c drill diameter on the GRG

### 4.2 Analysis of Variance

To determine the influence of process parameters on the performance characteristic, ANOVA is applied. ANOVA table was prepared by using MINITAB software.

ANOVA for the GRA is given in Table 7. It also shows the percentage involvement of each factor. By observing the values from the data collected, it can be seen that the most controlling parameter is feed. Means it is playing the main role in increasing the MRR and decreasing the surface roughness.

**Table 7** ANOVA of GRA values

Source	DF	Seq SS	Contribution	Adj SS	Adj MS	F-Value	P-Value
Speed	2	0.077500	32.00%	0.077500	0.038750	61.43	0.016
Feed	2	0.095884	39.60%	0.095884	0.047942	76.00	0.013
Drill diameter	2	0.067507	27.88%	0.067507	0.033754	53.51	0.018
Error	2	0.001262	0.52%	0.001262	0.000631		
Total	8	0.242153	100.00%				

## 5 Conclusion

In this study, the composite of Al7075-B<sub>4</sub>C was fabricated and drilling process was carried out. And then using the GRA, the optimization of drilling parameters has been performed. Taguchi L9 orthogonal array was used to carry out the experiments. MRR and surface roughness were considered as multi-performance characteristics.

The following conclusions have been made is the presented study.

- By using the stir casting method, a perfect metal matrix composite is fabricated.
- This study shows that it is feasible to carry out the drilling operation on Al 7075-B<sub>4</sub>C (6%) metal matrix composites.
- In this study, trends of surface roughness are estimated for Al 7075 reinforced with boron carbide with optimum drilling operation which was not done in previous studies.
- The result table gives that the highest value of GRG occurs when speed, feed, and drill bit diameter are at level 740 rpm, 0.015 in/rev, and 5 mm, respectively. Therefore, this the optimum parameters setting to get largest MRR and lowest surface roughness.

The ANOVA of grey relational grade for the multi-performance characteristic established that feed rate in drilling operation is the most significant parameter with percentage contribution of 39.60%, to get the better MRR and optimum surface roughness.

## References

1. Rana SK, Lata S (2018) GA based optimization of process parameters for drilling on Al-MgO metal matrix composite. *Mater Today Proc* 5(2):5837–5844
2. Aravind S, Shunmugesh K, Biju J, Vijayan JK (2017) Optimization of micro-drilling parameters by Taguchi grey relational analysis. *Mater Today Proc* 4(2):4188–4195
3. Nayak SK, Patro JK, Dewangan S, Gangopadhyay S (2014) Multi-objective optimization of machining parameters during dry turning of AISI 304 austenitic stainless steel using grey relational analysis. *Proc Mater Sci* 6:701–708

4. Baradeswaran A, Elyaperumal A (2013) Influence of B4C on the tribological and mechanical properties of Al 7075–B4C composites. *Compos B Eng* 54:146–152
5. Amran MA, Salmah S, Hussein NIS, Izamshah R, Hadzley M, Sivaraos et al (2013) Effects of machine parameters on surface roughness using response surface method in drilling process. *Proc Eng* 68:24–29
6. Khan IA, Zaidi A (2015) Analysis of CNC lathe environment with multi-performance characteristics. *Int J Artif Intell Mechatron* 4(3):95–99. ISSN: 2320-5121
7. Khan IA, Khan H, Anwer F (2018) Optimization of CNC lathe operation by ANOVA and validation using gradient descent. *Int J Mech Prod Eng* 6(6):49–54. ISSN: 2320-2092
8. Khan IA, Mittal A (2011) Predicting surface roughness in machining: a review. Conference: recent advances in mechanical engineering, India, pp 101–109. ISBN: 978-81-906515-3-0
9. Fathipour M, Zoghipour P, Tarighi J, Yousefi R (2012) Investigation of reinforced SiC particles percentage on machining force of metal matrix composite. *Mod Appl Sci* 6(8):9–20
10. Rajmohan T, Palanikumar K, Kathirvel M (2012) Optimization of machining parameters in drilling hybrid aluminium metal matrix composites. *Trans Nonferrous Metals Soc China* 22(6):1286–1297
11. Ramu I, Srinivas P, Vekatesh K (2018) Taguchi based grey relational analysis for optimization of machining parameters of CNC turning steel 316. *IOP Conf Series Mater Sci Eng* 377



# Critical Analysis of Manufacturing of Manganese Steel Liners Used in Crushing and Mining Sector for Improved Performance



Rahul Nagar, Anant Prakash Agrawal, Ajay Kumar, and Shyam Lal

**Abstract** The scope of this paper is to understand the manufacturing process of austenitic manganese steel (AMS) casting liners specifically for cone crushers (consumable liners) used in the mining sector. During review work, an orthodox manganese steel manufacturing process was studied along with the heat treatment process's silent parameters, which directly affect the austenitic manganese steel wear properties and internal cast integrity. Also, the effect of the heat treatment of Austenitic manganese steel was discussed, which helps to improve austenitic microstructure with minimal carbides precipitation on grain boundaries. Various other silent factors in the heat treatment process, like effective quenching by controlling quenching time lag, medium temperature control, parts stacking gap, churning of the tank medium, etc., were also discussed and controlled during the heat treatment process. This helped to increase the toughness values significantly from 27 to 188 J, i.e., up to 7 times approximately. Also, there is a marginal increase in hardness from 209 to 237 BHN, around 15%, which helps sustain the impacts during application and improves wear life without failures. This was concluded that the manufacturing process of crusher liners followed by an adequate heat treatment process produces an improved austenitic microstructure with improved mechanical properties, resulting in higher wear life of consumable crusher liners in mining and crushing applications.

**Keywords** Quenching · Wear life · Abrasion resistance · Crushing liners · Precipitation · Carbides · Grain boundaries

---

*Present Address:*

R. Nagar (✉) · A. P. Agrawal · A. Kumar · S. Lal  
Department of Mechanical Engineering, Noida Institute of Engineering and Technology, Greater Noida, Uttar Pradesh 201306, India  
e-mail: [rnagar2005@gmail.com](mailto:rnagar2005@gmail.com)

A. P. Agrawal  
e-mail: [anant.agraawal@gmail.com](mailto:anant.agraawal@gmail.com)

## 1 Introduction

Austenitic manganese steels (AMS) are widely used in the mining segment globally due to their excellent wear resistance properties with good ductility and high toughness properties under variable impact loads [1]. The initial chemical composition of AMS for such applications was about 12% manganese and 1.2% carbon. However, medium manganese, i.e., 18% manganese content along with 2% chromium, is becoming famous due to its increased mechanical properties and improved wear life [2]. Initially, British metallurgist Sir R Hadfield first developed the manganese steel in 1882 and observed that AMS achieved high toughness when Mn levels were above 10%, along with effective heat treatment. Since then, extensive work has been carried out in this field, and various amendments have been proposed based on the end applications [3]. The original AMS, containing about 1.2–1.4% carbon and 12–14% manganese (around 1:10 ratio), is unique in its properties. This had higher toughness and ductility with improved work hardening [4]. Many efforts have been made to improve its wear resistance properties, driven mainly by the continuous demand for lower production costs in the crushing and mining segment [3].

Later, AMS gained acceptance as a suitable engineering material and is still being used in various fields of crushing and mining. The high hardness of this alloy, with good ductility and toughness properties, makes it a valuable source for crushing liners. Manganese steel castings are currently being extensively used for stone-crusher in the crushing and mining sector globally [1].

The higher manganese content in AMS is considered to be one of the oldest materials having an enriched amount of hardness, toughness, and ductility, due to which same can be used for the variable load high impact applications along with its higher wear resistance properties [3]. Manganese steel contains a work hardening phenomenon due to its higher manganese content, which is costly and not much required for the lower impact loads applications, so medium content (18% Mn) steel was developed. Medium AMS achieved an increased wear resistance property under medium/lower impact applications. This steel grade had comparatively lesser wear resistance properties and issues with delayed cracks origination due to unstable internal austenite structure [5]. Various works have been carried out to improve liner wear resistance and overall life by enhancing the chemistry with add-on alloys like nickel, chromium, and molybdenum, followed by the controlled heat treatment process. All add-on alloys have their properties, and considering all factors (feasibility and cost), higher manganese (18% and above) with added chromium grade is proven as the optimum commercially viable solution to overcome the failures that usually occur during the crushing application process [1]. Refer to Fig. 1 for cone-type crushers (secondary crushers) consumable liner sets.

In the crushing industry, we have two types of crushers—primary type and secondary. Output material of primary Jaw type crushers is an input material for secondary type (cone) crushers. Both types of crushers have extensive usage of consumable liner sets. As per Fig. 2, it can be noticed that the thicker type of stone is

**Fig. 1** Cone crusher—consumable liner (fixed and moving type)

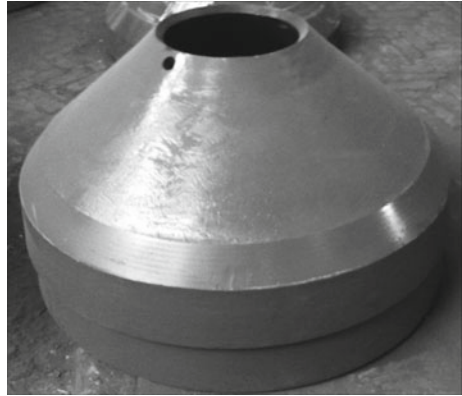
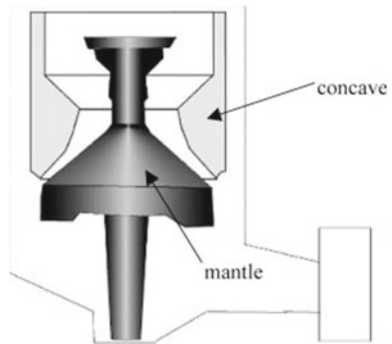


**Fig. 2** Cone liner—wear areas while stone crushing [5]

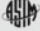


getting crushed between the concave and the mantle. This is delivered as an output material of a smaller size.

This work's novelty and objective are to understand the importance and analyze the various silent heat treatment parameters like parts time lag for quenching, stacking gap (for effective heating/cooling), tank medium temperature, churning of the tank water, etc. The outcome specimen testing follows this to assess the internal integrity of the produced liner castings, which in turn directly affects the performance of crushing liners. So far, no direct work has been carried out to assess the crusher casting liners' integrity by monitoring and controlling the above silent heat treatment factors.

**Table 1** Standard manganese steel chemical composition

Element	C	Mn	Cr	Mo	Ni	Si	P
wt.%	1.15–1.25	18.2 max	1.8–2.0	0.5 max	0.2 max	0.6 max	0.07 max



**A 128/A 128M – 93 (2003)**

**TABLE 1 Chemical Requirements**

Grade <sup>A</sup>	Composition, %						
	Carbon	Manganese	Chromium	Molybdenum	Nickel	Silicon	Phosphorus
A <sup>B</sup>	1.05–1.35	11.0 min	...	...	...	1.00 max	0.07 max
B-1	0.9 –1.05	11.5–14.0	...	...	...	1.00 max	0.07 max
B-2	1.05–1.2	11.5–14.0	...	...	...	1.00 max	0.07 max
B-3	1.12–1.28	11.5–14.0	...	...	...	1.00 max	0.07 max
B-4	1.2 –1.35	11.5–14.0	...	...	...	1.00 max	0.07 max
C	1.05–1.35	11.5–14.0	1.5–2.5	...	...	1.00 max	0.07 max
D	0.7 –1.3	11.5–14.0	...	...	3.0–4.0	1.00 max	0.07 max
E-1	0.7 –1.3	11.5–14.0	...	0.9–1.2	...	1.00 max	0.07 max
E-2	1.05–1.45	11.5–14.0	...	1.8–2.1	...	1.00 max	0.07 max
F (J91340)	1.05–1.35	6.0–8.0	...	0.9–1.2	...	1.00 max	0.07 max

<sup>A</sup> Section size precludes the use of all grades and the producer should be consulted as to grades practically obtainable for a particular design required. Final selection shall be by mutual agreement between manufacturer and purchaser.

<sup>B</sup> Unless otherwise specified, Grade A will be supplied.

**Fig. 3** Standard material grades for manganese steel [Ref. ASTM A128/A 128M]

## 2 Material and Method

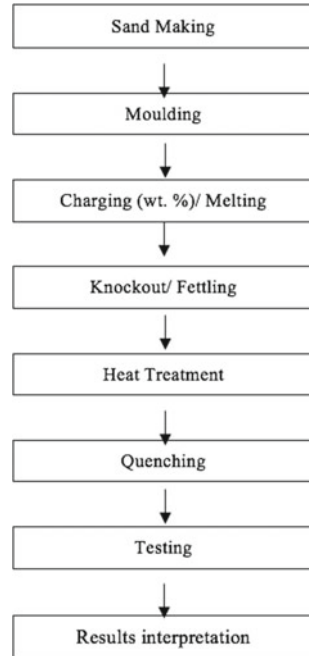
### 2.1 Material Grades

Referring to ASTM, A 128/A 128M–93, “Standard Specification for Austenitic Manganese Steel Castings,” initially had many grades available in lower/medium grade Mn steel with Cr, Mo, & Ni alloys. Nowadays, medium Mn steel of up to 18% Mn and higher grades Mn steel containing up to 22% Mn, along with various alloys like Cr, Ni, and Mo, is getting more famous due to their extended wear life. However, the same is not very cost-effective due to the high prices of added special alloys. Various works have been carried out to optimize the overall output by adding various alloys to medium and high manganese steel of various combinations, and 18% Mn and 2% added chrome became an optimum solution for liner cost and overall performance. This paper considers chemistry as medium manganese steel with added alloys like Cr, Ni, and Mo, refer to Table 1 (Fig. 3).

### 2.2 Manufacturing of Austenitic Manganese Steel Cone Liners

Figure 4 refers below the process flow chart made for the manufacturing of manganese steel cone liners.

**Fig. 4** Process flow chart for manufacturing Mn steel cone liners



### 2.3 Molding Process

*Sand preparation.* All critical parameters, like cohesiveness, refractoriness, binding properties, moisture content, binder ratio, etc., were checked and controlled during sand preparation and mixing.

*Pattern.* Due to dynamic and variable loads, the pattern geometry is essential for crushing liners and needs a thoroughly validated design with close due allowances. Also, various other critical factors include cost, weight, durability, and versatility. In the present work, wood has been used as pattern material with due consideration to the various pattern allowances. Figure 5 shows the pattern being machined by using a CNC machine.

*Mold box.* While carrying out mold-making for cone liners, two-part molding was considered to be the best option due to its critical geometry and design. Refer to Fig. 6a, b for core making, and Fig. 7 for two-part molds.

*Melting and Charging.* For AMS raw material, inputs for the melting and charging process are Mn steel return scrap, regular steel scrap, and element alloys (refer to Fig. 8). Separately fused elements (raw alloys) are also used to control the final chemistry ratio during the final charging process (refer to Fig. 9 showing manganese steel raw alloy).



**Fig. 5** Cone liner pattern manufacturing at CNC VTL machine

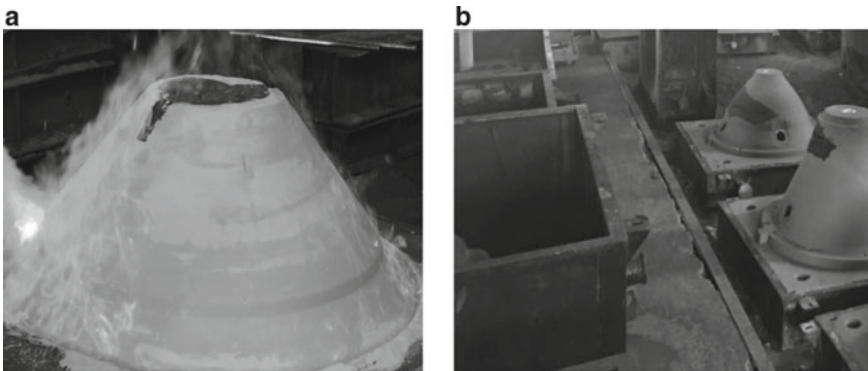


**Fig. 6** **a** Core preparation. **b** Mold box core preparation

*Chemistry verification.* Quick chemistry verification occurs via bath sample and post confirmation of elements content after the final pouring process. Refer to Table 1 considered for this paperwork.

*Pouring.* The top basin ladle carried outpouring by controlling the molten metal temperature within range as uncontrolled temperature leads to the variable grain size and structure and adversely impacts the overall strength of the casting (by adversely affecting various physical properties). Because melt temperature was continuously monitored and verified by the calibrated pyrometer, during this work, the pouring temperature for AMS was observed as 1348 °C against a specified range of 1330–1450 °C, refer to Fig. 9. Lower pouring temperature also adversely affects the fluidity of the molten metal and results in various internal and surface casting defects (shrinkage, etc.) along with the loss of desired physical properties.

*Knock out.* Knock out is done post-solidification in a sand reclamation area where castings are kept open for atmospheric cooling, followed by the fettling and making



**Fig. 7** Mold box preparation



**Fig. 8** Return manganese steel scrap [4]

them ready for heat treatment. During the mold's cooling process, the cooling rate is generally very low. Due to the slow cooling rate, austenite tends to decompose in ferrite and carbide forms. Mechanical hammers (impactors) knock down the castings (to break runners, risers, gates, etc.).

*Heat treatment.* Due to the slow cooling rate inside the mold, embrittling and intergranular carbides are formed in manganese steels. Such brittle microstructures with intergranular carbides are removed by a heat treatment process above 900 °C and a rapid quenching [1]. Due to variable thick sections of liners, the heating in the furnace takes place step by step with a temperature increase of up to 1100 °C at desired soaking time, which varies for various section thicknesses. Also, it has been



**Fig. 9** Raw manganese alloy

concluded before that 750 °C is not a suitable temperature for homogenizing Mn steel. On the contrary, about 95% of the carbide is dissolved at 1050 °C; only very few precipitates can be found across the noticeable at 1050 °C [6].

The kinetics of carbide formation follow the typical C-curve of an isothermal transformation, with the fastest growth (carbide nose) occurring at 550–600 °C. Majorly, there are 2 types of carbides:

- “Thin” carbides form very rapidly and appear as grain boundary delineations in the etched structure at 50× to 200×.
- “Thick” carbides nucleate on thin carbides and grow/participate along the grain boundaries.

Thin carbides do not embrittle the steel significantly, and however, thick carbides have embrittling phenomenon severely on cast steel. Thicker ones are distinguished from the thin carbides by having a resolvable cementite with a clear austenite/carbide interphase boundary on both sides of the cementite film. In regular manganese steels, the thin carbide delineations are less than 0.2 μm thick, and the thick carbides have a starting thickness of 0.5–1.5 μm and appear as a step where they meet the thin carbides [7].

*Austenitic microstructure—Pre- and post-heat treatment.* Figures 10 and 11 show micro-examination at various scales to understand the visual appearance changes in austenitic manganese steel before and after heat treatment (Figs. 12, 13 and 14).

The figures show higher chances of developing cracks/internal stresses in AMS if the heat treatment process is not practical. Due to this, thick carbides are developed and can lead to generating immediate cracks. In contrast, finer ones (precipitated on grain boundaries) may lead to delayed/ time lag cracks during application runs. Figure 15 shows the effective HT process outcome at a micro-level.

*Parts stacking.* The heat treatment experiment was carried out by assigning two heat numbers for identification and traceability—i.e., AB-167 and BB-185. Parts stacking



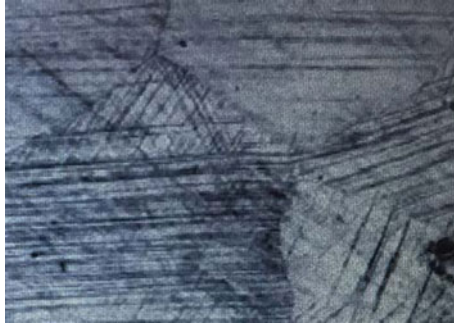


**Fig. 10** Pre-heat treatment



**Fig. 11** Post-heat treatment [8] Scale—200×

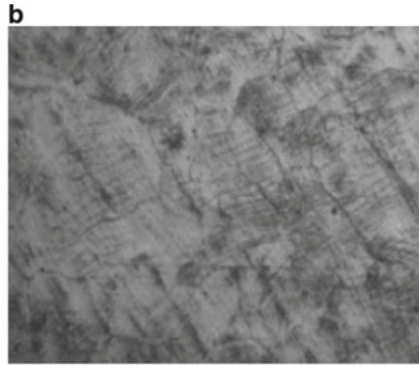
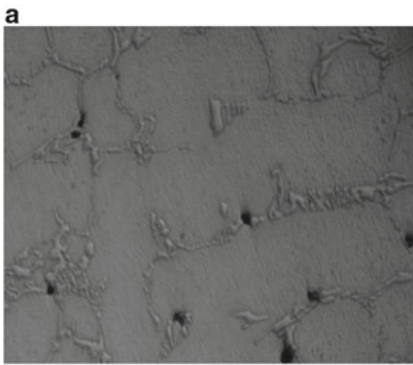


**Fig. 12** **a** Pre-heat treatment. **b** Post-heat treatment [9] Scale—100×

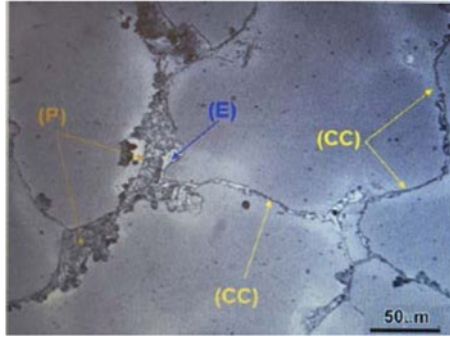


Fig. 13 Before HT (as cast) [4]

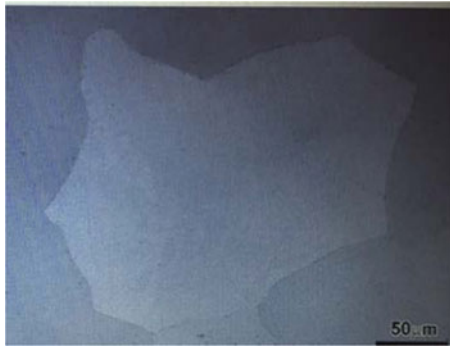


Fig. 14 Post-HT [4] Scale—500×

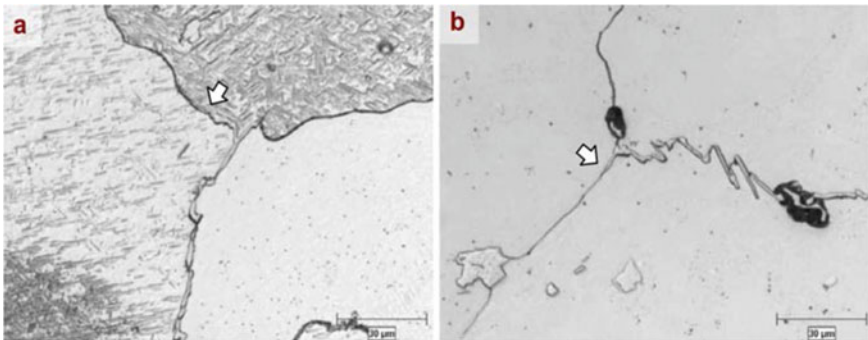


Fig. 15 AMS microstructure—effective HT process image [7] Scale—500×



**Fig. 16** Stacking gap

is again a silent but critical factor for effective heating during heat treatment. Stacking gap plays an essential role in achieving effective heating/cooling. Due to variable thick sections in crusher liners, there should be a gap of around 4–5 in. while staking them on a loading tray. A stacking gap of around 4–5 in. was kept in this work, as shown in Fig. 16 [pictures taken during experimentation].

*Quenching process.* Quenching is an essential part of the manganese steel heat treatment process. It helps to transform the internal microstructure into the austenitic structure. Figure 18 shows manganese austenite transforms between  $< 700\text{ }^{\circ}\text{C}$  (UC, i.e., upper critical temp) and  $350\text{ }^{\circ}\text{C}$  temperature range. During this transformation phase, cementite tends to originate (coming out of austenite). This transformation of austenite ( $\gamma$ ) results in the formation of carbides ( $\gamma + \text{carbides}$ ), which results in embrittlement in the casting and ultimately makes it more brittle and non-favorable in crushing/mining sector usage (increased fracture chances during impact wear application run).

AMS needs rapid water quenching with high-temperature soaking in a tank-based medium. The cutting of Mn casting liners needs to take place immediately once the castings are removed from the heat treatment furnace. The time-based rate of this quenching bath needs to be high enough to prevent any possible precipitation of carbides during microstructural transformation. A slack quenching (delayed or at a higher temperature) can adversely affect the toughness of the casting. Due to thick carbide formation, it may lead to a failure in actual working load applications.

Referring to the TTT curve as shown in Fig. 18,  $350\text{ }^{\circ}\text{C}$  and  $700\text{ }^{\circ}\text{C}$ , occurrences of carbides (intergranular) tend to begin after a short time lag (a few seconds). However, peripheral carbides (acicular) form after a time lag as per the 2nd C type curve (TTT curve) with a nose located at around  $580\text{ }^{\circ}\text{C}$  with around 60 s incubation time. Later at the end, carbides + pearlite structure originates after a long time (around 12 min, i.e., 700 s approx.) In a lesser temperature range (around  $410\text{ }^{\circ}\text{C}$  and  $680\text{ }^{\circ}\text{C}$ ), the boundary precipitated carbide formation occurs.

*Medium temperature control.* Water tank temperature plays a vital role during the quenching process. Suppose water temperature tends to increase while submerging hot cast liners. In that case, there will not be an effective quenching which will lead to poor austenitic microstructure and support the generation of thick carbides. This will affect the strength of the casting and may lead to premature failure during the application (Fig. 19).

To control and maintain the water temperature, tank water circulation was connected with a cooling tower, continuously moving the tank water to the tower and receiving the cold water. This helped maintain the tank water temperature at less than 35 °C and an effective quenching process. Refer to Fig. 20 for tank medium temperature observed as 32 °C and 35 °C, respectively.

*Quenching tank.* Refer to Fig. 17 [actual picture] shows a water tank with a capacity of 20,000 L. When the heated liner parts come out of the heating furnace and rapidly go into the quenching water tank, they get surrounded by a steam blanket due to water vaporization, which adversely affects the rapid quenching phenomenon followed by poor microstructure and leads to embrittlement due to thick carbides generation. To minimize this phenomenon, a 10HP submersible pump inside the water tank was used, which helped to break the steam blanket and supports to achieve effective quenching.

*Time lag factor.* Referring to the TTT curve as presented in Fig. 18, the quenching time lag factor plays an important role in controlling the austenite microstructure formation along with minimal carbide precipitation at grain boundaries. Ideally, lag time should be as lesser as possible during quenching. To control the time lag during the quenching process, it was maintained for up to 55 s, which helped to control the intergranular embrittlement by converting them into hypereutectoid carbide precipitation. Referring to Figs. 21 and 22, the opening time of furnace gates until merging the tray into the quenching tank, the maximum time consumed was less than 60 s.

*Other silent factors.* Water tank temperature must be continuously controlled and maintained at less than 35 °C.

**Fig. 17** Tank capacity—20,000L

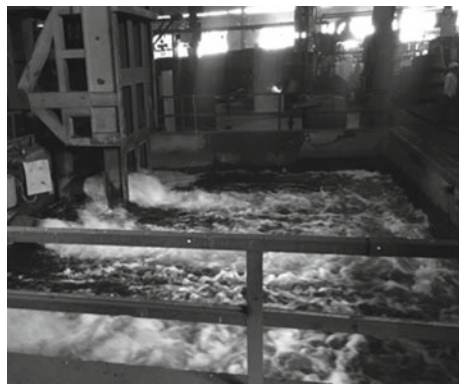


**Fig. 18** TTT curve for austenite formation [10]

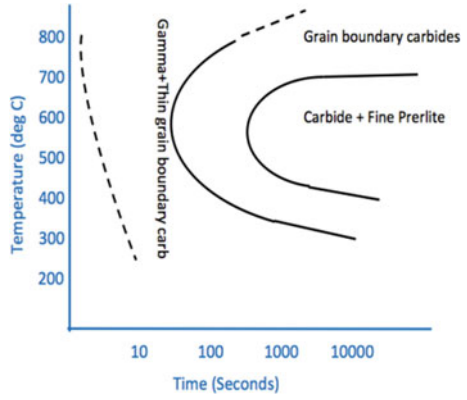


**Fig. 19** Tank temp rise [11]

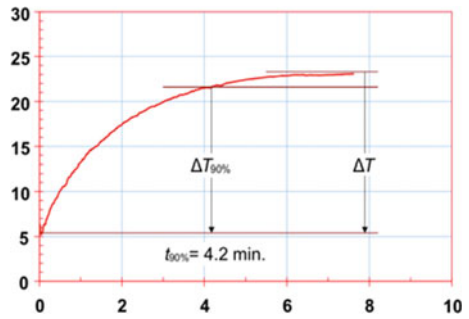


**Fig. 20** Tank temp monitoring

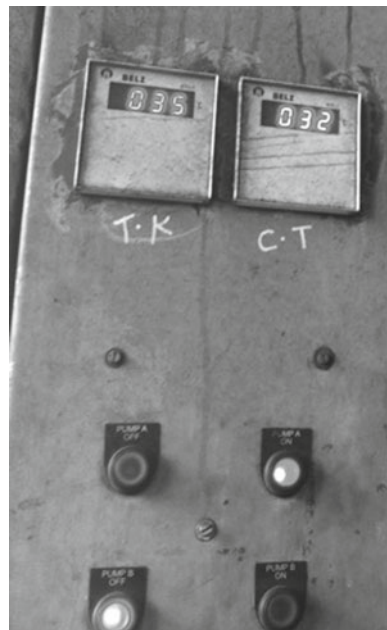


**Fig. 21** Heated cone liners

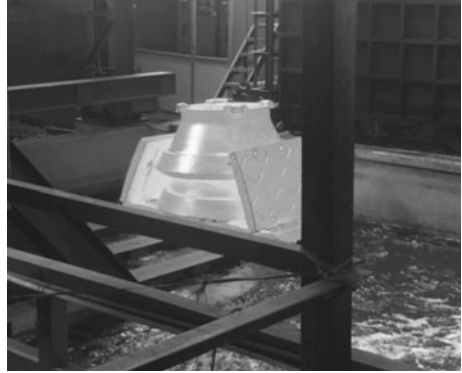


**Fig. 22** Quenching process



### 3 Results and Discussion

Based on the work and analysis of the AMS liners manufacturing process, below are the mechanical testing results of 2 sample liners (different heat samples maintaining identical chemistry)- microstructure, hardness, impact, grain size, grain nos.

#### 3.1 *Microstructure Testing*

During microstructure analysis, post-heat treatment austenite with limited carbides precipitation to the grain boundaries, the desired microstructure with minimal micro-embrittlement was observed. It helped to cast liners to give an increased wear life without premature failures during the run. Figures 23 and 24 refer to the microstructure images achieved during the microstructure examination post-heat treatment.

**Fig. 23** (100×) —microstructure at shrinking time lag

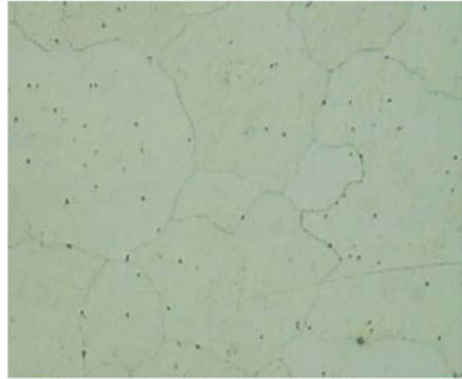
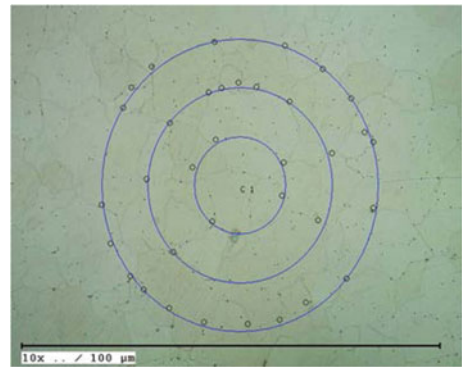


**Fig. 24** (100×) —grains distribution (as per ASTM E 112-grid method)



### 3.2 Hardness

After heat treatment, it was observed that there was a marginal increase in the hardness levels. However, also it signifies the overall grain refinement with a desired ductility, which is a favorable property for the casting liners application perspective. While running in the crusher machine, the surface hardness of the liner goes up to 550 BHN due to the work hardening phenomenon. However, the inner surface has lesser hardness with good ductility, which prevents it from fracture failure. Refer to Fig. 25 for pre- and post-heat treatment hardness results (Table 2).

### 3.3 Impact Properties

A significant increase was observed in the impact properties of casting liners after heat treatment. Increased impact values signify the increased toughness of the casting

**Fig. 25** Hardness (BHN)—pre/post-HT

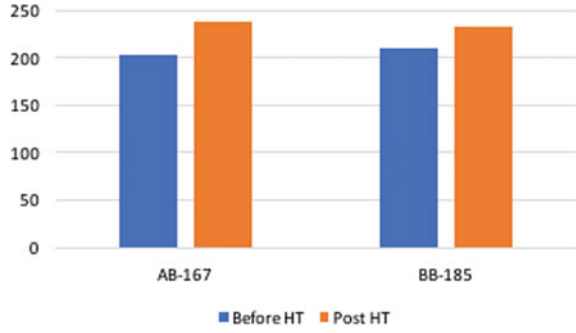


**Table 2** Hardness

HT batch code	Before heat treatment	After heat treatment
AB-167	203 BHN	237 BHN
BB-185	209 BHN	233 BHN

liner, which means a significant improvement in energy absorption properties and an increased life during variable impact load applications (Fig. 26; Table 3).

**Fig. 26** Impact values (J) enhancement—pre/post-HT

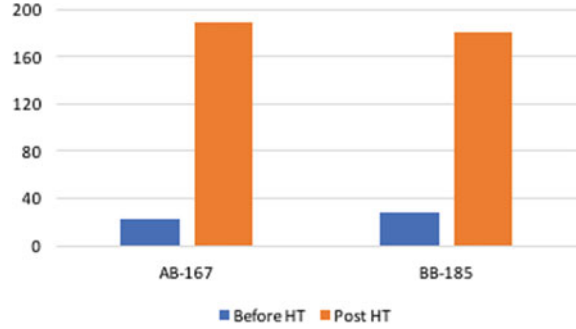


**Table 3** Impact values

HT batch code	Before heat treatment (J)	After heat treatment (J)
AB-167	22.6	188.7
BB-185	27.3	179.8



**Fig. 27** Grain size and grain nos. pre/post-HT as per ASTM E562-02 and ASTM E112

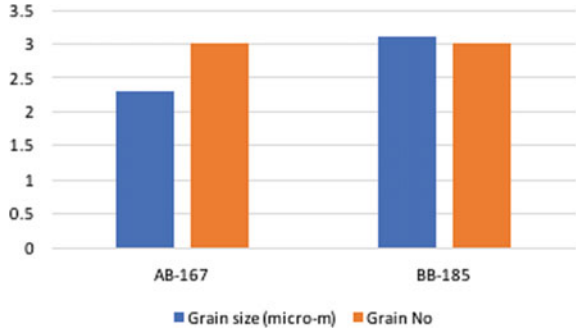


**Table 4** Grain size and grain number

HT batch code	Grain size ( $\mu$ )	Grain (nos.)
AB-167	2.8	3
BB-185	3.1	3

### 3.4 Grain Size and Grain Numbers

Grain size and grain numbers were compared with the standard ASTM E 562-02 (for no) and grain size as per ASTM E 112-10 to confirm the desired outcome. Grain size and numbers were analyzed at 100 $\times$  and were observed to be acceptable for this grade of casting (Fig. 27; Table 4).

## 4 Conclusion

The manufacturing process of concave liners was investigated, and critical manufacturing parameters (heat treatment) were analyzed, which directly affect the strength of manganese cast steel in terms of its overall life during the application run in the crushing machine.

Based on the work, below conclusions are derived:

1. Additional controls in the quenching process (silent factors- time lag control within the 60 s, medium temperature control within 35  $^{\circ}$ C, stacking gap of around 5 inches, tank water churning) helped to increase the toughness values significantly from 27 to 188 J, i.e., up to 7 times increase. This massive increase in toughness values gives liners high-energy absorption ability and helps to decrease the fracture/crack chances during variable impact load conditions.
2. Lesser precipitation of carbides over grain boundaries was observed (refer to Fig. 23, showing microstructure at 100 $\times$ ), which minimizes the embrittlement in castings and increases the overall life of the liners during the application run.

3. Time lag control (within 60 s) from the heating furnace to entirely dip in the quenching tank helped to transform the microstructure into the fully austenitic state (Refer Fig. 23, of microstructure at 100×) that gives lesser precipitation of carbides on grain boundaries, thus avoiding the premature failures of liners in crushing machine.
4. Though a marginal increase (around 15%, refer to Fig. 25, increase in hardness from 209 to 237 BHN) was observed in hardness, the same helps sustain the impacts during application. During crushing, due to the work hardening phenomenon of austenitic manganese steel, the surface hardness shoots very high (up to 500 BHN), and that's why lesser subsurface hardness (237 BHN, refer to Table 2) which is lesser than the 50% of the work hardened surface hardness, helps to absorb the shocks during crushing application and gives tensile properties to the casting.

**Acknowledgements** The author acknowledges the support of the entire faculty of the Mechanical Engineering Department—NIET, Greater Noida, India, for their continuous support, guidance, and help throughout the present work.

## References

1. Panchal K (2016) Life improvement of Hadfield manganese steel castings. ISSN: 2455-2631
2. Chen H, Zhao D, Wang Q, Qiang Y, Qi J (2017) Effects of impact energy on the wear resistance and work hardening mechanism of medium manganese austenitic steel. *Friction* 5(4):447–454
3. Su G, Gao X, Zhang D, Du L, Hu J, Liu Z (2018) Impact of reversed austenite on the impact toughness of the high-strength steel of low carbon medium manganese. *JOM* 70(5):672–679
4. Mahlami C, Pan X, Madzivhandila T (2009) An overview on high manganese steel casting
5. Gupta A, Yan DS (2006) Mineral processing design and operation
6. Agunsoye JO, Balogun SA, Esezobor DE, Nganbe M, Wear of Hadfield austenitic manganese steel casting
7. Kuyucak S et al (2004) HT processing of austenetic manganese steel
8. Kumar A (2019) Reducing the time of heat treatment cycle of the manganese steel. ISSN 2278-3075
9. SemanticScholar.org/paper/Cast-High-Manganese-Steel---the-Effect-of-on-Wear-Kalandyk-Tecza/ebb3147c818ba7ceb8444202822010b78b7f10ae
10. Omar B et al (2012) Dimensional transient heat transfer Axi-symmetric MM to predict the hardness. <https://doi.org/10.5772/51947>
11. Meng Z, Zhou C, Liu X (2019) Effect of self-tempering temperature on precipitation of secondary phase in V-Ti-N high-strength seismic bars. *Trans Indian Inst Met* 72(7):1757–1763
12. Herring DH (2010) The influence of manganese in steel
13. Srivastava AK, Das K (2010) The abrasive wear resistance of TiC and (Ti, W) C-reinforced Fe-17 Mn austenitic steel matrix composites. *Tribol Int* 43(5–6):944–950
14. Razavi M, Yaghmaee MS, Rahimpour MR, Razavi-Tousi SS (2010) The effect of production method on properties of Fe-TiC composite. *Int J Miner Process* 94(3–4):97–100
15. He Z-M, Jiang Q-C, Fu S-B, Xie J-P (1987) Improved work-hardening ability and wear resistance of austenitic manganese steel under non-severe impact-loading conditions. *Wear* 120(3):305–319

16. Ge S, Wang Q, Wang J (2017) The impact wear-resistance enhancement mechanism of medium manganese steel and its applications in mining machines. *Wear* 376–377:1097–1104
17. Zhou R, Tong ZP, Sun GF, Ni ZH, Zhang W (2018) Microstructure and wear behavior of 38CrMoAl steel laser-processed with the addition of MoS<sub>2</sub> or WS<sub>2</sub>. *Lasers Eng* 41(1–3):1–25
18. Lin T, Guo Y, Wang Z, Shao H, Lu H, He X (2018) Effects of chromium sources on the microstructure and properties of TiC-steel composites. *Powder Metall* 61(4):334–341
19. Ma H, Liao S-L, Wang S-F (2014) Effect of Ti on austenite grain growth behavior in high carbon steels. *J Iron Steel Res Int* 21(7):702–709
20. Wu CL, Zhang S, Zhang CH, Zhang JB, Liu Y (2018) Formation mechanism and phase evolution of in situ synthesizing TiC-reinforced 316L stainless steel matrix composites by laser melting deposition. *Mater Lett* 217:304–307
21. Sha Q, Sun Z (2009) Grain growth behavior of coarse-grained austenite in a Nb–V–Ti microalloyed steel. *Mater Sci Eng A* 523(1–2):77–84
22. David Havel PE (2017) Austenitic manganese steel—a complete overview
23. Lee MK, Park EK, Park JJ, Rhee CK (2013) A nanoscale dispersion of TiC in cast carbon steel through a reaction in melt. *Mater Chem Phys* 138(2–3):423–426
24. Tecza G, Sobula S (2014) Effect of heat treatment on change microstructure of cast high-manganese Hadfield steel with elevated chromium content. *ISSN* 1897-3310
25. Peng HB, Chen WQ, Chen L, Guo D (2015) Effect of rare earth yttrium on hot ductility of 20CrMnTi steel with 0.05% tin. *Metall Res Technol* 112(3):307
26. Su G, Gao X, Yan T, Zhang D, Cui C, Du L, Liu Z, Tang Y, Hu J (2018) Intercritical tempering enables nanoscale austenite/ε-martensite formation in low-C medium-Mn steel: a pathway to control mechanical properties. *Mater Sci Eng A* 736:417–430

# Productivity Improvement Using Systematic Layout Planning: A Cement Refractory Case Study



Ramkrishna Bharsakade , Atharwa Kharkar , Himanshu Kurzekar ,  
Arnav Hardas , Ameya Panshikar , and Nilay Diwan 

**Abstract** The present study relates to the cement refractory layout configuration. The objective of the proposed research is to boost the inventory space and reduce the unnecessary travel of the material by applying the systematic layout planning approach to understand the movement of the material and the utilization of the region occupied by the machinery. The proposed layouts aim to boost the inventory area and reduce the unnecessary travel of the material by implementing the proposed configuration developed by analyzing the activity areas, the outline process chart, process flow diagram, affinity analysis diagram and space relationship diagram across 8 departments. Analyzing these data, an alternative configuration was developed, which reduced the transport distance significantly between the two departments and spread up the inventory space, allowing a better storage and travel area.

**Keywords** Optimization · Facility layout planning · Relationship activity diagram · Material flow optimization · Cement refractory · Inventory space optimization

## Nomenclature

SLP Systematic layout planning  
BBM Batch ball mill  
CBM Continuous ball mill  
WIP Work in progress

---

R. Bharsakade (✉) · A. Kharkar · H. Kurzekar · A. Hardas · A. Panshikar · N. Diwan  
Vishwakarma Institute of Technology, Pune, India  
e-mail: [ramkrishna.bharsakade@vit.edu](mailto:ramkrishna.bharsakade@vit.edu)

© The Author(s), under exclusive license to Springer Nature Singapore Pte Ltd. 2024  
R. K. Tyagi et al. (eds.), *Advances in Engineering Materials*, Lecture Notes in  
Mechanical Engineering, [https://doi.org/10.1007/978-981-99-4758-4\\_26](https://doi.org/10.1007/978-981-99-4758-4_26)

295

# 1 Introduction

## 1.1 Background

This paper is based on the field study conducted at a medium-scale cement refractory unit involved in manufacturing high-quality refractory cement used for various specialized applications. The company is working continuously towards increasing the production and productivity of the complete plant. The company plans to improve its productivity by optimizing its existing plant layout.

This study was conducted in a cement refractory industry in Nagpur, India. The company is involved in manufacturing high-quality refractory cement required for various specialized applications. The company has been functional for the last two decades and the top management is always keen to apply process improvement tools and techniques.

The major objective of this study is to increase production and enhance productivity by optimizing the plant layout with such an aspect that improper space and worker utilization concerns could be resolved. The proposed work focuses on expanding the inventory space, reduce the non-essential travel of material by performing a systematic layout planning analysis approach, which would lead to an enormous amplification in the productivity at the refractory and would help to understand the motion of materials and the utilization of area occupied by the machinery. This could be achieved by modifying the plant layout to fit their component family better. In the absence of a solid strategy, rearranging will always result in wasting time, human disturbance, and idle equipment. Furthermore, it may result in substantial mistakes in utilizing a factory's available space, expensive reshuffles, or demolishing operational infrastructure, later proving to pose challenges to efficiency and operating at a cheap operational cost [8]. Many academics believe that plant architecture is one approach to cutting manufacturing costs while increasing productivity [11].

The paper is organized as follows: Sect. 1 discusses the background, the study's primary objective, and a supportive literature review. In Sect. 2, we discuss the research methodology used in this study, the SLP technique and developed the analysis based on the collected data from the cement refractory. Section 3 discusses the results and discussion, and finally, Sect. 4 presents the conclusion of this study.

## 1.2 Literature Review

Despite the fact that many innovative technologies are present in the domain of facility design, and the systematic layout planning (SLP) technique remains extensively employed by businesses and universities [3]. Systematic layout planning entails a collection of design issues, including placing elements that define capacity utilization systems in a coverage location [10]. To compete against their market rivals, industrial

facilities must increase their manufacturing capacity and effectiveness to keep up with rising demand. Simultaneously, the production process should be able to reduce costs and increase efficiency. The recent iron production plant architecture was created using SLP for better efficiency, and the results discovered the developed layout cut down the distance of movement of material from cutting to warehousing. As a result, plant architecture may be a viable option for increasing output [14]. Simplified systematic layout planning, also known as Muther's pen-and-paper-based graphical approach, is one way to upgrade the layout [6].

Since the last few decades, layout design difficulties have been a hot research topic [7]. The SLP tool was used to enrich the architecture of existing machines and lower reject rates [13]. This strategy gives the architecture of new machines that can increase material flow and help the plant utilize space more efficiently [11]. Planning an efficient building layout may cut your company's operating costs by 10–30% [1]. The SLP technique helps to enhance the current arrangement. The application should produce the fastest possible material movement at a lower cost and with less material handling [12]. The synchronization and movement of material should be considered while preparing the model [2].

A factory in Bayan Lepas, Penang that produces meatballs and soup paste was chosen for a case study to identify a workable layout that reduces movement distance, material handling, and shortfalls. The study showed that even the best-chosen layout might be improved, and facility and layout design should be completed prior to any factory set-up to ensure long-term efficiency and loss reduction [9].

The layout of operation theatre is created using the SLP tactic on logistics and non-logistics links. The SLP is a method for organizing a workplace in a factory by putting two sections in the immediate vicinity of high frequency and logical links [5].

On the one hand, many researchers view the challenge of assigning facilities in order to refine the product flow from sourcing to end product. This is done through decreasing the total cost of material handling. On the other hand, layout planning may be considered a design difficulty [15]. SLP has been widely used in businesses and academia because of the abovementioned positions.

Literature suggests that changing plant architecture may be a viable option for increasing output. The first step in improving plant layout should be to identify the issues with the current configuration to enhance productivity while minimizing expenditure and will reduce the excess material movement. This study attempts to identify those significantly influencing factors for increasing the productivity of the overall plant using the systematic layout planning approach. The elements are found in the literature compiled from research papers. A new design for the cement refractory plant layout was proposed using the SLP approach. The existing layout, alternative plant structure, and material movement analyses, involving distance and area among the unit activities, were investigated through refactored cement.

## 2 Research Methodology

Making changes in the plant architecture may be a viable option for increasing output and enhancing productivity while minimizing expenditure. The SLP approach is utilized to study the existing layout and create a better version of the plant layout. The sequential approach to implement systematic layout planning of the cement refractory is as shown in Fig. 1.

### 2.1 Data Collection

We have carried out a field study in the cement refractory and collected operational data for its layout improvement. The data related to plant’s operations, equipment and working area is shown in Table 1. Table 2 shows the manufacturing sequence and the distance travelled within the plant.

**Fig. 1** Method for systematic layout planning [12]

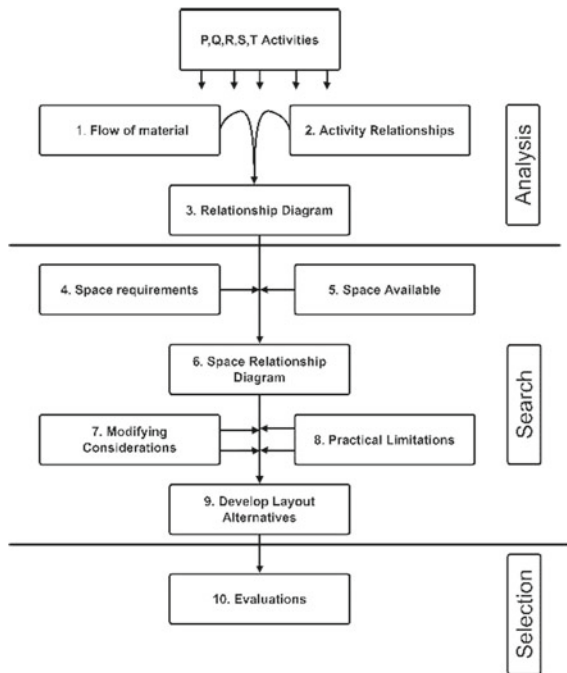


**Table 1** List of operations and equipment size and working area

Department	Operations	Number of equipment	Equipment area (m <sup>2</sup> )	Total working area (m <sup>2</sup> )
Inventory	Storage	–	182	182
Batch ball mill-1	Mixer	1	34.33	103
Nodulizer	Nodulizing	1	68.72	150
Rotatory kiln	Heating	1	120.9	204
Cooling section	Cooling	–	98.6	100
CBM	Grinding	3	493	500
Batch ball mill-2	Blending	2	194	210

## 2.2 Develop the Analysis

In the analysis, the activity areas, the outline process chart, process flow diagram, affinity analysis diagram and space relationship diagram across 8 departments were employed using the data collected. Third, the operation process chart and material flow for product manufacturing were investigated, and the issues with the current plant layout were shown. To plan the interaction between the equipment and the region, the fundamentals of plant planning based on SLP were reviewed, and a new configuration was designed and proposed based on changing plant layout and the practical constraints. The operational flow chart in Fig. 2 represents operations flow in the refractory.

The processed material travels a long distance that results in a loss of time and energy, at a significant expense, as given in Tables 1 and 2 such as moving it from BBM machine, where the calcium aluminate and lime are mixed together. A uniform consistency is obtained by tumbling the mixture inside the BBM drums. The mix travels further for a distance of 25 m to reach nodulizer machine, resulting in wasted time and more energy in material movement. There the nodules are created of 2–3 cm in diameter. The region near the nodulizer machine was not utilized to its full potential since huge supplies remained in the working area, resulting in an unused space in the factory. The area near the nodulizer was much more than the area required for the actual machinery, thereby increasing the travel distance of the material processed on the BBM machine. The raw materials material handling equipment was inadequate, i.e., a shovel was used to fill the raw materials and move them in hand trolleys, and the route was inflexible due to a messy arrangement of the items. The storage for cement or the raw material was 150 m<sup>2</sup>. The working capacity of the plant is 620 tons. Now, it could contain 500 tons per month. After the improvement, it would have more space to contain the cement or the raw materials.

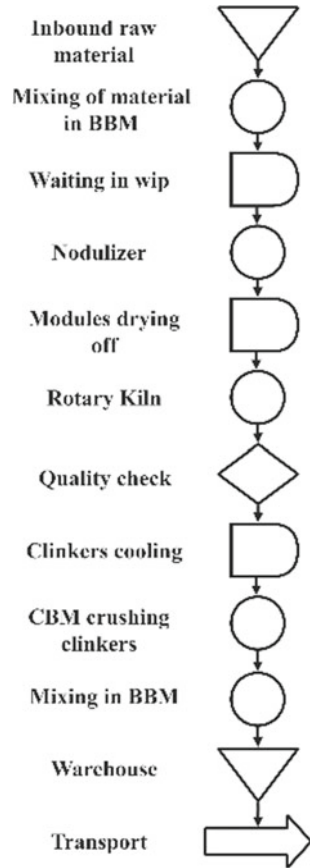
The WIP material needs to be placed properly as it hinders material movement. This would be addressed in the improvement by allotting a proper area for it. The nodules were then kept to dry off the moisture. These dried nodules were then thrown into the rotary kiln to heat them at a temperature of 1450 °C and convert those nodules



**Table 2** Distance and manufacturing sequence for the refactored cement

Activity description	Time (min)	Distance (m)
Storage of raw materials	–	–
Transport to batch ball mill	–	15
Filling up/weighing sacks	7	3
Transport weighing machine to crane trunk	6	7
Transport of lime to weighing machine	1	4
Transport of lime to crane weighing machine	4	7
Delay (deposits earlier batch mixed product)	6	–
Pulls trolley out (earlier batch)	1	–
Transport of trunk into batch ball mill	2	–
Delay (no worker, machine at rest)	15	–
Batch ball mill mixes raw material	45	–
Workers pulls trolley out	1	–
Delay (worker brings sacks)	2	–
Filling sacks of mixed products	15	–
Stalking bags on one another	2	–
Delay	30	–
Transport to nodulizer	20	10
Pouring into the nodulizer	–	–
Travel of one trolley of nodulizer to dry	5	5
Delay (kept for drying)	–	–
Transport of nodules to rotary kiln	1	6
Loading the rotary kiln for heating	–	–
Trolley filled with hot nodules	–	–
Quality check	–	–
Transport to cooling room	–	15
Delay (cooling the nodules)	–	–
Transport of nodules to trunk	22	10
Transport of trunk to CBM machine	3	6
Pouring nodules into the CBM machine	30	–
Nodules filled into the sack	4	–
Transport to small sacks to fill the big sack	11	3
Transport to BBM machines	3	5
Nodules poured into BBM machine	45	–
Filling final product in sacks out of BBM machines	16	–
Transport to storage	14	3

Fig. 2 Operations flow chart



into clinkers. The clinkers are moved to the continuous ball mill machines to grind the clinkers into the powered form again by tumbling into the drums. This process inculcates specific properties into the mixture so that it can be used at places with high-temperature requirements. Finally, the crushed mixture is again tumbled into the BBM machines to obtain a uniform consistency of the material. The entire process can be reviewed in Fig. 2 to get a better view of the processes.

According to a review of the production process, it was discovered that the long distance for transferring raw materials mix from BBM to nodulizer could be decreased, and the problem of less space for raw materials could be resolved. The effective strategy to optimize the plant was to use the SLP technique to create a continuous workflow by rearranging the essential production sequence. Then, to make the relationship of each activity in the operational flow chart, as shown in Fig. 2, the closeness rating is used to develop the relationship between the activities, as given in Table. 3. The relationship between these activities is evaluated considering the various criteria shown in Fig. 3. The activities are listed as follows, raw material

**Table 3** Closeness rating [4]

Code	Closeness rating
A	Absolutely important
E	Especially important
I	Important
O	Ordinary closeness
U	Unimportant
X	Undesirable

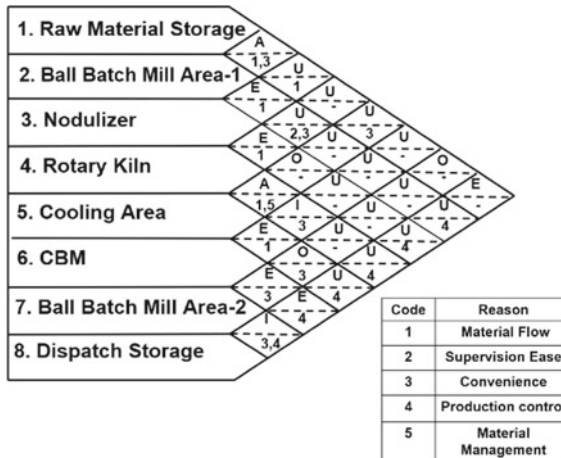


**Fig. 3** Relationship chart

storage, ball batch mill area-1, nodulizer, rotary kiln, cooling area, continuous ball mill, and ball batch mill area-2.

Several configurations were designed based on changing plant layout and practical constraints evaluated in Fig. 4. As shown in Fig. 5, there were two options for improving the plant architecture. Figure 5a depicts the original plant layout, while Fig. 5b shows the proposed plant layout.

### 3 Outcome of the Research

The new plant layout architecture enhances process flow and allows for more space in the facility’s raw material storage area. After analysing the tables, we have found that the travel distance between Department 2 and Department 3 was around 27 m, which has been further lowered to 17 m. Additionally, the area for Department 1 (raw material storage area), which was being used for storing the raw materials, increased from 182 to 285 m<sup>2</sup>. This rearrangement of the layout resulted in an efficient flow of

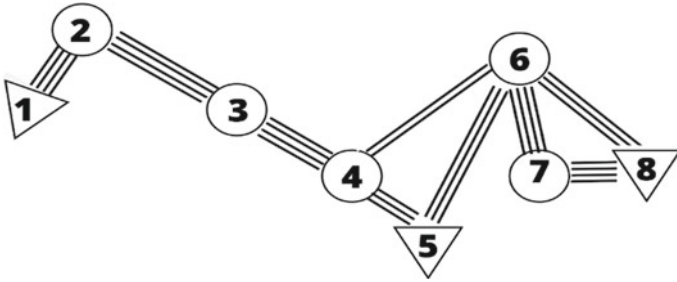


Fig. 4 Flow intensities diagram

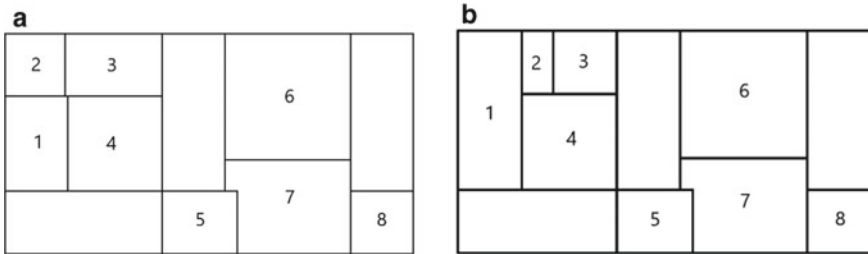


Fig. 5 (a) Earlier layout, (b) proposed layout

materials and more space for the inventory, which resulted in increased productivity. The results are shown in Table 4.

## 4 Conclusion

In this study, we have successfully implemented the SLP approach to enhance the overall efficiency of the processes in the cement refractory. The significant conclusion from the study is listed below:

1. The space use was being studied, and a new layout was proposed to reduce the travel distance of material and increase the inventory space.
2. The problem of excess material travel was views, and the study resulted in lowering the transport distance by 37% from Department 2 to Department 3.
3. The reduction in transportation also reduced the time required for the carrying of the material.
4. With the change in the layout configuration, the inventory space spread has been boosted by almost 56%.
5. Finally, we can conclude that the systematic layout planning approach is highly effective in improving the existing layout or constructing a new layout.
6. It will be helpful to utilize the available resources and reduce the coordinial waste present in the manufacturing system.

**Table 4** Amount and sequence for manufacturing the refactored cement

Activity description	Time (min)	Distance (m)
Storage of raw materials	–	–
Transport to batch ball mill	–	15
Filling up/weighing sacks (Ca10)	6	3
Transport weighing machine to crane trunk	1	7
Transport of lime to weighing machine	4	4
Transport of lime to crane weighing machine	6	7
Delay (deposits earlier batch mixed product)	1	–
Pulls trolley out (earlier batch)	2	–
Transport of trunk into batch ball mill	15	1
Delay (no worker, machine at rest)	45	–
Batch ball mill mixes raw material	1	–
Workers pulls trolley out	2	–
Delay (worker brings sacks)	15	–
Filling sacks of mixed products	2	–
Stalking bags on one another	30	–

(continued)

**Table 4** (continued)

Activity description	Time (min)	Distance (m)
Delay	20	10
Transport to nodulizer	–	–
Pouring into the nodulizer	5	5
Travel of one trolley of nodulizer to dry	–	–
Delay (kept for drying)	1	6
Transport of nodules to rotary kiln	–	–
Loading the rotary kiln for heating	–	–
Trolley filled with hot nodules	–	–
Quality check	–	15
Transport to cooling room	–	–
Delay (cooling the nodules)	22	10
Transport of nodules to trunk	3	6
Transport of trunk to CBM machine	30	–
Pouring nodules into the CBM machine	4	–
Nodules filled into the sack	11	3
Transport to small sacks to fill the big sack	–	–
Delay (WIP)	3	5
Transport to BBM machines	45	–
Nodules poured into BBM machine	16	–
Filling final product in sacks out of BBM machines	14	3
Transport to storage	–	–

## References

1. Barnwal S, Dharmadhikari P (2019) Optimization of plant layout using SLP method. *Int J Innovative Res Sci Eng Technol* 5(3):3008–3015. <https://doi.org/10.15680/IJRSET.2016.0503046>
2. Bharsakade RS, Nandangiri O, Biyani N, Pazare S (2018) Layout improvement through lean tools application for healthcare facility. *Asian J Convergence Technol* IV(I):5
3. Chien TK (2004) An empirical study of facility layout using a modified SLP procedure. *J Manuf Technol Manag* 15(6):455–465. <https://doi.org/10.1108/17410380410547861>
4. Jerin Leno I, Saravana Sankar S, Victor Raj M, Ponnambalam SG (2013) An elitist strategy genetic algorithm for integrated layout design. *Int J Adv Manuf Technol* 66(9–12):1573–1589
5. Lin QL, Liu HC, Wang DJ, Liu L (2015) Integrating systematic layout planning with fuzzy constraint theory to design and optimize the facility layout for operating theatre in hospitals. *J Intell Manuf* 26(1):87–95. <https://doi.org/10.1007/s10845-013-0764-8>
6. Mardberg P, Fredby J, Engström K, Li Y, Berglund J, Carlson JS, Vallhagen J (2018) A novel tool for optimization and verification of layout and human logistics in digital factories. In: 51st CIRP conference on manufacturing systems, vol 72. pp 545–550. <https://doi.org/10.1016/j.procir.2018.03.158>
7. Meiler RD, Gau KY (1996) The facility layout problem: recent and emerging trends and perspectives. *J Manuf Syst* 15(5):351–366. [https://doi.org/10.1016/0278-6125\(96\)84198-7](https://doi.org/10.1016/0278-6125(96)84198-7)

8. Muther R, Hales L (2015) Systematic layout planning. In: Management and industrial research publications, 4th edn
9. Ojaghi Y, Khademi A, Yusof NM, Renani NG, Hassan SAHBS (2015) Production layout optimization for small and medium scale food industry. In: 12th global conference on sustainable manufacturing production, vol 26. pp 247–251
10. Perez-Gosende P, Mula J, Diaz-Madronero M (2021) Facility layout planning. An extended literature review. *Int J Prod Res* 59(12):3777–3816. <https://doi.org/10.1080/00207543.2021.1897176>
11. Shewale PP, Shete MS, Sane PDSM (2012) Improvement in plant layout using Systematic Layout Planning (SLP) for increased productivity. *Int J Adv Eng Res Stud I(III)*:259–261
12. Suhardini D, Septiani W, Fauziah S (2017) Design and simulation plant layout using systematic layout planning. *IOP Conf Ser: Mater Sci Eng* 277(1). <https://doi.org/10.1088/1757-899X/277/1/012051>
13. Sutari O, Rao US (2014) Development of plant layout using systematic layout planning (SLP) to maximize production—a case study. *Int J Mech Prod Eng* 2(8):1–4
14. Wiyaratn W, Watanapa A (2010) Improvement plant layout using Systematic Layout Planning (SLP) for increased productivity. *World Acad Sci Eng Technol* 72(12):373–377
15. Ye M, Zhou G (2007) A local genetic approach to multi-objective, facility layout problems with fixed aisles. *Int J Prod Res* 45(22):5243–5264. <https://doi.org/10.1080/00207540600818179>

# Study on the Flexural Strength of Glass Fiber-Reinforced M20 Grade Self-Healing Concrete Using a Novel Technique Microbial-Induced Calcite Precipitation



S. Hemanth and B. Ramesh

**Abstract** The objective of this study is to quantify the influence of glass fiber on flexural strength of the M20 grade self-healing concrete by using a novel technique microbial-induced calcite precipitation. Two groups consisting of 18 samples in each were prepared for collection of data. One is prepared without the addition of glass fiber and the other is with the addition of glass fiber. Bacteria *Bacillus subtilis* was prepared in the bioinformatics laboratory using a strain brought from Hi media laboratories. The data were analyzed using statistical software called SPSS. The mean flexural strength of bacterial concrete without fiber was 7.944 N/mm<sup>2</sup> and the mean flexural strength of glass fiber-reinforced concrete was 8.666 N/mm<sup>2</sup>. The significance of the events was 0.028 ( $p < 0.05$ ). Glass fiber-reinforced M20 grade self-healing concrete had more flexural strength compared to conventional M20 grade self-healing concrete which were made by using a novel technique microbial-induced calcite precipitation. The percentage increase in strength of glass fiber-reinforced M20 grade self-healing concrete was 9%.

**Keywords** Flexural strength · Glass fiber · Reinforced · M20 grade · Self-healing concrete · Novel technique · Microbial-induced calcite precipitation

## 1 Introduction

Bio-concrete is a self-healing form of concrete designed to repair its own cracks by producing calcium in the cracks and that process is known as microbial-induced calcite precipitation (MICP). Bacteria belong to the *Bacillus* family and calcium acetate was added to the concrete for self-healing [1]. A mechanism to increase life span of concrete structure in the autonomous healing of cracks [2]. Today's world

---

S. Hemanth · B. Ramesh (✉)

Department of Mechanical Engineering, Saveetha School of Engineering, Saveetha Institute of Medical and Technical Sciences, Saveetha University, Chennai, Tamil Nadu 602105, India  
e-mail: [vasudevana.sse@saveetha.com](mailto:vasudevana.sse@saveetha.com)



brings different types of structures which are mostly high raised ones and require high strength so this type of concrete can make it happen with low maintenance cost and with good efficiency. It also shows a positive impact on the surroundings as well as on the environment [3]. Bacterial concrete with fiber added to it has a lot of advantages when compared to normal conventional concrete. Bacterial concrete automatically fills the cracks which had formed in the concrete structure due to different factors like weathering and load on the structure. It enhances the durability of cementitious materials. It prevents the cracks at the earliest stage and reduces maintenance and rehabilitation costs. It also minimizes corrosion in steel by filling the cracks [4].

A lot of research has been done on bacteria concrete by using a novel technique microbial-induced calcite precipitation previously by many scholars. Over the last five years, several study articles have been published on this topic. There are around sixty articles published in Google scholar and around thirty in PubMed journals. Application of bacteria as a self-healing agent for the creation of long-lasting concrete, in which bacteria cement stone specimens appeared to create much more crack-plugging minerals. The potential minerals of bacteria spores as self-healing agents seem promising [5]. The capacity to repair wounds is one of the genuinely astonishing characteristics of the biological system, according to modeling of self-healing materials [6]. Self-healing materials are man-made materials that have the built-in capability to repair damage [7–9]. The evaluation of concrete durability improvement in a sulfate environment using bacteria demonstrates the examination of concrete durability improvement in a sulfate environment using bacteria [10].

The impact of glass fiber-reinforced self-healing concrete in the flexural strength of the concrete was not fully understood in any of the articles published in recent years. In the past, researchers studied bacterial concrete and discovered the effect of bacteria as a self-healing agent, as well as concrete characteristics such as compression strength, split tensile strength, and flexural strength. In this paper, the influence of glass fiber-reinforced M20 grade self-healing concrete by using a novel technique microbial-induced calcite precipitation was checked and the flexural strength was quantified.

## 2 Materials and Methods

This research was carried out in the concrete slab of the Department of Civil Engineering. The bacteria were produced in the Biotechnology lab, Department of Bioinformatics, Saveetha School of Engineering. There was a total of two groups prepared. The first is made without glass fiber, whereas the second is made with it. The total number of samples prepared for each group was 18 in total. Concrete prism of size  $500 \times 100 \times 100$  mm was prepared to find out the flexural strength of concrete. Figure 1a shows the concrete prism of size  $500 \times 100 \times 100$  mm which was casted and Fig. 1b glass fiber used for the study respectively [11]. Properties of the Glass fiber were mentioned in Table 1. The fiber was brought from nectar composites,

poonamallee, Chennai. Bacteria used for the preparation of biological concrete were bacillus subtilis [12]. Bacillus bacteria are bacteria that belong to the bacillus family.

The bacterium strip, which contains 10 spores, was obtained from the hi medium in T Nagar, Chennai. The materials used for the preparation of bacteria were also brought from hi media, T Nagar, Chennai. Soybean casein digest medium (tryptone soya bath), L-alanine ( $C_3H_7NO_2$ ) and manganous sulfate ( $Mnso_4H_2o$ ) were employed to cultivate bacterial cultures. Calcium acetate was employed in the calcite precipitation process. In a mother culture, the bacteria were grown. Following that, bacteria were produced in 100 ml glass tubes which is shown in Fig. 2. Then, the bacteria were prepared in a 2-L jar. The amount of materials used for growing 2-L bacteria growth were 60 gms of soybean medium, 0.4 gms of alanine, 0.2 gms of  $Mnso_4H_2o$ , 200 ml of water. Haecyometer was used to determine the bacteria concentration. The two-liter media solution was shown in Fig. 2. A light microscope at 60× magnification was used to check bacterial presence and viability in the culture which was shown

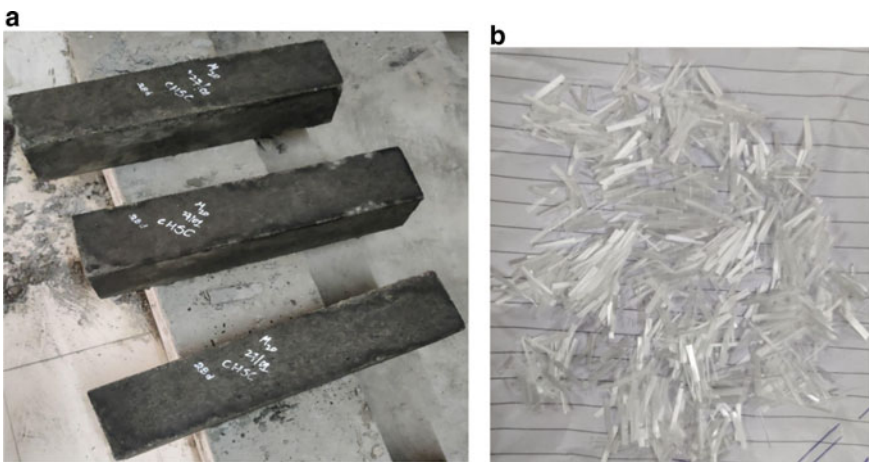


**Fig. 1** a Concrete prism of size 500 × 100 × 100 mm which was casted. b Glass fiber used for the study, respectively

**Table 1** Properties of the fiber which are added for the group-2 samples (glass)

S. No	Properties	Values
1	Length	20 mm
2	Modulus of elasticity	72.5 Gpa
3	Color	White
4	Shape	Straight
5	Density	0.94 g/cm <sup>3</sup>
6	Reaction with water	Hydrophobic
7	% of fiber added	3%
8	Amount of fiber used to cast 18 prisms	1088.64 gms

in Fig. 3. The cell concentration was discovered to be  $10^7$  cells/ml [13]. In comparison with the water used to prepare the concrete, the percentage of bacteria added to the concrete was 3%. Cement, fine aggregate, coarse aggregate, and calcium acetate were utilized in concrete production. Cement (2.016 kg), sand (3.3 kg), and coarse aggregate (6.3 kg) were combined to make one cement prism. Quantity of materials required for the preparation of a single prism was given in Table 2. The water-cement ratio was calculated to be 0.44. M20 grade was used in the concrete mix (1:1.5:3) [14]. Calcium acetate was also put to the concrete, in addition to microorganisms. With regard to prism size, 30% calcium acetate was added.

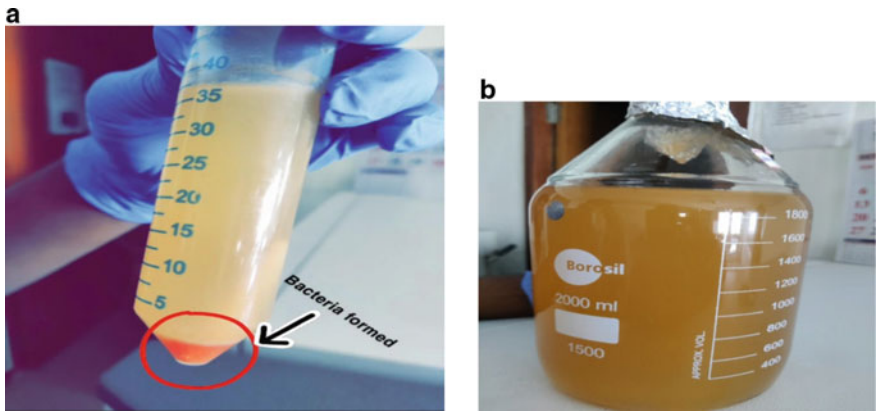


Fig. 2 a Growth of bacteria in a 100 ml tube and b 2 L reagent bottle with prepared media

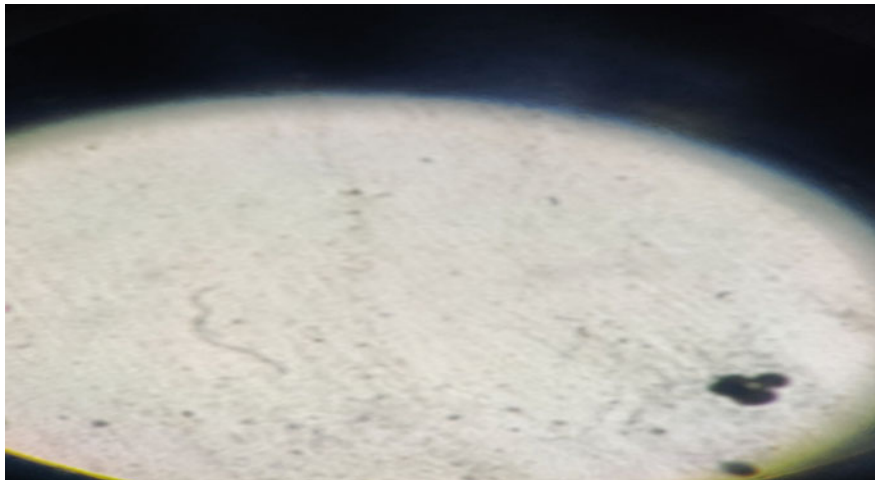


Fig. 3 Bacteria under a microscope of 60× magnification were used to check bacterial presence and viability in the culture

**Table 2** Quantity of materials required to cast a single sample (prism of dimension 500 × 100 × 100 mm)

S. No	Material	Quantity (kg/L)
1	Cement	2.016 kg
2	Fine aggregates	3.36 kg
3	Coarse aggregates	6.3 kg
4	Glass fiber (3%)	60.48 gms
5	Water	0.88704 L
6	Bacteria	26.6112 ml
7	Calcium acetate	0.2 gms

Specimens were produced without the addition of fiber in the first group. The second group was cast in an identical way as the first, with the exception of the inclusion of fiber. The second group was created by mixing all of the foregoing components with glass fiber. The water-cement ratio was calculated to be 0.44. M20 was the concrete mix (1:1.5:3) [15]. All of the ingredients were combined, and the prisms were cast. For a period of 28 days, the cast prisms were submerged in water to cure.

The prism's flexural strength was determined using flexural testing equipment. It possesses the following characteristics. 250 kN was the maximum load capacity. It was operated by hand. The flexural testing machine's ram dia was 90 mm. The distance between the load roller and the supporting roller is 133 mm and 400 mm, respectively. The flexural testing machine was shown in Fig. 4. Different equipment was utilized to guarantee that the bacteria were alive and free of contamination during the preparation process. The preparation jars, as well as the medium, are sterilized in an autoclave first.

This is done to keep bacteria from being contaminated. Autoclave was a piece of equipment that used steam under pressure to destroy bacteria, viruses, and even spores, providing a physical form of sterilizing. In this experiment, the autoclave was set to 121 °C for 15 min at a pressure of 15 lb/sec. Following the sterilization of the jars, the bacteria were grown in a shaking incubator [16]. By shaking chemicals in a 2 L reagent bottle, a shaking incubator might mix, blend, or agitate them. It was run for four days at 37 °C and 90 rpm. The concentration of cells was found using spectrometer. The concentration of cells was found to be  $10^7$  cells/ml shown in Fig. 5.

After the bacteria had reached a stable stage, the bacterium cells were separated from the medium using a centrifuge. A centrifuge is a device that separates different components of a fluid using centrifugal force. The centrifuge was run at a speed of 4000 revolutions per minute at a temperature of 27 °C for ten minutes. The centrifuge apparatus was shown in Fig. 6a. Finally, the extracted bacteria were added with the distilled water which is shown in Fig. 6b. The extracted bacteria were mixed in with the calcium acetate in the concrete. All of the aforementioned were blended together, and prisms were created. For 28 days, the specimens were submerged in water for curing. The water was 27 (±) 2 °C. After 28 days, the specimens were dried for



**Fig. 4** Manually handled flexural testing machine at the time of sampling testing which was used for the study

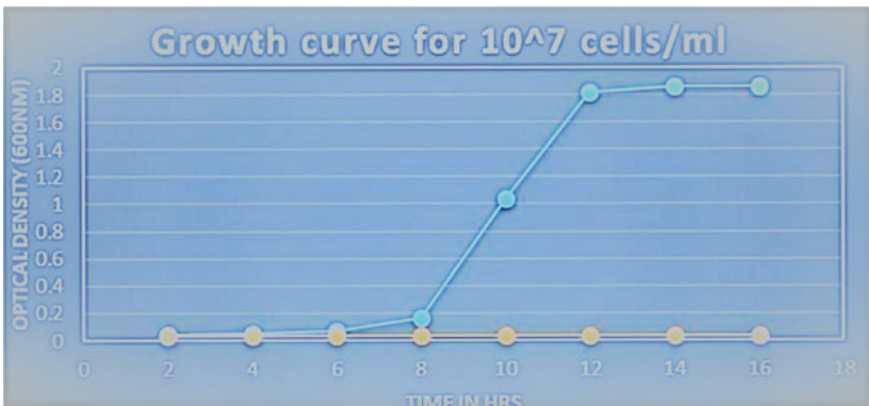


**Fig. 5** Graph representing the growth of the bacteria at a concentration of  $10^7$  cells/ml. It shows that the bacteria growth is constant up to 6 h then it starts growing up to the maximum level then again at a certain point it comes to the constant position

testing. The tested specimens were shown in Fig. 7. The statistical analysis was represented with respect to the bar chart in Fig. 8.

The flexural strength of 18 specimens from group-1, i.e., traditional self-healing specimens, was determined. Similarly, the flexural strength of 18 specimens of group-2, i.e., glass fiber-reinforced self-healing concrete specimens, was determined.

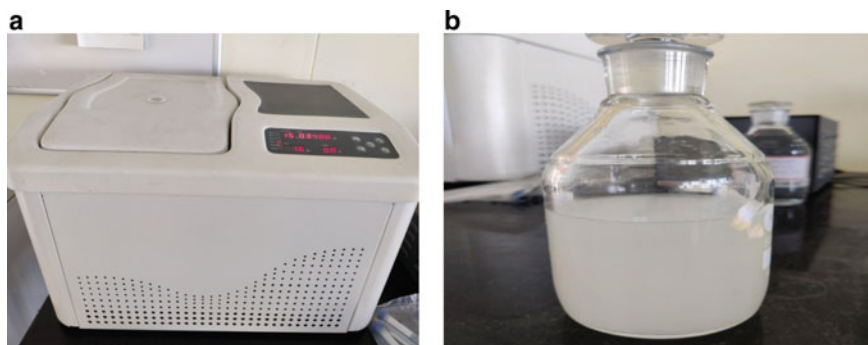


**Fig. 6** a Centrifuge apparatus which was used for separation of the bacteria from the medium. b Final collection of the bacteria after being mixed with distilled water



**Fig. 7** Samples after testing on which the cracks are clearly visible



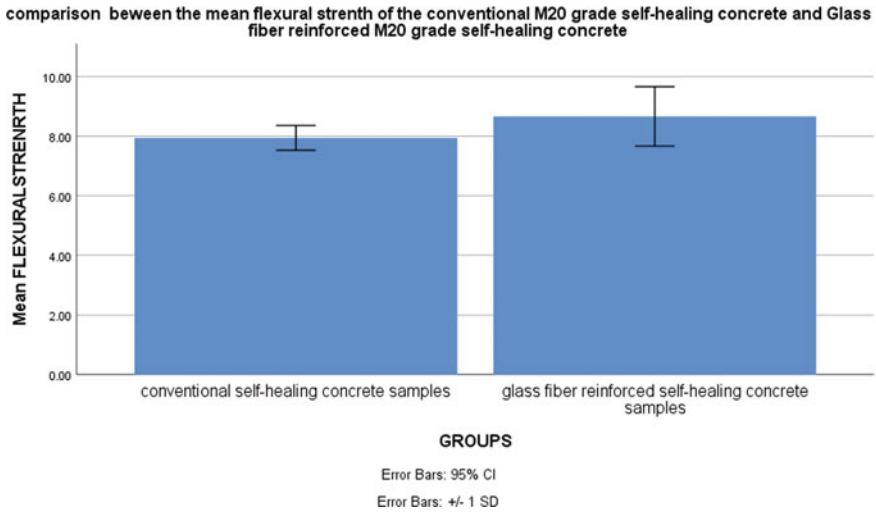


**Fig. 8** Bar chart representing the comparison of mean flexural strength of glass fiber-reinforced concrete and bacterial concrete (independent sample *t*-test means =  $\pm 1$  SD). It shows that the mean flexural strength is more in glass fiber-reinforced M20 grade self-healing concrete than conventional self-healing concrete, where *X*-axis represents the conventional self-healing concrete, glass fiber-reinforced self-healing concrete and *Y*-axis represents the mean flexural strength (N/mm<sup>2</sup>) of the samples

### 3 Statistical Analysis

The experiment's results were evaluated with SPSS version 21 software. An independent sample *t*-test was used to determine the statistical significance of the study and control groups [17–19]. In this study, flexural strength, concrete grade, water/cement ratio, cement grade, and curing days were all considered independent variables. This tool was also used to calculate the mean and standard deviation of flexural strength.

### 4 Results

For both groups, the mean flexural strength was determined. The group-1 samples have a mean flexural strength of 7.944 N/mm<sup>2</sup> which was given in Table 3, whereas the group-2 samples have a mean flexural strength of 8.666 N/mm<sup>2</sup> which was given in Table 4. When comparing group-2 samples to group-1 samples, the mean flexural strength was found to be higher in group-2. The increase in mean flexural strength in group-2 was 9% given in Table 5. The statistical parameters also show that there is a substantial difference between the two groups. The standard deviation values for both groups were found to be extremely low. Group-1 has a standard deviation of

**Table 3** Flexural strength value of the group-1 samples (conventional M20 grade self-healing concrete samples)

Flexural strength of the conventional concrete (group-1)				
S. No	Weight (Kg)	Collapse load (KN)	Flexural strength (N/mm <sup>2</sup> )	Average flexural strength (N/mm <sup>2</sup> )
1	13.18	16	8	7.9444 N/mm <sup>2</sup>
2	13.31	17	8.5	
3	13.39	15	7.5	
4	13.196	16	8	
5	13.528	16	8	
6	13.527	17	8.5	
7	13.755	16	8	
8	13.775	15	7.5	
9	13.882	14	7	
10	13.752	16	8	
11	14.060	16	8	
12	14.315	17	8.5	
13	13.173	16	8	
14	13.490	15	7.5	
15	13.766	17	8.5	
16	13.765	15	7.5	
17	13.982	16	8	
18	13.717	16	8	

0.41618, whereas group-2 has a standard deviation of 0.23570. When the fiber is a glass, the values were taken.

## 5 Discussion

The flexural strength of glass fiber-reinforced M20 grade self-healing concrete was found to be greater than that of conventional M20 grade self-healing concrete in this investigation. The data were statistically analyzed and compared using SPSS version 21 [20]. As a result, the addition of glass fiber to regular M20 grade self-healing concrete strengthens the concrete in terms of flexural strength [21]. Similar results were found by some other researchers in their paper as discussed below.

In recent years, research articles on bacterial concrete have shown mixed findings in terms of flexural strength values. If the fracture in an FRCC with synthetic fibers is smaller than 0.1 mm, the FRCC’s water-tightness will be recovered to the same degree as an uncracked FRCC, regardless of fiber type [22]. As the maximum healable crack width has more than doubled, a biochemical self-healing agent consisting of



**Table 4** Flexural strength value of the group-2 samples (glass fiber-reinforced M20 grade self-healing concrete)

Flexural strength of the fiber-reinforced self-healing concrete (group-2)				
S. No	Weight (Kg)	Collapse load (KN)	Flexural strength (N/mm <sup>2</sup> )	Average flexural strength (N/mm <sup>2</sup> )
1	13.487	18	9	8.666 N/mm <sup>2</sup>
2	13.276	16	8	
3	13.288	17	8.5	
4	13.590	18	9	
5	13.479	17	8.5	
6	13.600	16	8	
7	13.114	15	7.5	
8	13.665	23	11.5	
9	13.520	16	8	
10	13.569	18	9	
11	13.540	17	8.5	
12	13.228	16	8	
13	13.558	18	9	
14	13.556	15	7.5	
15	13.842	16	8	
16	13.067	17	8.5	
17	13.908	18	9	
18	13.069	21	10.5	

a combination of bacterial spores and calcium lactate may be successfully applied to promote and increase the self-healing ability of concrete using a novel technique microbial-induced calcite precipitation [23]. In another paper, it was found that the application of bacteria in concrete to compressive strength and tensile strength of concrete increased with a decrease in permeability, water absorption, and corrosion of reinforcement compared to that of conventional concrete [24]. The use of polymeric capsules to obtain self-healing properties in concrete seems promising [25]. Both self-healing approaches under investigation have some potential to be applied on a real scale with both positive and negative results [26]. The utilization of glass powder addition on the concrete relieves the provision, affordability, quality, and contamination issue [27, 28]. There may be some factors that may affect the entire investigation as it is a manual process and error may happen at any place and such factors are a selection of aggregate size, water/cement ratio, grade of cement, air voids, and compaction during casting [29].

The limitation of the study is that the result will be different if the percentage of fiber is taken different other than 3% or if the fiber selected is different because the fiber used for this study was only glass fiber and the concrete used was only M20 grade, only one type of bacteria was used for the self-healing purpose, i.e., bacillus

**Table 5** Comparison of group-1 and group-2 which shows the increment in the mean flexural strength of group-2 by 9%

Flexural strength (N/mm <sup>2</sup> )	Groups		N	Mean	Std. deviation	Std. error mean
	Without fiber	With fiber				
	Without fiber		18	7.944	0.41618	0.09809
	With fiber		18	12.6944	1.00000	0.23570
t-test for equality of members						
	Levene's test of equality of variance					
	<i>f</i>	<i>sig</i>	<i>t</i>	Df	Sig (2-tailed)	Mean difference
Flexural strength	Equal variances assumed	0.028	- 2.829	34	0.008	- 0.72222
	Equal variances not assumed		- 2.829	22.717	0.010	- 0.72222
						Std. error
						95% confidence interval of the difference
						Lower
						Upper
						- 1.24105
						- 0.203395
						- 1.25071
						- 0.19373

Here, the difference between the std deviation is 0.58382

subtilis. The testing apparatus which was used for sample testing was a manual one so there may be some kind of error in the result [30].

By varying the concrete grade, bacteria kind, and other factors in the future, this idea may function in a variety of ways. It may be done by combining several types of concrete, microorganisms, and a superplasticizer to increase the strength value [31]. Fiber dispersion, bacterium distribution, and calcium carbonate formation may all be studied using SEM and XRD analyses [32]. It has a great possibility since it is a highly helpful idea for the construction industry that saves maintenance costs and enhances the service life of the structure [33]. It may be discovered slowly by doing various types of study on it.

## 6 Conclusion

The glass fiber-reinforced M20 grade self-healing concrete's flexural strength was determined  $w$ . The addition of glass fiber to M20 grade self-healing concrete can enhance the concrete's flexural strength, as demonstrated in this article. Flexural strength increased by 9% as a proportion of total strength. Adding this type of fiber to M20 grade, self-healing concrete can boost its strength, which is highly beneficial and can extend the structure's service life. This type of method is extremely beneficial to buildings, as it leads to the development of new and creative construction materials.

**Acknowledgements** The author would like to express their gratitude toward Saveetha School of Engineering, Saveetha Institute of Medical and Technical Sciences (Formerly known as Saveetha University) for providing the necessary infrastructure to carry out this work successfully.

### Funding

We thank the following organizations for providing financial support that enables us to complete the study.

1. MV Construction, Nellore, AP
2. Saveetha University
3. Saveetha Institute of Medical and Technical Sciences
4. Saveetha School of Engineering.

### Declaration

#### Conflicts of Interest

No conflict of interest in this manuscript.

**Author Contribution** Author SH is involved in data collection, experimental study and manuscript writing. Author RB involved in conceptualization, guidance, and critical review of the manuscript.

## References

1. Ahad M, Gheena S (2016) Awareness, attitude and knowledge about evidence based dentistry among the dental practitioner in Chennai City. *J Adv Pharm Technol Res* 9(11):1863
2. Alquier M, Kassim C, Bertron A, Sablayrolles C, Rafrafi Y, Albrecht A, Erable B (2014) Halomonas desiderata as a bacterial model to predict the possible biological nitrate reduction in concrete cells of nuclear waste disposals. *J Environ Manage* 132(January):32–41
3. Cuenca E, Ferrara L (2017) Self-healing capacity of fiber reinforced cementitious composites. State of the art and perspectives. *KSCE J Civ Eng*. <https://doi.org/10.1007/s12205-017-0939-5>
4. Dhinesh B, Niruban Bharathi R, Isaac Joshua Ramesh Lalvani J, Parthasarathy M, Annamalai K (2017) An experimental analysis on the influence of fuel borne additives on the single cylinder diesel engine powered by Cymbopogon flexuosus biofuel. *J Energy Inst* 90(4):634–45
5. Franzoni E (2011) Materials selection for green buildings: Which tools for engineers and architects? *Procedia Eng*. <https://doi.org/10.1016/j.proeng.2011.11.2090>
6. Girija SA, Jayaseelan VP, Arumugam P (2018) Prevalence of VIM- and GIM-producing Acinetobacter baumannii from patients with severe urinary tract infection. *Acta Microbiol Immunol Hung* 65(4):539–550
7. Gokulnath V, Ramesh B, Priyadharsan K (2020) Influence of M-sand in self compacting concrete with addition of glass powder in M-25 grade. *Mater Today: Proc*. <https://doi.org/10.1016/j.matpr.2019.08.188>
8. Gupta G, Tyagi RK (2021) Theoretical analysis of plasma parameters on film deposition in planer and cylindrical magnetron sputtering. *IJPAP* 59(03):174–179. Retrieved from <http://nopr.niscair.res.in/handle/123456789/56518>
9. Gupta G, Tyagi RK, Rajput SK (2021) A statistical analysis of sputtering parameters on superconducting properties of niobium thin film. *Evergreen* 8(1):44–50. <https://doi.org/10.5109/4372259>
10. Gupta V, Ramani P (2016) Histologic and immunohistochemical evaluation of mirror image biopsies in oral squamous cell carcinoma. *J Oral Biol Craniofac Res* 6(3):194–197
11. Hilloulin B, Van Tittelboom K, Gruyaert E, De Belie N, Loukili A (2015) Design of polymeric capsules for self-healing concrete. *Cement Concr Compos*. <https://doi.org/10.1016/j.cemconcomp.2014.09.022>
12. Jangid K, Alexander AJ, Jayakumar ND, Varghese S, Ramani P (2015) Ankyloglossia with cleft lip: a rare case report. *J Indian Soc Periodontol* 19(6):690–693
13. Jogi PK, Vara Lakshmi TV (2021) Self healing concrete based on different bacteria: a review. *Mater Today: Proc*. <https://doi.org/10.1016/j.matpr.2020.08.765>
14. Jonkers HM, Thijssen A, Muyzer G, Copuroglu O, Schlangen E (2010) Application of bacteria as self-healing agent for the development of sustainable concrete. *Ecol Eng*. <https://doi.org/10.1016/j.ecoleng.2008.12.036>
15. Karthiga P, Rajeshkumar S, Annadurai G (2018) Mechanism of Larvicidal activity of antimicrobial silver nanoparticles synthesized using Garcinia mangostana bark extract. *J Cluster Sci* 29(6):1233–1241
16. Kim S, Yoo D-Y, Kim M-J, Banthia N (2019) Self-healing capability of ultra-high-performance fiber-reinforced concrete after exposure to cryogenic temperature. *Cement Concr Compos*. <https://doi.org/10.1016/j.cemconcomp.2019.103335>
17. Uma TN, Venugopal A, Sureshbabu NM, Ramani P (2018) Salivary micro RNA as a potential biomarker in oral potentially malignant disorders: a systematic review. *Ci Ji Yi Xue Za Zhi = Tzu-Chi Med J* 30(2):55–60
18. Manohar J, Abilasha R (2019) A study on the knowledge of causes and prevalence of pigmentation of Gingiva among dental students. *Indian J Public Health Res Dev*. <https://doi.org/10.5958/0976-5506.2019.01859.x>
19. Gupta G, Tyagi RK (2019) An experimental evaluation of mechanical properties and microstructure change on thin-film-coated AISI-1020 steel. *Mater Perf Charact* 8(3):20180143. <https://doi.org/10.1520/MPC20180143>

20. Nishiwaki T, Kwon S, Homma D, Yamada M, Mihashi H (2014) Self-healing capability of fiber-reinforced cementitious composites for recovery of watertightness and mechanical properties. *Materials*. <https://doi.org/10.3390/ma7032141>
21. Saxena P, Vashisth A, Mehndiratta S (2020) PVD based thin film deposition methods and characterization/property of different compositional coatings—a critical analysis. *Mater Today: Proc.* <https://doi.org/10.1016/j.matpr.2020.07.132>
22. Nosouhian F, Mostofinejad D, Hasheminejad H (2016) Concrete durability improvement in a sulfate environment using bacteria. *J Mater Civ Eng.* [https://doi.org/10.1061/\(asce\)mt.1943-5533.0001337](https://doi.org/10.1061/(asce)mt.1943-5533.0001337)
23. Poorni S, Srinivasan MR, Nivedhitha MS (2019) Probiotic streptococcus strains in caries prevention: a systematic review. *J Conserv Dent: JCD* 22(2):123–128
24. Portland Cement Association (2018) Design and control of concrete mixtures. Franklin Classics
25. Rajeshkumar S, Menon S, Kumar SV, Tambuwala MM, Bakshi HA, Mehta M, Satija S et al (2019) Antibacterial and antioxidant potential of biosynthesized copper nanoparticles mediated through *Cissus Arnotiana* plant extract. *J Photochem Photobiol B, Biol* 197(August):111531
26. Seifan M, Berenjian A (2018) Application of microbially induced calcium carbonate precipitation in designing bio self-healing concrete. *World J Microbiol Biotechnol.* <https://doi.org/10.1007/s11274-018-2552-2>
27. Sheriff KA, Hilal KA, Sheriff H, Santhanam A (2018) Knowledge and awareness towards oral biopsy among students of Saveetha dental college. *Res J Pharm Technol.* <https://doi.org/10.5958/0974-360x.2018.00101.4>
28. Maan R, Jacob S, Verma S (2021) Review on thermal spray coating methods and property of different types of metal-based coatings. In: *Lecture notes in mechanical engineering*. pp. 427–439. [https://doi.org/10.1007/978-981-33-6029-7\\_40](https://doi.org/10.1007/978-981-33-6029-7_40)
29. Subashri A, Uma Maheshwari TN (2016) Knowledge and attitude of oral hygiene practice among dental students. *J Adv Pharm Technol Res* 9(11):1840
30. Tittelboom V, Kim ND, Belie FL, Grosse CU (2012) Acoustic emission analysis for the quantification of autonomous crack healing in concrete. *Constr Build Mater.* <https://doi.org/10.1016/j.conbuildmat.2011.08.079>
31. Tittelboom V, Kim JW, Araújo M, Snoeck D, Gruyaert E, Debbaut B, Derluyn H et al (2016) Comparison of different approaches for self-healing concrete in a large-scale lab test. *Constr Build Mater.* <https://doi.org/10.1016/j.conbuildmat.2015.12.186>
32. Tyagi RK, Gupta G (2019) Investigation of titanium as thin film deposited material thereon effect on mechanical properties. In: *Advances in industrial and production engineering*. pp 315–323. [https://doi.org/10.1007/978-981-13-6412-9\\_30](https://doi.org/10.1007/978-981-13-6412-9_30)
33. Wiktor V, Jonkers HM (2011) Quantification of crack-healing in novel bacteria-based self-healing concrete. *Cement Concr Compos.* <https://doi.org/10.1016/j.cemconcomp.2011.03.012>

# Spectroscopic Study of Eco-Friendly Slow Release Micronutrient Delivery System



Manpreet Kaur Takkar and Khushbu Gumber

**Abstract** For optimum plant growth, micronutrients are just as important as macronutrients. These micronutrients are present in the soil naturally, but because they are not phytoavailable, a way must be found to make them accessible to plants from the outside. The highest quantity of nutrients supplied directly to plant systems leaches off, causing soil toxicity rather than fortification, which is another significant difficulty. Therefore, one of the main considerations is the introduction of a carrier material to improve the availability of the additional nutritional molecules. To carry the copper micronutrients for a slow release study, nano-zeolite was used in the design of the current study as a support material. FT-IR spectroscopy is used to establish the synthesis of nano-zeolite (NZ) and the loaded nutrient NZ (LNZ). And using UV–Visible spectroscopy as a foundation, the gradual release study of the nutrient particles is created. As a result, the plant will have access to the doped nutrients for the entirety of the crop culture time, which is great for promoting germination, development, flowering, and fruiting. The findings allow for the safe use of produced LNZ materials as an environmentally friendly fertilizer.

**Keywords** Fertilizer · Copper · Nano-zeolite · Slow release · Micronutrient · Spectroscopy

## 1 Introduction

Agriculture practices are essential for supplying food to people worldwide, but they are currently dealing with a number of global problems. One such challenge is the rapid population growth, which has put tremendous pressure on agricultural productions, which must be raised while using the same constrained land and water resources. As a result, the usage of fertilizers to enhance soil health increased significantly, enabling a quicker increase in output per hectare [5]. Fertilizers, however,

---

M. K. Takkar · K. Gumber (✉)

Department of Chemistry, University Institute of Sciences, Chandigarh University, Gharaura,  
Punjab, India

e-mail: [khushbu.e9433@cumail.in](mailto:khushbu.e9433@cumail.in)

contribute less to plant development and more to environmental challenges due to their high solubility, which results in leaching losses of 40–75% [5, 16], all of which have a negative impact on human health. Additionally, this wastes a substantial amount of fertilizer, costing money. Together, all of these issues have the potential to place a significant financial burden on society, which is a grave problem for both developed and developing nations working to achieve sustainability. It is urgently necessary to change agronomic practices by creating innovative, environmentally friendly fertilizers that can also increase crop productivity by facilitating optimal nutrient uptake.

Nanotechnology can help to promote sustainable agriculture by offering slow or controlled release fertilizers, herbicides, and insecticides [1, 6, 11]. Numerous studies have been done in this regard on the creation of nanoparticles or nano-composites to promote plant growth through direct nutrient uptake or nutrient release over time. A total of 16 nutrients are needed by plants, and 13 of those are normally absorbed from the soil. Through progressive release, nano-fertilizers have helped to ensure that these vital nutrients are always available to the soil. This gradual release encourages better nutrient uptake by the plants, which leads to early germination, quicker growth, and higher nutritional levels.

Zeolite is generally believed to benefit crop cultivation by enhancing soil quality by boosting nutrient and water consumption efficiency, biological activity, and fertility, and decreasing ammonia volatilization and soil salinity [8, 12–14, 17]. Zeolite's greater ability to retain nutrients in the soil makes nutrients more readily available to plants for longer periods of time because of its sluggish rate of breakdown and disintegration [11]. Given all of these advantages, zeolite has recently attracted a lot of attention and is currently utilized to gradually supply plants with fertilizer following small structural alterations [3, 7, 9, 10]. Only a little amount of study has been done on using nano-zeolite as a slow release fertilizer, and it is done by Subramanian et al. [15]. They showed that these nano-zeolites release nutrients over a far longer length of time than standard fertilizers do, significantly reducing nutrient leaching losses [15]. One of the crucial micronutrients for plants, copper is needed for the development of chlorophyll, seeds, and other enzymatic processes that take place in the plant system. Because of its lack, grain crops are more prone to illnesses like ergot. Thus, copper serves as both a fertilizer and a seed priming agent, protecting seeds from a variety of fungi.

In order to improve nutrient absorption capacity and reduce the likelihood of fungal disease while minimizing the environmental effects brought on by the use of conventional and environmentally hazardous materials, a simple and affordable method for the synthesis of copper micronutrient loaded nano-zeolite system is designed and analyzed for slow release in water.

## 2 Experimental Section

### 2.1 *Materials and Methods*

Sodium hydroxide pellets AR (NaOH, caustic soda,  $40 \text{ g mol}^{-1}$ ),  $\text{Al}_2(\text{SO}_4)_3 \cdot 16\text{H}_2\text{O}$  ( $630.38 \text{ g mol}^{-1}$ ),  $\text{Na}_2\text{SiO}_3 \cdot 9\text{H}_2\text{O}$  ( $284.2 \text{ g mol}^{-1}$ ),  $\text{C}_2\text{H}_6\text{O}_2$  ( $62.07 \text{ g mol}^{-1}$ ) were purchased from Central Drug House India.  $\text{CuCl}_2 \cdot 2\text{H}_2\text{O}$  ( $170.48 \text{ g mol}^{-1}$ ) was purchased from Qualikems Fine Chem India. Fourier transformation infrared (FT-IR) spectroscopy was used to analyze each manufactured composite material. On a Perkin Elmer Spectra Two-IR Fourier-Transform spectrophotometer, the FT-IR spectrum of nano-zeolite and its composite was captured in the  $400\text{--}4000 \text{ cm}^{-1}$  region. UV-Visible analysis was used to check for micronutrient presence in the water release research sample. On a SHIMADZU MODEL UV-1900, the UV-Visible spectrum of the water release research was obtained between  $200$  and  $1000 \text{ cm}^{-1}$ .

### 2.2 *Synthesis of Loaded Micronutrient Nano-zeolite (LNZ)*

According to a study by, Lateef et al. [4] nano-zeolite (NZ) was made using a modified co-precipitation technique. In this procedure, ethylene glycol (2.5 ml) and sodium silicate (22 g/30 ml distilled water) were added to a round-bottomed flask. To create a uniform mixture, the mixture was swirled for a half-hour at a temperature of  $50\text{--}60 \text{ }^\circ\text{C}$ . Aluminum sulfate (7.87 g/25 ml) and sodium hydroxide (3 g/25 ml) were added drop by drop to the aforementioned mixture while being continuously stirred and heated at  $50\text{--}60 \text{ }^\circ\text{C}$ . Following the whole addition, the pH of the mixture was brought back to neutral using concentrated HCl. Thereafter, filtration and oven drying at  $100 \text{ }^\circ\text{C}$  were performed. The mixture was ground, then put into a muffle furnace and calcined at  $650 \text{ }^\circ\text{C}$  for five hours. The finished sample was chilled to room temperature after calcination. The sample was marked as NZ and was gray in color. Simply impregnating nutrients into nano-zeolite produced more LNZ. To get the most nutrient impregnation into the nano-zeolite, a 5% solution of the micronutrient (Cu) in the form of its salts ( $\text{CuCl}_2 \cdot 2\text{H}_2\text{O}$ ) was added to the previously synthesized nano-zeolite in distilled water (5 g/10 ml). The finished product was then dried, filtered, and finely ground. The final LNZ product was tagged and kept in an airtight container.

### 2.3 *Slow Release Studies in Water*

By conducting an experiment in centrifuge tubes (15 ml) with 0.5 g of LNZ in distilled water (pH 7) and acidic media, the seven-day gradual release or leaching pattern of LNZ in water was determined (pH 5). Throughout the experiment, the volume of



each tube was kept at the 5 ml threshold. To ascertain the release of nutrients over the course of seven days, water samples in increments of 4 ml were taken at intervals of 2 h, 24 h, 3 days, 5 days, and 7 days.

### 3 Result and Discussion

#### 3.1 Characterization of NZ and LNZ

In Fig. 1, FT-IR spectra of NZ and LNZ are presented. Peaks at 1102.13 (doublet) and 613.52  $\text{cm}^{-1}$  are attributed to Al–O and Si–O bending and stretching in the zeolite (NZ) structure [4]. The peak shift in the FT-IR spectra for LNZ, or micronutrient doped nano-zeolite, to 979.32 (merged) and 709.77  $\text{cm}^{-1}$  for copper doped micronutrient, respectively, relates to the nutrient incorporation into the zeolite structure leading to the doped product. The IR spectra for the NZ and LNZ are depicted in Fig. 1.

#### 3.2 Water Release Study

To examine the release pattern of LNZ for copper in water at two different pH values, the UV–Vis spectral analysis was used (5 and 7). In both cases, experiments were carried out in triplicate, and the findings were averaged out based on the total amount of nutrients present in LNZ. The % release was estimated using a standard curve created for cupric chloride at various concentrations (0.001, 0.005, 0.01, 0.025, and 0.05 g/ml) showed in Fig. 2. The first indicator was that the release of nutrients is much higher at pH 5 than in neutral medium, and the second was that there is a burst release after a set amount of time, such as after seven days in neutral medium. Existing research on slow release fertilizers, which reveals a substantial nutrient release in an acidic medium, supports the findings [2]. Therefore, the synthesized sample's gradual release behavior can be used to promote germination, growth, flowering, and fruiting.

### 4 Conclusion

The current study focuses on the synthesis of an environmentally friendly fertilizer that is a slow release micronutrient carrier based on zeolite. In order to extend the plant's access to nutrients, nano-porous zeolite's properties were used to integrate micronutrients. The progressive provision of nutrients under neutral soil conditions is further supported by slow release research, which reduces the traditional fertilizers' tendency to leak from the soil. As a result, utilizing nano-fertilizers to boost plant growth and productivity may open up new avenues for agricultural practice. Plant

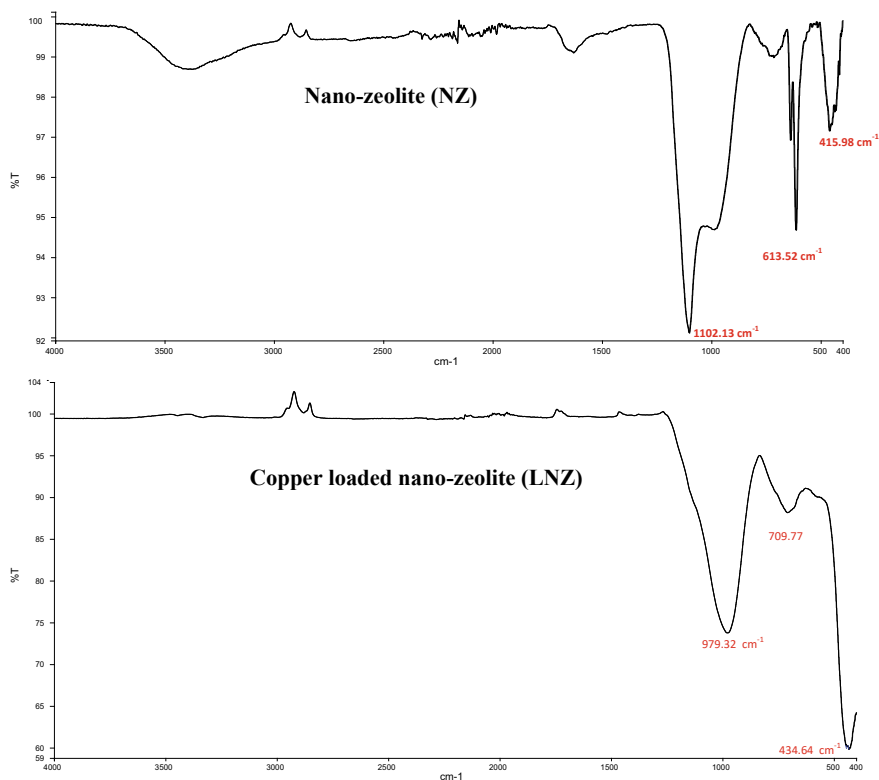


**Fig. 1** IR spectra of NZ and LNZ

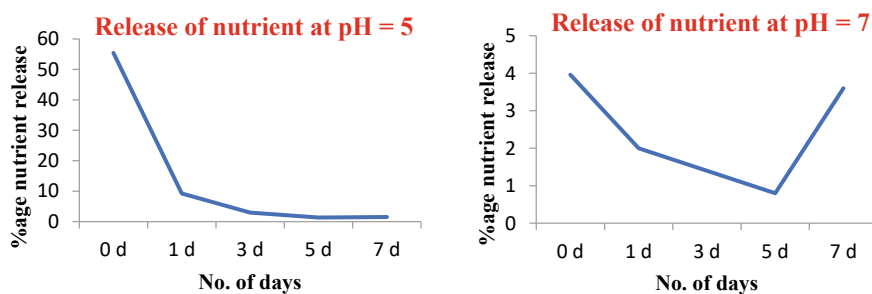


**Fig. 2** Release of nutrient at pH 5 and pH 7

response to nano-fertilizers, on the other hand, varies depending on the plant species, growth stage, and nanomaterial composition. The safety, bioavailability, and toxicity of various NFs or NPs used in agricultural production should be the focus of future research.

## References

1. Baruah S, Dutta J (2009) Nanotechnology applications in pollution sensing and degradation in agriculture. *Environ Chem Lett* 7(3):191–204. <https://doi.org/10.1007/s10311-009-0228-8>
2. Bindra P, Kaur K, Rawat A, De Sarkar A, Singh M, Shanmugam V (2019) Nano-hives for plant stimuli controlled targeted iron fertilizer application. *Chem Eng J* 375(June):121995. <https://doi.org/10.1016/j.cej.2019.121995>
3. de Campos Bernardi AC, de Souza GB, Polidoro JC, Paiva PRP, de Mello Monte MB (2011) Yield, quality components, and nitrogen levels of silage corn fertilized with urea and zeolite. *42(11):1266–1275*. <https://doi.org/10.1080/00103624.2011.571980>
4. Lateef A, Nazir R, Jamil N, Alam S, Shah R, Khan MN, Saleem M (2016) Synthesis and characterization of zeolite based nano-composite: an environment friendly slow release fertilizer. *Microporous Mesoporous Mater* 232:174–183. <https://doi.org/10.1016/j.micromeso.2016.06.020>
5. Liu R, Lal R (2015) Potentials of engineered nanoparticles as fertilizers for increasing agro-nomic productions. *Sci Total Environ* 514(2015):131–139. <https://doi.org/10.1016/j.scitotenv.2015.01.104>
6. Mura S, Seddaiu G, Bacchini F, Roggero PP, Greppi GF (2013) Advances of nanotechnology in agro-environmental studies. *Ital J Agron* 8(3):127–140. <https://doi.org/10.4081/ija.2013.e18>
7. Noori M, Zendehelel M, Ahmadi A (2007) Using natural zeolite for the improvement of soil salinity and crop yield. *88(1):77–84*. <https://doi.org/10.1080/02772240500457928>
8. Omar OL, Ahmed OH, Muhamad AMN (2010) Minimizing ammonia volatilization in water-logged soils through mixing of urea with zeolite and sago waste water. *Int J Phys Sci* 5(14):2193–2197. <https://doi.org/10.5897/IJPS.9000372>
9. Pereira EI, Minussi FB, Da Cruz CCT, Bernardi ACC, Ribeiro C (2012) Urea-montmorillonite-extruded nanocomposites: a novel slow-release material. *J Agric Food Chem* 60(21):5267–5272. [https://doi.org/10.1021/JF3001229/ASSET/IMAGES/MEDIUM/JF-2012-001229\\_006.GIF](https://doi.org/10.1021/JF3001229/ASSET/IMAGES/MEDIUM/JF-2012-001229_006.GIF)
10. Perrin TS, Drost DT, Boettinger JL, Norton JM (2008) Ammonium-loaded clinoptilolite: a slow-release nitrogen fertilizer for sweet corn. *21(3):515–530*. <https://doi.org/10.1080/01904169809365421>
11. Rai V, Acharya S, Dey N, Rai V, Acharya S, Dey N (2012) Implications of nanobiosensors in agriculture. *J Biomater Nanobiotechnol* 3(2):315–324. <https://doi.org/10.4236/JBNB.2012.322039>
12. Ramesh K, Reddy DD, Biswas AK, Rao AS (2011) Zeolites and their potential uses in agriculture. *Adv Agron* 113:215–236. <https://doi.org/10.1016/B978-0-12-386473-4.00009-9>
13. Reháková M, Čuvanová S, Dzivák M, Rimár J, Gaval'ová Z (2004) Agricultural and agro-chemical uses of natural zeolite of the clinoptilolite type. *Curr Opin Solid State Mater Sci* 8(6):397–404. <https://doi.org/10.1016/J.COSSMS.2005.04.004>
14. Saadat S, Sepaskhah AR, Azadi S (2012) Zeolite effects on immobile water content and mass exchange coefficient at different soil textures. *43(22):2935–2946*. <https://doi.org/10.1080/00103624.2012.724748>
15. Subramanian KS, Manikandan A, Thirunavukkarasu M, Rahale CS (2015) Nano-fertilizers for balanced crop nutrition. *Nanotechnol Food Agric* 69–80. [https://doi.org/10.1007/978-3-319-14024-7\\_3](https://doi.org/10.1007/978-3-319-14024-7_3)
16. Trenkel (2013) Slow and controlled-release and stabilized fertilizers. *J Chem Inf Model* 53(9)
17. Xiubin H, Zhanbin H (2001) Zeolite application for enhancing water infiltration and retention in loess soil. *Resour Conserv Recycl* 34(1):45–52. [https://doi.org/10.1016/S0921-3449\(01\)00094-5](https://doi.org/10.1016/S0921-3449(01)00094-5)

# Mechanical Behavior of Friction Stir Welded Al-Alloy AA6063 + 5%SiC<sub>p</sub>



Pardeep Gahlot, Narinder Kaushik , Naveen Hooda, Rajkumar Duhan, and Rakesh Kumar Phanden

**Abstract** Friction stir welding of Al-alloy AA6063-5%SiC<sub>p</sub> was carried out by applying various permutations of tool rotating velocity and tool traverse velocity using vertical milling machine (VMC). FSW is termed as the green joining technique of the present and future generation. In this research work, the welded joints have been obtained by altering input variables at two-level variation ranges. Tool rotating velocity, tool traverse speed and dwell time were the input variables in this experimental research. Sound weld joints thus obtained were tested for various mechanical properties, namely hardness, tensile strength, etc., during welding process. The results showed that there is a sharp increase in the hardness and tensile strength of the SiC particulate reinforced AA6063. The obtained results were complied with graphs and optical images to analyze the exact behavior.

**Keywords** Friction stir welding (FSW) · VMC-vertical milling machine · FSW · SiC<sub>p</sub>

## 1 Introduction

FSW does not need consumable filler material and can eliminate some welding faults like cracks and porosity. It is usually referred to as a green welding technology as well as a promising welding procedure that can produce high-strength joints [1]. The Welding Institute (TWI) invented friction stir welding in 1991 [2]. Numerous researchers have used the FSW approach to combine comparable and dissimilar

---

P. Gahlot · N. Hooda · R. Duhan  
Mechanical Engineering Department, UIET, MDU, Rohtak, India

N. Kaushik (✉)  
Mechanical and Automation Engineering Department, MAIT, Rohini, Delhi, India  
e-mail: [narinderk@mae.mait.ac.in](mailto:narinderk@mae.mait.ac.in)

R. K. Phanden  
Mechanical Engineering Department, Amity School of Engineering & Technology, Amity University Noida, Noida, India

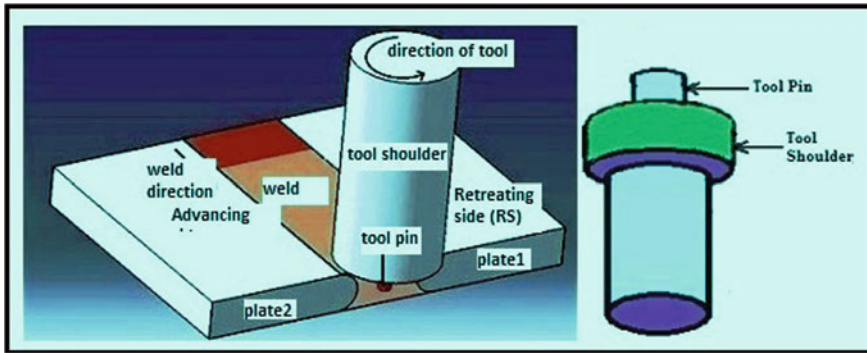


**Fig. 1** Mechanism of friction stir welding process

metals, particularly aluminum alloys and its series, since its discovery [3–7]. When welding aluminum alloys and aluminum-based composite materials, green welding technologies like FSW approaches are preferable.

As in the case of solid state welding method, the metals does not undergo melting and so the problems of cracks arising during solidification occurs. The other disadvantages of fusion welding like porosity, development of HAZ, segregation and development of brittle intermetallics are also minimized. FSW promised to be the most attractive solid state joining technique for the fusion of al-based alloys and aluminum-based composites in producing variety of joints such as butt joints as shown in Fig. 1 and lap joints, etc. [8, 9]. In order to impart properties that are not achievable with discrete phases, metallic matrix composites are intermetallic compounds made up of two or more chemically and physically distinct metal phases that are implanted inside a metallic matrix [10].

The literature lists various manufacturing processes for creating aluminum matrix composites. Based on the reinforcement and matrix material, a production method is selected. The most popular, economical and practical method for creating AMCs is stir casting. The right manufacturing technique has an impact on the microstructure of the produced composite, the dispersion of the reinforcement particles into the alloy matrix and the interfacial bonding of particles between the matrix and reinforcement phase [11, 12].

In this paper, AA6063 reinforced with  $\text{SiC}_p$  has been friction stir welded. The parameters under consideration were tool feed rate, tool rotating velocity and dwell time. The level of variation has been kept as two. The produced welds have been examined for the tensile strength, macro hardness. The results have analyzed and optimized using full factorial method, and each parameter's percentage contribution is calculated.

## 2 Materials and Methods

In this experimental work, AA6063 reinforced with 5% particulate Sic composite matrix was manufactured via stir casting method and cut in the dimensions of thickness 6 mm, width 50 mm and length 100 mm. The optical pictures of as produced AA6063 strengthen with 5% SiC particulates is shown in Fig. 2. AA6063 is an Mg-Si alloy. AA6063 finds application in many industrial and architectural framework irrigation pipes, tubes and automobile sector, etc. The welding samples, 100 × 50 × 6 mm, were butt welded using CNC milling machine with a special designed fixture as shown in Fig. 3. In this experiment, the tool used was made to have pin geometry. It was made from EN-24. The tools were made on the lathe machine and had cylindrical shoulder. The tool's pin was threaded and tapered for speedy metal removal and to facilitate the rapid transmission of heat from the metal. To strengthen the tool's strength, it was further heated in a muffle furnace to a temperature of 850 °C. Tool rotational speeds of 1800 and 2300 rpm were used in combination with traverse speeds of 20 and 40 mm/min and dwell time of 20 and 50 s as depicted in Table 1 to produce the butt-welded joints. Full factorial method was used to prepare the matrix for experimentation [8].

The samples for tensile testing were prepared in accordance with ASTM E08 standards. The test specimens have been set at 90° to the welding joint route and then machined and finished as per test dimension specifications. Three testing specimens for tensile examination have been cut from each plate to get the average tensile strength across each joint. The 100 KN capacity of computer operated universal tensile testing machine (FIE UNITEK-94100) was used to measure the tensile

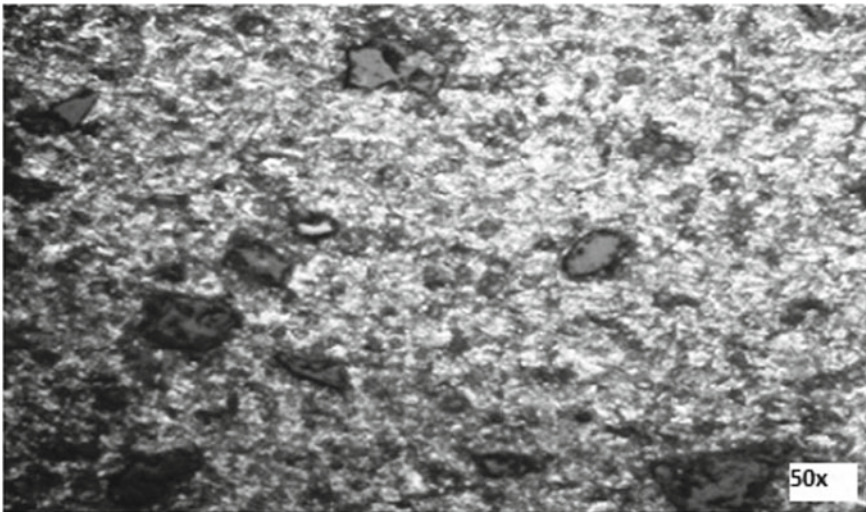


**Fig. 2** As-cast AA6063 + 5%SiC<sub>p</sub>

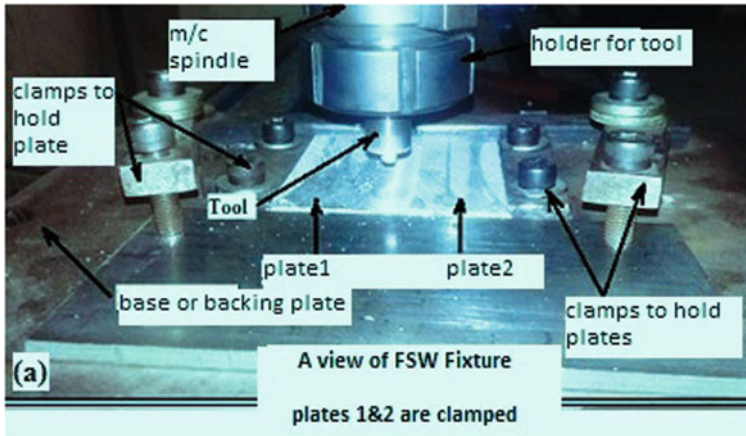


**Fig. 3** View of fixture

**Table 1** Experimental matrix

Sample number	Rotational velocity (rpm)	Traverse velocity (mm/min)	Dwell time (sec)
1	2300	40	20
2	2300	20	50
3	1800	40	50
4	1800	20	20
5	2300	20	20
6	1800	20	50
7	2300	40	50
8	1800	40	20

strength of the test samples. Specimens for measuring hardness were set in accordance with standard metallographic procedures. A Brinell hardness tester at a load of 100 kgf was used to measure the macro hardness of the samples [8].

### 3 Results and Discussion

#### 3.1 Tensile Test

100 KN capacity of computer operated universal tensile testing machine (FIE UNITEK-94100) was employed to measure the tensile strength of test samples at a strain rate of 0.4 mm/min. Test samples were cut by using WEDM. The dimensions



of the test samples were kept 20 mm × 10 mm × 6 mm as length, width and thickness, respectively. Load against displacement and stress against strain graphs have been plotted for the test samples. A relative plot as shown in Fig. 5 depicting the test specimen number 5 with greater tensile strength at the weld nugget from all of the 8 test samples. The related welding parameters with the sample having maximum tensile strength can be described as:

Tool spindle speed: 2300 rpm

Feed: 20 mm/min

Dwell time: 20 s.

For each weld sample, the rotating velocity, feed rate and dwell time were maintained constant during the whole experiment. An analysis of the variation in the tensile strength was done using the tensile strength data that was gathered for several samples at varied welding conditions. The graph that was created for all 8 samples revealed that sample No. 5 had the highest tensile strength, which was 105 Mpa. The graph unequivocally demonstrates the greater tensile strength of the low feed weld area. Figure 4 displays an optical view of a 5% SiC Al AMC weld nugget. The sharp increase in the tensile strength of sample no. 5 is due to the smashing of SiC particles in the weld region which is depicted in Fig. 5 [13, 14].

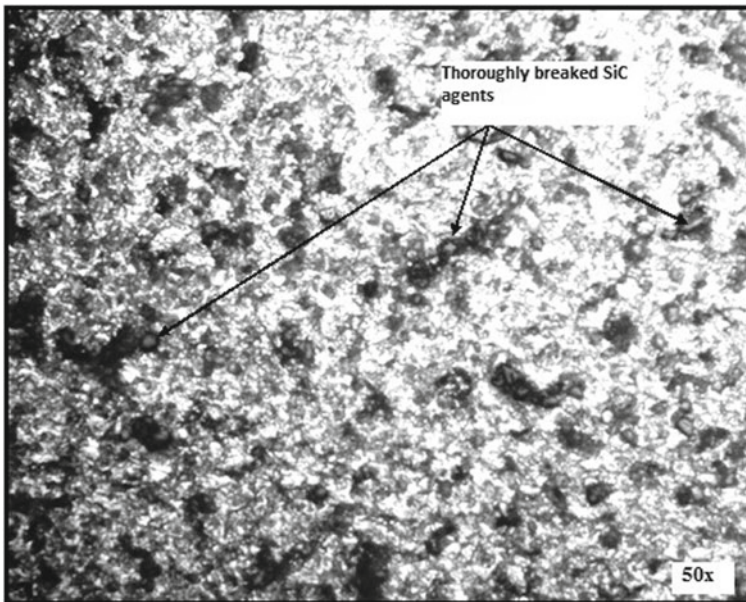


**Fig. 4** Optical image showing weld nugget of 5% SiC Al AMC welded joint (sample no. 5)



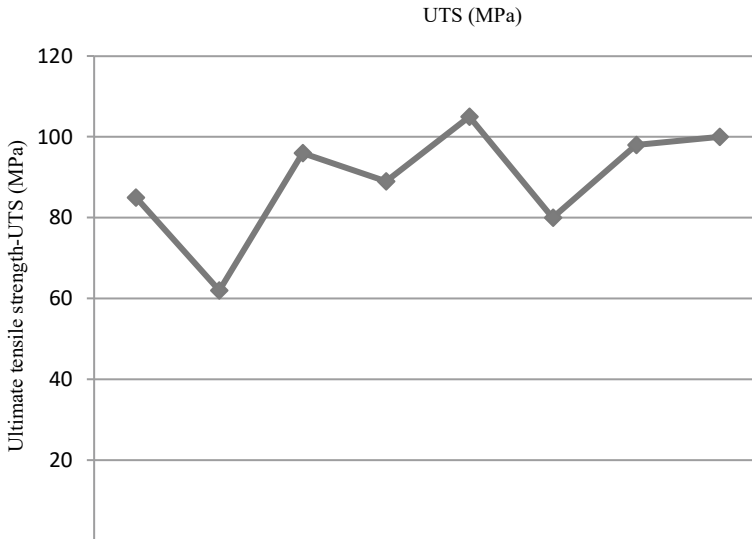


**Fig. 5** Comparison of UTS at the weld center

### 3.2 Macro Hardness Test

A Brinell hardness tester at a load of 100 kgf was used to measure the macro hardness of the samples. The indenter diameter was 10 mm. The indentation was made on the weld samples at the 5 points. These points are the weld center, 2 points in HAZ and 2 points on the base metal on the either side of the center. In each of the specimen, the hardness was calculated at the middle of the weld and a graph is plotted to analyze the sample with maximum hardness at the weld nugget and also to describe the related welding parameters. In Fig. 4, the optical image showing the weld nugget of 5% SiC Al AMC welded joint. The sharp increase in the hardness in weld zone of sample no. 3 is due to the smashing and scattering of SiC agents in the joint area [13, 14]. The fine distribution of SiC particulates, and grain refinement in the weld nugget of sample no. 3 with the associated welding parameters was responsible for the increase in hardness. A sufficient amount of heat generated at the selected welding parameters was responsible for the fine grain refinement and ultimately increase in the hardness of the welded joint as displayed in Fig. 6.

The graph as shown in Fig. 7 represents the hardness of the various 8 samples welded at different welding parameters. The graph clearly depicts that the sample no. 3 exhibits the maximum hardness of 138BHN with its associated welding parameters as:

Tool spindle speed: 1800 rpm  
 Feed: 40 mm/min  
 Dwell time: 50 s.

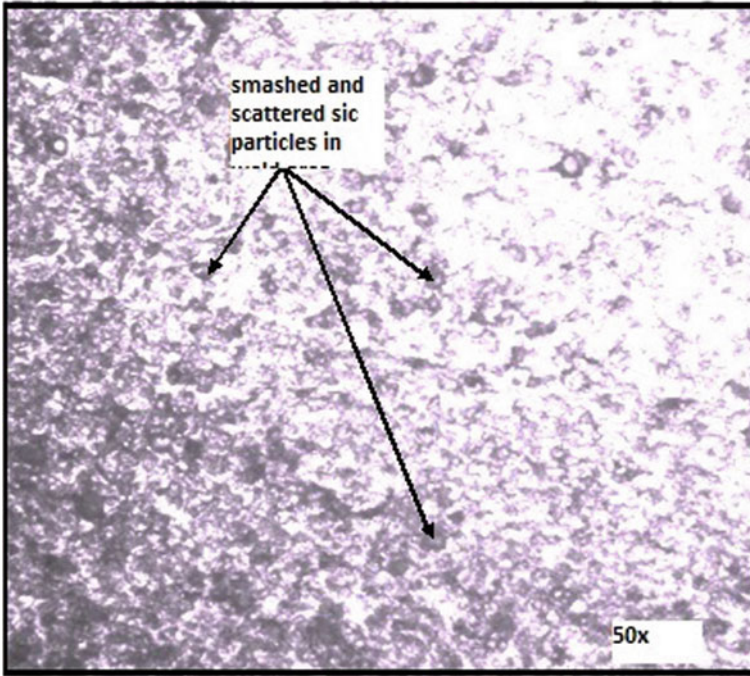


Fig. 6 Optical picture showing weld nugget of 5% SiC Al AMC welded joint (sample no. 3)

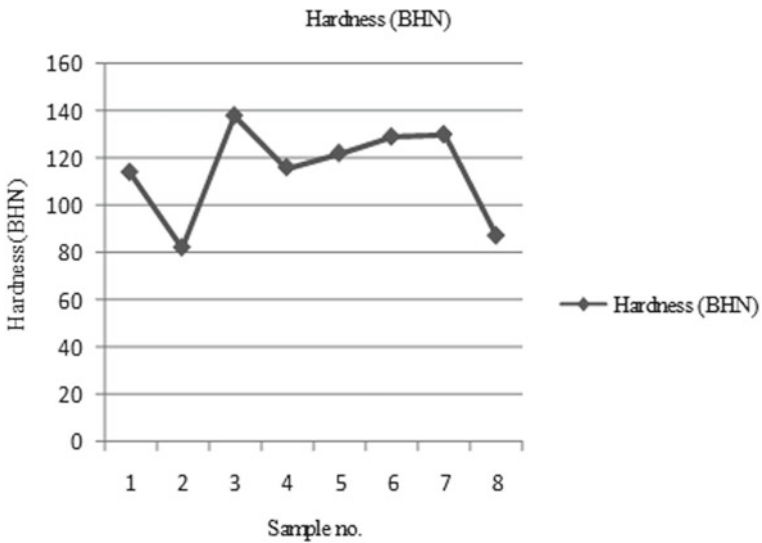


Fig. 7 Comparison of hardness at the weld center

## 4 Conclusions

FSW seems to be a useful method for joining AA6063 AMC strengthen with 5% SiC particles. In this experiment, the FSW of 6 mm thick AA6063 with 5 weight percent SiC composite plates was performed. It was determined how the eight samples of AA6063/SiC matrix composite plates that were friction stir welded at various welding conditions compared in terms of tensile strength and hardness. The welded joint's maximum tensile strength was seen at low feed rates and dwell times combined with a high tool rotational speed of 2300 rpm. The sharp rise in tensile strength in the weld nugget was caused by the fine grain structure, crushing, and scattering of SiC particles. At lower tool rotating speeds of 1300 rpm, as well as high feed rates and dwell times, the weld joint's maximum hardness was noted. Due to the increased quantity of SiC reinforcing agents in the nugget zone, some agglomeration was also noted. The variance in the joints' ultimate tensile strength is responsible for the agglomeration. Agglomeration caused a reduction in UTS in some samples, which was noted. Some locations in the joint showed variance in the joint's hardness value, and as a result, some locations showed a decline in hardness.

## References

1. Kaushik N, Singhaal S (2017) Mechanical and metallurgical examinations of stir cast aluminum matrix composites: a review study. *Int J Eng Technol* 9:3203–3217
2. Reynolds AP (2000) Visualisation of material flow in autogenous friction stir welds. *Sci Technol Welding Joining* 5(2):120–124; Chen T (2009) Process parameter study on FSW joints of dissimilar metal for aluminium steel alloys. *J Mater Sci* 44(10):2573–2580
3. Venkateswaran P, Xu ZH, Li X, Reynolds AP (2009) Determination of mechanical properties of Al–Mg alloys dissimilar friction stir welded interface by indentation methods. *J Mater Sci* 44(15):4140–4147
4. Watanabe T, Takayama H, Yanagisawa A (2006) Joining of aluminum alloy to steel by friction stir welding. *J Mater Process Technol* 178(1–3):342–349
5. Kaushik N, Singhal S, Rajesh R, Gahlot P, Tripathi BN (2018) Experimental investigations of friction stir welded AA6063 aluminum matrix composite. *J Mech Eng Sci* 12(4):4127–4140
6. Kumar BA, Murugan N (2014) Optimization of friction stir welding process parameters to maximize tensile strength of stir cast AA6061-T6/AlNp composite. *Mater Des* 57:383–393
7. Koilraj M, Sundareswaran V, Vijayan S, Rao SK (2012) Friction stir welding of dissimilar aluminum alloys AA2219 to AA5083—optimization of process parameters using Taguchi technique. *Mater Des* 42:1–7
8. Kaushik N, Singhal S (2019) Experimental investigations on microstructural and mechanical behavior of friction stir welded aluminum matrix composite. *Int J Eng* 32(1):162–170
9. McGuire PF (1992) Aluminum composites come in for a landing. *Mach Des* 64:71–74
10. Surappa MK (2003) Aluminium matrix composites: challenges and opportunities. *Sadhana* 28(1):319–334
11. Aigbodion VS, Hassan SB (2007) Effects of silicon carbide reinforcement on microstructure and properties of cast Al–Si–Fe/SiC particulate composites. *Mater Sci Eng, A* 447(1–2):355–360
12. Verma S, Misra JP (2015) A critical review of friction stir welding process. *DAAAM Int Sci Book* 14:249–266

13. Kaushik N, Singhal S (2018) A case study of mechanical and metallurgical properties of friction stir welded AA6063 AMC. *Int J Microstruct Mater Prop* 13(3–4):240–255
14. Baxter SC, Reynolds AP (2001) Characterization of reinforcing particle size distribution in a friction stir welded AL-SiC extrusion. In: *Lightweight alloys for aerospace application*. pp 283–293

# 3D Printing of Phase Change Materials: Issues and Challenges



Deepak Kumar Yadav, Basant Singh Sikarwar, Arvind Kumar Gupta, and Rajeev Kumar Singh

**Abstract** Latent heat storage offers most preferable technique for thermal energy storage because of invariable working temperature and high energy storage density. Latent heat storage systems use phase change materials (PCM) for energy storage. These systems suffer from low thermal conductivity of PCM which elongates charging and discharging time. A lot of research is being carried out to enhance the performance of PCM by using high thermal conductivity additives and porous media to enhance thermal conductivity, using cascaded or multistage latent heat technique to ameliorate heat transfer uniformity, using encapsulated PCM and finned structure to increase heat transfer surface. This paper reviews fabrication methods of PCM-based system using 3D printing technique. In addition, the research gaps in this field are also discussed and some recommendation for further research are also proposed.

**Keywords** PCM · Latent heat storage systems · 3D printing

## 1 Introduction

Today, there is a key issue for effective energy utilization due to concern over greenhouse gas emissions and finite reserve of fossil fuels. PCMs for thermal energy storage (TES) offer a viable solution for efficacious energy management and without greenhouse gas emissions. PCM in TES systems enhances the storage efficiency and these systems find their application in industrial (automobile, electronic, biomedical, construction, textile, etc.) and domestic sectors. The utilization of PCMs in energy storage systems preserves energy, improves reliability, and fills the gap between supply and demand. PCMs exhibit high energy density with the capability to store

---

D. K. Yadav · B. S. Sikarwar · R. K. Singh (✉)

Department of Mechanical Engineering, Amity University Uttar Pradesh, Noida, UP, India

e-mail: [rksingh4@amity.edu](mailto:rksingh4@amity.edu)

A. K. Gupta

Department of Mechanical Engineering, YMCA University, Faridabad, Haryana, India

© The Author(s), under exclusive license to Springer Nature Singapore Pte Ltd. 2024

R. K. Tyagi et al. (eds.), *Advances in Engineering Materials*, Lecture Notes in Mechanical Engineering, [https://doi.org/10.1007/978-981-99-4758-4\\_30](https://doi.org/10.1007/978-981-99-4758-4_30)

337

and release large amount of thermal energy during melting and solidification, respectively, at nearly constant temperature. These materials store and release energy in the form of latent heat. PCMs include polymeric materials like polyethylene glycol (PEG), organic compounds like fatty acids and paraffins and inorganic compounds like salt and salt hydrates [1].

The desirable properties of ideal PCMs are high thermal conductivity in solid and liquid phase, high energy density, high specific heat, insignificant volume change during phase change, congruent melting, low vapor pressure at the operating temperature, high nucleation rate, no supercooling, adequate rate of crystallization, non-flammable, non-toxic, non-explosive, non-corrosive, long-term chemical stability, and completely reversible freeze/melt cycle. Apart from this, it should be abundantly available at low cost [2].

## 2 Conventional Manufacturing Methods for PCM Systems

The favored way of preparation of PEG-based phase change systems are chemical modification for realizing PEG solid–solid PCM (such as polyurethane, hexamethylene diisocyanate biuret, and halloysite nanotubes), physical blending of PEG with other supporting materials (such as microcrystalline cellulose and graphene aerogels), and vacuum impregnation in porous materials (such as mesoporous silica) [3]. The paraffin wax has large latent heat capacity but poor thermal conductivity ( $\sim 0.2$  W/m K). The thermal conductivity of paraffin wax can be enhanced by using nanoadditives like graphene [4], carbon nanotube [5], nanoparticles of zinc oxide, alumina, titania, silica [6], copper oxide [7], etc. The paraffin wax is melted, and these nanoadditives/nanoparticles are added and stirred. Upon cooling, the wax solidifies with uniformly dispersed nanoparticles. This method is known as dispersion method. Fins or extended surfaces render additional heat transfer surface in concentric double pipe and shell and tube heat exchangers. In these systems, heat is dissipated from inner tube surface and PCM is stored in annulus/shell. There is an increase in thermal resistance between liquid PCM which is away from inner tube and solidified PCM adjacent to inner tube during discharging. This results in poor heat transfer to the liquid PCM. Attachment of fins to the tube renders superior thermal contact with heat transfer surface resulting in decreased thermal resistance [8]. Paraffin wax can be encapsulated in polymeric shell by cross-linking of polymerizable vinyl monomers via facial suspension polymerization in order to enhance thermal conductivity as well as latent heat [9]. Fatty acids like lauric acid, capric acid, palmitic acid, stearic acid, etc., are used as PCM because of fairly high latent heat. Their melting temperature can be adjusted by mixing different fatty acids in different proportions. The constituent fatty acids are mixed in liquid state by melting them, holding them at that temperature, and then solidifying at room temperature [10].

Salt hydrates possess moderate to high latent heat but large supercooling and incongruent melting limits their use as PCM in thermal energy storage systems. Anhydrous salt form solid crystalline structure in the presence of water in specific

molar ratio and is then known as salt hydrates. The examples of salt hydrates are sodium sulfate decahydrate ( $\text{Na}_2\text{SO}_4 \cdot 10\text{H}_2\text{O}$ ) (also known as Glauber's salt), lithium chlorate trihydrate ( $\text{LiClO}_3 \cdot 3\text{H}_2\text{O}$ ), potassium fluoride tetrahydrate ( $\text{KF} \cdot 4\text{H}_2\text{O}$ ), dipotassium hydrogen phosphate hexahydrate ( $\text{K}_2\text{HPO}_4 \cdot 6\text{H}_2\text{O}$ ), calcium chloride hexahydrate ( $\text{CaCl}_2 \cdot 6\text{H}_2\text{O}$ ), calcium nitrate tetrahydrate ( $\text{Ca}(\text{NO}_3)_2 \cdot 4\text{H}_2\text{O}$ ), sodium thiosulfate pentahydrate ( $\text{Na}_2\text{S}_2\text{O}_3 \cdot 5\text{H}_2\text{O}$ ), etc. As compared to paraffins, salt hydrates possess lower material energy cost and high thermal energy density for melting temperature over 20 °C. Upon charging (gaining heat), salt hydrates melts and releases water and forms aqueous solution. There is insufficient released water to completely dissolve anhydrous salt. This results in incongruent melting. Upon discharging (releasing heat), anhydrous salt fails to recombine with water [11].

### 3 3D Printing Methods for PCM

#### 3.1 Thermoplastic Polyurethane Blends

3D printing of thermoplastic polyurethane blends was performed using fused deposition modeling (FDM) machine for sports applications to provide thermal comfort to athletes. The polyurethane blends consisted of polyurethane and encapsulated paraffin wax. The paraffin wax particles were encapsulated in melamine formaldehyde resin which formed hard shells of size  $\sim 20 \mu\text{m}$ . The paraffin wax had 85–90 wt% in encapsulated particles with latent heat of 157–167 kJ/kg. Polyurethane in granular form was mixed with encapsulated particles in different proportions and then extruded to form 1.75 mm diameter wire form to be used as filament material in FDM machine. During 3D printing process, deposition rate, bed temperature, nozzle temperature, and layer thickness were maintained at 40 mm/sec, 40 °C, 240 °C, and 0.20 mm, respectively, in FDM machine as these were optimized parameter for this composite. As the concentration of encapsulated particles in composite was increased, melt flow index (MFI) was increased indicating enhanced flowability. The melting and crystallization temperature of 3D printed composite were 5 °C and –9 °C, respectively, and were almost invariable for change in encapsulated particles concentration. With increase in encapsulated particles concentration, the ductility of 3D printed composite decreased (enhanced embrittlement). Higher elastic modulus of shell material in composite was responsible for this embrittlement. In creep analysis of 3D printed composite, no tertiary creep was observed and by increasing concentration of encapsulated particles, decrease in creep compliance was observed. Latent heat of 3D printed composite was 70 kJ/kg for encapsulated particles concentration of 50 wt% [12].

### 3.2 Concrete Mixed with PCM

The PCM was added to building materials and then it is 3D printed to obtain excellent thermoregulatory properties. The PCM in concrete absorbs heat when ambient temperature is rising and releases heat when ambient temperature is declining. In this way, PCM enhances thermal comfort inside the building. The PCM consisted of paraffin wax encapsulated in polymethyl methacrylate with particle size 2–10  $\mu\text{m}$ . Since 3D printers for printing concrete are not available commercially, so indigenously designed and built 3D printer with accuracy of 0.1 mm was used as shown in Fig. 1.

Ordinary concrete mixture could not be used in 3D concrete printer because limitations of fluidity, low compressive strength and extrusion efficiency and less workability, plasticity, viscosity, and hydration rate. So certain additives were added in concrete apart from PCM to enhance its viability to be used in 3D concrete printer. Glass beads were added in concrete in place of fine sand to enhance compressive strength and extrusion efficiency. Fly ash, hydroxypropyl methylcellulose, lithium carbonate, and magnesium aluminum silicate were added in concrete mixture to improve workability, viscosity, hydration, and fluidity, respectively.

As the PCM concentration was increased, the compressive and flexural strengths were decreased by 24% and 44% and 4% and 39% for PCM concentration of 10% and 20%, respectively, as compared to without PCM concrete mixture. Although, the 3D printed hollow and solid blocks made by concrete mixture with PCM fulfilled the minimum requirement of compressive strength from buildings code viewpoint. The thermal conductivity of 3D printed concrete was also decreased with increasing

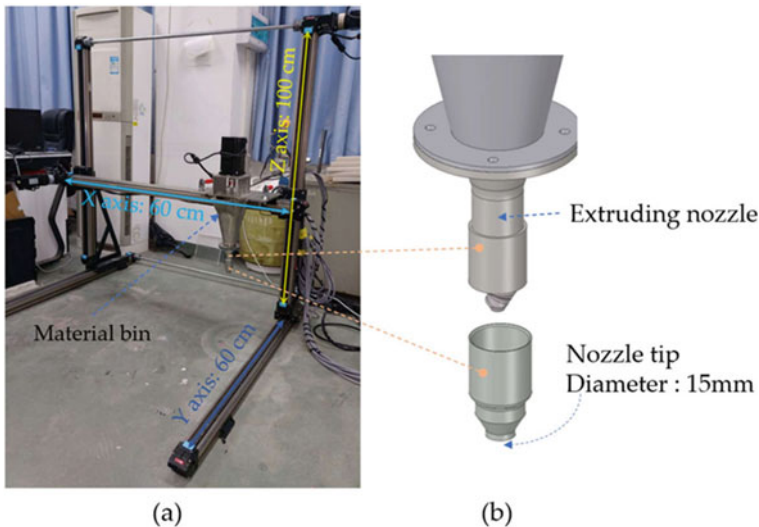


**Fig. 1** 3D concrete printer **a** printing system along with nozzle **b** details of nozzle [13]



concentration of PCM. This decrease was  $\sim 24\%$  for both concentration of 10 and 20%. Interfacial gap and porosity in concrete were responsible for reduced thermal conductivity. Maximum indoor temperature of 3D printed room was reduced to  $6^\circ\text{C}$  and  $8^\circ\text{C}$  for PCM concentration of 10% and 20%, respectively. This decrease in room temperature balances the grid load and reduces the building energy consumption [13].

### 3.3 *Aluminum Silicon Alloy Grid*

The thermal conductivity of PCM-based thermal energy storage system can be enhanced by employing grid structure. These grid structures with complex shape can be rapidly and accurately fabricated using 3D selective laser melting process as shown in Fig. 2a–c.

The material for the grid structure was aluminum silicon alloy (AlSi10Mg) and three types of grid structures, viz. uniform fin thickness, non-uniform fin thickness, and tapering fin thickness were fabricated in heat exchanger as shown in Fig. 2a–c. Two PCMs, viz. paraffin wax and myristic acid were used for the study. Due to highest alloy content in case of non-uniform fin thickness heat exchanger, charging time was fastest indicating more efficacious heat transfer. The charging power (W)/time (min) was 450/9.67, 430/11, and 405/10 and discharging power (W)/time (min) was 670/6, 545/7.85, and 604/7.33 for uniform fin thickness, non-uniform fin thickness, and tapering fin thickness type heat exchanger, respectively, for paraffin wax. Discharging time was shorter as compared to charging time in all three cases because of higher temperature difference between heat transfer fluid and melting temperature of PCM. Also discharging power was more as compared to charging power in all three cases for paraffin wax as PCM. Heat transfer was enhanced due to 3D printed alloy grid skeleton which escalates the phase transition rate of the PCM which was responsible for enhanced efficiency of heat energy storage and release. The superior performance of grid type heat exchanger was accredited by low convection thermal resistance and high conduction. Similar results were obtained for myristic acid. Average power for massive phase change were 435 W and 895 W during charging and discharging respectively for myristic acid PCM [14].

### 3.4 *Fused Filament Fabrication*

The composite PCM can be 3D printed using fused filament fabrication. For it, composite is made in wire form (wire diameter 1.75 mm) using extrusion process then it is supplied to heated nozzle of the fused filament system. The composite consists of polymer and PCM. Fused filament system prints the structure as per computer-aided design (CAD) using composite wire.

High density polyethylene (HDPE) and PureTemp 42 were used as polymer and PCM, respectively, for making wire of 1.75 mm using the extrusion process to use

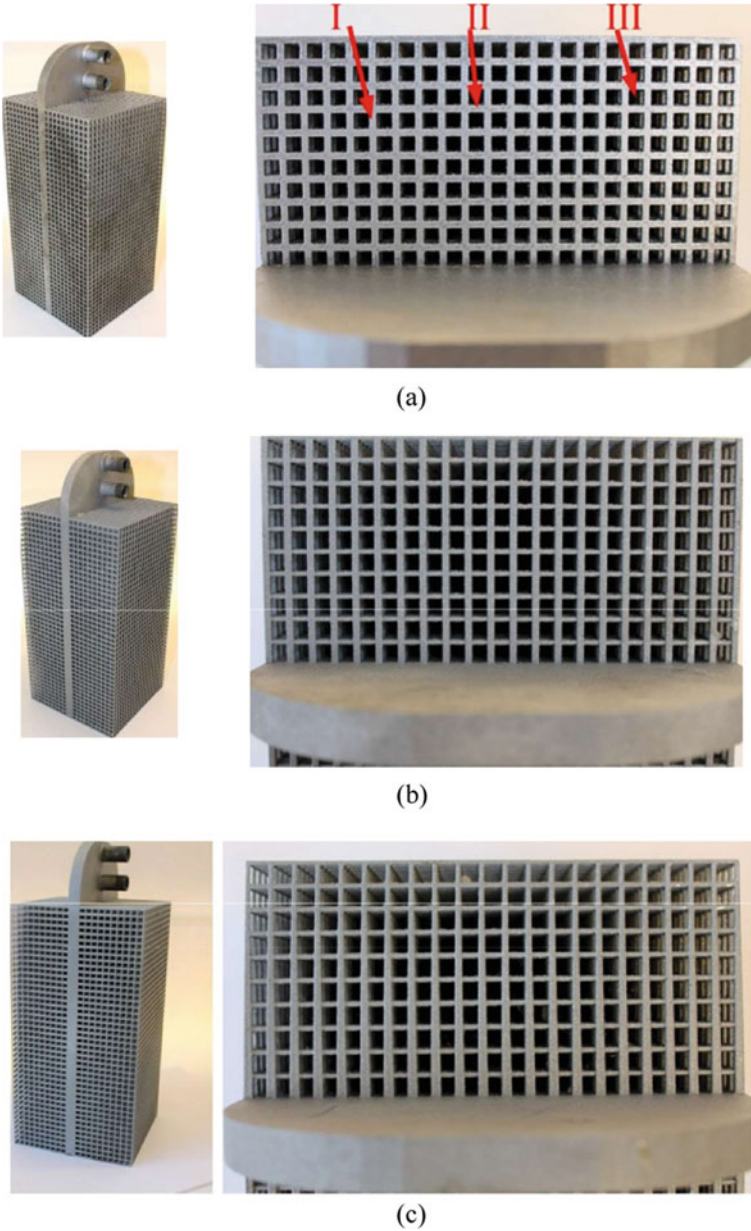


**Fig. 2** Grid type heat exchanger **a** uniform fin thickness **b** non-uniform fin thickness and **c** tapering fin thickness (I, II, and III in **a** indicating orthogonal grid, parallel grid, and grid spacing, respectively) made by 3D selective laser melting machine [14]

in fused filament system. This system printed the composite PCM by moving the nozzle in *X*- and *Y*-directions. Pure PCM and pure HDPE had melting temperature of 44 °C and 133 °C, respectively, while PCM and HDPE in composite had melting temperature of 40 °C and 124 °C, respectively, in case of 3D printed structure. Similarly, for the same 3D printed structure, the latent heat of melting for pure PureTemp 42 and pure HDPE was 64 kJ/kg and 120 kJ/kg, respectively. The thermal conductivity of 3D printed composite PCM was 0.365 W/m K which was in between the thermal conductivity of pure PCM ( $k = 0.276$  W/m K) and pure HDPE ( $k = 0.576$  W/m K) [15].

### **3.5 Aluminum Honeycomb with Prickly Structure**

3D printed aluminum honeycomb with prickly structure (3D Al-Hc) was filled with paraffin wax (PW), expanded graphite (EG), high-density polyethylene (HDPE), and carbon fibers (CF) by melt blending to make form stable composite phase change material (CPCM). Prickly structures were extended surfaces inside hexagonal structure. These prickly structures were added to enhance compressive strength and thermal conductivity of CPCM. In this CPCM, paraffin wax acted as phase change material, expanded graphite, and high-density polyethylene acted as support material, whereas role of carbon fibers was to enhance thermal conductivity.

Experimental investigation revealed that PW (82.5 wt%)/EG (7 wt%)/HDPE (6 wt%)/CF (4.5 wt%)/3D Al-Hc attained maximum thermal conductivity (5.723 W/m K). The thermal conductivity of same CPCM with honeycomb structure (i.e., without prickly structure) attained was 4.465 W/m K. This indicated the role of extended surface in increasing thermal conductivity. Reduction in the carbon fiber content lowered the thermal conductivity of CPCM. Increase in carbon fiber content lowered the melting temperature and enhanced the freezing temperature of CPCM. There was a trend of decrease in latent heat of fusion and freezing with increase in carbon fiber content. Compressive strength in increasing order was PW/EG/HDPE/CF, PW/EG/HDPE/CF/Al-Hc (i.e., simple hexagonal structure and without prickly structure) and PW/EG/HDPE/CF/3D Al-Hc. The deformation for 100 kPa compressive stress in these CPCM was 8 mm, 4.9 mm, and 1.25 mm, respectively [16].

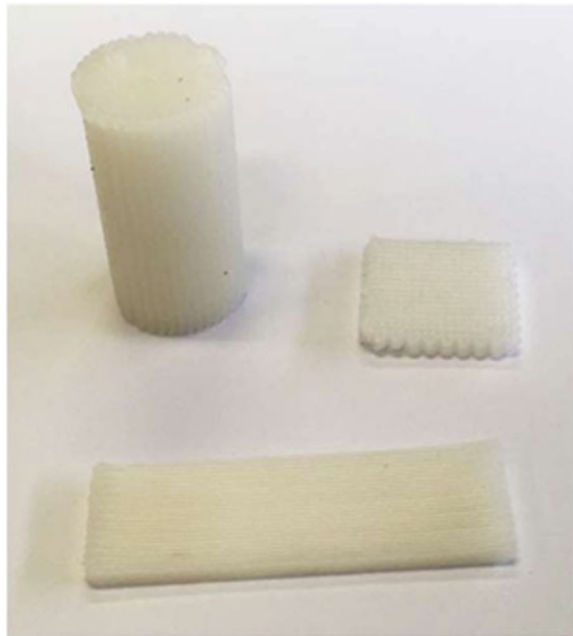
### **3.6 Biopolymer**

The polyester polycaprolactone, which is a biopolymer, is a suitable candidate material for additive manufacturing technology. This polymer can be processed in fused deposition modeling system. Shape stabilized composite PCMs (SS-CPCM) were

formed by mixing paraffin RT27 (Rubitherm) and Micronal DS5040 (Microencapsulated PCM) (Microtek Labs) in it via dissolution method. Experimental investigation demonstrated that increase in PCM content enhanced the latent heat of fusion in both SS-CPCM (i.e., polycaprolactone + RT27 and polycaprolactone + Micronal DS5040). No significant change was observed in melting temperature of RT27 and polycaprolactone for RT27 content from 10 to 60% in RT27-based SS-CPCM. Due to shell damage during SS-CPCM formation, slight variation in melting temperature of Micronal DS5040 was observed for DS5040 content from 10 to 60% in DS5040-based SS-CPCM. There was no significant change in the melting temperature of polycaprolactone in this CPCM for all wt%.

Different objects were printed (as shown in Fig. 3) by fused deposition modeling method using polycaprolactone/RT27 (20 wt%). These 3D printed material had latent heat of fusion and melting temperature as 10 kJ/kg and 27 °C, respectively. The 3D printed material had lower latent heat of fusion than material formed by dissolution method. Reduction in latent heat capacity of 3D printed material can be attributed to high temperature of extruder which was responsible for phase separation in composite PCM. Enthalpy loss was detected in both SS-CPCM after large number of thermal cycling [17].

**Fig. 3** 3D printed sample using polycaprolactone/RT27 (20 wt%) [17]



### ***3.7 Cold Source Design***

In selective freezing 3D printing process, there is a requirement of uniform temperature over the substrate and platform. Methods for this requirement are application of PCM, peltier cooling, and metal block cooling. Among these methods, PCM is capable to provide uniform temperature over the entire surface of substrate/platform. In order to print uniform porous structure by selective freezing 3D printing process, uniform temperature of substrate is prime requirement.

Aqueous ammonium chloride and sodium chloride in different concentrations were tried as PCM to obtain cold source in selective freezing 3D printing process. Both aqueous salts were capable to provide extremely stable temperature up to 150 min that was sufficient for one printing round. Higher concentration of aqueous salts resulted in longer phase change time which was the desirable characteristic of selective freezing 3D printing process. 400 ml volume of aqueous salt was sufficient to provide cold temperature up to 4 h in selective freezing 3D printing process. Fin structure in platform enhanced heat transfer efficiency resulting in a more stable cooling system. Fin structure in platform doubled the phase change duration compared to platform without fin structure. Spatially temperature of the platform was fairly constant till 70 min indicating that PCM can provide stable temperature for this duration in selective freezing 3D printing process. More homogeneous interior structure was obtained when parts were fabricated using PCM as cold source [18].

### ***3.8 Hydrogel as the Cooling Phase Change Medium***

One of the probable applications of hydrogel is in cooling, where it acts as phase change material. Water-based hydrogels possesses the property of stability, non-toxicity, eco-friendliness, affordability, superior softness, biocompatibility, wetness, and bioactivity. High water content in it provides liquid like attributes like transparency to optical and acoustic waves and permeability to different types of biological and chemical molecules to it. Water content in it absorbs heat which makes water-based hydrogels a candidate material for cooling devices.

A CPCM, consisted of layers of Ca-alginate/polyacrylamide hydrogel and polydimethylsiloxane (PDMS), was demonstrated a suitable material for cooling application. In this CPCM, PDMS served as thermal insulation barrier and prevented the dehydration of hydrogel layer. This CPCM can absorb large amount of water. It was experimentally demonstrated that optimum value of water in hydrogel was 85 wt% to control the temperature increment rate by maintaining a balance of conduction pathway between polymer network and water. A linear relationship was obtained between cold retention capacity and hydrogel layer thickness in CPCM. If hydrogel layer thickness increases, cold retention capacity also increases. Cooling capacity of CPCM increased by 60 min for every added layer of hydrogel. Hydrogel with 80 wt% and 95 wt% water exhibited highest young's modulus (1500 kPa) and

highest flexibility, respectively. Toughness of hydrogel decreases with increasing water content. Experimental investigation demonstrated that for optimum overall performance (Young's modulus:  $1.4 \times 10^5$  Pa and minimum cooling capacity: 192 min) was obtained for 85 wt% water content in hydrogel. Introduction to fumed silica in hydrogel enhanced flexibility as well as cooling capacity.

3D printing of the CPCM was performed by stereolithography process. In this process, cross-linking of polymer was initiated by UV light. The printed hydrogel lattice indicated super-elastic performance suitable for sports applications. In uniaxial compression test of printed sample, deformation was fully recoverable below 80% strain. Large improvement in the cooling capacity of the hydrogel was observed if PDMS was filled into porous lattice structure of hydrogel during 3D printing [19].

### ***3.9 3D Printing of Polyethylene Glycol with Form Stabilized Cellulose Nanofibrils***

Most existing PCM suffer from instability, leakage, fossil fuel-based origin, and volume change. There is a need to develop a PCM that is leak proof, form stable, and tunable melting temperature. A form stable phase change nanohybrid (PCN) was formed by polyethylene glycol (PEG) and cellulose nanofibrils (CNFs) through aqueous blending process. CNF originates from renewable sources like microorganisms, wood, and plants. In this PCN, cellulose nanofibrils served as matrix with its content varying 15–25%. Molecular mass and fusion temperature of PEG varied from 600 to 8000 and  $\sim 20$ –65 °C, respectively. PEG and CNF were crystalline and amorphous, respectively. Solid to gel transition takes place in PCN as opposed to conventional PCM, where solid to liquid transition takes place during phase change.

The PCN was 3D printed by bioprinter with pneumatic print heads. The substrate in this printing was plastic Petri dish and rectilinear infill pattern was followed for fabrication. PCN film had failure at 1% strain and corresponding tensile strength was 28 MPa. Due to physical interactions and high miscibility of CNF with PEG, PCN exhibits form stable structure at the melt state. It is experimentally demonstrated that thermal energy stored during melting and released during solidification increased with increasing content of PEG. Larger molecular mass of PEG resulted in higher latent heat. The stored and released heat in PCN was 81–146 kJ/kg and 71–142 kJ/kg during melting and crystallization, respectively, for PEG molecular mass of 600–8000. Reduction in fusion temperature was obtained as CNF content increased. The thermal conductivity of 3D printed PCN (75% PEG 4000) was 0.040 W/m K. The PCN is suitable for thermal management of waste heat generating electronics, smart energy buildings, and aerospace equipment [20].

## 4 Conclusions

3D printing is versatile fabrication method that has enormous possibilities for CPCM fabrication. Fused deposition modeling is suitable for printing polyurethane-based CPCM, HDPE-based CPCM, and polycaprolactone-based CPCM. This process requires the CPCM to be extruded into wire of diameter 1.75 mm. This wire later on used as feed material in extrusion head. This process can be controlled by varying deposition rate, bed/platform temperature, nozzle temperature, and layer thickness. To print concrete-based PCM, large sized printer with extruding nozzle is required due to the large size of the building structure. The CPCM suitable for this 3D printing application must have high compressive strength and extrusion efficiency, good workability, viscosity, hydration, and fluidity.

The application of grid structure in PCM-based thermal energy storage system enhances the thermal conductivity of the system. 3D selective laser melting process is suitable for printing aluminum silicon alloy-based grid structure. Various geometries can be printed using this technique based on design. Similarly, aluminum honeycomb with prickly structure, printed using 3D printing process, enhances the thermal conductivity of CPCM.

3D printing process can be improved by using PCM. In selective freezing 3D printing process, ammonium chloride and sodium chloride can be used to make platform temperature uniform spatially and temporally. Stereolithography can be used to print Ca-alginate/polyacrylamide hydrogels which can hold large amount of water. These hydrogels are CPCM and suitable for cooling applications. PEG-based PCM can be 3D printed using bioprinter. In this CPCM, high PEG loading is possible due to the affinity of cellulose nanofibrils.

## 5 Future Methods

3D printing of HDPE, polyurethane, and polycaprolactone-based CPCM was demonstrated using fused deposition modeling technique. Other polymers with same PCM or same polymers with other PCM can also be printed using same technique. Further evaluation of thermal cycling for long-term stability, leakage issues, and mechanical testing including tensile and flexural testing should be conducted on these CPCMs. Geopolymer is a candidate material in building material. The possibility of 3D printing of geopolymer-based CPCM should be explored. In case of grid structure to enhance thermal conductivity of CPCM, more grid design (with fin)/grid material like copper, etc., should be investigated by 3D printing process to obtain maximum thermal conductivity.



## References

1. Pielichowska K, Pielichowski K (2014) Phase change materials for thermal energy storage. *Prog Mater Sci* 65:67–123. <https://doi.org/10.1016/j.pmatsci.2014.03.005>
2. Sharma A, Tyagi VV, Chen CR, Buddhi D (2009) Review on thermal energy storage with phase change materials and applications. *Renew Sustain Energy Rev* 13(2):318–345. <https://doi.org/10.1016/j.rser.2007.10.005>
3. Kou Y et al (2019) Thermal analysis and heat capacity study of polyethylene glycol (PEG) phase change materials for thermal energy storage applications. *J Chem Thermodyn* 128:259–274. <https://doi.org/10.1016/j.jct.2018.08.031>
4. Kumar K, Sharma K, Verma S, Upadhyaya N (2019) Experimental investigation of graphene-paraffin wax nanocomposites for thermal energy storage. *Mater Today: Proc* 5158–5163. [Online]. Available: <https://www.sciencedirect.com/science/article/pii/S2214785319327026>
5. Kuziel AW et al (2021) Ultra-long carbon nanotube-paraffin composites of record thermal conductivity and high phase change enthalpy among paraffin-based heat storage materials. *J Energy Storage* 36:102396. <https://doi.org/10.1016/j.est.2021.102396>
6. Teng T-P, Yu C-C (2012) Characteristics of phase-change materials containing oxide nano-additives for thermal storage. *Nanoscale Res Lett* 7(1):611. <https://doi.org/10.1186/1556-276X-7-611>
7. Jesumathy S, Udayakumar M, Suresh S (2012) Experimental study of enhanced heat transfer by addition of CuO nanoparticle. *Heat Mass Transf* 48(6):965–978. <https://doi.org/10.1007/s00231-011-0945-y>
8. Bose P, Amirtham VA (2016) A review on thermal conductivity enhancement of paraffin wax as latent heat energy storage material. *Renew Sustain Energy Rev* 65:81–100. <https://doi.org/10.1016/j.rser.2016.06.071>
9. Pradhan R, Ramaswamy AP (2019) Encapsulation of paraffin wax by rigid cross-linked poly (styrene divinylbenzene-acrylic acid) and its thermal characterization. *SN Appl Sci* 1(8):859. <https://doi.org/10.1007/s42452-019-0891-8>
10. Kant K, Shukla A, Sharma A (2016) Ternary mixture of fatty acids as phase change materials for thermal energy storage applications. *Energy Rep* 2:274–279. <https://doi.org/10.1016/j.egy.2016.10.002>
11. Hirsche J, Gluesenkamp KR, Mallow A, Graham S (2018) Review of inorganic salt hydrates with phase change temperature in range of 5 °C to 60 °C and material cost comparison with common waxes. In: 5th international high performance buildings conference. pp 1–10. [Online]. Available: <https://www.osti.gov/servlets/purl/1468092>
12. Rigotti D, Dorigato A, Pegoretti A (2018) 3D printable thermoplastic polyurethane blends with thermal energy storage/release capabilities. *Mater Today Commun* 15:228–235. <https://doi.org/10.1016/j.mtcomm.2018.03.009>
13. Cui H, Yu S, Cao X, Yang H (2022) Evaluation of printability and thermal properties of 3D printed concrete mixed with phase change materials. *Energies* 15(6):1978. <https://doi.org/10.3390/en15061978>
14. Yazdani MR et al (2021) Efficient storage and recovery of waste heat by phase change material embedded within additively manufactured grid heat exchangers. *Int J Heat Mass Transf* 181:121846. <https://doi.org/10.1016/j.ijheatmasstransfer.2021.121846>
15. Freeman TB, Messenger MA, Troxler CJ, Nawaz K, Rodriguez RM, Boetcher SKS (2021) Fused filament fabrication of novel phase-change material functional composites. *Addit Manuf* 39:101839. <https://doi.org/10.1016/j.addma.2021.101839>
16. Cao M, Huang J, Liu Z (2020) The enhanced performance of phase-change materials via 3D printing with prickly aluminum honeycomb for thermal management of ternary lithium batteries. *Adv Mater Sci Eng* 2020:1–11. <https://doi.org/10.1155/2020/8167386>
17. Salgado-Pizarro R, Padilla JA, Xuriguera E, Barreneche C, Fernández AI (2021) Novel shape-stabilized phase change material with cascade character: synthesis, performance and shaping evaluation. *Energies* 14(9):2621. <https://doi.org/10.3390/en14092621>



18. Yang F, Zhao G, Zhou C, Lin D (2018) Phase change materials (PCM) based cold source for selective freezing 3D printing of porous materials. *Int J Adv Manuf Technol* 95(5–8):2145–2155. <https://doi.org/10.1007/s00170-017-1295-9>
19. Gogoi P et al (2020) Ductile cooling phase change material. *Nanoscale Adv* 2(9):3900–3905. <https://doi.org/10.1039/D0NA00465K>
20. Yazdani MR, Ajdary R, Kankkunen A, Rojas OJ, Seppälä A (2021) Cellulose nanofibrils endow phase-change polyethylene glycol with form control and solid-to-gel transition for thermal energy storage. *ACS Appl Mater Interfaces* 13(5):6188–6200. <https://doi.org/10.1021/acsami.0c18623>

# Challenges and Possibilities in the Welding of Advanced High-Strength Steels



Marcell Gáspár  and Raghawendra P. S. Sisodia 

**Abstract** In numerous industrial fields, there is a demand for the application of high strength steels (HSS). Steel producers have an increased attention to develop new generation of HSS with good weldability properties. The users of HSS in welded structures generally face with the problem of cold cracking, significant deterioration of mechanical properties in the heat-affected zone and the arising questions related to the mismatch ratio between the base and the filler material. Gas metal arc welding (GMAW) is the commonly used technology for HSS, although welding equipment with the function of advanced pulsed process variants is recommended to achieve minimized heat input and acceptable penetration at the same time. Beam welding processes can offer new opportunities with the combination of preheating, welding and post-weld heat treatment by the same heat source. Present paper provides a brief overview about weldability challenges and the advanced technological solutions regarding HSS. A strong relation can be identified between the steel processing route, weldability and the recommended welding technology.

**Keywords** High strength steels · Weldability ·  $t_{8/5}$  cooling time · Beam welding processes

## 1 Introduction

In order to realize sustainable development, the reduction of CO<sub>2</sub> emission is one of the key factors. The structure of vehicles is often needed to fulfil different expectations. On the one hand, weight reduction should be realized to reduce the fuel consumption, and so the pollutant emission. On the other hand, more safety and convenience device should be implemented into the vehicles which can easily increase their weight. The weight reduction and the fulfilment of safety requirements at the same time cannot be imagined without high strength steels (HSS). Besides vehicle industry, HSS also appears in different kind of welded structures,

---

M. Gáspár (✉) · R. P. S. Sisodia  
University of Miskolc, Miskolc 3515, Hungary  
e-mail: [marcell.gaspar@uni-miskolc.hu](mailto:marcell.gaspar@uni-miskolc.hu)

where the main motivation is basically originated from aesthetic considerations of designers for slim structures. Therefore, there is an increasing demand nowadays for the application of HSS, although their welding, especially in the higher grades, is challenging for welding engineers.

By the combination of special rolling (e.g. thermomechanical rolling) and heat treating technologies, and the application of various microalloying elements, the steel producers aim to develop new generations of HSS with good elongation, toughness and weldability properties [1]. Since the origin of high strength is often originated from a partially or fully martensitic microstructure, especially in the higher grades, therefore the irreversible change of the non-equilibrium microstructure should not be neglected. In the heat-affected zone (HAZ), softened and brittle subzones can form depending on the welding heat cycle and peak temperature. Present paper provides an overview about the development tendencies and microstructural background of HSS, HAZ characterization and weldability difficulties, mismatch phenomena, welding process window ( $t_{8/5}$ ), post-weld heat treatment (PWHT) and the advanced welding technologies (e.g. pulsed MIG/MAG, beam welding processes).

## 2 Steel Grades and Their Production

The available highest strength structural steels have nearly four times higher yield strength than a structural steel one hundred years ago (Fig. 1). Although the ratio between yield and tensile strength is increasing towards one by the upper steel grades, so their plastic reserve is relatively low. Thanks to the implementation of quenching and tempering (Q&T) high strength steels have been produced with outstanding toughness properties for decades. These steels have generally a tempered martensitic and partially bainitic microstructure with relatively high (0.15–0.25) carbon content, alloying with Mo, Cr, Ni and microalloying elements (Al, Ti, Nb, Zr, V and B) depending on the steel producers. The high yield strength can be originated by the martensitic-bainitic microstructure, grain refinement, solid solution of alloying elements and higher dislocation density. Although they are outstanding base materials, their relatively high carbon equivalent raises numerous difficulties during welding.

By the appearance of thermomechanical rolling (TMCP), the same yield strength can be achieved by less carbon content and less macro alloying elements, however microalloying has also an important role in their case. Their microstructure is generally bainitic-martensitic with even finer grain size compared to Q+T steels. Their widespread application is limited by their plate thickness in the range of medium-thick plates since the thermomechanical rolling cannot be realized in larger cross sections. In case of both production routes, the steel producers try to minimize the contamination (especially S, P) content to guarantee high toughness at low temperature.

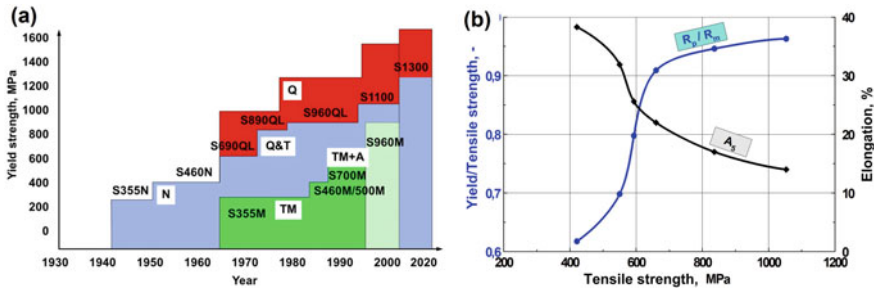


**Fig. 1** Development trends (a) of high strength structural steels and their mechanical characteristics (b)

### 3 Weldability Challenges

When the weldability of a given structural steel is investigated, the first step is to analyse its position in the Graville diagram (Fig. 2), which separates structural steels into three zones rated by their ease of weldability: zone I easily weldable, zone II weldable with care and zone III difficult to weld. The diagram highlights that with increasing carbon equivalent, the weldability decreases but it also emphasizes the extremely important effect of carbon content on weldability. In Fig. 2, the positions of different steel grades were determined based on the information provided in the 3.1 type base material certificate of several steel producers according to EN 10204. Based on the diagram, Q+T steels generally fall into the most problematic third area indicating high cold cracking sensitivity, while advanced TMCP steels fall into the zone I, so they are expected to be welded without the risk of cold cracking and the necessity of preheating.

In HSS, cold cracks can occur both in the weld (transversal direction) and HAZ due to the presence of hydrogen, brittle microstructure and residual stresses. The risk of cold cracking is relatively high in Q+T steels if too low welding heat input is used without preheating.

Another significant phenomenon is the deterioration of mechanical properties in HAZ. Depending on the steel category and welding heat input, hardened and softened zones can form. Especially hardened, brittle coarse-grained zone (CGHAZ) is identified in Q+T steels, while in TMCP steels, generally lower hardening is observed. The toughness can also significantly reduce in HSS, and not only in CGHAZ, but in the intercritical zone (ICHAZ), too. In multipass welding, especially the intercritical coarse-grained zone (ICCGHAZ) can be considered as the lowest toughness with the presence of local brittle zone (LBZ), especially in Q+T steels. The problem with the low impact energy in HAZ that it cannot be quantified with non-destructive testing (NDT), while cold cracks can be generally identified by penetration testing (PT) or ultrasonic testing (UT).

The third weldability problem of HSS is the limited availability of matching filler metals. While steel producers can optimize the microstructure with the combination

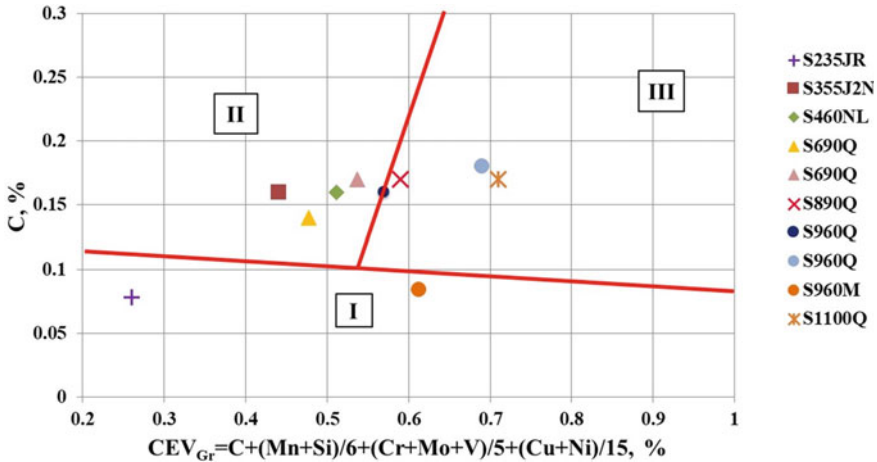


Fig. 2 Different structural steel grades in the Graville diagram

of heat treating, rolling and alloying, filler material producers' only chance is to find the ideal alloying elements to achieve the desired mechanical properties. Matching type filler materials, with increased amount of nickel compared to base material, nowadays are available up to the S1100 grade, however in case of S1300, only undermatching consumables can be selected. Depending on the location of the welded joint in the welded structure and the loading circumstances, numerous research investigate the effect of mismatch ratio on the fatigue resistance of the welded joints [2]. There are combinations of base and filler materials when undermatching can be more advantageous, while in other case, matching consumable is more expedient.

Since in welded structures, gas metal arc welding (GMAW) is the commonly used technology, therefore the presence of increased porosity may occur. Compared to mild steel, all literature emphasize that minimal welding heat input is recommended to HSS to preserve the mechanical, especially toughness properties. However, in practice, low welding heat input may increase the porosity level if the proper precautions (e.g. surface cleaning, grinding between the layers, appropriate purity level of shielding gas) are neglected. Due to the short welding cycle and so the fast solidification, there is not enough time for gas to leave from the weld pool.

### 4 Technological Considerations

During the welding technology planning, a relatively narrow  $t_{8/5}$  cooling time range is recommended for HSS (e.g. 6–10 for S960QL, 5–15 for S960M). The  $t_{8/5}$  conception considers the effect of preheating and welding heat input together. However, in many

HSS grades, there is not any theoretical background for the investigation of this 800–500 °C interval, since generally austenite to martensite transformation occurring during welding under 500 °C depending on the chemical composition.

Nowadays, GMAW is the spreadly used welding technology for HSS. Especially, there is a great future for the application of advanced process variants which can minimize the welding heat input and the HAZ extension with ensuring the appropriate weld penetration at the same time. Since waving of the weld torch should be avoided, therefore the weld built-up generally includes more welding pass compared to conventional steels. In order to achieve acceptable productivity, the application of metal-cored wire electrode can be prosperous.

There is an increasing tendency for the application of laser and electron beam welding processes for HSS. The core advantage of both technologies is the high energy density, and so deep penetration with minimal HAZ area. During special applications, both heat sources can be used for preheating and PWHT. Solutions can be elaborated when the welding and PWHT is realized by the same heat source equipment. Thanks to PWHT the risk of cold cracking can be minimized and the toughness of weld and HAZ can be significantly increased after welding.

## 5 Conclusion

In present paper, a short overview is provided about different high strength steel grades and their production, weldability and technological considerations. There is a strong relation between the steel processing route, weldability and the recommended welding technology. Thermomechanically rolled steels seem to be less sensitive to welding heat input in terms of the deterioration of mechanical properties in the heat-affected zone (HAZ) compared to quenched and tempered steel. Within gas metal arc welding, advanced pulsed process variants with metal-cored wire electrodes are the most prosperous, while the application of beam welding technologies can be advantageous due to the minimized area of weld and HAZ and to the opportunity of post-weld heat treatment by the same heat source.

## References

1. Porter DA (2015) Weldable high-strength steels: challenges and engineering applications. In: Portevin lecture, IIW 2015 international conference on high strength steels—challenges and applications, Helsinki, Finland, Paper IIW 2015 0102
2. Lukács J, Dobosy Á (2019) Matching effect on fatigue crack growth behaviour of high-strength steels GMA welded joints. *Weld World* 63:1315–1327

# CNT-Reinforced Metal Matrix Composites: A Review



Garvit Kumar, Anirudh Sharma, Bhavish Sharma, and Prateek Mittal

**Abstract** Materials have been an important part of human life from its very existence. Especially metals have played a vital role in the development of human kind. From tools to utensils, metals have been used extensively. In today's scenario, pure metals and metal alloys have become a bit less popular as compared to metal matrix composites (MMCs). This has happened because of the extraordinary properties possessed by MMCs. Properties such as high compressive and yield strength, good creep and wear resistance, good fatigue and corrosion resistance, ability to withstand high temperatures, high thermal conductivity and low coefficient of thermal expansion make MMCs suitable for most demanding applications such as aerospace, defense, surgical, automobile, structural and thermal management applications. MMCs have gained popularity over the years due to above-mentioned properties which distinguish them from pure metals and traditional alloys which possess very few of them taken together. There are several ways for the synthesis of MMCs such as sintering, powder metallurgy (P/M), squeeze casting, liquid infiltration and stir casting. This paper presents the latest developments in the field of metal matrix composites reinforced with carbon nanotubes (CNTs) including synthesis and applications. Some of the classical papers from the past have also been included to present a comprehensive picture as far as microstructure and alignment of CNT within the metal matrix is concerned. The paper indicates toward the challenges in the processing of CNT-reinforced MMCs and also points toward the potential future applications of these materials in the future.

**Keywords** CNT · MMC · Composites · Microstructure · Mechanical properties · CNT-reinforced MMCs

---

G. Kumar · A. Sharma · B. Sharma · P. Mittal (✉)

Department of Mechanical Engineering, Manav Rachna International Institute of Research and Studies, Faridabad, Haryana, India

e-mail: [prateekmittal.fet@mrii.edu.in](mailto:prateekmittal.fet@mrii.edu.in)

## 1 Introduction

The requirement of materials in the last few decades has changed to a great extent due to changing requirements of domestic and industrial applications [1]. There are different materials for different needs which arise out of requirements of the society. The usage of these materials leads to the discovery of newer materials which can substitute the older ones in functionality and performance [2]. The selection of materials is based on their physical and chemical properties [3]. For instance, a structural material is required to possess good compressive strength. The physical and chemical properties of a material generally make them suitable for a desired application [4]. Composite materials are the ones which two different materials are joined together in such a way that their combined physical and chemical properties result in the final properties of the composite. In composite materials, the constituent materials which are joined together remain in their individual form, bearing their own properties, while the properties of the composite are a result of their combination composite materials which are being used in the society from the time of oldest civilizations [5]. In today's world, metal matrix composites (MMCs) have gained tremendous popularity due to their extraordinary properties as compare to pure metals and metal alloys [6]. Properties such as high tensile and compressive strength, low weight to strength ratio high endurance limit, high resistance to creep, high thermal conductivity, low coefficient of thermal expansion, high scratch resistance, high wear resistance and excellent corrosion properties make MMCs stand apart as the choice of material for human kind [7]. MMCs are used in wide range of applications such as aerospace, defense, medical and surgical equipment, automotive components and locomotives [8]. CNT-aluminum composites are found to be extremely efficient against wear with very good temperature resistance, hence are most commonly used in aerospace applications. Cu-CNT composites having very low thermal expansion coefficient and extraordinarily high thermal conductivity up to the order of 6000 W/m-K are generally used in thermal management applications. Various research works have shown that Cu-CNT composites have very high strength and damping properties, hence is used in structural applications [9]. The addition of CNT in CU matrix not only increases wear resistance but also improves electrical conductivity, hence it is used in high energy electrical applications. CNT-reinforced steel nano-composites are potentially identified as structural materials for future with respect to petroleum industry. However, there are some challenges associated with uniform dispersion of CNT in steel matrix and alignment of CNT within the matrix. Various researchers have suggested solutions to these challenges and future applications of CNT-reinforced steel composites [10]. In automobile industry, brake shoes and cylinder liners are manufactured using CNTs due to their low density and high strength with excellent wear resistance. Aircraft brakes and landing gears are also produced with CNT-reinforced MMCs due to the aforementioned properties. Heat sinks for thermal management in electronic devices like large servers, databanks and high performance computers use CNT-reinforced MMCs due to their excellent thermal properties [11]. MMCs have at least two constituents; one of them



is required to be a metal. Other constituent can be a ceramic material or any other material suitable for a specific application. MMCs which have more than two components are known as hybrid MMCs. These hybrid MMCs also necessarily have one base metal, in which two or more other constituents are added which are known as reinforcements [12]. There are several materials which are used as base metals such as Al, Fe, Cu and Ti. The reinforcements which are added in to the base metal matrix can be ceramic or non-ceramic in nature and are generally added to provide specific properties to the MMCs. The ceramics are generally added as reinforcements in order to provide hardness, wear resistance and corrosion resistance to the MMCs [13]. The electronic devices and machines are reducing in size which creates a requirement of smaller components with desired properties in light MMCs [14]. CNTs are thin rolled graphene sheets. Graphene sheet is rolled in itself to create singled walled carbon nanotube (SWCNT) when these tubes are attached to other tube creating concentric multiple tubes, then the material is called multi-walled carbon nanotube (MWCNT) (Fig. 1). CNTs are known to possess extraordinary properties like extremely high thermal conductive (6000 W/mK), high yield strength (Up to 100 GPa) and extremely high stiffness. These CNT fibers can transform the properties of a metal completely and make it suitable for a demanding application [15]. In graphene-reinforced composites, the reinforcement materials are equally important as the matrix material as far as improvement in the properties of the composite is concerned [16]. In this paper, studies pertaining to recent articles on CNT-reinforced MMCs have been included with highlights on methods and materials and characterization. This paper discusses various research works carried out in the last 5 years in the field of CNT-reinforced MMCs. The need of this work is that very few review papers are present on CNT-reinforced MMCs. Although there are many research gaps as far as studies on CNT-reinforced MMCs are concerned [17]. These research gaps are listed asunder:

1. Uniform distribution of CNT in the metal matrix.
2. Orientation of the CNTs upon application of stress and heat.
3. Effect on microstructure of metal matrix upon addition of CNTs.
4. Effect of CNT properties on the microstructure of the final MMC.
5. Effect of processing parameter on the properties of the MMC.
6. Effect of matrix attributes on the composite properties.

## 2 Introduction

There are several methods available for synthesis of CNT-reinforced MMCs; the list of prominent methods is indicated in Fig. 2. Although all the methods are useful for synthesis of CNT-reinforced composites, powder metallurgy (P/M) remains as the most popular method for synthesis of CNT-reinforced MMCs. Electro-deposition acts as the second most popular method especially in case of thin film deposition of metals on CNTs and vice-versa. Metals having low melting point are processed

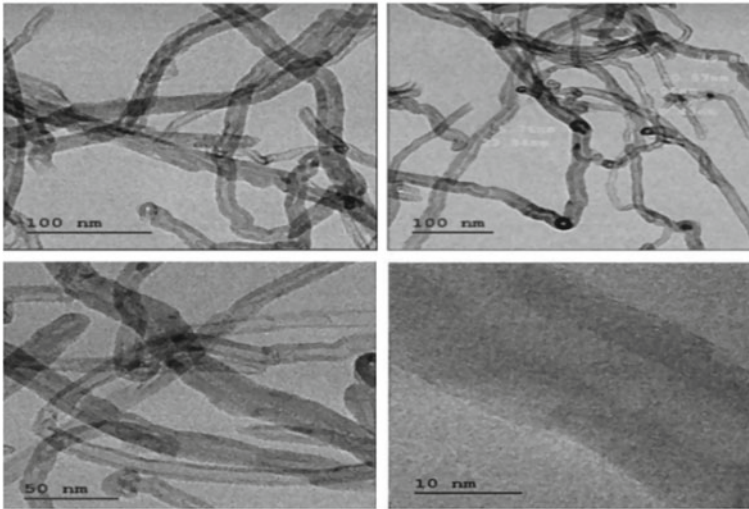


Fig. 1 Multi-walled carbon nanotube (MWCNT)

through liquid processing techniques such as stir casting and squeeze casting, and liquid processing may also be used in case of metals such as aluminum and copper [18].

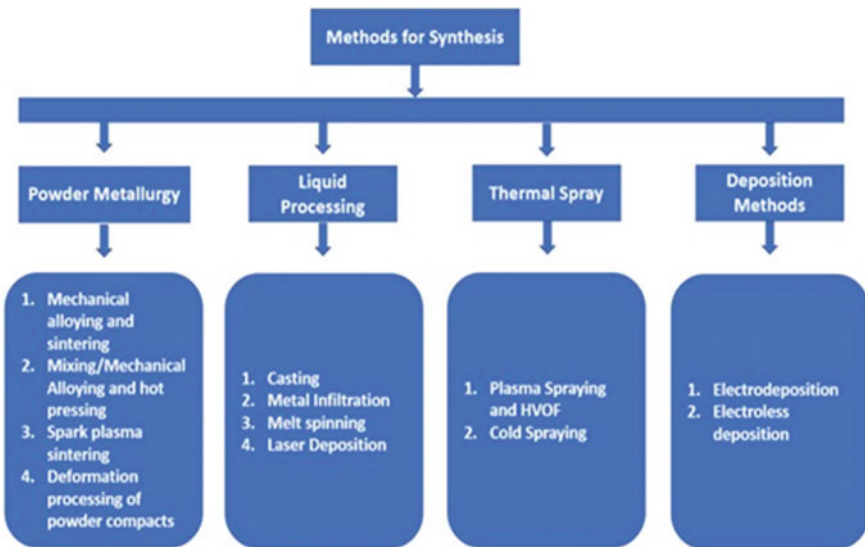


Fig. 2 Prominent methods for synthesis of CNT-reinforced MMCs

## 2.1 *P/M Method*

In P/M process, metal powders are created using ball milling or other similar techniques and are mixed with CNTs by grinding or mechanical alloying [19]. After proper mixing of metal powder and CNTs, compaction is done. This is done by hot or cold pressing and the consolidated mixture is heated in a sintering furnace. This sintering process may also be done through spark plasma sintering (SPS). SPS is a recently developed technique, in which pulsed direct current is passed which creates extraordinarily high temperature in a very short span of time. This process is better as compared to traditional sintering as it does not allow the MMC for grain growth. Hence, superior quality MMC is synthesized in less time. Generally, after sintering, the CNT-reinforced MMCs are subjected to some forming process such as rolling and extrusion. Hindrances in synthesizing the composites through P/M method are listed as under:

1. Even distribution of CNTs in the matrix.
2. Conservation if the aspect ratio of fibers in the composite.
3. Developmental reactions at the interface between CNT fibers and metal matrix.
4. Compound formation at the interface as a result of CNT-metal bonding [20].

## 2.2 *Liquid Processing*

This type of processing is also referred to as melting and solidification; it is one of the most primitive and traditional processing techniques for metals, and this method is simpler and cheaper as compared to the other methods but there are chances of generation of unwanted compounds at metal-CNT interface as a result of the chemical reaction. Hence, this method is primarily used for metals with low melting points such as Mg [21–24]. Another drawback of this method is formation of clusters of CNT which remains suspended in the matrix thereby resulting in non-homogenous distribution of reinforcement phase. This phenomenon is known as agglomeration [6]. Very few papers are present which indicate about the distribution of CNTs in the metal matrix. Also, this process involves porosity in the casted MMCs which may reduce the endurance limit of the MMCs [25, 26]. The addition of even a small amount of CNT may enhance the mechanical properties of the formed MMC [24, 27].

## 2.3 *Thermal Spray*

In thermal spray process, particles in molten or semi-molten form are sprayed on a substrate thereby forming a coating due to the impact of high velocity high temperature particle and its solidification [19]. This process has large cooling rates which help in the formation of nanocrystalline structures. Depending on the heating source

utilized for conducting this process, it can be classified into flame process and plasma process. In flame process, high temperature flame is used for melting the material to be sprayed on the substrate, which may be obtained by combustion of gases as in case of oxy-acetylene flame. In plasma spray, high temperature plasma is used for heating the particles, and this plasma is stream of ionized gases by means of a spark or radio waves. The properties of MMCs synthesized by means of high velocity oxy-fuel (HVOF) spraying were found to be better than the ones synthesized through plasma spray especially with reference to modulus of elasticity and hardness. This could be attributed to the low porosity of the MMCs synthesized through HVOF [28].

## ***2.4 Deposition Methods***

Electro-deposition is a technique which involves breaking of material into ions by means of passage of electric current in the presence of electrolyte. These ions are deposited on the other material. Electro-deposition is mainly used for Ni-CNT [29–33] and Cu-CNT [34–37] MMCs as indicated in past literature.

## ***2.5 High Energy Ball Milling (HEBM)***

High energy ball milling is the process of converting bulk metal, alloys and other high-strength materials in the powder form. The metals and alloys generally possess coarse-grained structure which is broken down in the form of powder for use in various applications. The breaking of bulk material occurs because of the cyclic loading induced by the action of hardened steel balls in high energy ball mill. The minimum particle size produced through HEBM is of the order of 1–30 nm [38].

## **3 Characterization**

Ngo et al. compared the microstructure and mechanical behavior of pure Al- and CNT-reinforced composites [39]. It was found that strength of the composites was more than pure Al both in static and dynamic loading. Orowan strengthening mechanism was the closest to the phenomenon noted in the study. The increase in strength was higher in case of dynamic loading than in static loading. The agglomeration of CNTs was given due consideration in the study as clusters of CNTs were seen in the microstructure. The general model which considers uniform distribution of reinforcement phase was not considered for strength prediction rather a new prediction model which considers the effect of agglomeration was considered for the prediction of strength [39]. Wang et al. prepared a model representing multiphase interfacial

structures of SiC/CNT/Al composites. The study revealed that there was significant increase in ductility, toughness and uniaxial tensile strength [40]. Qiu et al. prepared ex situ and in situ CNT-reinforced Al matrix composites through spark plasma sintering. It was found that in situ processed composites showed better strain hardening behavior than ex situ processed composites [41]. Usef et al. prepared Al alloy-CNT MMCs through gravity die casting. It was observed from the study that interfacial heat transfer coefficient increased around 4% of the existing value [42]. It resulted in reduction in grain size at the interface. The strength and hardness was also found to improve due to grain refinement and strengthening mechanism [42]. Kim et al. fabricated Ag-CNT/Cu composites through friction stir welding [43]. The comparison between CNT/Cu composites and Ag-CNT/Cu composites revealed that thermal diffusivity was enhanced when Ag-CNT was used as reinforcement in the Cu matrix. The number of passes was also found to increase in case of the latter one. It was observed that beyond two passes, the thermal properties were found to diminish, which means that at there was a certain combination of parameters which yielded best thermal properties [43]. Zhang et al. prepared the Mg matrix composites using cold gas dynamic spray with Al coating with and without CNTs. The modulus of elasticity and hardness of the composites with coating of Al with CNT was found to be higher than the ones containing pure Al coating. The corrosion and wear resistance of the Al-CNT coating composites were found to be lower than the pure Al coating composites. The enhancement in corrosion resistance was found to be seen due to filling of pores and inhibition to crack propagation by the CNTs [44]. Graphene nanosheets coated with Ni nanoparticles were used as reinforcements in the Mg matrix by Ye et al. [45]. Interfacial bonding was found to improve between graphene nanosheets and Mg due to reaction between Mg and Ni particles. The compressive strength was found to improve significantly due to grain refinement and improved interfacial bonding [45]. In a study conducted by Luo et al., CNT-reinforced Al alloy matrix composites were prepared using selective laser melting. The Al alloy powder was created using ball milling process. The hardness and tensile strength of the composites were found to increase significantly as compared to the original matrix [46]. Abbas et al. fabricated CNT-reinforced Mg alloy matrix composites through stir casting. The wear rates were found to reduce significantly and the hardness was found to increase due to homogeneous distribution of reinforcement phase in the metal matrix [47]. Figure 3 indicates the worn-out surfaces of CNT-reinforced Mg alloy. Hu et al. fabricated the graphene nanosheets-reinforced Al matrix composite through P/M route, and the tensile strength of the formed composite was found to be 249 MPa which was 62% more than the pure Al matrix [48]. Hu et al. also prepared graphene-iron composites through laser sintering technique and the hardness was found to be 600 HV which was 93.5% more than the original matrix material [48]. Chen et al. observed that during effective load transfer in the Al matrix composites reinforced with CNTs, the outer walls of CNTs were damaged, while the inner walls remained intact and stable which lead to the conclusion that CNT-reinforced MMCs possess extraordinary properties for structural applications [49]. Azarnia et al. observed the CNT phase at high temperatures and it was found that CNTs do not lose their original properties up to 2000 °C [50]. Up to this temperature, CNTs do not attain any allotropic form



**Fig. 3** Worn out surfaces of CNT-reinforced Mg alloy composite [47]

and preserve their original properties. Merino et al. produced the polyvinyl alcohol composites reinforced with CNTs through magnetic stirring and sonification. The composites were found to possess enhanced mechanical properties as compared to the base material [51]. Naseer et al. reviewed the works done on CNT MMCs and focused not only on the popular sintering technique but also on the less popular but important techniques such as shot peening, annealing, hot extrusion and hot rolling [52].

## 4 Challenges

Although addition of CNTs in the metal matrix as reinforcement enhances the properties of the composite to great extent, it has some challenges associated with it. These challenges have been enumerated below as reported by Azarmia et al. [53]:

1. Non-uniform dispersion of the CNTs in the metal matrix [54].
2. Poor interfacial adhesion.
3. Thermal decomposition of CNTs and reaction with the metals.

## 5 Conclusions

The development of CNT-reinforced composites has shown remarkable progress in the recent past, wherein CNT-reinforced MMCs have been used in thermal management, hydrogen storage, wear resistant coatings, structural members and micro-electromechanical systems (MEMS). The use of CNTs in metal-based composites has been marked with increase in strength and stiffness. The use of CNTs as reinforcement in Ni- and Cu matrix-based composites has shown lower friction coefficient and improved wear rates. It has been observed that the CNT-metal interface has been one

of the deciding factors for determining the strength of the composite. If the bonding is not proper than load sharing by CNTs will be non-homogeneous and there will be weak sections in the composite material [11].

After reviewing the quoted articles, following conclusions can be drawn:

1. Homogeneous distribution of CNTs in the matrix is essential for enhancement hardness and strength.
2. Compound formation with some secondary agent like Ni acts as a catalyst in interfacial bonding of CNTs with the metal matrix.
3. Length of the CNT and its alignment in the matrix is one of the factors, on which mechanical properties of the composite depend.
4. Wear rates, tensile strength and compressive strength are found to be improved due to the presence of CNT in the reinforcement phase. This may be attributed to the fact that CNTs prevent crack propagation and fill the pores.
5. Thermal properties are found to enhance due to the presence of CNTs in the matrix up to certain reinforcement concentration beyond which they are found to decrease.

## References

1. Kumar A, Arafath MY, Gupta P, Kumar D, Hussain CM, Jamwal A (2020) Microstructural and mechano-tribological behavior of Al reinforced SiC-TiC hybrid metal matrix composite. *Mater Today Proc* 21:1417–1420
2. Hossain S, Rahman MM, Jamwal A, Gupta P, Thakur S, Gupta S (2019) Processing and characterization of pine epoxy based composites. In: AIP conference proceedings, vol 2148, no 1. AIP PublishingLLC, p 030017
3. Sohag MAZ, Gupta P, Kondal N, Kumar D, Singh N, Jamwal A (2020) Effect of ceramic reinforcement on the microstructural, mechanical and tribological behavior of Al-Cu alloy metal matrix composite. *Mater Today Proc* 21:1407–1411
4. Nayim STI, Hasan MZ, Seth PP, Gupta P, Thakur S, Kumar D, Jamwal A (2020) Effect of CNT and TiC hybrid reinforcement on the micro-mechano-tribo behaviour of aluminium matrix composites. *Mater Today Proc* 21:1421–1424
5. Jamwal A, Vates UK, Gupta P, Aggarwal A, Sharma BP (2019) Fabrication and characterization of Al<sub>2</sub>O<sub>3</sub>-TiC-reinforced aluminum matrix composites. In: *Advances in industrial and production engineering*. Springer, Singapore, pp 349–356
6. Mittal P, Paswan MK, Sadasivuni KK, Gupta P (2020) Structural, wear and thermal behaviour of Cu-Al<sub>2</sub>O<sub>3</sub>-graphite hybrid metal matrix composites. *Proc Inst Mech Eng Part L J Mater Des Appl* 234(8):1154–1164
7. Jamwal A, Mittal P, Agrawal R, Gupta S, Kumar D, Sadasivuni KK, Gupta P (2020) Towards sustainable copper matrix composites: manufacturing routes with structural, mechanical, electrical and corrosion behaviour. *J Compos Mater* 54(19):2635–2649
8. Mittal P, Raghav V, Chawla D, Mehta J, Paswan MK, Gupta P (2021) Structural, wear and thermal behavior of copper metal matrix composites: a review. *Adv Eng Mater* 319–327
9. Tsai PC, Jeng YR, Lee JT, Stachiv I, Sittner P (2017) Effects of carbon nanotube reinforcement and grain size refinement mechanical properties and wear behaviors of carbon nanotube/copper composites. *Diam Relat Mater* 74:197–204



10. Radhamani AV, Lau HC, Ramakrishna S (2018) CNT-reinforced metal and steel nanocomposites: a comprehensive assessment of progress and future directions. *Compos A Appl Sci Manuf* 114:170–187
11. Bakshi SR, Lahiri D, Agarwal A (2010) Carbon nanotube reinforced metal matrix composites—a review. *Int Mater Rev* 55(1):4
12. Mittal P, Sengar SS, Paswan MK, Mehta J, Chawla D, Gupta P (2021) Challenges and opportunities in synthesis of hybrid Cu-Al<sub>2</sub>O<sub>3</sub>-C and Cu-ZrO<sub>2</sub>-C composites through stir casting route. In: *Adv Eng Mater*. Springer, Singapore, pp 1–9
13. Zhu J, Qi J, Guan D, Ma L, Dwyer-Joyce R (2020) Tribological behaviour of self-lubricating Mg matrix composites reinforced with silicon carbide and tungsten disulfide. *Tribol Int* 146:106253
14. Gupta P, Kumar D, Quraishi MA, Parkash O (2016) Influence of processing parameters on corrosion behavior of metal matrix nanocomposites. *J Mater Env Sci* 7(7):2505–2512
15. Bakshi SR, Agarwal A (2011) An analysis of the factors affecting strengthening in carbon nanotube reinforced aluminum composites. *Carbon* 49(2):533–544
16. Güler Ö, Bağcı N (2020) A short review on mechanical properties of graphene reinforced metal matrix composites. *J Market Res* 9(3):6808–6833
17. Sundaram RM, Sekiguchi A, Sekiya M, Yamada T, Hata K (2018) Copper/carbon nanotube composites: research trends and outlook. *Royal Soc Open Sci* 5(11):180814
18. Thirumaran B, Babu SK (2020) Corrosion behaviour of Stir-Squeeze cast optimised AA7075 CuCNT/CuGrP reinforced metal matrix composites. *Mater Today Proc* 27:2774–2781
19. Bakshi SR, Lahiri D, Agarwal A (2010) Carbon nanotube reinforced metal matrix composites—a review. *Int Mater Rev* 55(1):41–64
20. Shirvanimoghaddam K, Hamim SU, Akbari MK, Fakhrhoseini SM, Khayyam H, Pakseresht AH, ... Naebe M (2017) Carbon fiber reinforced metal matrix composites: fabrication processes and properties. *Compos Part A Appl Sci Manuf* 92:70–96
21. Li S, Song S, Yu T, Zhang YS, Chen H (2005) Microstructure and fracture surfaces of carbon nanotubes/magnesium matrix composite. In: *Materials science forum*, vol 488. Trans Tech PublicationsLtd, pp 893–896
22. Goh CS, Wei J, Lee LC, Gupta M (2005) Development of novel carbon nanotube reinforced magnesium nanocomposites using the powder metallurgy technique. *Nanotechnology* 17(1):7
23. Goh CS, Wei J, Lee LC, Gupta M (2008) Ductility improvement and fatigue studies in Mg-CNT nanocomposites. *Compos Sci Technol* 68(6):1432–1439
24. Goh CS, Wei J, Lee LC, Gupta M (2006) Simultaneous enhancement in strength and ductility by reinforcing magnesium with carbon nanotubes. *Mater Sci Eng A* 423(1–2):153–156
25. Uozumi H, Kobayashi K, Nakanishi K, Matsunaga T, Shinozaki K, Sakamoto H, Yoshida M (2008) Fabrication process of carbon nanotube/light metal matrix composites by squeeze casting. *Mater Sci Eng A* 495(1–2):282–287
26. Munir KS, Kingshott P, Wen C (2015) Carbon nanotube reinforced titanium metal matrix composites prepared by powder metallurgy—a review. *Crit Rev Solid State Mater Sci* 40(1):38–55
27. Zhou SM, Zhang XB, Ding ZP, Min CY, Xu GL, Zhu WM (2007) Composites part A. *Appl Sci* 38:301–306
28. Balani K, Bakshi SR, Chen Y, Laha T, Agarwal A (2007) Role of powder treatment and carbon nanotube dispersion in the fracture toughening of plasma-sprayed aluminum oxide—carbon nanotube nanocomposite. *J Nanosci Nanotechnol* 7(10):3553–3562
29. Arai S, Fujimori A, Murai M, Endo M (2008) Excellent solid lubrication of electrodeposited nickel-multiwalled carbon nanotube composite films. *Mater Lett* 62(20):3545–3548
30. Chen B, Zhou XY, Zhang B, Kondoh K, Li JS, Qian M (2020) Microstructure, tensile properties and deformation behaviors of aluminium metal matrix composites co-reinforced by ex-situ carbon nanotubes and in-situ alumina nanoparticles. *Mater Sci Eng A* 795:139930
31. Tan J, Yu T, Xu B, Yao Q (2006) Microstructure and wear resistance of nickel—carbon nanotube composite coating from brush plating technique. *Tribol Lett* 21(2):107–111
32. Xu Q, Zhang L, Zhu J (2003) Controlled growth of composite nanowires based on coating Ni on carbon nanotubes by electrochemical deposition method. *J Phys Chem B* 107(33):8294–8296



33. Chen XH, Peng JC, Li XQ, Deng FM, Wang JX, Li WZ (2001) Tribological behavior of carbon nanotubes—reinforced nickel matrix composite coatings. *J Mater Sci Lett* 20(22):2057–2060
34. Chen XH, Cheng FQ, Li SL, Zhou LP, Li DY (2002) Electrodeposited nickel composites containing carbon nanotubes. *Surf Coat Technol* 155(2–3):274–278
35. Kang X, Mai Z, Zou X, Cai P, Mo J (2007) A sensitive nonenzymatic glucose sensor in alkaline media with a copper nanocluster/multiwall carbon nanotube-modified glassy carbon electrode. *Anal Biochem* 363(1):143–150
36. Zhang K, Chai Y, Yuen MMF, Xiao DGW, Chan PCH (2008) Carbon nanotube thermal interface material for high-brightness light-emitting-diode cooling. *Nanotechnology* 19(21):215706
37. Ferrer-Anglada N, Gomis V, El-Hachemi Z, Weglikovska UD, Kaempgen M, Roth SJPS (2006) Carbon nanotube based composites forelectronic applications: CNT–conducting polymers. *CNT–Cu. physica status solidi (a)* 203(6):1082–1087
38. Munir KS, Li Y, Qian M, Wen C (2016) Identifying and understanding the effect of milling energy on the synthesis of carbon nanotubes reinforced titanium metal matrix composites. *Carbon* 99:384–397
39. Ngo Q, Cruden BA, Cassell AM, Walker MD, Ye Q, Koehne JE, ... Yang CY (2004) Thermal conductivity of carbon nanotube composite films. In: *MRS Online Proceedings Library (OPL)*, p 812
40. Wang M, Li Y, Chen B, Shi D, Umeda J, Kondoh K, Shen J (2021) The rate-dependent mechanical behavior of CNT-reinforced aluminum matrix composites under tensile loading. *Mater Sci Eng A* 808:140893
41. Qiu C, Su Y, Yang J, Wang X, Chen B, Ouyang Q, Zhang D (2021) Microstructural characteristics and mechanical behavior of SiC (CNT)/Al multiphase interfacial micro-zones via molecular dynamics simulations. *Compos Part B Eng* 220:108996
42. Usef AP, Bhajantri V, Kannoth V, Jambagi SC (2021) Influence of carbon nanotube reinforcement on the heat transfer coefficient, microstructure, and mechanical properties of a die cast Al-7Si-0.35 Mg alloy. *J Alloys Compounds* 160844
43. Kim JH, Lee YR, Park HJ, Kim S, Jung SB (2020) Microstructures and thermal properties of Ag-CNT/Cu composites fabricated by friction stir welding. *J Mater Sci Mater Electron* 31(3):2280–2287
44. Zhang Y, Wang Q, Chen G, Ramachandran CS (2020) Mechanical, tribological and corrosion physiognomies of CNT-Al metal matrix composite (MMC) coatings deposited by cold gas dynamic spray (CGDS) process. *Surf Coat Technol* 403:126380
45. Ye J, Chen X, Li J, Liu C, Wu B, Pan F (2020) Microstructure and compressive properties of Mg–9Al composite reinforced with Ni-coated graphene nanosheets. *Vacuum* 181:109629
46. Luo S, Li R, He P, Yue H, Gu J (2021) Investigation on the microstructure and mechanical properties of CNTs-AlSi10Mg composites fabricated by selective laser melting. *Materials* 14(4):838
47. Abbas A, Huang SJ, Balloková B, Sülleiová K (2020) Tribological effects of carbon nanotubes on magnesium alloy AZ31 and analyzing aging effects on CNTs/AZ31 composites fabricated by stir casting process. *Tribol Int* 142:105982
48. Hu Z, Tong G, Lin D, Chen C, Guo H, Xu J, Zhou L (2016) Graphene-reinforced metal matrix nanocomposites—a review. *Mater Sci Technol* 32(9):930–953
49. Chen B, Kondoh K, Umeda J, Li S, Jia L, Li J (2019) Interfacial in-situ Al<sub>2</sub>O<sub>3</sub> nanoparticles enhance load transfer in carbon nanotube (CNT)-reinforced aluminum matrix composites. *J Alloy Compd* 789:25–29
50. Azarniya A, Azarniya A, Sovizi S, Hosseini HRM, Varol T, Kawasaki A, Ramakrishna S (2017) Physicomechanical properties of spark plasma sintered carbon nanotube-reinforced metal matrix nanocomposites. *Prog Mater Sci* 90:276–324
51. Merino CAI, Sillas JL, Meza JM, Ramirez JH (2017) Metal matrix composites reinforced with carbon nanotubes by an alternative technique. *J Alloy Compd* 707:257–263
52. Naseer A, Ahmad F, Aslam M, Guan BH, Harun WSW, Muhamad N, ... German RM (2019) A review of processing techniques for graphene-reinforced metal matrix composites. *Mater Manuf Process* 34(9):957–985

53. Azarniya A, Safavi MS, Sovizi S, Azarniya A, Chen B, Madaah Hosseini HR, Ramakrishna S (2017) Metallurgical challenges in carbon nanotube-reinforced metal matrix nanocomposites. *Metals* 7(10):384
54. Mittal P, Acharya V, Kumar S, Paswan M, Sadasivuni KK, Gupta P (2022) Synthesis and characterization of stir casted Cu-ZrO<sub>2</sub>-Graphite hybrid metal matrix composites for thermal management structures. *Proc Inst Mech Eng C J Mech Eng Sci.* <https://doi.org/10.1177/09544062221078197>

# Nonlinear Static and Dynamic Analysis of Composite Riser



Manander Singh, Rajeev Kumar Singh, Sanatan Ratna, Shubham Sharma, and Priyank Srivastava

**Abstract** The dynamic response of composite production risers w.r.t periodic and erratic waves was derived in the time domain. The harmonic superposition method is used to model the time series of sea surface elevation, water particle kinematics, and vessel top motion in the context of random sea states. Instantaneous updates to the stiffness matrix account for the intrinsically unpredictable variations in axial tension. Time domain examination of the riser structure takes into account some significant nonlinearities. For a range of tides typical of the deep offshore fields in the Indian Ocean, the bending stresses in the presence of variable axial tension are calculated. Obtaining power spectral density functions helps researchers look for signs of resonance. As a result of their high strength-to-weight ratio, composite risers are highlighted in the research as a potential means of increasing safety margins. In order to provide input for the probabilistic evaluation of riser safety in a harsh ocean environment, we extract the statistical features of the reaction, which are of stochastic nature.

**Keywords** Nonlinear · Random sea · Composite riser · Dynamic analysis

## 1 Introduction

Risers are long slender pipes used to establish connection between the drilling facilities on an offshore platform and an oil well head at the seabed. Production riser systems are used to transport fluid and gas from an underwater oil field to an offshore platform. There is a special sort of pipeline called a riser that was designed for this purpose of vertical transfer. Existing risers are typically manufactured from steel. Many academics, however, have been looking at composite risers for some time now, and not only for shallow water applications. The advantages of composites are not limited to their lightweight construction; they also offer superior fatigue strength,

---

M. Singh (✉) · R. K. Singh · S. Ratna · S. Sharma · P. Srivastava  
Department of Mechanical Engineering, Amity University Uttar Pradesh, Noida, Uttar Pradesh, India  
e-mail: [msingh19@amity.edu](mailto:msingh19@amity.edu)

damping, thermal (insulation), and corrosion resistance. For a tension leg platform system, components are reduced by switching from traditional riser to composite risers, and the transition is unavoidable despite the high cost of riser fabrication.

Institute Francais du Petrole (IFP) and Aerospatiale of France [1, 2] began the first effort to construct and analyse a composite production riser back in the 1980s. The concrete TLP that the IFP/Aerospatiale riser was made for is between 500 and 1000 m deep in the sea. Midway through the 1990s, the industry came together for a project funded by the NIST Advanced Technology Programme (ATP) to create the first composite production riser [3, 4] and the first composite drilling riser [5–7]. Another industry-wide initiative, the Magnolia composite production riser [8], was only just launched. This project aims to prove that a composite production riser joint can be fabricated that meets all of the same specifications. A 3D nonlinear big deformation model for maritime risers was created by Bernitsas et al. [9]. Nonlinearities' stiffening effects and the loads' dependence on deformation are highlighted as crucial considerations for both two- and three-dimensional riser studies.

Multiple parametric investigations on the response of composite risers to dynamic excitations to the regular wave have been published using the aforementioned techniques. Even yet, a literature review reveals that further parametric research is required to fully comprehend the dynamics of composite risers subjected to random wave stress. This paper's goal is to examine how changing the following variables affects the reaction of composite risers:

- (i) Nonlinearity's produced by drag force and fluctuation in top tension.
- (ii) Long-term periodic platform motion
- (iii) Current in hydrodynamic loading.

## 2 Mathematical Model of Composite Riser

Including the riser joints, the composite riser system includes a wellhead, two stress joint, one tensioner joint, and one surface tree (Fig. 1). The present study includes some number of steel riser joints and will be used near to the stress joint and mean water level, where significant local loads are anticipated.

Principal modelling assumptions for composite risers are as expounded by Singh and Ahmed [10].

### 2.1 Motion Equations

To demonstrate the evolution of the dynamic equation regulating the motion of the riser under the anticipated horizontal action of hydrodynamic loading, the riser is considered to undergo mostly horizontal movements. Singh and Ahmed [4] have formulated the equation for it. To compute this force, we assume the mass of the

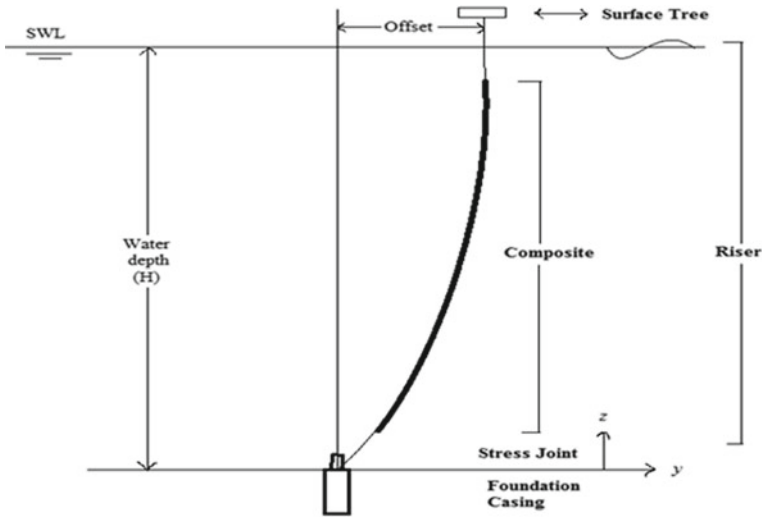


Fig. 1 Mathematical model of composite riser system

riser’s separate components is consolidated into a single mass. From [10, 11], the equation follows:

$$[M]\{\ddot{x}\} + [C]\{\dot{x}\} + [K]\{x\} = \{F(t)\} \tag{1}$$

where the terms are expounded in [10].

The riser system’s total mass matrix comprises of structural mass and additional mass component. The riser system’s overall mass matrix is composed of elemental consistent mass matrices.

$$[M_e] = [M_{em}] + [M_{ea}] \tag{2}$$

where  $[M_{em}]$  represents the element’s mass and  $[M_{ea}]$  represents the increased mass effect. Up to the level of still water, the submerged part of the riser is evaluated for an increased mass impact.

Due to the water surrounding the whole structure, the  $[M_{em}]$  structural mass of the element is determined by the extra mass of the structure  $M_{ea}$ . Considering the oscillation of the free surface, Wheeler’s method simulates this changeable submergence effect. The structure’s extra mass per unit length is provided by

$$M_{ea} = \rho_w(C_m - 1) \frac{\pi D^2}{4} \ddot{X} \tag{3}$$

where  $\rho_w$ ,  $C_m$ ,  $D$ , and  $\ddot{X}$  are the density of water, the moment of inertia, the diameter of the member, and the acceleration of the structure, respectively.

The stiffness matrix includes both elastic and geometric stiffness. Due to the mechanical qualities of the riser, such as Young's modulus and Poisson's ratio, the riser has elasticity. The geometric stiffness matrix is not a function of mechanical qualities, but rather the geometry of the riser and the force exerted against it. Geometric stiffness occurs in all structures; however, it is only significant if it is greater than the structural system's mechanical stiffness. The exhaustive stiffness matrix  $[K]$  may be expressed as

$$[K] = [K_E] + [K_G] \quad (4)$$

where  $[K]$  = Total stiffness matrix,  $[K_E]$  = Elastic stiffness matrix,  $[K_G]$  = Geometric stiffness matrix.

The damping matrix  $[C]$  is not explicitly specified, but it is assumed to be a linear combination of  $[M]$  and  $[K]$ . Therefore, it is necessary to know the modal damping ratio to calculate the dynamic response of the riser.

Structural and hydrodynamic damping provide the overall damping for the full riser system. Significant damping is caused by the hydrodynamic effect. Rayleigh damping calculates the structural damping as follows.

$$[C] = \alpha[M] + \beta[K] \quad (5)$$

where ' $\alpha$ ' and ' $\beta$ ' are the constants.

## 2.2 Loading Equation

Hydrodynamic loading owing to random wave and current is regarded as a source of dynamic loading in this research [10]. Using Morison's equation for hydrodynamic loading under some assumption, the equation  $\{F(t)\}$  is (Fig. 2) [11]

$$\{F(t)\} = \frac{1}{2}\rho_w C_D D (\dot{U}_i - \dot{x}_i + \dot{V}_{ci}) |\dot{U}_i - \dot{x}_i + \dot{V}_{ci}| + \rho_w \frac{\pi}{4} D^2 C_M \ddot{U}_i - m \ddot{x}_v \quad (6)$$

where  $m$  is the mass of the riser per unit length and is given by [4].

## 2.3 Finite Element Model

Using the finite element approach, it is feasible to do a study of a composite deep water riser subjected to time-varying hydrodynamic stress and real-world physical circumstances. In genuine field issues, both wave and current hydrodynamic stresses operate concurrently on composite risers. In the FEM, the riser's structure as a whole behaves as a continuum. This model is capable of including all nonlinearities, loads,

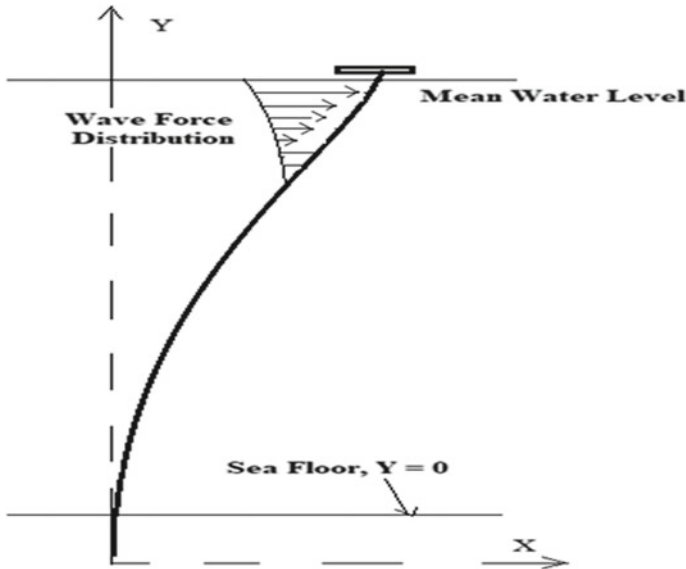


Fig. 2 Wave forces on composite riser

and boundary conditions. The ABAQUS/AQUA module of the commercial finite element package ABAQUS is deemed acceptable for this project. A second argument for using ABAQUS is because its module AQUA represents an offshore environment accurately.

Using the aforementioned finite element algorithm, the motion equation has been resolved. It can describe thin and stiff bodies with realistic boundary conditions, such as fluid inertia and viscous drag. All forms of important nonlinearities are integrated into the model of the composite riser. In the study, the B21H element is used. It is a Timoshenko beam element, which is used because it is suited for long buildings with huge cross sections. In addition to displacements and rotation, axial and shear forces are major variables for hybrid elements.

The bottom end of the riser is hinged, while the top end is horizontally constrained. The approach incorporates nonlinearities caused by substantial deformations, variable in time, submergence, buoyancy, and power of resistance.

### 2.4 Composite Riser Specification

The study includes the composite risers in deep water (approximately 2000 m). Consideration is given to a general composite riser design (Fig. 1) that is indicative of current technology in the Krishna Godavari basin in the Indian Ocean. The

composite riser assists to establish probability approach and comprehend the sensitivity of numerous components leading to composite riser failure scenarios. The riser system includes the well head, the stress joint, the steel riser joint, the composite joint, the tensioner, and the surface tree. For this research, an 1860-m long single-string composite riser system is explored. The length of each composite riser joint is 18.9 m. The composite riser joints stretch from 31.1 m to 1906.25 m in height. Above 1220.42 m, fairings will be fitted to minimise vortex-induced vibration (VIV). There is a standard steel riser junction between the top of the stress joint and the bottom of the composite riser, and there are two steel joints between the top of the composite riser and the bottom of the tensioner joint. Singh and Ahmed [10] have shown the specifications of the composite riser.

### **3 Results and Discussion**

This section contains validation study, static, and dynamic analysis carried out for the composite riser mentioned in the above section.

#### ***3.1 Validation Study***

It is essential to conduct the validation research, in which the acquired findings are compared to previously published data. A 639-element beam model is subjected to the stresses and the axial tension, bending moment profiles, and natural frequencies are derived. Stress Engineering Services, Inc. matched the study's findings to previously published results and existing finite element analysis data. The magnitudes of the applied loads are as described in the preceding section. The charts for axial tension and bending moment along the elevation from the sea bottom in Fig. 3 of the validation study are in excellent agreement with existing data.

#### ***3.2 Static Loads of Composite Riser***

For static loading, just component weights and top tension are applied to the model. Depending on the service situation, the top tension is typically 1.5 times more than the total of the riser weight and the effective weights of all the joints. Keeping the whole composite riser under tension serves primarily to regulate its deflection and avoid buckles caused by axial compression. In this investigation, a tension factor of 1.3 is used, resulting in a notional peak tension of 141.8308 kN.

The tensioner's stiffness is set at 596.94 kN/m. Due to the fact that the top tension exceeds the entire effective weight, the riser system is stretched when the weight and top tension are applied. When the basic setup and tensioner are complete, the



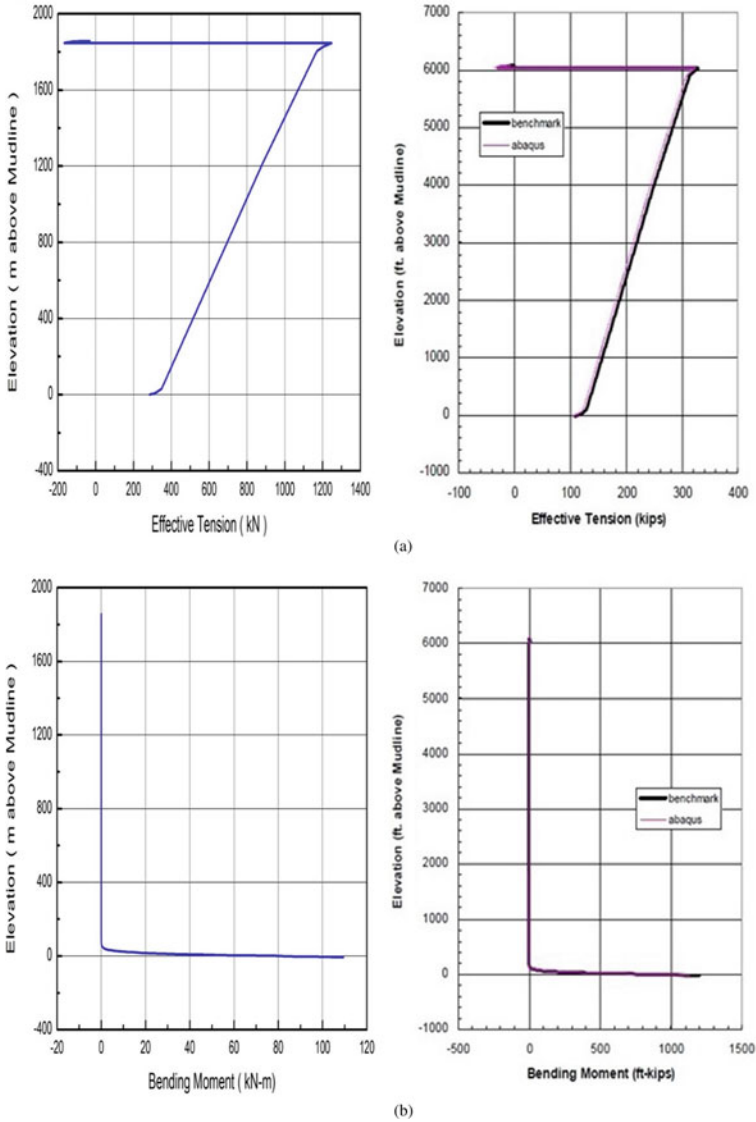


**Fig. 3** Validation study: **a** Axial tension **b** Bending moment

platform’s mean offset is implemented. The highest offset is 109 m. The lateral displacement of the composite riser is seen in Fig. 4.

On the same, deep water composite riser stated in this section. For the following load situations, dynamic responses have been obtained: I regular waves (ii) random waves. The period ( $H_s$ ,  $T_z$ ) of 15 m–15 s and 15 m–10 s was selected for the current research in order to investigate the behaviour of the composite riser under severe,

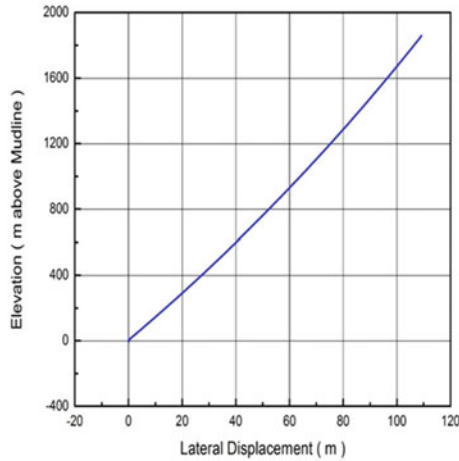


**Fig. 4** Lateral displacement of the composite riser

near-resonant, and non-resonant dynamic excitations. The offset for the composite riser is determined to be 109 m.

Effect of Normal Wave on Composite Riser.

Figure 5 depicts simply the plot for the 15 m/15 s (Case I) regular wave. It was observed, that the regular wave time domain analysis underestimates the riser system's bending stress because it does not accurately describe the actual wave state, in which many regular waves coexist.

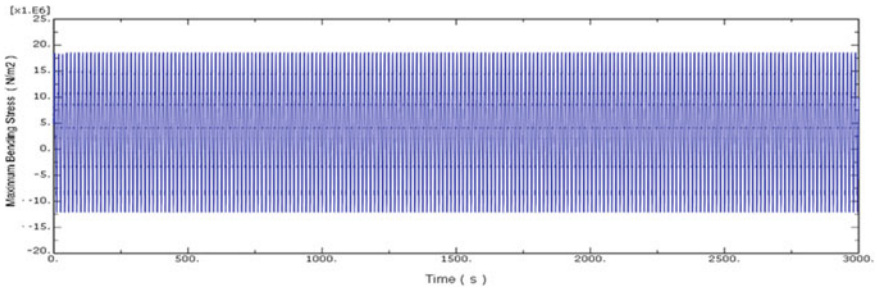


**Fig. 5** Regular wave time history

### 3.3 Effect of Random Waves Without Current on Composite Riser Response

To study the effect of long-crested random sea on composite riser, bending stress time histories are plotted. Figure 6 show the plots under 15 m/15 s (Case II) random sea states for bending stress time history. Maximum and minimum bending moments are taken at every node from its corresponding moment time histories. Bending stress history is plotted. Bending moment envelope is drawn and is shown in Fig. 7.

Maximum bending stress is calculated using flexural equation at point just below the sea surface, where maximum bending moments are observed.

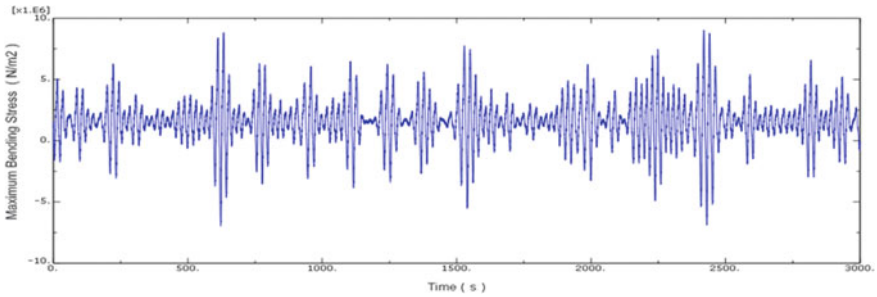


Fig. 6 Maximum bending stress

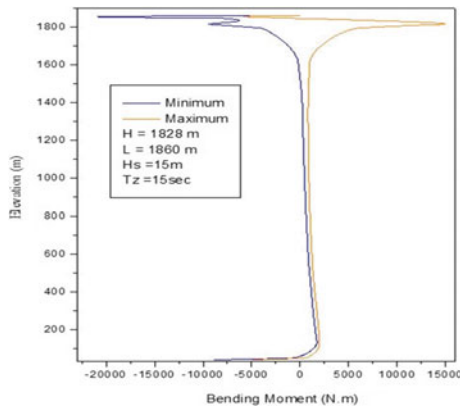


Fig. 7 Maximum bending stress time history

## 4 Conclusions

In time domain, a P-M spectrum simulation of the sea state is used to conduct a dynamic study of a composite riser for an irregular, long-crested, random sea. In the study of the dynamic response, the relative velocity squared drag term, the long-term drift oscillation, and the present velocity are taken into account. Until steady state is established, time records for different outcomes are created. For the random sea state alone, the reaction of the structure is dictated primarily by the excitation force resulting from the dominant sea state under consideration. Maximum bending strains are seen towards the riser's apex in the wave splash zone. In the given scenario, the frequency response at low frequencies predominates. When the current velocity is added to the water particle velocity in the calculation of the hydrodynamic loading, the composite riser's dynamic response may be significantly altered. The magnitude of change is determined by the ratio of wave period to structure period. For the resonance situation, the addition of a modest current may result in a significant shift in dynamic responsiveness. It has been discovered that the addition of no current velocity to a random sea with lengthy crests reduces the bending stress.

## References

1. Sparks CP, Odru P (1988) Mechanical testing of high-performance composite tubes for TLP production risers. In: Offshore technology conference proceedings, OTC-5797, Houston, Texas, May 2–5, 1988, pp 467–472
2. Sparks CP (1986) Lightweight composite production risers for a deep-water tension leg platform. In: 5th International conference on offshore mechanics and arctic engineering, Tokyo, Japan, pp 86–93
3. Baldwin DD, Newhouse NL (1997) Composite production riser design. In: Offshore technology conference proceedings, OTC 8431, Houston, Texas, May 5–8, 1997, pp 11–18
4. Johnson DB, Baldwin DD, Long JR (1999) Mechanical performance of composite production risers. In: Offshore technology conference proceedings, OTC-11008, Houston, Texas, May 3–6, 1999, pp 1–11
5. Andersen WF, Anderson JJ, Mickelson CS, Sweeney TF (1997) The application of advanced composite technology to marine drilling riser systems: design, manufacturing and test. In: Offshore technology conference, OTC 8433, Houston, Texas, May 5–8, 1997
6. Andersen WF, Burgdorf O, Sweeney TF (1998) Comparative analysis of 12,500 Ft. water depth steel and advanced composite drilling risers. In: Offshore technology conference, OTC 8732, Houston, Texas, May 4–7, 1998
7. Andersen WF, Anderson JJ, Landriault LS (1998) Full-scale testing of prototype composite drilling riser joints—interim report. In: Offshore technology conference, OTC-8668, Houston, Texas, May 4–7, 1998
8. Lindsey CG, Masudi H (2002) Stress analysis of composite tubes under tensile fatigue loading in a simulated seawater environment. In: ASME engineering technology conference on energy, Houston, Texas
9. Bernitsas MM, Kokarakkis JE, Imron A (1985) Large deformation three-dimensional static analysis of deep-water marine riser. *Appl Ocean Res* 7(4)
10. Singh M, Ahmad S (2015) Fatigue life calculation of deep-water composite production risers by rain flow cycle counting method. In: International conference on offshore mechanics and arctic engineering, vol 56529. American Society of Mechanical Engineers, p V05BT04A010

11. Singh M, Ahmad S, Jain AK (2020) S-N curve model for assessing cumulative fatigue damage of deep-water composite riser. In: Proceedings of the international conference on offshore mechanics and arctic engineering—OMAE, 1, V001T01A024. <https://doi.org/10.1115/OMAE2020-18555>